



**Università
degli Studi
di Ferrara**

**DOCTORAL COURSE IN
CHEMISTRY**

CYCLE XXXV

DIRECTOR Prof. Alberto Cavazzini

*Design and synthesis of potential cardioprotective agents
targeting mitochondria.*

Scientific/Disciplinary Sector (SDS) CHIM/08

Candidate

Dott.ssa Martina Fabbri

Supervisor

Prof.ssa Delia Preti

Years 2019/2022

LIST OF CONTENTS.

1. INTRODUCTION.....	1
1.1 Ischemia-reperfusion injury (IRI).....	1
<i>1.1.1 Pathophysiology of IRI.....</i>	<i>3</i>
<i>1.1.2 Mitochondrial ischemia and reperfusion.....</i>	<i>6</i>
1.2 MPT and the mitochondrial permeability transition pore (mPTP).....	9
<i>1.2.1 The ATP-synthase.....</i>	<i>12</i>
<i>1.2.2 mPTP and cell death.....</i>	<i>17</i>
1.3 mPTP: a promising pharmacological target against IRI.....	20
<i>1.3.1 Known inhibitors of the mitochondrial permeability transition (MPT).....</i>	<i>20</i>
2. DESIGN, SYNTHESIS AND BIOLOGICAL EVALUATION OF CLINICALLY USEFUL SPIRO-DERIVATIVES AS mPTP INHIBITORS.	26
2.1 INTRODUCTION.....	26
2A. Project 1: NOVEL SPIRO-ISATIN DERIVATIVES.....	29
2a.1 AIM AND OBJECTIVES.....	29
2a.2 RESULTS AND DISCUSSION.....	30
<i>2a.2.1 Chemistry.....</i>	<i>30</i>
<i>2a.2.2 Biological evaluation.....</i>	<i>37</i>
2a.3 EXPERIMENTAL SECTION.....	41
<i>2a.3.1 Materials and Methods.....</i>	<i>41</i>
<i>2a.3.2 General synthetic procedures.....</i>	<i>42</i>
General procedure for the preparation of compounds 4-6.....	42
General procedure for the preparation of compounds 7-11.....	43
General procedure for the preparation of compounds 12a-n.....	43
General procedure for the preparation of compounds 12o-p.....	46
General procedure for the preparation of compounds 13a-p.....	47
General procedure for the preparation of compounds 14a-p.....	49
General procedure for the preparation of compounds 15a-p.....	52
2B. Project 2: DISPIRO-PIPERIDINE AND DISPIRO-ISATIN DERIVATIVES.....	57
2b.1 AIM AND OBJECTIVES.....	57
2b.2 RESULTS AND DISCUSSION.....	59
<i>2b.2.1 Chemistry.....</i>	<i>59</i>
<i>2b.2.2 Biological evaluation.....</i>	<i>63</i>
2b.3 EXPERIMENTAL SECTION.....	67

2b.3.1 <i>Materials and Methods</i>	67
2b.3.2 <i>General synthetic procedures</i>	68
Preparation of 2-diazo-5,5-dimethylcyclohexane-1,3-dione 17	68
General procedure for the preparation of compounds 23a-j and 24a-j	68
General procedure for the preparation of compounds 25a-h	74
General procedure for the preparation of compounds 26-27	76
Preparation of compound 30	77
General procedure for the preparation of compounds 33a-b	77
General procedure for the preparation of compound 34a-b	77
General procedure for the preparation of compounds 35-36	78
General procedure for the preparation of compounds 39-42	79
General procedure for the preparation of compounds 44a-e	79
2C. Project 3: SPIRO-PIPERIDINE DERIVATIVES	82
2c.1. AIM AND OBJECTIVES	82
2c.1.1 <i>Overview of solid phase peptide synthesis (SPPS)</i>	83
2c.2. RESULTS AND DISCUSSION	85
2c.2.1 <i>Chemistry</i>	85
2c.2.2 <i>Biological evaluation</i>	87
2c.3. EXPERIMENTAL SECTION	89
2c.3.1 <i>Materials and Methods</i>	89
2c.3.2 <i>General synthetic procedures</i>	90
General procedure for dipeptide synthesis on solid-phase	90
General procedure for condensation of N-benzyl-4-piperidone from AmphiSpheres resin (50a-f)	90
General procedure for condensation of N-benzyl-4-piperidone from Glycine preloaded-Wang resin (55a-f)	91
General procedure for the cleavage of synthesized final derivatives 51a-f and 56a-f	91
2.2 GENERAL CONCLUSIONS	95
3. DESIGN AND SYNTHESIS OF PHO AFFINITY PROBES (PAPs) FOR BINDING SITE DECONVOLUTION STUDIES AND DETECTION OF POSSIBLE OFF-TARGETS	97
3.1 INTRODUCTION	97
3.1.1 <i>Photo-affinity labeling (PAL) in chemical proteomics</i>	97
3.2 AIM AND OBJECTIVES	99
3.3 RESULTS AND DISCUSSION	100

3.3.1 Chemistry.....	100
3.3.2 Biological evaluation.....	102
3.4 CONCLUSION AND FUTURE PERSPECTIVES.....	103
3.5 EXPERIMENTAL SECTION.....	104
3.5.1 Materials and Methods.....	104
3.5.2 General synthetic procedures.....	105
Preparation of 1-benzyl-4-(phenylamino)piperidine-4-carbonitrile 58.....	105
Preparation of 1-benzyl-4-(phenylamino)piperidine-4-carboxamide 59.....	105
Preparation of 8-benzyl-1-phenyl-1,3,8-triazaspiro[4.5]dec-2-en-4-one 60.....	106
Preparation of 8-benzyl-1-phenyl-1,3,8-triazaspiro[4.5]decan-4-one 61.....	106
Preparation of 1-phenyl-1,3,8-triazaspiro[4.5]decan-4-one 62.....	107
Preparation of 1-phenyl-8-(4-(3-(trifluoromethyl)-3H-diazirin-3-yl)benzoyl)-1,3,8-triazaspiro[4.5]decan-4-one 65.....	107
Preparation of 1-phenyl-8-((4-(3-(trifluoromethyl)-3H-diazirin-3-yl)phenyl)sulfonyl)-1,3,8-triazaspiro[4.5]decan-4-one 66.....	107
General procedure for the preparation of compounds 67-68.....	108
4. DESIGN AND SYNTHESIS OF NOVEL MITOCHONDRIA-TARGETED CARDIOPROTECTIVE AGENTS POTENTIALLY ABLE TO SCAVENGE REDOX-ACTIVE TRANSITION METAL IONS.....	110
4.1 INTRODUCTION.....	110
4.2 AIM AND OBJECTIVES.....	114
4.3 RESULTS AND DISCUSSION.....	116
4.3.1 Chemistry.....	116
4.4 CONCLUSION AND FUTURE PERSPECTIVES.....	122
4.5 EXPERIMENTAL SECTION.....	122
4.5.1 Materials and Methods.....	122
4.5.2 General synthetic procedures.....	123
Preparation of 3,14,25-trihydroxy-2,10,13,21,24,32-hexaoxo-3,9,14,20,25,31-hexaazapentatriacontan-35-oic acid 70.....	123
General procedure for the synthesis realized on solid-phase support.....	124
4.5.3 Appendix: HPLC chromatograms and ESI mass spectra of the final derivative	125
5. REFERENCES.....	133
6. PUBLICATIONS.....	144
6.1 Structure-Activity Relationship Studies on Oxazolo[3,4-a]pyrazine Derivatives Leading to the Discovery of a Novel Neuropeptide S Receptor Antagonist with Potent In Vivo Activity.	

6.2 Novel Mixed NOP/Opioid Receptor Peptide Agonists.

6.3 Synthesis and NLRP3-Inflammasome Inhibitory Activity of the Naturally Occurring Velutone F and of Its Non-Natural Regioisomeric Chalconoids.

1. INTRODUCTION.

According to the Global Burden of Disease Study 2017, ischemic heart disease (IHD) is still the leading cause of death worldwide. Data show that the global number of IHD-related deaths is drastically increased by 52.3%, from 5.9 million in 1990 to 8.9 million in 2017. In this scenario, one of the most frequent forms of IHD is the acute myocardial infarction (MI) and, despite recent advances in interventional coronary reperfusion strategies by using either thrombolytic therapy or primary percutaneous coronary intervention (PPCI), it remains the main burden of death in Western countries. ^[1]

1.1 Ischemia-reperfusion injury (IRI).

In 2019 statistics by the World Health Organization have shown that cardiovascular (ischemic heart disease, stroke), respiratory (chronic obstructive pulmonary disease, lower respiratory infections) and neonatal conditions (birth asphyxia and birth trauma, neonatal sepsis and infections, and preterm birth complications) are recognized as the top global reasons of death. ^[2]

In particular, it is estimated that globally ischemic heart disease (IHD) affects around 126 million individuals, which is approximately 1.72% of the world's population, accounting for 9 million deaths each year. ^[3] Also referred to as coronary artery disease and atherosclerotic cardiovascular disease, IHD manifests clinically as myocardial infarction (MI), wherein a 40% of cases exhibit an ST segment elevation MI (STEMI).

Despite timely reperfusion strategies, STEMI is associated with 6-12% mortality and 14-36% prevalence of heart failure (HF) within 1 year. These data are usually due to the damaging effects of myocardial ischemia-reperfusion injury (IRI). ^[4] Indeed, it is estimated that IRI is responsible for up to the 50% of the final infarct size and left ventricular remodelling processes, which in clinical practice are known as strong and independent predictors of heart failure and mortality. ^[5]

Briefly, ischemia is associated to a partial or total occlusion of the coronary artery, a condition of reduced blood supply, hence oxygen and nutrients, to the various tissues or organs. Depending on its duration and extent, this pathological state might give rise to a series of changes that result in cell death. Paradoxically, during reperfusion the rapid restoration of blood flow triggers a series of events that cause a profound inflammatory response and oxidative stress rather than a return to normal tissue function, with serious and

irreversible consequences. This phenomenon is the so-called "reperfusion injury" (RI), an irreversible cellular damage that overlaps with the original ischemic insult. [4] [6] (Fig. 1a)

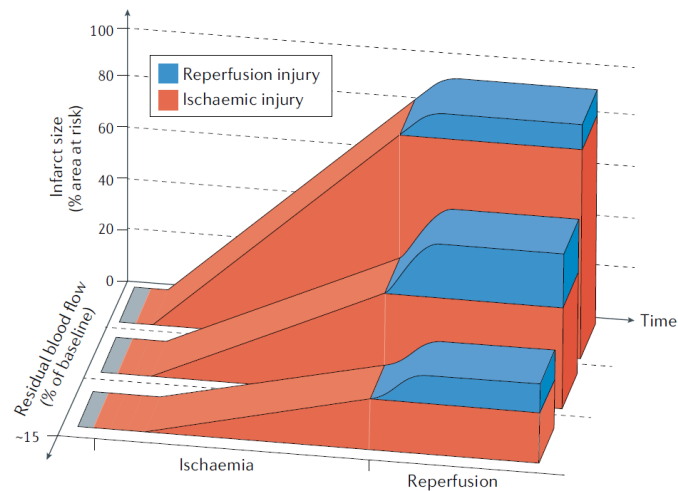


Figure 1a: Reperfusion consequences overlap to the ischemic insult. [7]

Four forms of cardiac dysfunction are recognized [6], which occur as a result of the myocardium injury during reperfusion: the “*myocardial stunning*” [8] is the long-lasting mechanical dysfunction after reperfusion, a consequence of the oxidative stress and intracellular calcium overload on the myocardial contractile apparatus; the “*reperfusion-induced arrhythmias*” may occur after the sudden reperfusion and, although the available treatment, it might be destructive [9]; the “*no-reflow phenomenon*”, the inability to reperfuse a previously ischemic region due to microvascular obstruction [10], might be an independent causal factor of reperfusion-induced cardiomyocyte death or merely a biomarker of severe myocardial IRI; eventually, the “*lethal myocardial reperfusion injury*”, a dysfunction responsible for a remarkable fraction of the final MI size, may represent an important target for cardioprotection in PPCI patients. [5] Whereas the first two forms of cardiac dysfunction are reversible, the second two are irreversible.

In order to reduce the lethal effects of myocardial reperfusion injury, a number of emerging therapeutic strategies have shown promise in small proof-of-concept clinical studies [4]. One of these is the so-called “*ischemic postconditioning (IPost)*”, an intermittent reperfusion of the acute ischemic myocardium that was demonstrated to be beneficial in the form of gradual reperfusion. [11] Although IPost has various clinical applications, most investigations currently conducted on IPost involve healthy myocardium.

Unlike IPost, which requires an invasive therapeutic intervention directly applied to the heart, the “*remote ischemic conditioning (RIC)*” is regarded as an innovative approach that

can be realized noninvasively. RIC describes the intriguing phenomenon in which one or more cycles of brief, reversible ischemia and reperfusion of one organ or tissue, confers global protection, rendering remote tissues and organs resistant to a subsequent episode of lethal IRI. ^[12] ^[13] Although RIC has been reported to be beneficial in patients undergoing cardiac surgery and in patients undergoing elective PCI, it is unknown whether RIC can actually improve clinical outcomes following PPCI. Therapeutic hyperoxemia ^[14] ^[15] and hypothermia are two other mechanical interventions ^[16], both potentially promising in PPCI patients ^[4]. In particular, hyperbaric oxygen therapy (HBO) can reduce myocardial injury by decreasing tissue edema, dropping formation of lipid peroxide radicals, altering nitric oxide synthase expression, and inhibiting leukocyte adherence and plugging in the microcirculation. However, treating patients in an HBO chamber or with a conventional oxygenator is impractical and difficult. A safe and well tolerated strategy after PCI is the intracoronary hyperoxemic reperfusion strategy applied by using a newly developed solution containing extremely high oxygen concentrations (1-3ml O₂/mL saline) namely aqueous oxygen. It is still hard to determine whether it will actually improve ventricular function or clinical outcome in anterior infarction.

The effects of these strategies on clinical outcomes in PPCI patients are currently under investigation, and there is a constant unmet need with respect to specific treatments to protect the myocardium against the damaging effects that occurs in MI.

In this regard, recent advances in understanding the complex and undoubtedly multifactorial pathophysiology of IRI may lead to the discovery of innovative therapeutic strategies/targets to prevent myocardial reperfusion injury.

1.1.1 Pathophysiology of IRI.

As anticipated, IRI is a condition that affects tissues in which blood flow is restored after a previous period of ischemia. Specifically, the ischemic event promotes a state in which the rapid reactivation of blood flow exacerbates the intracellular alterations, instead of allowing the return to the normal function. For this reason, IRI is linked to a wide range of diseases, such as myocardial infarction, ischemic stroke and acute kidney injury, besides being a major complication in organ transplantation and cardiothoracic, vascular and general surgery. ^[17]

IRI is described as a complex process wherein a wide range of critical mediators are involved, contributing to the injury as well as myocardial cells death. ^[18]

During ischemia the inadequate blood flow causes an imbalance between inputs and needs of oxygen and nutrient of the myocardium, which leads to important consequences. In particular, the hypoxic condition promotes a switch from aerobic to anaerobic glycolysis: pyruvate is reduced to lactate, and only 2 ATP molecules per molecule of glucose are produced. A drastic reduction, from 30 to 2, in ATP production and a gradual consumption of residual ATP, besides an intracellular load of lactate and protons, are noticed, resulting in inhibition of myocardial contractility. The ATP reduction occurs in the first minutes of the ischemic event and becomes almost complete (approximately 90-95%) after 40 to 60 minutes. [19]

Opie et al. suggest that the accumulation of lactate and the production of CO₂ from the Krebs cycle, might be responsible for the decrease of the intracellular pH. [20] Indeed, Garlick et al. report that in rat model, after global ischemia, the intracellular pH decreases to 6.2 after 10 min. [21] [22] This rapid drop and the increase in cofactors such as NADH and FADH₂ cause a slowdown in the activation of myocardium glycogenolysis.

Furthermore, the perturbation in intracellular ions is closely related to the pH drop and the blockage of the ATP synthase activity. (Fig. 1b) In fact, intracellular pH plays a critical role in the regulation of cardiac excitability and contractility, since affecting the function of ion channels and transport/contractile proteins. Moreover, the blockage of the ATP synthase activity causes consequences on ATP-dependent enzyme complexes such as the Na⁺/K⁺ ATPase pump engaged in maintaining membrane potential under homeostatic conditions. Therefore, Na⁺/H⁺ exchanger, in order to restore intracellular pH to homeostatic values, causes an initial intracellular Na⁺ overload, which is exacerbated by the block of the Na⁺/K⁺ ATPase. In response to the increase in Na⁺ ions, the 2Na⁺/Ca²⁺ exchanger is activated to function in “reverse mode”, causing a sudden increase in intracellular Ca²⁺ ions. At the same time, sarco/endoplasmic reticulum Ca²⁺-ATPase (SERCA or SR Ca²⁺-ATPase) is unable to reabsorb Ca²⁺ ions, thus contributing to an increase in Ca²⁺ intracellular concentration. [23]

In addition, the release of free fatty acids promotes the rapid β-oxidation's arrest, which causes the inhibition of mitochondrial ATP-dependent K⁺ channel (mitoKATP), resulting in the alteration of mitochondrial membrane potential (Δψ), hence arrhythmia. In fact, a study shows how activation of mitoKATP channels can prevent the collapse of membrane potential, protecting cardiomyocytes from IRI. [24]

Eventually, cell swelling ensues as a result of a gradual accumulation of metabolites from glycogenolysis (lactates, protons), from the usage of the phosphocreatines (creatine,

inorganic phosphates), and the catabolism of the high energy phosphate. ^[23] An irreversible tissue change can thus be expected when intervention strategies fail.

Although the reperfusion allows the recovery of ATP production and the normalization of intracellular pH, it also induce detrimental effects. ^{[19][25]} (Fig. 1b)

Further abrupt intracellular changes are known. ^[23] Indeed, a strong gradient of H^+ across the cell membrane, resulting in restoring of physiological pH and washout of lactate, promotes a massive flux of Na^+ ions within the cell by the Na^+/H^+ and Na^+/HCO_3^- exchangers. The increase of intracellular Na^+ induces the $2Na^+/Ca^{2+}$ exchanger and thus a further intracellular Ca^{2+} overload. ^[26] This is also promoted by the damaged sarcoplasmic reticulum as a consequence of oxidative stress, besides the disruption of the plasma membrane and mitochondrial re-energisation.

Intracellular Ca^{2+} overload is involved in a series of events that immediately accelerate myocardial damage: ^[27]

- * activation of lipases, nucleases and proteases, which damage cellular structure;
- * myofibril contractures;
- * mitochondrial Ca^{2+} accumulation which triggers the opening of a pore known as mitochondrial permeability transition pore (mPTP).

Moreover, following reperfusion, the still inactive electron transport chain (ETC) leads to the production of radical oxygen species (ROS), also generated from endothelial cells (xanthine oxidase) and neutrophils (NADPH oxidase). Besides inducing mPTP opening and mediating dysfunction of the sarcoplasmic reticulum, ROS also acts as neutrophil chemoattractant (along with cytokines and the activated complement). In fact, during the first 6 hours of myocardial reperfusion neutrophils are pulled into the infarct area, and after several hours they migrate into the myocardial tissue. Suggestions also show that a high release of ROS is associated with a high issue of inflammatory mediators and chemotactic agents. Among these, platelets play an important role, contributing to inflammation and ventricular remodelling. ^{[28][29]}

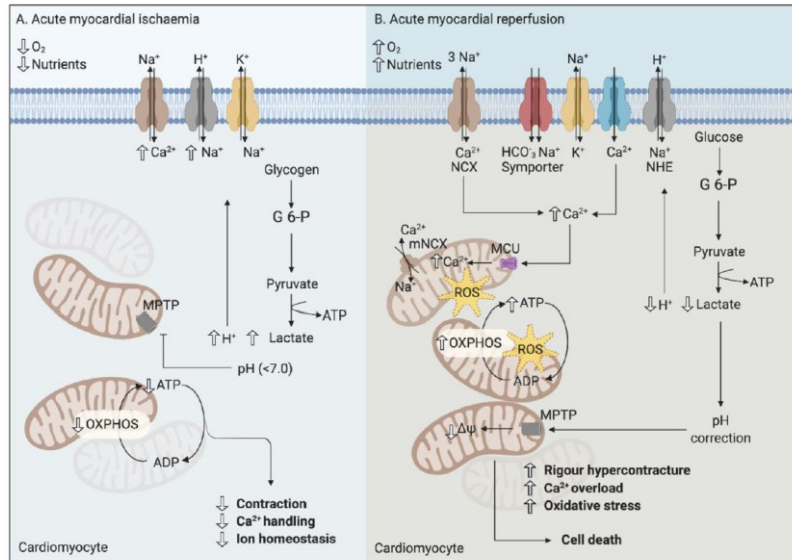


Figure 1b: Cardiomyocyte environment during ischemia and reperfusion. [30]

These changes act together inducing mitochondrial dysfunction in the cardiomyocyte. Actually, rising data indicate that the onset of reperfusion injury (RI) involves many biochemical and metabolic intracellular perturbations that culminate in the final abrupt increase in the permeability of the inner mitochondrial membrane (IMM) through the opening of a channel known as the mitochondrial permeability transition pore (mPTP). [31] [32] In particular, it has been shown that during ischemia mPTP remains closed and only during reperfusion the mitochondrial Ca^{2+} and inorganic phosphate overload, the oxidative stress (ROS production), the ATP depletion, the reduction in mitochondrial membrane potential ($\Delta\psi$) and also the rapid correction of pH, promote its opening. [33] (Fig. 1b)

Therefore, many of the perturbations described above are reflected adversely on mitochondria, especially on the final opening of mPTP, which plays a pivotal role in a perspective of cardioprotection.

1.1.2 Mitochondrial ischemia and reperfusion.

During IRI, mitochondria are closely involved in the final lethal injury. Hence, the discovery of novel approaches able to prevent mitochondrial dysfunction induced by IRI may be an important therapeutic strategy for cardioprotection. [30]

Briefly, mitochondria are small cytoplasmatic organelles engaged in a wide variety of cellular processes. They have a typical double membrane structure, which divides them into four different compartments: the outer mitochondrial membrane (OMM), the inter-membrane space (IMS), the inner mitochondrial membrane (IMM) and the matrix. The

matrix includes the soluble enzymes that facilitate reactions responsible for the production of ATP, such as the citric acid cycle, oxidative phosphorylation, oxidation of pyruvate and the beta oxidation of fatty acids, besides containing the mitochondrial DNA and ribosomes. The OMM is easily permeable to ions and small solutes ($M_w < 5000$), which freely move through porins, a crossing-membrane proteins family. The IMM, in contrast to the OMM, is an extremely tight barrier totally impermeable to small size molecules and to the most part of ions, including H^+ , but it is permeable to oxygen, carbon dioxide and water. IMM consists of cristae that increase the area containing the electron transport chain (ETC) and ATP synthase.

Mitochondria are involved in several pathways in order to ensure cellular homeostasis, among which: ATP supply, mitochondrial biogenesis, reactive oxygen species (ROS) production, mitochondrial signalling, calcium homeostasis, activation of the innate immune system by release of damage-associated molecular patterns (DAMPs) and regulation of cell death programs, with apoptotic or necrotic features. (Fig. 1c) Therefore, mitochondria contain essential enzymes that carry out vital chemical reactions. In fact, following glycolysis, which occurs in the cytosol, the subsequent citric acid cycle (Krebs cycle) and oxidative phosphorylation take place in these organelles. It is well known that, under normal aerobic conditions glucose, through glycolysis, is changed to pyruvate, which is then converted to Acetyl-CoA. Afterwards, Acetyl-CoA takes part in the citric acid cycle and the electron transport chain (ETC), allowing the production of 30 molecules of ATP for each molecule of glucose. (Fig. 1c)

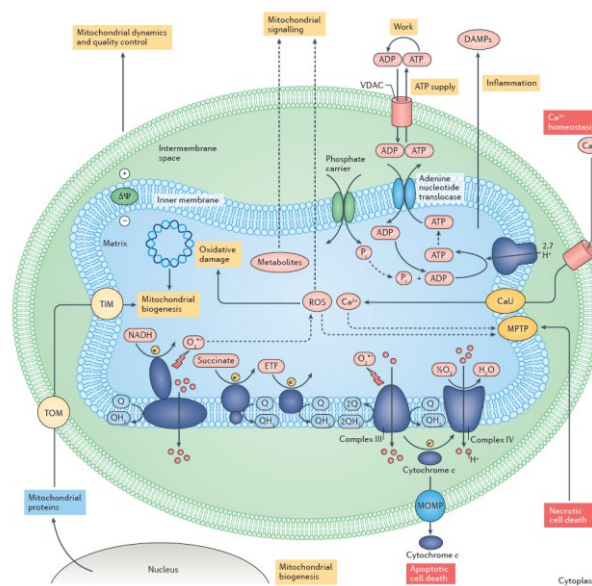


Figure 1c: Mitochondrial and cellular homeostasis. [34]

However, during ischemia, the hypoxic state induces the activation of an anaerobic glycolysis with important consequences on ATP production and pH reduction. Indeed, the absence of oxygen inhibits the regeneration of ETC and pyruvate must follow anaerobic glycolysis. This leads to a drastic reduction of ATP production, only 2 per glucose molecule, and an accumulation of lactate and protons, which causes a fall in pH. [18] Moreover, the crash of ion pumps, as described above, promotes a final rise in intracellular Ca^{2+} .

During reperfusion the supply of oxygen and nutrients allows mitochondrial re-energisation, leading to a further increase of intracellular Ca^{2+} and thus to mitochondrial Ca^{2+} accumulation. This condition, along with the production of ROS from the still inactive ETC, and the rapid correction of pH, induces rigour hypercontractures and mPTP opening, that determines osmotic perturbation, release of pro-apoptotic factors into the cytosol, mitochondrial swelling and in most cases cell death. (Fig. 1d)

In this dramatic scenario the mitochondrial permeability transition (MPT) is considered as a cellular catastrophe implicated in the pathophysiology of major human conditions as myocardial (Morciano et al., 2017) and hepatic (Panel et al., 2019) IRI, traumatic brain injury (Hånell et al., 2015), premature aging (Zhou et al., 2019), and Parkinson's disease (Ludtmann et al., 2018). [35]

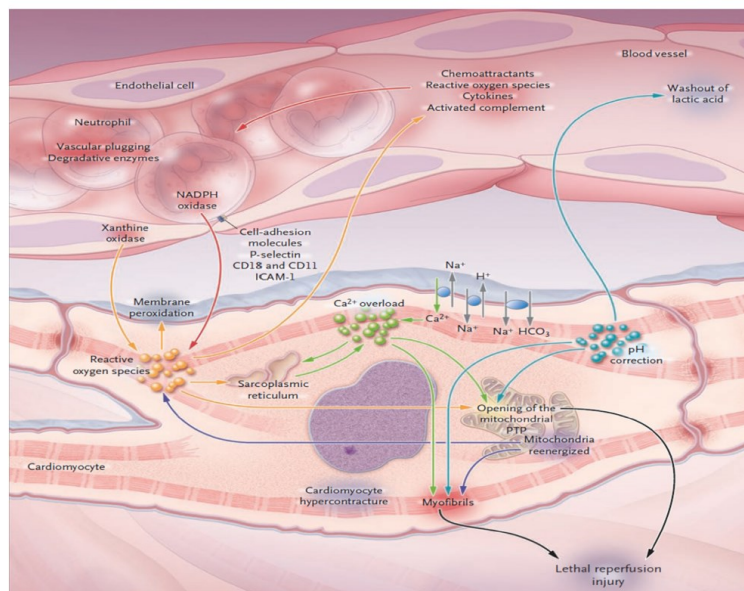


Figure 1d: Opening of mPTP, a main trigger of the lethal reperfusion injury. [36]

MPT is described as the consequence of the opening of the so-called mitochondrial permeability transition pore (mPTP), which is emerging as a major therapeutic target for cardioprotection. [32] (Fig. 1d)

1.2 MPT and the mitochondrial permeability transition pore (mPTP).

Approximately 40 years ago Haworth and Hunter reported the first biochemical description of the mitochondrial permeability transition (MPT) in isolated mitochondria, [37] as a sudden flux of low molecular weight solutes (molecules up to 1.5 kDa) across the generally impermeable inner mitochondrial membrane (IMM).

MPT has been studied for almost four decades and it was firstly believed to be a result of the degradation of the IMM, and thus an artefactual event. However, several data have shown that MPT is mediated by the opening of a hydrophilic supramolecular entity, namely the mitochondrial permeability transition pore (mPTP), whose complex bio architecture has long been discussed and, as yet, remains unresolved.

mPTP is depicted as a multiprotein platform assembled at the interface of the inner and outer mitochondrial membranes, crucial for signal transduction or material transfer. (Fig. 1e) Many components/modulators of this complex have been revealed in recent years, nevertheless the exact proteins involved in the channel-forming fraction are still under intensive investigation. [38]

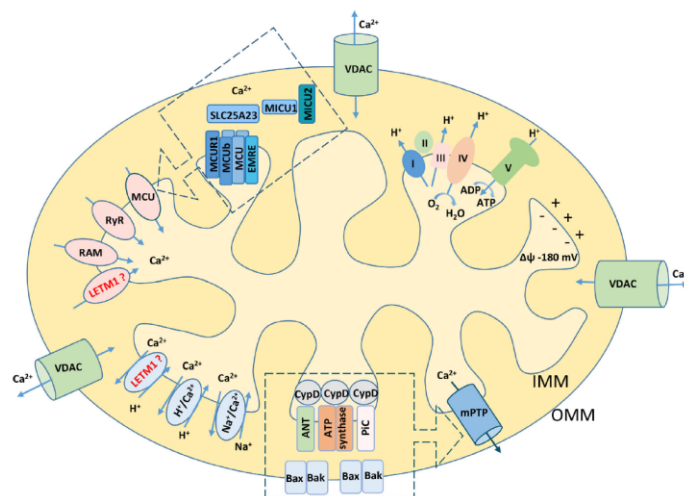


Figure 1e: The current proposal about the mPTP. [39]

Originally, the mPTP model suggested the adenine nucleotide translocator (ANT) and the voltage-dependent anion-selective channel (VDAC), sited in the IMM and OMM respectively, as the core components of mPTP. [32] However, conflicting data reported that none of them might be part of the pore. [40] Firstly, a study based on knockout (KO) animal model was performed to investigate the role of ANT. Especially, using ANT1 and ANT2 knockout mice, it was demonstrated that the MPT occurs despite the loss of ANTs, and although they have an essential role in regulating permeability transition by modulating the

sensitivity of the mPTP to Ca^{2+} activation and ANT ligands, they are non-essential structural components of the mPTP. [41] Similarly, a recent experiment with VDAC-deficient null mitochondria did not show any significant differences in the Ca^{2+} threshold for mPTP induction or in cell death in response to various types of stimuli, indicating that VDAC might not be an essential structural element of the mPTP. [42]

The metalloprotease spastic paraplegia 7 (SPG7) has been proposed as an essential and conserved component of the mPTP at the OMM and IMM contact site. [43] A study recognized a necessary role for SPG7 in Ca^{2+} - and ROS-induced mPTP opening using RNAi-based screening. Indeed, loss of SPG7 yielded mitochondrial performance that could best be described as enhanced and robust. However, the only consolidation of the exact mPTP complex will allow manipulation of these structures to rigorously investigate SPG7-dependent mPTP function in health and disease.

It has long been recognized that inorganic phosphate sensitized the mPTP pore, suggesting that it could possess a Pi-binding site. Some results, together with the finding that a nonspecific pore is generated in liposomes by reconstituting the inorganic phosphate-carrier (PiC), proposed it as a strong mPTP core-forming candidate. This idea was well accepted until experiments based on gene silencing have shown that Ca^{2+} threshold for MPT onset was not significantly affected by PiC knockdown expression. This carrier was thus recognized as a minor regulator of mPTP rather than its structural component. [44]

Even though the minimal structure required for mPTP activity is difficult to identify, an amount of mPTP modulators has been described. The mitochondrial translocator protein (TSPO), an 18-kDa protein localized in the OMM, was initially characterized as the peripheral benzodiazepine receptor. Then, the interaction of TSPO with the VDAC and the ANT showed that it was a potential component of mPTP. This assumption remained debated for a long time, [45] [46] [47] and a TSPO KO study critically assessed the role of TSPO, pointing out that it could exert only minor regulatory effect. [48] The participation of the well-known pro-apoptotic BCL-2 family members, BAK and BAX, in the formation of mPTP clarified the crucial role of MPT in the lethal injury. [49] Supplementary regulators have then attracted attention, such as the glycogen synthase kinase 3 beta (GSK3- β) and the isoform ϵ of the protein kinase C (PKC ϵ), besides p53, and the complement component 1Q subcomponent-binding protein (C1QBP), but further elucidations of their role in the MPT are required. [50] [51]

The mitochondrial matrix protein Cyclophilin D (CypD) is the only unambiguously accepted as regulator of mPTP opening, which has similar but opposite binding sensitivities to Ca^{2+} and ADP. CypD is a known 21-kDa cyclophilin that catalyses the *cis-trans* isomerisation of peptidyl-prolyl bonds in target proteins. The CypD enzymatic activity (Peptidyl-Proline Isomerases, PPIase) is necessary for positive regulation of pore opening, [52] abolition of which affords the mechanism for CsA-mediated mPTP inhibition. [53] Genetic or pharmacological ablation of CypD supported its engagement in mPTP formation. Indeed, cells of Cyp-D KO mice were shown to be more resistant to stress-induced conditions, the mitochondrial Ca^{2+} overload and the oxidative stress. In particular, it was demonstrated that a higher mitochondrial Ca^{2+} load is needed for mPTP opening in Cyp-D KO mice. The studies point out that a Cyp-D-independent conformational change can happen in the presence of high Ca^{2+} overload, making the role of Cyp-D appear regulatory in facilitating channel formation rather than being a component of the pore. [38]

The possibility to modulate mPTP opening by targeting its structural proteins is of particular interest for the development of novel therapeutic strategies to treat IRI in the clinical practice. However, the limited knowledge of the bio architecture of mPTP is the main obstacle in drug discovery programs.

Basing on the available evidence MPT seems to be sustained by two types of currents, each interesting a different pore. The low conductance current (amplitude of 0.3-0.7 nS) ensues during physiological conditions of mitochondria and is defined as a reversible event; whereas the high conductance one (amplitude of 1.5 nS) occurs as a consequence of extremely stressful states, impacting on mitochondrial structure and functions, thus causing the activation of mitophagy or cell death, with necrotic or apoptotic features, depending on ATP availability. [54]

Of note for this thesis, while ANT seems to be the most likely candidate generating the low conductance current, the high conductance would be sustained by a pore within the ATP synthase. The two currents are closely correlated due to the involvement of ANT and ATP synthase in the formation of the so-called “ATP synthasome”. This recent data focused the attention on the engagement of the ATP synthase in mPTP formation, and according to this model, suitable conditions during reperfusion may convert the energy-supplying ATP synthase machine into an energy-dissipating supramolecular entity, mPTP.

1.2.1 The ATP-synthase.

ATP synthase is the enzymatic complex that crosses the IMM and is responsible for the ATP synthesis via rotary catalysis from ADP and inorganic phosphate (Pi), essential for cell bioenergy.

It is composed of 18 protein subunits, 16 nuclear DNA (nDNA) encoded and two mitochondrial DNA (mtDNA) encoded, organized in two well-defined domains, ^[55] F_O and F₁, each of which in turn consists of multiple subunits (Fig. 1f). F_O is the membrane-embedded domain, which contains the c-ring (a number of hydrophobic c-subunits organized to form a ring structure, whose stoichiometry is species-dependent) in close contact with the a-, e-, f- and g-subunits; whereas F₁ is the water-soluble domain, located in the matrix, which includes the (αβ)₃ hexameric structure wherein only the β-subunits catalyse the ATP synthesis or hydrolysis, driven by the transmembrane proton-motive force (Δp) or ATP phosphorylation potential respectively. In addition, two stalks are defined: an asymmetrical central stalk that contains the γ-, δ- and ε-subunits and a peripheral one (also known as stator) composed of hydrophilic and hydrophobic subunits. The formers are the oligomycin sensitivity-conferring protein (OSCP), F6, the soluble portion of b-, d- subunit bound to (αβ)₃ hexameric structure, whereas the hydrophobic portion of b- and A6L constitute the embedded portion in the IMM of the peripheral stalk (Fig. 1f). F₁ motor promotes the ATP synthesis by a three steps rotational mechanism, based on a constantly alternate affinity of each one of the 3 β-subunit to ADP and phosphate, to ATP and to none of them. This rotational mechanism is supported by the proton translocation across the IMM, that is coupled to the rotation of the c-ring. As a result of the described ATP-synthase structure, proton influx and ATP synthesis are deeply connected.

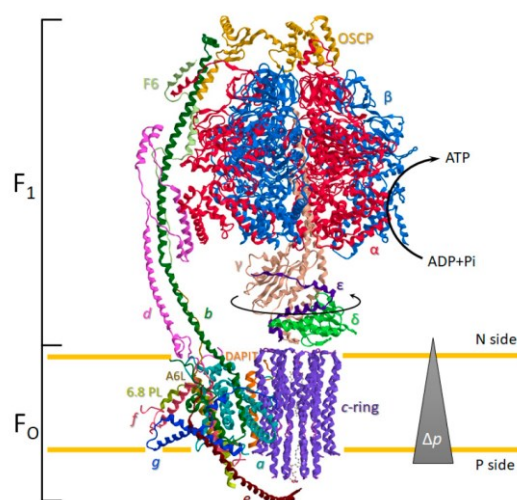


Figure 1f: ATP synthase general structure in mammalian mitochondria. ^[56]

It is known that the ATP synthases are organized in dimers, promoting the typical shape of cristae of the IMM, and that one of the main triggers of mPTP opening is the mitochondrial Ca^{2+} overload. In this regard, a recent hypothesis (Fig. 1g) explicates that the pore forms from ATP synthase dimers following Ca^{2+} -binding to the catalytic site located in the soluble F_1 domain, causing a conformational change. [57] Conversely, divalent cations like Mg^{2+} , Sr^{2+} , Mn^{2+} and Ba^{2+} act as mPTP inhibitors. [58] In particular, Mg^{2+} contends with Ca^{2+} through a competitive mechanism, whereas Sr^{2+} , Mn^{2+} and Ba^{2+} obstruct Ca^{2+} influx inhibiting mPTP. [37] [59] [60]

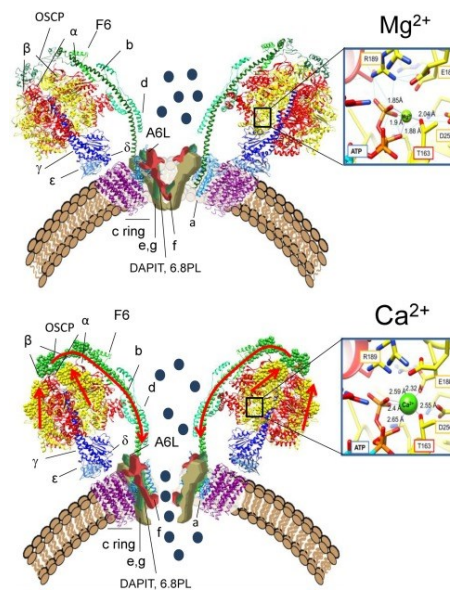


Figure 1g: ATP synthase dimers structure with Mg^{2+} (upper panel) or Ca^{2+} (lower panel) bound at the catalytic sites. [57]

Moreover, in pathophysiology settings the ATP enzyme can convert its catalytic activity, causing the ATP hydrolysis and thus a drastic reduction of ATP level. This process can be avoided by the physiological inhibitory factor 1 (IF1) that binds the ATP synthase dimer, inhibiting both the synthetic and hydrolytic activities. (Fig. 1h) This regulator is active only in its dimerization form, which ensues after the pH decreases under 6.5, as well as in the presence of an extensive proton motive force.

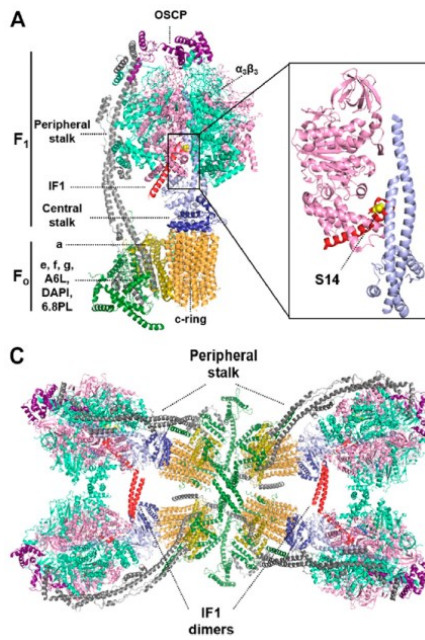


Figure 1h: IF1, the physiological inhibitory factor 1 of the ATP synthase dimer. [61]

Hence, under hypoxic conditions, oxidative phosphorylation is gradually blocked, ATP synthase does not function but at the same time IF1 is active, stabilizing the ATP synthase dimer and preventing hydrolysis of the still remaining ATP reserves. During reperfusion, as a consequence of the pH increase, the dimer IF1 becomes unstable, forming tetramers by interaction of two dimer pairs (Fig. 1i), and thus the inhibition of the ATPase is removed.

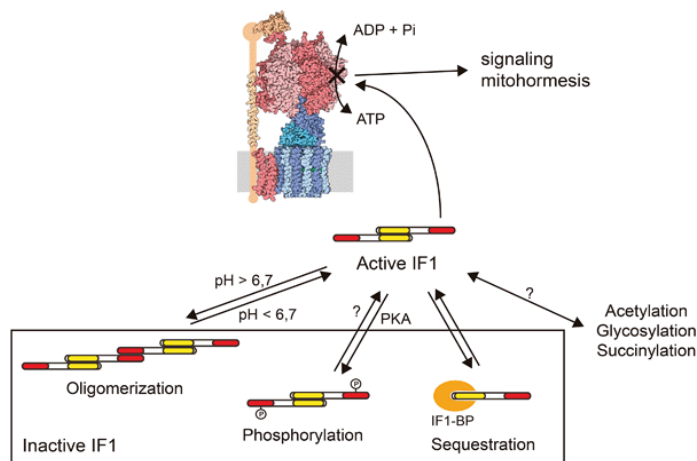


Figure 1i: Active and inactive forms of IF1. [62]

In this regard, items of evidence join in the suggestion that a failed stabilization of the ATP synthase dimer, along with the involvement of crucial triggers, causes a deep rearrangement, closely related to the mPTP opening. [63] [64] Nevertheless, a molecular model that clarifies the ATP synthase dimers transition to the mPTP is still lacking.

As mentioned above, following the binding of the two positive modulators, Ca^{2+} and CypD, two forms of currents are recorded, a low and a high conductance current, through ANT and a pore within the ATP synthase respectively (Fig. 1j panel b). Concerning to the high conductance state of the MPT, two working models of pore formation are currently proposed: the “dimer hypothesis” and the “c-ring or death finger hypothesis”. (Fig. 1j panel c). The first model proposed that a reconfiguration of the dimer origins a high conductance current at the interface of two ATP synthase monomers. Conversely, the second one supports that a significant conformational change induced by Ca^{2+} allows the c-ring to generate the pore.

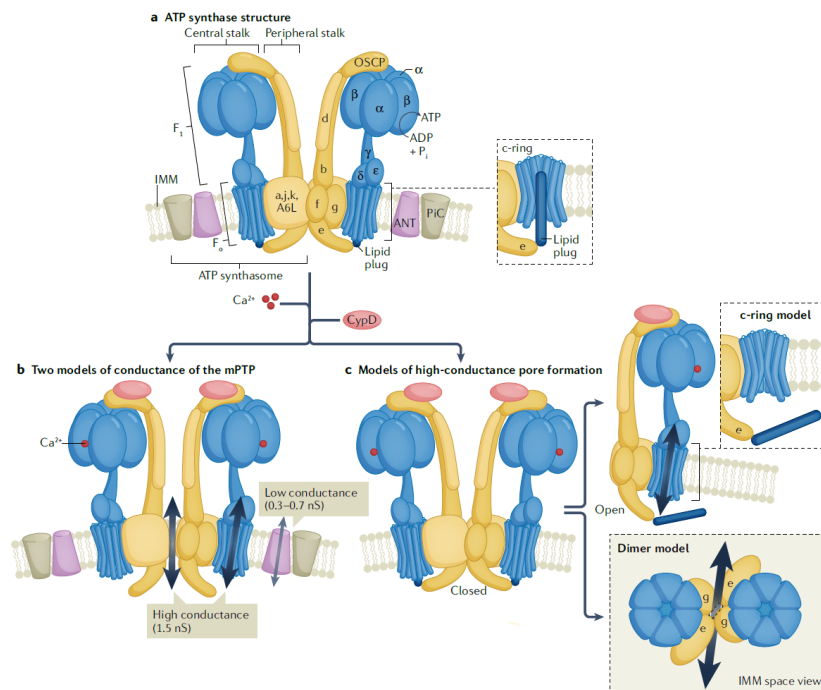


Figure 1j: The “dimer hypothesis” and the “c-ring or death finger hypothesis”.^[54]

Although studies provided criticism of both the models,^[65] ^[66] independent experiments have shown that: the depletion of the c-subunit reduces the lethal effects in response to calcium overload- and oxidative stress-induced stimuli, whereas its overexpression enhances mPTP opening.^[67] ^[68] Supporting the hypothesis that the long-sought pore might reside in the Fo-ATP synthase, a further investigation has assessed c-subunit in patients with STEMI. This study was the first evidence that c-subunit is detectable in serum from STEMI patients and that its elevated levels in the early phase of MI correlate to several myocardial reperfusion markers and outcome in terms of death and HF.^[69] Moreover, M. Bonora *et al.* by genetic approaches have revealed that mPTP opening is a multistep process that involves disassembly of F₁F_o-ATP synthase dimers and rearrangement of c-rings.^[70]

Of note, the recent Cryo-EM ^[71] structure of the entire mammalian F-type ATP synthase, with the Ca²⁺ bound to catalytic sites of the enzyme, has strengthened the “c-ring hypothesis”. In particular, it has been evidenced that under physiological conditions the c-ring lumen is occupied by a lipid plug, holding in place by a fragment of the e-subunit. Since Ca²⁺ has a higher atomic radius than the natural cofactor Mg²⁺, it is able to induce an alteration of the F₁ domain, which is transmitted by the peripheric stalk to the F₀ domain. As a result of the significant rearrangement of the ATP synthase, the shift of e-subunit promotes the deprivation of the lipid plug and the exposition of c-ring lumen which also appears enlarged. ^[54] (Fig.1j(c)) Especially, the obtained 3D classes of F₁F₀ exposed to calcium have been tentatively assigned to sequential stages in mPTP opening. As depicted in Figure 1k, the initial pulling out can lead to a reversible partial opening, wherein water molecules come into the c-ring, destabilizing the second lipid plug on the matrix side and creating a ‘leak’ across the membrane. This condition can be followed by the c-ring widening to 2-3 nm due to destabilization of its hydrophobic interior by the incoming water molecules, F₁ detachment and opening of the full conductance pore.

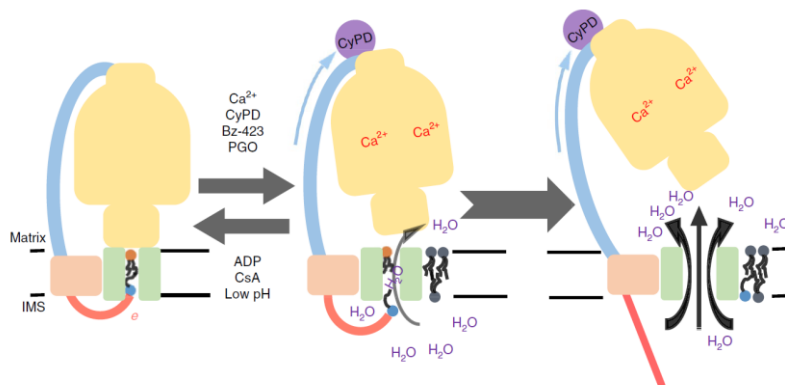


Figure 1k: Proposed model of mPTP opening. ^[71]

The unexpected double role of e-subunit as a second anchor point for the stator (along with OSCP) and a holder for the lipid plug in the c-ring helps to understand the enigmatic link between F₁F₀ and the mPTP. ^[71]

Eventually, literature conveyed that the low conductance current promotes a redistribution of ions across the IMM and a brief depolarization ($\Delta\psi$), which only temporarily modifies mitochondrial physiological conditions. However, the high conductance current alters persistently the mitochondrial depolarization, besides a redistribution of ions and solutes. A series of cellular responses are thus activated. ^[54]

1.2.2 *mPTP and cell death.*

Programmed cell death (PCD) is a physiological, evolutionarily conserved event. Nevertheless, excessive PCD may be the basis of many diseases, including cardiovascular and neurodegenerative disorders. Several types of PCD exist, including mitochondrial permeability transition (MPT) driven apoptosis, which is related to the onset of ischemia-reperfusion injury (IRI).^[31]

Especially, following MI the mPTP opening plays a dual role as arbiter of different cellular responses, from the physiological regulation of mitophagy, the clearance of mitochondria affected (as a supporter of cell survival), to the activation of necrosis or apoptosis (as a promoter of cell death).

Necrosis and apoptosis are two forms of cell death in the myocardium that differently contribute to MI. In order to clarify the possible correlation between mPTP and cell death in cardiomyocytes,^[72] some investigations have suggested that the mechanism of heart failure in cell death involves the mPTP, besides a complex network of cellular signals.

In this regard, it has been well documented that necrosis is a frequent outcome of ischemia and reperfusion that rapidly leads to a destruction of a large group of cells, whereas apoptosis, primarily during reperfusion, may independently contribute to the extension of cell death.

Necrosis is characterized by depletion of high-energy stores, cell and organelle swelling and disruption of cellular membrane, with its subsequent irreversible rupture and the spilling of their intracellular contents.^[17] Moreover, if the cellular stress is a severe insult, the extent of mPTP opening is a catastrophic event and necrotic cell death is inevitable.

Otherwise, apoptosis involves an orchestrated caspase signalling cascade that induces a self-contained program of cell death. Since this form is recognized as the final event in a cascade of energy dependent events, following reperfusion the final fate of the cells, whether by apoptotic or necrotic features, is determined by the amount of ATP.

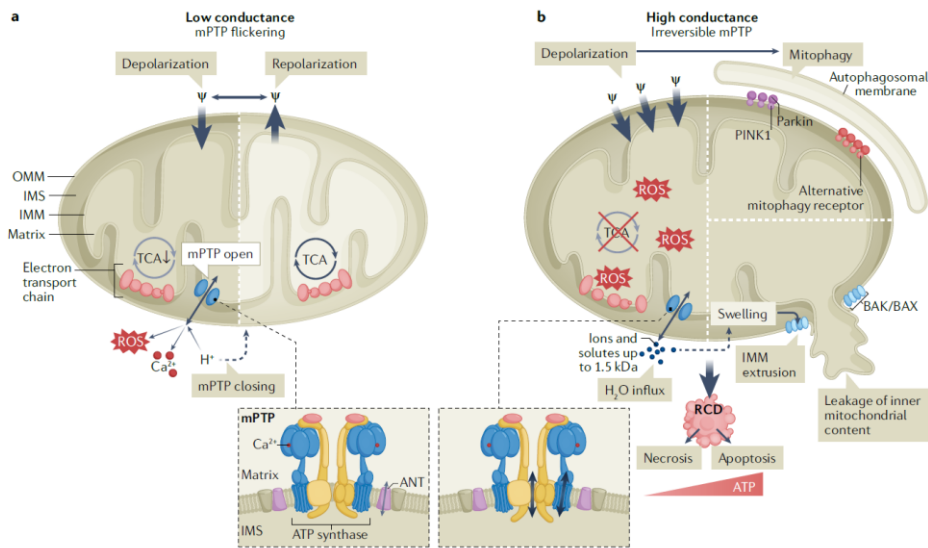


Figure 11: The high conductance and the different cellular responses. ^[54]

Especially, the apoptotic cell death can be initiated via two different pathways, which depend on the nature of the death signals: the death receptor pathway (extrinsic apoptotic pathway) and the mitochondrial pathway (intrinsic apoptotic pathway). ^[32]

Basically, the extrinsic pathway is activated in response to inflammation, which is required for healing and scar formation in the infarct. Hence, proinflammatory ligands (such as Fas, THF- α and TNF-related apoptotic inducing ligand (TRAIL)) bind their own receptor, that is a plasma membrane protein with a death domain (DD). The DD, in turn, is involved in binding an adaptor protein (FADD) with a death effector domain (DED) and sited between the receptor and the procaspase 8. Therefore, in the presence of the appropriate ligand the complex that is formed consists of: the receptor, the adaptor protein and the procaspase 8. It is the so-called DISC (Death Inducing Signalling Complex), the corresponding apoptosome of the intrinsic pathway. (Fig. 11)

The involved caspases are also termed cysteine-aspartate proteases. They are mainly distinguished into initiator caspases, such as caspases 8 (extrinsic pathway) and 9 (intrinsic pathway) and effector caspases, such as caspase 3, 6 and 7, which are responsible for inducing apoptosis. Out of their important role in cell death, they are normally in an inactive form, named procaspase, which can be cleaved to give the corresponding active form.

As anticipated, apoptosis may follow a second intrinsic pathway, wherein the main cause seems to be mitochondrial permeability transition (MPT), driven by the mPTP opening. Besides the accumulation of Ca^{2+} ions in the mitochondrial matrix and the decrease in IMM transmembrane potential ($\Delta\psi$), another important role in the induction of apoptosis is played by ROS, which can be generated by the electron transport chain (ETC). Indeed, ROS are able to induce lipid peroxidation and thus the OMM fragmentation, driving the release into

the cytosol of a number of apoptotic activators, such as cytochrome c, apoptosis-induction factor (AIF) and Smac/DIABLO. Cytochrome c-mediated apoptosis is significant in cardiomyocytes, thereby in the cytosol it is bound by the protein APAF (Fig. 11), which subsequently polymerizes and binds procaspase 9 thus activating into caspase 9. Thus, a complex called apoptosome is formed. However, the various steps of apoptosome formation, as well as the activation of caspase 9, being ATP-dependent processes, require energy. Therefore, in case of severe ATP depletion or advanced cell damage, the cell is unable to activate an apoptotic death process and might veer toward a necrotic process.

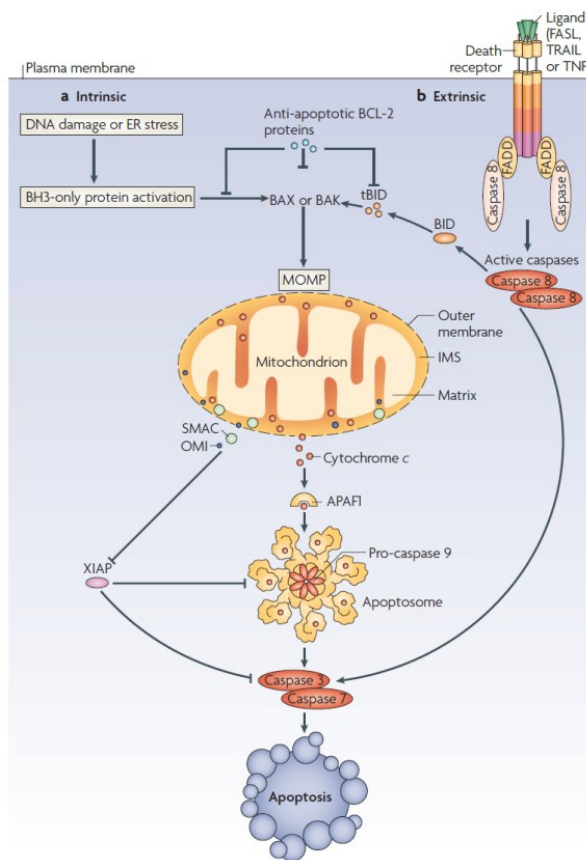


Figure 1m: Intrinsic (a) and extrinsic (b) pathway of apoptosis. [73]

1.3 mPTP: a promising pharmacological target against IRI.

The main triggers of mPTP opening are the increase of intramitochondrial calcium concentration and of reactive oxygen species byproducts, both typical conditions occurring when the blood flow is restored after an ischemic insult in a tissue. Because the combination of these conditions ensues in multiple diseases, from neurodegeneration to IRI-related heart disease, the prevention of MPT at the onset of reperfusion with specific inhibitors have been proposed as a possible cardioprotective strategy.

1.3.1 Known inhibitors of the mitochondrial permeability transition (MPT).

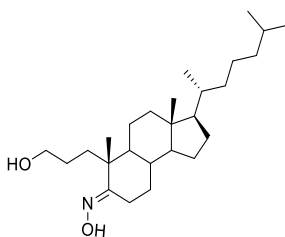
Currently, the few available inhibitors can be classified into two categories: CypD-dependent mPTP inhibitors, that act indirectly via interaction with the CypD; CypD-independent mPTP inhibitors, whose mechanism of action is still unknown or involves an alternative mitochondrial target.

The best characterised member of the first class of inhibitors, with a CypD-dependent mechanism, is Cyclosporin A (CsA), a hydrophobic cyclic peptide of 11 amino acids. It has been well established that CsA inhibits mPTP opening by binding a highly conserved domain of CypD, ^[74] occluding its active site and thus its ability to associate other protein components of the pore. It was evaluated in preclinical models of IRI, ^[75] ^[76] showing a narrow therapeutic window that is hard to achieve in clinical practise. ^[77] ^[78] ^[79] Moreover, some small clinical studies on efficacy in improving cardiac outcomes following IRI have summarized the occurrence of off-target effects, such as immunosuppression and hypertension, as well as significant differences in patient inclusion criteria between studies.

In order to overcome its immunosuppression behaviour, two semisynthetic analogues of CsA lacking in calcineurin binding domain, *N*-methyl-isoleucine-4-cyclo-sporin (NIM-811) and *N*-methyl-D-alanine-3-*N*-ethyl-valine-4-cyclosporin (Debio025) respectively, were developed. These are both potent and nonselective cyclophilin inhibitors and they have demonstrated activity in multiple in vivo models of myopathy. ^[80] ^[81] ^[82]

Inhibitors acting by CypD-dependent mechanism raise the threshold of mPTP sensitivity to higher Ca^{2+} concentrations, but do not entirely suppress the pore opening. [52] It is unclear whether this would result in a therapeutic advantage, given the recognized physiological activity of the mPTP pore. Therefore, research has been guided to the identification of molecules that can act through a different mechanism (CypD-independent mPTP inhibitors), thus avoiding just desensitization.

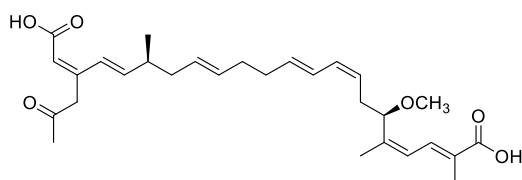
Among these, TRO-40303 was the first compound to be identified. It is a steroid analogue that binds the cholesterol binding site of the translocator protein TSPO, sited in the OMM. It was initially shown to be effective in vitro and in vivo, delaying pore opening following oxidative stress caused by reperfusion. [83] Subsequently, studies discussed whether TSPO was effectively involved in the organization of the mPTP platform and disappointing results were achieved. [48] However, TRO-40303 was further investigated in a Phase II clinical trial, called MITOCARE, not demonstrating any effect in limiting myocardial injury after percutaneous coronary interventions (PCI). [84] [85]



TRO-40303

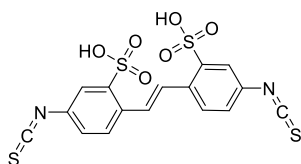
It has been proposed that the disappointing results with the molecules, CsA and TRO-40303 which have reached clinical trials, may be in part due to their indirect mechanism of action. CsA is a Cyclophilin D (CypD)-dependent inhibitor while TRO-40303 binds the mitochondrial translocator protein (TSPO) located in the OMM. Both CypD and TSPO are known regulator of mPTP and not structural components of the pore.

Another target for the regulation of mPTP opening could be the ANT. It has been recognised that the ANT inhibitor, Bongkreikic acid, in $\text{G}\alpha\text{q}$ -signaling induced cardiomyocytes apoptosis, shows an anti-apoptotic effect (Adams et al., 2000), besides a decreased ROS production (Roussel et al., 2015). However, ANT inhibitors are known to be potent mitochondrial toxins. Consequently, they cannot be considered for the development of further cardioprotective agents.



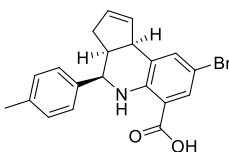
Bongkreikic acid

In 2016 was assessed, in vitro on cisplatin-treated HeLa cells, the anti-apoptotic effect of the VDAC1 oligomerization inhibitor, 4,4-diisothiocyanatodihydrostilbene-2,2-disulfonic acid (H2DIDS). However, an in vivo evaluation of the cardioprotective action of VDAC1 blockers is needed.



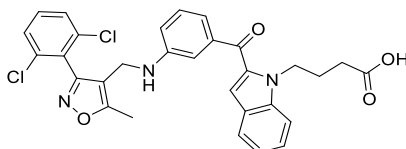
H2DIDS

DS44170716 is a small molecule whose mechanism of action apparently consists of blocking mitochondrial Ca^{2+} uptake. Actually, it promotes a loss of mitochondrial membrane potential ($\Delta\psi$) and inhibition, by acting on the electron transport chain (ETC). The inhibition of respiration, however, reducing its therapeutic potential and further investigation are needed. [86]



DS44170716

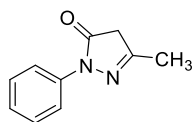
DS16570511 is a novel inhibitor of the mitochondrial Ca^{2+} uniporter (MCU), and thus preventing mitochondrial Ca^{2+} uptake is a potential inhibitor of mPTP opening. Studies expose encouraging data on the use of the compound to control cardiac function. [87]



DS16570511

Modulation of ETC function and Ca^{2+} uptake has been reported as alternative approaches for mPTP inhibition, besides the modulation of mitochondrial redox state. In this regard, the

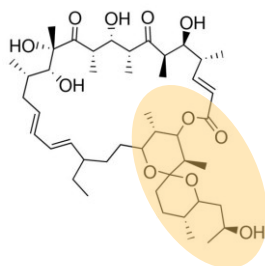
most significant result was obtained with the derivative Edaravone (RadicutTM), a potent antioxidant and inhibitor of mPTP opening. Its action is expressed against free radicals, as a scavenger, thus preventing oxidative damage to cells as well as subsequent necrosis or apoptosis. [88]



Edaravone (RadicutTM)

As previously described, CsA reduces the mitochondrial permeability transition by binding CypD, which is in turn an important regulator of ATP synthase. This awareness, together with recent findings showing that ATP-synthase is involved not only in regulation but also in mPTP formation, has increased attention in this enzyme as therapeutic target. In the past, it has been extensively studied as pharmacological target for therapies aimed in blocking adenosine triphosphate (ATP) synthesis in cells, especially those of pathogens, cause of infective pathologies in humans. Deprivation of ATP stores often means death for an organism and this is what has been reached in medicine by the use of antimicrobials such as a diarylquinoline (Bedaquiline, to fight Tuberculosis) and 1,4-benzodiazepine (Bz-423, to treat autoimmune disorders), both selectively targeting proteins of ATP synthase: the c-subunit and the oligomycin sensitivity conferral protein (OSCP), respectively.

Among the classes of Fo inhibitors, macrolides are one of the more representative derivatives. Oligomycin A (OA) is a macrolide consisting of a 26 membered lactone ring, isolated from *Streptomyces diastatochromogenes*, that lies at the interface between the a- and c-subunits of the enzyme ATP synthase, blocking the rotary proton translocation in Fo. The mechanism provides that the oligomycin-sensitivity conferring protein (OSCP) is the subunit that connect portion F₁ with Fo, hence, if the enzyme is well coupled, F₁ activity is also blocked. Since, the amino acid residues that form the oligomycin-binding site are 100% conserved between human and yeast, the high-resolution (1.9 Å) crystal structure of oligomycin bound to the subunit c₁₀-ring of the yeast mitochondrial ATP synthase has exploit to clarify how the general spiranic portion of OA (in orange) may inhibit the ATP synthesis: [89] each c-subunit has an H⁺-binding site defined by a conserved acidic side chain (Glu⁵⁹) on the C-terminal helix in the middle of IMM that is essential for proton translocation. It forms an H-bond with an ester carbonyl oxygen of OA via a bridging water molecule, and a bond with a hydroxyl group of OA. The remaining contacts between OA and c-subunit are mainly hydrophobic. [90]



Oligomycin A

Thereby, the 1,7-dioxaspiro[5.5]undecane moiety of Oligomycin A (in orange), closely engaged in the binding cavity of the c-ring, could be an interesting starting point for the design of novel derivatives libraries, avoiding the inhibition of the ATP synthesis.

2. DESIGN, SYNTHESIS AND BIOLOGICAL EVALUATION OF CLINICALLY USEFUL SPIRO-DERIVATIVES AS mPTP INHIBITORS.

2.1 INTRODUCTION.

Acute myocardial infarction (MI) is one of the leading reasons of death and disability worldwide. The standard treatment of patients with ST-segment-elevation MI (STEMI) for reducing ischemic injury is the prompt restoration of blood flow, via either primary percutaneous coronary intervention (PCI) or thrombolytic therapy. ^[91] Despite timely reperfusion strategies, STEMI is associated with 6-12% mortality and 14-36% prevalence of heart failure within 1 year, thus novel therapeutic approaches are needed to improve the clinical outcomes in this patient group. In particular, the so-called reperfusion injury (RI) contributes for up to the 50% of the final infarct size, restricting the efficacy of PCI. ^[92] There is a clear unmet need with respect to RI therapy and this is mainly due to the incomplete understanding of the complex pathophysiology of this condition. ^[91] ^[7] Rising data indicate that the onset of RI involves several molecular and cellular factors that culminate in the opening of a large pore in the mitochondrial membrane, namely the mitochondrial permeability transition pore (mPTP). ^[31] ^[32] mPTP is defined as the key actor in the final step of RI and the main responsible for cardiomyocyte death, which makes it a major therapeutic target for cardioprotection. It is recognized that mPTP opening mediates mitochondrial permeability transition (MPT)-driven apoptosis, ^[51] during which the inner mitochondrial membrane, usually highly impermeable, undergoes to a sudden and irreversible increase of permeability. This phenomenon allows the free entry into the matrix of all molecules <1.5 kDa, which translates into ATP depletion, mitochondrial swelling and release of cytochrome c and other apoptotic proteins ultimately leading to cell death. ^[31] The main triggers of mPTP opening are the increase of intra-mitochondrial calcium levels and oxygen species by-products, both typical conditions occurring when the blood flow is restored in a tissue after an ischemic insult.

mPTP is defined as a multiprotein entity including pore-forming elements and modulators, allocated at the crosstalk of inner and outer mitochondrial membranes, that contribute to its opened/closed conformational state. ^[50] Although many components/modulators of mPTP have been discovered in recent years, the proteins involved in the channel-forming fraction are still under intensive investigation. Several mPTP inhibitors have been identified, among which Cyclosporin A (CsA) and TRO-40303 have reached clinical studies. ^[50] However, inconsistent results have been achieved as far as their cardioprotective action. It has been suggested that the disappointing results may in part be due to their indirect mechanism of

action. CsA is a Cyclophilin D (CypD)-dependent inhibitor, while TRO-40303 binds the mitochondrial translocator protein (TSPO) sited in the outer mitochondrial membrane. (c) Both CypD and TSPO are known regulator of mPTP and not structural components of the pore.

The incomplete knowledge of the bio architecture of mPTP is the main obstacle in drug discovery programs. Of note, recent data point to a role for ATP synthase in mPTP formation. [63] [64] According to this model, the increase of mitochondrial calcium during reperfusion can convert the energy-supplying ATP synthase machine into an energy-dissipating supramolecular entity, mPTP. [64] Currently, two working models of pore formation have been proposed. [54] However, independent studies provided that the c-subunit of F₁F₀-ATP synthase play a pivotal role in mPTP formation: depletion of the c-subunit reduces the channel opening in response to calcium- and oxidative stress-induced stimuli, whereas its over expression enhances mPTP opening. [67] [68] [70] Moreover, elevated levels of c-subunits in serum of STEMI patients correlate to myocardial reperfusion markers and are determinants of poor clinical outcomes. [69] In addition, the recent Cryo-EM structure of the mammalian F-type ATP synthase, with the Ca²⁺ bound to catalytic sites of the enzyme, has provided solid validation of the “c-ring hypothesis”. [71]

Sharing a dual role as both generator of cell life and key participant in death mechanisms, in the past F₁F₀-ATP synthase has been extensively studied as pharmacological target for therapies aimed in blocking adenosine triphosphate (ATP) synthesis in cells, specifically those of pathogens that cause infective pathologies in humans. Lack of ATP stores often means death for an organism, and this is what has been reached in medicine by the use of antimicrobials such as a diarylquinoline (Bedaquiline, to fight Tuberculosis) and 1,4-benzodiazepine (Bz-423, to treat autoimmune disorders), both selectively targeting proteins of ATP synthase: the c-subunit and the oligomycin sensitivity conferral protein (OSCP), respectively.

Considering the available information and, looking for novel potential pharmacological approach for the treatment of RI, my research group recently reported the design and synthesis of different series of mPTP inhibitors targeting the c-subunit of F₁F₀-ATP synthase. [93] [94] Oligomycin A (OA) and dicyclohexylcarbodiimide (DCC) has been considered as starting points for the investigated derivatives due to their known capability of binding c-subunit to Glu⁵⁹. [90] [95]

Especially, the crystal structure of the OA-ATP synthase complex indicated that the spiro bicyclic portion of OA, with a general structure 1,7-dioxaspiro[5.5]-undecane, is closely

engaged by the binding cavity of the c ring.^[90] In the effort to simplify the structure of OA to the putative pharmacophore portion towards easy and accessible synthesis, a small internal library of spirocyclic compounds was initially screened. On this basis, it has been investigated the hypothesis that the spiro bicyclic fragment may be mandatory for mPTP inhibition. **PP11** was selected as a valuable hit-compound with an *in vitro* inhibitory potency comparable to that of OA, but at a 10-fold lower concentration; the increased performance at lower concentrations was ascribed to its better localization to the mitochondrial compartment, as assessed by HPLC-HRMS.

Considering the higher chemical stability of the aza-spiro moiety compared to the spiro-ketal function of OA, further SAR optimization led to compound **10** with improved *in vitro* potency. Moreover, in an *ex vivo* model of MI, the treatment with **10** during reperfusion showed beneficial effects in preserving cardiac functions with significant reduction of apoptotic cell death.^[93] Noteworthy, conversely from OA the inhibition of mPTP by **10** was not associated with a depletion of the mitochondrial ATP content.

In light of these prominent results, in this doctoral thesis we focused on the design, synthesis and biological evaluation of novel spiro derivatives as potential mPTP inhibitors, for the clinical management of ischemic events. To this end, the first goal of this doctoral thesis was to develop three series of molecules characterized by new spiro fusions capable of mimicking the spiroketal core of OA (projects 1, 2 and 3).

2A. Project 1: NOVEL SPIRO-ISATIN DERIVATIVES.

2a.1 AIM AND OBJECTIVES.

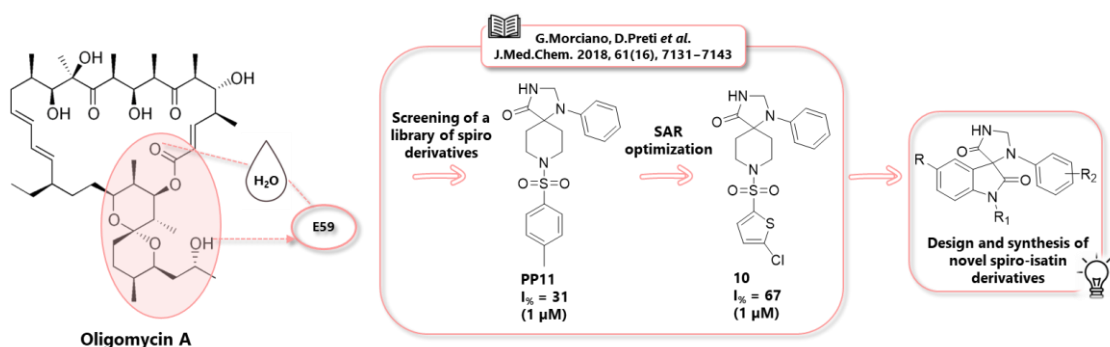


Figure 2a.1: Rational design Project 1.

With the aim to identify novel spiro derivatives as potential cardioprotective agents, we firstly considered the isatin ring, a scaffold that has attracted strong interest in organic and medicinal chemistry due to its potential in biological and pharmacological activities.

Briefly, the synthesis of new medicinal compounds based on candidate molecules with known biological activity offers an opportunity to design effective safe drugs with minimal toxicity.

Heterocyclic derivatives represent an important class of organic compounds having biological and pharmacological properties. Among nitrogen-containing heterocyclic compounds, indoline-2,3-dione, commonly known as isatin, is a versatile chemical building block able to form a wide category of biologically useful heterocyclic molecules.^[96] Structurally, it consists of an indole nucleus and two types of carbonyl group, lactam and keto respectively. It is a well-known natural product and an endogenous polyfunctional heterocyclic compound found in mammalian tissues and body fluids, where its concentrations vary significantly from <0.1 to >10 μ M.^[97] It was first obtained in 1841 by Erdman and Laurent as a product from the oxidation of indigo dye by nitric acid and chromic acids. The unique potential of isatin to participate in a broad range of synthetic reactions has allowed its extensive use as a precursor molecule in medicinal chemistry.^[98] In particular, the isatin moiety has been used by many researchers by taking advantage of N^1 position, C^2 and C^3 carbonyl positions for the synthesis of a wide variety of derivatives possessing several biological activities^[96], such as anticancer, anti-inflammatory, antiviral, anticonvulsant, anti-tubercular, antidiabetic, antimicrobial. Apart from N -substitutions, nucleophilic additions at

the C-O bond and condensation reactions, the isatin ring can undergo electrophilic aromatic substitution at position C^5 and C^7 of the phenyl ring, chemoselective reductions, oxidations and ring expansions.

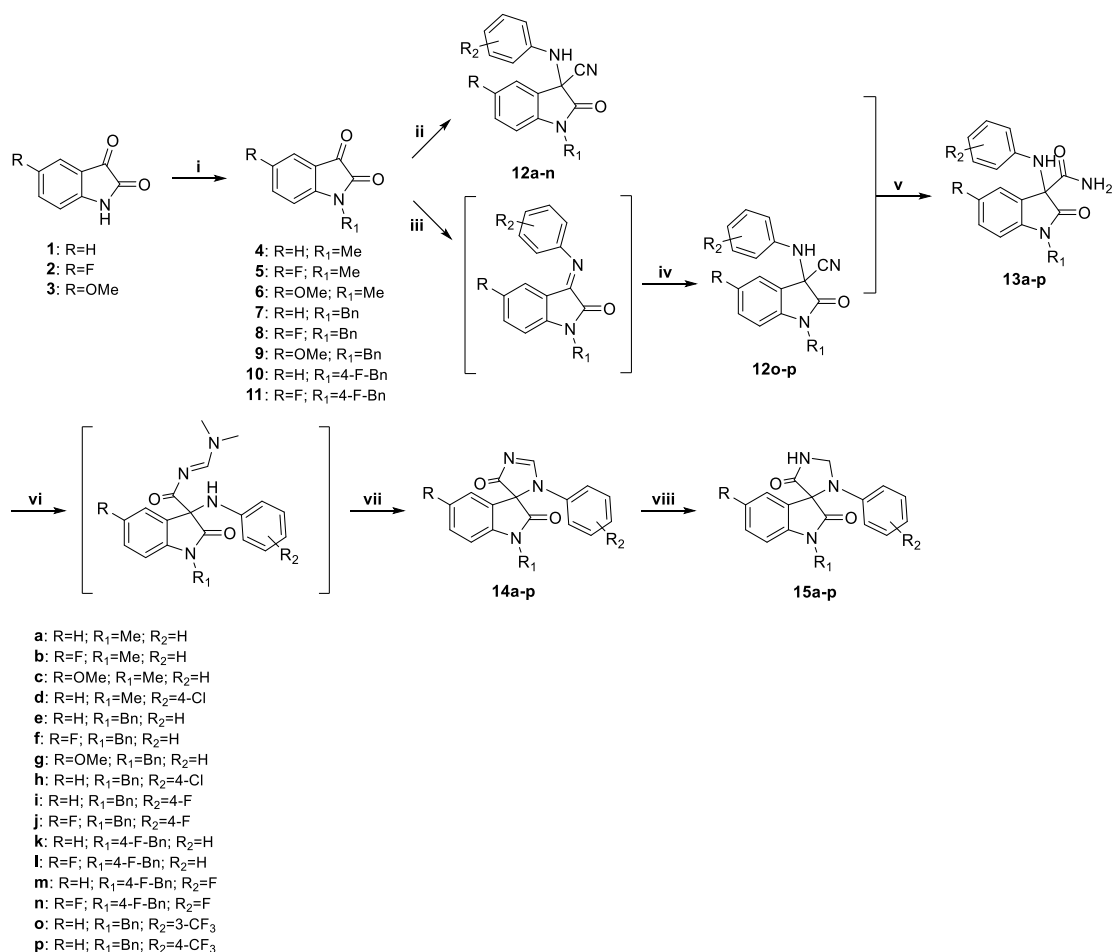
In light of the attractive features of the isatin ring, we focused on the possibility to exploit it as core structure in order to develop novel spiro derivatives as promising cardioprotective agents. Notably, it has been observed that sometimes the presence of two oxo groups at positions 2 and 3 becomes insignificant as a fusion with a heterocycle at these positions resulted in a biologically relevant compound. [99] Considering this evidence, we designed a series of isatin-based spirocycles, wherein the imidazolidinone cycle of the previous series [93] was created in an isatin scaffold instead of a piperidine one. Because of the peculiar chemical behaviour of the isatin ring, for the synthesis of the desired derivatives we optimized some reaction steps, identifying the ideal conditions after several attempts.

The efficacy of these new spiro compounds against mPTP opening was measured through a preliminary *in vitro* screening (in living cells, AC16: human ventricular cardiomyocytes), recognising **15f** as the best performing compound that was further investigated to explore its biological profile

2a.2 RESULTS AND DISCUSSION.

2a.2.1 Chemistry.

As depicted in **Scheme 2a.1**, the optimized synthetic pathway allowed us to set up a library of spiro-isatin compounds. The reported derivatives, with general structure 1'-methyl-3-phenylspiro[imidazolidine-4,3'-indoline]-2',5-dione derivatives (**15a-d**) and 1'-benzyl-3-phenylspiro[imidazolidine-4,3'-indoline]-2',5-dione (**15e-p**) respectively, were synthesized starting from opportunely substituted commercially available 1H-indole-2,3-diones **1-3**. They were first alkylated and then a Strecker reaction, between compounds **4-11** and anilines in presence of trimethyl silyl cyanide (TMSCN), led to the α -amino nitriles **12a-n**. However, for the preparation of the α -amino nitriles **12o-p** we exploited a different strategy. Compound **7** was transformed to the corresponding ketimine intermediate, by reaction with the appropriate aniline, which was subsequently implemented to react with TMSCN. Nitrile groups were then converted to amide functions by treatment with an alkaline solution of 30% H_2O_2 . The obtained amino-amide intermediates **13a-p** were reacted with DMF-DMA and the **14a-p** spiro derivatives were obtained by acid catalysis via acetic acid. Finally, the unsaturated imidazolidinone cycles were reduced with $NaBH_4$, leading to the final saturated products **15a-p**.

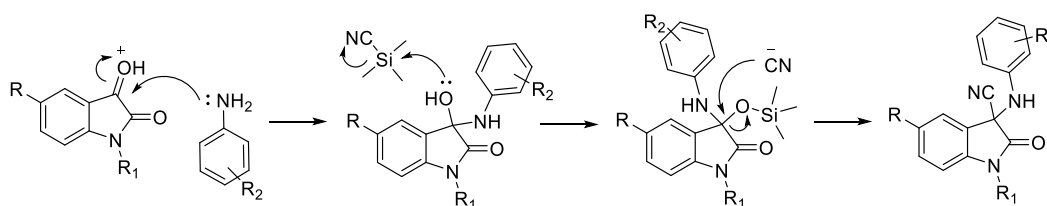


Scheme 2a.1: Synthesis of substituted 1'-methyl-3-phenylspiro[imidazolidine-4,3'-indoline]-2',5-dione and 1'-benzyl-3-phenylspiro[imidazolidine-4,3'-indoline]-2',5-dione derivatives - Reagents and conditions - i. MeI, NaH, DMF, 0°C 2h to rt 2h (except for 7-11: Substituted benzyl bromides, K₂CO₃, MeCN, reflux 16h); ii. Substituted anilines, TMSCN, AcOH, 0°C to rt 18h (except for 12o-p); iii. Substituted anilines, AcOH, 0°C to rt 3h; iv. TMSCN, MeOH 50°C 18h; v. H₂O₂ 30%, Na₂CO₃ 1N, acetone, rt 2h; vi. DMF-DMA, MeOH, 50°C 2h; vii. AcOH, MeOH, 50°C 2h; viii. NaBH₄, MeOH, rt 2h.

All the synthesized compounds are reported in **Table 2a.1**. In this regard, we applied a versatile synthetic approach that first led to two groups of isatin-based spirocycles (compound **15a-d** and **15e-h**). We investigated the effect of placing a methyl or a benzyl group at the *N*^{1'} position of the isatin moiety, combining these general scaffolds with various substitutions at the *C*⁵ or at the *N*³ position. In particular, examining the most promising spiroperidines of the previous work,^[93] we considered to implement *N*³-phenyl ring bearing an electron-withdrawing group (EWG) at the para position (see compounds **15d** and **15h**).

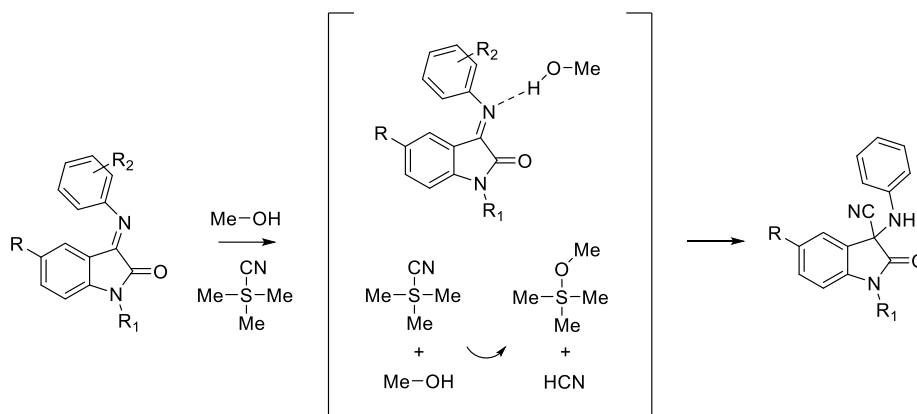
The results of the *in vitro* biological assay indicated that compound **15f**, with a benzyl group at the *N*^{1'} position and a fluorine atom at the *C*⁵ position, exhibited the best profile, thus we investigated various fluorinated compounds (**15i-p**), all of them bearing a benzyl group at the *N*^{1'} position.

For the preparation of all the final compounds, a previous pathway ^[93] was optimized and the ideal conditions of some reaction steps were achieved after critical attempts. The first improved step was the Strecker reaction. As shown above, α -amino nitriles **12a-n** were synthesized starting from the commercially available isatins **1-3**. Regarding the mechanism of this one-pot three-component condensation (Scheme 2a.2), we assumed that, in presence of acetic acid, the reaction of ketone with aniline readily provides the corresponding hemiaminal. ^[100] The obtained hydroxyl group, by attacking TMSCN, ensures the release of a cyanide that then promotes the elimination of an efficient leaving group, as well as the trimethylsilyloxy one (S_N2 substitution).



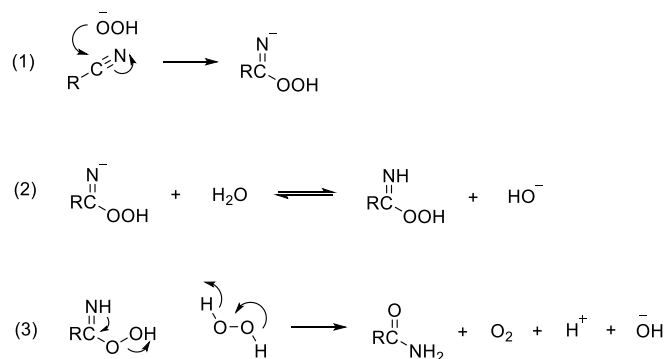
Scheme 2a.2: Proposed mechanism for preparation of compounds 12a-n.

For the synthesis of the α -amino nitriles **12o-p** we did not use the described one-pot strategy. In particular, we split the reaction into two steps in order to gain pure product with high yields (Scheme 2a.3): we first obtained ketimine intermediates that were then efficiently converted into the corresponding α -amino nitrile derivatives. Substituted anilines with a strong electron-withdrawing group (EWG), as CF₃, in the para/meta position were less nucleophilic compared to the others. To promote the reaction, it was necessary to push the complete conversion of isatin **7** to the corresponding ketimine intermediate by adding TMSCN at a later stage. Since the solvent acted as a catalyst, its choice was crucial. In this regard, the data showed that MeOH may activate ketimine intermediates via hydrogen-bonding (as a more electrophilic intermediate) and it may interact with TMSCN promoting the cyanide transfer (nucleophilic addition). [100] [101]



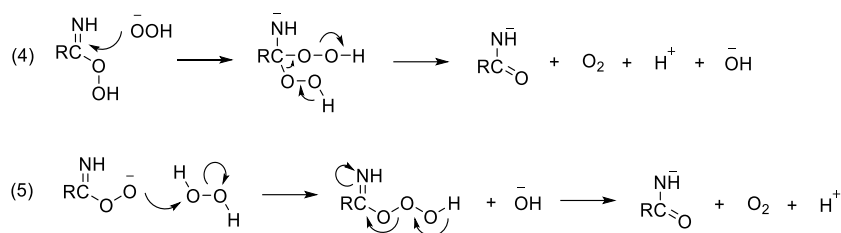
Scheme 2a.3: Two steps proposed mechanism for preparation of compounds 12o-p.

In the following step, the conversion of nitriles to amides, we did not perform an acid-catalyzed reaction but a base-catalyzed one. In fact, it has been noted that the isatin scaffold did not support the strong acid condition used in the previous work.^[93] For this reason, we explored the possibility to involve a different reaction setting that allowed the preparation of amino-amide derivatives (**13a-p**) through a base-catalysed conversion of nitriles to amides by hydrogen peroxide. The mechanism of this well-tolerated procedure at pH range 7-8 has been investigated by Wiberg. As shown below (Scheme 2a.4), Wiberg's mechanism, eq 1-3, involves nucleophilic attack of the anion of hydrogen peroxide on the nitrile carbon (1) followed by a rapid reaction of the intermediate peroxy-carboximidic acid with hydrogen peroxide (3).^[102]



Scheme 2a.4: Wiberg's mechanism.

However, Wiberg's mechanism cannot be operating exclusively. Edwards and co-workers have suggested that peroxy-carboximidic acid may decompose simultaneously via two distinctive paths: involving nucleophilic attack by the peroxy acid anion upon the carbonyl carbon of the peroxy acid (no scrambling, eq 4) or involving nucleophilic attack of the peroxy acid anion upon the outer oxygen of the peroxy acid (scrambling, eq 5) (see below Scheme 2a.5). They suggested that the transition states for these pathways must be of similar energy, but sp^2 carbon is the preferred site for attack.^[102]



Scheme 2a.5: Edwards' paths for the peroxycarboxylic acid decomposition.

Unlike to the spiropiperidine series, ^[93] the cyclization step using *N,N*-dimethylformamide dimethyl acetal (DMF-DMA) did not lead to the desired spiroisatin derivative. Specifically, in the first step, checking the reaction by MS (ESI), we found the molecular weight of the molecular ion corresponding to the expected product which was then appropriately isolated and purified. However, by NMR spectroscopy analysis, we did not detect the characteristic signals and, following an in-depth analysis of the ¹H NMR spectrum, we highlighted the hypothetical achievement of a product with a dimethylamino imine group (Fig. 2a.2).

In this regard, it is well-known that DMF-DMA is one of the commonly used reagents in the synthesis of many heterocyclic compounds and that it can react with different functional groups of organic compounds. [103] Methylene, methyl and amino groups are the most important of these functional groups, allowing the synthesis of the corresponding enamine, enamionone and dimethylamino imine structures. Concerning the organic compounds with amine, it has been shown that when they react with DMF-DMA they can form imine, as a result of condensation reaction. Especially, amino groups that act as nucleophiles attack the partially positive carbon atom of the DMF-DMA reagent to give the imine group. The reaction mechanism is similar to the addition of amino group into carbonyl groups.

With regard to the final compound **15a**, shown as an example of the series (Fig. 2a.2), the ¹H NMR spectrum shows the typical signals of the assumed dimethylamino imine intermediate. In particular, the relevant peaks are: singlet at 8.45 ppm corresponding to the imminic proton (in red) and singlets at 3.07 ppm and 2.85 ppm matching to the protons of the two methyl groups of the dimethylamine unit (in blue).

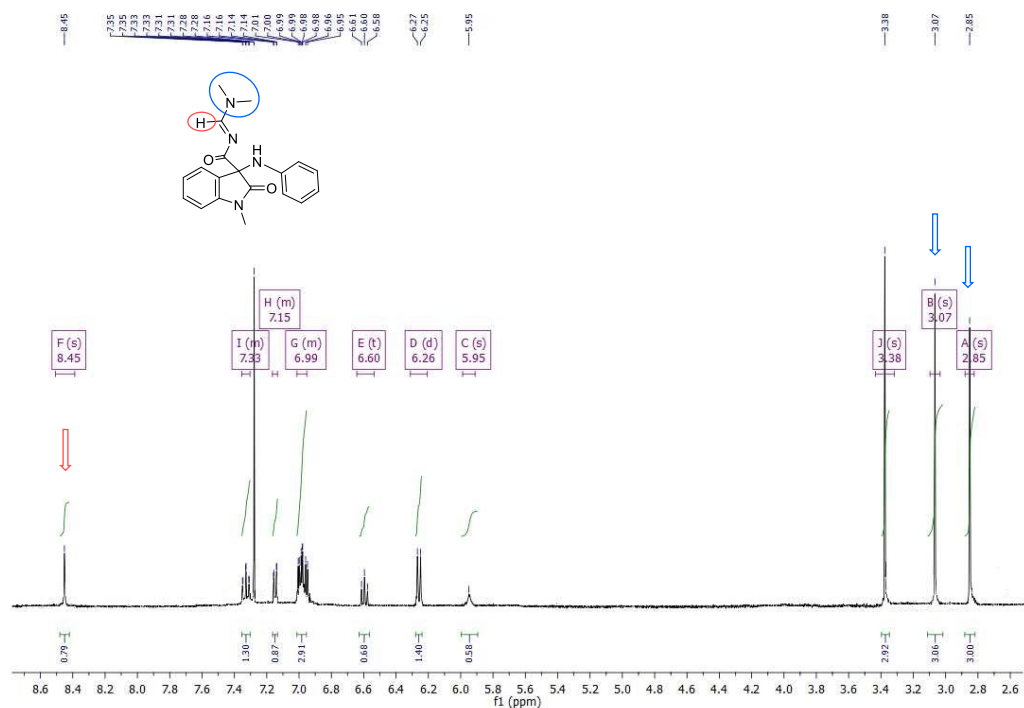


Figure 2a.2: ^1H NMR spectrum of the dimethylamino imine intermediate.

Once attributed the putative product obtained by treating the amino-amide intermediate with DMF-DMA, we focused on the next step. Since we observed the molecular weight of the desired spiro derivative by mass spectrometry, and considering that the mass sample was prepared in a solution of acetonitrile, water and trifluoroacetic acid (60/40/0.1), we assumed that an acidic catalysis may promote the nucleophilic attack of the aromatic amine, making the dimethylamine unit a better leaving group. Thus, we dissolved the intermediate in MeOH and added few drops of acetic acid (AcOH) to this solution, heating the mixture at 55°C . After 1h, we observed, by TLC, a complete conversion of the intermediate and after purification, NMR confirmed its structure. In particular, we observed that: singlet at 8.45 ppm of the imminic proton was replaced by a singlet at 9.80 ppm, corresponding to the proton of the spiro cycle, and above all, the singlets of protons of the two methyl groups of the dimethylamine unit were not detected (Fig. 2a.3).

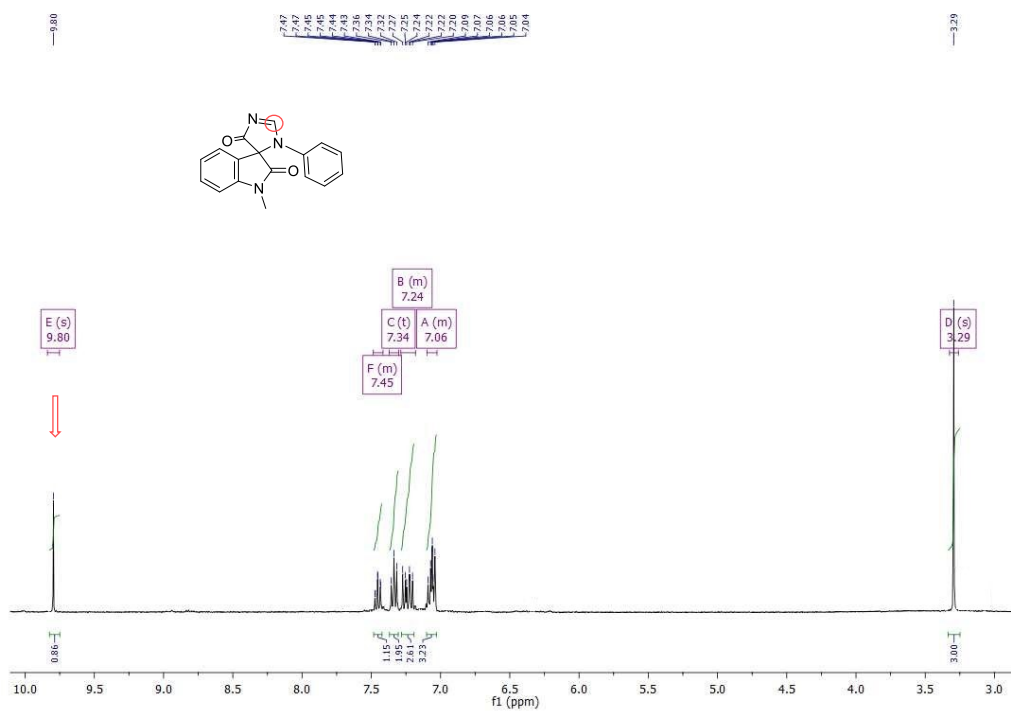


Figure 2a.3: ^1H NMR spectrum of the unsaturated spiro derivative.

Lastly, the saturated spiro cycle was quickly obtained by treatment with the reducing agent NaBH_4 . As indicated by ^1H NMR spectrum we noted the emergence of the typical peaks as a singlet at 9.43 ppm of the amidic proton (in red) and two doublets of protons of the obtained saturated carbon (in blue, Fig. 2a.4).

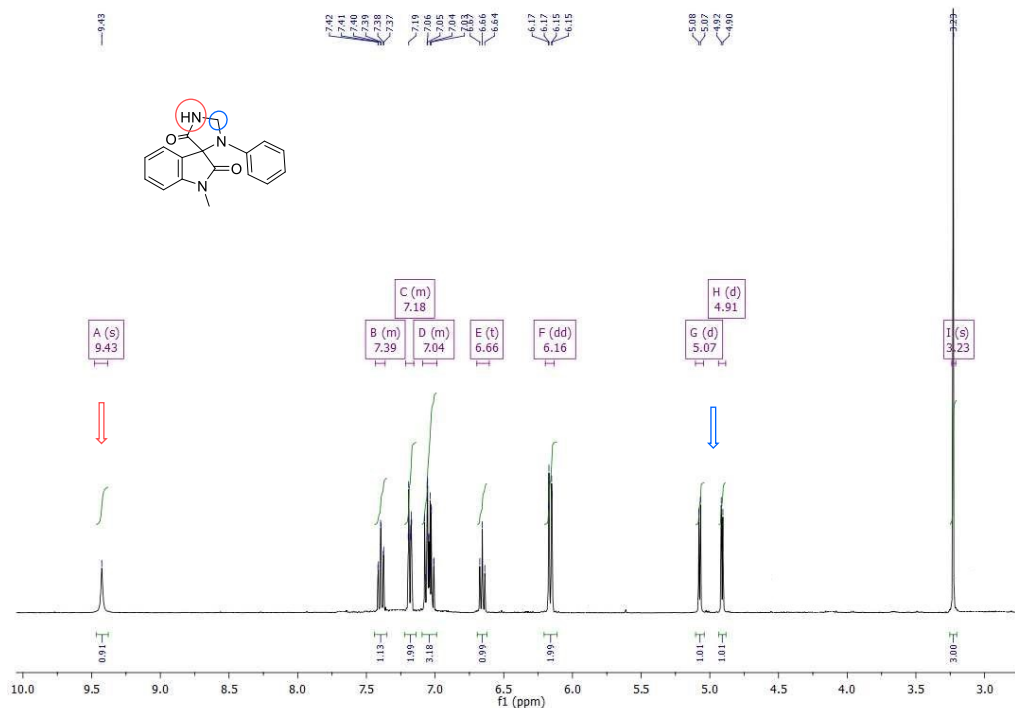


Figure 2a.4: ^1H NMR spectrum of the saturated spiro derivative.

As detailed above, we have optimized some steps. Regarding the formation of the imidazolidinone spirocycle, it was a very critical step and, the difficulties encountered could be attributed to the distinctive chemical behaviour of the isatin moiety. In fact, in contrast to the spiropiperidine series of the previous work, ^[93] herein we designed the same spiro imidazolidinonic cycle on a five-member ring and not on a six one. It can be speculated that due to ring strain the five-member ring of isatin hinders the formation of the desired spiro bicycle, requiring an acid catalysis.

2a.2.2 Biological evaluation.

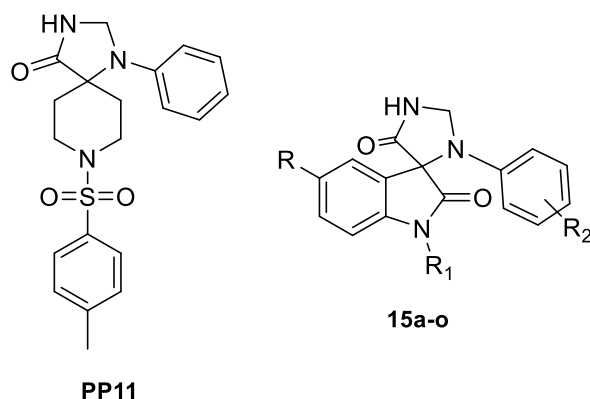
The biological assays reported below were realized in collaboration with the research group of Professor Paolo Pinton of the University of Ferrara (Dept. of Medical Sciences).

Preliminary screening-cobalt-calcein assay.

Mitochondrial permeability transition (MPT) is a fascinating but quite obscure event that needs careful investigation in living cells. For this reason, three different methods that can be exploited to monitor mPTP activity have been described: the cobalt-calcein assay, mitochondrial membrane depolarization, and the swelling technique.

Herein we measured the biological activity of all the investigated final compounds in human ventricular cardiomyocytes (AC16) by using the cobalt-calcein assay. A preliminary screening of the synthesized derivatives with this type of assay has been performed as it efficiently allows measuring mPTP opening. Briefly, the protocol is based on the decrease in calcein fluorescence, which is directly related to the mPTP opening. ^[104] Compounds that prevent cobalt (Co^{2+}) entry into mitochondria and calcein quenching, in the first minute post stimulation with ionomycin, are active as potential inhibitors of mPTP opening. In this condition, the slope of the calcein fluorescence trace (in terms of kinetics data) is lower compared to that of the vehicle.

Table 2a.1: *In vitro* potency of the novel spiro-isatin derivatives as mPTP opening inhibitors.



Compd	R	R ₁	R ₂	mPTP inhibition (% ₁ , 1μM)	Statistic
PP11	-	-	-	40,19	P<0.0001
15a (MF 18)	H	Me	H	49,18	P<0.0001
15b (MF 19)	F	Me	H	47,39	P<0.0001
15c (MF 22)	OMe	Me	H	42,59	P<0.0001
15d (MF 20)	H	Me	4-Cl	44,77	P<0.0001
15e (MF 15)	H	Bn	H	51,90	P<0.0001
15f (MF 16)	F	Bn	H	62,60	P<0.0001
15g (MF 17)	OMe	Bn	H	59,48	P<0.0001
15h (MF 21)	H	Bn	4-Cl	54,22	P<0.0001
15i (MF 44)	H	Bn	4-F	4,86	n.s.
15j (MF 45)	F	Bn	4-F	11,37	P<0.05
15k (MF 46)	H	4-F-Bn	H	20,64	P<0.0001
15l (MF 47)	F	4-F-Bn	H	4,17	n.s.
15m (MF 48)	H	4-F-Bn	F	6,43	n.s.
15n (MF 49)	F	4-F-Bn	F	-8,71	n.s.
15o (MF 50)	H	Bn	3-CF ₃	19,99	P<0.0001
15p (MF 51)	H	Bn	4-CF ₃	-21,06	n.s.

As shown in Table 2a.1, many of the first synthesized derivatives exhibited an encouraging *in vitro* potency against the target. In detail, it is well-known that substitution of a hydrogen atom by a fluorine one is a common classical bioisosteric replacement. Indeed, it has been reviewed that the incorporation of fluorine into a biologically active compound can simultaneously influence the electronic, lipophilic and steric parameters and could critically

improve the pharmacokinetics increasing the intrinsic activity and the chemical stability.^[105] Since replacement of hydrogen by fluorine enhances lipophilicity and functional groups such as CF₃, CF₃O and CF₃S are the most lipophilic groups known, we also evaluated the effects of placing a strong EWG, as CF₃, at the para/meta position of the N³ phenyl ring. Unfortunately, this planned series (compounds **15i-p**) did not show an improvement in terms of potency against mPTP opening. In particular, the biological results obtained through the *in vitro* screening highlighted that the placement of different substitutions at the N³-phenyl ring and/or at the N^{1'}-benzyl group could be not well tolerated in the mechanism of mPTP inhibition.

However, the addition of 1 μM ionomycin to cells pretreated with 1 μM **15f** resulted in desensitization of mPTP opening by approximately 62%. Because **15f** was selected as a potent spiro derivative, additional *in vitro* assays were performed to explore its biological behaviour towards the target.

Biological profile of the most promising compound (15f).

Overall, the preliminary *in vitro* assay revealed compound **15f** as a potent inhibitor with the greatest effects on reducing calcein quenching (Table 2a.1) compared to **PP11** (reference compound).

Given the crucial role of the c-subunit in ATP synthase assembly and cellular energy production as a component of the membrane rotor, the basal mitochondrial ATP content and agonist-induced ATP production were monitored by the luciferin-luciferase method.^[106] The most sensitive and reliable technique for measuring ATP is based on the bio luminescent luciferin-luciferase reaction. Luciferase is an enzyme derived from the North American firefly *Photinus pyralis* that chemically generates light as a byproduct of the oxidation of the small-molecule substrate D-luciferin. Especially, the reaction catalyzed by luciferase in the presence of magnesium ions implicates the conversion of D-luciferin into oxyluciferin, producing a flash of yellow-green light proportional to the amount of ATP present. The *in vitro* luciferin-luciferase assay includes cell transfection and expression of a luciferase probe targeted to a given organelle and the detection of the yellow-green light by a luminometer. It is known that increased mitochondrial Ca²⁺ accumulation induced by agonist stimulation triggers activation of the mitochondrial metabolic machinery. Therefore, not only the basal mitochondrial ATP content but also Ca²⁺-stimulated ATP synthesis can be measured.

Especially, we aimed to assess the effects of **15f** either at resting conditions (normoxia) or at hypoxia (2h) - reoxygenation (48h) conditions. As depicted in Figure 2a.5 panel A and panel D, compound **15f** did not affect the basal mitochondrial ATP content, and it slightly but significantly increased the relative amount of ATP upon Bradykinin/Histamine

(Brad/His) induced calcium uptake at hypoxia-reperfusion conditions (Fig. 2a.5, panel E).

[107]

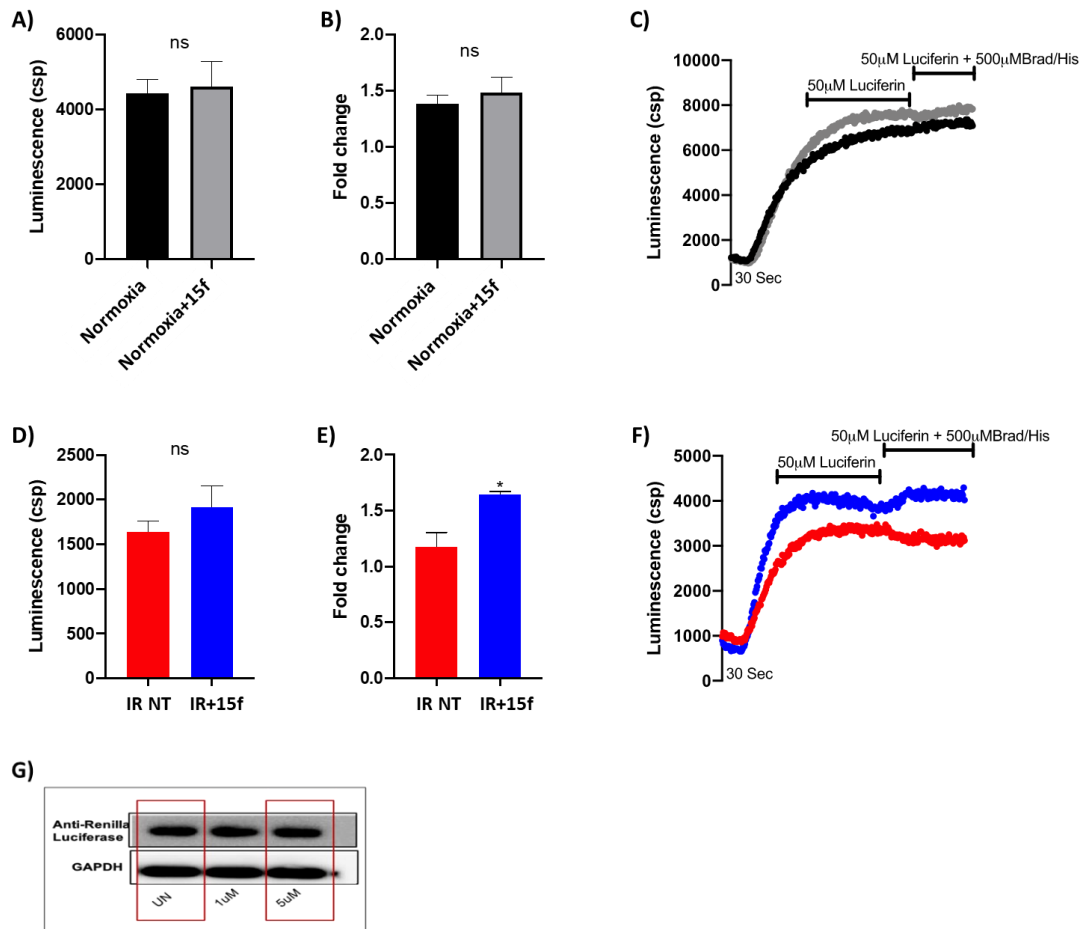


Figure 2a.5: A) Mitochondrial ATP content in living cells at resting conditions (normoxia) using the luciferase-luciferin method. B) Mitochondrial ATP production upon agonist-induced Ca^{2+} uptake in living cells at resting conditions (normoxia) using the luciferase-luciferin method. C) Representative kinetics of the luciferase-luciferin assay at resting conditions (normoxia). D) Mitochondrial ATP content in living cells at hypoxia-reperfusion conditions using the luciferase-luciferin method. E) Mitochondrial ATP production in living cells upon agonist-induced Ca^{2+} uptake at hypoxia-reperfusion conditions using the luciferase-luciferin method. F) Representative kinetics of the luciferase-luciferin assay at hypoxia-reperfusion conditions. G) Immunoblot assay with an antibody against luciferase. Brad/His indicate the agonists (500 μ M) used to induce Ca^{2+} -dependent ATP production. NT: untreated. IR: hypoxia-reperfusion. ns: not significant. (*) p value < 0.05. (**) p value < 0.01. (***) p value < 0.0001.

In addition, in order to evaluate the cardioprotective effect of compound **15f**, a cell-death assay and a cell-viability assay were performed, by western blot and fluorescence flow cytometry respectively. In Figure 2a.6 panel A is depicted the western blot of the two proteins engaged in the mechanism of cell-death, cleaved Parp and cleaved Caspase 3, besides the β -Actin as well as an internal control. In a context of hypoxia-reoxygenation, it can be noticed that the levels of cleaved Parp and cleaved Caspase 3 are reduced comparing the untreated sample and the treated one with compound **15f**. In Figure 2a.6 panel B are

reported the relative cell-viability in various settings. The assay was executed by using propidium iodide (PI) and fluorescein isothiocyanate (FITC)-labeled annexin V (annexin V-FITC) to selectively detect in culture the necrotic and apoptotic cells respectively. In particular, the blue bar highlights that the relative cell viability is improved when, in a context of hypoxia-reoxygenation, compound **15f** (5 μ M) is administered during reperfusion.

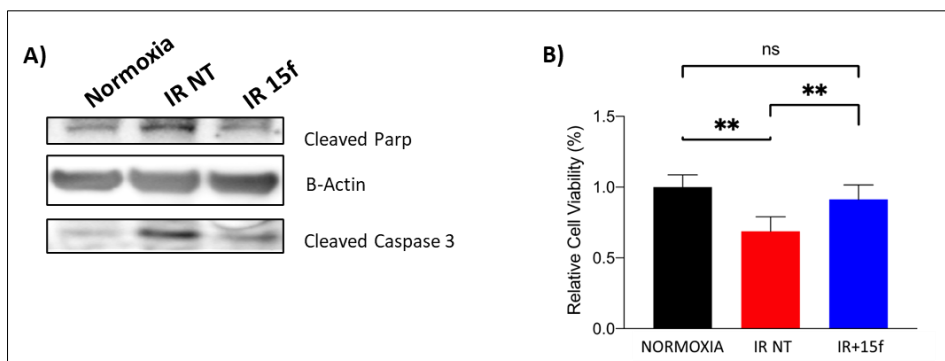


Figure 2a.6: A) Western blot. B) Cell-viability assay. NT: untreated. IR: hypoxia-reperfusion. ns: not significant. (*) p value < 0.05. (**) p value < 0.01. (****) p value < 0.0001.

Notably, compound **15f** was selected from a cobalt-calcein preliminary screening as the most promising derivatives, and as a result of its ability to increase the relative cell viability and to protect cells from cell death, it can also be considered as a useful cardioprotective agent. Therefore, considering its encouraging biological profile, it will be attractive to inquire the mechanism by which compound **15f** can improve the ATP production upon Brad/His induced calcium uptake, besides the possible engagement of the c-subunit in its inhibitory activity on the mPTP target.

2a.3 EXPERIMENTAL SECTION.

2a.3.1 Materials and Methods.

Reagents and solvents were provided by BLD, Fluorochem and Sigma-Aldrich.

Reaction progress and product mixture were monitored by thin-layer chromatography (TLC) on pre-coated F₂₅₄ Macherey-Nagel plates of silica gel, visualized with a UV lamp (254 nm light source), and/or by ESI MICROMASS ZMD 2000 electrospray mass spectrometer, after dissolution of compounds in a solution composed by 40:60:0.1 of H₂O:CH₃CN:TFA. Compounds were purified by crystallization/trituration, flash chromatography or via reverse-phase purification using a Waters Delta 600 high-performance liquid chromatography (HPLC) system with a Jupiter column C18 (250 × 30 mm, 300 Å, 15 μ m spherical particle size), using a binary mobile phase consisting of solution A (100% H₂O, 0.1% v/v TFA) and solution B (40% H₂O, 60% CH₃CN, 0.1% v/v TFA) at a flow rate of 20 mL/min. Gradient

was established individually considering the analytical HPLC profile of the crude product. Analytical HPLC was performed with a Beckman 126 liquid chromatograph furnished of a UV detector Beckman 168 and equipped with KARAT32 software. The purity of all the derivatives was assessed with an Agilent Zorbax C18 column (4.6×150 mm, $3.5 \mu\text{m}$ particle size) at a flow rate of 0.7 mL/min using a linear gradient from 100% of A (water + 0.1% TFA) to 100% of B (acetonitrile + 0.1% TFA) over a period of 25 min. All final compounds were monitored at 220 nm showing $\geq 96\%$ purity. ^1H NMR and ^{13}C NMR spectra were performed on a Varian Mercury Plus 400 MHz spectrometer. The signals were referenced to residual ^1H shift of the deuterated solvents (respectively δ H 7.26 for CDCl_3 ; δ H 2.50 for $\text{DMSO-}d_6$). Chemical shifts (δ) are expressed in parts per million (ppm) using the peak of deuterated solvents as an internal standard, while values of coupling constants (J) are reported in Hertz (Hz). Splitting patterns are designed as s, singlet; d, doublet; dd, double doublet; t, triplet; m, multiplet; and bs, broad signal. Melting points for purified products were determined in a glass capillary on a Stuart Scientific electrothermal apparatus SMP30.

2a.3.2 General synthetic procedures.

General procedure for the preparation of compounds 4-6.

NaH (60% dispersion in mineral oil, 1.1 eq) was added to a cooled solution of derivatives **1-3** (1 eq, 6.8 mmol) in DMF (25 mL), and the mixture was stirred at 0°C for 15 min. MeI (1.1 eq) was successively added dropwise and the reaction mixture was stirred at 0°C for 2 h and at room temperature for 1 h. Upon completion, as indicated by TLC and MS (ESI), the mixture was concentrated under vacuum. The resulting residue was then extracted with EtOAc (3x15 mL), and the combined organic layers were washed with water (1x15 mL), brine (1x10 mL) and dried over Na_2SO_4 . The solvent was then evaporated to obtain a solid, which was triturated (Et_2O) and filtered to yield derivatives **4-6** as orange-red solids, used in the next step without further purification. ^[108]

1-methylindoline-2,3-dione (4): Orange solid (yield 81%). ^1H NMR (400 MHz, $\text{DMSO-}d_6$) δ 7.68-7.62 (m, 1H), 7.52 (dd, $J = 8.0, 2.0$ Hz, 1H), 7.13-7.08 (m, 2H), 3.12 (s, 3H). MS (ESI): calculated for $\text{C}_9\text{H}_8\text{NO}_2$ $[\text{M}+\text{H}]^+$ 162.06; found 162.45.

5-fluoro-1-methylindoline-2,3-dione (5): Dark orange solid (yield 85%). ^1H NMR (400 MHz, $\text{DMSO-}d_6$) δ 7.58-7.52 (m, 1H), 7.47-7.43 (m, 1H), 7.20-7.14 (m, 1H), 3.14 (s, 3H). MS (ESI): calculated for $\text{C}_9\text{H}_7\text{FNO}_2$ $[\text{M}+\text{H}]^+$ 180.05; found 180.12.

5-methoxy-1-methylindoline-2,3-dione (6): Red solid (yield 71%). ¹H NMR (400 MHz, DMSO-d₆) δ 7.26-7.21 (m, 1H), 7.11-7.09 (m, 1H), 7.06 (d, *J* = 8.0 Hz, 1H), 3.75 (s, 3H), 3.09 (s, 3H). MS (ESI): calculated for C₁₀H₁₀NO₃ [M+H]⁺ 192.07; found 192.14.

General procedure for the preparation of compounds 7-11.

K₂CO₃ (3 eq) and the appropriate benzyl bromide (1.5 eq) were added to a solution of derivatives **1-3** (1 eq, 6.8 mmol) in MeCN (0.10 M) at room temperature. The resulting mixture was then heated at reflux overnight. Upon completion, as indicated by TLC and MS (ESI), the reaction mixture was cooled, filtered and concentrated. The crude residue was then triturated (Et₂O) and filtered to yield derivatives **7-11** as orange-red solids, which were used in the next step without further purification. ^[109]

1-benzylindoline-2,3-dione (7): Orange solid (yield 82%). ¹H NMR (400 MHz, DMSO-d₆) δ 7.62-7.54 (m, 2H), 7.43 (d, *J* = 7.2 Hz, 2H), 7.39-7.24 (m, 3H), 7.14-7.08 (m, 1H), 6.97 (d, *J* = 8.4 Hz, 1H), 4.91 (s, 2H). MS (ESI): calculated for C₁₅H₁₂NO₂ [M+H]⁺ 238.09; found 238.30.

1-benzyl-5-fluoroindoline-2,3-dione (8): Dark orange solid (yield 89%). ¹H NMR (400 MHz, DMSO-d₆) δ 7.53-7.40 (m, 4H), 7.38-7.24 (m, 3H), 6.98-6.93 (m, 1H), 4.91 (s, 2H). MS (ESI): calculated for C₁₅H₁₁FNO₂ [M+H]⁺ 256.08; found 256.37.

1-benzyl-5-methoxyindoline-2,3-dione (9): Red solid (yield 93%). ¹H NMR (400 MHz, DMSO-d₆) δ 7.44-7.39 (m, 2H), 7.37-7.24 (m, 3H) 7.19-7.14 (m, 2H), 6.93-6.87 (m, 1H), 4.88 (s, 2H), 3.74 (s, 3H). MS (ESI): calculated for C₁₆H₁₄NO₃ [M+H]⁺ 268.10; found 268.25.

1-(4-fluorobenzyl)indoline-2,3-dione (10): Dark orange solid (yield 79%). ¹H NMR (400 MHz, DMSO-d₆) δ 7.62-7.44 (m, 4H), 7.24 -7.04 (m, 3H), 6.98 (d, *J* = 7.7 Hz, 1H), 4.90 (s, 2H). MS (ESI): calculated for C₁₅H₁₁FNO₂ [M+H]⁺ 256.08; found 256.17.

5-fluoro-1-(4-fluorobenzyl)indoline-2,3-dione (11): Red solid (yield 78%). ¹H NMR (400 MHz, CDCl₃) δ 7.37-7.29 (m, 3H), 7.26-7.19 (m, 1H), 7.10-7.03 (m, 2H), 6.76-6.71 (m, 1H), 4.91 (s, 2H). MS (ESI): calculated for C₁₅H₁₀F₂NO₂ [M+H]⁺ 274.07; found 274.30.

General procedure for the preparation of compounds 12a-n.

To a solution of derivatives **4-11** (1 eq, 4.2 mmol) in glacial AcOH (15 mL) was added the appropriate aniline (1 eq) at 0°C. Trimethylsilyl cyanide (TMSCN) (3 eq) was then added at 0°C and the reaction mixture was stirred at room temperature overnight. Upon completion, as indicated by TLC and MS (ESI), the reaction mixture was basified to pH 10 using 2M

NaOH and suspended with Ac₂OEt (20 mL). The organic layers were then washed with water (2x15 mL), brine (1x10 mL) and dried over Na₂SO₄. The solvent was evaporated under reduced pressure to give a crude solid residue, which was triturated (Et₂O) and filtered. Derivatives **12a-n** were obtained as pale orange solids and used in the next step without further purification.

1-methyl-2-oxo-3-(phenylamino)indoline-3-carbonitrile (12a): Pale orange solid (yield 59%). ¹H NMR (400 MHz, DMSO-d₆) δ 7.59-7.49 (m, 2H), 7.26-7.18 (m, 2H), 7.15 (s, 1H), 7.13-7.07 (m, 2H), 6.77-6.71 (m, 3H), 3.25 (s, 3H). MS (ESI): calculated for C₁₆H₁₄N₃O [M+H]⁺ 264.11; found 264.26.

5-fluoro-1-methyl-2-oxo-3-(phenylamino)indoline-3-carbonitrile (12b): Pale orange solid (yield 52%). ¹H NMR (400 MHz, DMSO-d₆) δ 7.54 (dd, *J* = 7.7, 2.7 Hz, 1H), 7.46-7.38 (m, 1H), 7.29-7.23 (m, 1H), 7.18 (s, 1H), 7.15-7.08 (m, 2H), 6.76-6.73 (m, 3H), 3.25 (s, 3H). MS (ESI): calculated for C₁₆H₁₃FN₃O [M+H]⁺ 282.10; found 282.34.

5-methoxy-1-methyl-2-oxo-3-(phenylamino)indoline-3-carbonitrile (12c): Pale orange solid (yield 54%). ¹H NMR (400 MHz, DMSO-d₆) δ 7.17-7.11 (m, 2H), 7.12-7.04 (m, 4H), 6.73-6.68 (m, 3H), 3.73 (s, 3H), 3.21 (s, 3H). MS (ESI): calculated for C₁₇H₁₆N₃O₂ [M+H]⁺ 294.12; found 294.04.

3-((4-chlorophenyl)amino)-1-methyl-2-oxoindoline-3-carbonitrile (12d): Pale orange solid (yield 48%). ¹H NMR (400 MHz, DMSO-d₆) δ 7.62-7.50 (m, 2H), 7.29 (s, 1H), 7.26-7.14 (m, 4H), 6.83-6.80 (m, 2H), 3.24 (s, 3H). MS (ESI): calculated for C₁₆H₁₃ClN₃O [M+H]⁺ 298.07; found 298.27.

1-benzyl-2-oxo-3-(phenylamino)indoline-3-carbonitrile (12e): Pale orange solid (yield 75%). ¹H NMR (400 MHz, DMSO-d₆) δ 7.62-7.56 (m, 1H), 7.47-7.43 (m, 1H), 7.39-7.25 (m, 6H), 7.21-7.16 (m, 2H), 7.06-7.00 (m, 2H), 6.74 (t, *J* = 7.3 Hz, 1H), 6.71-6.63 (m, 2H), 5.07 (d, *J* = 15.7 Hz, 1H), 4.94 (d, *J* = 15.7 Hz, 1H). MS (ESI): calculated for C₂₂H₁₈N₃O [M+H]⁺ 340.14; found 340.35.

1-benzyl-5-fluoro-2-oxo-3-(phenylamino)indoline-3-carbonitrile (12f): Pale orange solid (yield 72%). ¹H NMR (400 MHz, DMSO-d₆) δ 7.58 (dd, *J* = 7.6, 2.7 Hz, 1H), 7.39-7.27 (m, 7H), 7.24-7.18 (m, 1H), 7.10-6.99 (m, 2H), 6.81-6.71 (m, 1H), 6.67 (dd, *J* = 8.6, 1.0 Hz, 2H), 5.08 (d, *J* = 15.7 Hz, 1H), 4.94 (d, *J* = 15.7 Hz, 1H). MS (ESI): calculated for C₂₂H₁₇FN₃O [M+H]⁺ 358.14; found 358.30.

1-benzyl-5-methoxy-2-oxo-3-(phenylamino)indoline-3-carbonitrile (12g): Pale orange solid (yield 81%). ¹H NMR (400 MHz, DMSO-d₆) δ 7.38-7.26 (m, 6H), 7.21-7.18 (m, 1H), 7.13-7.09 (m, 1H), 7.06-6.99 (m, 3H), 6.74 (t, *J* = 7.3 Hz, 1H), 6.67-6.64 (m, 2H), 5.05 (d, *J* = 15.6 Hz, 1H), 4.94 (d, *J* = 15.6 Hz, 1H), 3.73 (s, 3H). MS (ESI): calculated for C₂₃H₂₀N₃O₂ [M+H]⁺ 370.16; found 370.24.

1-benzyl-3-((4-chlorophenyl)amino)-2-oxoindoline-3-carbonitrile (12h): Pale orange solid (yield 71%). ¹H NMR (400 MHz, DMSO-d₆) δ 7.63-7.59 (m, 1H), 7.48-7.44 (m, 1H), 7.40 (s, 1H), 7.37-7.25 (m, 5H), 7.22-7.16 (m, 2H), 7.11-7.05 (m, 2H), 6.77-6.69 (m, 2H), 5.03 (d, *J* = 15.7 Hz, 1H), 4.92 (d, *J* = 15.7 Hz, 1H). MS (ESI): calculated for C₂₂H₁₇ClN₃O [M+H]⁺ 374.11; found 374.21.

1-benzyl-3-((4-fluorophenyl)amino)-2-oxoindoline-3-carbonitrile (12i): Pale orange solid (yield 69%). ¹H NMR (400 MHz, DMSO-d₆) δ 7.61-7.57 (m, 1H), 7.48-7.06 (m, 9H), 6.94-6.86 (m, 2H), 6.79-6.71 (m, 2H), 5.02 (d, *J* = 15.7 Hz, 1H), 4.89 (d, *J* = 15.7 Hz, 1H). MS (ESI): calculated for C₂₂H₁₇FN₃O [M+H]⁺ = 358.14; found 358.56.

1-benzyl-5-fluoro-3-((4-fluorophenyl)amino)-2-oxoindoline-3-carbonitrile (12j): Pale orange solid (yield 71%). ¹H NMR (400 MHz, DMSO-d₆) δ 7.59 (dd, *J* = 7.7, 2.7 Hz, 1H), 7.35-7.26 (m, 6H), 7.17-7.12 (m, 1H), 7.11 (s, 1H), 6.91 (t, *J* = 8.9 Hz, 2H), 6.79-6.72 (m, 2H), 5.02 (d, *J* = 15.8 Hz, 1H), 4.88 (d, *J* = 15.8 Hz, 1H). MS (ESI): calculated for C₂₂H₁₆F₂N₃O [M+H]⁺ 376.13; found 376.24.

1-(4-fluorobenzyl)-2-oxo-3-(phenylamino)indoline-3-carbonitrile (12k): Pale orange solid (yield 84%). ¹H NMR (400 MHz, DMSO-d₆) δ 7.60-7.56 (m, 1H), 7.48-7.42 (m, 1H), 7.38-7.32 (m, 2H), 7.27 (s, 1H), 7.23-7.14 (m, 4H), 7.04-6.99 (m, 2H), 6.75-6.70 (m, 1H), 6.66-6.60 (m, 2H), 5.04 (d, *J* = 15.6 Hz, 1H), 4.91 (d, *J* = 15.6 Hz, 1H). MS (ESI): calculated for C₂₂H₁₇FN₃O [M+H]⁺ 358.14; found 358.71.

5-fluoro-1-(4-fluorobenzyl)-2-oxo-3-(phenylamino)indoline-3-carbonitrile (12l): Pale orange solid (yield 87%). ¹H NMR (400 MHz, DMSO-d₆) δ 7.56 (dd, *J* = 7.6, 2.6 Hz, 1H), 7.37-7.32 (m, 3H), 7.28 (s, 1H), 7.26-7.22 (m, 1H), 7.21-7.13 (m, 2H), 7.05-7.00 (m, 2H), 6.77-6.72 (m, 1H), 6.66-6.61 (m, 2H), 5.04 (d, *J* = 15.6 Hz, 1H), 4.91 (d, *J* = 15.6 Hz, 1H). MS (ESI): calculated for C₂₂H₁₆F₂N₃O [M+H]⁺ 376.13; found 376.42.

1-(4-fluorobenzyl)-3-((4-fluorophenyl)amino)-2-oxoindoline-3-carbonitrile (12m): Pale orange solid (yield 89%). ¹H NMR (400 MHz, DMSO-d₆) δ 7.61-7.57 (m, 1H), 7.48-7.42 (m, 1H), 7.30 (dd, *J* = 8.80, 5.40 Hz, 2H), 7.22-7.13 (m, 5H), 7.10 (s, 1H), 6.90 (t, *J* = 8.9

Hz, 2H), 6.76-6.71 (m, 2H), 5.01 (d, $J = 15.7$ Hz, 1H), 4.88 (d, $J = 15.7$ Hz, 1H). MS (ESI): calculated for $C_{22}H_{16}F_2N_3O$ $[M+H]^+$ 376.13; found 376.68.

5-fluoro-1-(4-fluorobenzyl)-3-((4-fluorophenyl)amino)-2-oxindoline-3-carbonitrile

(12n): Pale orange solid (yield 83%). 1H NMR (400 MHz, DMSO- d_6) δ 7.60 (dd, $J = 7.7$, 2.7 Hz, 1H), 7.37-7.26 (m, 3H), 7.23-7.12 (m, 3H), 7.11 (s, 1H), 6.96-6.88 (m, 2H), 6.77-6.72 (m, 2H), 5.00 (d, $J = 15.7$ Hz, 1H), 4.87 (d, $J = 15.7$ Hz, 1H). MS (ESI): calculated for $C_{22}H_{15}F_3N_3O$ $[M+H]^+$ 394.12, found 394.41.

General procedure for the preparation of compounds 12o-p.

To a solution of derivative **7** (1 eq, 4.2 mmol) in glacial AcOH (15 mL) was added the appropriate aniline (1 eq) at 0°C, and the mixture was stirred at room temperature for 3 h. Upon completion, as indicated by TLC, the solution was basified to pH 10 using 2M NaOH and suspended with Ac₂OEt (20 mL). The organic layers were washed with water (2x15 mL), brine (1x10 mL) and dried over Na₂SO₄. The solvent was then evaporated under reduced pressure to give imine intermediates, as orange solids, which were used in the next step without further purification.

To a solution of the obtained imine intermediates (1 eq, 4.0 mmol) in MeOH (15 mL) was added TMSCN, and the mixture was stirring at 50°C for 18 h. Upon completion, as indicated by TLC and MS (ESI), the solution was basified to pH 10 using a solution NaHCO₃ 5%. The resulting mixture was then suspended with Ac₂OEt (20 mL), and then washed with water (2x15 mL), brine (1x10 mL) and dried over Na₂SO₄. The organic layers were evaporated under reduced pressure to give a solid residue which was purified by flash chromatography (EtOAc/PE as the eluent). Derivatives **12o-p** were obtained as orange pale solids.

1-benzyl-2-oxo-3-((3-(trifluoromethyl)phenyl)amino)indoline-3-carbonitrile (12o):

Orange solid (yield 49%). 1H NMR (400 MHz, DMSO- d_6) δ 7.69-7.62 (m, 2H), 7.52-7.45 (m, 1H), 7.34-7.25 (m, 6H), 7.25-7.18 (m, 3H), 7.10-7.05 (m, 1H), 7.03-6.98 (m, 1H), 5.03 (d, $J = 15.8$ Hz, 1H), 4.94 (d, $J = 15.8$ Hz, 1H). MS (ESI): calculated for $C_{23}H_{17}F_3N_3O$ $[M+H]^+$ 408.13; found 408.68.

1-benzyl-2-oxo-3-((4-(trifluoromethyl)phenyl)amino)indoline-3-carbonitrile (12p):

Orange solid (yield 53%). 1H NMR (400 MHz, DMSO- d_6) δ 7.94 (s, 1H), 7.65-7.61 (m, 1H), 7.52-7.45 (m, 1H), 7.41-7.18 (m, 9H), 6.84 (d, $J = 8.5$ Hz, 2H), 5.04 (d, $J = 15.6$ Hz, 1H), 4.96 (d, $J = 15.6$ Hz, 1H). MS (ESI): calculated for $C_{23}H_{17}F_3N_3O$ $[M+H]^+$ 408.13; found 408.37.

General procedure for the preparation of compounds 13a-p.

Carbonitrile derivatives **12a-p** (1 eq, 3.0 mmol) was dissolved in acetone (25 mL) and stirred for 10 min. A solution 1N Na₂CO₃ (3eq) was then added to the reaction solution, followed by the addition of H₂O₂ (30% w/w, 27 eq). The resulting mixture was stirred at room temperature for 2 h. Upon completion, as indicated by TLC and MS (ESI), the volatile organic solvent was evaporated. The residue was suspended with CH₂Cl₂ (3x15 mL), and the organic layers were washed with water (2x15 mL), brine (1x10 mL) and dried over Na₂SO₄. The solvent was then evaporated under reduced pressure and the crude material was purified by flash chromatography (EtOAc/PE as the eluent) to yield derivatives **13a-p** as pale-yellow solids. ^[110]

1-methyl-2-oxo-3-(phenylamino)indoline-3-carboxamide (13a): Pale yellow solid (yield 70%). ¹H NMR (400 MHz, DMSO-d₆) δ 7.53 (s, 1H), 7.42-7.36 (m, 1H), 7.32-7.24 (m, 2H), 7.13 (d, *J* = 7.8 Hz, 1H), 7.08-7.02 (m, 1H), 6.94-6.91 (m, 2H), 6.54 (t, *J* = 7.3 Hz, 1H), 6.38-6.31 (m, 3H), 3.20 (s, 3H). MS (ESI): calculated for C₁₆H₁₆N₃O₂ [M+H]⁺ 282.12; found 282.26.

5-fluoro-1-methyl-2-oxo-3-(phenylamino)indoline-3-carboxamide (13b): Pale yellow solid (yield 46%). ¹H NMR (400 MHz, DMSO-d₆) δ 7.58 (s, 1H), 7.37 (s, 1H), 7.26-7.10 (m, 3H), 6.99-6.89 (m, 2H), 6.59-6.49 (m, 1H), 6.40 (s, 1H), 6.35-6.31 (m, 2H), 3.17 (s, 3H). MS (ESI): calculated for C₁₆H₁₅FN₃O₂ [M+H]⁺ 300.11; found 300.30.

5-methoxy-1-methyl-2-oxo-3-(phenylamino)indoline-3-carboxamide (13c): Pale yellow solid (yield 65%). ¹H NMR (400 MHz, DMSO-d₆) δ 7.50 (s, 1H), 7.26 (s, 1H), 7.08-7.01 (m, 1H), 6.96-6.86 (m, 4H), 6.60-6.45 (m, 1H), 6.38-6.27 (m, 3H), 3.67 (s, 3H), 3.15 (s, 3H). MS (ESI): calculated for C₁₇H₁₈N₃O₃ [M+H]⁺ 312.13; found 312.40.

3-((4-chlorophenyl)amino)-1-methyl-2-oxoindoline-3-carboxamide (13d): Pale yellow solid (yield 71%). ¹H NMR (400 MHz, DMSO-d₆) δ 7.52 (s, 1H), 7.41-7.34 (m, 2H), 7.32-7.26 (m, 1H), 7.14-7.02 (m, 2H), 7.00-6.93 (m, 2H), 6.56 (s, 1H), 6.43-6.37 (m, 2H), 3.17 (s, 3H). MS (ESI): calculated for C₁₆H₁₅ClN₃O₂ [M+H]⁺ 316.08; found 316.30.

1-benzyl-2-oxo-3-(phenylamino)indoline-3-carboxamide (13e): Pale yellow solid (yield 87%). ¹H NMR (400 MHz, DMSO-d₆) δ 7.58 (s, 1H), 7.49 (s, 1H), 7.45-7.20 (m, 7H), 7.07-6.94 (m, 2H), 6.93-6.84 (m, 2H), 6.59-6.54 (m, 1H), 6.49 (s, 1H), 6.42-6.37 (m, 2H), 5.02 (d, *J* = 15.7 Hz, 1H), 4.84 (d, *J* = 15.7 Hz, 1H). MS (ESI): calculated for C₂₂H₂₀N₃O₂ [M+H]⁺ 358.16; found 358.74.

1-benzyl-5-fluoro-2-oxo-3-(phenylamino)indoline-3-carboxamide (13f): Pale yellow solid (yield 73%). ¹H NMR (400 MHz, DMSO-d₆) δ 7.68-7.53 (m, 2H), 7.43-7.21 (m, 6H), 7.21-7.05 (m, 1H), 7.01-6.95 (m, 1H), 6.92-6.85 (m, 2H) 6.57 (t, *J* = 7.3 Hz, 2H), 6.38 (d, *J* = 7.7 Hz, 1H), 4.99 (d, *J* = 15.7 Hz, 1H), 4.84 (d, *J* = 15.7 Hz, 1H). MS (ESI): calculated for C₂₂H₁₉FN₃O₂ [M+H]⁺ 376.15; found 376.23.

1-benzyl-5-methoxy-2-oxo-3-(phenylamino)indoline-3-carboxamide (13g): Pale yellow solid (yield 60%). ¹H NMR (400 MHz, DMSO-d₆) δ 7.55 (s, 1H), 7.45 (s, 1H), 7.41-7.33 (m, 2H), 7.34-7.19 (m, 3H), 7.02-6.99 (m, 1H), 6.92-6.82 (m, 4H), 6.55 (t, *J* = 7.3 Hz, 1H), 6.47 (s, 1H), 6.37 (d, *J* = 7.7 Hz, 2H), 4.97 (d, *J* = 15.7 Hz, 1H), 4.79 (d, *J* = 15.7 Hz, 1H), 3.65 (s, 3H). MS (ESI): calculated for C₂₃H₂₂N₃O₃ [M+H]⁺ 388.17; found 388.24.

1-benzyl-3-((4-chlorophenyl)amino)-2-oxoindoline-3-carboxamide (13h): Pale yellow solid (yield 45%). ¹H NMR (400 MHz, DMSO-d₆) δ 7.59 (s, 2H), 7.45-7.24 (m, 7H), 7.07-6.98 (m, 2H), 6.95-6.89 (m, 2H), 6.73 (s, 1H), 6.52-6.43 (m, 2H), 4.97 (d, *J* = 15.7 Hz, 1H), 4.86 (d, *J* = 15.7 Hz, 1H). MS (ESI): calculated for C₂₂H₁₉ClN₃O₂ [M+H]⁺ 392.12; found 392.33.

1-benzyl-3-((4-fluorophenyl)amino)-2-oxoindoline-3-carboxamide (13i): Pale yellow solid (yield 63%). ¹H NMR (400 MHz, DMSO-d₆) δ 7.58-7.53 (m, 2H), 7.42-7.38 (m, 1H), 7.35-7.22 (m, 6H), 7.05-6.98 (m, 1H), 6.95 (d, *J* = 7.8 Hz, 1H), 6.76-6.68 (m, 2H), 6.47 (s, 1H), 6.46-6.39 (m, 2H), 4.95 (d, *J* = 15.8 Hz, 1H), 4.82 (d, *J* = 15.8 Hz, 1H). MS (ESI): C₂₂H₁₉FN₃O₂ [M+H]⁺ 376.15; found 376.29.

1-benzyl-5-fluoro-3-((4-fluorophenyl)amino)-2-oxoindoline-3-carboxamide (13j): Pale yellow solid (yield 61%). ¹H NMR (400 MHz, DMSO-d₆) δ 7.63 (s, 2H), 7.37-7.23 (m, 6H), 7.17-7.08 (m, 1H), 6.97-6.91 (m, 1H), 6.79-6.71 (m, 2H), 6.55 (s, 1H), 6.47-6.39 (m, 2H), 4.94 (d, *J* = 15.8 Hz, 1H), 4.84 (d, *J* = 15.8 Hz, 1H). MS (ESI): calculated for C₂₂H₁₈F₂N₃O₂ [M+H]⁺ 394.14; found 394.23.

1-(4-fluorobenzyl)-2-oxo-3-(phenylamino)indoline-3-carboxamide (13k): Pale yellow solid (yield 70%). ¹H NMR (400 MHz, DMSO-d₆) δ 7.56 (s, 1H), 7.49 (s, 1H), 7.45-7.38 (m, 2H), 7.36 (dd, *J* = 7.6, 1.1 Hz, 1H), 7.32-7.25 (m, 1H), 7.19-7.08 (m, 2H), 7.03-6.98 (m, 2H), 6.90-6.80 (m, 2H), 6.57-6.51 (m, 1H), 6.47 (s, 1H), 6.35 (dd, *J* = 8.7, 1.0 Hz, 2H), 4.97 (d, *J* = 15.7 Hz, 1H), 4.83 (d, *J* = 15.7 Hz, 1H). MS (ESI): calculated for C₂₂H₁₉FN₃O₂ [M+H]⁺ 376.15; found 376.33.

5-fluoro-1-(4-fluorobenzyl)-2-oxo-3-(phenylamino)indoline-3-carboxamide (13l): Pale yellow solid (yield 56%). ¹H NMR (400 MHz, DMSO-d₆) δ 7.64 (s, 1H), 7.58 (s, 1H), 7.48-7.35 (m, 2H), 7.30 (dd, *J* = 8.0, 2.7 Hz, 1H), 7.19-7.08 (m, 3H), 7.04-6.99 (m, 1H), 6.92-6.86 (m, 2H), 6.61-6.53 (m, 2H), 6.35 (dd, *J* = 8.6, 1.0 Hz, 2H), 4.96 (d, *J* = 15.7 Hz, 1H), 4.85 (d, *J* = 15.7 Hz, 1H). MS (ESI): calculated for C₂₂H₁₈F₂N₃O₂ [M+H]⁺ 394.14; found 394.68.

1-(4-fluorobenzyl)-3-((4-fluorophenyl)amino)-2-oxoindoline-3-carboxamide (13m): Pale yellow solid (yield 61%). ¹H NMR (400 MHz, DMSO-d₆) δ 7.62-7.58 (m, 2H), 7.45-7.36 (m, 3H), 7.33-7.27 (m, 1H), 7.19-7.11 (m, 2H), 7.08-6.98 (m, 2H), 6.78-6.72 (m, 2H), 6.51 (s, 1H), 6.47-6.41 (m, 2H), 4.94 (d, *J* = 15.7 Hz, 1H), 4.85 (d, *J* = 15.7 Hz, 1H). MS (ESI): calculated for C₂₂H₁₈F₂N₃O₂ [M+H]⁺ 394.14; found 394.05.

5-fluoro-1-(4-fluorobenzyl)-3-((4-fluorophenyl)amino)-2-oxoindoline-3-carboxamide (13n): Pale yellow solid (yield 58%). ¹H NMR (400 MHz, DMSO-d₆) δ 7.69-7.66 (m, 2H), 7.42-7.33 (m, 3H), 7.21-7.12 (m, 3H), 7.03-6.98 (m, 1H), 6.83-6.73 (m, 2H), 6.59 (s, 1H), 6.48-6.41 (m, 2H), 4.93 (d, *J* = 15.7 Hz, 1H), 4.87 (d, *J* = 15.7 Hz, 1H). MS (ESI): calculated for C₂₂H₁₇F₃N₃O₂ [M+H]⁺ 412.13; found 412.25.

1-benzyl-2-oxo-3-((3-(trifluoromethyl)phenyl)amino)indoline-3-carboxamide (13o): Pale yellow solid (yield 52%). ¹H NMR (400 MHz, DMSO-d₆) δ 7.69 (s, 1H), 7.60 (s, 1H), 7.44 (dd, *J* = 7.5, 0.9 Hz, 1H), 7.41-7.34 (m, 2H), 7.34-7.23 (m, 4H), 7.12-7.01 (m, 3H), 7.01-6.95 (m, 2H), 6.89-6.84 (m, 1H), 6.69-6.64 (m, 1H), 4.93 (d, *J* = 15.8 Hz, 1H), 4.88 (d, *J* = 15.8 Hz, 1H). MS (ESI): calculated for C₂₃H₁₉F₃N₃O₂ [M+H]⁺ 426.14; found 426.57.

1-benzyl-2-oxo-3-((4-(trifluoromethyl)phenyl)amino)indoline-3-carboxamide (13p): Pale yellow solid (yield 78%). ¹H NMR (400 MHz, DMSO-d₆) δ 7.65-7.58 (m, 2H), 7.40 (dd, *J* = 6.4, 1.5 Hz, 3H), 7.35-7.26 (m, 4H), 7.22-7.16 (m, 3H), 7.07-7.01 (m, 2H), 6.58 (d, *J* = 8.6 Hz, 2H), 4.96 (d, *J* = 15.7 Hz, 1H), 4.87 (d, *J* = 15.7 Hz, 1H). MS (ESI): calculated for C₂₃H₁₉F₃N₃O₂ [M+H]⁺ 426.14; found 426.30.

General procedure for the preparation of compounds 14a-p.

To a solution of carboxamide derivatives **13a-p** (1 eq, 1.3 mmol) in MeOH (5 mL) was added DMF-DMA (3 eq) and the reaction mixture was then stirred at 55°C for 1-2 h. After formation of the formamidine intermediates, as indicated by TLC, few drops of AcOH were added to the mixture, which was stirred at 55°C for 2 h. Upon completion, as indicated by TLC, the volatile fraction was evaporated and the crude residue was suspended with EtOAc (3x15 mL). The organic layers were washed with water (1x10 mL), brine (1x10 mL), and

dried over Na₂SO₄. The solvent was then evaporated under reduced pressure and the obtained crude residue was purified by flash chromatography (AcOEt/PE as the eluent) to yield bicyclic derivatives **14a-p** as pale white solids. In addition, a small amount of derivatives **14a-p** was then purified by semi-preparative HPLC to improve the chemical characterization performed by NMR.

1'-methyl-3-phenylspiro[imidazole-4,3'-indoline]-2',5(3H)-dione (14a): Pale white solid (yield 37%). ¹H NMR (400 MHz, DMSO-d₆) δ 9.80 (s, 1H), 7.48-7.42 (m, 1H), 7.34 (t, *J* = 8.0 Hz, 2H), 7.28-7.16 (m, 3H), 7.09-7.04 (m, 3H), 3.29 (s, 3H). MS (ESI): calculated for C₁₇H₁₄N₃O [M+H]⁺ 292.11; found 392.28.

5'-fluoro-1'-methyl-3-phenylspiro[imidazole-4,3'-indoline]-2',5(3H)-dione (14b): Pale white solid (yield 32%). ¹H NMR (400 MHz, DMSO- d₆) δ 9.77 (s, 1H), 7.38-7.24 (m, 5H), 7.23-7.16 (m, 1H), 7.06-7.02 (m, 2H), 3.27 (s, 3H). MS (ESI): calculated for C₁₇H₁₃FN₃O₂ [M+H]⁺ 310.10; found 310.33.

5'-methoxy-1'-methyl-3-phenylspiro[imidazole-4,3'-indoline]-2',5(3H)-dione (14c): Pale white solid (yield 37%). ¹H NMR (400 MHz, DMSO- d₆) δ 9.74 (s, 1H), 7.36-7.29 (m, 2H), 7.22-7.12 (m, 2H), 7.07-7.02 (m, 2H), 7.00-6.93 (m, 2H), 3.64 (s, 3H), 3.24 (s, 3H). MS (ESI): calculated for C₁₈H₁₆N₃O₃ [M+H]⁺ 322.19; found 322.39.

3-(4-chlorophenyl)-1'-methylspiro[imidazole-4,3'-indoline]-2',5(3H)-dione (14d): Pale white solid (yield 41%). ¹H NMR (400 MHz, DMSO-d₆) δ 9.76 (s, 1H), 7.51-7.34 (m, 2H), 7.29-6.98 (m, 4H), 6.37-6.24 (m, 2H), 3.27 (s, 3H). MS (ESI): calculated for C₁₇H₁₃ClN₃O₂ [M+H]⁺ 326.07; found 326.26.

1'-benzyl-3-phenylspiro[imidazole-4,3'-indoline]-2',5(3H)-dione (14e): Pale white solid (yield 31%). ¹H NMR (400 MHz, DMSO-d₆) δ 9.78 (s, 1H), 7.42-6.97 (m, 14H), 5.05 (d, *J* = 15.8 Hz, 1H), 5.00 (d, *J* = 15.8 Hz, 1H). MS (ESI): calculated for C₂₃H₁₈N₃O₂ [M+H]⁺ 368.14; found 368.22.

1'-benzyl-5'-fluoro-3-phenylspiro[imidazole-4,3'-indoline]-2',5(3H)-dione (14f): Pale white solid (yield 28%). ¹H NMR (400 MHz, DMSO-d₆) δ 9.78 (s, 1H), 7.48-6.68 (m, 12H), 6.34-6.28 (m, 1H), 5.06 (d, *J* = 15.8 Hz, 2H), 4.96 (d, *J* = 15.8 Hz, 2H); MS (ESI): calculated for C₂₃H₁₇FN₃O₂ [M+H]⁺ 386.13; found 386.17.

1'-benzyl-5'-methoxy-3-phenylspiro[imidazole-4,3'-indoline]-2',5(3H)-dione (14g): Pale white solid (yield 35%). ¹H NMR (400 MHz, DMSO-d₆) δ 9.76 (s, 1H), 7.36-7.17 (m,

7H), 7.06-6.97 (m, 4H), 6.92-6.87 (m, 2H), 5.01 (d, $J = 15.8$ Hz, 1H), 4.97 (d, $J = 15.8$ Hz, 1H), 3.62 (s, 3H). MS (ESI): calculated for $C_{24}H_{20}N_3O_3$ $[M+H]^+$ 398.15; found 398.24.

1'-benzyl-3-(4-chlorophenyl)spiro[imidazole-4,3'-indoline]-2',5(3H)-dione (14h): Pale white solid (yield 29%). 1H NMR (400 MHz, DMSO- d_6) δ 9.76 (s, 1H), 7.46-7.24 (m, 7H), 7.12-6.93 (m, 4H), 6.35-6.28 (m, 2H), 5.01 (d, $J = 15.8$ Hz, 1H), 4.97 (d, $J = 15.8$ Hz, 1H). MS (ESI): calculated for $C_{23}H_{17}ClN_3O_2$ $[M+H]^+$ 402.10; found 402.28.

1'-benzyl-3-(4-fluorophenyl)spiro[imidazole-4,3'-indoline]-2',5(3H)-dione (14i): Pale white solid (yield 34%). 1H NMR (400 MHz, DMSO- d_6) δ 9.66 (s, 1H), 7.38-7.23 (m, 7H), 7.21-7.02 (m, 6H), 5.04 (d, $J = 15.9$ Hz, 1H), 4.97 (d, $J = 15.9$ Hz, 1H). MS (ESI): calculated for $C_{23}H_{17}FN_3O_2$ $[M+H]^+$ 386.13; found 386.74.

1'-benzyl-5'-fluoro-3-(4-fluorophenyl)spiro[imidazole-4,3'-indoline]-2',5(3H)-dione (14j): Pale white solid (yield 48%). 1H NMR (400 MHz, DMSO- d_6) δ 9.66 (s, 1H), 7.43 (dd, $J = 7.9, 2.6$ Hz, 1H), 7.38-7.23 (m, 6H), 7.23-7.16 (m, 3H), 7.16-7.09 (m, 2H), 5.04 (d, $J = 15.9$ Hz, 1H), 4.97 (d, $J = 15.9$ Hz, 1H). MS (ESI): calculated for $C_{23}H_{16}F_2N_3O_2$ $[M+H]^+$ 404.12; found 404.31.

1'-(4-fluorobenzyl)-3-phenylspiro[imidazole-4,3'-indoline]-2',5(3H)-dione (14k): Pale white solid (yield 39%). 1H NMR (400 MHz, DMSO- d_6) δ 9.79 (s, 1H), 7.39-7.33 (m, 3H), 7.30-7.24 (m, 3H), 7.23-7.14 (m, 4H), 7.07-6.98 (m, 3H), 5.05 (d, $J = 15.9$ Hz, 1H), 4.99 (d, $J = 15.9$ Hz, 1H). MS (ESI): calculated for $C_{23}H_{17}FN_3O_2$ $[M+H]^+$ 386.13; found 386.35.

5'-fluoro-1'-(4-fluorobenzyl)-3-phenylspiro[imidazole-4,3'-indoline]-2',5(3H)-dione (14l): Pale white solid (yield 45%). 1H NMR (400 MHz, DMSO- d_6) δ 9.79 (s, 1H), 7.51-7.45 (m, 1H), 7.40-7.32 (m, 2H), 7.29-7.21 (m, 1H), 7.18-7.09 (m, 5H), 7.03-7.96 (m, 3H), 5.05 (d, $J = 15.8$ Hz, 1H), 4.99 (d, $J = 15.8$ Hz, 1H). MS (ESI): calculated for $C_{23}H_{16}F_2N_3O_2$ $[M+H]^+$ 404.12, found 404.18.

1'-(4-fluorobenzyl)-3-(4-fluorophenyl)spiro[imidazole-4,3'-indoline]-2',5(3H)-dione (14m): Pale white solid (yield 39%). 1H NMR (400 MHz, DMSO- d_6) δ 9.66 (s, 1H), 7.60-6.77 (m, 10H), 6.58-6.14 (m, 2H), 5.03 (d, $J = 15.8$ Hz, 1H), 4.95 (d, $J = 15.8$ Hz, 1H). MS (ESI): calculated for $C_{23}H_{16}F_2N_3O_2$ $[M+H]^+$ 404.12; found 404.35.

5'-fluoro-1'-(4-fluorobenzyl)-3-(4-fluorophenyl)spiro[imidazole-4,3'-indoline]-2',5(3H)-dione (14n): Pale white solid (yield 40%). 1H NMR (400 MHz, DMSO- d_6) δ 9.66 (s, 1H), 7.60-6.77 (m, 9H), 6.58-6.14 (m, 2H), 5.03 (d, $J = 15.3$ Hz, 1H), 4.96 (d, $J = 15.3$ Hz, 2H). MS (ESI): calculated for $C_{23}H_{15}F_3N_3O_2$ $[M+H]^+$ 422.11; found 422.40.

1'-benzyl-3-(3-(trifluoromethyl)phenyl)spiro[imidazole-4,3'-indoline]-2',5(3H)-dione (14o): Pale white solid (yield 40%). ¹H NMR (400 MHz, DMSO-d₆) δ 9.94 (s, 1H), 7.55-7.45 (m, 1H), 7.40-7.25 (m, 7H), 7.21-7.05 (m, 5H), 5.06 (d, *J* = 15.9 Hz, 1H), 4.99 (d, *J* = 15.9 Hz, 1H). MS (ESI): calculated for C₂₄H₁₇F₃N₃O₂ [M+H]⁺ 436.13; found 436.46.

1'-benzyl-3-(4-(trifluoromethyl)phenyl)spiro[imidazole-4,3'-indoline]-2',5(3H)-dione (14p): Pale white solid (yield 37%). ¹H NMR (400 MHz, DMSO-d₆) δ 10.00 (s, 1H), 7.56-7.26 (m, 7H), 7.19-7.04 (m, 3H), 6.56 (s, 1H), 6.43 (d, *J* = 8.7 Hz, 2H), 5.04 (d, *J* = 15.7 Hz, 1H), 4.95 (d, *J* = 15.7 Hz, 1H). MS (ESI): calculated for C₂₄H₁₇F₃N₃O₂ [M+H]⁺ 436.13, found 436.39.

General procedure for the preparation of compounds 15a-p.

To a cooled solution of unsaturated spiro derivatives **14a-p** (1 eq, 0.2 mmol) in MeOH (10 mL) was added in small portions NaBH₄ (1.3 eq), and the reaction mixture was then stirred at room temperature for 3-4 h. Upon completion, as indicated by TLC and MS (ESI), the mixture was quenched with water. The volatile fraction was then concentrated under reduced pressure and the resulting residue was suspended with EtOAc (2x15 mL). The organic layers were washed with water (1x15 mL), brine (1x10 mL), and dried over Na₂SO₄. The solvent was then evaporated and the obtained crude material was purified by flash chromatography (AcOEt/PE as the eluent) to yield the final derivatives **15a-f** as white solids.

1'-methyl-3-phenylspiro[imidazolidine-4,3'-indoline]-2',5-dione (15a): White solid (yield 44%). mp 230-231 °C. ¹H NMR (400 MHz, DMSO-d₆) δ 9.43 (bs, 1H), 7.43-7.36 (m, 1H), 7.21-7.16 (m, 2H), 7.09-6.99 (m, 3H), 6.66 (t, *J* = 7.3 Hz, 1H), 6.16 (dd, *J* = 8.7, 0.9 Hz, 2H), 5.07 (d, *J* = 4.8 Hz, 1H), 4.91 (d, *J* = 4.8 Hz, 1H), 3.23 (s, 3H). ¹³C NMR (101 MHz, DMSO-d₆) δ 172.42 (C), 167.83 (C), 143.75 (C), 142.85 (C), 129.88 (CH), 129.12 (CH), 126.13 (C), 123.10 (CH), 122.90 (CH), 118.05 (CH), 111.87 (CH), 109.46 (CH), 70.50 (C), 59.76 (CH₂), 26.45 (CH₃). MS (ESI): calculated for C₁₇H₁₆N₃O₂ [M+H]⁺ 294.1237; found 294.4462. HPLC: t_R = 15.07.

5'-fluoro-1'-methyl-3-phenylspiro[imidazolidine-4,3'-indoline]-2',5-dione (15b): White solid (yield 70%). mp 212-232 °C. ¹H NMR (400 MHz, DMSO-d₆) δ 9.52 (bs, 1H), 7.31-7.19 (m, 3H), 7.13-7.06 (m, 2H), 6.70 (d, *J* = 7.3 Hz, 1H), 6.17 (dd, *J* = 8.7, 0.8 Hz, 2H), 5.10 (d, *J* = 4.6 Hz, 1H), 4.92 (d, *J* = 4.6 Hz, 1H), 3.25 (s, 3H). ¹³C NMR (101 MHz, DMSO-d₆) δ 172.30 (C), 167.28 (C), 158.75 (C, ¹*J*_{C-F} = 240 Hz), 142.65 (C), 139.99 (C), 129.23 (CH), 127.94 (C, ³*J*_{C-F} = 8 Hz), 118.20 (CH), 116.27-116.03 (CH, ²*J*_{C-F} = 24 Hz), 111.83 (CH), 111.30 (CH, ²*J*_{C-F} = 25 Hz), 110.53 (CH, ³*J*_{C-F} = 8 Hz), 70.68 (C), 59.71 (CH₂), 26.66

(CH₃). MS (ESI): calculated for C₁₇H₁₅FN₃O₂ [M+H]⁺ 312.1143; found 312.4261. HPLC: t_R = 16.10.

5'-methoxy-1'-methyl-3-phenylspiro[imidazolidine-4,3'-indoline]-2',5-dione (15c):

White solid (yield 45%). mp 229-230°C. ¹H NMR (400 MHz, DMSO-d₆) δ 9.40 (bs, 1H), 7.16-7.01 (m, 3H), 6.95 (dd, 1H, *J* = 8.5, 2.6 Hz), 6.87-6.82 (m, 1H), 6.66 (t, *J* = 7.3 Hz, 1H), 6.23-6.12 (m, 2H), 5.08 (d, *J* = 4.7 Hz, 1H), 4.89 (d, *J* = 4.7 Hz, 1H), 3.66 (s, 3H), 3.20 (s, 3H). ¹³C NMR (101 MHz, DMSO-d₆) δ 172.62 (C), 168.35 (C), 156.40 (C), 143.47 (C), 137.62 (C), 129.69 (CH), 128.06 (C), 118.58 (CH), 114.75 (CH), 112.42 (CH), 110.75 (CH), 110.55 (CH), 71.34 (C), 60.28 (CH₂), 56.02 (CH₃), 27.06 (CH₃). MS (ESI): calculated for C₁₈H₁₈N₃O₃ [M+H]⁺ 324.1343; found 324.3919. HPLC: t_R = 16.02.

3-(4-chlorophenyl)-1'-methylspiro[imidazolidine-4,3'-indoline]-2',5-dione (15d):

White solid (yield 60%). mp 228-229°C. ¹H NMR (400 MHz, DMSO-d₆) δ 9.48 (bs, 1H), 7.46-7.38 (m, 1H), 7.26-7.17 (m, 2H), 7.14-7.00 (m, 3H), 6.22-6.15 (m, 2H), 5.08 (d, *J* = 4.6 Hz, 1H), 4.92 (d, *J* = 4.6 Hz, 1H), 3.24 (s, 3H). ¹³C NMR (101 MHz, DMSO-d₆) δ 172.07 (C), 167.58 (C), 143.75 (C), 141.73 (C), 130.05 (CH), 128.89 (CH), 125.66 (C), 123.14 (CH), 122.99 (CH), 121.95 (C), 113.43 (CH), 109.60 (CH), 70.51 (C), 59.84 (CH₂), 26.51 (CH₃). MS (ESI): calculated for C₁₇H₁₅ClN₃O₂ [M+H]⁺ 328.0847; found 328.4014. HPLC: t_R = 16.22.

1'-benzyl-3-phenylspiro[imidazolidine-4,3'-indoline]-2',5-dione (15e):

White solid (yield 48%). mp 234-235°C. ¹H NMR (400 MHz, DMSO-d₆) δ 9.48 (bs, 1H), 7.49-7.24 (m, 6H), 7.21 (dd, *J* = 7.4, 0.8 Hz, 1H), 7.08 (d, *J* = 7.8 Hz, 1H), 7.03-6.96 (m, 3H), 6.69-6.63 (m, 1H), 6.16 (d, *J* = 7.9 Hz, 2H), 5.10 (d, *J* = 4.8 Hz, 1H), 4.99 (d, *J* = 2.5 Hz, 2H), 4.94 (d, *J* = 4.8 Hz, 1H). ¹³C NMR (101 MHz, DMSO-d₆) δ 173.21 (C), 168.35 (C), 143.34 (C), 143.25 (C), 136.27 (C), 130.32 (CH), 129.56 (CH), 129.02 (CH), 128.01 (CH), 126.75 (C), 123.87 (CH), 123.56 (CH), 118.74 (CH), 112.60 (CH), 110.63 (CH), 71.18 (C), 60.36 (CH₂), 43.66 (CH₂); MS (ESI): calculated for C₂₃H₂₀N₃O₂ [M+H]⁺ 370.1550; found 370.1786. HPLC: t_R = 18.43.

1'-benzyl-5'-fluoro-3-phenylspiro[imidazolidine-4,3'-indoline]-2',5-dione (15f):

White solid (yield 49%). mp 238-239°C. ¹H NMR (400 MHz, DMSO-d₆) δ 9.54 (bs, 1H), 7.46-6.96 (m, 11H), 6.68 (t, *J* = 7.3 Hz, 1H), 6.15 (d, *J* = 7.8 Hz, 2H), 5.10 (d, *J* = 4.5 Hz, 1H), 5.00 (s, 2H), 4.93 (d, *J* = 4.5 Hz, 1H). ¹³C NMR (101 MHz, DMSO-d₆) δ 173.08 (C), 167.78 (C), 159.31 (C, ¹*J*_{C-F} = 241 Hz), 143.13 (C), 139.43 (C), 136.07 (C), 129.64 (CH), 129.06 (CH), 128.61 (C, ³*J*_{C-F} = 9Hz), 128.11 (CH), 128.03 (CH), 118.86 (CH), 116.67 (CH, ²*J*_{C-F}

= 23 Hz), 112.53 (CH), 112.02 (CH, $^2J_{C-F} = 26$ Hz), 111.66 (CH, $^3J_{C-F} = 7$ Hz), 71.34 (C), 60.30 (CH₂), 43.78 (CH₂). MS (ESI): calculated for C₂₃H₁₉FN₃O₂ [M+H]⁺ 388.1456; found 388.2196; HPLC: t_R = 23.17.

1'-benzyl-5'-methoxy-3-phenylspiro[imidazolidine-4,3'-indoline]-2',5-dione (15g):

White solid (yield 52%). mp 240-241°C. ¹H NMR (400 MHz, DMSO-d₆) δ 9.45 (bs, 1H), 7.45-7.37 (m, 2H), 7.37-7.24 (m, 3H), 7.07-6.93 (m, 3H), 6.88-6.82 (m, 2H), 6.67 (t, *J* = 7.3 Hz, 1H), 6.16 (d, *J* = 7.8 Hz, 2H), 5.11 (d, *J* = 4.5 Hz, 1H), 4.96 (d, *J* = 6.6 Hz, 2H), 4.92 (d, *J* = 4.6 Hz, 1H), 3.63 (s, 3H). ¹³C NMR (101 MHz, DMSO-d₆) δ 172.84 (C), 168.30 (C), 156.42 (C), 143.39 (C), 136.45 (C), 136.34 (C), 129.56 (CH), 128.99 (CH), 128.13 (C), 128.01 (CH), 118.69 (CH), 114.71 (CH), 112.59 (CH), 111.21 (CH), 110.86 (CH), 71.45 (C), 60.32 (CH₂), 55.99 (CH₃), 43.69 (CH₂). MS (ESI): calculated for C₂₄H₂₂N₃O₃ [M+H]⁺ 400.1656; found 400.0746; HPLC: t_R = 17.85.

1'-benzyl-3-(4-chlorophenyl)spiro[imidazolidine-4,3'-indoline]-2',5-dione (15h):

White solid (yield 49%). mp 255-256°C. ¹H NMR (400 MHz, DMSO-d₆) δ 9.52 (bs, 1H), 7.45-7.38 (m, 2H), 7.38-7.27 (m, 6H), 7.26-7.20 (m, 1H), 7.10 (d, *J* = 7.8 Hz, 1H), 7.07-6.97 (m, 3H), 6.20-6.09 (m, 2H), 5.09 (d, *J* = 4.8 Hz, 1H), 4.99 (d, *J* = 9.2 Hz, 2H), 4.94 (d, *J* = 4.8 Hz, 1H). ¹³C NMR (101 MHz, DMSO-d₆) δ 172.85 (C), 168.09 (C), 143.28 (C), 142.22 (C), 136.21 (C), 130.52 (CH), 129.30 (CH), 129.05 (CH), 128.07 (CH), 127.94 (CH), 126.25 (C), 123.93 (CH), 123.67 (CH), 122.60 (C), 114.10 (CH), 110.75 (CH), 71.18 (C), 60.45 (CH₂), 43.72 (CH₂). MS (ESI): calculated for C₂₃H₁₉ClN₃O₂ [M+H]⁺ 404.1160; found 404.4582. HPLC: t_R = 24.08.

1'-benzyl-3-(4-fluorophenyl)spiro[imidazolidine-4,3'-indoline]-2',5-dione (15i):

White solid (yield 46%). mp 228-229°C. ¹H NMR (400 MHz, DMSO-d₆) δ 9.50 (bs, 1H), 7.44-7.39 (m, 2H), 7.39-7.34 (m, 2H), 7.34-7.29 (m, 2H), 7.23 (dd, *J* = 7.4, 0.8 Hz, 1H), 7.10 (d, *J* = 7.8 Hz, 1H), 7.06-7.00 (m, 1H), 6.90-6.84 (m, 2H), 6.20-6.13 (m, 2H), 5.10 (d, *J* = 4.7 Hz, 1H), 5.00 (d, *J* = 4.9 Hz, 2H), 4.94 (d, *J* = 4.7 Hz, 1H). ¹³C NMR (101 MHz, DMSO-d₆) δ 172.50 (C), 167.76 (C), 155.37 (C, $^1J_{C-F} = 236$ Hz), 142.73 (C), 139.54 (C), 135.65 (C), 129.86 (CH), 128.48 (CH), 127.48 (CH), 127.34 (CH), 125.92 (C), 123.36 (CH), 123.06 (CH), 115.56 (CH, $^2J_{C-F} = 22$ Hz), 113.07 (CH, $^1J_{C-F} = 7$ Hz), 110.12 (CH), 70.82 (C), 60.07 (CH₂), 43.10 (CH₂). MS (ESI): calculated for C₂₃H₁₈FN₃O₂ [M+H]⁺ 388.4219; found 388.1456. HPLC: t_R = 21.40.

1'-benzyl-5'-fluoro-3-(4-fluorophenyl)spiro[imidazolidine-4,3'-indoline]-2',5-dione (15j):

White solid (yield 54%). mp 242-243°C. ¹H NMR (400 MHz, DMSO-d₆) δ 9.55 (bs,

1H), 7.41-7.32 (m, 4H), 7.31-7.23 (m, 2H), 7.20-7.14 (m, 1H), 7.09 (dd, $J = 8.7, 4.2$ Hz, 1H), 6.87 (t, $J = 8.9$ Hz, 2H), 6.17-6.11 (m, 2H), 5.08 (d, $J = 4.6$ Hz, 1H), 4.99 (d, $J = 6.7$ Hz, 2H), 4.92 (d, $J = 4.6$ Hz, 1H). ^{13}C NMR (101 MHz, DMSO- d_6) δ 172.96 (C), 167.77 (C), 159.34 (C, $^1J_{\text{C-F}} = 241$ Hz), 156.00 (C, $^1J_{\text{C-F}} = 236$ Hz), 139.88 (C), 139.48 (C), 136.03 (C), 129.09 (CH), 128.12 (CH), 127.93 (CH), 116.80 (CH, $^2J_{\text{C-F}} = 23$ Hz), 116.22 (CH, $^2J_{\text{C-F}} = 22$ Hz), 113.59 (CH, $^3J_{\text{C-F}} = 7$ Hz), 112.08 (CH, $^2J_{\text{C-F}} = 25$ Hz), 111.75 (C, $^3J_{\text{C-F}} = 8$ Hz), 111.75 (CH, $^3J_{\text{C-F}} = 8$ Hz), 71.56 (C), 60.58 (CH₂), 43.79 (CH₂). MS (ESI): calculated for C₂₃H₁₈F₂N₃O₂ [M+H]⁺ 406.1362; found 406.3859. HPLC: $t_{\text{R}} = 23.92$.

1'-(4-fluorobenzyl)-3-phenylspiro[imidazolidine-4,3'-indoline]-2',5-dione (15k): White solid (yield 49%). mp 241-242°C. ^1H NMR (400 MHz, DMSO- d_6) δ 9.48 (bs, 1H), 7.51-7.40 (m, 2H), 7.32-7.28 (m, 1H), 7.24-7.08 (m, 4H), 7.03-6.96 (m, 3H), 6.66 (t, $J = 7.3$ Hz, 1H), 6.14 (dd, $J = 8.7, 0.9$ Hz, 2H), 5.10 (d, $J = 4.8$ Hz, 1H), 4.99 (s, 2H), 4.94 (d, $J = 4.8$ Hz, 1H). ^{13}C NMR (101 MHz, DMSO- d_6) δ 173.20 (C), 168.31 (C), 162.02 (C, $^1J_{\text{C-F}} = 244$ Hz), 143.32 (C), 143.09 (C), 132.49 (C), 130.35 (CH), 130.10 (CH, $^3J_{\text{C-F}} = 8$ Hz), 129.57 (CH), 126.75 (C), 123.91 (CH), 123.63 (CH), 118.76 (CH), 115.85 (CH, $^2J_{\text{C-F}} = 21$ Hz), 112.54 (CH), 110.59 (CH), 71.17 (C), 60.36 (CH₂), 42.92 (CH₂). MS (ESI): calculated for C₂₃H₁₉FN₃O₂ [M+H]⁺ 388.1456; found 388.4308. HPLC: $t_{\text{R}} = 20.77$.

5'-fluoro-1'-(4-fluorobenzyl)-3-phenylspiro[imidazolidine-4,3'-indoline]-2',5-dione (15l): White solid (yield 51%). mp 249-250°C. ^1H NMR (400 MHz, DMSO- d_6) δ 9.54 (bs, 1H), 7.46-7.42 (m, 2H), 7.25 (dd, $J = 7.7, 2.5$ Hz, 1H), 7.22-7.11 (m, 4H), 7.04-6.98 (m, 2H), 6.68 (t, $J = 7.3$ Hz, 1H), 6.13 (dd, $J = 8.7, 0.9$ Hz, 2H), 5.10 (d, $J = 4.7$ Hz, 1H), 4.99 (s, 2H), 4.93 (d, $J = 4.7$ Hz, 1H). ^{13}C NMR (101 MHz, DMSO- d_6) δ 173.10 (C), 167.76 (C), 162.06 (C, $^1J_{\text{C-F}} = 244$ Hz), 159.34 (C, $^1J_{\text{C-F}} = 241$ Hz), 143.11 (C), 139.27 (C), 132.32 (C), 130.12 (CH, $^3J_{\text{C-F}} = 8$ Hz), 129.65 (CH), 128.61 (C, $^3J_{\text{C-F}} = 8$ Hz), 118.89 (CH), 116.70 (CH, $^2J_{\text{C-F}} = 24$ Hz), 115.89 (CH, $^2J_{\text{C-F}} = 21$ Hz), 112.47 (CH), 112.07 (CH, $^2J_{\text{C-F}} = 25$ Hz), 111.63 (CH, $^3J_{\text{C-F}} = 8$ Hz), 71.33 (C), 60.30 (CH₂), 43.04 (CH₂). MS (ESI): calculated for C₂₃H₁₈F₂N₃O₂ [M+H]⁺ 406.1362; found 406.2602. HPLC: $t_{\text{R}} = 23.48$.

1'-(4-fluorobenzyl)-3-(4-fluorophenyl)spiro[imidazolidine-4,3'-indoline]-2',5-dione (15m): White solid (yield 52%). mp 237-238°C. ^1H NMR (400 MHz, DMSO- d_6) δ 9.49 (bs, 1H), 7.46-7.41 (m, 2H), 7.34-7.29 (m, 1H), 7.25-7.15 (m, 3H), 7.11 (d, $J = 7.8$ Hz, 1H), 7.05-6.99 (m, 1H), 6.86 (t, $J = 8.90$ Hz, 2H), 6.18-6.10 (m, 2H), 5.08 (d, $J = 4.7$ Hz, 1H), 5.00-4.95 (m, 2H), 4.92 (d, $J = 4.7$ Hz, 1H). ^{13}C NMR (101 MHz, DMSO- d_6) δ 173.08 (C), 168.29 (C), 162.02 (C, $^1J_{\text{C-F}} = 244$ Hz), 155.95 (C, $^1J_{\text{C-F}} = 236$ Hz), 143.15 (C), 140.07 (C), 132.46 (C), 130.47 (CH), 129.98 (CH, $^3J_{\text{C-F}} = 8$ Hz), 126.48 (C), 123.96 (CH), 123.70 (CH),

116.17 (CH, $^2J_{C-F} = 23$ Hz), 115.89 (CH, $^2J_{C-F} = 21$ Hz), 113.57 (CH, $^3J_{C-F} = 7$ Hz), 110.66 (CH), 71.40 (C), 60.63 (CH₂), 42.93 (CH₂). MS (ESI): calculated for C₂₃H₁₈F₂N₃O₂ [M+H]⁺ 406.1362; found 406.4291. HPLC: t_R = 23.20.

5'-fluoro-1'-(4-fluorobenzyl)-3-(4-fluorophenyl)spiro[imidazolidine-4,3'-indoline]-2',5-dione (15n): White solid (yield 51%). mp 221-222°C. ¹H NMR (400 MHz, DMSO-d₆) δ 9.57 (bs, 1H), 7.47-7.42 (m, 2H), 7.30-7.11 (m, 5H), 6.90 (t, $J = 8.8$ Hz, 2H), 6.17-6.12 (m, 2H), 5.10 (d, $J = 4.6$ Hz, 1H), 5.03-4.97 (m, 2H), 4.93 (d, $J = 4.6$ Hz, 1H). ¹³C NMR (101 MHz, DMSO-d₆) δ 172.39 (C), 167.17 (C), 161.48 (C, $^1J_{C-F} = 244$ Hz), 158.80 (C, $^1J_{C-F} = 241$ Hz), 155.44 (C, $^1J_{C-F} = 236$ Hz), 139.29 (C), 138.75 (C), 131.69 (C), 129.43 (CH, $^3J_{C-F} = 8$ Hz), 127.77 (C, $^3J_{C-F} = 9$ Hz), 116.26 (CH, $^2J_{C-F} = 23$ Hz), 115.68 (CH, $^2J_{C-F} = 22$ Hz), 115.35 (CH, $^2J_{C-F} = 22$ Hz), 112.95 (CH, $^3J_{C-F} = 8$ Hz), 111.54 (CH, $^2J_{C-F} = 25$ Hz), 111.15 (CH, $^3J_{C-F} = 8$ Hz), 70.98 (C), 60.00 (CH₂), 42.48 (CH₂). MS (ESI): calculated for C₂₃H₁₇F₃N₃O₂ [M+H]⁺ 424.1267; found 424.4342. HPLC: t_R = 23.43.

1'-benzyl-3-(3-(trifluoromethyl)phenyl)spiro[imidazolidine-4,3'-indoline]-2',5-dione (15o): White solid (yield 58%). mp 238-239°C. ¹H NMR (400 MHz, DMSO-d₆) δ 9.59 (bs, 1H), 7.44-7.38 (m, 2H), 7.37-7.23 (m, 5H), 7.18 (t, $J = 7.9$ Hz, 1H), 7.11 (d, $J = 7.8$ Hz, 1H), 7.05-6.97 (m, 2H), 6.51 (s, 1H), 6.30 (dd, $J = 8.3, 2.4$ Hz, 1H), 5.18 (d, $J = 5.0$ Hz, 1H), 5.07-4.92 (m, 3H). ¹³C NMR (101 MHz, DMSO-d₆) δ 172.74 (C), 167.84 (C), 143.68 (C), 143.29 (C), 136.14 (C), 130.67 (CH), 130.63 (CH), 129.05 (CH), 128.03 (CH), 127.80 (CH), 125.86 (C), 124.43 (C), 123.99 (CH), 123.77 (CH), 116.22 (CH), 114.96 (CH), 110.74 (CH), 108.55 (CH), 71.11 (C), 60.38 (CH₂), 43.75 (CH₂). MS (ESI): calculated for C₂₄H₁₉F₃N₃O₂ [M+H]⁺ 438.1424; found 438.1981. HPLC: t_R = 25.42.

1'-benzyl-3-(4-(trifluoromethyl)phenyl)spiro[imidazolidine-4,3'-indoline]-2',5-dione (15p): White solid (yield 46%). mp 251-252°C. ¹H NMR (400 MHz, DMSO-d₆) δ 9.61 (bs, 1H), 7.47-7.41 (m, 2H), 7.39-7.25 (m, 7H), 7.15 (d, $J = 7.9$ Hz, 1H), 7.04 (t, $J = 7.5$ Hz, 1H), 6.29 (d, $J = 8.7$ Hz, 2H), 5.19 (d, $J = 5.1$ Hz, 1H), 5.03 (m, 3H). ¹³C NMR (101 MHz, DMSO-d₆) δ 171.96 (C), 167.17 (C), 145.48 (C), 142.72 (C), 135.60 (C), 130.08 (CH), 128.46 (CH), 127.50 (CH), 127.42 (CH), 126.25 (CH), 125.90 (C), 125.35 (C), 123.37 (CH), 123.18 (CH), 118.23 (C), 111.88 (CH), 110.28 (CH), 70.42 (C), 59.79 (CH₂), 43.23 (CH₂). MS (ESI): calculated for C₂₄H₁₉F₃N₃O₂ [M+H]⁺ 438.1424; found 438.4498. HPLC: t_R = 24.82.

2B. Project 2: DISPIRO-PIPERIDINE AND DISPIRO-ISATIN DERIVATIVES.

2b.1 AIM AND OBJECTIVES.

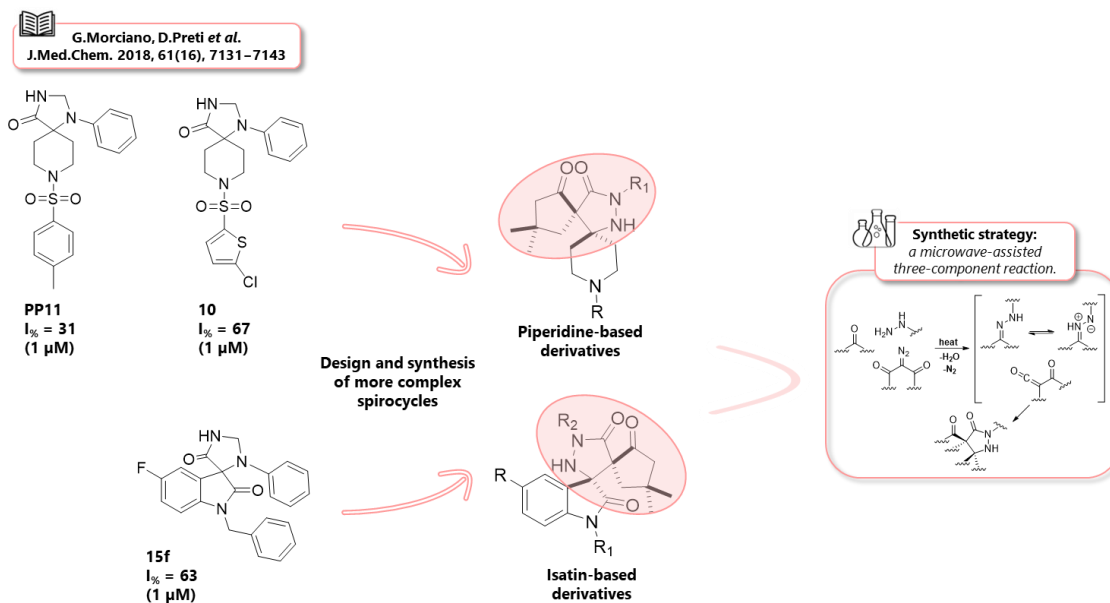


Figure 2b.1: Rational design Project 2.

Considering the unmet need with respect to RI therapy, we have firstly focused on the design and synthesis of piperidine- and isatin-based monospiro derivatives, identifying **PP11**, **10** [93] and **15f** (previous chapter) as the most promising inhibitors of mPTP opening, as well as potential cardioprotective agents. Based on these prominent results we then explored more complex spiro templates (Fig. 2b.1), with the perspective of expanding the range of chemotypes in this medchem area. Especially, we replaced the imidazolidinone ring from the previous series with two spiro-cycles fused either with a piperidine ring or with an isatin bicycle. By exploiting a known microwave-assisted three-component strategy (a type of multiple bond-forming transformations (MBFTs) [111]) two series of dispiro-piperidine- and dispiro-isatin-based compounds have been synthesized.

Synthetic organic chemistry has developed in a fascinating way over the past decades so that several highly selective procedures have been advanced which allow the preparation of complex molecules with excellent regio-, chemo-, diastereo-, and enantioselectivity. However nowadays it is not only a question of what can be synthesized, but how it can be done. Major problems in chemical production are the handling of waste, the search for environmental tolerable procedures, the preservation of resources, and the increase in efficiency. Efficiency can, of course, be evaluated from overall yield and sustainability

criteria such as waste production, toxicity and hazard of the chemicals and the protocols involved. ^[112] In this scenario, MBFTs are defined as chemical transformations that allow the creation of several covalent C-C or C-heteroatom bonds in a single chemical operation. ^[113] The invention of new highly chemoselective methods and controlled MBFTs is expected to provide step-economical syntheses, thereby largely contributing to the development of sustainable chemistry. Step-economical synthesis can be approached in different ways and is established as one of the most important conceptual frameworks towards efficient modern organic synthetic chemistry. For millions of years, the biosynthesis of complex molecules occurring in living organisms (secondary metabolites) has been largely based on such extremely efficient enzyme-mediated chemoselective MBFTs. Alternatively, to achieve this goal it is possible to rely on the development of efficient non-concerted MBFTs. According to the definitions proposed by Tietze, non-concerted MBFTs can be categorized into two main classes, domino reactions and consecutive reactions respectively. A domino (or cascade) reaction is a process involving two or more bond-forming transformations (usually C-C bonds) without changes in the reaction conditions, and in which the subsequent reactions result as a consequence of the functionality formed in the previous step. ^[112] In comparison, consecutive reactions describe MBFTs for which the introduction of the reagent(s) and/or additional solvent(s) and substrate(s) is performed in a stepwise manner to a single reaction mixture from which nothing is removed. Whether the reaction sequence requires any kind of workup of the intermediate product mixture, even one keeping the crude product in the same reactor (e.g. the removal of solvent and/or volatiles by simple evaporation), the reaction sequence may be considered as multiple-step without purification of the intermediate performed in one-pot manner.

In order to synthesize more complex spiro templates we employed a published catalyst-free domino three-component reaction involving a 1,3-dipolar cycloaddition of azomethine imines obtained from hydrazone with α -oxo-ketene generated *in situ*. ^[111] Regarding α -oxo-ketenes, they are recognized as a class of densely functionalized 1,3-dicarbonyls particularly suited for the conceptualization of new MBFTs. It is well-known that α -oxo-ketenes react with nucleophiles to produce 1,3-dicarbonyl compounds, and in contrast with simple ketenes, they almost exclusively react as 1-oxadienes with unsaturations in inverse electron demand [4+2] oxa-Diels-Alder cycloadditions. However, it was recently discovered that in the presence of 1-aza-dienes, α -oxo-ketenes can also react as excellent dienophiles in microwave-assisted [2+4] aza-Diels-Alder cycloadditions.

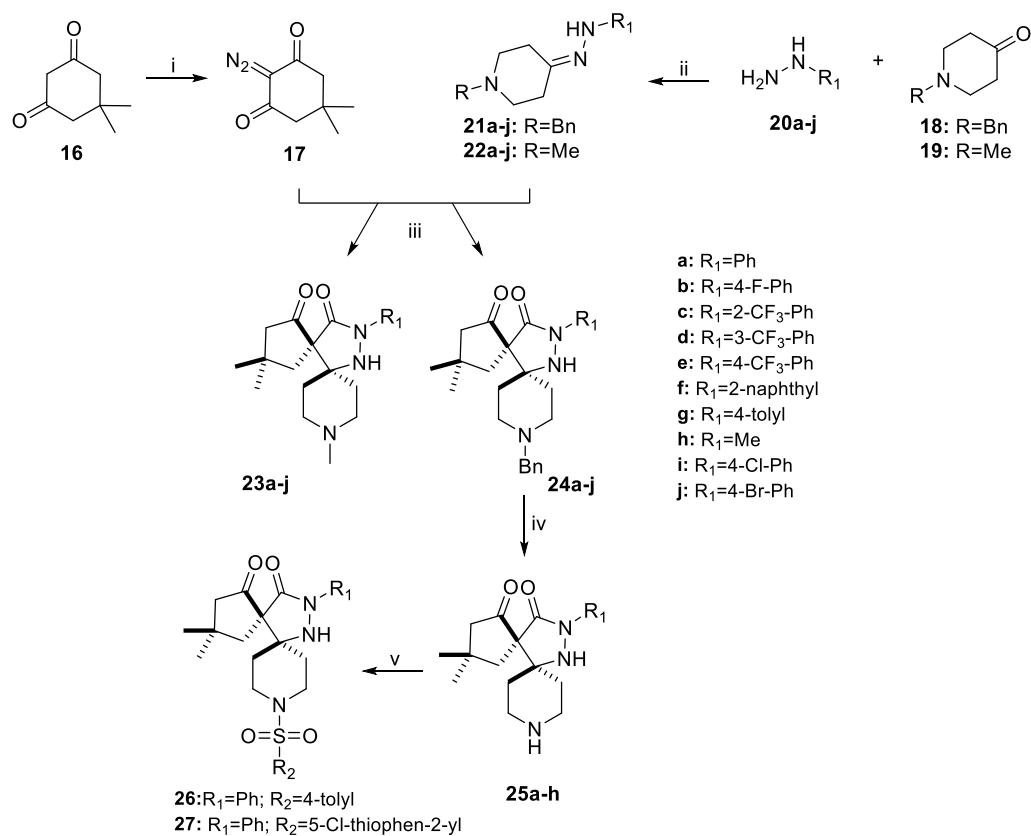
Based on this unique reactivity a series of pyrazolidin-3-one-based dispiro derivatives (specifically dispiro-piperidine and dispiro-isatin compounds) was obtained from a carbonyl derivative, a substituted hydrazine and a diazo compound (Fig. 2b.1).^[111] Compared to the previous monospiro derivatives, the described series features the replacement of the imidazolidinone ring with a pyrazolidin-3-one one, besides the insertion of an additional core connected to this unit by spiro junction.

2b.2 RESULTS AND DISCUSSION.

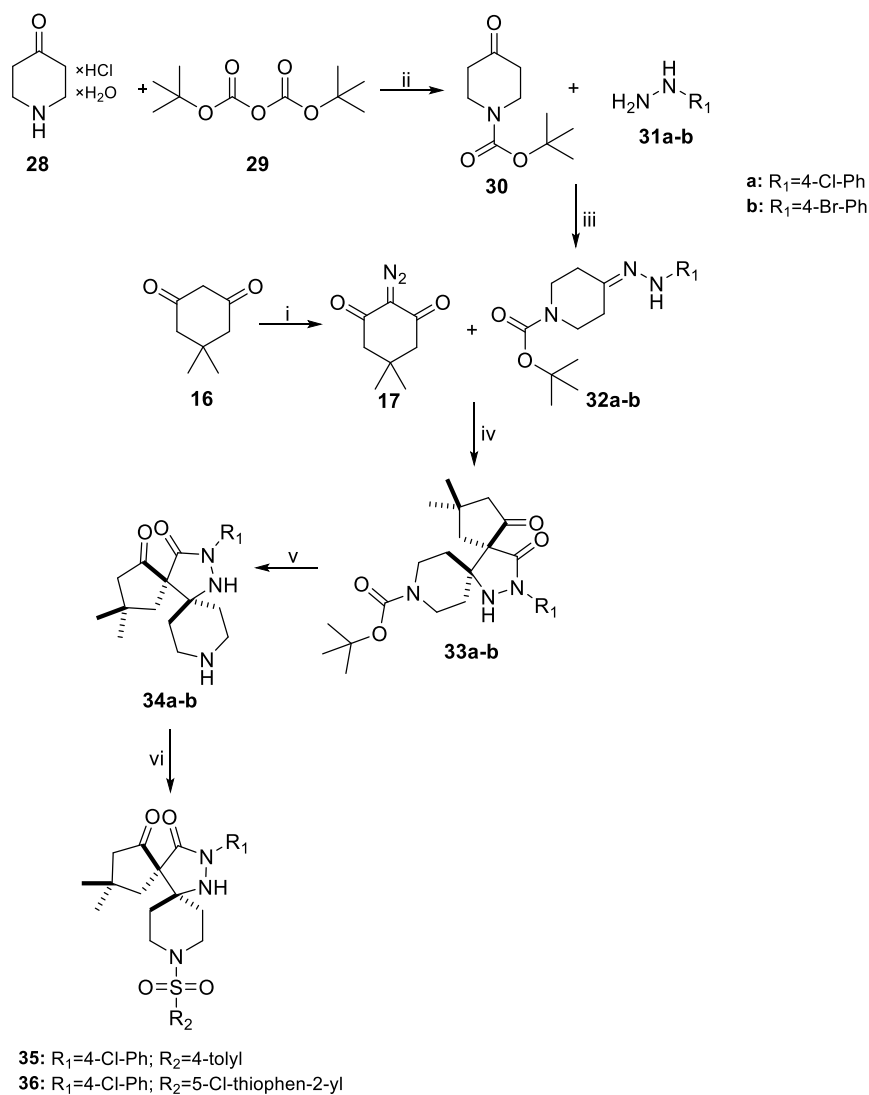
2b.2.1 Chemistry.

The synthetic approach to the obtainment of the target compounds involves a known microwave-assisted strategy realized in a short time and with an excellent control of the diastereoselectivity. The 1,3-dipolar cycloaddition reaction was performed starting from different carbonyl compounds, piperidine (in Scheme 2b.1 and Scheme 2b.2) or isatin compounds (in Scheme 2b.3) respectively. Especially, *N*-methyl-4-piperidone and *N*-benzyl-4-piperidone were commercially available, whereas substituted *N*¹-benzyl-isatins were previously obtained by treatment with substituted benzyl bromide (in Scheme 2b.3). Carbonyl compounds were initially reacted with hydrazines to realize the corresponding hydrazone intermediates. In this regard, for the dispiro-piperidine series, a wide range of substituted hydrazines has been applied, while for the dispiro-isatin series only alkyl and substituted alkyl hydrazines were admitted.^[111] Moreover, for the preparation of dispiro-piperidine derivatives with the *N*^{1,3} phenyl ring substituted at the para position with halogens we optimized the protocol described in Scheme 2b.2. In this case, *N*-Boc-protected 4-piperidinone was prepared from commercially 4-piperidone monohydrate hydrochloride by treatment with Boc-anhydride and then used as carbonyl compound. In this way, the desired final derivatives were achieved processing the obtained intermediates with acid conditions (mixture of trifluoro acetic acid (TFA) and CH₂Cl₂). Considering the most promising spiro-piperidines of the previous work,^[93] compounds **PP11** and **10**, we also synthesized some *N*⁹ substituted derivatives (**26**, **27** and **35**, **36**) by merging the same substituted sulfonyl units to the dispiro-piperidine scaffold herein investigated.

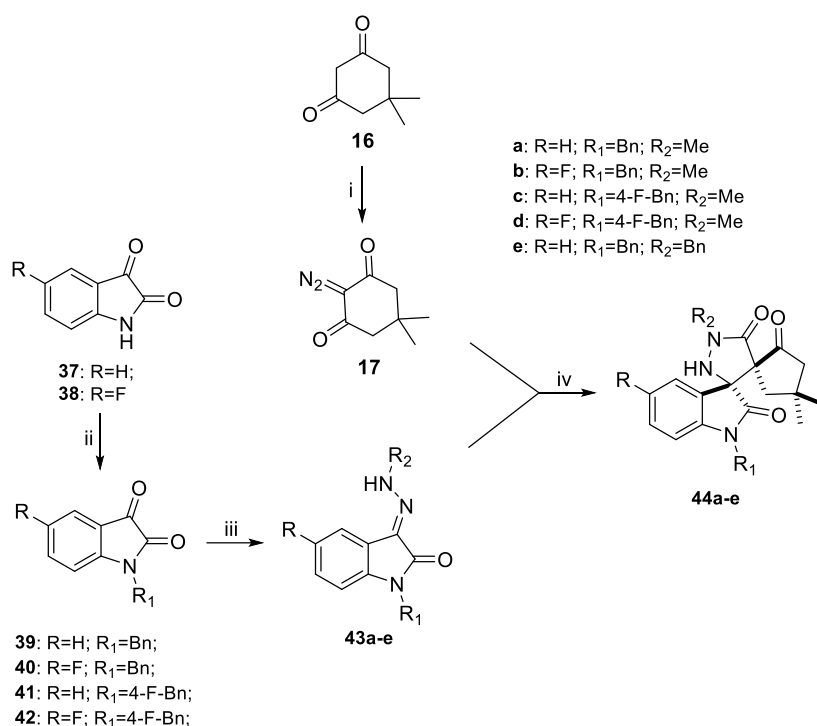
In addition, for all the synthesized derivatives we employed the same diazo compound, synthesized through a standard liquid-phase reaction between dimedone, a 1,3-diketone, and the *p*-toluenesulfonyl azide in the presence of potassium carbonate (K₂CO₃).



Scheme 2b.1. Synthesis of N^9, N^{13} substituted 3,3-dimethyl-9,12,13-triazadispiro[4.0.5⁶.3⁵]tetradecane-1,14-dione - Reagents and conditions - i. TsN₃, K₂CO₃, MeCN, 0°C to rt 2h; ii. Toluene, microwave 140°C 15 min; iii. Toluene, microwave 140°C 15 min; iv. H₂, 10% C/Pd, EtOH, AcOH 7h; v. R₂SO₂Cl, DIPEA, THF, rt 2h.



Scheme 2b.2. Synthesis of N⁹,N¹³ substituted 3,3-dimethyl-9,12,13-triazadispiro[4.0.5⁶.3⁵]tetradecane-1,14-dione - Reagents and conditions - i. TsN₃, K₂CO₃, MeCN, 0°C to rt 2h; ii. K₂CO₃, H₂O:1,4-Dioxane (2:1), 0°C to rt overnight; iii. Toluene, microwave 140°C 15 min; iv. Toluene, microwave 140°C 15 min; v. TFA:CH₂Cl₂ (2:1), rt 2h; vi. R₂SO₂Cl, DIPEA, THF, rt 2h.



Scheme 2b.3. Synthesis of substituted 4,4-dimethyldispiro[cyclopentane-1,4'-pyrazolidine-3',3''-indoline]-2,2'',5'-trione - Reagents and conditions - i. TsN₃, K₂CO₃, MeCN, 0°C to rt 2h; ii. Substituted benzyl bromides, K₂CO₃, MeCN, reflux 16h; iii. R₂NHNH₂, toluene, microwave 140°C 15min; iv. toluene, microwave 140°C 15min.

Since the faster formation of the hydrazone compared to the α -oxo-ketene is crucial to prevent the irreversible nucleophilic addition of hydrazines to the diazo compound, we decided to split the global reaction into two steps (consecutive protocol): an initial microwave-assisted reaction between the carbonyl compound and the hydrazine to give the hydrazone intermediate and a subsequent microwave-assisted reaction between the obtained intermediate and the added diazo compound (**17**). This strategy also avoided the hydrolysis of the α -oxo-ketene by water produced concomitantly with hydrazone formation.

Upon heating the two main partners of the pivotal 1,3-dipolar cycloaddition reaction were supplied as follows: a 1,2-hydrogen shift of the hydrazone intermediate provided the corresponding azomethine imine 1,3-dipole, while a Wolff rearrangement of the diazo compound led to the corresponding α -oxo-ketene. (Fig. 2b.2) ^[111]

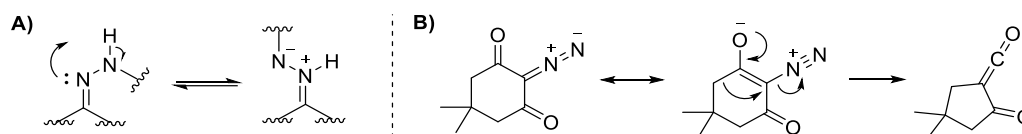


Figure 2b.2: Proposed 1,2-hydrogen shift (A) and Wolff rearrangement (B).

Moreover, it has been highlighted that the reaction is highly atom-economical, producing only water and nitrogen gas coproducts under additive-free conditions. Researchers have also resolved the structure of analogues synthesized through this approach by X-ray diffraction analyses, confirming the chemo-, regio- and stereochemical outcome of the reaction. ^[111] In this regard it has been speculated that, for both the observed regio- and diastereoselectivity, the reaction involved a thermodynamically controlled stepwise (or concerted very asynchronous) process via disrotatory 6π electrocyclicization of a zwitterionic species (Figure 2b.3). ^[111]

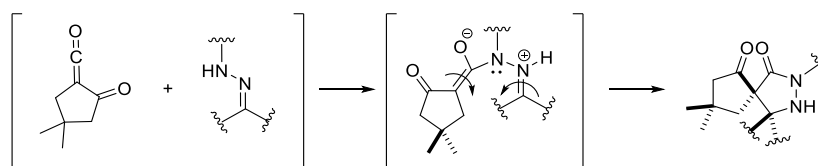


Figure 2b.3: Proposed pathway. ^[111]

Notably, the described synthetic approach allowed the creation of four covalent bonds and two contiguous chiral quaternary centers with excellent diastereoselectivity.

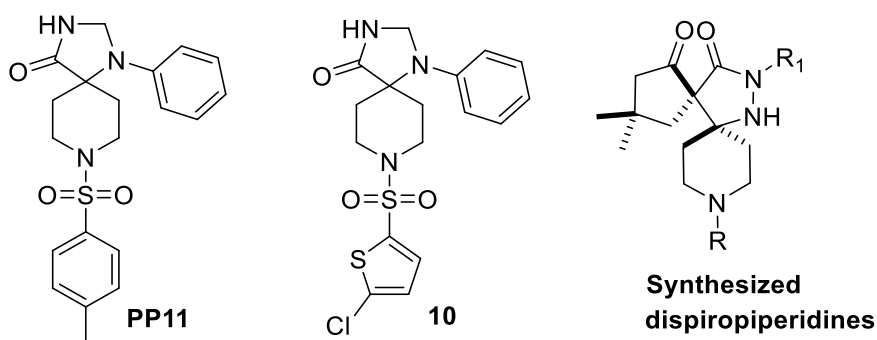
2a.2.2 Biological evaluation.

The biological assay reported below was realized in collaboration with the research group of Professor Paolo Pinton of the University of Ferrara (Dept. of Medical Sciences).

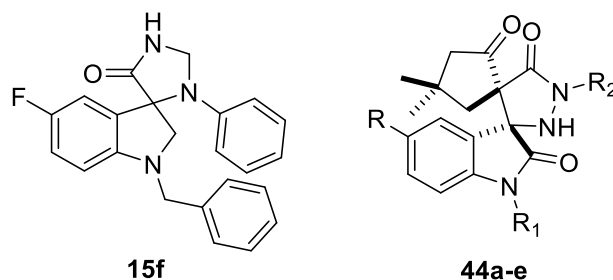
Preliminary screening-cobalt-calcein assay.

The biological activity of the investigated dispiro derivatives was tested by using the cobalt-calcein assay ^[104] performed in human ventricular cardiomyocytes (AC16). All cells were pretreated with vehicle (DMSO), 1 μM **PP11** (first reference compound), 1 μM **10** (second reference compound) or 1 μM inquired derivative, and then loaded with 1 μM calcein acetoxymethyl ester and 2 mM Co^{2+} . According to the described assay and under conditions of mitochondrial calcium overload (by the administration of 1 μM ionomycin), the resulting kinetics data are reported in Table 2b.1 and Table 2b.2.

Table 2b.1. *In vitro* potency of dispiro-piperidine derivatives as mPTP opening inhibitors.



Compd	R	R ₁	mPTP inhibition (% 1μM)	Statistic
PP11	-	-	40,19	P<0.0001
10	-	-	66,80	P<0.0001
24a (MF 09)	Bn	Ph	15,59	P<0.001
23a (MF 05)	Me	Ph	25,36	P<0.0001
25a (MF 13)	H	Ph	57,56	P<0.0001
26 (MF 26)	Tosyl	Ph	66,41	P<0.0001
27 (MF 25)	(5-Cl-thiophen-2-yl)-sulfonyl	Ph	51,39	P<0.0001
24b (MF 10)	Bn	4-F-Ph	34,69	P<0.0001
23b (MF 06)	Me	4-F-Ph	6,42	n.s.
25b (MF 53)	H	4-F-Ph	15,34	P<0.001
24i (MF 11)	Bn	4-Cl-Ph	69,51	P<0.0001
23i (MF 07)	Me	4-Cl-Ph	24,12	P<0.0001
34a (MF 27)	H	4-Cl-Ph	71,32	P<0.0001
35 (MF 52)	Tosyl	4-Cl-Ph	28,73	P<0.0001
36 (MF 28)	(5-Cl-thiophen-2-yl)-sulfonyl	4-Cl-Ph	36,37	P<0.0001
24f (MF 12)	Bn	2-Naphthyl	37,79	P<0.0001
23f (MF 08)	Me	2-Naphthyl	14,59	P<0.001
25f (MF 54)	H	2-Naphthyl	18,45	P<0.001

Table 2b.2. *In vitro* potency of dispiro-isatin derivatives as mPTP opening inhibitors.

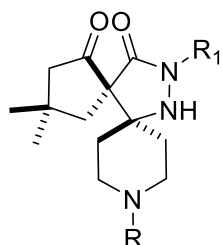
Compd	R	R ₁	R ₂	mPTP inhibition (% ₁ , 1μM)	Statistic
15f	-	-	-	62,60	P<0.0001
44a (MF 01)	H	Bn	Me	19,36	P<0.001
44b (MF 02)	F	Bn	Me	29,84	P<0.0001
44c (MF 03)	H	4-F-Bn	Me	23,84	P<0.0001
44d (MF 04)	F	4-F-Bn	Me	38,71	P<0.0001
44e (MF 14)	H	Bn	Bn	30,93	P<0.0001

Regarding the design of the investigated compounds, we firstly synthesized two series of dispiro compounds, dispiro-piperidine- (Table 2b.1) and dispiro-isatin- (Table 2b.2) compounds. For the dispiro-piperidine series, we employed various carbonyl reactants, such as *N*-methyl-4-piperidone, *N*-benzyl-4-piperidone and *N*-Boc-protected 4-piperidone (Scheme 2b.1 and Scheme 2b.2). The resulting three groups of derivatives were designed as follows: keeping unchanged the substitution at the *N*⁹ position of the piperidine core (i.e. free *N*⁹ or substituted with methyl or benzyl), different changes were respectively introduced at position *N*¹³ of the pyrazolidinone core, in some cases jointly with further precise substitutions at the *N*⁹ position. Whereas, for the dispiro-isatin series we synthesized a unique group of derivatives starting from substituted *N*-benzyl-isatins (Scheme 2b.3).

Among the dispiro-piperidine derivatives (in Table 2b.1) we identified three promising candidates, **26**, **24i** and **34a**, with a significantly more potent behaviour in inhibiting mPTP opening than **PP11**. In light of these encouraging results and with the goal to better inquire about the SAR, we extended the dispiropiperidine series (in Table 2b.3) by placing various substitution to the general scaffold. The *in vitro* potency of these dispiro-piperidine analogues have been only partially evaluated to date through a slightly different protocol performed in human cardiac fibroblasts (in Figure 2b.4). A complete SAR analysis of the dispiro-piperidine derivatives will be elucidated only after the acquisition of these data.

Unfortunately, among the dispiro-isatin derivatives (in Table 2b.2) we did not find an improvement of activity compared to the reference derivative **15f**. Thus, for this subset of molecules the increase of molecular complexity seems to correspond to a decrease of potency.

Table 2b.3. Dispiro-piperidine analogues under biological evaluation.



**New synthesized
dispiropiperidines**

Compd	R	R₁
24c (BC 01)	Bn	2-CF ₃ -Ph
23c (BC 02)	Me	2-CF ₃ -Ph
25c (BC 03)	H	2-CF ₃ -Ph
24d (BC 04)	Bn	3-CF ₃ -Ph
23d (BC 05)	Me	3-CF ₃ -Ph
25d (BC 06)	H	3-CF ₃ -Ph
24e (BC 07)	Bn	4-CF ₃ - Ph
23e (BC 08)	Me	4-CF ₃ -Ph
25e (BC 09)	H	4-CF ₃ - Ph
24j (BC 16)	Bn	4-Br-Ph
23j (BC 17)	Me	4-Br-Ph
34b (BC 18)	H	4-Br-Ph
24g (BC 10)	Bn	4-Tolyl
23g (BC 11)	Me	4-Tolyl
25g (BC 12)	H	4-Tolyl
24h (BC 13)	Bn	Me
23h (BC 14)	Me	Me
25h (BC 15)	H	Me

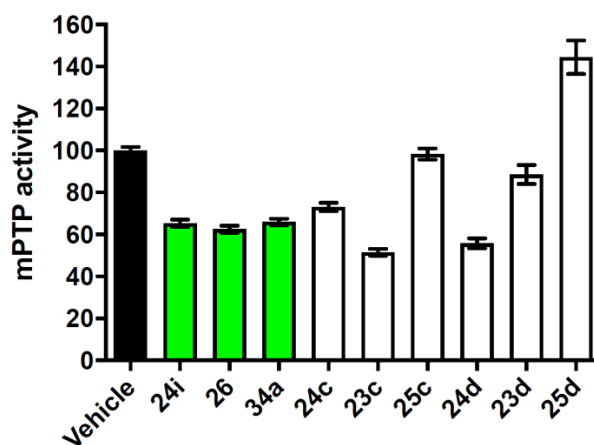


Figure 2b.4: Preliminary cobalt-calcein assay of the new dispiropiperidine analogues.

2b.3 EXPERIMENTAL SECTION.

2b.3.1 Materials and Methods.

Reagents and solvents were purchased by BLD, Fluorochem and Sigma Aldrich.

Microwave-assisted three-component reactions were conducted with a Biotage[®] Initiator+. Reaction progress and product mixture were monitored by thin-layer chromatography (TLC) on pre-coated F₂₅₄ Macherey-Nagel plates of silica gel, visualized with a UV lamp (254 nm light source), and/or by ESI MICROMASS ZMD 2000 electrospray mass spectrometer, after dissolution of compounds in a solution composed by 40:60:0.1 of H₂O:CH₃CN:TFA. Derivatives were purified by, flash chromatography or via reverse-phase purification using a Waters Delta 600 high-performance liquid chromatography (HPLC) system with a Jupiter column C18 (250 × 30 mm, 300 Å, 15 μm spherical particle size), using a binary mobile phase consisting of solution A (100% H₂O, 0.1% v/v TFA) and solution B (40% H₂O, 60% CH₃CN, 0.1% v/v TFA) at a flow rate of 20 mL/min. Gradient was established individually considering the analytical HPLC profile of the crude product. Analytical HPLC was performed with a Beckman 126 liquid chromatograph furnished of a UV detector Beckman 168 and equipped with KARAT32 software. The purity of all the derivatives was assessed with an Agilent Zorbax C18 column (4.6 × 150 mm, 3.5 μm particle size) at a flow rate of 0.7 mL/min using a linear gradient from 100% of A (water + 0.1% TFA) to 100% of B (acetonitrile + 0.1% TFA) over a period of 25 min. All final compounds were monitored at 220 nm showing ≥ 96% purity. ¹H NMR and ¹³C NMR spectra were performed on a Varian Mercury Plus 400 MHz spectrometer. The signals were referenced to residual ¹H shift of the deuterated solvents (respectively δ H 7.26 for CDCl₃; δ H 2.50 for DMSO-*d*₆). Chemical shifts (δ) are expressed in parts per million (ppm) using the peak of deuterated solvents as an internal standard, while values of coupling constants (*J*) are reported in Hertz (Hz).

Splitting patterns are designed as s, singlet; d, doublet; dd, double doublet; t, triplet; m, multiplet; and bs, broad signal. Melting points for purified products were determined in a glass capillary on a Stuart Scientific electrothermal apparatus SMP30.

2b.3.2 General synthetic procedures.

Dispiro-piperdine derivatives.

Preparation of 2-diazo-5,5-dimethylcyclohexane-1,3-dione 17. ^[114] To a solution of dimedone **16** (1 eq, 7.13 mmol) in MeCN (15 mL) were added tosyl azide (1 eq) and K₂CO₃ (1.1 eq) at 0°C. The mixture was stirred at 0°C for 1h and then at room temperature for 3h. Upon completion, as indicated by TLC, the volatile fraction was evaporated under reduced pressure. The resulting crude material was directly purified by flash chromatography (EtOAc/PE as the eluent) to yield derivative **17** as pale white solid (stored at -25°C).

diazo-5,5-dimethylcyclohexane-1,3-dione (17): Pale yellow solid (yield 97%) ¹H NMR (400 MHz, DMSO-d₆) δ 2.42 (s, 2H), 1.01 (s, 3H). ¹³C NMR (101 MHz, DMSO-d₆) δ 189.91, 49.50, 30.64, 27.57. MS (ESI): calculated for C₈H₁₁N₂O₂ [M+H]⁺ 167.08; found 167,25.

General procedure for the preparation of compounds 23a-j and 24a-j. To a solution of carbonyl derivatives **18-19** (1 eq, 0.80 mmol) in toluene (3 mL), in a specific vial, was added the appropriate hydrazine (2 eq). The reaction mixture was sealed and irradiate with microwaves (400 W) at 140 °C for 15 min, and then cooled down to 50°C by airflow. When the hydrazone intermediate was achieved, as indicated by MS(ESI), the diazo compound (2.5 eq) was added to the resulting mixture, which was sealed again, irradiate with microwaves (400 W) at 140 °C for 15 min and then cooled down to 50°C by airflow. Upon completion, as indicated by MS (ESI), the solvent was evaporated and the obtained crude material was directly purified by semi-preparative HPLC, to yield derivatives **23a-j** and **24a-j** as white solids.

9-benzyl-3,3-dimethyl-13-phenyl-9,12,13-triazadispiro[4.0.5⁶.3⁵]tetradecane-1,14-dione (24a): White solid (yield 43%). mp 68-70°C. ¹H NMR (400 MHz, DMSO-d₆) δ 9.76 (bs, 1H), 7.82 (dd, *J* = 8.6, 0.9 Hz, 2H), 7.56-7.46 (m, 5H), 7.44-7.36 (m, 2H), 7.16 (t, *J* = 7.4 Hz, 1H), 6.24 (s, 1H), 4.41 (s, 2H), 3.46-3.06 (m, 4H), 2.39 (d, *J* = 17.0 Hz, 1H), 2.24-1.98 (m, 3H), 1.87-1.71 (m, 2H), 1.73 (d, *J* = 14.0 Hz, 1H), 1.48 (d, *J* = 15.0 Hz, 1H), 1.20 (s, 3H), 1.08 (s, 3H). ¹³C NMR (101 MHz, DMSO-d₆) δ 212.66, 169.44, 138.90, 131.06, 129.80, 129.53, 128.81, 128.55, 124.27, 118.39, 67.41, 60.79, 58.81, 53.75, 47.60, 47.34,

39.54, 32.89, 29.33, 28.05, 26.33, 25.03. MS (ESI): calculated for C₂₆H₃₂N₃O₂ [M+H]⁺ 418.2489; found 418.3768. HPLC: t_R = 18.26 min.

3,3,9-trimethyl-13-phenyl-9,12,13-triazadispiro[4.0.5⁶.3⁵]tetradecane-1,14-dione (23a):

White solid (yield 51%). mp 57-59°C. ¹H NMR (400 MHz, DMSO-d₆) δ 9.84 (bs, 1H), 7.83 (dd, *J* = 8.7, 1.1 Hz, 2H), 7.42-7.36 (m, 2H), 7.19-7.11 (m, 1H), 6.22 (s, 1H), 3.42-3.27 (m, 3H), 3.17-3.05 (m, 1H), 2.83-2.82 (m, 3H), 2.42 (d, *J* = 17.0 Hz, 1H), 2.21-2.05 (m, 3H), 1.87-1.73 (m, 3H), 1.51-1.45 (m, 1H), 1.22 (s, 3H), 1.09 (s, 3H). ¹³C NMR (101 MHz, DMSO-d₆) δ 212.71, 169.51, 138.91, 128.53, 124.21, 118.32, 67.39, 60.29, 53.74, 49.63, 49.09, 42.25, 39.54, 32.87, 29.32, 28.07, 26.53, 25.23. MS (ESI): calculated for C₂₀H₂₈N₃O₂ [M+H]⁺ 342.2176; found 342.3223. HPLC: t_R = 14.65 min.

9-benzyl-13-(4-fluorophenyl)-3,3-dimethyl-9,12,13-triazadispiro[4.0.5⁶.3⁵]tetradecane-1,14-dione (24b):

White solid (yield 48%). mp 65-68°C. ¹H NMR (400 MHz, DMSO-d₆) δ 9.73 (bs, 1H), 7.86-7.78 (m, 2H), 7.57-7.46 (m, 5H), 7.30-7.20 (m, 2H), 6.30 (s, 1H), 4.40 (s, 2H), 3.42-3.11 (m, 4H), 2.39 (d, *J* = 17.0 Hz, 1H), 2.21-2.01 (m, 3H), 1.86-1.70 (m, 2H), 1.48 (d, *J* = 14.0 Hz, 1H), 1.20 (s, 3H), 1.07 (s, 3H). ¹³C NMR (101 MHz, DMSO-d₆) δ 213.15, 169.82, 160.27, 158.15, 135.83, 131.57, 130.20, 129.35, 120.92, 115.70, 67.77, 61.40, 59.35, 54.26, 48.14, 47.85, 39.66, 33.42, 29.85, 28.56, 26.85, 25.56. MS (ESI): calculated for C₂₆H₃₁FN₃O₂ [M+H]⁺ 436.2395; found 436.4203. HPLC: t_R = 18.37 min.

13-(4-fluorophenyl)-3,3,9-trimethyl-9,12,13-triazadispiro[4.0.5⁶.3⁵]tetradecane-1,14-

dione (23b): White solid (yield 40%). mp 59-61°C. ¹H NMR (400 MHz, DMSO-d₆) δ 9.82 (bs, 1H), 7.89-7.80 (m, 2H), 7.28-7.21 (m, 2H), 6.28 (s, 1H), 3.40-3.29 (m, 3H), 3.14-3.03 (m, 1H), 2.83-2.81 (m, 3H), 2.42 (d, *J* = 17.2 Hz, 1H), 2.21-2.05 (m, 3H), 1.86-1.72 (m, 3H), 1.48 (d, *J* = 15.6 Hz, 1H), 1.21 (s, 3H), 1.09 (s, 3H). ¹³C NMR (101 MHz, DMSO-d₆) δ 212.67, 169.29, 158.51, 135.32, 120.29, 115.29, 67.22, 60.36, 53.72, 49.60, 49.05, 42.25, 39.55, 32.88, 29.31, 28.05, 26.51, 25.22. MS (ESI): calculated for C₂₀H₂₇FN₃O₂ [M+H]⁺ 360.2082; found 360.4147. HPLC: t_R = 15.94 min.

9-benzyl-3,3-dimethyl-13-(2-(trifluoromethyl)phenyl)-9,12,13-

triazadispiro[4.0.5⁶.3⁵]tetradecane-1,14-dione (24c): White solid (yield 48%). mp 67-69°C. ¹H NMR (400 MHz, DMSO-d₆) δ 9.60 (bs, 1H), 7.84-7.77 (m, 2H), 7.66-7.60 (m, 1H), 7.54-7.42 (m, 6H), 6.16 (s, 1H), 4.42-4.26 (m, 2H), 3.21-3.27 (m, 3H), 3.03-2.85 (m, 1H), 2.36 (d, *J* = 17.2 Hz, 1H), 2.23-1.97 (m, 3H), 1.95-1.65 (m, 4H), 1.17 (s, 3H), 1.02 (s, 3H). ¹³C NMR (101 MHz, DMSO-d₆) δ 212.47, 171.65, 136.57, 134.45, 131.56, 130.64, 130.25, 130.07, 129.91, 129.36, 127.43, 127.42, 127.32, 66.12, 63.07, 59.26, 54.16, 47.96,

47.82, 39.15, 33.42, 29.89, 28.54, 26.92, 25.63. MS (ESI): calculated for C₂₇H₃₁F₃N₃O₂ [M+H]⁺ 486.2363; found 486.3757. HPLC: t_R = 18.31 min.

3,3,9-trimethyl-13-(2-(trifluoromethyl)phenyl)-9,12,13-

triazadispiro[4.0.5⁶.3⁵]tetradecane-1,14-dione (23c): White solid (yield 44%). mp 65-67°C. ¹H NMR (400 MHz, DMSO-d₆) δ 9.67 (bs, 1H), 7.88-7.72 (m, 2H), 7.63 (t, *J* = 7.7 Hz, 1H), 7.50 (d, *J* = 7.9 Hz, 1H), 6.17 (s, 1H), 3.42-3.14 (m, 3H), 3.03-2.86 (m, 1H), 2.80-2.77 (m, 3H), 2.39 (d, *J* = 17.2 Hz, 1H), 2.22-2.00 (m, 3H), 1.94-1.69 (m, 4H), 1.19 (s, 13H), 1.03 (s, 3H). ¹³C NMR (101 MHz, DMSO-d₆) δ 212.60, 171.70, 136.57, 134.45, 130.63, 129.91, 127.44, 127.43, 66.13, 62.55, 54.18, 50.04, 49.67, 42.78, 39.40, 33.44, 29.90, 28.58, 27.15, 25.85. MS (ESI): calculated for C₂₁H₂₇F₃N₃O₂ [M+H]⁺ 410.2050; found 409.8189. HPLC: t_R = 16.56 min.

9-benzyl-3,3-dimethyl-13-(3-(trifluoromethyl)phenyl)-9,12,13-

triazadispiro[4.0.5⁶.3⁵]tetradecane-1,14-dione (24d): White solid (yield 71%). mp 47-49°C. ¹H NMR (400 MHz, DMSO-d₆) δ 9.67 (bs, 1H), 8.16 (s, 1H), 8.09 (d, *J* = 8.2 Hz, 1H), 7.64 (t, *J* = 8.1 Hz, 1H), 7.57 – 7.42 (m, 6H), 6.43 (s, 1H), 4.40 (s, 1H), 3.34 – 3.09 (m, 4H), 2.40 (d, *J* = 16.8 Hz, 1H), 2.21 – 2.02 (m, 3H), 1.85-1.69 (m, 3H), 1.52 (d, *J* = 13.5 Hz, 1H), 1.19 (s, 3H), 1.06 (s, 3H). ¹³C NMR (101 MHz, DMSO-d₆) δ 213.02, 170.68, 158.43, 140.25, 131.62, 130.48, 130.24, 130.08, 130.08, 129.90, 129.34, 122.26, 122.26, 121.09, 114.47, 68.00, 61.46, 59.20, 54.25, 48.32, 47.67, 39.21, 33.28, 29.66, 28.57, 26.66, 25.65. MS (ESI): calculated for C₂₇H₃₁F₃N₃O₂ [M+H]⁺ 486,2363; found 485.9183. HPLC: t_R = 20.73 min

3,3,9-trimethyl-13-(3-(trifluoromethyl)phenyl)-9,12,13-

triazadispiro[4.0.5⁶.3⁵]tetradecane-1,14-dione (23d): White solid (yield 52%). mp 55-57°C. ¹H NMR (400 MHz, DMSO-d₆) δ 9.75 (bs, 1H), 8.21 (s, 1H), 8.09 (d, *J* = 8.0 Hz, 1H), 7.63 (t, *J* = 8.0 Hz, 1H), 7.50 (d, *J* = 7.8 Hz, 1H), 6.40 (s, 1H), 3.42-3.25 (m, 3H), 3.15-3.06 (m, 1H), 2.82-2.85 (m, 3H), 2.43 (d, *J* = 17.0 Hz, 1H), 2.23-2.03 (m, 3H), 1.85-1.73 (m, 3H), 1.52 (d, *J* = 12.9 Hz, 1H), 1.21 (s, 3H), 1.07 (s, 3H). ¹³C NMR (101 MHz, DMSO-d₆) δ 212.98, 170.71, 139.81, 130.64, 130.03, 129.90, 122.15, 120.81, 114.66, 68.00, 60.81, 54.53, 50.61, 49.60, 42.69, 40.09, 33.59, 29.96, 28.61, 27.02, 25.78. MS (ESI): calculated for C₂₁H₂₇F₃N₃O₂ [M+H]⁺ 410.2050; found 409.8156. HPLC: t_R = 16.67 min.

9-benzyl-3,3-dimethyl-13-(4-(trifluoromethyl)phenyl)-9,12,13-

triazadispiro[4.0.5⁶.3⁵]tetradecane-1,14-dione (24e): White solid (yield 62%). mp 74-76°C. ¹H NMR (400 MHz, DMSO-d₆) δ 9.67 (bs, 1H), 8.03 (d, *J* = 8.6 Hz, 2H), 7.75 (d, *J* = 8.8 Hz, 2H), 7.54-7.43 (m, 5H), 6.40 (s, 1H), 4.39 (s, 2H), 3.42-3.11 (m, 4H), 2.41 (d, *J* =

17.1 Hz, 1H), 2.21-2.03 (m, 3H), 1.86-1.72 (m, 3H), 1.47 (d, $J = 12.8$ Hz, 1H), 1.19 (s, 3H), 1.06 (s, 3H). ^{13}C NMR (101 MHz, DMSO- d_6) δ 212.86, 170.87, 142.62, 131.58, 130.31, 130.09, 129.38, 129.36, 126.43, 124.56, 118.62, 68.03, 61.50, 59.37, 54.27, 48.14, 47.79, 39.55, 33.47, 29.80, 28.54, 26.81, 25.54. MS (ESI): calculated for $\text{C}_{27}\text{H}_{31}\text{F}_3\text{N}_3\text{O}_2$ $[\text{M}+\text{H}]^+$ 486.2363; found 486.6895. HPLC: $t_{\text{R}} = 20.62$ min.

3,3,9-trimethyl-13-(4-(trifluoromethyl)phenyl)-9,12,13-

triazadispiro[4.0.5⁶.3⁵]tetradecane-1,14-dione (23e): White solid (yield 66%). mp 54-56°C. ^1H NMR (400 MHz, DMSO- d_6) δ 9.70 (bs, 1H), 8.05 (d, $J = 8.7$ Hz, 2H), 7.74 (d, $J = 8.8$ Hz, 2H), 6.38 (s, 1H), 3.42-3.27 (m, 3H), 3.17-3.01 (m, 1H), 2.85-2.80 (m, 3H), 2.42 (s, 1H), 2.21-2.06 (m, 3H), 1.86-1.71 (m, 3H), 1.48 (d, $J = 14.2$ Hz, 1H), 1.21 (s, 3H), 1.08 (s, 3H). ^{13}C NMR (101 MHz, DMSO- d_6) δ 212.93, 170.89, 142.63, 126.42, 126.39, 124.56, 118.61, 68.02, 61.00, 54.29, 50.13, 49.59, 42.82, 40.14, 33.47, 29.83, 28.59, 27.04, 25.77. MS (ESI): calculated for $\text{C}_{21}\text{H}_{27}\text{F}_3\text{N}_3\text{O}_2$ $[\text{M}+\text{H}]^+$ 410.2050; found 409.7831. HPLC: $t_{\text{R}} = 21.73$ min.

9-benzyl-3,3-dimethyl-13-(naphthalen-2-yl)-9,12,13-

triazadispiro[4.0.5⁶.3⁵]tetradecane-1,14-dione (24f): White solid (yield 43%). mp 185-187°C. ^1H NMR (400 MHz, DMSO- d_6) δ 9.73 (bs, 1H), 8.25-8.24 (m, 1H), 8.06-8.03 (m, 1H), 7.97-7.86 (m, 3H), 7.60-7.42 (m, 7H), 6.39 (s, 1H), 4.44 (s, 2H), 3.39-3.19 (m, 4H), 2.42 (d, $J = 17.1$ Hz, 1H), 2.24-2.06 (m, 3H), 1.93-1.73 (m, 3H), 1.55 (d, $J = 14.3$ Hz, 1H), 1.22 (s, 3H), 1.11 (s, 3H). ^{13}C NMR (101 MHz, DMSO- d_6) δ 212.65, 169.72, 136.53, 132.83, 131.64, 130.10, 129.49, 129.37, 128.80, 128.26, 127.98, 127.18, 126.64, 125.75, 119.06, 115.79, 67.45, 60.92, 58.85, 53.78, 47.68, 47.31, 39.62, 32.93, 29.34, 28.05, 26.38, 25.05. MS (ESI): calculated for $\text{C}_{30}\text{H}_{34}\text{N}_3\text{O}_2$ $[\text{M}+\text{H}]^+$ 468.2646; found 468.4977. HPLC: $t_{\text{R}} = 19.86$ min.

3,3,9-trimethyl-13-(naphthalen-2-yl)-9,12,13-triazadispiro[4.0.5⁶.3⁵]tetradecane-1,14-

dione (23f): White solid (yield 49%). mp 157-159°C. ^1H NMR (400 MHz, DMSO- d_6) δ 9.83 (bs, 1H), 8.26-8.25 (m, 1H), 8.08-8.04 (m, 1H), 7.96-7.84 (m, 3H), 7.53-7.41 (m, 2H), 6.36 (s, 1H), 3.46-3.29 (m, 3H), 3.21-3.08 (m, 1H), 2.87-2.84 (m, 3H), 2.44 (d, $J = 17.1$ Hz, 1H), 2.23-2.06 (m, 3H), 1.92-1.74 (m, 3H), 1.53 (d, $J = 14.7$ Hz, 1H), 1.22 (s, 3H), 1.11 (s, 3H). ^{13}C NMR (101 MHz, DMSO- d_6) δ 213.25, 170.27, 137.09, 133.39, 130.63, 128.78, 127.97, 127.95, 127.13, 125.70, 119.05, 115.74, 67.99, 60.98, 54.34, 50.22, 49.68, 42.85, 39.97, 33.46, 29.89, 28.63, 27.14, 25.82. MS (ESI): calculated for $\text{C}_{24}\text{H}_{30}\text{N}_3\text{O}_2$ $[\text{M}+\text{H}]^+$ 392.2333; found 392.3768. HPLC: $t_{\text{R}} = 16.83$ min.

9-benzyl-3,3-dimethyl-13-(p-tolyl)-9,12,13-triazadispiro[4.0.5⁶.3⁵]tetradecane-1,14-dione (24g): White solid (yield 51%). mp 51-53°C. ¹H NMR (400 MHz, DMSO-d₆) δ 9.69 (bs, 1H), 7.67 (d, *J* = 8.5 Hz, 2H), 7.54-4.43 (m, 5H), 7.18 (d, *J* = 8.7 Hz, 2H), 6.17 (s, 1H), 4.39 (s, 2H), 3.41-3.10 (m, 4H), 2.36 (d, *J* = 17.1 Hz, 1H), 2.27 (s, 3H), 2.18-1.99 (m, 3H), 1.86-1.65(m, 3H), 1.44 (d, *J* = 12.8 Hz, 1H), 1.18 (s, 3H), 1.05 (s, 3H). ¹³C NMR (101 MHz, DMSO-d₆) δ 213.28, 169.67, 137.09, 133.96, 131.60, 130.33, 130.07, 129.43, 129.34, 118.95, 67.87, 61.33, 59.33, 54.28, 48.14, 47.87, 39.97, 33.41, 29.88, 28.58, 26.88, 25.55, 20.89. MS (ESI): calculated for C₂₇H₃₄N₃O₂ [M+H]⁺ 432.2646; found 431.8159. HPLC: t_R = 19.10 min.

3,3,9-trimethyl-13-(p-tolyl)-9,12,13-triazadispiro[4.0.5⁶.3⁵]tetradecane-1,14-dione (23g): White solid (yield 50%). mp 48-50°C. ¹H NMR (400 MHz, DMSO-d₆) δ 9.66 (bs, 1H), 7.68 (d, *J* = 8.6 Hz, 2H), 7.17 (d, *J* = 8.3 Hz, 2H), 6.15 (s, 1H), 3.32-3.29 (m, 3H), 3.15-3.01 (m, 1H), 2.85-2.80 (m, 3H), 2.40 (d, *J* = 17.1 Hz, 2H), 2.27 (s, 3H), 2.21-2.01 (m, 4H), 1.86-1.67 (m, 3H), 1.44 (d, *J* = 14.7 Hz, 1H), 1.19 (s, 3H), 1.07 (s, 3H). ¹³C NMR (101 MHz, DMSO-d₆) δ 213.36, 169.67, 137.11, 133.93, 129.44, 118.89, 67.87, 60.83, 54.29, 50.19, 49.67, 42.81, 40.18, 33.42, 29.93, 28.62, 27.12, 25.80, 20.88. MS (ESI): calculated for C₂₁H₃₀N₃O₂ [M+H]⁺ 356.2333; found 356.4444. HPLC: t_R = 17.03 min.

9-benzyl-3,3,13-trimethyl-9,12,13-triazadispiro[4.0.5⁶.3⁵]tetradecane-1,14-dione (24h): White solid (yield 55%). mp 44-46°C. ¹H NMR (400 MHz, DMSO-d₆) δ 9.88 (bs, 1H), 7.52-7.42 (m, 5H), 5.63 (s, 1H), 4.34 (s, 2H), 3.26-3.12 (m, 3H), 2.93 (s, 3H), 2.25 (d, *J* = 17.0 Hz, 1H), 2.10-1.81 (m, 3H), 1.78-1.58 (m, 3H), 1.40 (d, *J* = 12.7 Hz, 1H), 1.13 (s, 3H), 1.00 (s, 3H). ¹³C NMR (101 MHz, DMSO-d₆) δ 213.62, 170.62, 131.61, 130.21, 130.04, 129.32, 65.96, 62.23, 59.21, 54.17, 48.05, 47.82, 39.75, 33.35, 32.80, 29.86, 28.49, 26.94, 25.48. MS (ESI): calculated for C₂₁H₃₀N₃O₂ [M+H]⁺ 356.2333; found 356.34. HPLC: t_R = 16.02 min.

3,3,9,13-tetramethyl-9,12,13-triazadispiro[4.0.5⁶.3⁵]tetradecane-1,14-dione (23h): White solid (yield 47%). mp 50-52°C. ¹H NMR (400 MHz, DMSO-d₆) δ 10.12 (bs, 1H), 5.61 (s, 1H), 3.32-3.12 (m, 3H), 2.93 (s, 3H), 2.94-2.84 (m, 1H), 2.76 (s, 3H), 2.26 (d, *J* = 17.0 Hz, 1H), 2.10-1.88 (m, 3H), 1.76-1.62 (m, 3H), 1.39 (d, *J* = 12.1 Hz, 1H), 1.14 (s, 3H), 1.01 (s, 3H). ¹³C NMR (101 MHz, DMSO-d₆) δ 213.70, 170.64, 65.96, 61.75, 54.19, 50.19, 49.65, 42.77, 39.73, 33.34, 32.78, 29.83, 28.52, 27.13, 25.67. MS (ESI): calculated for C₁₅H₂₆N₃O₂ [M+H]⁺ 280.2020; found 280.33. HPLC: t_R = 12.92 min.

9-benzyl-13-(4-chlorophenyl)-3,3-dimethyl-9,12,13-triazadispiro[4.0.5⁶.3⁵]tetradecane-1,14-dione (24i): White solid (yield 51%). mp 81-

83°C. ¹H NMR (400 MHz, DMSO-d₆) δ 9.73 (bs, 1H), 7.85-7.810 (m, 2H), 7.55-7.41 (m, 7H), 6.30 (s, 1H), 4.39 (s, 2H), 3.39-3.11 (m, 4H), 2.38 (d, *J* = 17.1 Hz, 1H), 2.19-2.01 (m, 3H), 1.85-1.68 (m, 3H), 1.45 (d, 1H, *J* = 14.8 Hz), 1.18 (s, 3H), 1.05 (s, 3H). ¹³C NMR (101 MHz, DMSO-d₆) δ 213.04, 170.08, 138.32, 131.57, 130.33, 130.07, 129.35, 129.00, 128.47, 120.37, 67.88, 61.40, 59.35, 54.27, 48.13, 47.81, 39.80, 33.43, 29.82, 28.55, 26.83, 25.53. MS (ESI): calculated for C₂₆H₃₁ClN₃O₂ [M+H]⁺ 452.2099; found 452.3963. HPLC: t_R = 19.93 min.

13-(4-chlorophenyl)-3,3,9-trimethyl-9,12,13-triazadispiro[4.0.5⁶.3⁵]tetradecane-1,14-dione (23i): White solid (yield 47%). mp 73-75°C. ¹H NMR (400 MHz, DMSO-d₆) δ 9.79 (bs, 1H), 7.85 (d, *J* = 9.1 Hz, 2H), 7.44 (d, *J* = 9.1 Hz, 2H), 6.28 (s, 1H), 3.40-3.26 (m, 3H), 3.13-3.02 (m, 1H), 2.83-2.81 (m, 3H), 2.41 (d, *J* = 17.1 Hz, 1H), 2.19-2.03 (m, 3H), 1.85-1.70 (m, 3H), 1.45 (d, *J* = 14.4 Hz, 1H), 1.20 (s, 3H), 1.07 (s, 3H). ¹³C NMR (101 MHz, DMSO-d₆) δ 213.11, 170.19, 138.33, 128.99, 128.42, 120.33, 67.88, 60.92, 54.28, 50.13, 49.59, 42.80, 39.98, 33.44, 29.85, 28.59, 27.06, 25.77. MS (ESI): calculated for C₂₀H₂₇ClN₃O₂ [M+H]⁺ 376.1786; found 376.3745. HPLC: t_R = 16.27 min.

9-benzyl-13-(4-bromophenyl)-3,3-dimethyl-9,12,13-triazadispiro[4.0.5⁶.3⁵]tetradecane-1,14-dione (24j): White solid (yield 65%). mp 70-72°C. ¹H NMR (400 MHz, DMSO-d₆) δ 9.64 (bs, 1H), 7.81-7.74 (m, 2H), 7.57 (d, *J* = 8.5 Hz, 2H), 7.54-7.43 (m, 5H), 6.30 (s, 1H), 4.39 (s, 2H), 3.39-3.10 (m, 4H), 2.38 (d, *J* = 17.0 Hz, 1H), 2.19-1.99 (m, 3H), 1.85-1.67 (m, 3H), 1.45 (d, *J* = 13.1 Hz, 1H), 1.18 (s, 3H), 1.05 (s, 3H). ¹³C NMR (101 MHz, DMSO-d₆) δ 213.02, 170.19, 138.74, 131.90, 131.58, 130.33, 130.08, 129.36, 120.69, 116.57, 67.90, 61.40, 59.36, 54.26, 48.14, 47.81, 39.77, 33.44, 29.84, 28.54, 26.84, 25.54. MS (ESI): calculated for C₂₆H₃₁BrN₃O₂ [M+H]⁺ 496.1594; found 496.40. HPLC: t_R = 20.47 min.

13-(4-bromophenyl)-3,3,9-trimethyl-9,12,13-triazadispiro[4.0.5⁶.3⁵]tetradecane-1,14-dione (23j): White solid (yield 49%). mp 51-53°C. ¹H NMR (400 MHz, DMSO-d₆) δ 9.73 (bs, 1H), 7.79 (d, *J* = 8.5 Hz, 1H), 7.56 (d, *J* = 8.5 Hz, 1H), 6.28 (s, 1H), 3.40-3.27 (m, 3H), 3.14-3.02 (m, 1H), 2.83-2.80 (m, 3H), 2.41 (d, *J* = 17.1 Hz, 1H), 2.20-2.03 (m, 3H), 1.84-1.69 (m, 3H), 1.45 (d, *J* = 12.3 Hz, 1H), 1.20 (s, 3H), 1.07 (s, 3H). ¹³C NMR (101 MHz, DMSO-d₆) δ 213.09, 170.22, 138.76, 131.90, 120.66, 116.52, 67.90, 60.91, 54.28, 50.13, 49.60, 42.81, 39.81, 33.44, 29.85, 28.59, 27.06, 25.77. MS (ESI): calculated for C₂₀H₂₇BrN₃O₂ [M+H]⁺ 420.1281; found 420.25. HPLC: t_R = 18.33 min.

General procedure for the preparation of compounds 25a-h. A solution of dispiropiperidine derivatives **24a-h** (1 eq, 0.45 mmol) in EtOH (5 mL) and glacial AcOH (1 mL) was treated with a catalytic amount (0.045 mmol) of palladium on activated charcoal (10% Pd basis) in an atmosphere of hydrogen. Upon completion, as indicated by TLC and MS (ESI), the mixture was filtered through celite, washed with fresh EtOH and then concentrated under reduced pressure. The resulting solid residue was directly purified by semi-preparative HPLC to yield the final derivatives **25a-h** as white solids.

3,3-dimethyl-13-phenyl-9,12,13-triazadispiro[4.0.5⁶.3⁵]tetradecane-1,14-dione (25a): White solid (yield 40%). mp 52-53°C. ¹H NMR (400 MHz, DMSO-d₆) δ 8.70 (bs, 1H), 8.49 (bs, 1H), 7.83-7.77 (m, 2H), 7.44-7.35 (m, 2H), 7.17-7.12 (m, 1H), 6.21 (s, 1H), 3.29-3.19 (m, 3H), 3.12-2.99 (m, 1H), 2.41 (d, *J* = 17.0 Hz, 1H), 2.22-1.98 (m, 3H), 1.83-1.72 (m, 3H), 1.41 (d, *J* = 15.2 Hz, 1H), 1.22 (s, 3H), 1.09 (s, 3H). ¹³C NMR (101 MHz, DMSO-d₆) δ 212.74, 169.45, 138.88, 128.57, 124.17, 118.18, 67.83, 61.01, 53.79, 39.56, 39.54, 39.14, 32.89, 29.35, 28.05, 25.64, 24.48. MS (ESI): calculated for C₁₉H₂₆N₃O₂ [M+H]⁺ 328.2020; found 328.3370. HPLC: t_R = 15.31 min.

13-(4-fluorophenyl)-3,3-dimethyl-9,12,13-triazadispiro[4.0.5⁶.3⁵]tetradecane-1,14-dione (25b): White solid (yield 44%). mp 48-50°C. ¹H NMR (400 MHz, DMSO-d₆) δ 8.50 (bs, 1H), 8.21 (bs, 1H), 7.82-7.75 (m, 2H), 7.30-7.15 (m, 2H), 6.25 (s, 1H), 3.22-3.15 (m, 3H), 3.05-2.94 (m, 1H), 2.41 (d, *J* = 16.9 Hz, 1H), 2.20-1.95 (m, 3H), 1.77-1.70 (m, 3H), 1.40 (d, *J* = 13.6 Hz, 1H), 1.21 (s, 3H), 1.07 (s, 3H). ¹³C NMR (101 MHz, DMSO-d₆) δ 213.27, 175.04, 169.83, 135.85, 120.70, 115.82, 68.21, 61.61, 54.33, 42.80, 40.46, 39.94, 33.48, 29.98, 28.61, 26.22, 25.06. MS (ESI): calculated for C₁₉H₂₅FN₃O₂ [M+H]⁺ 346.1925; found 346.3879. HPLC: t_R = 17.67 min.

3,3-dimethyl-13-(2-(trifluoromethyl)phenyl)-9,12,13-triazadispiro[4.0.5⁶.3⁵]tetradecane-1,14-dione (25c): White solid (yield 51%). mp 61-63°C. ¹H NMR (400 MHz, DMSO-d₆) δ 8.59 (bs, 1H), 8.40 (bs, 1H), 7.85-7.74 (m, 2H), 7.62 (t, *J* = 7.7 Hz, 1H), 7.47 (d, *J* = 7.9 Hz, 1H), 6.15 (s, 1H), 3.28-3.06 (m, 3H), 2.96-2.82 (m, 1H), 2.38 (d, *J* = 17.2 Hz, 1H), 2.20-1.96 (m, 3H), 1.97-1.64 (m, 4H), 1.19 (s, 3H), 1.03 (s, 3H). ¹³C NMR (101 MHz, DMSO-d₆) δ 212.65, 171.72, 136.55, 134.47, 130.48, 129.84, 127.43, 127.38, 109.99, 66.59, 63.18, 54.25, 40.10, 39.95, 39.70, 33.46, 29.92, 28.57, 26.23, 25.09. MS (ESI): calculated for C₂₀H₂₅F₃N₃O₂ [M+H]⁺ 396,1893; found 396.4466. HPLC: t_R = 15.49 min.

3,3-dimethyl-13-(3-(trifluoromethyl)phenyl)-9,12,13-

triazadispiro[4.0.5⁶.3⁵]tetradecane-1,14-dione (25d): White solid (yield 55%). mp 70-72°C. ¹H NMR (400 MHz, DMSO-d₆) δ 8.62 (bs, 1H), 8.52 (bs, 1H), 8.17 (s, 1H), 8.08 (d, *J* = 8.8 Hz, 1H), 7.64 (t, *J* = 8.1 Hz, 1H), 7.49 (d, *J* = 7.7 Hz, 1H), 6.38 (s, 1H), 3.29-2.98 (m, 4H), 2.42 (d, *J* = 17.0 Hz, 1H), 2.23-2.00 (m, 3H), 1.81-1.71 (m, 3H), 1.43 (d, *J* = 13.5 Hz, 1H), 1.21 (s, 3H), 1.07 (s, 3H). ¹³C NMR (101 MHz, DMSO-d₆) δ 213.04, 170.78, 140.01, 130.58, 129.90, 122.04, 121.01, 114.49, 68.48, 61.74, 54.33, 40.24, 40.09, 39.65, 33.49, 29.83, 28.60, 26.11, 25.02. MS (ESI): calculated for C₂₀H₂₅F₃N₃O₂ [M+H]⁺ 396,1893; found 396.37. HPLC: t_R = 19.23 min.

3,3-dimethyl-13-(4-(trifluoromethyl)phenyl)-9,12,13-

triazadispiro[4.0.5⁶.3⁵]tetradecane-1,14-dione (25e): White solid (yield 44%). mp 75-77°C. ¹H NMR (400 MHz, DMSO-d₆) δ 8.63 (bs, 1H), 8.40 (bs, 1H), 8.01 (d, *J* = 8.6 Hz, 2H), 7.76 (d, *J* = 8.6 Hz, 2H), 6.37 (s, 1H), 3.32-2.94 (m, 4H), 2.43 (d, *J* = 17.1 Hz, 1H), 2.22-2.05 (m, 3H), 1.80-1.69 (m, 3H), 1.40 (d, *J* = 14.6 Hz, 1H), 1.21 (s, 3H), 1.08 (s, 3H). ¹³C NMR (101 MHz, DMSO-d₆) δ 212.98, 170.93, 142.61, 126.52, 124.56, 118.48, 68.49, 61.74, 54.35, 40.07, 39.62, 39.44, 33.51, 29.86, 28.58, 26.16, 25.01. MS (ESI): calculated for C₂₀H₂₅F₃N₃O₂ [M+H]⁺ 396,1893; found 396.4119. HPLC: t_R = 17.90 min.

3,3-dimethyl-13-(naphthalen-2-yl)-9,12,13-triazadispiro[4.0.5⁶.3⁵]tetradecane-1,14-

dione (25f): White solid (yield 50%). mp 70-72°C. ¹H NMR (400 MHz, DMSO-d₆) δ 8.65 (bs, 1H), 8.44 (bs, 1H), 8.24-8.21 (m, 1H), 8.06-8.02 (m 1H), 7.96-7.84 (m, 3H), 7.54-7.40 (m, 2H), 6.34 (s, 1H), 3.32-3.03 (m, 4H), 2.43 (d, *J* = 17.0 Hz, 1H), 2.23-2.01 (m, 3H), 1.82-1.75 (m, 3H), 1.45 (d, *J* = 12.7 Hz, 1H), 1.22 (s, 3H), 1.11 (s, 3H). ¹³C NMR (101 MHz, DMSO-d₆) δ 213.30, 170.27, 137.09, 133.38, 130.60, 128.85, 127.95, 127.15, 127.16, 125.71, 118.87, 115.61, 68.46, 61.69, 54.39, 40.19, 39.97, 39.56, 33.51, 29.94, 28.64, 26.27, 25.09. MS (ESI): calculated for C₂₃H₂₈N₃O₂ [M+H]⁺ 378,2176; found 378.4529. HPLC: t_R = 20.98 min.

3,3-dimethyl-13-(p-tolyl)-9,12,13-triazadispiro[4.0.5⁶.3⁵]tetradecane-1,14-dione (25g):

White solid (yield 52%). mp 78-80°C. ¹H NMR (400 MHz, DMSO-d₆) δ 8.63 (bs, 1H), 8.43 (bs, 1H), 7.65 (d, *J* = 8.3 Hz, 2H), 7.17 (d, *J* = 8.3 Hz, 2H), 6.15 (s, 1H), 3.25-2.97 (m, 4H), 2.38 (d, *J* = 17.0 Hz, 1H), 2.26 (s, 3H), 2.20-1.96 (m, 3H), 1.78-1.70 (m, 3H), 1.37 (d, *J* = 13.3 Hz, 1H), 1.20 (s, 3H), 1.07 (s, 3H). ¹³C NMR (101 MHz, DMSO-d₆) δ 213.39, 169.72, 137.11, 133.89, 129.48, 118.77, 68.34, 61.58, 54.35, 40.39, 40.12, 39.70, 33.45, 29.94, 28.62, 26.23, 25.04, 20.88. MS (ESI): calculated for C₂₀H₂₈N₃O₂ [M+H]⁺ 342.2176; found 342.4488. HPLC: t_R = 17.48 min.

3,3,13-trimethyl-9,12,13-triazadispiro[4.0.5⁶.3⁵]tetradecane-1,14-dione (25h): White solid (yield 50%). mp 55-57°C. ¹H NMR (400 MHz, DMSO-d₆) δ 8.42 (bs, 1H), 8.11 (bs, 1H), 5.60 (s, 1H), 3.14-3.08 (m, 3H), 2.85 (d, *J* = 15.2 Hz, 1H), 2.57 (d, *J* = 17.9 Hz, 1H), 2.30 (d, *J* = 17.0 Hz, 2H), 2.11-2.03 (m, 1H), 1.98-1.84 (m, 2H), 1.68-1.58 (m, 3H), 1.35-1.28 (m, 1H), 1.16 (s, 3H), 1.02 (s, 3H). ¹³C NMR (101 MHz, DMSO-d₆) δ 213.72, 170.65, 66.37, 62.48, 54.24, 41.80, 40.55, 39.73, 36.22, 33.41, 32.84, 30.02, 28.52, 26.33, 25.00. MS (ESI): calculated for C₁₄H₂₄N₃O₂ [M+H]⁺ 266,1863; found 266.39. HPLC: t_R = 12.07 min.

General procedure for the preparation of compounds 26-27. To a solution of dispiropiperidine derivative **25a** (1 eq, 0.60 mmol) in THF (8 mL) were added DIPEA (1 eq) and the appropriate sulfonyl chloride (1.2 eq). The resulting mixture was stirred at room temperature 2-3h. Upon completion, as indicated by TLC and MS (ESI), the solvent was evaporated under reduce pressure. The resulting solid residue was extracted with EtOAc (3x15 mL) and the combined organic layers were washed with water (1x15 mL), brine (1x10 mL), and then dried over Na₂SO₄. The volatile fraction was then evaporated and the crude solid was purified by semi-preparative HPLC to yield derivatives **26-27** as white solids.

3,3-dimethyl-13-phenyl-9-tosyl-9,12,13-triazadispiro[4.0.5⁶.3⁵]tetradecane-1,14-dione (26): White solid (yield 45%). mp 200-202°C. ¹H NMR (400 MHz, DMSO-d₆) δ 7.65 (d, *J* = 8.1 Hz, 2H), 7.58 (d, *J* = 7.8 Hz, 2H), 7.46 (d, *J* = 8.0 Hz, 2H), 7.30 (t, *J* = 7.9 Hz, 2H), 7.07 (t, *J* = 7.4 Hz, 1H), 5.92 (s, 1H), 3.59-3.54 (m, 2H), 2.72-2.63 (m, 1H), 2.41 (s, 3H), 2.34 (d, *J* = 16.6 Hz, 1H), 2.06 (d, *J* = 16.4 Hz, 1H), 1.99-1.87 (m, 2H), 1.76 (d, *J* = 14.0 Hz, 1H), 1.62-1.47 (m, 2H), 1.31-1.21 (m, 2H), 1.19 (s, 3H), 1.02 (s, 3H). ¹³C NMR (101 MHz, DMSO-d₆) δ 213.40, 170.48, 144.05, 139.48, 133.78, 130.41, 129.03, 127.88, 124.60, 118.78, 68.38, 62.64, 54.32, 42.46, 41.86, 40.20, 39.82, 33.47, 29.50, 28.59, 27.39, 21.50. MS (ESI): calculated for C₂₆H₃₂N₃O₄S [M+H]⁺ 482,2108; found 482.5256. HPLC: t_R = 25.17 min.

9-((5-chlorothiophen-2-yl)sulfonyl)-3,3-dimethyl-13-phenyl-9,12,13-triazadispiro[4.0.5⁶.3⁵]tetradecane-1,14-dione (27): White solid (yield 51%). mp 166-168°C. ¹H NMR (400 MHz, DMSO-d₆) δ 7.70-7.65 (m, 2H), 7.61 (d, *J* = 4.0 Hz, 1H), 7.42 (d, *J* = 4.0 Hz, 1H), 7.38-7.31 (m, 2H), 7.14-7.08 (m, 1H), 5.99 (s, 1H), 3.59-3.54 (m, 2H), 2.90-2.81 (m, 1H), 2.74-2.63 (m, 1H), 2.38 (d, *J* = 16.6 Hz, 1H), 2.13-1.94 (m, 3H), 1.86 (d, *J* = 13.9 Hz, 1H), 1.70-1.58 (m, 2H), 1.34 (d, *J* = 13.7 Hz, 1H), 1.22 (s, 3H), 1.05 (s, 3H). ¹³C NMR (101 MHz, DMSO-d₆) δ 212.85, 169.89, 138.93, 135.42, 134.26, 132.83, 128.73, 128.51, 124.05, 118.15, 67.78, 61.87, 53.75, 42.03, 41.48, 39.26, 32.94, 28.93, 28.06, 27.97,

26.78. MS (ESI): calculated for C₂₃H₂₇ClN₃O₄S₂ [M+H]⁺ 508,1126; found 508.2773. HPLC: t_R = 26.16 min.

Preparation of compound 30. To a solution of carbonyl derivative **28** (1 eq, 5.2 mmol) in H₂O:1,4-Dioxane (2:1, 20 mL) was added K₂CO₃ (3 eq) at 0°C. To the resulting mixture was then added dropwise a solution of Boc-anhydride (1 eq) in H₂O:1,4-Dioxane (2:1, 10 mL) at 0°C. The reaction was stirred at room temperature overnight. Upon completion, the mixture was concentrated under reduce pressure. The resulting residue was extracted with EtOAc (3x15 mL) and the combined organic layers were washed with water (1x15 mL), brine (1x10 mL), and then dried over Na₂SO₄. The volatile fraction was then evaporated to yield derivative **30** as yellow solid.

tert-butyl 4-oxopiperidine-1-carboxylate (30): Yellow solid (yield 95%). ¹H NMR (400 MHz, DMSO-d₆) δ 3.59 (t, *J* = 6.0 Hz, 4H), 2.33 (t, *J* = 6.0 Hz, 4H), 1.40 (s, 9H). ¹³C NMR (101 MHz, DMSO-d₆) δ 208.01 (C), 79.47 (C), 39.55 (CH₂), 28.63 (CH₃).

General procedure for the preparation of compounds 33a-b. To a solution of *N*-Boc protected-carbonyl derivative **30** (1 eq, 0.60 mmol) in toluene (3 mL), in a specific vial, was added the appropriate hydrazine (2 eq). The reaction mixture was sealed, irradiate with microwaves (400 W) at 140 °C for 15 min, and then cooled down to 50°C by airflow. When the hydrazone intermediate was achieved, as indicated by MS(ESI), the diazo compound (2.5 eq) was added to the resulting mixture, which was sealed again, irradiate with microwaves (400 W) at 140 °C for 15 min, and then was cooled down to 50°C by airflow. Upon completion, the mixture was concentrated under reduce pressure. The resulting residue was extracted with EtOAc (3x15 mL) and the combined organic layers were washed with water (1x15 mL), brine (1x10 mL), and then dried over Na₂SO₄. The volatile fraction was then evaporated and the crude solid intermediates **33a-b** were used in the next step without further purification.

General procedure for the preparation of compound 34a-b. Intermediates **33a-b** (0.40 mmol) were suspended in TFA:CH₂Cl₂ (2:1, 5 mL), and the resulting mixture was stirred at room temperature for 2h. Upon completion, as indicated by MS (ESI), the solvent was evaporated under reduced pressure, and the resulting residue was directly purified by semi-preparative HPLC to yield derivatives **34a-b** as white solids.

13-(4-chlorophenyl)-3,3-dimethyl-9,12,13-triazadispiro[4.0.5⁶.3⁵]tetradecane-1,14-dione (34a): White solid (yield 48%). mp 56-59°C. ¹H NMR (400 MHz, DMSO-d₆) δ 8.67 (bs, 1H), 8.46 (bs, 1H), 7.85-7.76 (m, 2H), 7.49-7.40 (m, 2H), 6.27 (s, 1H), 3.31-2.94 (m,

4H), 2.40 (d, $J = 17.0$ Hz, 1H), 2.20-1.99 (m, 3H), 1.80-1.70 (m, 3H), 1.38 (d, $J = 14.4$ Hz, 1H), 1.20 (s, 3H), 1.07 (s, 3H). ^{13}C NMR (101 MHz, DMSO- d_6) δ 213.16, 170.22, 138.32, 129.07, 128.38, 120.21, 68.35, 61.67, 54.34, 40.58, 40.38, 39.97, 33.48, 29.88, 28.59, 26.18, 25.02. MS (ESI): calculated for $\text{C}_{19}\text{H}_{25}\text{ClN}_3\text{O}_2$ $[\text{M}+\text{H}]^+$ 362,1630; found 362.3550. HPLC: $t_{\text{R}} = 15.62$ min.

13-(4-bromophenyl)-3,3-dimethyl-9,12,13-triazadispiro[4.0.5⁶.3⁵]tetradecane-1,14-dione (34b): White solid (yield 51%). mp 67-69°C. ^1H NMR (400 MHz, DMSO- d_6) δ 8.65 (bs, 1H), 8.43 (bs, 1H), 7.76 (d, $J = 9.0$ Hz, 2H), 7.57 (d, $J = 9.0$ Hz, 2H), 6.27 (s, 1H), 3.26-3.12(m, 3H), 3.08-2.96 (m, 1H), 2.40 (d, $J = 17.0$ Hz, 1H), 2.20-1.96 (m, 3H), 1.78-1.71 (m, 3H), 1.37 (d, $J = 12.8$ Hz, 1H), 1.20 (s, 3H), 1.06 (s, 3H). ^{13}C NMR (101 MHz, DMSO- d_6) δ 213.14, 170.26, 138.74, 131.97, 120.53, 116.49, 68.36, 61.65, 54.34, 40.02, 39.68, 39.57, 33.48, 29.88, 28.58, 26.18, 25.02. MS (ESI): calculated for $\text{C}_{19}\text{H}_{25}\text{BrN}_3\text{O}_2$ $[\text{M}+\text{H}]^+$ 406.1125; found 406.26. HPLC: $t_{\text{R}} = 18.43$ min.

General procedure for the preparation of compounds 35-36. To a solution of derivative **34a** (1 eq, 0.50 mmol) in THF (8 mL) were added DIPEA (1 eq) and the appropriate sulphonyl-chloride (1.2 eq), and the reaction mixture was stirred at room temperature overnight. After the reaction was complete, as indicated by MS (ESI), the mixture was concentrated under reduced pressure. The resulting solid residue was extracted with EtOAc (2x10 mL), and the organic layers were washed with water (1x10 mL) and brine (1x10 mL). After drying over Na_2SO_4 , the solvent was evaporated to obtain a crude material, which was purified by semi-preparative HPLC to yield derivatives **35-36** as white solids.

13-(4-chlorophenyl)-3,3-dimethyl-9-tosyl-9,12,13-triazadispiro[4.0.5⁶.3⁵]tetradecane-1,14-dione (35): White solid (yield 42%). mp 181-183°C. ^1H NMR (400 MHz, DMSO- d_6) δ 7.67-7.60 (m, 4H), 7.46 (d, $J = 7.9$ Hz, 2H), 7.40-7.34 (m, 2H), 6.01 (s, 1H), 3.61-3.50 (m, 2H), 2.70-2.62 (m, 1H), 2.41 (s, 3H), 2.35 (d, $J = 16.6$ Hz, 1H), 2.09-2.03 (m, 1H), 1.98-1.87 (m, 2H), 1.81-1.73 (m, 1H), 1.61-1.47 (m, 2H), 1.25-1.20 (m, 2H), 1.19 (s, 3H), 1.01 (s, 3H). ^{13}C NMR (101 MHz, DMSO- d_6) δ 213.24, 170.68, 144.04, 138.35, 133.87, 130.43, 128.97, 128.22, 127.85, 120.18, 68.34, 62.73, 54.29, 42.41, 41.81, 40.19, 39.56, 33.48, 29.44, 28.56, 27.36, 21.50. MS (ESI): calculated for $\text{C}_{26}\text{H}_{31}\text{ClN}_3\text{O}_4\text{S}$ $[\text{M}+\text{H}]^+$ 516,1718; found 516.5870. HPLC: $t_{\text{R}} = 26.07$ min.

13-(4-chlorophenyl)-9-((5-chlorothiophen-2-yl)sulfonyl)-3,3-dimethyl-9,12,13-triazadispiro[4.0.5⁶.3⁵]tetradecane-1,14-dione (36): White solid (yield 45%). mp 165-167°C; ^1H NMR (400 MHz, DMSO- d_6) δ 7.71-7.66 (m, 2H), 7.59 (d, $J = 4.1$ Hz, 1H), 7.42-

7.37 (m, 3H), 6.07 (s, 1H), 3.60-3.50 (m, 2H), 2.83-2.75 (m, 1H), 2.69-2.62 (m, 1H), 2.37 (d, $J = 16.7$ Hz, 1H), 2.12-1.82 (m, 4H), 1.68-1.61 (m, 2H), 1.30 (d, $J = 11.7$ Hz, 1H), 1.20 (s, 3H), 1.02 (s, 3H). ^{13}C NMR (101 MHz, DMSO- d_6) δ 213.27, 170.66, 138.37, 136.00, 134.92, 133.37, 129.31, 129.01, 128.25, 120.16, 68.29, 62.53, 54.30, 42.54, 42.00, 39.96, 33.52, 29.44, 28.59, 28.53, 27.33. MS (ESI): calculated for $\text{C}_{23}\text{H}_{26}\text{Cl}_2\text{N}_3\text{O}_4\text{S}_2$ $[\text{M}+\text{H}]^+$ 542,0736; found 542.4138. HPLC: $t_{\text{R}} = 25.16$ min.

Dispiro-isatin derivatives.

General procedure for the preparation of compounds 39-42.

K_2CO_3 (3 eq) and the appropriate benzyl bromide (1.5 eq) were added to a solution of substituted isatins **37-38** (1 eq, 6.8 mmol) in MeCN (0.10 M) at room temperature. The resulting mixture was then heated at reflux overnight. Upon completion, as indicated by TLC and MS (ESI), the reaction mixture was cooled, filtered and concentrated. The crude residue was then triturated (Et_2O) and filtered to yield derivatives **39-42** as orange-red solids, which were used in the next step without further purification. ^[109]

1-benzylindoline-2,3-dione (39): Orange solid (yield 82%). ^1H NMR (400 MHz, DMSO- d_6) δ 7.62-7.54 (m, 2H), 7.43 (d, $J = 7.2$ Hz, 2H), 7.39-7.24 (m, 3H), 7.14-7.08 (m, 1H), 6.97 (d, $J = 8.4$ Hz, 1H), 4.91 (s, 2H). MS (ESI): calculated for $\text{C}_{15}\text{H}_{12}\text{NO}_2$ $[\text{M}+\text{H}]^+$ 238.09; found 238.30.

1-benzyl-5-fluoroindoline-2,3-dione (40): Dark orange solid (yield 89%). ^1H NMR (400 MHz, DMSO- d_6) δ 7.53-7.40 (m, 4H), 7.38-7.24 (m, 3H), 6.98-6.93 (m, 1H), 4.91 (s, 2H). MS (ESI): calculated for $\text{C}_{15}\text{H}_{11}\text{FNO}_2$ $[\text{M}+\text{H}]^+$ 256.08; found 256.37.

1-(4-fluorobenzyl)indoline-2,3-dione (41): Dark orange solid (yield 79%). ^1H NMR (400 MHz, DMSO- d_6) δ 7.62-7.44 (m, 4H), 7.24-7.04 (m, 3H), 6.98 (d, $J = 7.7$ Hz, 1H), 4.90 (s, 2H). MS (ESI): calculated for $\text{C}_{15}\text{H}_{11}\text{FNO}_2$ $[\text{M}+\text{H}]^+$ 256.08; found 256.17.

5-fluoro-1-(4-fluorobenzyl)indoline-2,3-dione (42): Red solid (yield 78%). ^1H NMR (400 MHz, CDCl_3) δ 7.37-7.29 (m, 3H), 7.26-7.19 (m, 1H), 7.10-7.03 (m, 2H), 6.76-6.71 (m, 1H), 4.91 (s, 2H). MS (ESI): calculated for $\text{C}_{15}\text{H}_{10}\text{F}_2\text{NO}_2$ $[\text{M}+\text{H}]^+$ 274.07; found 274.30.

General procedure for the preparation of compounds 44a-e. To a solution of carbonyl derivatives **39-42** (1 eq, 0.4 mmol) in toluene (3 mL), in a specific vial, was added the appropriate hydrazine (1 eq). The reaction mixture was sealed and irradiated with microwaves (400 W) at 140 °C for 15 min, and then cooled down to 50 °C by airflow. When the hydrazone intermediate was achieved, as indicated by TLC and MS(ESI), the diazo compound (2eq)

was added to the resulting mixture, which was sealed again, irradiated with microwaves (400 W) at 140 °C for 15 min and then cooled down to 50°C by airflow. Upon completion, as indicated by TLC and MS (ESI), the solvent was evaporated and the obtained crude material was directly purified by semi-preparative HPLC to yield derivatives **44a-e** as white solids.

1''-benzyl-1',4,4-trimethyldispiro[cyclopentane-1,4'-pyrazolidine-3',3''-indoline]-2,2'',5'-trione (44a): White solid (yield 50%). mp 202-204°C. ¹H NMR (400 MHz, CDCl₃) δ NH not detected, 7.35-7.24 (m, 7H), 7.05-6.98 (m, 1H), 6.79 (d, *J* = 7.9 Hz, 1H), 5.03 (d, *J* = 15.5 Hz, 1H), 4.69 (d, *J* = 15.5 Hz, 1H), 3.20 (s, 3H), 2.47 (d, *J* = 14.2 Hz, 1H), 2.21 (d, *J* = 17.4 Hz, 1H), 1.88 (d, *J* = 17.4 Hz, 1H), 1.34 (d, *J* = 14.2 Hz, 1H), 1.13 (s, 3H), 0.59 (s, 3H). ¹³C NMR (101 MHz, CDCl₃) δ 214.22, 174.05, 170.40, 144.23, 135.32, 131.12, 128.84, 127.95, 127.54, 124.97, 123.20, 121.70, 109.91, 70.40, 63.99, 54.27, 43.78, 42.19, 33.74, 33.63, 29.22, 28.98. MS (ESI): calculated for C₂₄H₂₆N₃O₃ [M+H]⁺ 404.1969; found 404.2409. HPLC: t_R = 20.98 min.

1''-benzyl-5''-fluoro-1',4,4-trimethyldispiro[cyclopentane-1,4'-pyrazolidine-3',3''-indoline]-2,2'',5'-trione (44b): White solid (yield 41%). mp 224-226°C. ¹H NMR (400 MHz, CDCl₃) δ NH not detected, 7.38-7.29 (m, 5H), 7.12-7.07 (m, 1H), 7.05-6.98 (m, 1H), 6.75-6.70 (m, 1H), 5.03 (d, *J* = 15.6 Hz, 1H), 4.71 (d, *J* = 15.6 Hz, 1H), 3.22 (s, 3H), 2.52 (d, *J* = 14.0 Hz, 1H), 2.28 (d, *J* = 17.5 Hz, 1H), 1.96 (d, *J* = 17.5 Hz, 1H), 1.37 (d, *J* = 14.0 Hz, 1H), 1.17 (s, 3H), 0.62 (s, 3H). ¹³C NMR (101 MHz, CDCl₃) δ 214.09, 173.74, 170.03, 158.99, 140.13, 134.87, 128.93, 128.09, 127.47, 123.13, 117.65, 113.65, 110.59, 70.33, 54.13, 43.84, 42.22, 33.71, 33.61, 29.24, 28.88. MS (ESI): calculated for C₂₄H₂₅FN₃O₃ [M+H]⁺ 422.1874; found 422.1902. HPLC: t_R = 21.25 min.

1''-(4-fluorobenzyl)-1',4,4-trimethyldispiro[cyclopentane-1,4'-pyrazolidine-3',3''-indoline]-2,2'',5'-trione (44c): White solid (yield 56%). mp 183-185°C. ¹H NMR (400 MHz, CDCl₃) δ NH not detected, 7.36-7.27 (m, 4H), 7.08-7.01 (m, 3H), 6.81 (d, *J* = 7.8 Hz, 1H), 4.97 (d, *J* = 15.5 Hz, 1H), 4.72 (d, *J* = 15.5 Hz, 1H), 3.23 (s, 3H), 2.47 (d, *J* = 14.2 Hz, 1H), 2.24 (d, *J* = 17.4 Hz, 1H), 1.90 (d, *J* = 17.4 Hz, 1H), 1.31 (d, *J* = 14.2 Hz, 1H), 1.15 (s, 3H), 0.60 (s, 3H). ¹³C NMR (101 MHz, CDCl₃) δ 214.09, 174.02, 170.44, 161.16, 143.98, 131.19, 131.12, 129.38, 125.10, 123.38, 121.63, 115.80, 109.75, 70.38, 63.99, 54.23, 43.11, 42.16, 33.74, 33.65, 29.25, 28.96. MS (ESI): calculated for C₂₄H₂₅FN₃O₃ [M+H]⁺ 422.1874; found 422.2532. HPLC: t_R = 21.04 min.

5''-fluoro-1''-(4-fluorobenzyl)-1',4,4-trimethyldispiro[cyclopentane-1,4'-pyrazolidine-3',3''-indoline]-2,2'',5'-trione (44d): White solid (yield 46%). mp 176-178°C. ¹H NMR

(400 MHz, CDCl₃) δ NH not detected, 7.32-7.26 (m, 2H), 7.15-6.97 (m, 4H), 6.75-6.70 (m, 1H), 4.96 (d, $J = 15.6$ Hz, 1H), 4.71 (d, $J = 15.6$ Hz, 1H), 3.22 (s, 3H), 2.51 (d, $J = 14.0$ Hz, 1H), 2.29 (d, $J = 17.5$ Hz, 1H), 1.96 (d, $J = 17.5$ Hz, 1H), 1.32 (d, $J = 14.0$ Hz, 1H), 1.17 (s, 3H), 0.61 (s, 3H). ¹³C NMR (101 MHz, CDCl₃) δ 213.98, 173.80, 170.13, 162.50, 159.15, 139.94, 130.74, 129.39, 123.21, 117.59, 115.89, 113.61, 110.51, 70.39, 63.98, 54.17, 43.24, 42.26, 33.77, 33.70, 29.34, 28.94. MS (ESI): calculated for C₂₄H₂₄F₂N₃O₃ [M+H]⁺ 440.1789; found 440.2499. HPLC: $t_R = 21.36$ min.

1',1''-dibenzyl-4,4-dimethyldispiro[cyclopentane-1,4'-pyrazolidine-3',3''-indoline]-2,2'',5'-trione (44e): White solid (yield 43%). mp 209-211°C. ¹H NMR (400 MHz, CDCl₃) δ NH not detected, 7.42-7.24 (m, 11H), 7.21 (dd, $J = 7.6, 0.7$ Hz, 1H), 7.02-6.95 (m, 1H), 6.79 (d, $J = 7.9$ Hz, 1H), 5.27 (d, $J = 15.0$ Hz, 1H), 5.04 (d, $J = 15.5$ Hz, 1H), 4.71 (d, $J = 15.5$ Hz, 1H), 4.38 (d, $J = 15.0$ Hz, 1H), 2.55 (d, $J = 14.3$ Hz, 1H), 2.27 (d, $J = 17.4$ Hz, 1H), 1.93 (d, $J = 17.4$ Hz, 1H), 1.41 (d, $J = 14.3$ Hz, 1H), 1.19 (s, 3H), 0.64 (s, 3H). ¹³C NMR (101 MHz, CDCl₃) 214.10, 173.86, 170.22, 144.24, 135.76, 135.29, 131.21, 128.92, 128.81, 128.16, 128.04, 127.70, 127.65, 125.13, 123.25, 121.57, 109.97, 70.14, 63.99, 54.34, 50.31, 43.82, 42.19, 33.70, 29.28, 29.03. MS (ESI): calculated for C₃₀H₃₀N₃O₃ [M+H]⁺ 480.23; found 480.53. HPLC: $t_R = 23.94$ min.

2C. Project 3: SPIRO-PIPERIDINE DERIVATIVES.

2c.1 AIM AND OBJECTIVES.

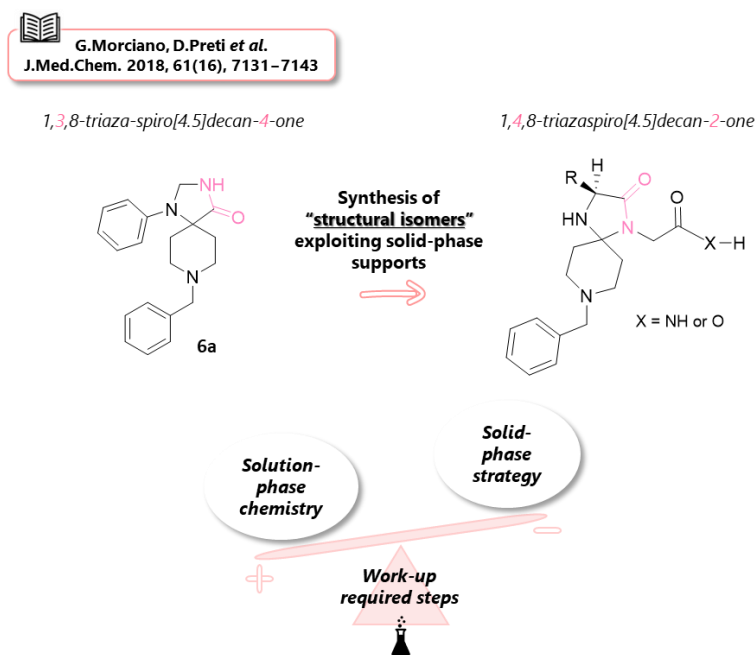


Figure 2c.1: Rational design Project 3.

My research group has reported the discovery of the first small-molecule inhibitors of mPTP that target the c-subunit of F₁F₀-ATP synthase.^[93] The synthesized spiro derivatives, with a general structure 1,3,8-triazaspiro[4.5]decan-4-one, were obtained by a synthetic approach exclusively based on standard liquid-phase methodologies. In this project we explored a different strategy which implement solid-phase supports in order to quickly synthesize a wide library of spiro derivatives.

In this regard, spiro-imidazolidinone compounds represent a molecular framework used with various pharmacological activities, and they may offer a useful template to which can be added a variety of functional groups. Since 1,4,8-triazaspiro[4.5]decan-2-one is recognized as a molecular architecture that constitutes interesting highly functionalized templates in the drug discovery process, [115] we decided to design a series of spiropiperidines whose general spirodecane scaffold can be defined as structural isomer of that of the spiropiperidines previously detailed.^[93] Moreover, considering that in drug design program particular attention is focused on the possibility to introduce hydrophilic or salifiable functions into the investigated derivatives, we have herein proposed spiro derivatives which can be converted in the corresponding salt form, increasing their water solubility to facilitate eventual future formulation in aqueous medium for *in vivo* administration. In particular, starting from compound **6a**^[93] we synthesized two groups of derivatives, as amide

spirocyclic and carboxylic acid spirocyclic derivatives respectively. (Fig. 2c.1) These compounds are made up of a piperidine moiety from *N*-benzyl-4-piperidone, and an imidazolidinone moiety from a dipeptide species. ^[115] To the achievement of the desired compounds, all the synthetic steps, including the preparation of the dipeptide and the subsequent condensation with *N*-benzyl-4-piperidone, were conducted on a solid-phase support. Only at the end of the synthesis the final derivatives were removed from the support (cleavage step) and purified. ^[115] It is therefore clear that the designed series were gained rapidly, reducing the reaction steps but especially all the work-up required procedures. Of note, this type of synthetic strategy allowed a quick preparation and investigation of a library of spiro-piperidine compounds, which differs from the previous one ^[93] in the mutual position of some functional groups that may be closely involved in the mechanism of mPTP inhibition.

2c.1.1 Overview of solid phase peptide synthesis (SPPS).

Since 1963, solid-phase peptide synthesis (SPPS) developed by R.B. Merrifield has been the widely used technique for the production of synthetic peptides. ^[116] Compared with the previous liquid-phase peptide synthesis, SPPS greatly simplifies the problems of compound solubility and purification through an approach inspired by protein biosynthesis in the human organism.

Solid-phase peptide synthesis involves sequential reactions on an accretion sequence bound to a "solid" support. The term "solid" refers more to the insolubility of this support in commonly used organic solvents, being porous polymer resin spheres. This polymer resin is chemically modified with reactive functions onto which the nascent peptide chain is grafted. They are available in either electrophilic (Br) or nucleophilic (OH, NH₂ and SH) form as well as derivatized with various linkers. Linkers are chemical entities used to "link" a compound to a resin bead during solid phase synthesis. The nature of the linker determines the kind of chemistry that can be performed, and the conditions under which products can be cleaved from the resin. There are a wide variety of linkers for polystyrene core resins. Peptide chemists can usually focus on just a few: Wang, Rink, and derivatives of each. Wang linkers produce carboxylic acid products while Rink linkers produce amide products. Both Wang and Rink resins are available with amino acids preloaded. The general procedure (Fig. 2c.2) involves the initial condensation of the first amino acid (aa), via the activated free C-terminal residue, to the resin support (Load). To prevent its polymerization, the alpha amino group (*N*_α) and the side chains are protected with a temporary protecting group. Indeed, the side chains of many amino acids are reactive and may form side products if left unprotected.

For successful peptide synthesis, these side chains must remain protected despite repeated exposure to *N*-deprotection conditions. Such a protection scheme is called “orthogonal” protection. Once the amino acid is attached to the resin, the resin is filtered and washed to remove by-products and excess reagents (Wash). The *N*-protecting group is then removed under appropriate conditions (Deprotect) and, following another washing step (Wash), the next amino acid is coupled to the attached resin-peptide (Couple). The cycle is repeated until the peptide sequence is complete. Then typically, all or most of the protecting groups are removed, the peptide resin is washed, and the peptide is cleaved from the resin (Cleave). This latter step is usually done using a "cleavage cocktail," consisting of a high percentage of a strong acid, among which the most commonly used is trifluoroacetic acid (TFA), and a small percentage of some "scavengers" such as thiols, alcohols, silanes or H₂O. Then, the obtained crude peptide may be precipitated in a cold organic solvent, such as Et₂O, centrifuged, and finally purified by semi-preparative HPLC. [117]

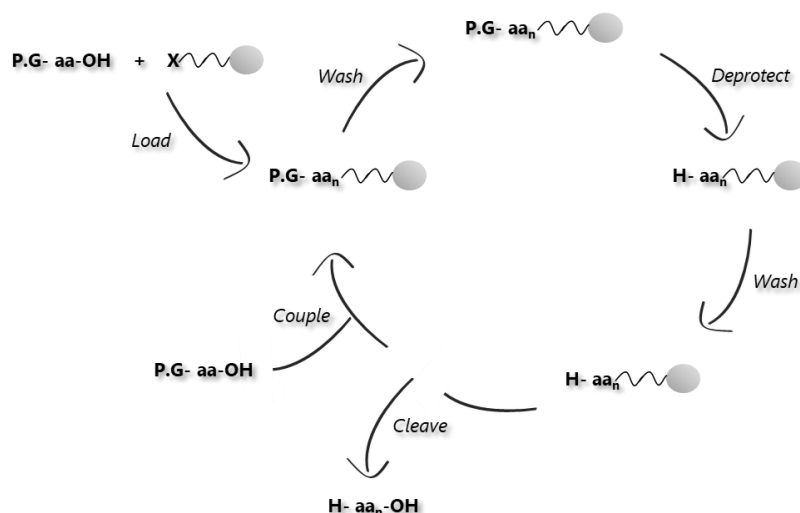


Figure 2c.2: General solid-phase peptide synthesis cycle.

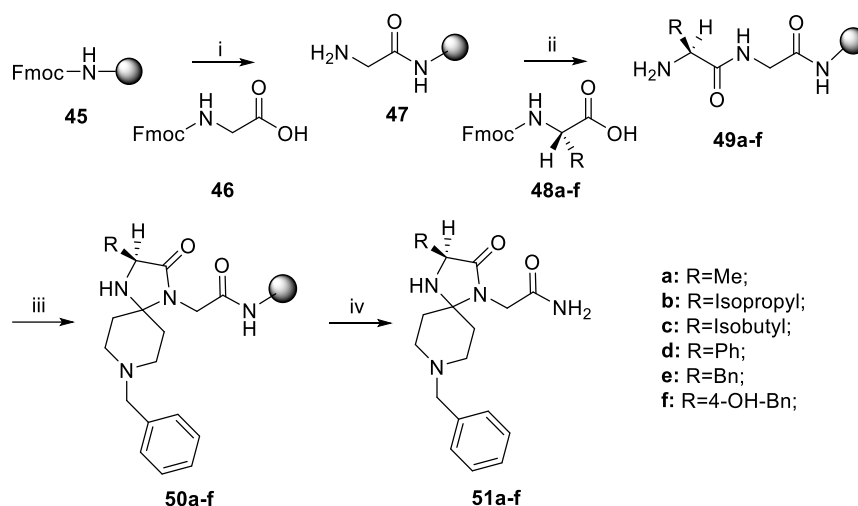
This synthetic method simplifies the work-up procedures and allows the use of reagents in large excess to drive reactions to completion, obtaining the product in relatively pure form with high yield. [118] Moreover, the use of a solid-phase support permits to automate the peptide synthesis process. Disadvantages of this type of synthesis include the lack of analytical control and purification following each step, besides a yield that tends to be inversely proportional to the length of the chain synthesized.

2c.2 RESULTS AND DISCUSSION.

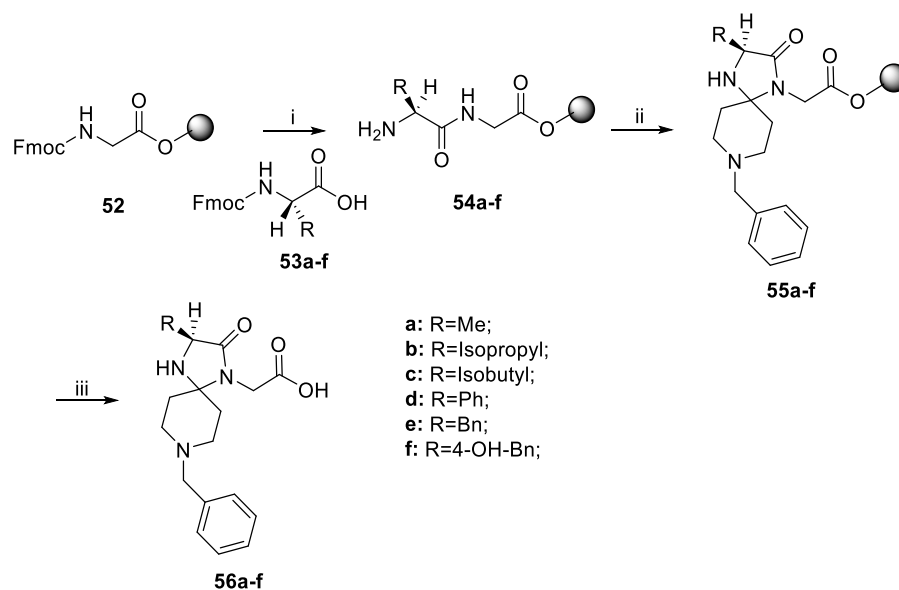
2c.2.1 Chemistry.

As depicted in Scheme 2c.1 and Scheme 2c.2, the synthetic pathway on solid-phase supports allowed us to quickly synthesize a library of spiropiperidines, as “structural isomers” of the spiropiperidines realized in the previous work.^[93] All the reported derivatives, with general structure 2-(8-benzyl-2-oxo-1,4,8-triazaspiro[4.5]decan-1-yl)acetamide (**51a-f**) and 2-(8-benzyl-2-oxo-1,4,8-triazaspiro[4.5]decan-1-yl)acetic acid (**56a-f**), were synthesized starting from commercially available natural Fmoc-protected amino acids (Fmoc-aa-OH), which were anchored on specific solid support by automatic coupling reactions. The obtained dipeptides were subsequently applied for the condensation reaction with *N*-benzyl-4-piperidone. This reaction was performed in different solvent conditions, according to the type of resin used: toluene for the AmphiSpheres resin and 2,2-Dimethoxypropane (DMP) for the Wang one.^[115] Especially, the AmphiSpheres resin was used as a functionalized support for the preparation of compounds **51a-f**, while the Glycine preloaded-Wang resin was used similarly for compounds **56a-f**. These final spiro derivatives were finally removed from the solid support and purified by semi-preparative HPLC.

Notably, we designed spiro derivatives starting from a dipeptide: the first amino acid bound to the solid-phase support, as well as the Glycine residue, was retained unaltered, changing the second one in order to first explore how this diverse portion, from a same general scaffold, can influence the activity towards the target. Moreover, since the employed commercially available amino acids were natural L-amino acids, all the synthesized final spiro derivatives exhibited a well-defined stereochemistry (as highlighted below).



*Scheme 2c.1. Synthesis of substituted 2-(8-benzyl-2-oxo-1,4,8-triazaspiro[4.5]decan-1-yl)acetamide (51a-f) - Reagents and conditions - i. 40% Piperidine in DMF, 2x7min; DIC, HOBt, DMF, 2x40min; NMM, Ac₂O, 2x5min; 40% Piperidine in DMF, 2x7min; ii. DIC, HOBt, DMF, 2x40min; NMM, Ac₂O, 2x5min; 40% Piperidine in DMF, 2x7min; iii. *N*-benzyl-4-piperidone, toluene, *p*-TsOH, 80°C overnight; iv. TFA:H₂O:Et₃SiH (95:2.5:2.5), rt 3h.*



*Scheme 2c.2. Synthesis of substituted 2-(8-benzyl-2-oxo-1,4,8-triazaspiro[4.5]decan-1-yl)acetic acid (56a-f) - Reagents and conditions - i. 40% Piperidine in DMF; 2x7min, DIC, HOBt, DMF, 2x40min; NMM, Ac₂O, 2x5min; 40% Piperidine in DMF, 2x7min; ii. *N*-benzyl-4-piperidone, DMP, *p*-TSOH, 80°C 5h; iii. TFA:H₂O:Et₃SiH (95:2.5:2.5), rt 3 h.*

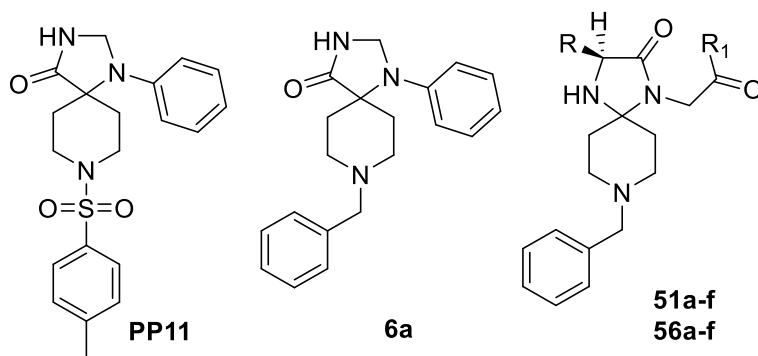
2c.2.2 Biological evaluation.

The biological assay reported below was realized in collaboration with the research group of Professor Paolo Pinton of the University of Ferrara (Dept. of Medical Sciences).

Preliminary screening-cobalt-calcein assay.

To assess the efficacy of the investigated spiro-piperidine derivatives in inhibiting Ca^{2+} -mediated mPTP opening, herein we measured their biological activity in human ventricular cardiomyocytes (AC16) by using the cobalt-calcein assay. ^[104] For the cobalt-calcein quenching assay, all cells were pretreated with vehicle (DMSO), 1 μM **PP11** (first reference compound), 1 μM **6a** (second reference compound) or 1 μM inquired derivative, and then loaded with 1 μM calcein acetoxymethyl ester and 2 mM Co^{2+} . According to the described assay and under conditions of mitochondrial calcium overload (by the administration of 1 μM ionomycin), the resulting kinetics data are reported in Table 2c.1.

The obtained outcomes indicate that changing R_1 does not result in a different behaviour towards the target, whereas varying R may modify the inhibitory potency. Especially, compounds **56e** and **56f** were slightly more potent than compound **6a** in inhibiting mPTP opening. Comparing these selected compounds with all the other synthesized, it can be noticed that, similarly to compound **6a** which bears an aniline fragment, the presence of an aromatic moiety at the imidazolidinone ring may be mandatory to ensure the desired activity.

Table 2c.1. *In vitro* potency of spiro-piperidine derivatives as mPTP opening inhibitors.

Compd	R	R ₁	mPTP inhibition (% 1 μM)	Statistic
PP11	-	-	40,19	P<0.0001
6a	-	-	37	P<0.0001
51a (MF 29)	Me	NH ₂	18,71	P<0.001
56a (MF 30)	Me	OH	19,40	P<0.001
51b (MF 31)	Isopropyl	NH ₂	28,71	P<0.0001
56b (MF 32)	Isopropyl	OH	-0,896	n.s.
51c (MF 33)	Isobutyl	NH ₂	29,13	P<0.0001
56c (MF 34)	Isobutyl	OH	23,01	P<0.001
51d (MF 39)	Ph	NH ₂	38,73	P<0.0001
56d (MF 40)	Ph	OH	36,63	P<0.0001
51e (MF 35)	Bn	NH ₂	30,72	P<0.0001
56e (MF 36)	Bn	OH	43,02	P<0.0001
51f (MF 37)	4-OH-Bn	NH ₂	32,17	P<0.0001
56f (MF 38)	4-OH-Bn	OH	42,11	P<0.0001

As shown in Table 2c.1, all the synthesized compounds showed a good inhibitory potential compared to the untreated mitochondrial sample. In particular, the addition of 1 μM ionomycin to cells pretreated with 1 μM **56e** or **56f** resulted in desensitization of mPTP opening by around 40-45%, which was approximately the same as that observed in compounds **PP11** and **6a** treated cells.

2c.3 EXPERIMENTAL SECTION.

2c.3.1 Materials and Methods.

Peptides were synthesized using a standard Fmoc/tBu strategy ^[119] through a Syro XP multiple peptide synthesizer (MultiSynTech GmbH, Witten Germany) on a AmphiSpheres 20 RAM resin (loading 0.55 mmol/g) or a Glycine preloaded-Wang resin (loading 1 mmol/g). Commercially available Fmoc-amino acids were used with a 4-fold excess on a 0.1 mM scale of the resin and double-coupled to the growing peptide chain using a 4-fold excess of *N,N'*-diisopropylcarbodiimide and 1-hydroxybenzotriazole (DIC/HOBt). Each Fmoc removal step was performed using 40% solution of piperidine in *N,N*-dimethylformamide (DMF), and the couplings were repeated until the desired dipeptide-bound resin was completed. After each coupling reaction a treatment with a solution of acetic anhydride (Ac₂O) and *N*-Methylmorpholine (NMM) in DMF was performed to quench the reactivity of randomly uncoupled amine groups (capping). The “cleavage cocktail” to obtain the final product from the resin consisted of 95% trifluoroacetic acid, 2.5% water, and 2.5% triethylsilane (TFA:H₂O:Et₃SiH). Reverse-phase purifications of crude derivative was carried out on a Waters Delta 600 high-performance liquid chromatography (HPLC) system with a Jupiter column C18 (250 × 30 mm, 300 Å, 15 μm spherical particle size), using a binary mobile phase consisting of solution A (100% H₂O, 0.1% v/v TFA) and solution B (40% H₂O, 60% CH₃CN, 0.1% v/v TFA) at a flow rate of 20 mL/min. Gradient was established individually considering the analytical HPLC profile of the crude product. Analytical HPLC was performed with a Beckman 126 liquid chromatograph furnished of a UV detector Beckman 168 and equipped with KARAT32 software. The purity of all the derivatives was assessed with an Agilent Zorbax C18 column (4.6 × 150 mm, 3.5 μm particle size) at a flow rate of 0.7 mL/min using a linear gradient from 100% of A (water + 0.1% TFA) to 100% of B (acetonitrile + 0.1% TFA) over a period of 25 min. All final compounds were monitored at 220 nm showing ≥95% purity. The molecular weights of the crude material and of the final compounds were determined using an electrospray mass spectrometer (ESI MICROMASS ZMD 2000). Enantiopure Fmoc-protected amino acids and the resins for SPPS were purchased from AAPPTec, Bachem (Bubendorf, Switzerland), BLDpharm (Kaiserslautern, Germany), Merck Life Science (Milan, Italy) and IrisBiotech (Marktredwitz, Germany). All solvents were purchased from VWR International.

2c.3.2 General synthetic procedures.

General procedure for dipeptide synthesis on solid-phase.

AmphiSpheres 20 RAM resin and Glycine preloaded-Wang resin were the two solid supports adopted as starting material (1eq). The resin was weighted into an empty syringe and then it was swelled in DMF at room temperature.

The main automatically repeated steps were:

- *N*-terminal deprotection: *N*-Fmoc, of the resin or of the first amino acid preloaded to it, was removed by treatment the resin with a 40% solution of piperidine in DMF (2 mL/0.15 g of resin), which selectively removed the base-labile *N*-protecting group in favour of the next amide coupling reaction;
- Amide coupling reaction: the free *N*-terminal residue of the growing peptide chain was coupled with the activated *C*-terminal of the following *N*-Fmoc-aa-OH (0.5M) of the sequence. HOBt (0.78 M) and DIC (1.09 M) were used as coupling reagents in DMF (1.1:0.7:0.5 v/v; 2.3 mL/0.15 g of resin);
- Capping: the acetylation reaction was performed to block the elongation of undesired peptide chains that may occur due to possible unsuccessful coupling reaction. Ac₂O (0.5 M) and NMM (0.25 M) were used as capping reagents in DMF (1.5:0.5 v/v; 2 mL/0.15 g of resin), to quench the reactivity of randomly uncoupled amine groups.

After each step the resin was washed for three times with fresh DMF (2 mL/0.15 g of resin). In the case of *N*-Fmoc deprotection it was preferred to wash the resin more carefully, for nine times with fresh DMF, to avoid an undesired *N*-deprotection of the next added amino acid.

Once the last amino acid was inserted and the *N*-terminal Fmoc protection was removed, a condensation reaction with *N*-benzyl-4-piperidone was performed, under specific condition depending on the solid support used as starting.

General procedure for condensation of *N*-benzyl-4-piperidone from AmphiSpheres resin (50a-f).

To a solution of *N*-benzyl-4-piperidone (1eq) in toluene (4mL), in a glass vial, were consecutively added a catalytic amount of *p*-toluenesulfonic acid monohydrate (0.01 eq) and the free *N*-terminal dipeptide anchored to Amphispheres resin (1eq, 0.083mmol). The reaction mixture was slowly stirred overnight at 80°C. The solution was filtered out and the solid support was washed three times with DMF and CH₂Cl₂ respectively.

General procedure for condensation of *N*-benzyl-4-piperidone from Glycine preloaded-Wang resin (55a-f).

To a solution of *N*-benzyl-4-piperidone (1eq) in DMP (4mL), in a glass vial, were consecutively added a catalytic amount of *p*-toluenesulfonic acid monohydrate (0.01 eq) and free *N*-terminal dipeptide anchored to the Glycine preloaded-Wang resin (1eq, 0.15mmol). The reaction mixture was slowly stirred for 5h at 80°C. The solution was filtered out and the solid support was consecutively washed three times with DMF and CH₂Cl₂ respectively.

General procedure for the cleavage of synthesized final derivatives 51a-f and 56a-f.

Upon completion, as indicated by MS(ESI), the final spiro derivatives **50a-f** and **55a-f**, which were anchored to the solid support, were treated with a cleavage solution composed by trifluoroacetic acid TFA, H₂O and Et₃SiH (95:2.5:2.5; v/v; 5 mL/0.15 g of resin) for 3 h at room temperature. After filtration of the exhausted resin, TFA was removed under vacuum, and the crude material was then precipitated in diethyl ether (Et₂O), isolated through centrifugation and finally purified by reverse-phase semi-preparative HPLC. After lyophilization the desired spiro derivatives **51a-f** and **56a-f** were obtained as tinted oils.

2-(8-benzyl-3-methyl-2-oxo-1,4,8-triazaspiro[4.5]decan-1-yl)acetamide (51a): Yellow oil (yield 38%). ¹H NMR (400 MHz, DMSO-d₆) δ 9.51 (bs, 1H), 7.55-7.43 (m, 6H), 7.34 (s, 1H), 7.12 (s, 1H), 4.33 (s, 2H), 3.71 (d, *J* = 17.1 Hz, 1H), 3.63-3.04 (m, 6H), 2.16-2.05 (m, 1H), 1.97-1.67 (m, 3H), 1.19 (d, *J* = 6.9 Hz, 3H). ¹³C NMR (101 MHz, DMSO-d₆) δ 175.14, 169.31, 131.12, 131.10, 129.53, 128.80, 73.55, 58.59, 52.40, 48.73, 48.04, 41.92, 31.72, 29.24, 16.17. MS (ESI): calculated for C₁₇H₂₅N₄O₂ [M+H]⁺ 317,1972; found 317.1975. HPLC: t_R = 10.69 min.

2-(8-benzyl-3-methyl-2-oxo-1,4,8-triazaspiro[4.5]decan-1-yl)acetic acid (56a): Yellow oil (yield 28%). ¹H NMR (400 MHz, DMSO-d₆) δ 9.62 (bs, 1H), 7.61-7.38 (m, 6H), 4.34 (s, 2H), 3.86-3.67 (m, 2H), 3.51-3.06 (m, 7H), 2.26-2.09 (m, 1H), 2.04-1.62 (m, 3H), 1.18 (d, *J* = 6.9 Hz, 3H). ¹³C NMR (101 MHz, DMSO-d₆) δ 175.60, 170.49, 131.66, 131.62, 130.08, 129.37, 74.05, 59.13, 52.86, 49.26, 48.58, 41.31, 32.41, 30.22, 17.07. MS (ESI): calculated for C₁₇H₂₄N₃O₃ [M+H]⁺ 318,1812; found 318.2321. HPLC: t_R = 11.30 min.

2-(8-benzyl-3-isopropyl-2-oxo-1,4,8-triazaspiro[4.5]decan-1-yl)acetamide (51b): Yellow oil (yield 31%). ¹H NMR (400 MHz, DMSO-d₆) δ 9.38 (bs, 1H), 7.53-7.43 (m, 6H), 7.33 (s, 1H), 7.06 (s, 1H), 4.33 (s, 2H), 3.69 (d, *J* = 17.1 Hz, 1H), 3.56 (d, *J* = 17.1 Hz, 1H), 3.38-3.13 (m, 5H), 2.08-1.80 (m, 3H), 1.72-1.60 (m, 2H), 0.96 (d, *J* = 6.8 Hz, 3H), 0.85 (d, *J* = 6.8 Hz, 3H). ¹³C NMR (101 MHz, DMSO-d₆) δ 174.01, 169.60, 131.64, 130.23, 130.10,

129.36, 73.51, 62.34, 59.23, 49.19, 48.93, 42.06, 33.20, 31.43, 29.86, 19.69, 18.13. MS (ESI): calculated for $C_{19}H_{29}N_4O_2$ $[M+H]^+$ 345,2285; found 345.4126. HPLC: t_R = 11.15 min.

2-(8-benzyl-3-isopropyl-2-oxo-1,4,8-triazaspiro[4.5]decan-1-yl)acetic acid (56b): Orange oil (yield 15%). 1H NMR (400 MHz, DMSO- d_6) δ 9.39 (bs, 1H), 7.52-7.43 (m, 6H), 4.33 (s, 2H), 3.85 (d, J = 17.8 Hz, 1H), 3.67 (d, J = 17.8 Hz, 1H), 3.36-3.15 (m, 5H), 2.13-1.83 (m, 3H), 1.72-1.61 (m, 2H), 0.96 (d, J = 6.8 Hz, 3H), 0.84 (d, J = 6.8 Hz, 3H). ^{13}C NMR (101 MHz, DMSO- d_6) δ 173.95, 170.38, 131.62, 130.23, 130.10, 129.37, 73.46, 62.25, 59.27, 49.20, 48.93, 41.05, 33.28, 31.50, 29.91, 19.59, 17.84. MS (ESI): calculated for $C_{19}H_{28}N_3O_3$ $[M+H]^+$ 346,2125; found 346.2477. HPLC: t_R = 13.57 min.

2-(8-benzyl-3-isobutyl-2-oxo-1,4,8-triazaspiro[4.5]decan-1-yl)acetamide (51c): Yellow oil (yield 30%). 1H NMR (400 MHz, DMSO- d_6) δ 9.36 (bs, 1H), 7.57-7.42 (m, 6H), 7.32 (s, 1H), 7.11 (s, 1H), 4.34 (s, 2H), 3.69 (d, J = 17.1 Hz, 1H), 3.53 (d, J = 17.1 Hz, 1H), 3.47-3.06 (m, 5H), 2.16-1.99 (m, 1H), 1.98-1.70 (m, 4H), 1.57-1.47 (m, 1H), 1.37-1.27 (m, 1H), 0.91 (d, J = 6.7 Hz, 3H), 0.87 (d, J = 6.7 Hz, 3H). ^{13}C NMR (101 MHz, DMSO- d_6) δ 175.67, 169.87, 131.62, 130.27, 130.08, 129.35, 74.25, 59.19, 55.67, 49.39, 48.88, 42.39, 40.94, 32.56, 30.24, 25.08, 23.67, 21.86. MS (ESI): calculated for $C_{20}H_{31}N_4O_2$ $[M+H]^+$ 359,2442; found 359.2592. HPLC: t_R = 18.23 min.

2-(8-benzyl-3-isobutyl-2-oxo-1,4,8-triazaspiro[4.5]decan-1-yl)acetic acid (56c): Orange oil (yield 29%). 1H NMR (400 MHz, DMSO- d_6) δ 9.35 (bs, 1H), 7.55-7.42 (m, 6H), 4.34 (s, 2H), 3.83 (d, J = 17.8 Hz, 1H), 3.70 (d, J = 17.8 Hz, 1H), 3.46-3.01 (m, 6H), 2.14-2.04 (m, 1H), 2.00-1.60 (m, 3H), 1.55-1.44 (m, 1H), 1.32-1.21 (m, 1H), 0.91 (d, J = 6.7 Hz, 3H), 0.87 (d, J = 6.7 Hz, 3H). ^{13}C NMR (101 MHz, DMSO- d_6) δ 175.69, 170.52, 131.61, 130.30, 130.08, 129.35, 74.14, 59.18, 55.59, 49.39, 48.93, 41.28, 40.17, 32.77, 30.62, 25.04, 23.68, 21.82. MS (ESI): calculated for $C_{20}H_{30}N_3O_3$ $[M+H]^+$ 360,2282; found 360.3399. HPLC: t_R = 10.69 min.

2-(8-benzyl-2-oxo-3-phenyl-1,4,8-triazaspiro[4.5]decan-1-yl)acetamide (51d): Yellow oil (yield 41%). 1H NMR (400 MHz, DMSO- d_6) δ 9.53 (bs, 1H), 7.53-7.39 (m, 8H), 7.37-7.23 (m, 4H), 7.11 (s, 1H), 4.63 (s, 1H), 4.34 (s, 2H), 3.72-3.68 (m, 2H), 3.49-3.12 (m, 4H), 2.20-1.95 (m, 2H), 1.89 (d, J = 13.2 Hz, 1H), 1.72 (d, J = 13.2 Hz, 1H). ^{13}C NMR (101 MHz, DMSO- d_6) δ 173.24, 169.56, 139.25, 131.68, 130.13, 130.10, 129.36, 128.54, 128.14, 127.87, 74.13, 60.85, 59.27, 49.11, 48.82, 42.44, 33.10, 31.25. MS (ESI): calculated for $C_{22}H_{27}N_4O_2$ $[M+H]^+$ 379,2129; found 379.3060. HPLC: t_R = 11.86 min.

2-(8-benzyl-2-oxo-3-phenyl-1,4,8-triazaspiro[4.5]decan-1-yl)acetic acid (56d): Orange oil (yield 28%). ¹H NMR (400 MHz, DMSO-d₆) δ 9.61 (bs, 1H), 7.56-7.38 (m, 8H), 7.38-7.24 (m, 3H), 4.64 (s, 1H), 4.34 (s, 2H), 3.94-3.74 (m, 2H), 3.42-3.20 (m, 4H), 2.21-2.04 (m, 2H), 1.87 (d, *J* = 13.8 Hz, 1H), 1.72 (d, *J* = 13.8 Hz, 1H). ¹³C NMR (101 MHz, DMSO-d₆) δ 173.13, 170.34, 139.24, 131.66, 130.14, 130.09, 129.36, 128.59, 128.13, 127.94, 74.06, 60.82, 59.27, 49.06, 48.81, 41.42, 40.59, 33.15, 31.31. MS (ESI): calculated for C₂₂H₂₆N₃O₃ [M+H]⁺ 380,1969; found 380.1863. HPLC: t_R = 14.85 min.

2-(3,8-dibenzyl-2-oxo-1,4,8-triazaspiro[4.5]decan-1-yl)acetamide (51e): Pale white solid (yield 35%). ¹H NMR (400 MHz, DMSO-d₆) δ 9.37 (bs, 1H), 7.52-7.41 (m, 6H), 7.35 (s, 1H), 7.32-7.09 (m, 6H), 4.31 (s, 2H), 3.73-3.54 (m, 3H), 3.39-2.98 (m, 5H), 2.72-2.62 (m, 1H), 2.08-1.86 (m, 2H), 1.74 (d, *J* = 13.6 Hz, 1H), 1.58 (d, *J* = 13.6 Hz, 1H). ¹³C NMR (101 MHz, DMSO-d₆) δ 174.69, 169.76, 139.36, 131.63, 130.24, 130.06, 129.60, 129.32, 128.62, 126.60, 74.34, 59.21, 59.04, 49.17, 48.85, 42.44, 38.06, 32.60, 30.71. MS (ESI): calculated for C₂₃H₂₉N₄O₂ [M+H]⁺ 393,2285; found 393.4768. HPLC: t_R = 12.93 min.

2-(3,8-dibenzyl-2-oxo-1,4,8-triazaspiro[4.5]decan-1-yl)acetic acid (56e): Yellow oil (yield 28%). ¹H NMR (400 MHz, DMSO-d₆) δ 12.85 (s, 1H), 9.40 (s, 1H), 7.53-7.41 (m, 5H), 7.32-7.16 (m, 6H), 4.32 (s, 2H), 3.83-3.65 (m, 2H), 3.40-2.96 (m, 6H), 2.68-2.61 (m, 1H), 2.14-1.90 (m, 2H), 1.72 (d, *J* = 13.3 Hz, 1H), 1.55 (d, *J* = 13.3 Hz, 1H). ¹³C NMR (101 MHz, DMSO-d₆) δ 174.52, 170.40, 139.20, 131.61, 130.24, 130.06, 129.65, 129.32, 128.59, 126.61, 74.28, 59.08, 59.06, 49.12, 48.88, 41.33, 38.27, 32.78, 30.97. MS (ESI): calculated for C₂₃H₂₈N₃O₃ [M+H]⁺ 394,2125; found 394.3277. HPLC: t_R = 20.05 min.

2-(8-benzyl-3-(4-hydroxybenzyl)-2-oxo-1,4,8-triazaspiro[4.5]decan-1-yl)acetamide (51f): Yellow oil (yield 34%). ¹H NMR (400 MHz, DMSO-d₆) δ 9.36 (bs, 1H), 7.54-7.39 (m, 6H), 7.32 (s, 1H), 7.12 (s, 1H), 7.04 (d, *J* = 8.2 Hz, 2H), 6.65 (d, *J* = 8.2 Hz, 2H), 4.31 (s, 2H), 3.66-3.56 (m, 3H), 3.37-3.01 (m, 4H), 2.93-2.87 (m, 1H), 2.62-2.54 (m, 1H), 2.07-1.86 (m, 2H), 1.73 (d, *J* = 12.8 Hz, 1H), 1.51 (d, *J* = 12.8 Hz, 1H). ¹³C NMR (101 MHz, DMSO-d₆) δ 174.78, 169.78, 156.19, 131.62, 130.51, 130.23, 130.05, 129.32, 129.18, 115.38, 74.27, 59.42, 59.08, 49.18, 48.87, 42.43, 37.15, 32.61, 30.79. MS (ESI): calculated for C₂₃H₂₉N₄O₃ [M+H]⁺ 409,2234; found 409.3512. HPLC: t_R = 11.09 min.

2-(8-benzyl-3-(4-hydroxybenzyl)-2-oxo-1,4,8-triazaspiro[4.5]decan-1-yl)acetic acid (56f): Yellow oil (yield 28%). ¹H NMR (400 MHz, DMSO-d₆) δ 9.45 (bs, 1H), 7.58-7.37 (m, 6H), 7.04 (d, *J* = 8.5 Hz, 2H), 6.65 (d, *J* = 8.5 Hz, 2H), 4.31 (s, 2H), 3.80-3.76 (m, 1H), 3.63-3.57 (m, 2H), 3.37-3.03 (m, 4H), 2.93-2.85 (m, 1H), 2.60-2.52 (m, 1H), 2.14-1.88 (m,

2H), 1.70 (d, $J = 13.4$ Hz, 1H), 1.49 (d, $J = 13.4$ Hz, 1H). ^{13}C NMR (101 MHz, DMSO- d_6) δ 174.62, 170.41, 156.20, 131.60, 130.56, 130.25, 130.05, 129.32, 129.01, 115.37, 74.20, 59.30, 59.07, 49.11, 48.87, 41.29, 37.32, 32.76, 31.02. MS (ESI): calculated for $\text{C}_{23}\text{H}_{28}\text{N}_3\text{O}_4$ $[\text{M}+\text{H}]^+$ 410,2074; found 410.5575. HPLC: $t_{\text{R}} = 11.24$ min.

2.2. GENERAL CONCLUSIONS.

Despite the efficacy of interventional coronary reperfusion strategies, morbidity and mortality from acute MI are still significant since, paradoxically, reperfusion negatively affects the post-MI healing.^[7] Reperfusion injury (RI) contributes for up to the 50% of the final infarct size and there is a clear unmet need with respect to specific cardioprotective therapies for such condition. It has been suggested that, when the blood flow is restored after an ischemic insult, the opening of the mitochondrial permeability transition pore (mPTP) is one of the key biochemical processes responsible for RI. mPTP is described as a multiprotein platform sited at the crosstalk of inner and outer mitochondrial membranes. Recent data point to a role for ATP synthase in mPTP formation: ^{[63][64]} the increase of mitochondrial calcium during reperfusion can convert the energy-supplying ATP synthase machine into an energy-dissipating supramolecular entity, the mPTP. In particular, the c ring of the mitochondrial F₁F₀-ATP synthase is emerged as a major target in this clinical area. In this scenario, my research group has reported the discovery of the first mPTP inhibitors that target the c-subunit of F₁F₀-ATP synthase.^[93] Promising derivatives, as **PP11** and **10**, were designed from the structure of Oligomycin A (OA), a known mPTP inhibitor that binds the c-subunit of F₁F₀-ATP synthase.

In the attempt to fill the gaps for the advancement of knowledge, with this doctoral thesis we aimed to consolidate these early studies on the validation of the c-subunit of the F₁F₀-ATP synthase as a novel therapeutic target for cardioprotection. Specifically, the research efforts were focused on the development of new classes of spiro derivatives as mPTP inhibitors (Project 1, 2 and 3).

In a first project we considered to design novel spiro derivatives by implementing the isatin ring, a scaffold that has attracted strong interest in organic and medicinal chemistry due to its potent biological and pharmacological activities. In particular, we described the discovery of spiroisatins among which compound **15f** has shown a promising *in vitro* potency. In the cobalt-calcein assay **15f** was recognised as the most potent compound with a 62% inhibition of mPTP activity at 1 μ M concentration. Moreover, the compound exhibited a cardioprotective behaviour in further *in vitro* evaluations demonstrating its capability to increase the relative cell viability and to protect cells from cell death without affecting basal mitochondrial ATP content. Future perspectives will be oriented towards the demonstration of the engagement of the c-subunit of ATP synthase as the effective mechanism of action leading to mPTP inhibition.

With the objective of expanding the range of chemotypes in this medchem area, in a second project we explored spiro derivatives with enhanced molecular complexity, namely dispiropiperidines and dispiroisatins. Among the dispiro-piperidine derivatives we identified three promising candidates, **26**, **24i** and **34a**, with a significantly more potent activity in inhibiting mPTP opening than the starting reference compound (**PP11**). In light of these encouraging results and with the goal to better inquire about the SAR, we then extended the series with a second round of dispiropiperidine derivatives for which only a preliminary biological evaluation is currently available. A complete SAR analysis of the dispiropiperidine derivatives will be elucidated only after the acquisition of these data.

In a third project, a solid-phase strategy was applied to quickly synthesize a small library of spiro-piperidines whose general spirodecane scaffold can be considered a structural isomer of the previously detailed compounds.^[93] Considering that a particular attention is paid in drug discovery program to increasing the water solubility of putative lead compounds in order to facilitate aqueous formulations for *in vivo* administration, we have proposed spiro-piperidine derivatives which may be easily converted in the corresponding salt form. Thanks to the approach we succeeded in identifying a further class of salified mPTP inhibitor endowed with improved water solubility. However additional SAR optimization work is required to improve *in vitro* potency before the preclinical investigation.

3. DESIGN AND SYNTHESIS OF PHO AFFINITY PROBES (PAPs) FOR BINDING SITE DECONVOLUTION STUDIES AND DETECTION OF POSSIBLE OFF-TARGETS.

3.1 INTRODUCTION.

As detailed in the previous chapters, my research group recently reported the design, synthesis and structure-activity relationship (SAR) optimization of the first series of mPTP inhibitors targeting the c-subunit of F₁F₀-ATP synthase as a new possible pharmacological approach for the treatment of RI. [93] This preliminary investigation led to the discovery of spiro compounds that demonstrated cardioprotective effects in an animal model of RI. The acquired preliminary findings strongly support the interaction of such molecules with F₁F₀-ATP synthase with an engagement of its c-ring. In particular: a) it has been demonstrated that the investigated molecules accumulate in the mitochondrial fraction of cells; b) the engagement of the c-subunit by the investigated molecules has been confirmed by a cellular thermal shift assay; c) by a proximity ligation assay, it has been provided evidence that our compounds stabilize ATP synthase dimers preventing their typical dissociation upon MPT induction. Despite these important results, the exact binding site of our molecules at the target protein is still unknown. Moreover, we cannot exclude that other cellular proteins can be enrolled by the explored chemical template.

3.1.1 Photo-affinity labeling (PAL) in chemical proteomics.

Photoaffinity labeling (PAL) is a validated chemoproteomics technique used in drug discovery for target identification studies or for probing the position and coordinates of ligand binding sites. Briefly, PAL was first introduced by Westheimer's group in the early 1960s [120] and has been newly revitalized by proteomic methods for the identification of labelled targets. It has traditionally been used with the goal of identifying proteins labelled by a probe but has increasingly been applied to locating specific sites within proteins. Actually, PAL (or photocrosslinking) is noted as a unique and emergent technique used for the study of protein-ligand interactions. It can identify unknown targets of ligands, assist in the explication of protein structures, functions and conformational changes, as well as recognize novel or alternative binding sites in proteins.

PAL consists in the use of multicomponent ligand that can covalently cross-link to its target upon irradiation with UV light. [121] The small molecule of interest, in other words the affinity/specificity motif, is responsible for reversible binding to target proteins. The simple combination of this unit with a "warhead", a photoreactive unit that remains inert until photoactivated, [122] [123] allows the permanent attachment to targets. Since PAL can be

performed either with recombinantly expressed proteins or in live cells, a reporter/purification tag may be included in the structure of the ligand for the detection and isolation of the PAL-target protein adducts. As shown in Figure 3.1, the general design of typical photoaffinity probes (PAPs) involves three structural components: the bioactive portion, a photoreactive group and an appropriate tag. ^[124]

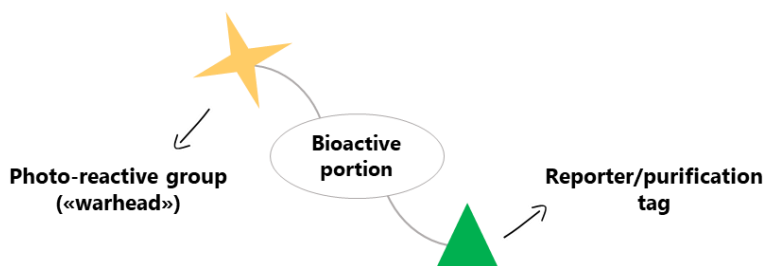


Figure 3.1: General design of PAPs.

In order to generate the best possible probe an extensive structure-activity relationship (SAR) work on a parent compound is often required as it will guide to incorporate the photoactivating group in strategic positions to retain the binding affinity to the expected target biomolecule. The length of the spacer groups between the main functionalities is a further key assignment. ^[125] Indeed, a probe with a linker that is too short may cross-link with itself while a probe with a linker that is too long may prevent the “warhead” to efficiently capture the target protein. Moreover, the nature of most reporter tags generally makes photoaffinity probes large and cell impermeable, avoiding the catch of protein targets in live cells. A strategy to overcome this issue may be the introduction of the reporter tag at a later stage ^[126] via click chemistry conjugation. Huisgen 1,3-dipolar cycloaddition of alkynes and azides to form 1,2,3-triazoles is one of the most successful examples of click chemistry in target identification strategies. Hence, the portion containing merely the pharmacophore, the photogroup and an alkyne moiety can enter cells. Following cell lysis, the terminal alkyne handle will serve to attach an azide-containing reporter/purification tag via copper-catalyzed azide-alkyne cycloaddition (CuAAC). Alternatively, the azide and the alkyne groups can switch positions.

The effort required to optimize simultaneously all the ideal components of a photoaffinity probe in a single molecule can be hard. Stability in the dark at a range of pHs, similarity to the parent compound with comparable activity and affinity, and little steric interference to binding are some of the main features in PAPs design programs. Even the choice of the photoreactive group can depend on various considerations such as activation at wavelengths that avoid damage to biological molecules (proteins absorb UV light at 280 and 200 nm), chemical synthetic accessibility, and minimal chemical perturbation.

The lead photoreactive groups used for PAL are phenylazides, phenyldiazirines and benzophenones which, as a result of the irradiation with specific wavelengths of light, formed the corresponding reactive intermediates, nitrene, carbene and diradical respectively. [124] As anticipated, to facilitate the successful isolation of photolabelled biomolecules, reporter/identification tags are incorporated either directly or indirectly in the photoprobe. Affinity tags are commonly used in PAL, where biotin is the most popular choice due to its extremely high affinity towards avidin. They allow easier enrichment and isolation of labelled proteins, representing the typical approach for target/binding site identification studies, whereas fluorophores, a group of reporter tags that has the largest variety available, are frequently used for visualization by in-gel fluorescence or imaging. [127]

3.2 AIM AND OBJECTIVES.

With this doctoral thesis we aimed to consolidate the early studies on the validation of the c-subunit of the F₁F₀ATP synthase as a novel therapeutic target for cardioprotection with the design and synthesis of photoaffinity probes to be used in future studies finalized to binding site deconvolution and off-targets identification.

Before starting a protocol for a photoaffinity labelling (PAL) probe strategy, two compounds are needed: a parent ligand and a PAL probe, which is designed from it and still retains the activity. The idea is that by preserving the crucial chemical unit of the parent ligand, a similar reversible binding to the protein target will be gained for the PAL probe. The conjugation of the pharmacophoric unit with a photoreactive group enables the capture of protein targets by establishing a covalent bond with close amino acid residues, while the further insertion of an alkyne handle can be useful to conjugate, via CuAAC click chemistry, an azide-containing reporter/purification tag for downstream analysis.

Our research group, provided indirect evidence that one of the most promising mPTP inhibitor with a spiro-piperidine nucleus (**PP11**, Fig 3.2), interacts with F₁F₀-ATP synthase with an engagement of its c-ring. [93] SAR information on PP11 guided us to incorporate the photoactivating group in strategical positions to retain its binding affinity to the expected target biomolecule without altering its functionality. In this regard, data suggested some tolerance for sterically demanding groups at the para position of the *N*' phenyl ring. In addition, the replacement of the *N*⁸ tosyl moiety did not interfere with the activity of the compound, leading in some cases to its enhancement. Considering the 1-phenyl-1,3,8-triazaspiro[4.5]decan-4-one scaffold as mandatory to ensure the optimal interactions with the putative biological target, we designed two series of PAPs which have been conceived

incorporating a photo-cross-linking unit alone (**65** and **66**, Fig. 3.2) or in combination with an alkyne handle (**67** and **68**, Fig 3.2). As photo reactive group, ^[124]^[128] we selected the trifluoromethylphenyl diazirine moiety, largely used in PAL due to its relatively high thermal/chemical stability and its peculiar activation conditions which require high wavelengths (350-355 nm) with low potential damage to biological molecules. ^[129] This “warhead” was merged to the parent portion through a carbonyl group (**65** and **67**), for reasons related to the accessibility of chemical reagents, or through a sulfonyl group, in analogy to **PP11** (**66** and **68**).

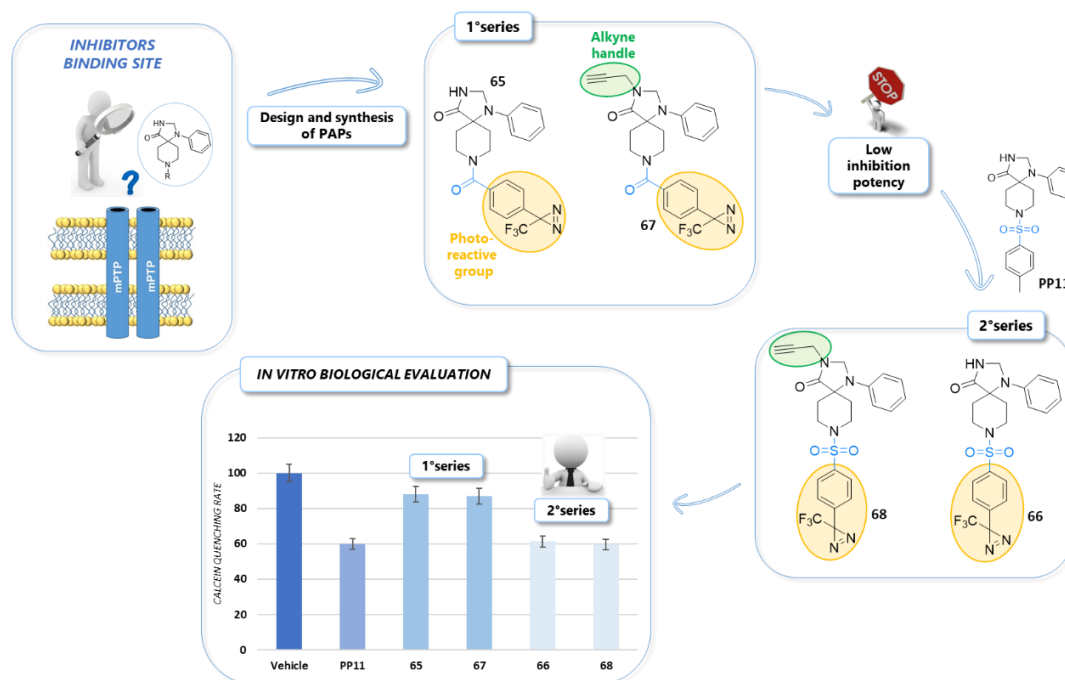


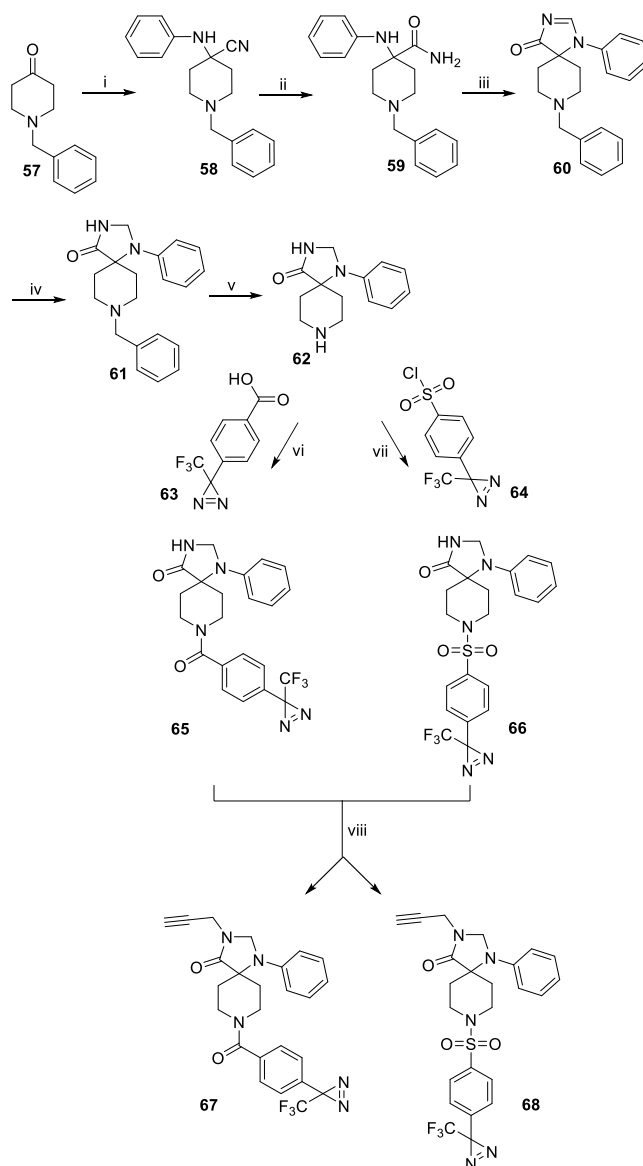
Figure 3.2: Rational design.

3.3 RESULTS AND DISCUSSION.

3.3.1 Chemistry.

The investigated PAMPs (**65-68**) were prepared through a liquid-phase methodology as depicted in Scheme 3.1. The general spiro-piperidine moiety **62** was easily synthesized in analogy to the versatile approach previously applied for synthesis of **PP11** analogues. ^[93] Specifically, a Strecker reaction between the commercially available *N*-benzyl-4-piperidone **57** and anilines in presence of trimethyl silyl cyanide (TMSCN) led to the α -aminonitrile **58**, whose nitrile group was then hydrolysed to the corresponding amide function by treatment with concentrated sulfuric acid. A spirocyclization of the obtained amino-amide intermediate **59** was carried out with DMF-DMA. Afterwards, the unsaturated spiro derivative **60** was reduced with NaBH₄, leading to the corresponding saturated product **61**. Debenzylation of

61, by hydrogenation using 10% palladium on carbon catalyst, yielded derivative **62** as well as the bioactive moiety used for the subsequent inclusion of the photo-reactive unit and the alkyne handle. The introduction of the “warhead” was realized through a HATU-mediated coupling and a reaction with 4-(3-(trifluoromethyl)-3H-diazirin-3-yl)benzenesulfonyl chloride in the presence of DIPEA, resulting in the final PAPs **65** and **66**, respectively. The final PAPs **67** and **68** were obtained through an alkylation reaction of **65** and **66** with propargyl bromide.



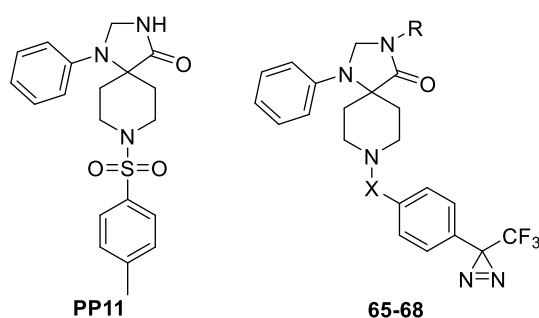
Scheme 3.1. Reagents and conditions - i. Aniline, TMSCN, AcOH, rt 2.5h ii. H₂SO₄, rt 18h; iii. DMF-DMA, MeOH, 55°C 16h; iv. NaBH₄, MeOH, rt 2h; v. H₂, 10% C/Pd, MeOH, CH₃COOH, 16h; vi. DIPEA, HATU, DMF, rt 20min; vii. DIPEA, THF, rt 1h; viii. NaH, Propargyl bromide, DMF, 0°C 30min, rt 2h.

3.3.2 Biological evaluation.

The biological assay reported below was realized in collaboration with the research group of Professor Paolo Pinton of the University of Ferrara (Dept. of Medical Sciences).

Preliminary screening-cobalt-calcein assay. To assess the efficacy of the designed PAPs in inhibiting Ca^{2+} -mediated mPTP opening, herein we measured their biological activity in human ventricular cardiomyocytes (AC16) by using the cobalt-calcein assay. ^[104] For the cobalt-calcein quenching assay, all cells were pretreated with vehicle (DMSO), 1 μM **PP11** (reference compound) or 1 μM inquired PAP, and then loaded with 1 μM calcein acetoxymethyl ester and 2 mM Co^{2+} . According to the described assay and under conditions of mitochondrial calcium overload (by the administration of 1 μM ionomycin), the resulting kinetics data are summarized in Table 3.1.

Table 3.1. *In vitro* potency of mPTP probes.



Compd	X	R	mPTP inhibition (% , 1 μM)	Statistic
PP11	-	-	40,19	P<0.0001
65 (PS 01)	CO	H	inactive	n.s.
67 (PS 02)	CO	prop-2-yn-1-yl	inactive	n.s.
66 (MF 23)	SO ₂	H	38,71	P<0.0001
68 (MF 24)	SO ₂	prop-2-yn-1-yl	43,27	P<0.0001

As shown in Table 3.1, the addition of 1 μM ionomycin to cells pretreated with 1 μM PAPs **66** or **68** resulted in desensitization of mPTP opening by approximately 40-45%, which was significantly higher than that observed in vehicle (DMSO) treated cells and approximately the same as that observed in **PP11** treated cells. Considering the lack of activity of PAP **65** and **67**, it can be speculated that the sulfonyl group used to join the photo reactive unit to the bioactive one may be mandatory for their activity on the target. This encouraging result

highlighted that starting from the general molecular scaffold of **PP11**, the introduction of the selected photo-reactive unit and the alkyne handle did not affect the inhibitory potency on the target. For this reason, PAPs **66** and **68** can be employed in future studies in order to identify the exact binding site of the synthesized molecules at the target protein, besides possible off-targets.

3.4 CONCLUSION AND FUTURE PERSPECTIVES.

Based on previous research efforts on assessing the role of the c ring of ATP synthase in mPTP opening ^[67] ^[70] to validate a new pharmacological approach for the treatment of IRI, in the first section of this doctoral thesis we detailed the design, synthesis and biological evaluation of various mPTP spirocyclic inhibitors. However, the exact binding site of all the examined molecules at the target protein is still unknown.

In order to guide the research towards a more rational structure-based drug design approach that could be helpful in generating more potent cardioprotective agents, a photoaffinity labelling (PAL) approach has been applied. We developed two series of PAL probes, containing a photoreactive unit, that after irradiation at a specific wavelength allows the permanent attachment to the target protein, and an alkyne handle for the detection and isolation of the PAL-target protein adducts.

Among the investigated PAPs, **66** and **68** retained the same mPTP inhibitory activity as **PP11** (the reference compound ^[93]). We can conclude that in this part of the doctoral thesis we have discovered two suitable tools which may be extremely useful to progress in this medchem area.

In particular, PAP **66** will be used in binding site deconvolution studies which involve the treatment of the purified c-subunit of eukaryotic ATP synthase ^[130] followed by irradiation at the required wavelength to activate the photophore. After enzymatic digestion of the protein, the resulting peptide fragments will be sequenced by LC-MS to determine the covalently linked fragments proteins. ^[124]

On the other hand, PAP **68** has all the structural requirements for performing PAL intracellular proteomics studies in cardiomyocytes (AC16 cells) (Fig. 3.3). After cells treatment with PAP **68** and irradiation, the reaction of the alkyne handle with rhodamine-azide can allow visualization of target proteins by fluorescence microscopy (bioimaging), whereas reaction with biotin-azide followed by LC-MS/MS experiments is the typical approach to confirm the interaction with the c-subunit of F₁F₀-ATP synthase and eventually other proteins that can be involved as off-targets. ^[131]

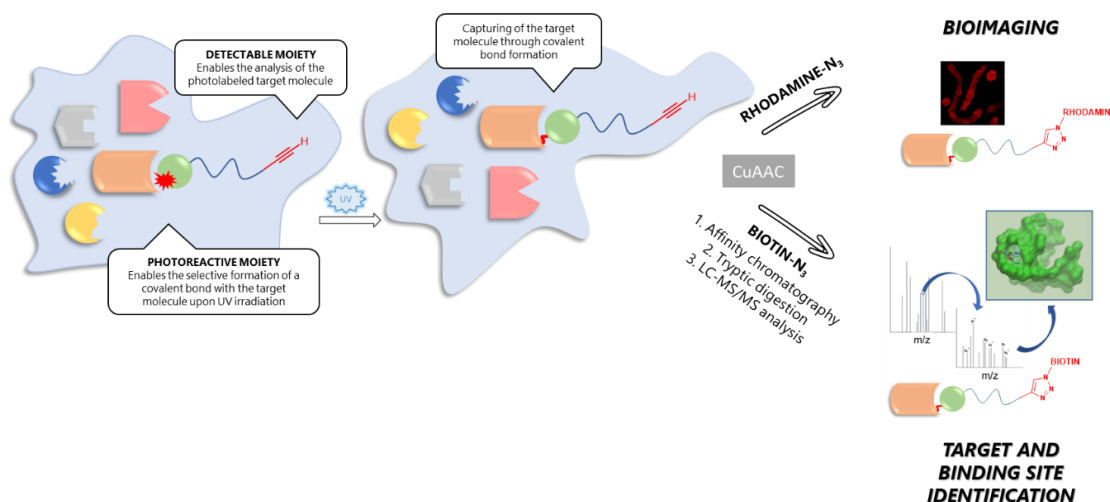


Figure 3.3: Typical PAL workflow.

We expect that the MS-based approach will provide structural and mechanistic information regarding the protein complex (ligand-receptor stoichiometry and a map of the binding pocket). The data obtained can be used to support a 3D model of the ligand-binding pocket that might provide better insight into the nature of the ligand-receptor interaction and will allow a structure-based drug design for further compound optimization. We also envision that the intracellular PAL proteomic approach can reveal or exclude the involvement of off-targets by our compounds. The early identification of off-target interactions in drug discovery represents an opportunity to reduce safety-related attrition rates during preclinical and clinical development.

3.5 EXPERIMENTAL SECTION.

3.5.1 Materials and Methods.

Reaction progress was checked by electrospray mass spectrometer ESI MICROMASS ZMD 2000 and/or by thin-layer chromatography (TLC) on pre-coated F₂₅₄ Macherey-Nagel plates of silica gel (UV lamp 254 nm light source). Compounds were purified by crystallization/trituration or flash chromatography with silica gel 60 (40-63 μ m). Chemical shifts (δ) are reported in parts per million (ppm) using the peaks of deuterated solvents as an internal standard (δ H 7.26 for CDCl₃; δ H 2.50 for DMSO-*d*₆ respectively), while coupling constants (*J*) are reported in Hertz. Splitting patterns are designed as s, singlet; d, doublet; dd, double doublet; t, triplet; m, multiplet; and bs, broad signal. Analytical HPLC was performed with a Beckman 126 liquid chromatograph furnished of a UV detector Beckman

168 and equipped with KARAT32 software. The purity of all the derivatives was assessed with an Agilent Zorbax C18 column (4.6 × 150 mm, 3.5 μm particle size) at a flow rate of 0.7 mL/min using a linear gradient from 100% of A (water + 0.1% TFA) to 100% of B (acetonitrile + 0.1% TFA) over a period of 25 min. All final compounds were monitored at 220 nm showing ≥ 96% purity. Melting points for purified products were determined in a glass capillary on a Stuart Scientific electrothermal apparatus SMP30.

Reagents and solvents were purchased by TCI, Iris Biotech, BLD, Fluorochem and Sigma Aldrich.

3.5.2 General synthetic procedures.

Preparation of 1-benzyl-4-(phenylamino)piperidine-4-carbonitrile 58. To a solution of *N*-benzyl-4-piperidone **57** (1 eq, 2g, 10.6 mmol) in glacial AcOH (40 mL) was added the appropriate aniline (1 eq) at 0°C. Trimethylsilyl cyanide (TMSCN) (3 eq) was then added at 0°C and the reaction mixture was stirred at room temperature overnight. Upon completion, as indicated by TLC and MS (ESI), the reaction mixture was basified to pH 10 using 2M NaOH and suspended with Ac₂OEt (20 mL). The organic layers were then washed with water (2x20 mL), brine (1x10 mL) and dried over Na₂SO₄. The solvent was evaporated under reduced pressure to give a crude solid residue, which was triturated (Et₂O) and filtered. The carbonitrile derivative **58** was obtained as pale yellow solid and used in the next step without further purification.

Pale yellow solid (yield 81%). mp 144-145°C. ¹H NMR (400 MHz, DMSO-d₆) δ 7.33-7.19 (m, 4H), 7.15 (t, *J* = 7.8 Hz, 2H), 6.83 (d, *J* = 7.9 Hz, 2H), 6.71 (t, *J* = 7.3 Hz, 1H), 6.01 (s, 1H), 3.50 (s, 2H), 3.31 (s, 1H), 2.74 (d, *J* = 11.3 Hz, 2H), 2.33-2.23 (m, 4H), 1.87-1.76 (m, 2H). ¹³C NMR (101 MHz, CDCl₃) δ 145.18, 138.53, 129.32, 129.24, 128.65, 127.43, 121.33, 118.78, 116.00, 62.14, 52.44, 49.38, 35.53. MS (ESI): calculated for C₁₉H₂₂N₃ [M+H]⁺ = 292.18; found 292.16.

Preparation of 1-benzyl-4-(phenylamino)piperidine-4-carboxamide 59. The carbonitrile derivative **58** (1 eq, 1.5g, 5.2 mmol) was dissolved in H₂SO₄ (96% w/w, 8 mL), and the resulting mixture was stirred at room temperature for 18h. Upon completion, as indicated by TLC and MS(ESI), it was slowly basified (pH>10) by dropwise addition of a NH₄OH solution (30% w/w) while maintaining the temperature below 0°C. Then, the mixture was extracted with CH₂Cl₂ (2x20 mL), and the organic layer was washed with water (2x10 mL) and brine (1x10 mL). After drying over Na₂SO₄, the solvent was evaporated under reduced pressure to yield a solid residue, which was triturated with Et₂O and filtered to yield the

carboxamide derivatives **59** as pale-yellow solids. The compound was used in the next step without further purification.

Pale yellow solid (yield 90%). mp 191-194°C. ¹H NMR (400 MHz, DMSO-d₆) δ 7.32-7.17 (m, 5H), 7.14 (s, 1H), 7.03 (t, *J* = 7.8 Hz, 2H), 6.97 (s, 1H), 6.59-6.51 (m, 3H), 5.44 (s, 1H), 3.40 (s, 2H), 3.31 (s, 2H), 2.23 (t, *J* = 10.7 Hz, 2H), 1.98 (t, *J* = 10.9, 2H), 1.84-1.77 (m, 2H). ¹³C NMR (101 MHz, CDCl₃) δ 178.08, 145.90, 139.14, 129.12, 128.90, 128.58, 127.24, 116.90, 115.14, 62.67, 57.49, 48.91, 31.84. MS (ESI): calculated for C₁₉H₂₄N₃O [M+H]⁺ = 310.19; found 310.28.

Preparation of 8-benzyl-1-phenyl-1,3,8-triazaspiro[4.5]dec-2-en-4-one 60. To a solution of carboxamide derivatives **59** (1 eq, 7.3 mmol) in MeOH (15 mL) was added DMF-DMA (3 eq) and the reaction mixture was then stirred at 55°C for 16h. Upon completion, as indicated by TLC and MS(ESI), the volatile fraction was evaporated under reduced pressure to yield a solid residue, which was triturated with Et₂O and filtered to yield the bicyclic compound **60** as white solid.

White solid (yield 88%). mp 158-159°C. ¹H NMR (400 MHz, DMSO-d₆) δ 8.68 (s, 1H), 7.53-7.44 (m, 3H), 7.39-7.33 (m, 2H), 7.28-7.14 (m, 5H), 3.46-3.22 (m, 4H), 2.79-2.64 (m, 2H), 1.81-1.62 (m, 4H). ¹³C NMR (101 MHz, CDCl₃) δ 194.64, 170.85, 138.85, 136.21, 130.11, 129.41, 129.11, 128.57, 128.44, 127.28, 64.16, 62.21, 46.98, 30.80. MS (ESI): calculated for C₂₀H₂₂N₃O [M+H]⁺ = 320.18; found 320.36.

Preparation of 8-benzyl-1-phenyl-1,3,8-triazaspiro[4.5]decan-4-one 61. To a cooled solution of bicyclic derivative **60** (1 eq, 5.5 mmol) in MeOH (25 mL) was added in small portions NaBH₄ (1.5 eq), and the reaction mixture was then stirred at room temperature for 2h. Upon completion, as indicated by TLC and MS (ESI), the mixture was quenched with water. The volatile fraction was then concentrated under reduced pressure and the resulting residue was suspended with EtOAc (2x20 mL). The organic layers were washed with water (1x15 mL), brine (1x10 mL), and dried over Na₂SO₄. The solvent was then evaporated and the obtained crude material was crystallized (MeOH) to yield derivative **61** as white pale solid.

White pale solid (yield 92%). mp 158-160°C. ¹H NMR (400 MHz, DMSO-d₆) δ 8.61 (s, 1H), 7.34-7.18 (m, 7H), 6.85 (d, *J* = 8.1 Hz, 2H), 6.74 (t, *J* = 7.2 Hz, 1H), 4.55 (s, 2H), 3.50 (s, 2H), 3.31 (s, 2H), 2.72-2.66 (m, 4H), 1.55 (d, *J* = 13.4 Hz, 2H). ¹³C NMR (101 MHz, DMSO-d₆) δ 176.63, 143.77, 139.20, 129.49, 129.12, 128.63, 127.25, 118.07, 114.69, 62.61,

59.10, 58.58, 49.70, 28.89. MS (ESI): calculated for C₂₀H₂₄N₃O [M+H]⁺ = 322.19; found 322.31.

Preparation of 1-phenyl-1,3,8-triazaspiro[4.5]decan-4-one 62. A solution of derivative **61** (1 eq, 3.1 mmol) in MeOH (30mL) and AcOH (2mL) was treated with a catalytic amount (0.3 mmol) of palladium on activated charcoal (10% Pd basis) in an atmosphere of hydrogen. Upon completion, as indicated by MS (ESI), the reaction mixture was filtered through Celite, concentrated under reduced pressure, diluted with water and alkalized with saturated sodium bicarbonate. The aqueous phase was then extracted with CH₂Cl₂ (3x20 mL), and the combined organic layers were dried over Na₂SO₄, filtered and concentrated under a vacuum to yield derivative **62** as white solid.

White solid (yield 91%). mp 172-173°C. ¹H NMR (400 MHz, DMSO-d₆) δ 8.57 (s, 1H), 7.19 (t, *J* = 7.9 Hz, 2H), 6.87 (d, *J* = 8.3 Hz, 2H), 6.71 (t, *J* = 7.2 Hz, 1H), 4.55 (s, 2H), 3.18-3.07 (m, 2H), 2.87-2.78 (m, 2H), 2.44-2.32 (m, 2H), 1.46 (d, *J* = 13.3 Hz, 2H). ¹³C NMR (101 MHz, DMSO-d₆) δ 176.87, 143.85, 129.35, 117.65, 114.35, 59.20, 59.01, 42.65, 29.72. MS (ESI): calculated for C₁₃H₁₈N₃O [M+H]⁺ = 232.14; found 232.16.

Preparation of 1-phenyl-8-(4-(3-(trifluoromethyl)-3H-diazirin-3-yl)benzoyl)-1,3,8-triazaspiro[4.5]decan-4-one 65. To a solution of 4-(3(trifluoromethyl)-3H-diazirin-3-yl) benzoic acid **63** (1.1 eq) in DMF (3 mL) were added HATU (1.1 eq) and DIPEA (1.2 eq). Then derivative **62** (1 eq, 0.24 mmol) was added and the reaction mixture was stirred at room temperature for 1 h. Upon completion, as indicated by TLC and MS (ESI), the volatile fraction was evaporated, and the resulting residue was extracted with CH₂Cl₂ (3x10 mL). The organic layers were washed with water (2x10 mL) and brine (1x10 mL). After drying over Na₂SO₄, the solvent was evaporated to obtain a crude solid which was purified by flash chromatography (AcOEt as the eluent) to yield derivative **65** as white solid.

White solid (yield 48%). ¹H NMR (400 MHz, DMSO-d₆) δ 8.84 (s, 1H), 7.60 (d, *J* = 8.2 Hz, 2H), 7.43-7.20 (m, 4H), 6.88-6.70 (m, 3H), 4.65-4.53 (m, 2H), 4.46-4.37 (m, 1H), 3.85-3.39 (m, 3H), 3.13 (s, 1H), 2.42-2.25 (m, 1H), 1.76 (d, *J* = 12.6 Hz, 1H), 1.60 (d, *J* = 12.6 Hz, 1H). ¹³C NMR (101 MHz, DMSO- d₆): δ 175.48, 168.11, 142.96, 137.80, 129.13, 128.45, 127.58, 126.56, 123, 38, 117.86, 114.08, 58.66, 58.34, 43.55, 38.33, 28.80, 27.92. MS (ESI): calculated for C₂₂H₂₁F₃N₅O₂ [M+H]⁺ = 444,16; found 444.42. HPLC: t_R = 19.04 min.

Preparation of 1-phenyl-8-((4-(3-(trifluoromethyl)-3H-diazirin-3-yl)phenyl)sulfonyl)-1,3,8-triazaspiro[4.5]decan-4-one 66. To a solution of derivative **62** (1 eq) in freshly distilled THF (3 mL) were added DIPEA (1.2 eq) and the appropriate sulphonyl-chloride **64**

(1.2 eq, 0.3 mmol), under an argon atmosphere. Then the solution was stirred at room temperature for 1 h. Upon completion, as indicated by TLC and MS (ESI), the mixture was concentrated under reduced pressure. The resulting residue was then extracted with CH₂Cl₂ (3x10 mL), and the organic layers were washed with water (2x10 mL) and brine (1x10 mL). After drying over Na₂SO₄, the solvent was evaporated to obtain a solid which was purified by flash chromatography (AcOEt/PE as the eluent) to yield derivative **66** as white solid.

White solid (yield 80%). ¹H NMR (400 MHz, DMSO-d₆) δ 8.74 (s, 1H), 7.97-7.85 (m, 2H), 7.54 (d, *J* = 8.2 Hz, 2H), 7.25-7.17 (m, 2H), 6.83-6.66 (m, 3H), 4.54 (s, 2H), 3.71-3.60 (m, 2H), 3.11-3.00 (m, 2H), 2.47-2.41 (m, 2H), 1.68 (d, *J* = 14.2 Hz, 2H). ¹³C NMR (101 MHz, DMSO- d₆) δ 175.68, 143.30, 138.22, 132.84, 129.59, 128.61, 127.92, 123.33, 119.08, 115.37, 59.08, 58.11, 43.10, 28.54. MS (ESI): calculated for C₂₁H₂₁F₃N₅O₃S [M+H]⁺ = 480,1312; found 480.3758. HPLC: t_R = 21.49 min.

General procedure for the preparation of compounds 67-68. To a solution of the appropriate spiro derivatives **65-66** (1 eq, 0.2 mmol) in DMF (2 mL) was added NaH (60% w/w, 1.2 eq) at 0°C. The resulting mixture was stirred for 10 min. Then propargyl bromide (1.2 eq) was added at 0°C, and the reaction mixture was stirred at 0°C for 30 min and at room temperature for 2 h. Upon completion, as indicated by TLC and MS (ESI), the volatile fraction was evaporated and the resulting residue was extracted with AcOEt (3x10 mL). The organic layers were washed with water (2x10 mL) and brine (1x10 mL). After drying over Na₂SO₄, the solvent was evaporated to obtain a solid which was purified by flash chromatography (AcOEt/PE as the eluent) to yield PAPs **67-68** as white solids.

1-phenyl-3-(prop-2-yn-1-yl)-8-(4-(3-(trifluoromethyl)-3H-diazirin-3-yl)benzoyl)-1,3,8-triazaspiro[4.5]decan-4-one (67): White solid (yield 49%). ¹H NMR (400 MHz, DMSO-d₆) δ 7.59 (d, *J* = 8.4 Hz, 2H), 7.43-7.23 (m, 4H), 6.90-6.85 (m, 1H), 6.93-6.86 (m, 3H), 5.64 (d, *J* = 6.4 Hz, 2H), 4.73-4.66 (m, 2H), 4.46-4.36 (d, 1H), 3.85-3.37 (m, 3H), 2.40-2.20 (m, 2H), 1.87 (d, *J* = 12.4 Hz, 1H), 1.71 (d, *J* = 12.4 Hz, 1H). ¹³C NMR (101 MHz, DMSO- d₆) δ 201.44, 170.82, 168.10, 142.29, 137.77, 129.24, 128.49, 127.62, 126.56, 123.31, 119.19, 115.66, 92.76, 88.36, 61.70, 60.75, 43.31, 38.05, 29.16, 28.22. MS (ESI): calculated for C₂₅H₂₃F₃N₅O₂ [M+H]⁺ = 482,18; found 482.34. t_R = 22.76 min.

1-phenyl-3-(prop-2-yn-1-yl)-8-((4-(3-(trifluoromethyl)-3H-diazirin-3-yl)phenyl)sulfonyl)-1,3,8-triazaspiro[4.5]decan-4-one (68): White solid (yield 55%). ¹H NMR (400 MHz, DMSO-d₆) δ 7.95-7.88 (m, 2H), 7.56 (d, *J* = 8.2 Hz, 2H), 7.29-7.24 (m, 2H), 7.00 (t, *J* = 6.5 Hz, 1H), 6.89 (t, *J* = 7.3 Hz, 1H), 6.81 (d, *J* = 7.9 Hz, 2H), 5.61 (d, *J* =

6.5 H, 2H z), 4.66 (s, 2H), 3.70-3.62 (m, 2H), 3.08-2.95 (m, 2H), 2.46-2.34 (m, 2H), 1.81 (d, $J = 14.0$ Hz, 2H). ^{13}C NMR (101 MHz, DMSO- d_6) δ 201.37, 170.34, 142.16, 137.51, 132.23, 129.09, 128.15, 127.38, 122.93, 119.56, 116.27, 92.64, 88.31, 61.72, 59.75, 42.40, 28.37. MS (ESI): calculated for $\text{C}_{24}\text{H}_{23}\text{F}_3\text{N}_5\text{O}_3\text{S}$ $[\text{M}+\text{H}]^+ = 518,1468$; found 518.2219. $t_{\text{R}} = 24.82$ min.

4. DESIGN AND SYNTHESIS OF NOVEL MITOCHONDRIA-TARGETED CARDIOPROTECTIVE AGENTS POTENTIALLY ABLE TO SCAVENGE REDOX-ACTIVE TRANSITION METAL IONS.

4.1 INTRODUCTION.

In the last decades, mitochondria have occupied a central position in developing innovative therapeutic strategies. ^[132] Within the cardiovascular system, mitochondria are involved in several pathways in order to ensure cellular homeostasis: ATP supply, regulation of calcium (Ca^{2+}) handling and reactive oxygen species (ROS), activation of the innate immune system, and regulation of cell death programs. One major determinant of the mitochondria-dependent cell loss is the opening of the mitochondrial permeability transition pore (mPTP), an unselective high conductance complex located in the inner mitochondrial membrane (IMM), which plays a dual role as arbiter of different cellular responses. mPTP opening and subsequent mitochondrial impairment are due to many factors among which P_i , high pH, overload of mitochondrial calcium (Ca^{2+}) and oxidative stress (ROS production). The combination of these conditions occurs in multiple diseases, including the ischemia-reperfusion-related pathologies. ROS generated in the mitochondria (hydrogen peroxide, superoxide anions, and hydroxyl radicals) lead to target-organ damage, dysfunction, hypertrophy, and inflammation. For these reasons the mPTP opening and the oxidative stress are noted as pivotal mediators of the ensuing pathological complications, thus amenable to drug therapy. ^[132]

In the previous sections we reported the design and synthesis of novel mPTP inhibitors as potential cardioprotective agents. However, single-target drug approaches are often limited in the treatment of complex diseases, since not fully addressing multiple and interconnected molecular mechanisms. Considering the importance of identifying adjuvant strategies in the clinical management of cardiovascular diseases, our efforts are herein focused on the development of mitochondria-targeted compounds able to counteract the mechanisms that sustain ROS generation during the ischemia-reperfusion event.

The term “oxidative stress” was originally introduced by Helmut Sies in 1985, denoting the shift in the balance between oxidants and antioxidants in favour of the former, potentially leading to many pathological conditions and diseases. Prooxidant (or free radicals) are compounds able to trigger a cascade of oxidative reactions to become electrically neutral. They induce oxidative stress, either through formation of ROS or by inhibiting the antioxidant system. Differently, antioxidants are elements that act as scavengers or convert the radical in an inert compound via oxyreductive reactions. The human body is equipped with a range of antioxidants that serve to counterbalance the effect of oxidants (Birben et al.

2012). However, antioxidants can exert a prooxidant activity under certain conditions,^[133] including alkaline pH, high concentrations of transition metal ions and the presence of oxygen molecules (Blokhina, Virolainen, and Fagerstedt 2003; Eghbaliferiz and Iranshahi 2016). ROS is a general term that includes both oxygen-derived free radicals, such as superoxide anions ($O_2^{\cdot-}$), hydroxyl radicals ($\cdot OH$), and nitric oxide ($\cdot NO$) with unpaired electrons in their outer orbital, and other prooxidant and non-radical oxygen derivatives that are easily converted into radicals, such as hydrogen peroxide (H_2O_2) and peroxynitrite ($ONOO^-$).^{[134][135]} Experimental evidence supported that the rapid ROS generation during reperfusion is the main responsible for cell and tissue damage,^{[136][137]} either by direct toxic effects (i.e. DNA nicking, membrane lipid peroxidation, protein degradation) or by pathways that lead indirectly to cell injury, as well as a consequence of the activation of signal transduction pathways that culminate in up- or down regulation of the expression of a number of genes.^{[138][139]} Aerobic organisms utilize molecular oxygen as a terminal electron acceptor during the process of energy producing oxidative catabolism. Even under normal conditions, a small portion of oxygen is reduced via a univalent pathway with concomitant formation of reactive intermediates, however only when ROS levels exceed the antioxidant ability of mitochondria, deleterious effects become hazardous for cell integrity. Although some data suggested that a limited formation of superoxide anions ($O_2^{\cdot-}$) was observed during the ischemic period,^{[140][141]} the greatest amount of ROS production and cellular injury occurs mainly during the reintroduction of oxygen following ischemia. In this case the exact sources of electrons are not clear; it is assumed that, as a consequence of the sudden increase in O_2 , other oxygen-dependending cellular redox systems, in addition to mitochondria, may produce ROS which collectively play an important role in postischemic myocardial injury.^[142] Both superoxide anions ($O_2^{\cdot-}$) and hydrogen peroxide (H_2O_2) are relatively weak oxidants that are continuously removed by endogenous nonenzymatic or enzymatic scavengers, such as superoxide dismutase, catalase, or glutathione (Fig. 4.1)

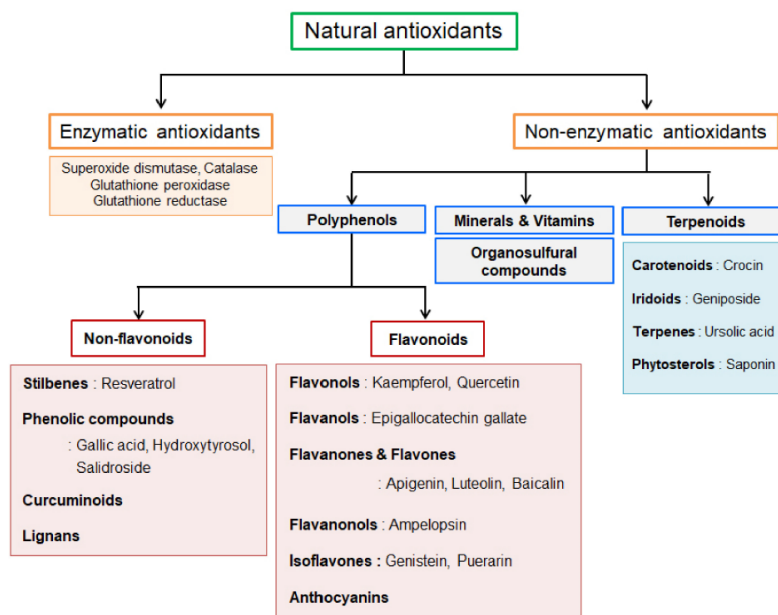


Figure 4.1: Enzymatic and non-enzymatic antioxidants. ^[143]

On the other hand, the lack of scavenger for the high reactive and cytotoxic hydroxyl radical ($\cdot\text{OH}$), causes irreversible cell damage by lipid peroxidation and alteration of protein structure. ^[144] This radical is produced from the superoxide anions and hydrogen peroxide in presence of trace amount of transition metal ions.

Of note, because ROS are implicated in IRI, the role of metal ions is of considerable importance. ^[145] Iron and copper have been shown to play a critical role in the formation of free radicals, as prooxidant agents. Their physiological plasma total concentrations (free and bound) are 11-31 μM and 14-19 μM , respectively (Letelier et al. 2010). Although the enzymatic mediation of redox reactions incorporating transition metal ions is of vital importance, iron and copper are particularly damaging when they exist in their unbound form because they can interact with oxygen by catalysing Haber-Weiss and/or Fenton reactions. ^[146] Conversely, selenium contributes to the detoxification of radicals as antioxidant agent. Zinc may also function in antioxidant pathways, disclosing an endogenous protective effect against IRI. Indeed, plasma zinc levels were found to be reduced after acute myocardial infarction, ^[147] a result of its increased uptake into mitochondria and microsomal fractions, both possible sites of production of reactive oxygen-derived intermediates. ^[148]

Since in ischemic conditions a large amount of iron is released, in this section we focused on the design of novel iron chelators to moderate production of ROS.

Briefly, iron is an essential nutrient for cell function and survival, but due to its redox nature it can act as a potential agent for toxicity. As iron is a transition metal with two oxidation states, ferrous (Fe^{2+}) and ferric (Fe^{3+}), its redox property is useful for biological systems but

it is also hazardous for the cells. During a global ischemia the pH decreases leading to release of iron from transferrin and other carrier proteins. A study showed that iron levels transiently increase with time and that the early treatment with iron chelators results in decreased ischemic damage as compared to later treatment (Millerot-Serruot et al. 2008). This low molecular weight free iron acts as a catalyst in free radical reactions (Lipscomb et al. 1998). Especially, Fe^{2+} is released and upon reperfusion is oxidized to Fe^{3+} , making the tissue susceptible to damage (Halliwell and Gutteridge 1989). As anticipated, iron ions produce hydroxyl free radicals, via Haber-Weiss and Fenton reactions, and enhances ^[149] the propagation of lipid peroxidation. (Fig. 4.2) The iron overload results in production of ROS which is directly proportional to time as well as its concentration.

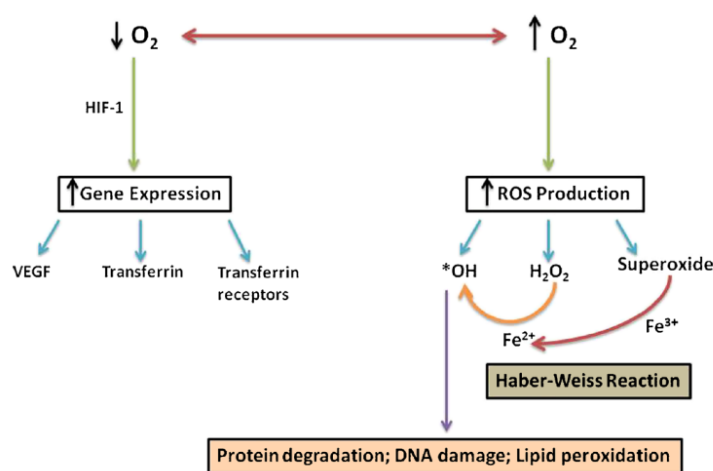


Figure 4.2: Role of iron in Ischemia-Reperfusion. ^[150]

Chelating agents are compounds that are known to be used as scavenger of metal ions and consequently as non-enzymatic scavenger of ROS. In this setting, iron chelators have already been described and have shown protective action. ^{[151] [152] [153]} Deferoxamine (DFO) is an iron chelator that has been tested in various animal models of stroke. It binds ferric iron by forming a hexadentate complex, making iron unavailable to cause any sort of injury. DFO is also a known activator of hypoxia-inducible factor 1 (HIF-1) (Wang and Semenza 1993), whose activation increases the expression of genes involved in adaptation to hypoxic conditions (Zaman et al. 1999). (Fig. 4.2)

However, a major challenge in this field is the selective delivery of these potential therapeutic agents to the cardiac tissue and to damaged mitochondria for successful clinical outcomes. The specific targeting of the treatment product to mitochondria may also minimize potential side effects.

4.2 AIM AND OBJECTIVES.

In this project we aimed to design, synthesize and characterize prooxidant metal ion chelators linked to a mitochondria-targeted drug delivery system, with an appropriate flexible spacer (Fig. 4.3).

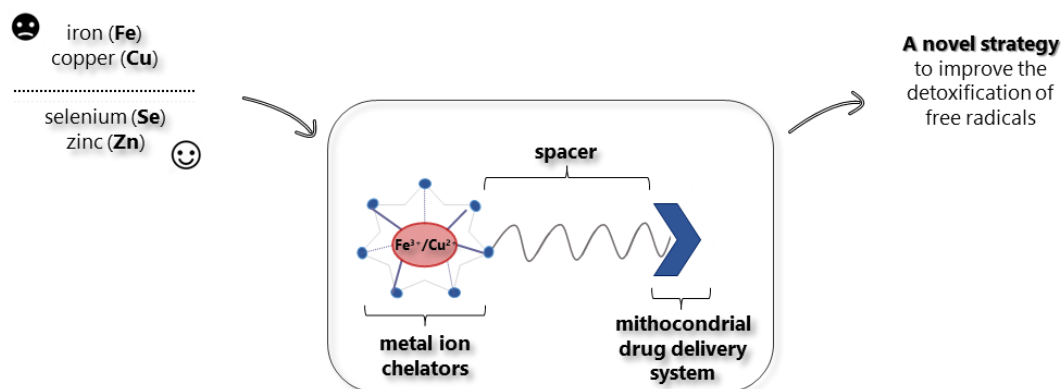


Figure 4.3: Rational design.

Two properties of mitochondria may facilitate this selective drug delivery: the larger membrane potential across the inner membrane (-150-200 mV), and the organelle's protein import machinery. The most common method for targeting compounds to mitochondria exploits the first mitochondria property, and thus we decided to consider a novel class of cell-permeable small peptides (Szeto-Schiller peptides, SS peptides), which selectively partition to the inner mitochondrial membrane and possess intrinsic mitoprotective properties. In fact, experiments with isolated mitochondrial preparations and cell cultures suggest that they can scavenge ROS, reduce mitochondrial ROS production, and inhibit mitochondrial permeability transition. They are small, water-soluble peptides composed of <10 amino acid residues. A common feature of these peptides is an alternating aromatic cationic motif, carrying a 3+ net charge at physiologic pH, which allows them to freely penetrate cells, in an energy-independent and non-saturable manner (1000-5000-fold). The SS peptides were first evaluated in ischemia-reperfusion injury in *ex vivo* guinea pig hearts undergoing retrograde perfusion in a Langendorff apparatus. Among them, the so-called SS31 and its acetate salt MTP-131 (also known as Bendavia or Elamipretide) was one of the most potent (nM) cardioprotective agents that can be used to reduce myocardial stunning without pre-ischemic treatment. ^[154] SS31 was initially thought to scavenge mitochondrial ROS through the activity of its dimethyltyrosine residue. ^[155]^[156] In fact, tyrosine is a known oxyradicals scavenger, forming relatively unreactive tyrosyl radicals, which can give

dityrosine, or react with superoxide to form tyrosine hydroperoxide. ^[157] In addition, dimethyltyrosine-containing peptides were found to be more effective than the tyrosine counterparts. Subsequent studies have revealed a further mechanism of SS31 action. Indeed, it can interfere with cardiolipin, preventing its oxidation, and probably interrupting a vicious cycle of cardiolipin oxidation, ROS formation and diminished ATP production. ^{[158][159]}

It is known that Cyclosporin A (CsA) is a potent inhibitor of MPT which has very high affinity for cyclophilin D. If CsA could be targeted to mitochondria, clinical outcomes would be improved. In fact, a recent and small trial (CAPRI) has shown that a single dose of CsA did not affect infarct size or left ventricular remodelling in STEMI patients. ^[160] In particular, the delineation of the lymphocyte kinetics and plasmatic concentration of CsA during the 24 h period post-injection has suggested that free CsA suffers of poor delivery at the injured tissue. For this reason, CsA was then loaded in PLGA NPs (poly(lactic-co-glycolic) acid nanoparticles) to improve its bioavailability and delivery to the injured cardiomyocyte. Although it has showed an enhanced cardioprotective effect than CsA alone, it could also present unfavourable features such as the unspecific uptake by the mononuclear phagocyte system in the blood circulation, reducing its accumulation in mitochondria of the ischemic cardiomyocytes. Hence, researchers formulated hybrid PLGA-CsA NPs by coating their surface with PEG (polyethylene glycol) and the mitochondriotropic SS31 peptide. This latter formulation exhibited significant cardioprotective effects against IR in rats by accumulating in the damaged mitochondria, protecting mitochondrial integrity, and decreasing cardiomyocyte cell death and myocardial infarct area. ^[132]

Considering the data highlighted above, we selected SS31 as useful drug delivery system which also combines ROS scavenging properties. Moreover, since DFO can tightly bind iron and copper, it was herein selected as specific chelator of transition metal ions. Deferoxamine (DFO) has been widely studied and several investigators were able to prove its cardioprotective effects in experimental and clinical studies. ^{[151][161]}

In this regard, we designed a series of derivatives (Fig. 4.4, panel A) characterized by the tetrapeptide SS31 conjugated to DFO through a Lys(N_ϵ -succ.) or a Lys(N_ϵ -(O₂Oc)_{n=1,3}-succ.) spacer, where succ. refers to a succinic acid unit.

Considering that SS31 is endowed with intrinsic ROS scavenging potential, a second series of derivatives (Fig. 4.4, panel B), lacking the chelating moiety, has been synthesized as internal reference.

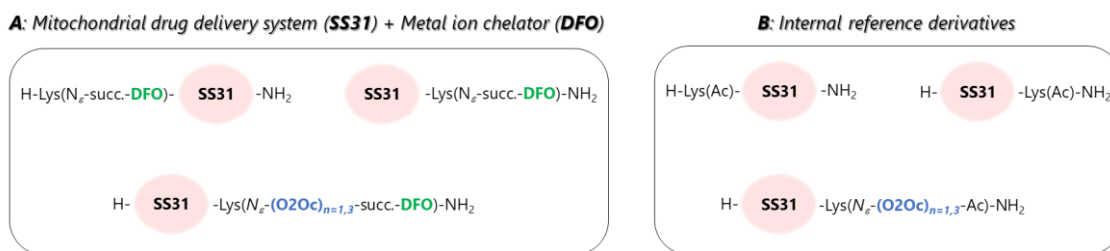


Figure 4.4: Synthesized derivatives.

4.3 RESULTS AND DISCUSSION.

4.3.1 Chemistry.

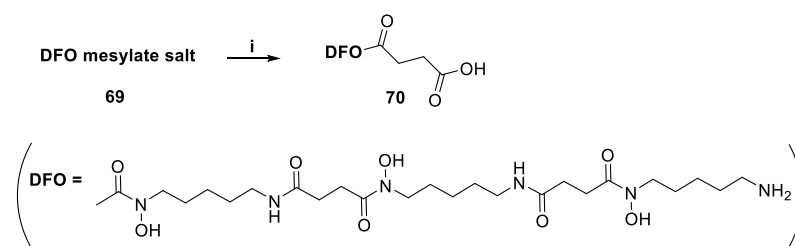
The designed derivatives reported in Table 4.1 and Table 4.2, were prepared through solid-phase Fmoc/tBu-based peptide synthesis (SPPS) ^[119] on a AmphiSpheres 20 RAM resin. Commercially available protected amino acids were employed as synthetic precursors of the target derivatives, except for the nonproteinogenic Fmoc-2',6' dimethyl-tyrosine (Fmoc-Dmt-OH), that was synthesized in analogy to an approach formerly described by our research unit, ^[162] the Fmoc-D-Arg(Pmc)-OH and the Boc-D-Arg(Pbf)-OH. Moreover, Deferoxamine (DFO) was employed as metal ion chelator, while polyoxyethylene chains (-O₂Oc-) as flexible spacers.

The synthetic pathway was planned considering that the common feature of tetrapeptide SS31 needs to be preserved as its 3+ net charge at physiologic pH allows it to freely penetrate cells, in an energy-independent and non-saturable manner. In order to perform a synthetic strategy on a solid-phase support, we implemented a Lysin residue as linker to join SS31 to selected flexible spacers or to the chelating agent DFO.

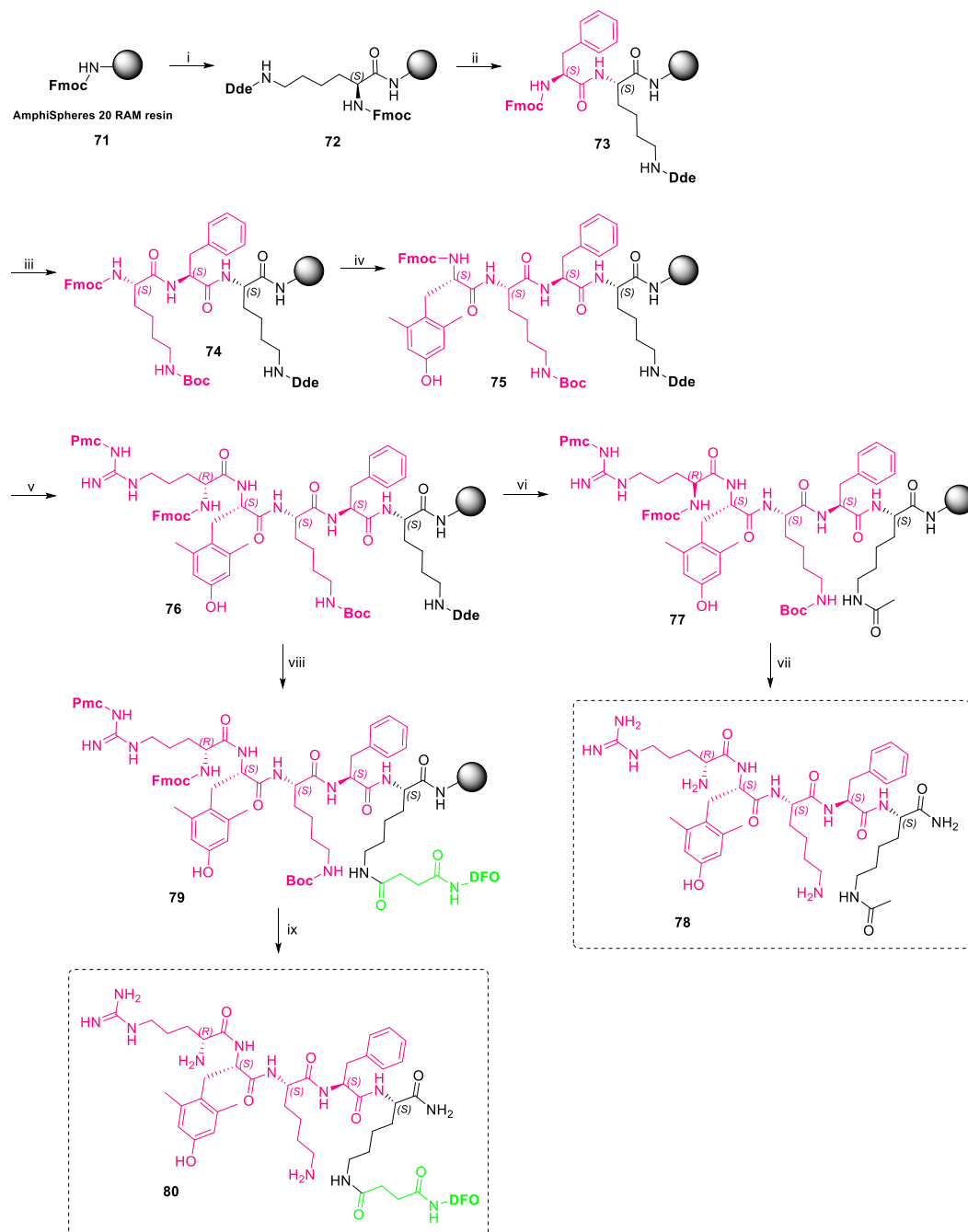
Apart from the standard liquid-phase reaction between DFO and succinic anhydride (Scheme 4.1), to promote its subsequent coupling reaction (succ.-DFO, in green), all the other synthetic steps were realized on solid-phase support, adding sequentially the protected building blocks of the target derivatives.

As depicted in Scheme 4.2 and Scheme 4.3 we designed two different orthogonal strategies wherein the Lysin residue (in black) was inserted at the N-terminal and at the C-terminal of the tetrapeptide SS31 (in pink) respectively.

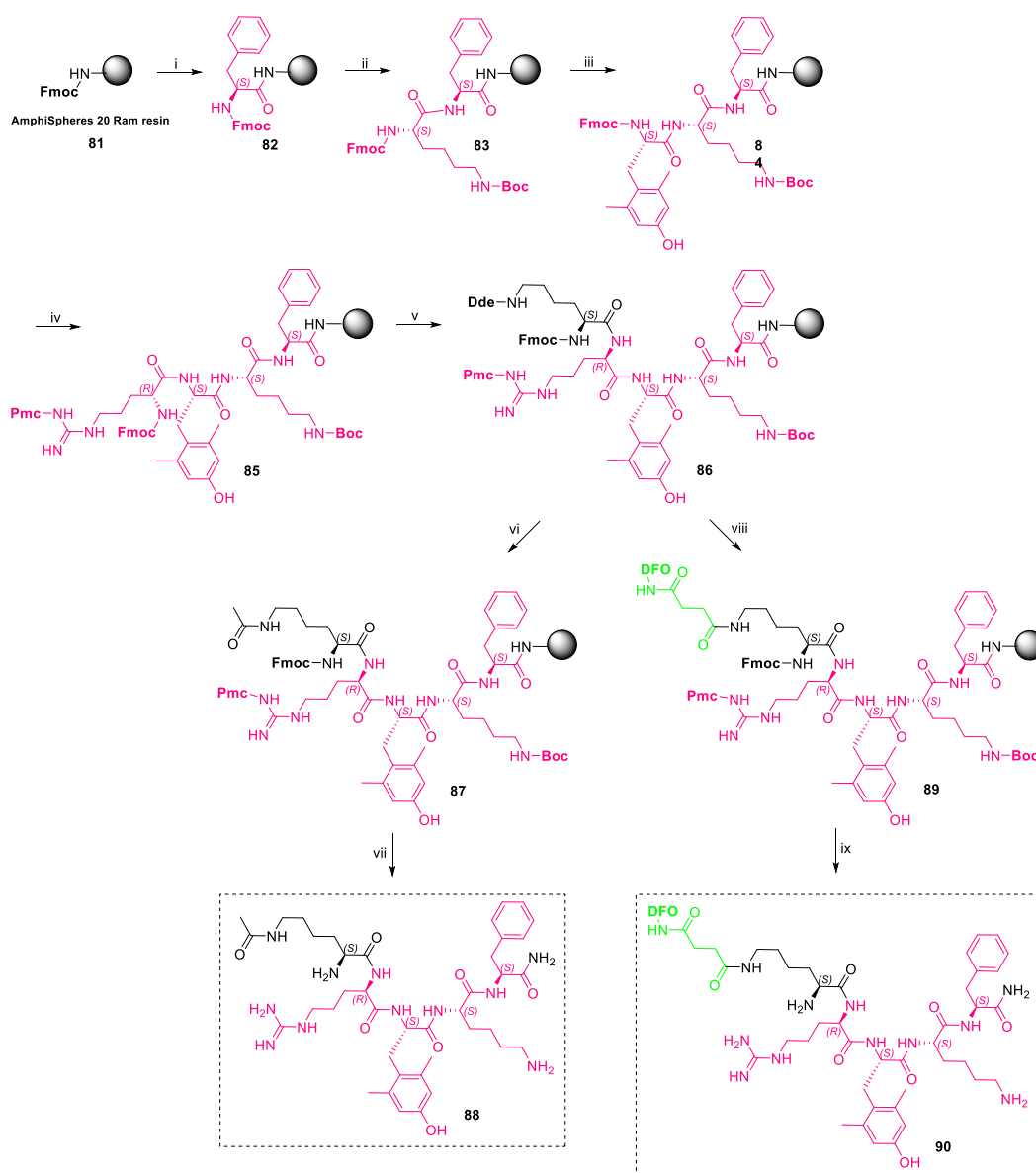
Whereas, in Scheme 4.4 is shown the strategy used for the preparation of the derivatives realized by the further insertion of polyoxyethylene chains (-O₂Oc-, in blue). In this regard, we considered to synthesize derivatives composed by tetrapeptide SS31 C-terminal-linked to these flexible chains, with the aim to first evaluate whether these units may alter or improve the drug delivery contribution of tetrapeptide SS31.



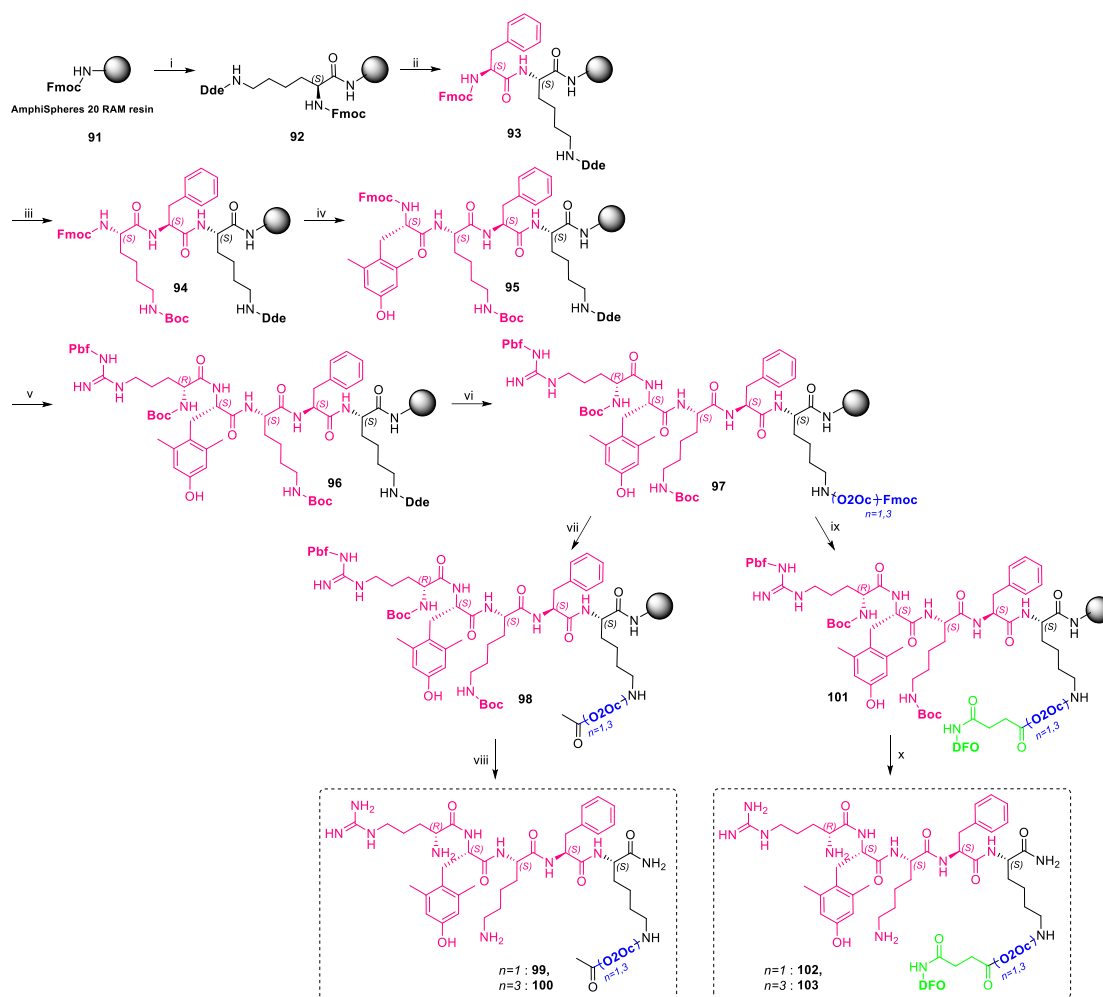
Scheme 4.1. Reagents and conditions - i. succinic anhydride, TEA, DMF, rt overnight.



Scheme 4.2. Reagents and conditions - i. 40% Piperidine in DMF; Fmoc-Lys(Dde)-OH, DIPEA, HATU, DMF; ii. 40% Piperidine in DMF; Fmoc-Phe-OH, DIC, HOBT, DMF; iii. 40% Piperidine in DMF; Fmoc-Lys(Boc)-OH, DIC, HOBT, DMF; iv. 40% Piperidine in DMF; Fmoc-DMT-OH, DIPEA, HATU, DMF; v. 40% Piperidine in DMF; Fmoc-D-Arg(Pmc)-OH, DIPEA, HATU, DMF; vi. NH₂OH·HCl/Imidazole in DMP; NMM, Ac₂O, DMF; vii. 40% Piperidine in DMF; TFA:H₂O:Et₃SiH (95:2.5:2.5); viii. NH₂OH·HCl/Imidazole in DMP; DFO-succ-OH, DIPEA, HATU, DMF; ix. 40% Piperidine in DMF; TFA:H₂O:Et₃SiH (95:2.5:2.5)



Scheme 4.3. Reagents and conditions - i. 40% Piperidine in DMF; Fmoc-Phe-OH, DIC, HOBT, DMF; ii. 40% Piperidine in DMF; Fmoc-Lys(Boc)-OH, DIC, HOBT, DMF; iii. 40% Piperidine in DMF; Fmoc-DMT-OH, DIPEA, HATU, DMF; iv. 40% Piperidine in DMF; Fmoc-D-Arg(Pmc)-OH, DIPEA, HATU, DMF; v. 40% Piperidine in DMF; Fmoc-Lys(Dde)-OH, DIPEA, HATU, DMF; vi. $\text{NH}_2\text{OH}\cdot\text{HCl}$ /Imidazole in DMP; NMM, Ac_2O , DMF; vii. 40% Piperidine in DMF; TFA: H_2O : Et_3SiH (95:2.5:2.5); viii. $\text{NH}_2\text{OH}\cdot\text{HCl}$ /Imidazole in DMP; DFO-succ.-OH, DIPEA, HATU, DMF; ix. 40% Piperidine in DMF; TFA: H_2O : Et_3SiH (95:2.5:2.5).



Scheme 4.4. Reagents and conditions - i. 40% Piperidine in DMF; Fmoc-Lys(Dde)-OH, DIPEA, HATU, DMF; ii. 40% Piperidine in DMF; Fmoc-Phe-OH, DIC, HOBT, DMF; iii. 40% Piperidine in DMF; Fmoc-Lys(Boc)-OH, DIC, HOBT, DMF; iv. 40% Piperidine in DMF; Fmoc-DMT-OH, DIPEA, HATU, DMF; v. 40% Piperidine in DMF; Boc-D-Arg(Pbf)-OH, DIPEA, HATU, DMF; vi. $\text{NH}_2\text{OH}\cdot\text{HCl}$ /Imidazole in DMF; Fmoc-O₂Oc-OH, DIPEA, HATU, DMF; vii. 40% Piperidine in DMF; NMM, Ac₂O, DMF; viii. TFA:H₂O:Et₃SiH (95:2.5:2.5); ix. 40% Piperidine in DMF; DFO-succ-OH, DIPEA, HATU, DMF; x. TFA:H₂O:Et₃SiH (95:2.5:2.5).

Table 4.1: Synthesized derivatives composed of SS31 and DFO

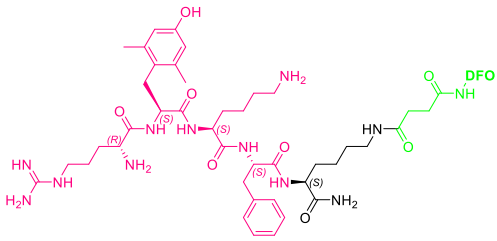
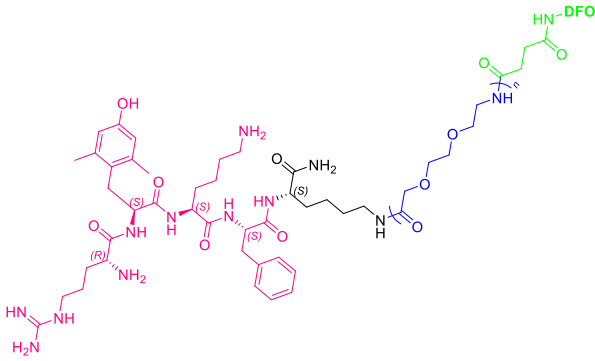
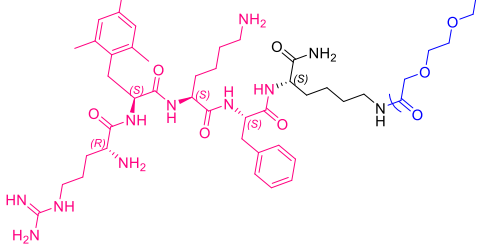
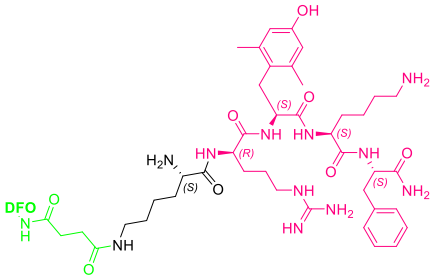
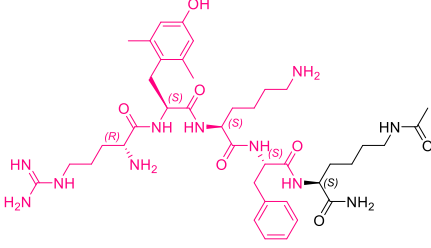
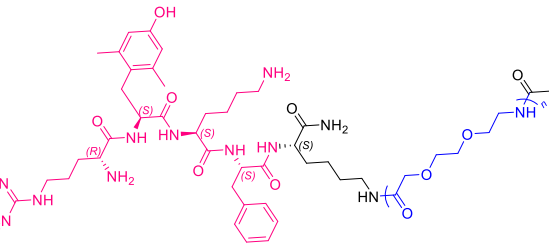
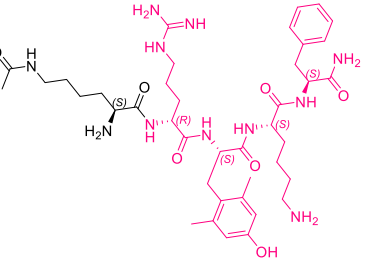
	<p>H-(D)Arg-Dmt-Lys-Phe-Lys(<i>N</i>_ε-succ.-DFO)-NH₂ (80)</p> <p>MW_s : 1752,73 g/mol - Yield : 9%</p>
	<p>H-(D)Arg-Dmt-Lys-Phe-Lys(<i>N</i>_ε-(O2Oc)_{n=1}-succ.-DFO)-NH₂ (102)</p> <p>MW_s : 1897,89 g/mol - Yield : 11%</p>
	<p>H-(D)Arg-Dmt-Lys-Phe-Lys(<i>N</i>_ε-(O2Oc)_{n=3}-succ.-DFO)-NH₂ (103)</p> <p>MW_s : 2188,20 g/mol - Yield : 10%</p>
	<p>H-Lys(<i>N</i>_ε-succ.-DFO)-(D)Arg-Dmt-Lys-Phe-NH₂ (90)</p> <p>MW_s : 1752,73 g/mol - Yield : 21%</p>

Table 4.2: Synthesized derivatives as internal reference

	<p>H-(D)Arg-Dmt-Lys-Phe-Lys(Ac)-NH₂ (78)</p> <p>MW_s: 1151,49 g/mol - Yield : 14%</p>
	<p>H-(D)Arg-Dmt-Lys-Phe-Lys(N_ε-(O₂Oc)_{n=1}-Ac)-NH₂ (99)</p> <p>MW_s: 1296,57 g/mol - Yield : 11%</p>
	<p>H-(D)Arg-Dmt-Lys-Phe-Lys(N_ε-(O₂Oc)_{n=3}-Ac)-NH₂ (100)</p> <p>MW_s: 1586,71 g/mol - Yield : 12%</p>
	<p>H-Lys(Ac)-(D)Arg-Dmt-Lys-Phe-NH₂ (88)</p> <p>MW_s: 1151,49 g/mol - Yield : 11%</p>

4.4 CONCLUSION AND FUTURE PERSPECTIVES.

As detailed above, mitochondrial ROS and mPTP opening have been suggested as primary targets for therapeutic intervention in cardiovascular disease.

In this section of the doctoral thesis, we focused on mitochondrial ROS and on the possibility to reduce the related oxidative damage for cardioprotective purposes. Hence, we designed, synthesized and characterized derivatives composed of an iron chelator (as DFO) linked to a mitochondria-targeted drug delivery system (as SS31), with appropriate spacers. All the novel synthesized derivatives will be evaluated in order to assess their potential behaviour in protecting mitochondria from the oxidative stress during the ischemic event. In particular, future perspectives will be oriented towards an *in vitro* biological assay performed in a hypoxia chamber. An evaluation in terms of mitochondrial cell protection against oxidative stress will select the derivatives with the best profile which may be further characterized by potentiometry and spectrophotometry techniques (such as mass spectrometry, UV-Vis spectrophotometry).

Moreover, a fascinating application field could exploit a push-and-pull mechanism for the synthesized compounds, when administered in complex with zinc instead of as free chelating derivatives: since iron and copper play a critical role in the formation of free radicals while zinc have antioxidant actions, and considering that iron ions have higher affinity to DFO than zinc ones, there is reason to assume synergistic cell protective effects from DFO-derivatives in their complexes with zinc. ^[153]

Most importantly, the two classes of compounds resulting from the final thesis, spirocyclic mPTP inhibitors and antioxidant agents, could exert synergistic cardioprotective actions that will be investigated in future studies.

4.5 EXPERIMENTAL SECTION.

4.5.1 Materials and Methods.

Peptides were synthesized using a standard Fmoc/tBu chemistry ^[119] through a Syro XP multiple peptide synthesizer (MultiSynTech GmbH, Witten Germany). The commercially available AmphiSpheres 20 RAM resin (loading 0.55 mmol/g) was used as a functionalized support for the designed derivatives. Protected amino acids, polyoxyethylene chains (Fmoc-O2Oc-OH), and precursor DFO-succinic acid-OH were coupled to the growing chain using *N,N*-Diisopropylethylamine and 1-[Bis(dimethylamino)methylene]-1H-1,2,3-triazolo[4,5-*b*]pyridinium 3-oxide hexafluorophosphate (DIPEA/HATU), or *N,N'*-

diisopropylcarbodiimide and 1-hydroxybenzotriazole (DIC/HOBt). N_{α} -Fmoc deprotection was performed using a 40% solution of piperidine in N,N -dimethylformamide (DMF), whereas N_{ε} -Dde deprotection ^[163] was realized using a solution of hydroxylamine hydrochloride ($\text{NH}_2\text{OH}\cdot\text{HCl}$) and imidazole in N -methyl-2-pyrrolidone (NMP), completely orthogonal to the N -Fmoc deprotection. All the couplings were repeated until the desired resin-bound derivative has been completed. After each coupling reaction a treatment with a solution of acetic anhydride (Ac_2O) and N -Methylmorpholine (NMM) in DMF was performed to quench the reactivity of randomly uncoupled amine groups (capping). The cleavage cocktail to obtain the desired derivative from the resin consisted of a mixture of 95% trifluoroacetic acid, 2.5% water and 2.5% triethylsilane ($\text{TFA}:\text{H}_2\text{O}:\text{Et}_3\text{SiH}$). Reverse-phase purifications of crude derivative was then carried out on a Waters Delta 600 high-performance liquid chromatography (HPLC) system with a Jupiter column C18 (250×30 mm, 300 \AA , $15 \mu\text{m}$ spherical particle size), using a binary mobile phase consisting of solution A (100% H_2O , 0.1% v/v TFA) and solution B (40% H_2O , 60% CH_3CN , 0.1% v/v TFA) at a flow rate of 20 mL/min. Gradient was established individually considering the analytical HPLC profile of the crude product. Analytical HPLC was performed with a Beckman 126 liquid chromatograph furnished of a UV detector Beckman 168 and equipped with KARAT32 software. The purity of all the derivatives was assessed with an Agilent Zorbax C18 column (4.6×150 mm, $3.5 \mu\text{m}$ particle size) at a flow rate of 0.7 mL/min using a linear gradient from 100% of A (water + 0.1% TFA) to 100% of B (acetonitrile + 0.1% TFA) over a period of 25 min. All final compounds were monitored at 220 nm showing $\geq 96\%$ purity. The molecular weights of the crude material and of the final compounds were determined using an electrospray mass spectrometer (ESI MICROMASS ZMD 2000). HPLC chromatograms and ESI mass spectra of the final derivatives have been reported below in the appendix (4.4.3). Enantiopure Fmoc-protected amino acids and the resins for SPPS were purchased from AAPPTec, Bachem (Bubendorf, Switzerland), BLDpharm (Kaiserslautern, Germany), Merck Life Science (Milan, Italy) and IrisBiotech (Marktredwitz, Germany). All solvents were purchased from VWR International.

4.5.2 General synthetic procedures.

Preparation of 3,14,25-trihydroxy-2,10,13,21,24,32-hexaoxo-3,9,14,20,25,31-hexaazapentatriacontan-35-oic acid 70.

To a solution of deferoxamine mesylate salt (1 eq, 0.76 mmol) in DMF (40 mL) were added succinic anhydride (1.3 eq) and TEA (2.3 eq). The reaction mixture was then stirred at room temperature overnight. Upon completion, as indicated by MS (ESI), the solvent was removed

under vacuum. The crude product was then precipitated in fresh diethyl ether (Et₂O) and isolated through centrifugation. The obtained white solid was used for the next step without further purification.

General procedure for the synthesis realized on solid-phase support.

AmphiSpheres 20 RAM resin was adopted as starting material (1eq, 0.083 mmol). The resin was weighted into an empty syringe, and then it was swelled in DMF at room temperature.

The main repeated steps were:

- *N*-terminal deprotection: *N*_α-Fmoc deprotection was removed by treatment the resin with a 40% solution of piperidine in DMF (2 mL/0.15 g of resin), which selectively removed the base-labile *N*-protecting group in favour of the next amide coupling reaction; while *N*_ε-Dde deprotection of Lysin residue was realized using a solution of NH₂OH·HCl (1.80 mmol) and imidazole (1.35 mmol) in NMP (5mL), which just before reaction was diluted CH₂Cl₂ (5:1 v/v; 2mL/0.15 g of resin).^[163] This completely orthogonal strategy was required to avoid the undesired *N*-Fmoc deprotection.
- Amide coupling reaction: for Fmoc-Phe-OH and Fmoc-Lys(Boc)-OH the *C*-terminals were activated using HOBt (0.78 M) and DIC (1.09 M) as coupling reagents in DMF (1.1:0.7:0.5 v/v; 2.3 mL/0.15 g of resin); for all the other building blocks (1.5 eq) of the sequence the *C*-terminals were activated with the coupling reagents HATU (1.5 eq) and DIPEA (1.5 eq) in DMF (2 mL/0.15 g of resin);
- Capping: the acetylation reaction was performed in order to block the elongation of undesired peptide chains that can occur due to possible unsuccessful coupling reaction. Ac₂O (0.5 M) and NMM (0.25 M) were used as capping reagents in DMF (1.5:0.5 v/v; 2 mL/0.15 g of resin), to quench the reactivity of randomly uncoupled amine groups.

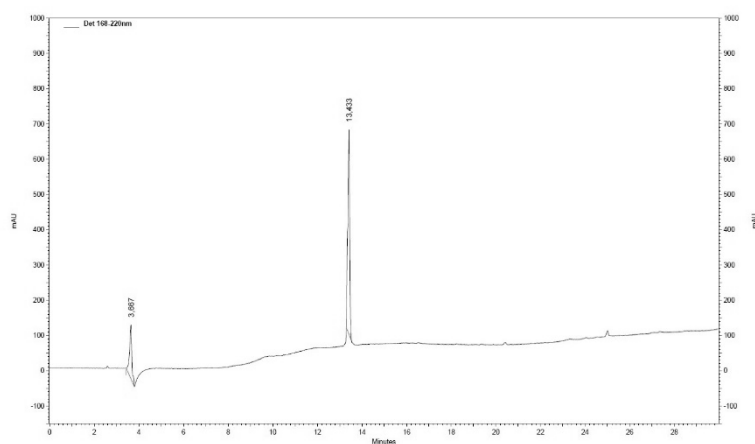
After each step the resin was washed for three times with fresh DMF (2 mL/0.15 g of resin). In the case of *N*_α-Fmoc and *N*_ε-Dde deprotection it was preferred to wash the resin more carefully, for nine times with fresh DMF, to avoid an undesired *N*-deprotection of the next added aa.

Once the last building block of the sequence was inserted and the *N*-terminal protection was removed, the desired final derivatives, which were anchored to the solid support, were treated with a cleavage solution composed by trifluoroacetic acid TFA, H₂O and Et₃SiH (95:2.5:2.5; v/v; 5 mL/0.15 g of resin) for 8 h at room temperature. After filtration of the

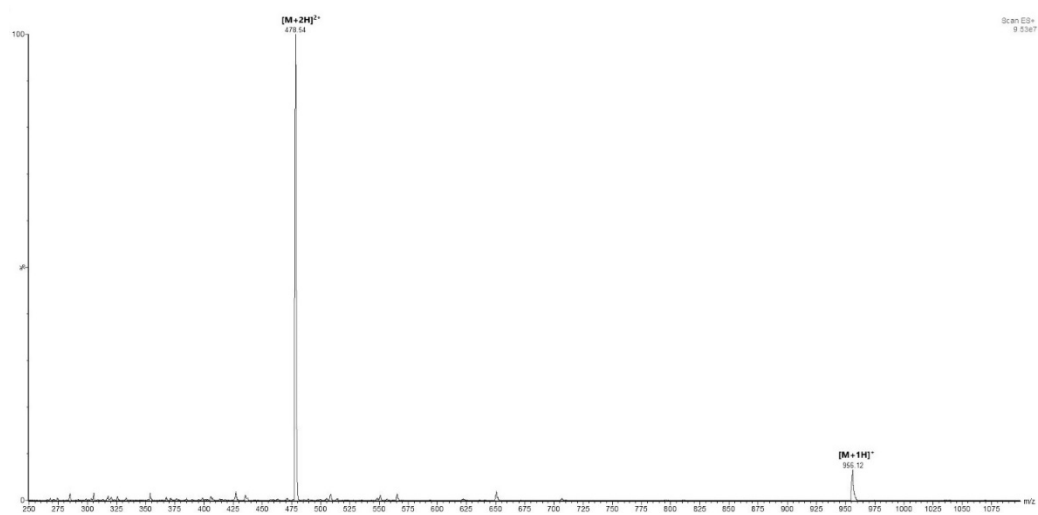
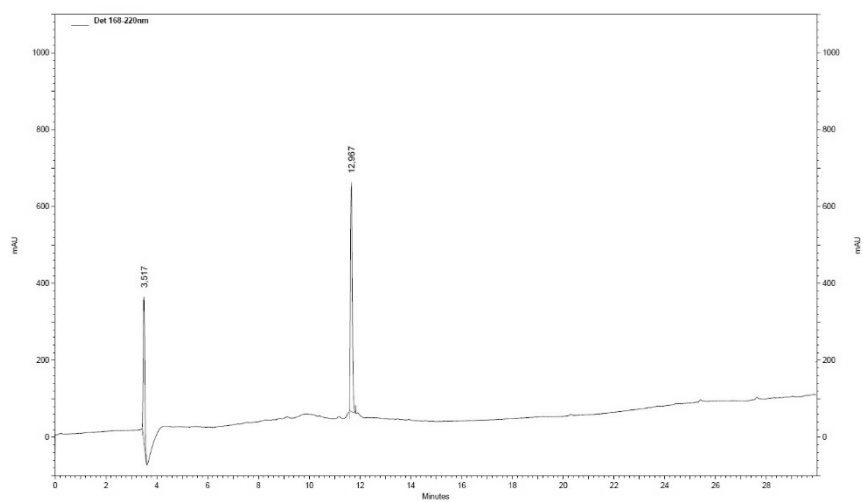
exhausted resin, TFA was removed under vacuum, and the crude material was then precipitated in fresh diethyl ether (Et₂O), isolated through centrifugation and finally purified by reverse-phase semi-preparative HPLC. After lyophilization the final spiro derivatives were obtained as white oils.

4.5.3 Appendix: HPLC chromatograms and ESI mass spectra of the final derivatives.

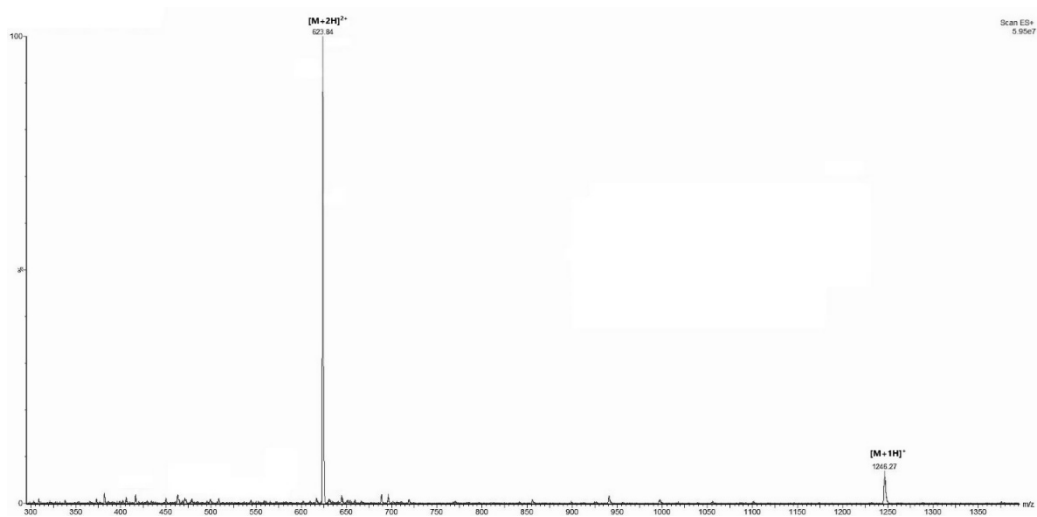
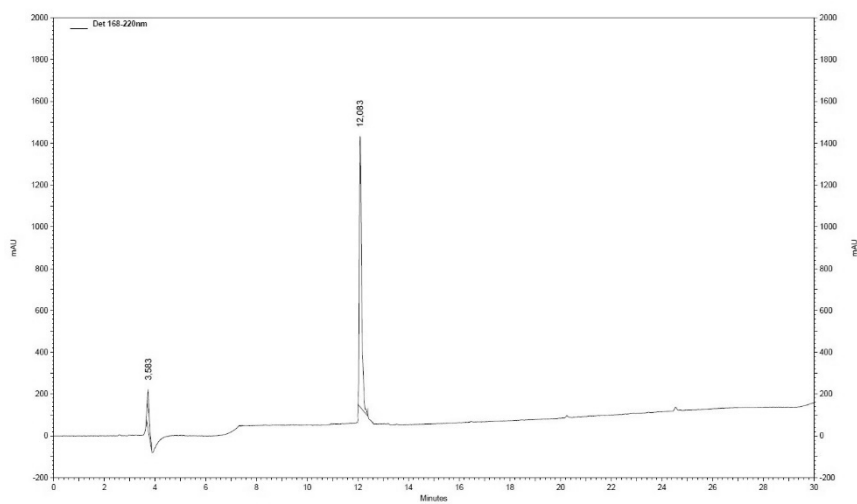
H-(D)Arg-Dmt-Lys-Phe-Lys(Ac)-NH₂ (78)



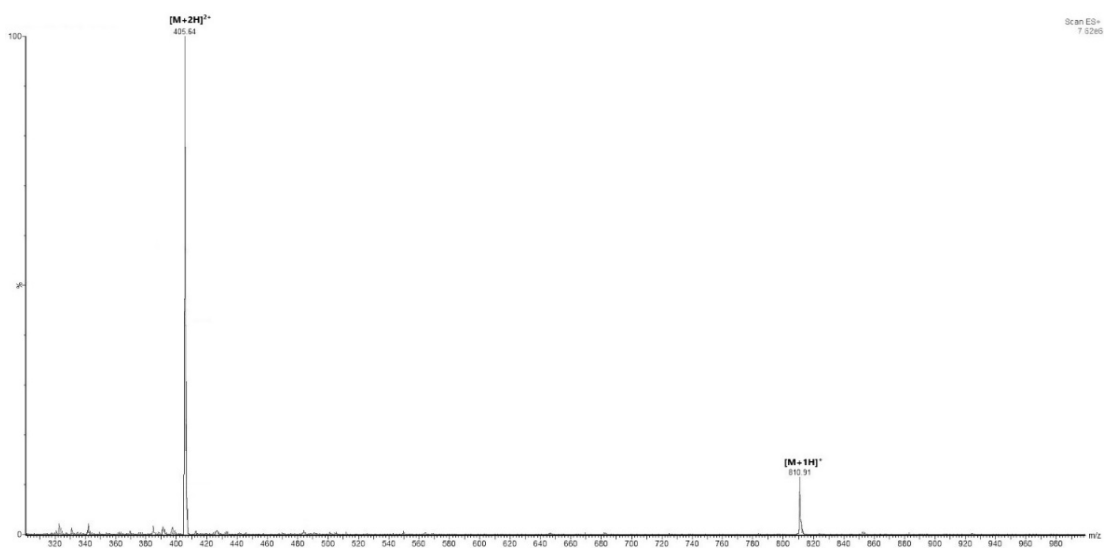
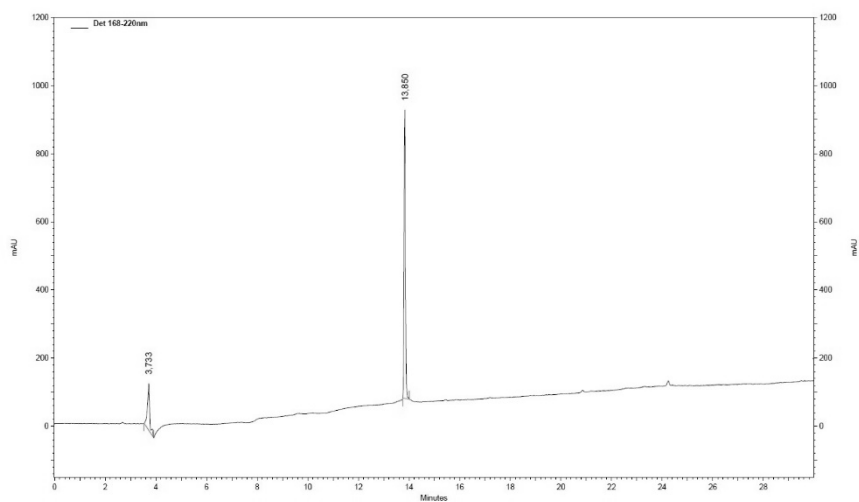
H-(D)Arg-Dmt-Lys-Phe-Lys(N ϵ -(O 2 O c) $n=1$ -Ac)-NH $_2$ (99)



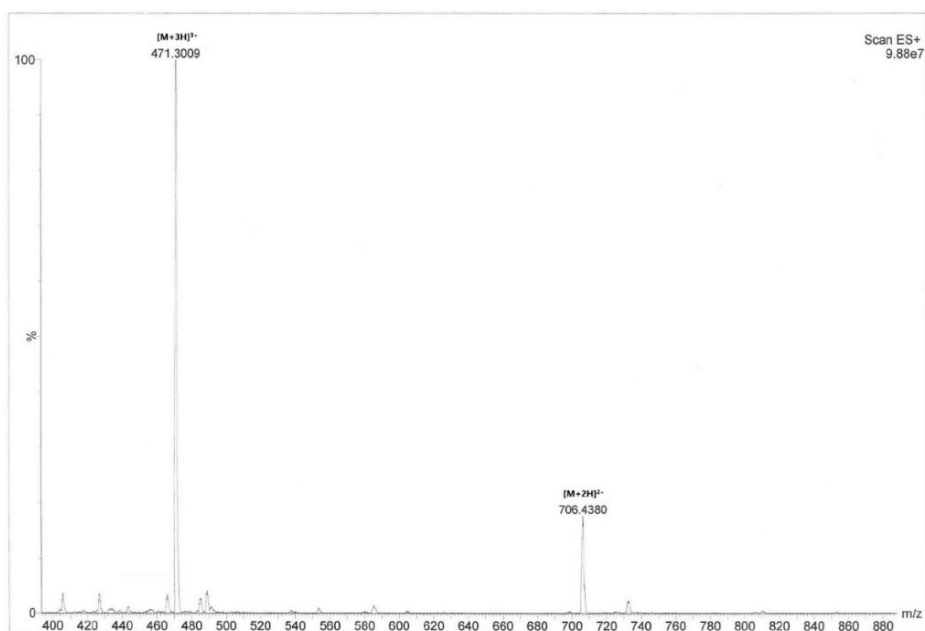
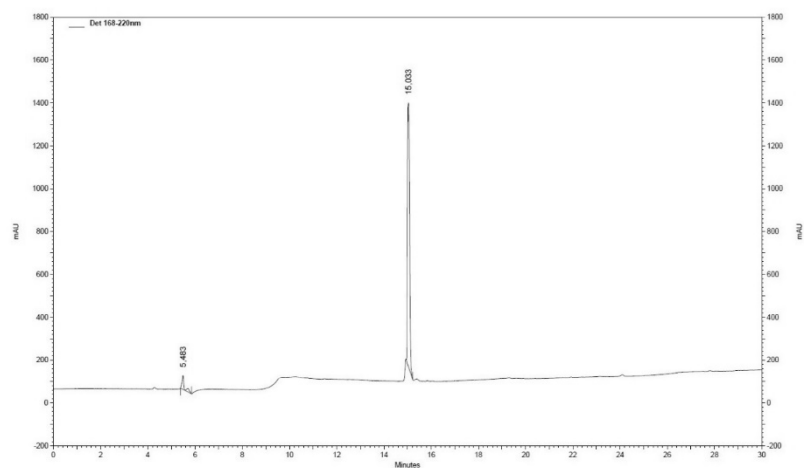
H-(D)Arg-Dmt-Lys-Phe-Lys(N ϵ -(O 2 O c) $_n=3$ -Ac)-NH $_2$ (100)



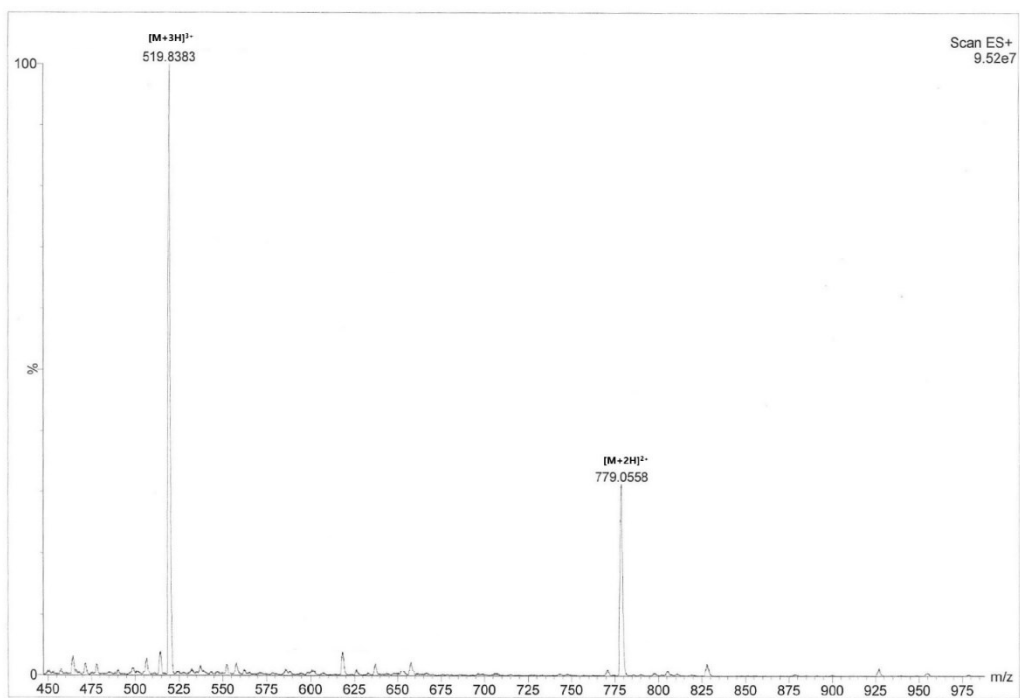
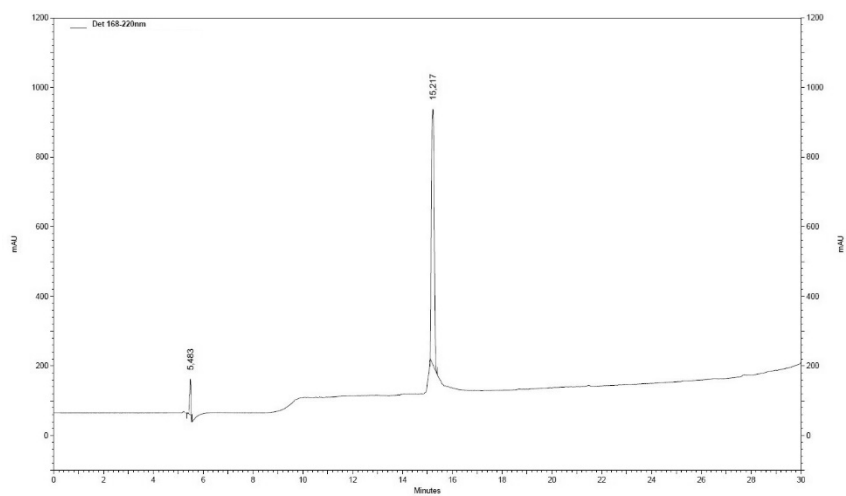
H-Lys(Ac)-(D)Arg-Dmt-Lys-Phe-NH₂ (88)



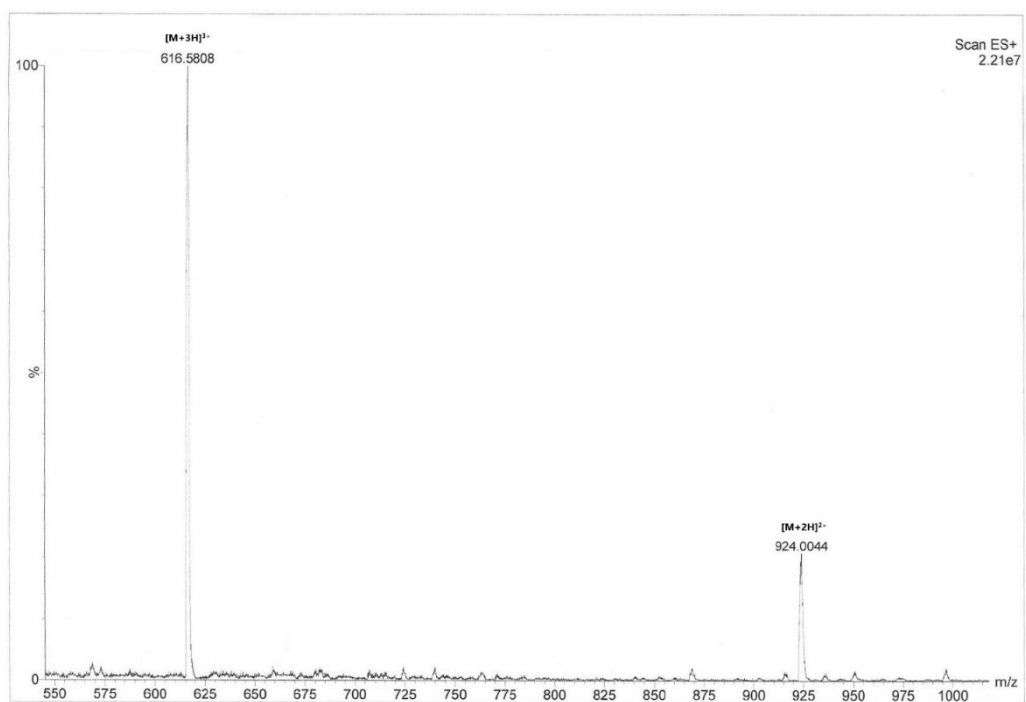
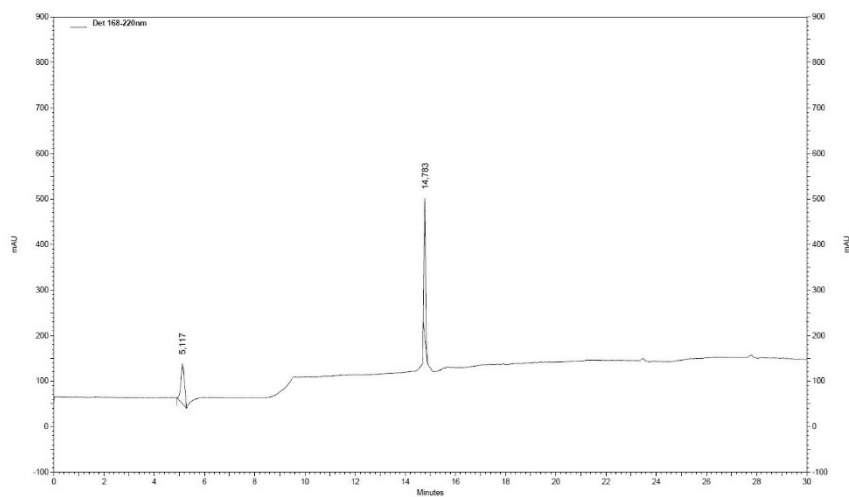
H-(D)Arg-Dmt-Lys-Phe-Lys(N_ε-succ.-DFO)-NH₂ (80)



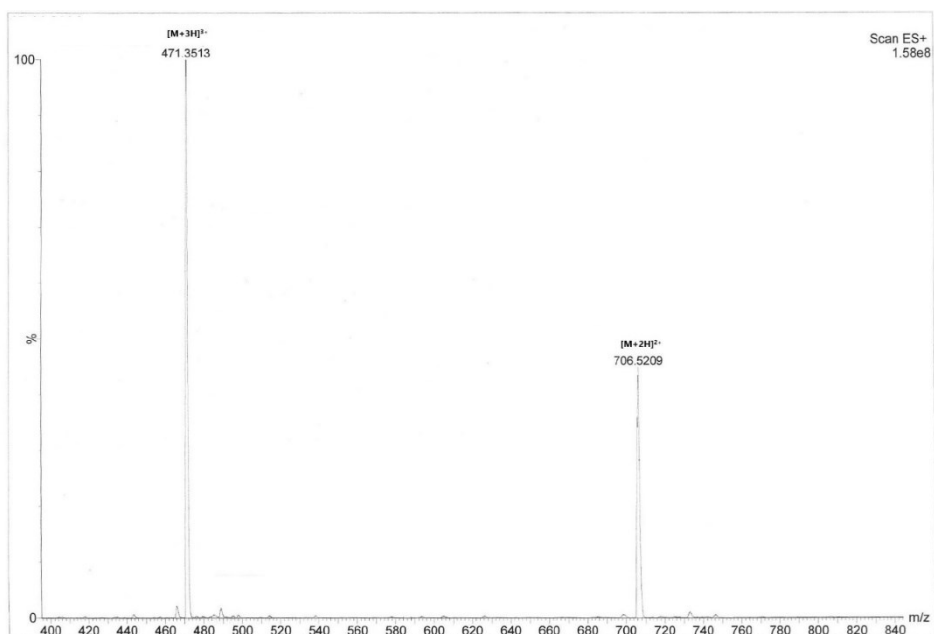
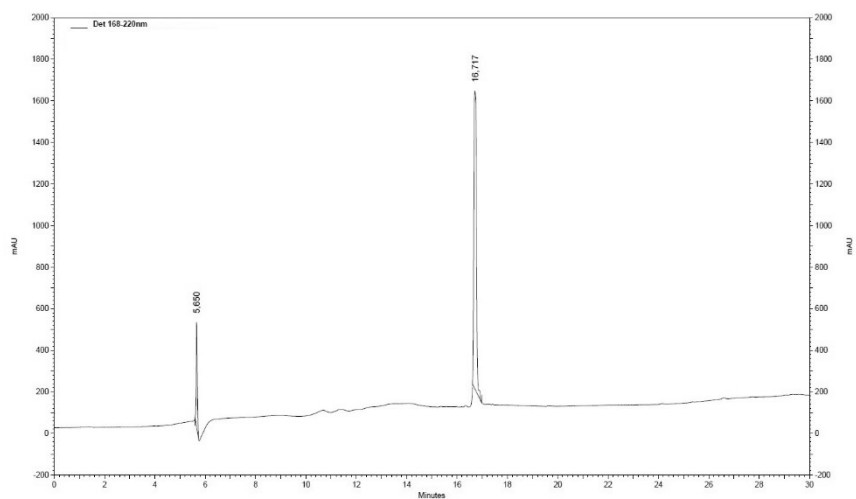
H-(D)Arg-Dmt-Lys-Phe-Lys(N ϵ -(O2Oc) $n=1$ -succ.-DFO)-NH $_2$ (102)



H-(D)Arg-Dmt-Lys-Phe-Lys(*N* ϵ -(O₂Oc)_{n=3}-succ.-DFO)-NH₂ (103)



H-Lys(N ϵ -succ.-DFO)-(D)Arg-Dmt-Lys-Phe-NH $_2$ (90)



5. REFERENCES.

- [1] Global, regional, and national burden of ischaemic heart disease and its attributable risk factors, 1990-2017: results from the Global Burden of Disease Study 2017. H. Dai, A. A. Much, E. Maor, E. Asher, A. Younis, Y. Xu, Y. Lu, X. Liu, J. Shu, N. L. Bragazzi. **2022**. *Eur Heart J Qual Care Clin Outcomes*. vol. 8(1):50-60.
- [2] https://www.who.int/healthinfo/global_burden_disease/estimates/en/
- [3] Global Epidemiology of Ischemic Heart Disease: Results from the Global Burden of Disease Study. M. AB Khan, M. J. Hashim, H. Mustafa, M. Y. Baniyas, S. K. B. M. Al Suwaidi, R. AlKatheeri, F. M. K. Alblooshi, M. E. A. Hassan Almatrooshi, M. E. Hazeem Alzaabi, R. S. Al Darmaki, S. N. A. Hussain Lootah. **2020**. *Cureus*. vol.12(7):e9349.
- [4] Myocardial ischemia-reperfusion injury: a neglected therapeutic target. D. J. Hausenloy, D. M. Yellon. **2013**. *J Clin Invest*. vol. 123(1):92-100.
- [5] Myocardial reperfusion injury. D. M. Yellon, D. J. Hausenloy. **2007**. *N Engl J Med*. vol. 357(11):1121-35.
- [6] Reperfusion Damage-A Story of Success, Failure, and Hope. R. Ferrari, C. Balla, M. Malagù, G. Guardigli, G. Morciano, M. Bertini, S. Biscaglia, G. Campo. **2017**. *Circ J*. vol. 81(2):131-141.
- [7] Myocardial ischaemia-reperfusion injury and cardioprotection in perspective. G. Heusch. **2020**. *Nat Rev Cardiol*. vol. 17(12):773-789.
- [8] The stunned myocardium: prolonged, postischemic ventricular dysfunction. E. Braunwald, R. A. Kloner. **1982**. *Circulation*. vol. 66(6):1146-9.
- [9] Reperfusion-induced arrhythmias: mechanisms and prevention. A. S. Manning, D. J. Hearse. **1984**. *J Mol Cell Cardiol*. vol. 16(6):497-518.
- [10] Blood supply of the myocardium after temporary coronary occlusion. A. Krug, D. M. de Rochemont, G. Korb. **1966**. *Circ Res*. vol. 19(1):57-62.
- [11] Effects of ischemic postconditioning on the hemodynamic parameters and heart nitric oxide levels of hypothyroid rats. S. Jeddi, J. Zaman, A. Ghasemi. **2015**. *Arq Bras Cardiol*. vol. 104(2):136-43.
- [12] Remote ischemic conditioning. G. Heusch, H. E. Bøtker, K. Przyklenk, A. Redington, D. Yellon. **2015**. *J Am Coll Cardiol*. vol. 65(2):177-95.
- [13] Remote ischaemic preconditioning: underlying mechanisms and clinical application. D. J. Hausenloy, D. M. Yellon. **2008**. *Cardiovasc Res*. vol. 79(3):377-86.
- [14] Acute Myocardial Infarction with Hyperoxemic Therapy (AMIHOT): a prospective, randomized trial of intracoronary hyperoxemic reperfusion after percutaneous coronary intervention. W. W. O'Neill, J. L. Martin, S. R. Dixon, A. L. Bartorelli, D. Trabattoni, P. V. Oemrawsingh, D. E. Atsma, M. Chang, W. Marquardt, J. K. Oh, M. W. Krucoff, R. J. Gibbons, J. R. Spears, AMIHOT Investigators. **2007**. *J Am Coll Cardiol*. vol. 50(5):397-405.
- [15] Hyperoxemic perfusion for treatment of reperfusion microvascular ischemia in patients with myocardial infarction. A. L. Bartorelli. **2003**. *Am J Cardiovasc Drugs*. vol. 3(4):253-63.
- [16] Effect of temperature on myocardial infarction in swine. D. J. Duncker, C. L. Klassen, Y. Ishibashi, S. H. Herrlinger, T. J. Pavsek, R. J. Bache. **1996**. *Am J Physiol*. vol. 270(4 Pt 2):H1189-99.

- [17] Ischemia and reperfusion-from mechanism to translation. H. K Eltzschig, T. Eckle. **2011**. *Nat Med*. vol. 17(11):1391-401.
- [18] Mechanisms underlying acute protection from cardiac ischemia-reperfusion injury. E. Murphy, C. Steenbergen. **2008**. *Physiol Rev*. vol. 88(2):581-609.
- [19] Pathophysiology of myocardial reperfusion injury: preconditioning, postconditioning, and translational aspects of protective measures. S. Sanada, I. Komuro, M. Kitakaze. **2011**. *Am J Physiol Heart Circ Physiol*. vol. 301(5):H1723-41.
- [20] Effects of regional ischemia on metabolism of glucose and fatty acids. Relative rates of aerobic and anaerobic energy production during myocardial infarction and comparison with effects of anoxia. L. H. Opie. **1976**. *Circ Res*. vol.38(5 Suppl 1):I52-74.
- [21] Studies of acidosis in the ischaemic heart by phosphorus nuclear magnetic resonance. P. B. Garlick, G. K. Radda, P. J. Seeley. **1979**. *Biochem J*. vol. 184(3):547-54.
- [22] Intracellular pH regulation in heart. R. D. Vaughan-Jones, K. W. Spitzer, P. Swietach. **2009**. *J Mol Cell Cardiol*. vol. 46(3):318-31.
- [23] Protection of the ischemic myocardium during the reperfusion: between hope and reality. J. C. Bopassa. **2012**. *Am J Cardiovasc Dis*. vol. 2(3):223-36.
- [24] Mitochondrial K(ATP) channel activation reduces anoxic injury by restoring mitochondrial membrane potential. M. Xu, Y. Wang, A. Ayub, M. Ashraf. **2001**. *Am J Physiol Heart Circ Physiol*. vol. 281(3):H1295-303.
- [25] Protective approaches against myocardial ischemia reperfusion injury. X. Li, M. Liu, R. Sun, Y. Zeng, S. Chen, P. Zhang. **2016**. *Exp Ther Med*. vol. 12(6):3823-3829.
- [26] Role of the reverse mode of the Na⁺/Ca²⁺ exchanger in reoxygenation-induced cardiomyocyte injury. C. Schäfer, Y. Ladilov, J. Inserte, M. Schäfer, S. Haffner, D. Garcia-Dorado, H. M. Piper. **2001**. *Cardiovasc Res*. vol. 51(2):241-50.
- [27] Calcium-mediated cell death during myocardial reperfusion. D. Garcia-Dorado, M. Ruiz-Meana, J. Inserte, A. Rodriguez-Sinovas, H. Michael Piper. **2012**. *Cardiovasc Res*. vol. 94(2):168-80.
- [28] Novel role of platelets in mediating inflammatory responses and ventricular rupture or remodeling following myocardial infarction. Y. Liu, Xiao-Ming Gao, L. Fang, N. L. Jennings, Y. Su, Xu Q, A. L. Samson, H. Kiriazis, Xin-Feng Wang, L. Shan, S. A. Sturgeon, R. L. Medcalf, S. P. Jackson, A. M. Dart, Xiao-Jun Du. **2011**. *Arterioscler Thromb Vasc Biol*. vol. 31(4):834-41.
- [29] Pretreatment with an inhibitor of mac-1 alters regional and systemic platelet function during ischemia-reperfusion in swine. P. A. Gurbel, V. L. Serebruany, S. F. Komiathy, M. E. Collins, G. D. Bittar, M. L. Schlossberg, W. Mergner. **1996**. *Pharmacology*. vol. 53(2):79-86.
- [30] Mitochondria in acute myocardial infarction and cardioprotection. C. J. A. Ramachandra, S. Hernandez-Resendiz, G. E. Crespo-Avilan, Ying-Hsi Lin, D. J. Hausenloy. **2020**. *EBioMedicine*. vol. 57:102884.
- [31] Mechanistic Role of mPTP in Ischemia-Reperfusion Injury. G. Morciano, M. Bonora, G. Campo, G. Aquila, P. Rizzo, C. Giorgi, M. R Wieckowski, P. Pinton. **2017**. *Adv Exp Med Biol*. vol. 982:169-189.

- [32] Molecular identity of the mitochondrial permeability transition pore and its role in ischemia-reperfusion injury. G. Morciano, C. Giorgi, M. Bonora, S. Punzetti, R. Pavasini, M. R. Wieckowski, G. Campo, P. Pinton. **2015**. *J Mol Cell Cardiol*. vol. 78:142-53.
- [33] Mitochondrial non-specific pores remain closed during cardiac ischaemia, but open upon reperfusion. E. J. Griffiths, A. P. Halestrap. **1995**. *Biochem J*. vol. 307(Pt 1):93-8.
- [34] Mitochondria as a therapeutic target for common pathologies. M. P. Murphy, R. C. Hartley. **2018**. *Nat Rev Drug Discov*. vol. 17(12):865-886.
- [35] Mitochondrial MPTP: A Novel Target of Ethnomedicine for Stroke Treatment by Apoptosis Inhibition. Y. Li, J. Sun, R. Wu, J. Bai, Y. Hou, Y. Zeng, Y. Zhang, X. Wang, Z. Wang, X. Meng. **2020**. *Front Pharmacol*. vol. 11:352.
- [36] Ischemia reperfusion injury as a modifiable therapeutic target for cardioprotection or neuroprotection in patients undergoing cardiopulmonary resuscitation. R. J. Madathil, R. S. Hira, M. Stoeckl, F. Sterz, J. B. Elrod, G. Nichol. **2016**. *Resuscitation*. vol. 105:85-91.
- [37] The Ca²⁺-induced membrane transition in mitochondria. II. Nature of the Ca²⁺ trigger site. R. A. Haworth, D. R. Hunter. **1979**. *Arch Biochem Biophys*. vol. 195(2):460-7.
- [38] Mitochondrial permeability transition pore: an enigmatic gatekeeper. B. Srinivasan. **2012**. *New Horizons in Science & Technology*, vol. 1(3):47-51.
- [39] The mitochondrial permeability transition pore: an evolving concept critical for cell life and death. G. Morciano, N. Naumova, P. Koprowski, S. Valente, V. A. Sardão, Y. Potes, A. Rimessi, M. R. Wieckowski, P. J. Oliveira. **2021**. *Biol Rev Camb Philos Soc*. vol. 96(6):2489-2521.
- [40] Mitochondrial permeability transition pore as a selective target for anti-cancer therapy. D. H. Suh, Mi-Kyung Kim, H. S. Kim, H. H. Chung, Y. S. Song. **2013**. *Front Oncol*. vol. 3:41.
- [41] The ADP/ATP translocator is not essential for the mitochondrial permeability transition pore. J. E. Kokoszka, K. G. Waymire, S. E. Levy, J. E. Sligh, J. Cai, D. P. Jones, G. R. MacGregor, D. C. Wallace. **2004**. *Nature*. vol. 427(6973):461-5.
- [42] Voltage-dependent anion channels are dispensable for mitochondrial-dependent cell death. C. P. Baines, R. A. Kaiser, T. Sheiko, W. J. Craigen, J. D. Molkentin. **2007**. *Nat Cell Biol*. vol. 9(5):550-5.
- [43] SPG7 Is an Essential and Conserved Component of the Mitochondrial Permeability Transition Pore. S. Shanmughapriya, S. Rajan, N. E. Hoffman, A. M. Higgins, D. Tomar, N. Nemani, K. J. Hines, D. J. Smith, A. Eguchi, S. Vallem, F. Shaikh, M. Cheung, N. J. Leonard, R. S. Stolakis, M. P. Wolfers, J. Ibetti, J. K. Chuprun, N. R. Jog, S. R. Houser, W. J. Koch, J. W. Elrod, M. Madesh. **2015**. *Mol Cell*. vol. 60(1):47-62.
- [44] The roles of phosphate and the phosphate carrier in the mitochondrial permeability transition pore. P. Varanyuwatana, A. P. Halestrap. **2012**. *Mitochondrion*. vol. 12(1):120-5.
- [45] Effect of peripheral benzodiazepine receptor (PBR/TSPO) ligands on opening of Ca²⁺-induced pore and phosphorylation of 3.5-kDa polypeptide in rat brain mitochondria. O. V. Krestinina, D. E. Grachev, I. V. Odinkova, G. Reiser, Yu V. Evtodienko, T. S. Azarashvili. **2009**. *Biochemistry (Mosc)*. vol. 74(4):421-9.
- [46] Targeting mitochondria for cancer therapy. S. Fulda, L. Galluzzi, G. Kroemer. **2010**. *Nat Rev Drug Discov*. vol. 9(6):447-64.

- [47] Specific ligands of the peripheral benzodiazepine receptor induce apoptosis and cell cycle arrest in human colorectal cancer cells. K. Maaser, M. Höpfner, A. Jansen, G. Weisinger, M. Gavish, A. P. Kozikowski, A. Weizman, P. Carayon, E. O. Riecken, M. Zeitz, H. Scherübl. **2001**. *Br J Cancer*. vol. 85(11):1771-80.
- [48] Regulation of the mitochondrial permeability transition pore by the outer membrane does not involve the peripheral benzodiazepine receptor (Translocator Protein of 18 kDa (TSPO)). J. Šileikytė, E. Blachly-Dyson, R. Sewell, A. Carpi, R. Menabò, F. Di Lisa, F. Ricchelli, P. Bernardi, M. Forte. **2014**. *J Biol Chem*. vol. 289(20):13769-81.
- [49] Bax and Bak function as the outer membrane component of the mitochondrial permeability pore in regulating necrotic cell death in mice. J. Karch, J. Q. Kwong, A. R. Burr, M. A. Sargent, J. W. Elrod, P. M. Peixoto, S. Martinez-Caballero, H. Osinska, E. H-Y Cheng, J. Robbins, K. W. Kinnally, J. D. Molkenin. **2013**. *Elife*. vol. 2:e00772.
- [50] Mitochondrial Permeability Transition: A Molecular Lesion with Multiple Drug Targets. T. Briston, D. L. Selwood, G. Szabadkai, M. R. Duchen. **2019**. *Trends Pharmacol Sci*. vol. 40(1):50-70.
- [51] The mitochondrial permeability transition pore and cancer: molecular mechanisms involved in cell death. M. Bonora, P. Pinton. **2014**. *Front Oncol*. vol. 4:302.
- [52] Loss of cyclophilin D reveals a critical role for mitochondrial permeability transition in cell death. C. P. Baines, R. A. Kaiser, N. H. Purcell, N. Scott Blair, H. Osinska, M. A. Hambleton, E. W. Brunskill, M. Richard Sayen, R. A. Gottlieb, G. W. Dorn, J. Robbins, J. D. Molkenin. **2005**. *Nature*. vol. 434(7033):658-62.
- [53] Inhibition by cyclosporin A of a Ca^{2+} -dependent pore in heart mitochondria activated by inorganic phosphate and oxidative stress. M. Crompton, H. Ellinger, A. Costi. **1988**. *Biochem J*. vol. 255(1):357-60.
- [54] Molecular mechanisms and consequences of mitochondrial permeability transition. M. Bonora, C. Giorgi, P. Pinton. **2022**. *Nat Rev Mol Cell Biol*. vol. 23(4):266-285.
- [55] Essentials for ATP synthesis by F1F0 ATP synthases. C. von Ballmoos, A. Wiedenmann, P. Dimroth. **2009**. *Annu Rev Biochem*. vol. 78:649-72.
- [56] From the Structural and (Dys)Function of ATP Synthase to Deficiency in Age-Related Diseases. C. Garone, A. Pietra, S. Nesci. **2022**. *Life (Basel)*. vol. 12(3):401.
- [57] Calcium and regulation of the mitochondrial permeability transition. V. Giorgio, L. Guo, C. Bassot, V. Petronilli, P. Bernardi. **2018**. *Cell Calcium*. vol. 70:56-63.
- [58] Molecular participants in mitochondrial cell death channel formation during neuronal ischemia. E. A. Jonas. **2009**. *Exp Neurol*. vol. 218(2):203-12.
- [59] The Ca^{2+} -induced membrane transition in mitochondria. III. Transitional Ca^{2+} release. D. R. Hunter, R. A. Haworth. **1979**. *Arch Biochem Biophys*. vol. 195(2):468-77.
- [60] The Ca^{2+} -induced membrane transition in mitochondria. I. The protective mechanisms. D. R. Hunter, R. A. Haworth. **1979**. *Arch Biochem Biophys*. vol. 195(2):453-9.
- [61] The ATPase Inhibitory Factor 1 is a Tissue-Specific Physiological Regulator of the Structure and Function of Mitochondrial ATP Synthase: A Closer Look Into Neuronal Function. S. Domínguez-Zorita, I. Romero-Carramiñana, J. M. Cuezva, P. B. Esparza-Moltó. **2022**. *Front Physiol*. vol. 13:868820.
- [62] Regulation of the H^{+} -ATP synthase by IF1: a role in mitohormesis. P. B. Esparza-Moltó, C. Nuevo-Tapióles, J. M. Cuezva. **2017**. *Cell Mol Life Sci*. vol. 74(12):2151-2166.

- [63] A mitochondrial megachannel resides in monomeric F₁F₀ ATP synthase. N. Mnatsakanyan, M. C. Llaguno, Y. Yang, Y. Yan, J. Weber, F. J. Sigworth, E. A. Jonas. **2019**. *Nat Commun*. vol. 10(1):5823.
- [64] Purified F-ATP synthase forms a Ca²⁺-dependent high-conductance channel matching the mitochondrial permeability transition pore. A. Urbani, V. Giorgio, A. Carrer, C. Franchin, G. Arrigoni, C. Jiko, K. Abe, S. Maeda, K. Shinzawa-Itoh, J. F. M. Bogers, D. G. G. McMillan, C. Gerle, I. Szabò, P. Bernardi. **2019**. *Nat Commun*. vol. 10(1):4341.
- [65] Persistence of the permeability transition pore in human mitochondria devoid of an assembled ATP synthase. J. Carroll, J. He, S. Ding, I. M. Fearnley, J. E. Walker. **2019**. *Proc Natl Acad Sci U S A*. vol.116(26):12816-12821.
- [66] Persistence of the mitochondrial permeability transition in the absence of subunit c of human ATP synthase. J. He, H. C. Ford, J. Carroll, S. Ding, I. M. Fearnley, J. E. Walker. **2017**. *Proc Natl Acad Sci U S A*. vol. 114(13):3409-3414.
- [67] Role of the c subunit of the FO ATP synthase in mitochondrial permeability transition. M. Bonora, A. Bononi, E. De Marchi, C. Giorgi, M. Lebiezinska, S. Marchi, S. Patergnani, A. Rimessi, J. M. Suski, A. Wojtala, M. R. Wieckowski, G. Kroemer, L. Galluzzi, P. Pinton. **2013**. *Cell Cycle*. vol. 12(4):674-83.
- [68] An uncoupling channel within the c-subunit ring of the F₁F₀ ATP synthase is the mitochondrial permeability transition pore. K. N. Alavian, G. Beutner, E. Lazrove, S. Sacchetti, Han-A Park, P. Licznarski, H. Li, P. Nabili, K. Hockensmith, M. Graham, G. A. Porter Jr, E. A. Jonas. **2014**. *Proc Natl Acad Sci U S A*. vol. 111(29):10580-5.
- [69] Fo ATP synthase C subunit serum levels in patients with ST-segment Elevation Myocardial Infarction: Preliminary findings. G. Campo, G. Morciano, R. Pavasini, M. Bonora, L. Sbrano, S. Biscaglia, M. Bovolenta, M. Pinotti, S. Punzetti, P. Rizzo, G. Aquila, C. Giorgi, R. Ferrari, P. Pinton. **2016**. *Int J Cardiol*. vol. 221:993-7.
- [70] Mitochondrial permeability transition involves dissociation of F₁F₀ ATP synthase dimers and C-ring conformation. M. Bonora, C. Morganti, G. Morciano, G. Pedriali, M. Lebiezinska-Arciszewska, G. Aquila, C. Giorgi, P. Rizzo, G. Campo, R. Ferrari, G. Kroemer, M. R. Wieckowski, L. Galluzzi, P. Pinton. **2017**. *EMBO Rep*. vol. 18(7):1077-1089.
- [71] Cryo-EM structure of the entire mammalian F-type ATP synthase. G. Pinke, L. Zhou, L. A. Sazanov. **2020**. *Nat Struct Mol Biol*. vol. 27(11):1077-1085.
- [72] The mitochondrial permeability transition pore and its role in cell death. M. Crompton. 1999. *Biochem J*. vol. 341(Pt 2):233-49.
- [73] Mitochondria and cell death: outer membrane permeabilization and beyond. S. W. G. Tait, D. R. Green. **2010**. *Nat Rev Mol Cell Biol*. vol. 11(9):621-32.
- [74] Structures of cyclophilin-ligand complexes. P. Taylor, H. Husi, G. Kontopidis, M. D. Walkinshaw. **1997**. *Prog Biophys Mol Biol*. vol. 67(2-3):155-81.
- [75] Protection by Cyclosporin A of ischemia/reperfusion-induced damage in isolated rat hearts. E. J. Griffiths, A. P. Halestrap. **1993**. *J Mol Cell Cardiol*. vol. 25(12):1461-9.
- [76] Inhibition of anoxia-induced injury in heart myocytes by cyclosporin A. W. Nazareth, N. Yafei, M. Crompton. **1991**. *J Mol Cell Cardiol*. vol. 23(12):1351-4.
- [77] Cyclosporine A in Reperfused Myocardial Infarction: The Multicenter, Controlled, Open-Label CYCLE Trial. F. Ottani, R. Latini, L. Staszewsky, L. La Vecchia, N.

- Locuratolo, M. Sicuro, S. Masson, S. Barlera, V. Milani, M. Lombardi, A. Costalunga, N. Mollichelli, A. Santarelli, N. De Cesare, P. Sganzerla, A. Boi, A. P. Maggioni, U. Limbruno, CYCLE Investigators. **2016**. *J Am Coll Cardiol*. vol. 67(4):365-374.
- [78] Cyclosporine before PCI in Acute Myocardial Infarction. J. Pottecher, P. Diemunsch, B. Geny. **2016**. *N Engl J Med*. Jan 7;374(1):88-9.
- [79] Cyclosporine before Coronary Artery Bypass Grafting Does Not Prevent Postoperative Decreases in Renal Function: A Randomized Clinical Trial. P. Ederoth, A. Dardashti, E. Grins, B. Brondén, C. Metzsch, A. Erdling, S. Nozohoor, A. Mokhtari, M. J. Hansson, E. Elmér, L. Algotsson, S. Jovinge, H. Bjursten. **2018**. *Anesthesiology*. vol. 128(4):710-717.
- [80] Alisporivir rescues defective mitochondrial respiration in Duchenne muscular dystrophy. M. Schiavone, A. Zulian, S. Menazza, V. Petronilli, F. Argenton, L. Merlini, P. Sabatelli, P. Bernardi. **2017**. *Pharmacol Res*. vol. 125(Pt B):122-131.
- [81] Debio-025 is more effective than prednisone in reducing muscular pathology in mdx mice. E. R. Wissing, D. P. Millay, G. Vuagniaux, J. D. Molkentin. **2010**. *Neuromuscul Disord*. vol. 20(11):753-60.
- [82] NIM811, a cyclophilin inhibitor without immunosuppressive activity, is beneficial in collagen VI congenital muscular dystrophy models. A. Zulian, E. Rizzo, M. Schiavone, E. Palma, F. Tagliavini, B. Blaauw, L. Merlini, N. M. Maraldi, P. Sabatelli, P. Braghetta, P. Bonaldo, F. Argenton, P. Bernardi. **2014**. *Hum Mol Genet*. vol. 23(20):5353-63.
- [83] TRO40303, a new cardioprotective compound, inhibits mitochondrial permeability transition. S. Schaller, S. Paradis, G. A. Ngoh, R. Assaly, B. Buisson, C. Drouot, M. A. Ostuni, Jean-Jacques Lacapere, F. Bassissi, T. Bordet, A. Berdeaux, S. P. Jones, D. Morin, R. M. Pruss. **2010**. *J Pharmacol Exp Ther*. vol. 333(3):696-706.
- [84] Effect of intravenous TRO40303 as an adjunct to primary percutaneous coronary intervention for acute ST-elevation myocardial infarction: MITOCARE study results. D. Atar, H. Arheden, A. Berdeaux, Jean-Louis Bonnet, M. Carlsson, P. Clemmensen, V. Cuvier, N. Danchin, Jean-Luc Dubois-Randé, H. Engblom, D. Erlinge, H. Firat, S. Halvorsen, H. S. Hansen, W. Hauke, E. Heiberg, S. Koul, Alf-Inge Larsen, P. Le Corvoisier, J. E. Nordrehaug, F. Paganelli, R. M. Pruss, H. Rousseau, S. Schaller, G. Sonou, V. Tuseth, J. Veys, E. Vicaut, S. E. Jensen. **2015**. *Eur Heart J*. vol. 36(2):112-9.
- [85] Administration of the Mitochondrial Permeability Transition Pore Inhibitor, TRO40303, prior to Primary Percutaneous Coronary Intervention, Does Not Affect the Levels of Pro-Inflammatory Cytokines or Acute-Phase Proteins. N. Butt, L. K. Bache-Mathiesen, J. E. Nordrehaug, V. Tuseth, P. S. Munk, V. Bonarjee, T. S. Hall, S. E. Jensen, S. Halvorsen, H. Firat, D. Atar, A. I. Larsen. **2017**. *Cardiology*. vol. 138(2):122-132.
- [86] A small-molecule DS44170716 inhibits Ca²⁺-induced mitochondrial permeability transition. N. Kon, A. Satoh, N. Miyoshi. **2017**. *Sci Rep*. vol. 7(1):3864.
- [87] DS16570511 is a small-molecule inhibitor of the mitochondrial calcium uniporter. N. Kon, M. Murakoshi, A. Isobe, K. Kagechika, N. Miyoshi, T. Nagayama. **2017**. *Cell Death Discov*. vol. 3:17045.
- [88] Edaravone, a radical scavenger, inhibits mitochondrial permeability transition pore in rat brain. Y. Takayasu, J. Nakaki, T. Kawasaki, K. Koda, Y. Ago, A. Baba, T. Matsuda. **2007**. *J Pharmacol Sci*. vol. 103(4):434-7.

- [89] Structure of the c(10) ring of the yeast mitochondrial ATP synthase in the open conformation. J. Symersky, V. Pagadala, D. Osowski, A. Krah, T. Meier, J. D. Faraldo-Gómez, D. M. Mueller. **2012**. *Nat Struct Mol Biol*. vol. 19(5):485-91.
- [90] Oligomycin frames a common drug-binding site in the ATP synthase. J. Symersky, D. Osowski, D. E. Walters, D. M. Mueller. **2012**. *Proc Natl Acad Sci USA*. vol. 109(35):13961-5.
- [91] Myocardial reperfusion injury: looking beyond primary PCI. G. M. Fröhlich, P. Meier, S. K. White, D. M. Yellon, D. J. Hausenloy. **2013**. *Eur Heart J*. vol. 34(23):1714-22.
- [92] Targeted pharmacotherapy for ischemia reperfusion injury in acute myocardial infarction. A. Rout, U. S. Tantry, M. Novakovic, A. Sukhi, P. A. Gurbel. **2020**. *Expert Opin Pharmacother*. vol. 21(15):1851-1865.
- [93] Discovery of Novel 1,3,8-Triazaspiro[4.5]decane Derivatives That Target the c Subunit of F₁/F₀-Adenosine Triphosphate (ATP) Synthase for the Treatment of Reperfusion Damage in Myocardial Infarction. G. Morciano, D. Preti, G. Pedriali, G. Aquila, S. Missiroli, A. Fantinati, N. Caroccia, S. Pacifico, M. Bonora, A. Talarico, C. Morganti, P. Rizzo, R. Ferrari, M. R. Wieckowski, G. Campo, C. Giorgi, C. Trapella, P. Pinton. **2018**. *J Med Chem*. vol. 61(16):7131-7143.
- [94] Identification of small-molecule urea derivatives as PTPC modulators targeting the c subunit of F₁/F₀-ATP synthase. A. Fantinati, G. Morciano, G. Turrin, G. Pedriali, S. Pacifico, D. Preti, V. Albanese, D. Illuminati, V. Cristofori, C. Giorgi, E. Tremoli, P. Pinton, C. Trapella. **2022**. *Bioorg Med Chem Lett*. vol. 72:128822.
- [95] Identification of amino acid substitutions in the dicyclohexylcarbodiimide-binding subunit of the mitochondrial ATPase complex from oligomycin-resistant mutants of *Saccharomyces cerevisiae*. W. Sebald, E. Wachter, A. Tzagoloff. **1979**. *Eur J Biochem*. vol. 100(2):599-607.
- [96] Isatin containing heterocycles for different biological activities: Analysis of structure activity relationship. R. Nath, S. Pathania, G. Grover, M. J. Akhtar. **2020**. *J Mol Structure*. vol. 1222.
- [97] Isatin, an endogenous nonpeptide biofactor: A review of its molecular targets, mechanisms of actions, and their biomedical implications. A. Medvedev, O. Buneeva, O. Gnedenko, P. Ershov, A. Ivanov. **2018**. *Biofactors*. vol. 44(2):95-108.
- [98] The chemistry of isatins: a review from 1975 to 1999. J. F. M. da Silva, S. J. Garden, A. C. Pinto. **2001**. *J. Braz. Chem. Soc*. vol.12 (3)
- [99] Isatin: A Scaffold with Immense Biodiversity. P. Nath, A. Mukherjee, S. Mukherjee, S. Banerjee, S. Das, S. Banerjee. **2021**. *Mini Rev Med Chem*. vol. 21(9):1096-1112.
- [100] Brønsted acid-catalyzed efficient Strecker reaction of ketones, amines and trimethylsilyl cyanide. Guang-Wu Zhang, Dong-Hua Zheng, J. Nie, T. Wang, Jun-An Ma. **2010**. *Org Biomol Chem*. vol. 8(6):1399-405.
- [101] A facile method for the synthesis of oxindole based quaternary alpha-aminonitriles via the Strecker reaction. Yun-Lin Liu, F. Zhou, Jun-Jie Cao, Cong-Bin Ji, M. Ding, J. Zhou. **2010**. *Org Biomol Chem*. vol. 8(17):3847-50.
- [102] Mechanism of the base-catalyzed conversion of nitriles to amides by hydrogen peroxide. John E. McIsaac Jr., R. E. Ball, E. J. Behrman. **1971**. *J Org Chem*. vol. 36(20):3048-3050.

- [103] Enamines and Dimethylamino Imines as Building Blocks in Heterocyclic Synthesis: Reactions of DMF-DMA Reagent with Different Functional Groups. M. Gümüş, İ. Koca. **2020**. *Chemistry Select* vol. 5:12377-12397.
- [104] Comprehensive analysis of mitochondrial permeability transition pore activity in living cells using fluorescence-imaging-based techniques. M. Bonora, C. Morganti, G. Morciano, C. Giorgi, M. R. Wieckowski, P. Pinton. **2016**. *Nat Protoc.* vol. 11(6):1067-80.
- [105] The Importance of Fluorine in the Life Science Industry. P. Maienfisch and R. G. Hall. **2004**. *CHIMIA International Journal for Chemistry.* vol. 58(3):93-99.
- [106] Use of luciferase probes to measure ATP in living cells and animals. G. Morciano, A. C. Sarti, S. Marchi, S. Missiroli, S. Falzoni, L. Raffaghello, V. Pistoia, C. Giorgi, F. Di Virgilio, P. Pinton. **2017**. *Nat Protoc.* vol. 12(8):1542-1562.
- [107] Regulation of mitochondrial ATP synthesis by calcium: evidence for a long-term metabolic priming. L. S. Jouaville, P. Pinton, .C Bastianutto, G. A. Rutter, R. Rizzuto. **1999**. *Proc Natl Acad Sci U S A.* vol. 96(24):13807-12.
- [108] A C=O...Isothiouonium Interaction Dictates Enantiodiscrimination in Acylative Kinetic Resolutions of Tertiary Heterocyclic Alcohols. M. D Greenhalgh, S. M. Smith, D. M. Walden, J. E. Taylor, Z. Brice, E. R. T. Robinson, C. Fallan, D. B. Cordes, A. M. Z. Slawin, H. C. Richardson, M. A. Grove, P. Ha-Yeon Cheong, A. D. Smith. **2018**. *Angew Chem Int Ed Engl.* vol. 57(12):3200-3206.
- [109] Reductive Coupling of Acrylates with Ketones and Ketimines by a Nickel-Catalyzed Transfer-Hydrogenative Strategy. C. S. Buxton, D. C. Blakemore, J. F. Bower. **2017**. *Angew Chem Int Ed Engl.* vol. 56(44):13824-13828.
- [110] The Quinine Thiourea-Catalyzed Asymmetric Strecker Reaction: An Approach for the Synthesis of 3-Aminooxindoles. D. Wang, J. Liang, J. Feng, K. Wang, Q. Sun, L. Zhao, D. Li, W. Yan, R. Wang. **2013**. *Adv. Synth. Catal.* vol. 355:548-558.
- [111] 1,3-Dipolar cycloaddition of hydrazones with α -oxo-ketenes: a three-component stereoselective entry to pyrazolidinones and an original class of spirooxindoles. M. Presset, K. Mohanan, M. Hamann, Y. Coquerel, J. Rodriguez. **2011**. *Org Lett.* vol. 13(15):4124-7.
- [112] Domino Reactions in Organic Synthesis. L. F. Tietze. **1996**. *Chem Rev.* vol. 96(1):115-136.
- [113] Stereoselective multiple bond-forming transformations (MBFTs): the power of 1,2- and 1,3-dicarbonyl compounds. D. Bonne, T. Constantieux, Y. Coquerel, J. Rodriguez. **2013**. *Chemistry.* vol. 19(7):2218-31.
- [114] Diazo-Transfer Reactions to 1,3-Dicarbonyl Compounds with Tosyl Azide. M. Presset, D. Mailhol, Y. Coquerel, J. Rodriguez. **2011**. *Synthesis.* vol. (16): 2549-2552.
- [115] Spiroimidazolidinone library derivatives on SynPhase lanterns. L. Feliu, G. Subra, J. Martinez, M. Amblard. **2003**. *J Comb Chem.* vol.5(4):356-61.
- [116] Solid Phase Peptide Synthesis: The Synthesis of a Tetrapeptide. R. B. Merrifield. **1963**. *J Am Chem Soc.* vol.85(14), 2149-2154.
- [117] HPLC analysis and purification of peptides. C. T. Mant, Y. Chen, Z. Yan, T. V. Popa, J. M. Kovacs, J. B. Mills, B. P. Tripet, R. S. Hodges. **2007**. *Methods Mol Biol.* vol. 386:3-55.
- [118] Solid-phase peptide synthesis. R. B. Merrifield. **1969**. *Adv Enzymol Relat Areas Mol Biol.* vol. 32:221-96.

- [119] Chemistry of peptide synthesis. N. L. Benoiton. **2005**. Taylor & Francis Oxford. 125-155.
- [120] The photolysis of diazoacetylchymotrypsin. A. Singh, E. R. Thornton, F. H. Westheimer. **1962**. *J Biol Chem*. vol. 237:3006-8.
- [121] Photochemical fishing approaches for identifying target proteins and elucidating the structure of a ligand-binding region using carbene-generating photoreactive probes. Y. Sadakane, Y. Hatanaka. **2006**. *Anal Sci*. vol. 22(2):209-18.
- [122] Photo-induced covalent cross-linking for the analysis of biomolecular interactions. G. W. Preston, A. J. Wilson. **2013**. *Chem Soc Rev*. vol. 42(8):3289-301.
- [123] Recent developments and applications of clickable photoprobes in medicinal chemistry and chemical biology. D. J. Lapinsky, D. S. Johnson. **2015**. *Future Med Chem*. vol. 7(16):2143-71.
- [124] Photoaffinity labeling in target- and binding-site identification. E. Smith, I. Collins. **2015**. *Future Med Chem*. vol. 7(2):159-83.
- [125] Design and synthesis of novel photoaffinity reagents for labeling VEGF receptor tyrosine kinases. Sun-Young Han, S. H. Choi, M. H. Kim, W. G. Lee, S. H. Kim, Y. K. Min, B. T. Kim. **2006**. *Tetrahedron Letters*. vol. 47(17):2915-2919.
- [126] The growing impact of click chemistry on drug discovery. H. C. Kolb, K. B. Sharpless. **2003**. *Drug Discovery Today*. vol. 8(24):1128-1137.
- [127] Fluorophores and Their Applications as Molecular Probes in Living Cells. J. Liu, C. Liu, W. He. **2013**. *Curr Org Chem*. vol. 17(6):564-579.
- [128] 2-Aryl-5-carboxytetrazole as a New Photoaffinity Label for Drug Target Identification. A. Herner, J. Marjanovic, T. M. Lewandowski, V. Marin, M. Patterson, L. Miesbauer, D. Ready, J. Williams, A. Vasudevan, Q. Lin. **2016**. *J Am Chem Soc*. vol. 138(44):14609-14615.
- [129] Fishing for Drug Targets: A Focus on Diazirine Photoaffinity Probe Synthesis. J. R. Hill, A. A. B. Robertson. **2018**. *J Med Chem*. vol. 61(16):6945-6963.
- [130] Mitochondrial ATP synthase c-subunit leak channel triggers cell death upon loss of its F1 subcomplex. N. Mnatsakanyan, Han-A Park, J. Wu, X. He, M. C. Llaguno, M. Latta, P. Miranda, B. Murtishi, M. Graham, J. Weber, R. J. Levy, E. V. Pavlov, E. A. Jonas. **2022**. *Cell Death Differ*. vol. 29(9):1874-1887.
- [131] Protocol for clickable photoaffinity labeling and quantitative chemical proteomics. W. Lee, Z. Huang, C. W. A. Ende, U. Seneviratne. **2021**. *STAR Protoc*. vol. 2(2):100593.
- [132] Mitochondria-Targeted Drug Delivery in Cardiovascular Disease: A Long Road to Nano-Cardio Medicine. F. Forini, P. Canale, G. Nicolini, G. Iervasi. **2020**. *Pharmaceutics*. vol. 12(11):1122.
- [133] Novel Iron(III)-Induced Prooxidant Activity Measurement Using a Solid Protein Sensor in Comparison with a Copper(II)-Induced Assay. E. Akyüz, K. S. Başkan, E. Tütem & R. Apak. **2020**. *Analytical Letters*. vol. 53(9):1489-1503.

- [134] Oxidative stress and microRNAs in vascular diseases. A. Magenta, S. Greco, C. Gaetano, F. Martelli. **2013**. *Int J Mol Sci*. vol. 14(9):17319-46.
- [135] ROS and RNS in plant physiology: an overview. L. A. Del Río. **2015**. *J Exp Bot*. vol. 66(10):2827-37.
- [136] Oxygen-derived free radicals in postischemic tissue injury. J. M. McCord. **1985**. *N Engl J Med*. vol. 312(3):159-63.
- [137] New concepts in reactive oxygen species and cardiovascular reperfusion physiology. L. B. Becker. **2004**. *Cardiovasc Res*. vol. 61(3):461-70.
- [138] Oxidative stress and cell signalling. G. Poli, G. Leonarduzzi, F. Biasi, E. Chiarotto. **2004**. *Curr Med Chem*. vol. 11(9):1163-82.
- [139] The broad spectrum of responses to oxidants in proliferating cells: a new paradigm for oxidative stress. K. J. Davies. **1999**. *IUBMB Life*. vol. 48(1):41-7.
- [140] Ischemic preconditioning alters real-time measure of O₂ radicals in intact hearts with ischemia and reperfusion. L. G. Kevin, A. K. S. Camara, M. L. Riess, E. Novalija, D. F. Stowe. **2003**. *Am J Physiol Heart Circ Physiol*. vol. 284(2):H566-74.
- [141] Generation of superoxide in cardiomyocytes during ischemia before reperfusion. L. B. Becker, T. L. vanden Hoek, Z. H. Shao, C. Q. Li, P. T. Schumacker. **1999**. *Am J Physiol*. vol. 277(6):H2240-6.
- [142] Oxidative stress in hepatic ischemia-reperfusion injury: the role of antioxidants and iron chelating compounds. D. Galaris, A. Barbouti, P. Korantzopoulos. **2006**. *Curr Pharm Des*. vol. 12(23):2875-90.
- [143] Regulation of miRNAs by Natural Antioxidants in Cardiovascular Diseases: Focus on SIRT1 and Enos. Y. Lee, E. Im. **2021**. *Antioxidants (Basel)*. vol. 10(3):377.
- [144] Effects of free radicals on the fluidity of myocardial membranes. M. Bagchi, M. R. Prasad, R. M. Engelman, D. K. Das. **1989**. *Free Radic Res Commun*. vol. 7(3-6):375-80.
- [145] The role of metals in ischemia/reperfusion injury of the liver. A. S. Arora, G. J. Gores. **1996**. *Semin Liver Dis*. vol. 16(1):31-8.
- [146] Mechanisms underlying iron and copper ions toxicity in biological systems: Pro-oxidant activity and protein-binding effects. M. E. Letelier, S. Sánchez-Jofré, L. Peredo-Silva, J. Cortés-Troncoso, P. Aracena-Parks. **2010**. *Chem Biol Interact*. vol. 188(1):220-7.
- [147] Serum zinc concentration in acute myocardial infarction. A. M. Handjani, J. C. Smith Jr, J. B. Herrmann, J. A. Halsted. **1974**. *Chest*. vol. 65(2):185-7.
- [148] Mitochondrial damage during cerebral ischemia. G. Fiskum. **1985**. *Annals of Emergency Medicine*. vol. 14(8):810-815.
- [149] The involvement of iron in lipid peroxidation. Importance of ferric to ferrous ratios in initiation. J. M. Braugher, L. A. Duncan, R. L. Chase. **1986**. *J Biol Chem*. vol. 261(22):10282-9.
- [150] Role of iron in ischemia-induced neurodegeneration: mechanisms and insights. G. Minhas, S. Modgil, A. Anand. **2014**. *Metab Brain Dis*. vol. 29(3):583-91.

- [151] Cardioplegic arrest superimposed on evolving myocardial ischemia. Improved recovery after inhibition of hydroxyl radical generation by peroxidase or deferoxamine. A 31P nuclear resonance study. M. Bernard, P. Menasché, S. Piétri, C. Grousset, A. Piwnica, P. J. Cozzone. **1988**. *Circulation*. vol. 78(5 Pt 2):III164-72.
- [152] TPEN, a transition metal chelator, improves myocardial protection during prolonged ischemia. M. Karck, Y. Appelbaum, H. Schwalb, A. Haverich, M. Chevion, G. Uretzky. **1992**. *J Heart Lung Transplant*. vol. 11(5):979-85.
- [153] The push-and-pull mechanism to scavenge redox-active transition metals: a novel concept in myocardial protection. M. Karck, S. Tanaka, E. Berenshtein, C. Sturm, A. Haverich, M. Chevion. **2001**. *J Thorac Cardiovasc Surg*. vol. 121(6):1169-78.
- [154] Mitochondria-targeted cytoprotective peptides for ischemia-reperfusion injury. H. H. Szeto. **2008**. *Antioxid Redox Signal*. vol. 10(3):601-19.
- [155] Mitochondria-targeted peptide prevents mitochondrial depolarization and apoptosis induced by tert-butyl hydroperoxide in neuronal cell lines. K. Zhao, G. Luo, S. Giannelli, H. H. Szeto. **2005**. *Biochem Pharmacol*. vol. 70(12):1796-806.
- [156] Do mitochondriotropic antioxidants prevent chlorinative stress-induced mitochondrial and cellular injury? M. Whiteman, J. P. E. Spencer, H. H. Szeto, J. S. Armstrong. **2008**. *Antioxid Redox Signal*. vol. 10(3):641-50.
- [157] Requirements for superoxide-dependent tyrosine hydroperoxide formation in peptides. C. C. Winterbourn, H. N. Parsons-Mair, S. Gebicki, J. M. Gebicki, M. J. Davies. **2004**. *Biochem J*. vol. 381(Pt 1):241-8.
- [158] First-in-class cardiolipin-protective compound as a therapeutic agent to restore mitochondrial bioenergetics. H. H. Szeto. **2014**. *Br J Pharmacol*. vol. 171(8):2029-50.
- [159] Targeting mitochondrial cardiolipin and the cytochrome c/cardiolipin complex to promote electron transport and optimize mitochondrial ATP synthesis. A. V. Birk, W. M. Chao, C. Bracken, J. D. Warren, H. H. Szeto. **2014**. *Br J Pharmacol*. vol. 171(8):2017-28.
- [160] Effect of ciclosporin on safety, lymphocyte kinetics and left ventricular remodelling in acute myocardial infarction. S. Cormack, A. Mohammed, P. Panahi, R. Das, A. J. Steel, T Chadwick, A. Bryant, M. Egred, K. Stellos, I. Spyridopoulos, CAPRI investigators. **2020**. *Br J Clin Pharmacol*. vol. 86(7):1387-1397.
- [161] Deferoxamine cardioplegia reduces superoxide radical production in human myocardium. G. Drossos, A. Lazou, P. Panagopoulos, S. Westaby. **1995**. *The Annals of Thoracic Surgery*. vol. 59(1):169-172.
- [162] Novel Mixed NOP/Opioid Receptor Peptide Agonists. S. Pacifico, V. Albanese, D. Illuminati, E. Marzola, M. Fabbri, F. Ferrari, V. A. D. Holanda, C. Sturaro, D. Malfacini, C. Ruzza, C. Trapella, D. Preti, E. Lo Cascio, A. Arcovito, S. Della Longa, M. Marangoni, D. Fattori, R. Nassini, G. Calò, R. Guerrini. **2021**. *J Med Chem*. vol. 64(10):6656-6669.
- [163] Full orthogonality between Dde and Fmoc: the direct synthesis of PNA--peptide conjugates. J. J. Díaz-Mochón, L. Bialy, M. Bradley. **2004**. *Org Lett*. vol. 6(7):1127-9.

6. PUBLICATIONS

Structure–Activity Relationship Studies on Oxazolo[3,4-*a*]pyrazine Derivatives Leading to the Discovery of a Novel Neuropeptide S Receptor Antagonist with Potent *In Vivo* ActivityValentina Albanese,[▽] Chiara Ruzza,[▽] Erika Marzola, Tatiana Bernardi, Martina Fabbri, Anna Fantinati, Claudio Trapella, Rainer K. Reinscheid, Federica Ferrari, Chiara Sturaro, Girolamo Calò, Giorgio Amendola, Sandro Cosconati,* Salvatore Pacifico,* Remo Guerrini, and Delia PretiCite This: <https://doi.org/10.1021/acs.jmedchem.0c02223>

Read Online

ACCESS |



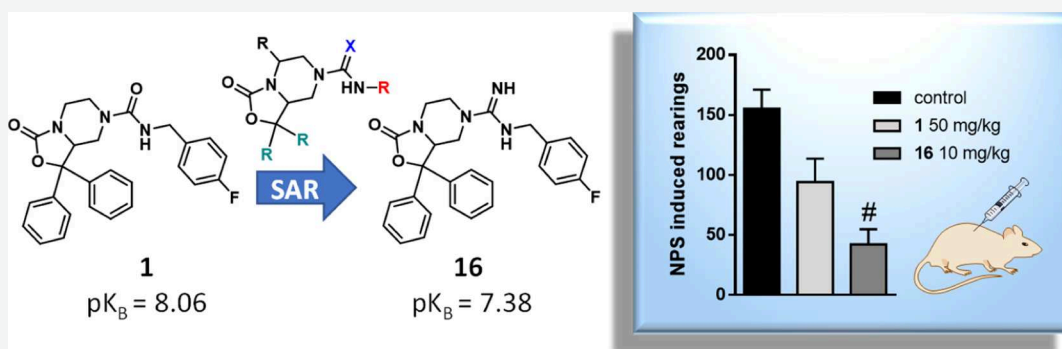
Metrics & More



Article Recommendations



Supporting Information



ABSTRACT: Neuropeptide S modulates important neurobiological functions including locomotion, anxiety, and drug abuse through interaction with its G protein-coupled receptor known as neuropeptide S receptor (NPSR). NPSR antagonists are potentially useful for the treatment of substance abuse disorders against which there is an urgent need for new effective therapeutic approaches. Potent NPSR antagonists *in vitro* have been discovered which, however, require further optimization of their *in vivo* pharmacological profile. This work describes a new series of NPSR antagonists of the oxazolo[3,4-*a*]pyrazine class. The guanidine derivative **16** exhibited nanomolar activity *in vitro* and 5-fold improved potency *in vivo* compared to **SHA-68**, a reference pharmacological tool in this field. Compound **16** can be considered a new tool for research studies on the translational potential of the NPSergic system. An in-depth molecular modeling investigation was also performed to gain new insights into the observed structure–activity relationships and provide an updated model of ligand/NPSR interactions.

INTRODUCTION

Neuropeptide S (NPS), identified in 2002 by a reverse pharmacology approach,¹ is the endogenous ligand of a previous orphan G protein-coupled receptor (GPCR), now named neuropeptide S receptor (NPSR). NPS is a 20 amino acid neuropeptide (primary sequence in humans: SFRNGVGTGMKKTSFQRAKS) highly conserved among different species, and it owes its name to the serine residue at the 1-position of the peptide sequence. NPSR shows a moderate homology with the other members of the GPCR family. The *in vitro* pharmacology of the human and mouse NPSR showed that NPS increases both intracellular calcium levels and cAMP accumulation with EC₅₀ values in the low nanomolar range. This indicates that NPSR can signal via both G_q and G_s pathways to increase cellular excitability.^{2,3} In the rodent brain, NPS is expressed only in few neurons in the perilocus coeruleus region. On the contrary, NPSR is widely expressed in several brain regions (i.e., hypothalamus,

endopiriform nucleus, amygdala, subiculum, cortex, and nuclei of the thalamic midline).^{4,5} *In vivo*, NPS has been shown to control several biological functions in rodents including stress, anxiety, social behavior, locomotor activity, wakefulness, food intake and gastrointestinal functions, memory processes, pain, and drug abuse.^{6,7} As far as the therapeutic potential of selective NPSR ligands is concerned, NPSR agonists may be useful as innovative anxiolytics devoid of sedative effects, analgesics, and nootropics. On the other hand, NPSR antagonists may be useful to treat substance abuse disorders against which there is an urgent need for the exploration of

Received: December 22, 2020

novel potential drug targets and for developing innovative therapeutic approaches.⁸

NPSR antagonists with potent *in vitro* activity have been developed in the last few years and a few compounds are currently in use as pharmacological tools.⁷ Among these, oxazolo[3,4-*a*]pyrazine derivatives have been first reported in 2005 by Takeda Pharmaceuticals,⁹ and **SHA-68** (**1**, Figure 1)

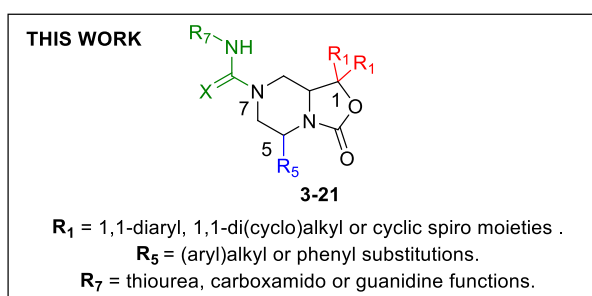
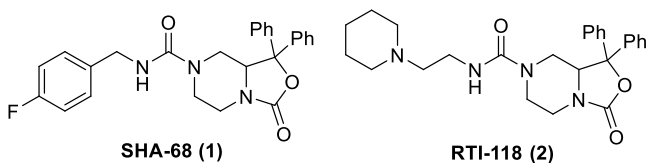


Figure 1. SAR extension performed in this work around the oxazolo[3,4-*a*]pyrazine nucleus of known NPSR antagonists **1** and **2**.

is the most representative member of this class.¹⁰ Compound **1** was shown to display nanomolar antagonist potency values (pA_2/pK_B) ranging from 7.28 to 8.16 toward the hNPSR-Asn¹⁰⁷ variant and from 7.55 to 8.03 toward the hNPSR-Ile¹⁰⁷ variant. Also, compound **1** exhibited high affinity for the hNPSR in radioligand-binding experiments ($pK_i = 7.32$) and high selectivity over several unrelated GPCRs.⁷

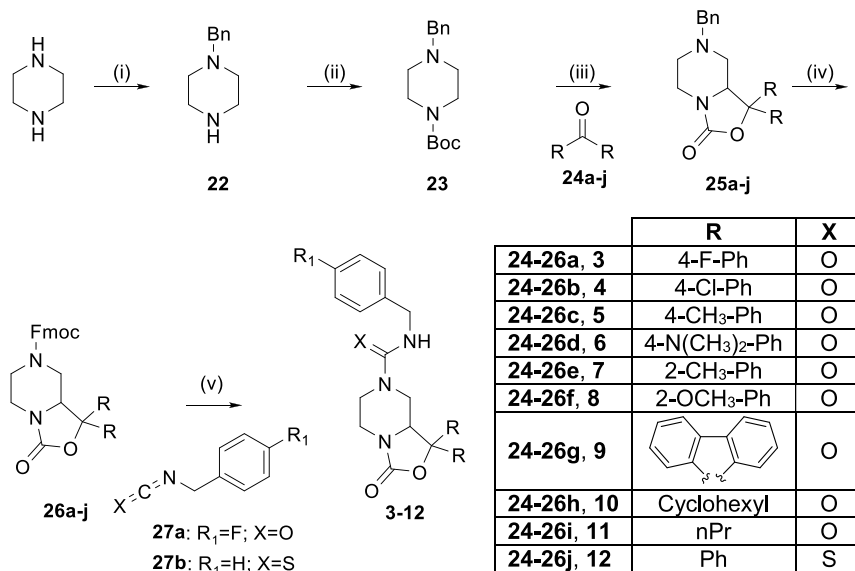
The *in vivo* pharmacological profile of **1** has been explored in various animal models in which considerably variable effectiveness was observed according to different assays,

which has been interpreted as due to suboptimal pharmacokinetic properties of the molecule.^{10–15} As a first attempt to overcome these limits, Hassler et al. developed the piperidine derivative **RTI-118** (**2**, Figure 1) that exhibited lower potency (hNPSR-Asn¹⁰⁷ $pA_2 = 6.31$; hNPSR-Ile¹⁰⁷ Ca^{2+} $pA_2 = 6.96$) *in vitro*¹⁶ but a slightly improved *in vivo* effectiveness in reducing cocaine self-administration and seeking behavior in rats; these results were ascribed to the higher water solubility of the molecule.¹⁷ Nonetheless, there is a generally recognized need for further optimizing the pharmacological profile and, above all, the drug-likeness properties of oxazolo[3,4-*a*]pyrazine ligands to obtain even more potent NPSR antagonist tools to be employed *in vivo* in preclinical studies. These ligands could be extremely useful for understanding the real therapeutic potential of the NPSergic system. This prompted us to extend the structure–activity relationship studies in this field investigating new and unexplored modifications of the bicyclic piperazine nucleus of compounds **1** and **2**. Thus, in this work, we describe the synthesis and the *in vitro* and *in vivo* biological evaluation of oxazolo[3,4-*a*]pyrazine derivatives resulting from a series of substitutions at the 1-, 5-, and 7-positions, as summarized in Figure 1. Moreover, molecular modeling studies were performed to gain new insights into the structure–activity relationships observed for the newly discovered NPSR ligands and provide an updated atomistic model of ligand/NPSR interactions.

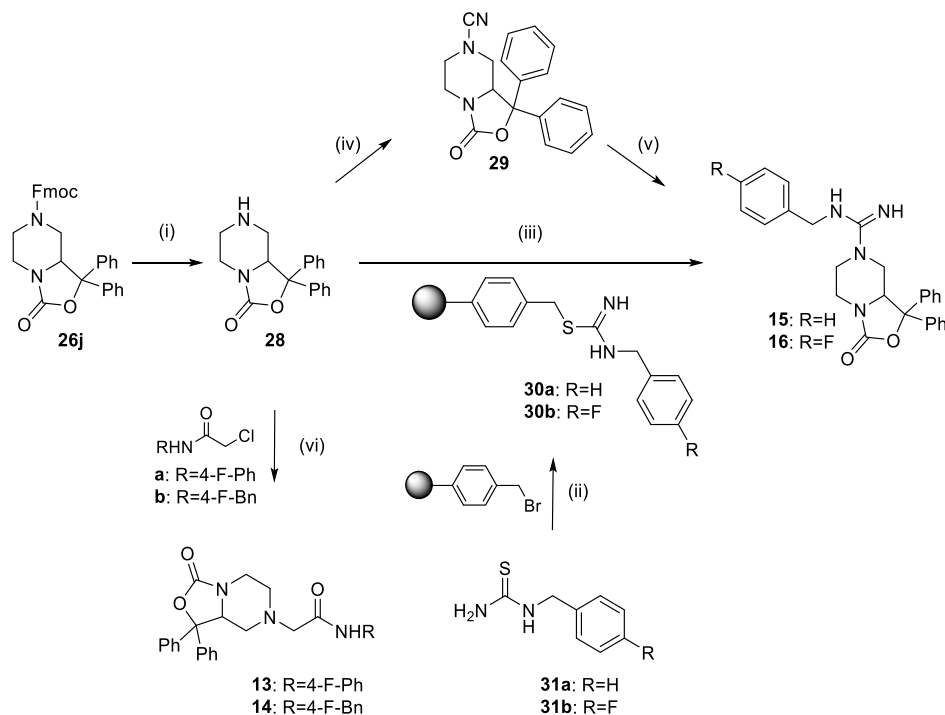
RESULTS AND DISCUSSION

Chemistry. As depicted in Scheme 1, *N*-Fmoc-oxazolo-piperazines with a general structure **26** were employed as synthetic precursors to obtain the final compounds **3–12** in analogy with the approach previously applied for the synthesis of **1** by Okamura et al.¹⁰ Specifically, intermediates **26** were obtained starting from unsubstituted piperazine that was first monoalkylated with benzyl-bromide and next Boc-protected on the second piperazine nitrogen to give compound **23**. Subsequently, the desired *N*-benzyl-protected oxazolo[3,4-

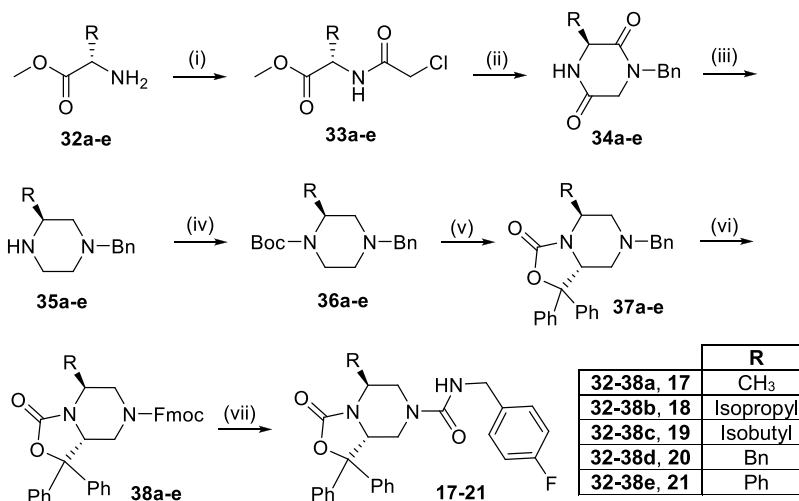
Scheme 1. Synthesis of Final Compounds **3–12**^a



^aReagents and conditions: (i) BnBr, EtOH, 75 °C, 5 h; (ii) Boc₂O, DMAP, tetraethylammonium, CH₂Cl₂, rt, 0.5 h; (iii) *sec*-BuLi, TMEDA, THF, –78 °C, 6 h; (iv) FmocCl, MeCN, 90 °C, 5 h; (v) DBU, THF, rt, 2 h.

Scheme 2. Synthesis of Final Compounds 13–16^a

^aReagents and conditions: (i) DBU, THF, rt, 2 h; (ii) CH₂Cl₂–DMF (2:1), 50 °C, 4 h; (iii) HgCl₂, CH₃CN, 90 °C, 24 h; (iv) BrCN, CH₂Cl₂, NaHCO₃, H₂O, 30 min at 0 °C, 24 h; (v) benzyl amine or 4-fluorobenzylamine, *p*-TsOH, DMSO, 60 °C, 18 h; (vi) K₂CO₃, CH₃CN, 90 °C, 4 h.

Scheme 3. Synthesis of Final Compounds 17–21^a

^aReagents and conditions: (i) NaHCO₃, chloroacetyl chloride, toluene, 0 °C to rt, overnight; (ii) Et₃N, benzylamine, dioxane, reflux, 20 h; (iii) LiAlH₄, THF, reflux, 3 h; (iv) Boc₂O, THF, 0 °C to rt, 1 h; (v) benzophenone, *sec*-BuLi, TMEDA, THF, –78 °C, 3 h; (vi) FmocCl, MeCN, 90 °C, 5 h and then rt, 18 h; (vii) 4-fluorobenzyl isocyanate, DBU, THF, rt, 2 h.

a]pyrazines **25a–j** were obtained through an ortho-lithiation reaction, in the presence of *sec*-butyllithium (*sec*-BuLi) as the base and various symmetric aromatic/aliphatic ketones (**24a–j**) as electrophiles. The benzyl function was next replaced with an Fmoc-group by treatment with FmocCl and finally, in order to achieve compounds **3–11**, **26a–i** were reacted with 4-F-benzyl-isocyanate, while compound **12** was obtained from **26j** by treatment with benzyl isothiocyanate.

The amide derivatives **13–14** and the guanidine analogues **15–16** were synthesized according to Scheme 2 starting from **26j** that was first deprotected by treatment with 1,8-

diazabicyclo[5.4.0]undec-7-ene (DBU). The *N*-alkylation of **28** with 2-chloro-*N*-(4-fluorophenyl)acetamide or 2-chloro-*N*-(4-fluorobenzyl)acetamide produced the final compounds **13** and **14**, respectively. In order to obtain the guanidine derivatives **15** and **16**, we explored two different synthetic strategies. The first approach, developed in the liquid phase, involved the reaction of **28** with cyanogen bromide, giving the key intermediate **29**. Then, the addition of benzylamine or 4-fluorobenzylamine in the presence of *p*-toluenesulfonic acid (*p*-TsOH) provided the desired final products.

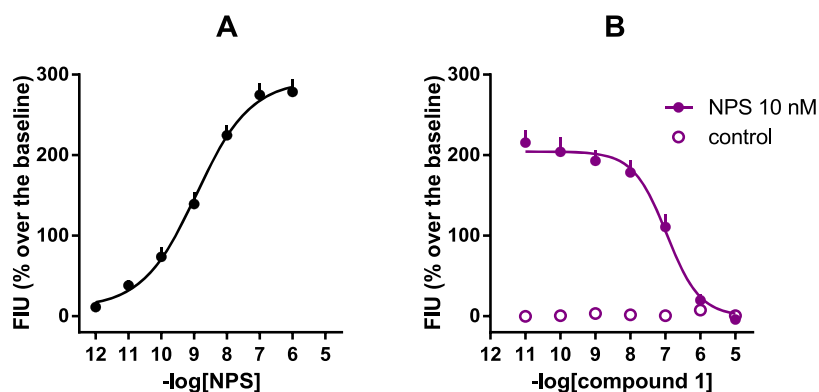


Figure 2. Calcium mobilization assay performed on HEK293_{mNPSR} cells. Concentration–response curve to NPS [panel (A)] and inhibition–response curves to **1** against the stimulatory effect of 10 nM NPS [panel (B)]. Data are mean \pm SEM of at least five separate experiments made in duplicate.

Table 1. *In Vitro* Pharmacological Activity of Compounds **1**, **3**–**21** as NPSR Antagonists^a

3-11			12-16			17-21		
	R	pK _B (CL _{95%})		R	pK _B (CL _{95%})		R	pK _B (CL _{95%})
1	Ph	8.06 (7.79–8.32)	12		7.35 (6.85–7.85)	13		Inactive up to 10 μ M
3	4-F-Ph	7.58 (6.71–8.45)	14		6.33 (5.76–6.90)	15		7.21 (6.40–8.02)
4	4-Cl-Ph	6.61 (6.41–6.81)	16		7.38 (6.94–7.82)	17	CH ₃	6.96 (6.53–7.39)
5	4-CH ₃ -Ph	6.51 (6.15–6.87)	18	Isopropyl	7.03 (6.53–7.53)	19	Isobutyl	6.74 (6.05–7.42)
6	4-N(CH ₃) ₂ -Ph	Inactive up to 10 μ M	20	Bn	6.62 (5.96–7.28)	21	Ph	7.82 (7.21–8.43)
7	2-CH ₃ -Ph	6.49 (5.88–7.10)						
8	2-OCH ₃ -Ph	Inactive up to 10 μ M						
9		Inactive up to 10 μ M						
10	Cyclohexyl	6.33 (6.17–6.49)						
11	CH ₂ CH ₂ CH ₃	Inactive up to 10 μ M						

^aCalcium mobilization assay performed in HEK293_{mNPSR} cells. Data are the mean of five separate experiments made in duplicate.

The second pathway resulted from the optimization of a known solid-phase approach.¹⁸ In this case, a bromomethyl polymeric resin was functionalized with 1-(4-fluorobenzyl)-thiourea or 1-(benzyl)thiourea affording **30a–b**. Subsequently, the loaded resin was reacted with **28** in the presence of HgCl₂ to produce the desired guanidine derivatives in good yields.

Finally, compounds **17–21** were prepared as depicted in **Scheme 3** starting from five different commercially available L-amino acid methyl esters (**32a–e**). Specifically, the piperazine-

diones **34a–e** were obtained in two simple steps involving a first amino acid acylation with chloroacetyl chloride, followed by cyclization with benzylamine.¹⁹ The subsequent reduction with LiAlH₄ gave **35a–e** that were then protected with di-*tert*-butyl dicarbonate (Boc₂O).²⁰ The resulting orthogonally protected piperazines **36a–e** were employed in the ortho-lithiation reaction to give the benzyl derivatives **37a–e**, followed by treatment with FmocCl and the final addition reaction with 4-fluorobenzyl isocyanate as described above.

The ortho-lithiation step is of key importance for the stereochemical course of the synthetic approach leading to the final compounds 17–21. This reaction takes advantage of the defined stereochemistry at C-2 of intermediates 36 that is imposed by the choice of the starting amino acid as demonstrated in the literature for analogous piperazine systems obtained through the same strategy.²¹ The spatial orientation of the substituents around the asymmetric C-8a, generated in the bicyclic derivatives 37 during the ortho-lithiation reaction, was driven by the absolute configuration previously introduced at C-2. A single diastereoisomer was isolated in all cases in which an antirelative stereochemistry between the substituent at the C-5 and the oxazole ring fused at C-8a was expected according to previous studies²¹ and as confirmed by NOE spectroscopy performed on the reference compound 17 (Figures S1 and S2). In this experiment, the irradiation of the methyl protons at the 5-position produced an important enhancement of the signal of the proton at the C-8a position which is in accordance with a syn relationship. Thus, the absolute (5*S*,8*aR*)-configuration was assigned to 17 and to the final compounds 18–21, the latter obtained from α -amino acid with even more hindered side chains. The maintenance of a significant *in vitro* activity of these derivatives would indirectly confirm that C-8a would assume the absolute configuration of the eutomer of 1 that has been previously identified following the separation of its enantiomers.²² According to this study, the interaction of 1 with the human NPSR would be markedly enantioselective with the *R*-isomer showing a pK_B value of 8.28 (hNPSR-N¹⁰⁷) in calcium mobilization experiments, while the *S*-enantiomer would display a considerably reduced potency ($pK_B < 6$).

In Vitro Structure–Activity Relationships. In the calcium mobilization assay, NPS increased intracellular calcium levels in a concentration-dependent manner with pEC_{50} and E_{max} values of 8.95 and $287 \pm 26\%$ over the basal values, respectively. Inhibition response curves to 1 (0.1 nM to 10 μ M), used as an internal reference, were performed against the stimulatory effect of 10 nM NPS, approximately corresponding to NPS EC_{80} . As shown in Figure 2, compound 1 concentration-dependently inhibited 10 nM NPS stimulatory effects with a pK_B value of 8.12. These results agree with previously reported data.¹¹ The pharmacological activity of compounds 3–21 was evaluated under the same experimental conditions, and the corresponding results are reported in Table 1.

None of the novel compounds stimulated calcium mobilization up to 10 μ M. On the other hand, the substitution or the replacement of the 1,1-diphenyl moiety of 1, such as in compounds 3–11, significantly affected the antagonist potency although to a different extent. In particular, the para-substitution of both the aromatic rings at the 1-position was slightly tolerated only in the case of the 4-fluoro derivative 3 which was only 3-fold less potent than 1, while a progressive reduction of potency was observed by increasing the steric hindrance of the para-substituents. For example, the bulky dimethylamino groups of compound 6 resulted in a complete loss of activity ($K_B > 10 \mu$ M). These data suggest that the phenyl rings at the 1-position could occupy the NPSR binding pocket in a region with highly stringent steric requirements.

Our results indicated that also a proper spatial orientation of the geminal phenyl groups relative to the oxazolidinone ring seems to be of particular importance to promote activity. Indeed, the ortho-substitution of the 1,1-diaryl moiety such as

in compounds 7 and 8 should induce a conformational distortion with respect to the nonsubstituted 1, determining a marked or total loss of potency. This observation was further confirmed by the inactivity of compound 9 in which the 1,1-phenyl rings were forced into a coplanar arrangement due to their inclusion in the spiro-fluorene fusion.

The aromaticity of 1,1-substituents seems to be important as well since the 1,1-dicyclohexyl derivative 10 was more than 50-fold less potent than 1. Even more unfavorable was the replacement of the diaryl template with linear propyl chains (compound 11, $K_B > 10 \mu$ M).

In compounds 12–16, we explored the effect of a few modifications at the 7-position of the oxazo[3,4-*a*]pyrazine core that has not been explored before.²³ In particular, we introduced side chains containing thiourea (12), *N*-substituted acetamide (13, 14) and guanidine (15, 16) functions. In this subset of molecules, compounds 13–16 have been specifically designed to modulate the hydrophilic/lipophilic balance of 1, which might be important for its *in vivo* effectiveness as suggested in different studies.^{10,11} In particular, it has been demonstrated that 1, at the high dose of 50 mg/kg, can only partially counteract NPS effects, with different levels of efficacy, depending on the assay used.^{10–15} These findings have been hypothetically attributed to suboptimal physicochemical properties of the compound, in particular, its high lipophilicity.⁷ Thus, in a first attempt to overcome these limits, the acetamide derivatives 13 and 14 have been synthesized as possible bioisosteres of 1 in which a methylene spacer was interposed between the piperazine nitrogen and the carbonyl function of the 7-side chain. The modification was conceived to increase the basicity of the piperazine nitrogen thus opening the possibility to obtain hydrochloride salts with improved water solubility. Nonetheless, the compounds were shown to display very low (14, $pK_B = 6.33$) or null activity (13, $K_B > 10 \mu$ M) in the calcium mobilization assay. However, the partial recovery of activity of compound 14, in which the 4-F phenyl moiety is not directly linked to the amide nitrogen, suggested that also the conformational freedom of this pharmacophoric portion may be important for the interaction with NPSR.

In compounds 15 and 16, we replaced the urea moiety of 1 with a guanidine function as an alternative strategy to obtain NPSR antagonists with improved hydrophilicity. The fluorinated derivative 16 was conceived as a close analogue of 1 bearing an NH-group in place of the urea oxygen atom. This modification does not interfere with the ability of the ligand to establish polar interactions with the receptor. Of note, compounds incorporating a guanidine moiety have aroused an increasing interest for their potential in the development of novel drugs due to the ability of the guanidinium group to form strong noncovalent interactions and to provide obvious advantages in terms of hydrophilicity.^{24–26} Compound 16 displayed low nanomolar potency in antagonizing the stimulatory activity of NPS with a pK_B value of 7.38. The nonfluorinated guanidine derivative 15 was slightly less potent ($pK_B = 7.21$) indicating some importance of the fluorine atom at the para position of the terminal benzyl moiety.

Finally, we introduced different substitutions at the 5-position of the oxazo[3,4-*a*]pyrazine core whose effect on NPSR modulation has not been explored before. To this aim, we developed a highly accessible diastereoselective synthesis that provided compounds 17–21 in which the 5-position was functionalized with the side chains of a series of *L*-amino acids employed as the starting material. The introduction of a $-CH_3$

(compound 17) or an isopropyl chain (compound 18) determined about a 10-fold reduction of potency if compared to 1. Even more detrimental was the introduction of a bulkier branched alkyl moiety (19) or a benzyl group (20). In contrast, the L-phenylglycine derivative 21 showed a recovery in activity becoming the most active compound of the newly reported series.

These data indicated that the 5-position tolerates substitutions with hydrophobic chemical groups of different size generating derivatives with 2 (21) to 30 (compound 20)—fold reduction of potency. Intriguingly, in the latter compounds, a subtle chemical modification such as the introduction of a methylene spacer between C5 and the phenyl ring promoted a consistent reduction of bioactivity. Given these data, we cannot exclude that the C5 phenyl ring of 21 might be recognized by a previously unexplored region of the NPSR binding pocket.

To confirm and better define the antagonist properties of compounds 16 and 21, the concentration–response curve of NPS has been reassessed in the absence and presence of 100 nM of 1, 16, and 21 (Figure 3). 1, 16, and 21 shifted the

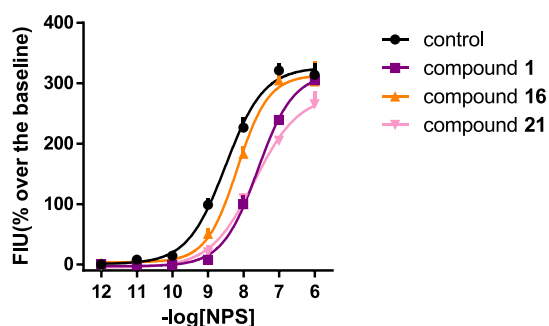


Figure 3. Calcium mobilization assay performed on HEK293_{mNPSR} cells. Concentration–response curve to NPS in the absence and in the presence of 100 nM of 1, 16, and 21. Data are mean \pm SEM of at least five separate experiments made in duplicate.

concentration–response curve of NPS to the right without changing its maximal effects. The following pA_2 values have been derived from these experiments: 7.82 (7.40–8.24) for 1; 7.10 (6.65–7.55) for compound 16; and 7.59 (7.08–8.10) for compound 21. Thus, the rank order of potency of these NPSR antagonists is 1 > 21 > 16. These results are superimposable to those obtained in inhibition experiments.

Molecular Modeling Studies. To gain major insights into the reasons for the structure–activity relationships (SARs) observed for the newly discovered NPSR ligands, molecular modeling studies were attempted. So far, the three-dimensional (3D) structure of the target receptor has not been determined so that homology-modeling techniques had to be employed to first construct a viable model of NPSR in its inactive state. The available SAR data were obtained from human HEK293 cells expressing the mouse NPSR (mNPSR). On the other hand, the sequence alignment between the human (hNPSR) and mNPSR revealed that the two proteins share 89.22% sequence identity with all the differences residing in the N-terminal region distant from the putative ligand-binding site. Thus, considering the high structural homology of NPSR across the two species, we decided to model the pharmacologically relevant hNPSR in its I107 variant in the present work. In 2010, Dal Ben et al.²⁷ published the first model of the two NPSR variants, namely, NPSR-N107 and -I107. In this seminal work, the authors modeled the NPSR receptors starting from the X-ray crystal structure of bovine rhodopsin.²⁸ The choice of using this latter structure as a template was dictated by preliminary modeling studies indicating that the NPSR extracellular loop 2 (ECL2) had a propensity to adopt a β -sheet conformation which was partially present in the bovine rhodopsin structure rather than in the structures of the human β_1 , β_2 adrenergic and adenosine A_{2A} receptors that were available at that time. Since then, more than 340 structures of GPCR have been deposited in the protein data bank (PDB) thereby allowing for a re-evaluation of the optimal template to employ in the *in silico* construction of the NPSR receptor variants. Thus, the hNPSR sequence (Uniprot entry code Q6WSP4) was used to interrogate the PDB and select the solved X-ray structures sharing the highest homology with the target structures. In this analysis, we decided to retain all the structures that shared with NPSR a sequence identity higher than 20%, a sequence coverage higher than 70%, and that were crystallized in their inactive states (i.e., bound to an antagonist ligand). These criteria allowed selecting 7 human GPCR structures in which, interestingly, 6 of them turned out to be receptors for endogenous peptides and 5 of these feature a twisted β -hairpin in the ECL2 region (Table S1). Indeed, the β -hairpin motif is usually found in the ECL2 of peptide-activated GPCRs such as Neuropeptide Y Y1 receptor,²⁹ orexin receptor type 1 (OX1R),³⁰ chemokine receptor type 4

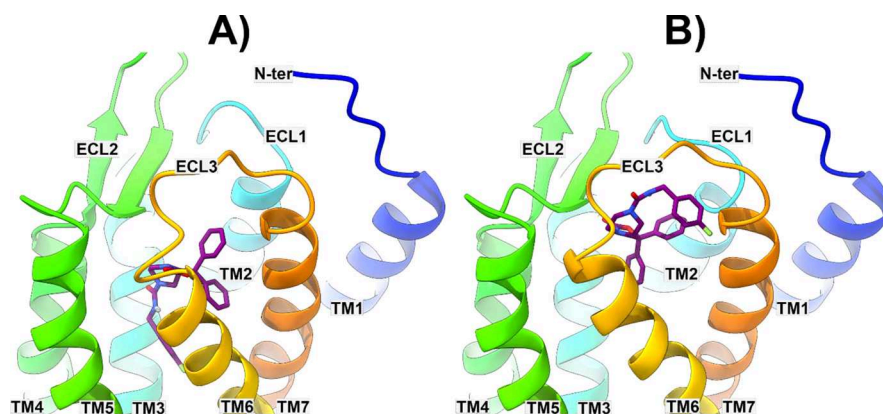


Figure 4. Energy-minimized docked poses of compound 1 in BM1 and BM2 (panels A and B, respectively) in the model of NPSR constructed starting from the human neuropeptide Y Y1 receptor (hNPY1R, PDB code 5ZBH).²⁹ 1 and the protein are represented as violet sticks and multicolored ribbons, respectively.

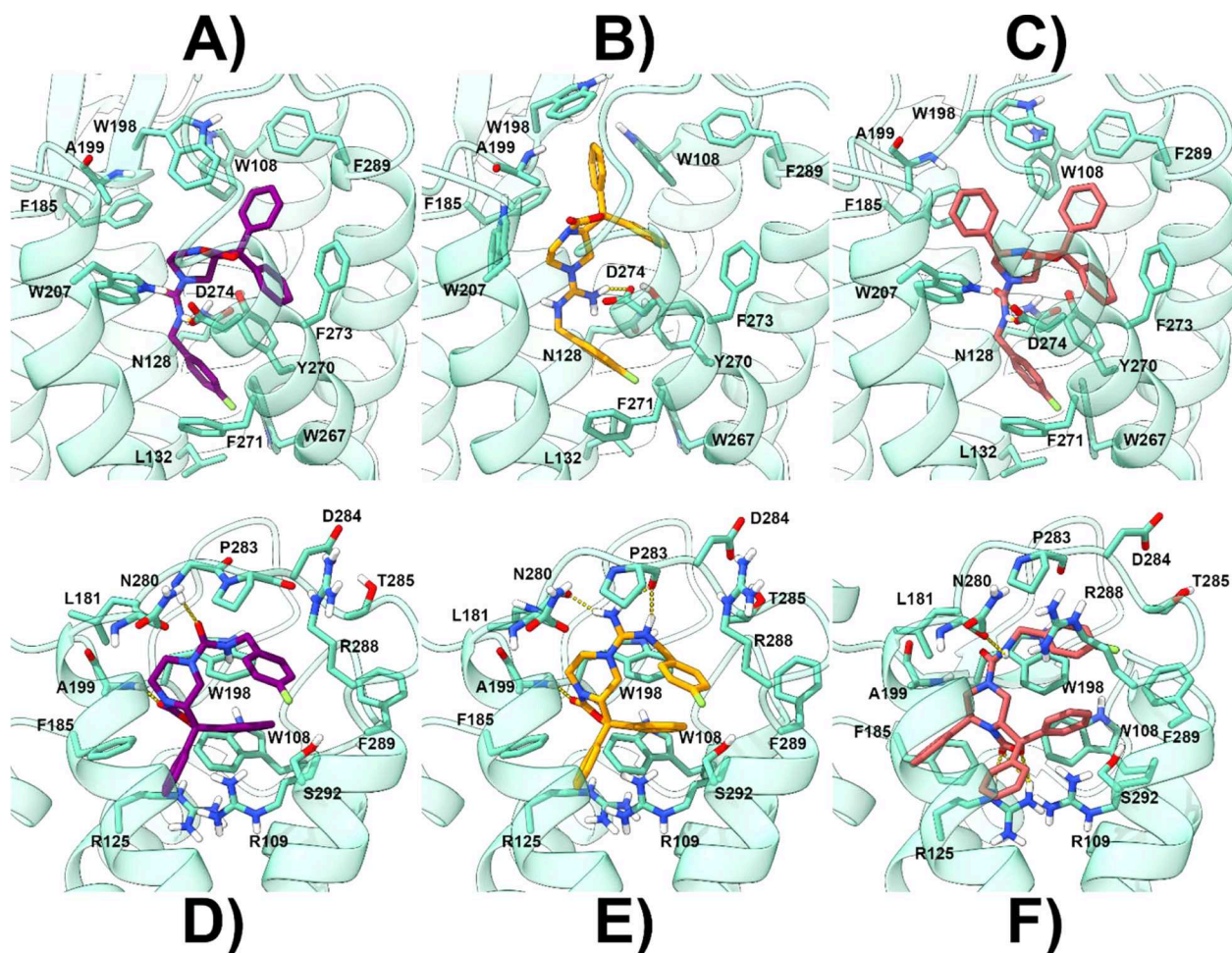


Figure 5. Energy-minimized docked poses of compound **1** [panel (A) for BM1 and (D) for BM2], **16** [panel (B) for BM1 and (E) for BM2], and **21** [panel (C) for BM1 and (F) for BM2] in the model of NPSR constructed starting from the human neuropeptide Y Y1 receptor (hNPY1R, PDB code 5ZBH).²⁹ **1**, **16**, and **21** are represented as violet, orange, and red sticks, respectively. The protein is represented as cyan ribbons and sticks. H-bonds are represented as dashed yellow lines.

(CXCR4),³¹ delta,³² and kappa³³ opioid receptors, protease-activated receptor 1 (PAR1),³⁴ neurotensin receptor 1 (NTR1),³⁵ endothelin ETB receptor,³⁶ and angiotensin receptors AT1³⁷ and AT2.³⁸ Unfortunately, for one of the selected 7 templates (Table S1), the human CC chemokine receptor type 9 (CCR9), ECL2 was unresolved; thus, this template structure was not considered further. Subsequently, the primary sequences of the remaining six GPCRs were all pairwise aligned to the one of the hNPSR-I107 variant, and the phylogenetic tree was calculated (see Figures S3–S9). Then, these templates were all used to construct six models of hNPSR, one for each template, using the Prime software within the Schrodinger's Maestro suite. The constructed models were all used to perform docking calculations of all the newly identified analogues employing the Glide program. The results of these simulations were then analyzed in light of the available SAR data. In this step, we first verified whether Glide was able to find a viable binding pose for each active compound reported in Table 1 (namely, **1**, **3–5**, **7**, **10**, **12**, and **14–21**) in each of the NPSR models constructed employing the aforementioned 6 template structures. This first analysis was instrumental for the selection of the best model structure that was able to host all the newly discovered NPSR ligands. In particular, the NPSR model constructed starting from the human neuropeptide Y Y1 receptor (hNPY1R, PDB code

5ZBH)²⁹ was the only one able to fulfill the above-mentioned selection criteria. Subsequently, we decided to analyze the docking results achieved for the most potent antagonists **16** and **21** as well as the control compound **1**. Interestingly, for all three ligands, Glide was able to suggest two possible binding poses (i.e. featuring comparable docking scores) in which the ligand pendant benzyl substituent is alternatively pointing downward [inside the transmembrane (TM) bundle] or upward (toward the NPSR extracellular region). In this work, the two alternative docked positions will be referred to as binding mode 1 (BM1) and 2 (BM2), respectively (Figure 4).

In BM1, the 1,1-diphenyl moiety of **1** is pointing toward TM7 and TM2 and establishes several π – π interactions with aromatic residues present in the outer region of NPSR (W108, W198, F273, and F289) (Figures 4A and 5A). The limited extension of the cleft lodging this moiety should explain why incrementing its steric hindrance has a detrimental effect on the antagonist potency of its analogues (compounds **3–8**). Moreover, the nature of the established ligand–protein interactions (charge transfer contacts) as well as the relative position of the two phenyl rings (not coplanar) explains why compounds **9–11** are less active or devoid of an evident antagonist potency. The **1** bicyclic piperazine core orients its pendant benzylamide chain inside the TM bundle between

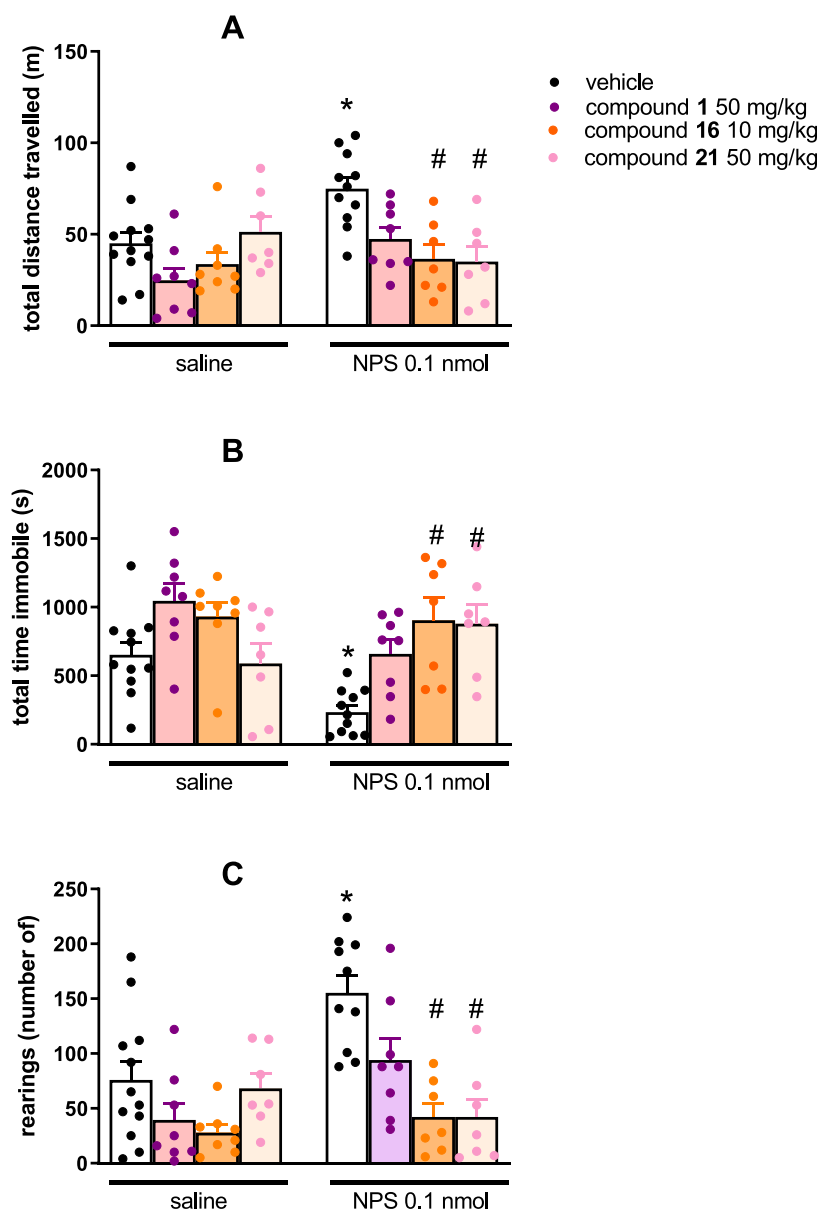


Figure 6. Effects of NPS, **1**, **16**, and **21** on mouse locomotor activity. The cumulative effects exerted on distance traveled are shown in panel (A), while the total time immobile and number of rearings over the 30 min observation period are shown in panels (B,C), respectively. Data are mean \pm SEM of four separate experiments (vehicle + saline, 12 mice; **1** + saline, 8 mice; **16** + saline, 8 mice; **21** + saline, 7 mice; vehicle + NPS, 11 mice; **1** + NPS, 8 mice; **16** + NPS, 7 mice; and **21** + NPS, 7 mice). The two-way ANOVA NPS \times antagonist revealed for the total distance traveled, an effect of NPS $F(1,59) = 6.63$ and of the interaction NPS \times antagonist $F(3,59) = 4.48$; for the immobility time, an effect of NPS $F(1,59) = 8.09$ and of the interaction NPS \times antagonist $F(3,59) = 4.26$; for the number of rearings, an effect of NPS $F(1,59) = 7.35$, of antagonist $F(3,59) = 10.65$, and of the interaction NPS \times antagonist $F(3,59) = 4.32$. * $p < 0.05$ vs saline, # $p < 0.05$ vs vehicle according to Bonferroni's test for multiple comparisons.

TM3 and TM6 where its NH forms a charged-reinforced H-bond with D274 and the terminal fluorophenyl ring is lodged in a well-defined lipophilic gorge establishing π - π interactions, reinforced by the electron-withdrawing effect of the fluorine atom, with W267, Y270, F271, and van der Waal contacts with L132 (Figure 5A). The tight interactions established by the benzamide chain in this receptor region would explain why modifications in this position result in a reduction (compound **14**) or abrogation (compound **13**) of the antagonist potency thereby indicating a limited tolerance for 7-position substituents.²³

Almost the same binding orientation was also found for **16** with all the aforementioned interactions being maintained

(Figure 5B). Here, the protonated guanidine group is now engaged in an ionic interaction with the D274 side chain. **21** is also predicted to adopt BM1 where the presence of the additional phenyl ring on the core structure allows to form supplementary charge-transfer and lipophilic interactions with F185, W198, A199, and W207 (Figure 5C). These contacts should explain why the substitution of the phenyl ring with alkyl or benzyl chains (compounds **17**–**20**) still allows observing an antagonist activity at NPSR, although resulting in less potent antagonists if compared to **21**.

In BM2, the 1,1-diphenyl moiety of **1** is predicted to point toward the inner part of NPSR making contact with TM2, TM6, and TM7 (Figure 4B). In this position, this moiety

established π - π and cation- π contacts with W108 and R109, respectively (Figure 5D). The carbonyl oxygen of the bicyclic piperazine scaffold accepts an H-bond from the A199 backbone NH while the pendant fluorobenzamide chain laced beneath ECL3 (Figure 4B) in a cleft lined by D284, T285, R288, F289, and S292. Almost the same interaction pattern is also predicted for **16** in BM2 (Figure 5E), and the presence of the protonated guanidine group allows the ligands to establish charge-reinforced H-bonds with N280 and P283 backbone COs as well as a cation- π interaction with W198. **21** recapitulates the same interactions established by **1** in BM2 (Figure 5F) and takes advantage of its additional phenyl ring in position 7 of the core scaffold to establish a π - π interaction with F185. Also in this case, BM2 would match the SAR data acquired in this manuscript as well as the ones already present in the literature.²³

The binary complexes calculated using the docking program for **1**, **16**, and **21** in both BM1 and BM2 were then subjected to 100 ns molecular dynamics (MD) simulations with Desmond³⁹ to refine the predicted binding geometries. Most importantly, given the dichotomy of binding modes predicted for these ligands, results of MD simulations could suggest a preferential binding orientation for each ligand. Analysis of the 6 MD simulations was attained through the Desmond SID tool which allowed us to analyze the ligand-receptor interactions during the MD trajectory. Attention was given to the ligand root-mean-square fluctuation (RMSF) (Figures S10-S15) and the stability of the ligand-residue interactions (Figures S16-S27).

The ligand RMSF was useful for characterizing changes in the ligand atom positions during the MD. Analysis of this parameter demonstrated that in BM1 and BM2, the three ligands display a different degree of flexibility. In particular, regardless of the adopted binding mode, the pendant fluorobenzamide chain is the most flexible part of the molecule with BM1 being more stable than BM2 (see Figures S10-S15). In the latter binding position, the fluorobenzamide moiety rapidly loses its interactions with the residues belonging to ECL3 to point toward the external part of the receptor without taking stable contacts with any NPSR residue. This is further outlined by plotting the most frequent (>30%) ligand-protein contacts (Figures S16-S27) showing that for the three ligands in BM2, the benzyl chain is always solvent exposed. On the contrary, in BM1, the same portion remains anchored to the receptor although experiencing a partial relocation during the MD. All in all, MD results would suggest that only in BM1, the fluorobenzamide chain would play a role in the ligand-receptor recognition as underscored by the experimental SAR data²³ available for this ligand moiety, thereby suggesting that **1**, **16**, and **21** should adopt this binding orientation. Plotting of the ligand-receptor interactions also shows that while binding of **1** is mainly governed by hydrophobic and charge-transfer contacts with the receptor, **16** is stably anchored to NPSR also through the polar interaction with D274 while **21** finds additional contacts with W207 and F185.

In Vivo Characterization in the Mouse Locomotor Activity Test. Among the synthesized molecules, **16** and **21** have been selected to be tested *in vivo* in the mouse locomotor activity assay. As shown in Figure 6 and in line with previous findings,^{11,40-42} NPS injected by the i.c.v. route at 0.1 nmol concentration was able to stimulate mouse locomotor activity by increasing the distance traveled (panel A) and the number

of rearings (panel C) and reducing the immobility time (panel B) with statistically significant effects. **1** (50 mg/kg) did not significantly modify mice locomotor activity and only partially counteracted NPS-induced stimulant effects, confirming previous studies.^{10,11} All mice treated with 50 mg/kg of **16** displayed an important reduction of locomotor activity (data not shown); thus, in the present study, the 10 mg/kg dose was used for this compound. The doses of 10 mg/kg for **16** and 50 mg/kg for **21** did not elicit by themselves statistically significant effects on mouse locomotor activity (Figure 6).

This result is in line with previous studies performed with different NPSR antagonists^{10,11,41} and with the lack of locomotor phenotype of NPSR knockout mice,⁴³⁻⁴⁵ collectively suggesting that the endogenous NPS does not control mouse locomotor activity in the open field. When administered 30 min before NPS, both **16** and **21** were able to completely block the stimulant effects of the peptide. Compound **21** was *in vivo* slightly more effective than **1** when injected intraperitoneally (ip) at the same dose (50 mg/kg). Compound **16**, despite its lower potency *in vitro*, was at least 5-fold more potent than **1** *in vivo*. It must be remarked that compound **2** (see the Introduction section) was shown to exert a significant blockade of NPS-induced locomotor activity at an i.p. dose of 50 mg/kg, thus being equipotent to the parental compound **1**.¹⁶ Of note, the ability of both **16** and **21** to completely block the stimulant NPS effects confirms previous studies demonstrating that the stimulant NPS effects are selectively due to the activation of the NPSR receptor (see Tables 1 and 2 of the recent review by Ruzza et al.).⁷ It is worth noting that at the higher doses tested, compound **1** was able to only partially block NPS effects. This may somewhat limit the usefulness of compound **1** as a research tool to explore the biological actions modulated by the endogenous NPS. Both compounds **16** and **21** seem to overcome this limitation; in fact, at doses statistically inactive, they were able to fully block NPS stimulant effects. This feature, that is, complete NPSR occupation and blockage, makes these compounds essential pharmacological tools for investigating those conditions in which the endogenous NPS/NPSR signaling is activated, for example, cocaine/alcohol seeking and relapse.⁴⁶⁻⁴⁸ On the other hand, in proposing compound **16** as an innovative research tool, we should also underline that selectivity concerns must be taken into account. In fact, at the high dose of 50 mg/kg, **16** strongly reduces mouse locomotor activity. This is most probably an off-target effect since NPSR selective peptide antagonists did not modify mouse locomotion at doses able to completely block NPS stimulatory effects,⁴¹ and NPSR(-/-) mice did not display a locomotor phenotype in this assay.⁴³ Thus, the high potency and antagonist effectiveness of compound **16** is associated with somewhat limited selectivity of action. Further studies, for example, CEREP receptorogram, are needed to eventually identify the mechanisms involved in the putative off-target effects of compound **16** at high doses. Based on these considerations, we certainly recommend the use of compound **16** but with special caution in selecting the range of doses to be used for NPSR physiopathological investigations. The *in vivo* action of **21** reflects the *in vitro* potency of the compound that was very similar to that of the reference tool **1**. On the other hand, the improved *in vivo* antagonist effectiveness of **16**, deriving from the bioisosteric replacement of the urea function of **1** with a guanidine moiety, may be attributed to its relatively higher hydrophilic properties that could compensate for the

slight loss of *in vitro* potency. Lipophilicity is indeed considered one of the most important physicochemical properties to be addressed for drug design purposes. Typically, highly hydrophilic compounds suffer from poor membrane permeability and faster renal clearance. On the other hand, water solubility and metabolism are more likely to be compromised at high lipophilicity values.⁴⁹ Noteworthy, the optimum region of lipophilicity for candidate drug molecules has been generally suggested to lie within a narrow range of log $D_{7.4}$ that has been approximately determined between 1 and 3.⁴⁹ Thus, the improved *in vivo* potency of **16** (Clog $P = 3.43 \pm 0.89$, ACDLabs; Clog $D_{7.4} = 1.87$, ChemAxon predictor) with respect to the known NPSR antagonist **1** (Clog $P = 4.32 \pm 0.86$, ACDLabs; Clog $D_{7.4} = 4.05$, ChemAxon predictor) can be reasonably justified in light of the optimization of lipophilicity parameters that are closer to the recommended values. This could also account for the lower *in vivo* potency of compound **21** (Clog $P = 6.18 \pm 0.87$, ACDLabs; Clog $D_{7.4} = 5.83$, ChemAxon predictor) despite its higher *in vitro* activity. However, we would like to underline the fact that these hypotheses are only supported by theoretical calculations; firm conclusions on this issue can be drawn only after performing experiments investigating the pharmacokinetic profile of compound **16** eventually in comparison with compounds **1** and **21**.

CONCLUSIONS

The therapeutic potential of selective NPSR ligands in psychiatric disorders is supported by a series of preclinical studies.⁷ In particular, NPSR antagonists were shown to reduce cocaine/alcohol seeking and relapse in animal models, and this makes them potentially useful for treating drug addiction. Patients suffering from such a condition typically show resistance to the very few treatments currently available. Thus, the identification of innovative drugs able to ameliorate these conditions, which are essentially untreated, is still urgent. Additionally, it can be speculated that NPSR antagonists may be useful also for the treatment of other types of drug abuse, although no preclinical data are currently available. NPSR antagonists may open new perspectives for addressing this unmet clinical need. Moreover, NPSR antagonists still represent important research tools to investigate the neurobiology of the NPS/NPSR system and to study those biological functions for which the NPSergic tone is important. However, even though *in vitro* potent NPSR antagonists have been reported, NPSR antagonists with a good *in vivo* pharmacological profile are still missing. This is probably due to pharmacokinetic issues and represents an undeniable limit for preclinical studies on the NPSergic system aimed at translating results from basic pharmacology into clinical utility. In the present study, the *in vitro* pharmacological activity of a new series of oxazolo[3,4-*a*]pyrazines as NPSR antagonists was investigated and a molecular-modeling study helped to rationalize the resulting SARs. The most promising compounds (**16** and **21**) in terms of *in vitro* potency and/or drug-likeness properties have been also evaluated *in vivo* for their capability to counteract NPS-induced stimulant effects on mouse locomotor activity. Our findings demonstrated that these compounds behave *in vitro* as pure NPSR antagonists with nanomolar potency in inhibiting the NPS stimulatory effects in the calcium mobilization assay (pK_B values of 7.38 and 7.82 for **16** and **21**, respectively). Importantly, the guanidine derivative **16** exhibited a significantly (5-fold)

improved potency and increased antagonist effectiveness *in vivo* when compared to the reference compound **1**, although this is associated with somewhat reduced selectivity of action. Collectively, our efforts can be considered an important advancement in this research field culminating in the identification of a new pharmacological tool that combines *in vitro* and *in vivo* potency in blocking NPSR. This could be useful to investigate possible pharmacological treatments in all the pathological conditions in which the endogenous NPSergic system is activated.

EXPERIMENTAL SECTION

Chemistry. Materials and Methods. The chemicals, including the 2-(4-bromomethyl-phenoxy)ethyl polystyrene HL resin for solid-phase synthesis, were purchased from Fluorochem, Novabiochem Iris Biotech GmbH, or Sigma-Aldrich. Reaction progress and product mixtures were monitored by thin-layer chromatography (TLC) on silica gel (precoated F254 Macherey-Nagel plates) and visualized with a UV lamp (254 nm light source). Compounds were purified through silica gel flash chromatography (silica gel 60, 40–63 μm) using appropriate eluent mixtures or on a reverse-phase Waters Prep 600 HPLC system equipped with a Jupiter column C18 (250 \times 30 mm, 300 \AA , 15 μm spherical particle size). Reverse-phase purification of crude compounds was carried out using a gradient of $\text{CH}_3\text{CN}/\text{H}_2\text{O}$ [with 0.1% trifluoroacetyl (TFA)] programmed time by time, with a flow rate of 20 mL/min and a UV detector with a wavelength of 220 nm. Analytical HPLC analyses were performed on a Beckman 116 liquid chromatograph equipped with a Beckman 166 diode array detector. Analytical purity of the final compounds were assessed using a XBridge C18 column (4.6 \times 150 mm, 5 μm particle size) at a flow rate of 0.7 mL/min with a linear gradient from 100% of solvent A ($\text{H}_2\text{O} + 0.1\%$ TFA) to 100% of solvent B ($\text{CH}_3\text{CN} + 0.1\%$ TFA) over 25 min. Analytical determinations were reported as column retention time (T_R) in minutes, and the purity of final compounds was >95% as determined by HPLC analysis carried out at a wavelength of 220 nm. Mass spectra were recorded with a Waters ESI Micromass ZQ dissolving the samples in a solution of $\text{H}_2\text{O}/\text{CH}_3\text{CN}/\text{TFA}$ (40:60:0.1). Melting points for purified products **3–21** were determined using glass capillaries on a Stuart Scientific electrothermal apparatus SMP3 and are uncorrected. NMR analyses were performed in CDCl_3 or $\text{DMSO}-d_6$ at ambient temperature using a Varian 200 or 400 MHz spectrometer. Chemical shifts (δ) are reported in parts per million (ppm) using the peak of tetramethylsilane as an internal standard in deuterated solvents, and coupling constants (J) are reported in Hertz. Splitting patterns are designed as s, singlet; d, doublet; t, triplet; q, quartet; m, multiplet; and b, broad. Optical rotations were measured on a Jasco P-2000 polarimeter dissolving the samples in methanol, with a path length of 1 dm, using sodium D line, 589 nm.

General Procedure for the Synthesis of 25a–j. Tetramethylethylenediamine (TMEDA, 2.7 mmol) was added under an argon atmosphere at room temperature to a stirring solution of **23**¹⁰ (1 mmol) in freshly distilled tetrahydrofuran (THF) (5 mL). After cooling at -78°C , *sec*-BuLi (2.7 mmol) was added and the reaction was allowed to reach -30°C over 2 h. A solution of appropriate benzophenone **24a–j** (2 mmol) in THF (5 mL) was added and the reaction solution was left stirring at -30°C for 30 min, then it was slowly warmed to rt and stirred for 16 h. The reaction was quenched with a saturated solution of NH_4Cl (15 mL), and the solvents were concentrated under vacuum to half volume and the aqueous phase was extracted with EtOAc (3 \times 15 mL). The organic layers were combined, dried over Na_2SO_4 , and the solvent was removed under vacuum. The resulting crude product was purified by flash column chromatography on silica gel using a mixture of EtOAc/Pet 1:2 as the eluent.

7-Benzyl-1,1-bis(4-fluorophenyl)tetrahydro-1H-oxazolo[3,4-*a*]pyrazin-3(5H)-one (25a). White solid (227 mg, 54% yield). ¹H NMR (200 MHz, CDCl_3): δ (ppm) 7.70–7.59 (m, 2H); 7.40–7.16 (m,

11H); 4.66 (dd, $J = 8.0, 4.0$ Hz, 1H); 3.62–3.49 (m, 2H); 3.38–3.21 (m, 1H); 3.16–2.98 (m, 1H); 2.63–2.58 (m, 2H); 1.88–1.69 (m, 1H); 1.52–1.38 (m, 1H). MS (ESI): m/z calcd for $C_{25}H_{23}F_2N_2O_2$ [$M + H$]⁺, 421.47; found, 421.03.

7-Benzyl-1,1-bis(4-chlorophenyl)tetrahydro-1H-oxazolo[3,4-*a*]pyrazin-3(5H)-one (25b). White solid (200 mg, 44% yield). ¹H NMR (200 MHz, $CDCl_3$): δ (ppm) 7.44–7.18 (m, 13H); 4.63–4.20 (m, 1H); 3.82 (dd, $J = 8.0, 4.0$ Hz, 1H); 3.44–3.04 (m, 2H); 2.76 (d, $J = 10.6$ Hz, 1H); 2.53 (d, $J = 11.1$ Hz, 1H); 2.01–1.88 (m, 1H); 1.60 (t, $J = 7.4$ Hz, 2H). MS (ESI): m/z calcd for $C_{25}H_{23}Cl_2N_2O_2$ [$M + H$]⁺, 454.37; found, 454.26.

7-Benzyl-1,1-di-*p*-tolyltetrahydro-1H-oxazolo[3,4-*a*]pyrazin-3(5H)-one (25c). Pale yellow solid (260 mg, 63% yield). ¹H NMR (200 MHz, $CDCl_3$): δ (ppm) 7.44 (d, $J = 8.4$ Hz, 2H); 7.31–7.12 (m, 11H); 4.60 (dd, $J = 11.1, 3.7$ Hz, 1H); 3.61–3.46 (m, 2H); 3.34 (s, 1H); 3.16–2.96 (m, 1H); 2.68–2.52 (m, 2H); 2.26 (d, $J = 3.4$ Hz, 6H); 1.84–1.65 (m, 1H); 1.58–1.39 (m, 1H). MS (ESI): m/z calcd for $C_{27}H_{29}N_2O_2$ [$M + H$]⁺, 413.54; found, 413.46.

7-Benzyl-1,1-bis(4-(dimethylamino)phenyl)tetrahydro-1H-oxazolo[3,4-*a*]pyrazin-3(5H)-one (25d). Dark blue solid (169 mg, 36% yield). ¹H NMR (200 MHz, $DMSO-d_6$): δ (ppm) 7.31–7.20 (m, 7H); 6.99 (d, $J = 8.6$ Hz, 2H); 6.66 (t, $J = 8.2$ Hz, 4H); 4.45 (d, $J = 8$ Hz, 1H); 3.53 (t, $J = 4$ Hz, 2H); 3.42–3.31 (m, 1H); 3.01 (d, $J = 12$ Hz, 1H); 2.87 (s, 12H); 2.63–2.41 (m, 2H); 1.78 (t, $J = 12$ Hz, 1H); 1.48 (t, $J = 12$ Hz, 1H). MS (ESI): m/z calcd for $C_{29}H_{35}N_4O_2$ [$M + H$]⁺, 471.63; found, 471.44.

7-Benzyl-1,1-di-*o*-tolyltetrahydro-1H-oxazolo[3,4-*a*]pyrazin-3(5H)-one (25e). White solid (82 mg, 28% yield). ¹H NMR (200 MHz, $CDCl_3$): δ (ppm) 7.89–7.79 (m, 1H); 7.67–7.55 (m, 1H); 7.40–6.96 (m, 11H); 4.88 (d, $J = 10.5$ Hz, 1H); 3.86 (d, $J = 11.2$ Hz, 2H); 3.52 (d, $J = 12.1$ Hz, 1H); 3.32–3.10 (m, 2H); 2.79–2.58 (m, 1H); 2.11–1.95 (m, 2H); 1.79 (d, $J = 9.8$ Hz, 6H). MS (ESI): m/z calcd for $C_{27}H_{29}N_2O_2$ [$M + H$]⁺, 413.54; found, 413.44.

7-Benzyl-1,1-bis(2-methoxyphenyl)tetrahydro-1H-oxazolo[3,4-*a*]pyrazin-3(5H)-one (25f). White solid (169 mg, 38% yield). ¹H NMR (200 MHz, $CDCl_3$): δ (ppm) 7.49–7.21 (m, 8H); 6.96–6.75 (m, 5H); 4.54 (d, $J = 8$ Hz, 1H); 3.90 (dd, $J = 8.0, 4.0$ Hz, 1H); 3.51 (s, 6H); 3.40–3.05 (m, 2H); 2.81–2.52 (m, 2H); 2.20–2.01 (m, 1H); 1.75–1.56 (m, 2H). MS (ESI): m/z calcd for $C_{27}H_{29}N_2O_4$ [$M + H$]⁺, 445.54; found, 445.30.

7-Benzyl-6',7',8',8a'-tetrahydrospiro[fluorene-9,1'-oxazolo[3,4-*a*]pyrazin]-3'(5'H)-one (25g). Yellow solid (279 mg, 73% yield). ¹H NMR (200 MHz, $CDCl_3$): δ (ppm) 7.85–7.79 (m, 4H); 7.61–7.09 (m, 9H); 4.20 (dd, $J = 10.6, 3.2$ Hz, 1H); 3.72 (d, $J = 11.1$ Hz, 1H); 3.43–3.36 (m, 2H); 3.20–3.05 (m, 1H); 2.80 (d, $J = 8.2$ Hz, 1H); 2.31–1.85 (m, 3H). MS (ESI): m/z calcd for $C_{25}H_{23}N_2O_2$ [$M + H$]⁺, 383.47; found, 383.29.

7-Benzyl-1,1-dicyclohexyltetrahydro-1H-oxazolo[3,4-*a*]pyrazin-3(5H)-one (25h). White solid (162 mg, 41% yield). ¹H NMR (200 MHz, $CDCl_3$): δ (ppm) 7.40–7.22 (m, 4H); 7.02 (s, 1H); 3.78–3.64 (m, 2H); 3.58–3.42 (m, 2H); 3.34 (s, 1H); 2.90–2.61 (m, 3H) 2.24 (t, $J = 12$ Hz, 1H); 1.97–1.41 (m, 13H); 1.28–0.98 (m, 9H). MS (ESI): m/z calcd for $C_{25}H_{37}N_2O_2$ [$M + H$]⁺, 397.58; found, 397.31.

7-Benzyl-1,1-dipropyltetrahydro-1H-oxazolo[3,4-*a*]pyrazin-3(5H)-one (25i). White solid (136 mg, 43% yield). ¹H NMR (200 MHz, $CDCl_3$): δ (ppm) 7.76 (d, $J = 6.8$ Hz, 1H); 7.44–7.25 (m, 4H); 4.80–4.44 (m, 2H); 4.30–4.00 (m, 2H); 3.67 (d, $J = 12.0$ Hz, 1H); 3.29–3.15 (m, 1H); 3.00–2.56 (m, 3H); 1.61–1.00 (m, 8H); 0.94–0.84 (m, 6H). MS (ESI): m/z calcd for $C_{19}H_{29}N_2O_2$ [$M + H$]⁺, 317.45; found, 317.46.

7-Benzyl-1,1-diphenyltetrahydro-1H-oxazolo[3,4-*a*]pyrazin-3(5H)-one (25j). White solid (277 mg, 72% yield). ¹H NMR (200 MHz, $CDCl_3$): δ (ppm) 7.60–7.49 (m, 1H); 7.38–7.16 (m, 14H); 4.52 (dd, $J = 8.0, 4.0$ Hz, 1H); 3.72–3.59 (m, 2H); 3.48–3.21 (m, 1H); 3.16–2.98 (m, 1H); 2.63–2.58 (m, 2H); 1.88–1.69 (m, 1H); 1.52–1.38 (m, 1H). MS (ESI): m/z calcd for $C_{25}H_{23}N_2O_2$ [$M + H$]⁺, 385.49; found, 385.28.

General Procedure for the Synthesis of 26a–j. 9-Fluorenylmethoxycarbonyl chloride (FmocCl, 1.1 mmol) was added to a solution of **25a–j** (1 mmol) in CH_3CN (5 mL). The reaction solution was heated at 90 °C for 5 h and then stirred at room temperature for 18 h.

The solvent was evaporated giving a residue that was dissolved in EtOAc (30 mL), and the resulting organic phase was washed with water (3×15 mL), dried over anhydrous Na_2SO_4 , and concentrated to dryness. All crude residues were finally purified via flash column chromatography on a silica gel using the appropriate mixture of petroleum ether and EtOAc as an eluent (see below).

(9H-Fluoren-9-yl)methyl 1,1-Bis(4-fluorophenyl)-3-oxotetrahydro-3H-oxazolo[3,4-*a*]pyrazine-7(1H)-carboxylate (26a). White solid (448 mg, 81% yield). Eluent for chromatography purification: EtOAc/PET 1:1; ¹H NMR (200 MHz, $DMSO-d_6$): δ (ppm) 7.94–7.84 (m, 2H); 7.62–7.18 (m, 14H); 4.65–4.39 (m, 3H); 4.25 (t, $J = 5.4$ Hz, 1H); 3.82 (d, $J = 10.5$ Hz, 1H); 3.56 (dd, $J = 10.6, 2.2$ Hz, 1H); 3.05–2.85 (m, 1H); 2.83–2.64 (m, 2H); 2.31–2.16 (m, 1H). MS (ESI): m/z calcd for $C_{33}H_{27}F_2N_2O_4$ [$M + H$]⁺, 553.59; found, 553.57.

(9H-Fluoren-9-yl)methyl 1,1-Bis(4-chlorophenyl)-3-oxotetrahydro-3H-oxazolo[3,4-*a*]pyrazine-7(1H)-carboxylate (26b). White solid (298 mg, 51% yield). Eluent for chromatography purification: EtOAc/PET 1:2; ¹H NMR (200 MHz, $DMSO-d_6$): δ (ppm) 7.90 (t, $J = 6.8$ Hz, 2H); 7.59–7.28 (m, 14H); 4.43–4.39 (m, 2H); 4.24 (t, $J = 5.6$ Hz, 2H); 3.82 (d, $J = 11.2$ Hz, 1H); 3.56 (d, $J = 10.6$ Hz, 1H); 3.19 (s, 1H); 3.07–2.64 (m, 2H); 2.24 (t, $J = 12.4$ Hz, 1H). MS (ESI): m/z calcd for $C_{33}H_{27}Cl_2N_2O_4$ [$M + H$]⁺, 586.49; found, 586.63.

(9H-Fluoren-9-yl)methyl 3-Oxo-1,1-di-*p*-tolyltetrahydro-3H-oxazolo[3,4-*a*]pyrazine-7(1H)-carboxylate (26c). White solid (327 mg, 60% yield). Eluent for chromatography purification: EtOAc/PET 1:4; ¹H NMR (200 MHz, $DMSO-d_6$): δ (ppm) 7.90 (t, $J = 7.4$ Hz, 2H); 7.59 (d, $J = 7.0$ Hz, 2H); 7.44–7.16 (m, 10H); 6.99 (s, 2H); 4.77–4.59 (m, 1H); 4.50–4.35 (m, 1H); 4.26 (s, 1H); 4.16–4.09 (m, 1H); 3.80 (d, $J = 10.6$ Hz, 1H); 3.53 (dd, $J = 11.2, 1.8$ Hz, 1H); 3.22–3.05 (m, 1H); 2.95–2.58 (m, 2H); 2.30 (d, $J = 4.6$ Hz, 6H); 2.20–2.08 (m, 1H). MS (ESI): m/z calcd for $C_{35}H_{33}N_2O_4$ [$M + H$]⁺, 545.66; found, 545.59.

(9H-Fluoren-9-yl)methyl 1,1-Bis(4-(dimethylamino)phenyl)-3-oxotetrahydro-3H-oxazolo[3,4-*a*]pyrazine-7(1H)-carboxylate (26d). Pink solid (380 mg, 63% yield). Eluent for chromatography purification: EtOAc/PET 1:4; ¹H NMR (200 MHz, $DMSO-d_6$): δ (ppm) 7.88 (t, $J = 6.6$ Hz, 2H); 7.59 (d, $J = 7.2$ Hz, 2H); 7.44–7.32 (m, 5H); 7.11 (s, 2H); 6.75–6.63 (m, 5H); 4.79–4.61 (m, 1H); 4.52–4.33 (m, 1H); 4.26 (t, $J = 5.6$ Hz, 1H); 4.01–3.90 (m, 1H); 3.82–3.60 (m, 1H); 3.53 (d, $J = 10.6$ Hz, 1H); 3.22–3.05 (m, 1H); 3.11–2.98 (m, 1H); 2.90 (d, $J = 4.8$ Hz, 12H); 2.83–2.77 (m, 1H); 2.22–2.06 (m, 1H). MS (ESI): m/z calcd for $C_{37}H_{39}N_4O_4$ [$M + H$]⁺, 603.74; found, 603.51.

(9H-Fluoren-9-yl)methyl 3-Oxo-1,1-di-*o*-tolyltetrahydro-3H-oxazolo[3,4-*a*]pyrazine-7(1H)-carboxylate (26e). White solid (408 mg, 75% yield). Eluent for chromatography purification: EtOAc/PET 3:7; ¹H NMR (200 MHz, $DMSO-d_6$): δ (ppm) 7.89–7.79 (m, 2H); 7.67–7.55 (m, 2H); 7.40–6.96 (m, 12H); 2.51–4.07 (m, 1H); 4.88 (d, $J = 10.5$ Hz, 1H); 3.86 (d, $J = 11.2$ Hz, 2H); 3.52 (d, $J = 12.1$ Hz, 1H); 3.32–3.10 (m, 2H); 2.79–2.58 (m, 1H); 2.11–1.95 (m, 2H); 1.79 (d, $J = 9.8$ Hz, 6H). MS (ESI): m/z calcd for $C_{35}H_{33}N_2O_4$ [$M + H$]⁺, 545.66; found, 545.25.

(9H-Fluoren-9-yl)methyl 1,1-Bis(2-methoxyphenyl)-3-oxotetrahydro-3H-oxazolo[3,4-*a*]pyrazine-7(1H)-carboxylate (26f). White solid (363 mg, 63% yield). Eluent for chromatography purification: EtOAc/PET 1:1; ¹H NMR (200 MHz, $CDCl_3$): δ (ppm) 7.72 (d, $J = 7.2$ Hz, 2H); 7.48–7.29 (m, 10H); 7.01–6.88 (m, 4H); 4.58–4.35 (s, 2H); 4.24–4.06 (m, 4H); 4.01–3.36 (m, 7H); 2.89–2.69 (m, 2H); 2.64–2.42 (m, 1H). MS (ESI): m/z calcd for $C_{35}H_{33}N_2O_6$ [$M + H$]⁺, 577.66; found, 577.65.

(9H-Fluoren-9-yl)methyl 3'-Oxo-5',6',8',8a'-tetrahydro-3'H,7'H-spiro[fluorene-9,1'-oxazolo[3,4-*a*]pyrazine]-7'-carboxylate (26g). White solid (283 mg, 55% yield). Eluent for chromatography purification: EtOAc/PET 1:4; ¹H NMR (200 MHz, $DMSO-d_6$): δ (ppm) 7.95 (s, 2H); 7.90–7.02 (m, 14H); 4.56–4.25 (m, 2H); 4.19–4.05 (s, 1H); 3.86 (d, $J = 12.40$ Hz, 2H); 3.69 (d, $J = 12.90$ Hz, 2H); 2.98–2.64 (m, 3H). MS (ESI): m/z calcd for $C_{33}H_{27}N_2O_4$ [$M + H$]⁺, 515.59; found, 515.50.

(9*H*-Fluoren-9-yl)methyl 1,1-Dicyclohexyl-3-oxotetrahydro-3*H*-oxazolo[3,4-*a*]pyrazine-7(1*H*)-carboxylate (**26h**). White solid (434 mg, 82% yield). Eluent for chromatography purification: EtOAc/PEt 1:4; ¹H NMR (200 MHz, DMSO-*d*₆): δ (ppm) 7.88 (d, *J* = 7.5 Hz, 2H); 7.65 (t, *J* = 7.0 Hz, 2H); 7.42 (t, *J* = 7.4 Hz, 2H); 7.33 (dd, *J* = 13.8, 7.1 Hz, 2H); 4.63–4.42 (m, 2H); 4.28 (t, *J* = 5.6 Hz, 1H); 3.94–3.58 (m, 2H); 3.50–3.18 (m, 3H); 2.98–2.63 (m, 2H); 1.78–1.03 (m, 22H). MS (ESI): *m/z* calcd for C₃₃H₄₁N₂O₄ [M + H]⁺, 529.70; found, 529.66.

(9*H*-Fluoren-9-yl)methyl 3-Oxo-1,1-dipropyltetrahydro-3*H*-oxazolo[3,4-*a*]pyrazine-7(1*H*)-carboxylate (**26i**). White solid (166 mg, 37% yield). Eluent for chromatography purification: EtOAc/PEt 3:7; ¹H NMR (200 MHz, CDCl₃): δ (ppm) 7.76 (d, *J* = 6.8 Hz, 2H); 7.55 (d, *J* = 7.2 Hz, 2H); 7.44–7.25 (m, 4H); 4.80–4.44 (m, 2H); 4.30–4.00 (m, 3H); 3.67 (d, *J* = 12.0 Hz, 1H); 3.29–3.15 (m, 1H); 3.00–2.56 (m, 3H); 1.61–1.00 (m, 8H); 0.94–0.84 (m, 6H). MS (ESI): *m/z* calcd for C₂₇H₃₃N₂O₄ [M + H]⁺, 449.57; found, 449.55.

(9*H*-Fluoren-9-yl)methyl 3-Oxo-1,1-diphenyltetrahydro-3*H*-oxazolo[3,4-*a*]pyrazine-7(1*H*)-carboxylate (**26j**). White solid (305 mg, 59% yield). Eluent for chromatography purification: EtOAc/PEt 1:1; ¹H NMR (200 MHz, DMSO-*d*₆): δ (ppm) 7.89 (t, *J* = 7.4 Hz, 2H); 7.59 (d, *J* = 7.4 Hz, 2H); 7.54–7.03 (m, 14H); 4.71–4.38 (m, 2H); 4.26 (t, *J* = 5.4 Hz, 2H); 3.79 (d, *J* = 10.6 Hz, 1H); 3.56 (dd, *J* = 11.4, 1.8 Hz, 2H); 3.00–2.84 (m, 2H); 2.28–2.09 (m, 1H). MS (ESI): *m/z* calcd for C₃₃H₂₉N₂O₄ [M + H]⁺, 517.61; found, 517.29.

General Procedure for the Synthesis of Final Compounds 3–12. The appropriate iso(thio)cyanate **27a–b** (2 mmol) and DBU (1.2 mmol) were sequentially added at room temperature to a stirring solution of **26a–j** (1 mmol) in anhydrous THF (5 mL). The reaction solution was continued stirring for 2 h after which it was quenched with a saturated solution of NH₄Cl (10 mL). The mixture was concentrated under vacuum to half volume, and the aqueous phase was extracted with EtOAc (3 × 15 mL). The organic layers were combined, dried over Na₂SO₄, and concentrated under vacuum. The crude products were purified by preparative RP-HPLC.

N-(4-Fluorobenzyl)-1,1-bis(4-fluorophenyl)-3-oxotetrahydro-1*H*-oxazolo[3,4-*a*]pyrazine-7(3*H*)-carboxamide (**3**). White solid (289 mg, 60% yield); mp 104–107 °C; ¹H NMR (400 MHz, DMSO-*d*₆): δ (ppm) 7.65–7.54 (m, 2H); 7.40–7.19 (m, 9H); 7.18–7.05 (m, 2H); 4.51 (dd, *J* = 11.2, 3.6 Hz, 1H); 4.21 (d, *J* = 5.5 Hz, 2H); 3.93 (d, *J* = 10.5 Hz, 1H); 3.82 (dd, *J* = 13.1, 2.9 Hz, 1H); 3.59 (dd, *J* = 13.2, 2.6 Hz, 1H); 3.05 (td, *J* = 12.8, 3.6 Hz, 1H); 2.68 (td, *J* = 12.9, 3.4 Hz, 1H); 2.17–2.00 (m, 1H). ¹³C NMR (DMSO-*d*₆): δ 162.94, 162.70, 162.12, 160.49, 160.27, 159.71, 157.05, 154.80, 138.44, 136.75, 134.48, 128.89, 128.09, 127.78, 115.45, 115.24, 114.70, 84.07, 59.51, 45.51, 42.79, 42.52, 41.09. MS (ESI): *m/z* calcd for C₂₆H₂₃F₃N₃O₃ [M + H]⁺, 482.48; found, 482.21. *T_R* = 24.77 min.

1,1-Bis(4-chlorophenyl)-*N*-(4-fluorobenzyl)-3-oxotetrahydro-1*H*-oxazolo[3,4-*a*]pyrazine-7(3*H*)-carboxamide (**4**). White solid (412 mg, 80% yield); mp 77–79 °C; ¹H NMR (400 MHz, DMSO-*d*₆): δ (ppm) 7.63–7.55 (m, 2H); 7.53–7.44 (m, 4H); 7.37–7.22 (m, 5H); 7.15–7.07 (m, 2H); 4.52 (dd, *J* = 11.2, 3.6 Hz, 1H); 4.21 (d, *J* = 5.2 Hz, 2H); 3.93 (d, *J* = 11.6 Hz, 1H); 3.83 (dd, *J* = 12.9, 2.9 Hz, 1H); 3.59 (dd, *J* = 13.1, 2.7 Hz, 1H); 3.05 (td, *J* = 12.7, 3.6 Hz, 1H); 2.68 (td, *J* = 13.0, 3.4 Hz, 1H); 2.11 (dd, *J* = 12.8, 11.4 Hz, 1H). ¹³C NMR (DMSO-*d*₆): δ 162.14, 159.73, 157.07, 154.68, 140.92, 136.96, 136.73, 133.18, 132.84, 128.92, 128.55, 127.77, 127.47, 114.71, 83.94, 59.33, 45.45, 42.81, 42.50, 41.14. MS (ESI): *m/z* calcd for C₂₆H₂₃Cl₂FN₃O₃ [M + H]⁺, 515.39; found, 515.45. *T_R* = 22.16 min.

N-(4-Fluorobenzyl)-3-oxo-1,1-di-*p*-tolyltetrahydro-1*H*-oxazolo[3,4-*a*]pyrazine-7(3*H*)-carboxamide (**5**). White solid (312 mg, 66% yield); mp 89–90 °C; ¹H NMR (400 MHz, DMSO-*d*₆): δ (ppm) 7.41–7.39 (m, 3H); 7.30–7.25 (m, 3H); 7.21–7.09 (m, 7H); 4.43 (dd, *J* = 11.1, 3.7 Hz, 1H); 4.20 (d, *J* = 5.3 Hz, 2H); 3.92 (d, *J* = 11.6 Hz, 1H); 3.84 (dd, *J* = 12.9, 2.9 Hz, 1H); 3.59 (dd, *J* = 13.3, 2.9 Hz, 1H); 3.02 (td, *J* = 12.7, 3.6 Hz, 1H); 2.64 (td, *J* = 12.9, 3.4 Hz, 1H); 2.29 (s, 3H); 2.27 (s, 3H), 2.08–2.02 (m, 1H). ¹³C NMR (DMSO-*d*₆): δ 162.66, 160.26, 157.63, 155.68, 140.15, 138.08, 137.59, 137.33, 136.28, 129.46, 129.38, 126.18, 125.93, 115.36, 115.15, 85.31, 60.08,

46.32, 43.33, 43.12, 41.52, 21.01. MS (ESI): *m/z* calcd for C₂₈H₂₉FN₃O₃ [M + H]⁺, 474.56; found, 474.43. *T_R* = 18.53 min.

1,1-Bis(4-(dimethylamino)phenyl)-*N*-(4-fluorobenzyl)-3-oxotetrahydro-1*H*-oxazolo[3,4-*a*]pyrazine-7(3*H*)-carboxamide (**6**). White solid (500 mg, 94% yield); mp 110–113 °C; ¹H NMR (400 MHz, DMSO-*d*₆): δ (ppm) 7.33–7.19 (m, 5H); 7.17–7.06 (m, 2H); 7.01–6.98 (m, 2H); 6.70–6.67 (m, 4H); 4.29 (dd, *J* = 11.2, 3.5 Hz, 1H); 4.22–4.17 (m, 2H); 3.93 (d, *J* = 11.2 Hz, 1H); 3.79 (dd, *J* = 13.0, 2.7 Hz, 1H); 3.59 (dd, *J* = 12.9, 2.7 Hz, 1H); 3.01 (td, *J* = 12.8, 3.4 Hz, 1H); 2.90–2.86 (m, 12H); 2.63 (td, *J* = 13.2, 3.5 Hz, 1H); 2.06 (dd, *J* = 13.0, 11.4 Hz, 1H). ¹³C NMR (DMSO-*d*₆): δ 162.11, 157.10, 155.50, 149.86, 149.44, 136.81, 129.87, 128.93, 128.85, 126.74, 126.41, 114.82, 114.61, 111.65, 111.54, 85.23, 59.63, 46.00, 42.77, 42.65, 40.84. MS (ESI): *m/z* calcd for C₃₀H₃₃FN₅O₃ [M + H]⁺, 532.64; found, 532.41. *T_R* = 11.44 min.

N-(4-Fluorobenzyl)-3-oxo-1,1-di-*o*-tolyltetrahydro-1*H*-oxazolo[3,4-*a*]pyrazine-7(3*H*)-carboxamide (**7**). White solid (260 mg, 55% yield); mp 217–219 °C; ¹H NMR (400 MHz, DMSO-*d*₆): δ (ppm) 7.92–7.81 (m, 1H); 7.68 (d, *J* = 7.5 Hz, 1H); 7.35–7.19 (m, 7H); 7.18–7.05 (m, 4H); 4.95 (dd, *J* = 11.1, 3.7 Hz, 1H); 4.24 (dd, *J* = 15.3, 5.7 Hz, 1H); 4.13 (dd, *J* = 15.1, 5.3 Hz, 1H); 3.88 (d, *J* = 11.4 Hz, 1H); 3.61 (dd, *J* = 13.3, 2.9 Hz, 1H); 3.38–3.22 (m, 2H); 2.81 (td, *J* = 13.3, 3.4 Hz, 1H); 2.19 (dd, *J* = 12.9, 11.2 Hz, 1H); 1.76 (s, 3H); 1.74 (s, 3H). ¹³C NMR (DMSO-*d*₆): δ 162.12, 159.73, 157.08, 154.97, 137.30, 137.00, 136.80, 136.21, 133.44, 132.71, 131.69, 128.98, 128.90, 128.69, 128.14, 126.74, 126.55, 125.54, 114.80, 114.60, 85.57, 56.28, 45.03, 43.11, 42.81, 41.26, 21.01, 20.45. MS (ESI): *m/z* calcd for C₂₈H₂₉FN₃O₃ [M + H]⁺, 474.56; found, 474.34. *T_R* = 19.20 min.

N-(4-Fluorobenzyl)-1,1-bis(2-methoxyphenyl)-3-oxotetrahydro-1*H*-oxazolo[3,4-*a*]pyrazine-7(3*H*)-carboxamide (**8**). White solid (435 mg, 86% yield); mp 172–173 °C; ¹H NMR (400 MHz, DMSO-*d*₆): δ (ppm) 7.45–7.42 (m, 1H); 7.39–7.22 (m, 4H); 7.20–7.15 (m, 1H); 7.14–6.89 (m, 7H); 4.37 (d, *J* = 8.1 Hz, 1H); 4.27–4.22 (m, 1H); 4.16–4.10 (m, 1H); 3.99–3.86 (m, 2H); 3.64 (s, 3H); 3.62 (s, 4H); 3.06 (td, *J* = 12.9, 3.6 Hz, 1H); 2.73 (td, *J* = 13.2, 3.6 Hz, 1H); 2.36–2.27 (m, 1H). ¹³C NMR (DMSO-*d*₆): δ 162.09, 159.68, 156.90, 156.78, 155.95, 154.76, 136.84, 129.64, 129.56, 128.90, 128.82, 128.20, 127.00, 125.98, 120.18, 119.93, 114.76, 114.55, 112.54, 111.90, 83.94, 59.04, 55.35, 55.29, 44.76, 42.78, 42.62, 40.57. MS (ESI): *m/z* calcd for C₂₈H₂₉FN₃O₅ [M + H]⁺, 506.55; found, 506.52. *T_R* = 18.71 min.

N-(4-Fluorobenzyl)-3'-oxo-5',6',8',8a'-tetrahydrospiro[fluorene-9,1'-oxazolo[3,4-*a*]pyrazine]-7'(3'*H*)-carboxamide (**9**). White solid (421 mg, 95% yield); mp 120–123 °C; ¹H NMR (400 MHz, DMSO): δ (ppm) 7.91–7.78 (m, 3H); 7.67 (d, *J* = 7.5 Hz, 1H); 7.56–7.47 (m, 2H); 7.42–7.36 (m, 2H); 7.20–7.15 (m, 3H); 7.11–6.95 (m, 2H); 4.19–4.00 (m, 4H); 3.74 (dd, *J* = 12.4, 2.4 Hz, 1H); 3.52 (dd, *J* = 13.0, 2.6 Hz, 1H); 3.08 (td, *J* = 12.3, 3.5 Hz, 1H); 2.88 (td, *J* = 13.1, 3.4 Hz, 1H); 2.70 (dd, *J* = 12.8, 11.4 Hz, 1H). ¹³C NMR (DMSO-*d*₆): δ 162.08, 156.81, 156.01, 142.93, 140.31, 139.82, 139.63, 136.66, 130.62, 130.52, 128.84, 128.77, 128.61, 128.00, 125.84, 124.86, 120.94, 120.45, 114.77, 114.56, 86.35, 58.93, 44.40, 42.66, 42.21, 41.00. MS (ESI): *m/z* calcd for C₂₆H₂₃FN₃O₃ [M + H]⁺, 444.49; found, 444.26. *T_R* = 18.91 min.

1,1-Dicyclohexyl-*N*-(4-fluorobenzyl)-3-oxotetrahydro-1*H*-oxazolo[3,4-*a*]pyrazine-7(3*H*)-carboxamide (**10**). White solid (105 mg, 23% yield); mp 94–95 °C; ¹H NMR (400 MHz, DMSO-*d*₆): δ (ppm) 7.37–7.24 (m, 3H); 7.18–7.05 (m, 2H); 4.31–4.16 (m, 2H); 4.06–3.93 (m, 2H); 3.55–3.42 (m, 2H); 2.98–2.72 (m, 3H); 2.00–1.40 (m, 12H); 1.38–0.85 (m, 10H). ¹³C NMR (DMSO-*d*₆): δ 162.14, 159.74, 157.13, 155.32, 136.82, 128.96, 128.89, 114.82, 114.61, 85.71, 55.26, 43.74, 42.82, 42.18, 40.90, 27.61, 26.54, 26.20, 25.84, 25.77, 25.53, 25.38. MS (ESI): *m/z* calcd for C₂₆H₃₇FN₃O₃ [M + H]⁺, 458.60; found, 458.47. *T_R* = 21.11 min.

N-(4-Fluorobenzyl)-3-oxo-1,1-dipropyltetrahydro-1*H*-oxazolo[3,4-*a*]pyrazine-7(3*H*)-carboxamide (**11**). White solid (189 mg, 50% yield); mp 74–77 °C; ¹H NMR (400 MHz, DMSO-*d*₆): δ (ppm) 7.34–7.21 (m, 3H); 7.15–7.10 (m, 2H); 4.23 (d, *J* = 5.5 Hz, 2H); 4.00 (t, *J* = 14.1 Hz, 2H); 3.52 (dd, *J* = 12.7, 2.6 Hz, 1H); 3.42–3.30

(m, 1H); 2.95–2.63 (m, 3H); 1.72–1.43 (m, 4H); 1.42–1.15 (m, 4H); 0.92–0.88 (m, 6H). ¹³C NMR (DMSO-*d*₆): δ 162.14, 159.73, 156.99, 155.22, 136.86, 128.92, 128.84, 114.84, 114.63, 83.14, 59.10, 44.12, 42.77, 42.58, 33.80, 16.11, 15.88, 14.26, 14.13. MS (ESI): *m/z* calcd for C₂₀H₂₉FN₃O₃ [M + H]⁺, 378.47; found, 378.38. T_R = 13.08 min.

N-Benzyl-3-oxo-1,1-diphenyltetrahydro-1H-oxazolo[3,4-*a*]pyrazine-7(3H)-carbothioamide (12). White solid (306 mg, 69% yield); mp 184–186 °C; ¹H NMR (400 MHz, DMSO-*d*₆): δ (ppm) 8.50 (s, 1H); 7.73–7.00 (m, 15H); 4.85–4.76 (m, 3H); 4.59–4.54 (m, 2H); 3.64 (d, *J* = 12.6 Hz, 1H); 3.15–2.98 (m, 2H); 2.40 (t, *J* = 12.2 Hz, 1H). ¹³C NMR (DMSO-*d*₆): δ 182.31, 155.12, 142.22, 139.22, 138.34, 128.54, 128.45, 128.36, 128.07, 127.99, 126.99, 126.58, 125.70, 125.42, 84.66, 59.42, 50.63, 48.53, 46.14, 40.82. MS (ESI): *m/z* calcd for C₂₆H₂₆N₃O₂S [M + H]⁺, 444.57; found, 444.23. T_R = 15.84 min.

1,1-Diphenylhexahydro-3H-oxazolo[3,4-*a*]pyrazin-3-one (28). DBU (1.2 mmol) was added to a stirring solution of **26j** (1 mmol) in anhydrous THF (10 mL). The reaction solution was allowed stirring at room temperature for 18 h and monitored by TLC. The solvent was removed under vacuum, and the residue was dissolved in EtOAc (20 mL) and washed with water (20 mL). The organic phase was separated, dried over Na₂SO₄, and the solvent was evaporated to give a residue that was purified via flash column chromatography on silica gel using a 1:3 mixture of petroleum ether and EtOAc as the eluent.

Off-white solid (256 mg, 87% yield). ¹H NMR (200 MHz, DMSO-*d*₆): δ (ppm) 7.52 (d, *J* = 7.2 Hz, 2H); 7.41–7.24 (m, 8H); 4.32 (d, *J* = 10.1 Hz, 1H); 4.10–3.71 (m, 2H); 3.16 (t, *J* = 5.6 Hz, 1H); 2.97–2.76 (m, 1H); 2.28 (td, *J* = 11.6, 3.4 Hz, 1H); 1.83–1.75 (m, 1H), 1.21 (br s, 1H). MS (ESI): *m/z* calcd for C₁₈H₁₉N₂O₂ [M + H]⁺, 295.36; found, 295.38.

General Procedure for the Synthesis of Final Compounds 13 and 14. 2-Chloro-*N*-(4-fluorobenzyl)acetamide or 2-chloro-*N*-(4-fluorophenyl)acetamide (1 mmol) was added to a mixture of compound **28** (1 mmol) and K₂CO₃ (1.5 mmol) in CH₃CN (15 mL). The reaction mixture was heated at 90 °C for 4 h after which the solvent was removed under vacuum, and the residue was partitioned between water (15 mL) and CH₂Cl₂ (15 mL). The aqueous phase was further extracted with CH₂Cl₂ (2 × 15 mL), and the combined organic layers were washed with brine (10 mL) and dried over Na₂SO₄. After evaporation, the residue was purified by flash column chromatography on silica gel using a 1:1 mixture of EtOAc/PET as the eluent.

***N*-(4-Fluorophenyl)-2-(3-oxo-1,1-diphenyltetrahydro-3H-oxazolo[3,4-*a*]pyrazin-7(1H)-yl)acetamide (13).** White solid (196 mg, 44% yield); mp 205–208 °C; ¹H NMR (400 MHz, DMSO-*d*₆): δ (ppm) 9.76 (s, 1H); 7.62–7.60 (m, 4H); 7.44–7.29 (m, 8H); 7.17–7.13 (m, 2H); 4.77 (dd, *J* = 11.2, 3.6 Hz, 1H); 3.59 (dd, *J* = 13.1, 2.9 Hz, 1H); 3.23–3.13 (m, 3H); 2.74 (d, *J* = 10.5 Hz, 1H); 2.61 (dd, *J* = 13.2, 2.6 Hz, 1H); 2.19 (td, *J* = 12.9, 3.4 Hz, 1H); 1.78 (t, *J* = 12.2 Hz, 1H). ¹³C NMR (DMSO-*d*₆): δ 167.92, 159.26, 156.88, 155.21, 142.80, 138.58, 134.74, 128.51, 128.36, 128.19, 127.72, 125.53, 125.18, 121.46, 115.24, 115.02, 84.54, 60.85, 60.11, 54.19, 50.66, 41.24. MS (ESI): *m/z* calcd for C₂₆H₂₅FN₃O₃ [M + H]⁺, 446.50; found, 446.69. T_R = 18.30.

***N*-(4-Fluorobenzyl)-2-(3-oxo-1,1-diphenyltetrahydro-3H-oxazolo[3,4-*a*]pyrazin-7(1H)-yl)acetamide (14).** White solid (170 mg, 37% yield); mp 137–140 °C; ¹H NMR (400 MHz, DMSO-*d*₆): δ (ppm) 8.41–8.37 (m, 1H); 7.56–7.54 (m, 2H); 7.43–7.39 (m, 2H); 7.37–7.25 (m, 8H); 7.17–7.13 (m, 2H); 4.76 (dd, *J* = 10.9, 3.4 Hz, 1H); 4.30–4.22 (m, 2H); 3.62–3.56 (m, 1H); 3.21–3.08 (m, 1H); 3.04 (d, *J* = 13.2 Hz, 1H); 2.88 (d, *J* = 12.9 Hz, 1H); 2.67–2.63 (m, 1H); 2.49–2.44 (m, 1H); 2.29–2.05 (m, 1H); 1.60 (t, *J* = 12.2 Hz, 1H). ¹³C NMR (DMSO-*d*₆): δ 168.94, 162.24, 155.12, 142.77, 138.49, 135.83, 129.10, 128.51, 128.28, 128.22, 127.72, 125.46, 125.10, 115.38, 101.57, 84.43, 60.51, 59.96, 54.32, 50.97, 41.14. MS (ESI): *m/z* calcd for C₂₇H₂₇FN₃O₃ [M + H]⁺, 460.53; found, 460.20. T_R = 18.16.

Method A for the Synthesis of Guanidine Derivatives 15 and 16.

A solution of NaHCO₃ (1.7 mmol) in H₂O (1 mL) was added at 0 °C to a stirring solution of **28** (1 mmol) in CH₂Cl₂ (5 mL). At the same temperature, a solution of cyanogen bromide (1.2 mmol) in CH₂Cl₂ (5 mL) was added. The heterogeneous mixture was vigorously stirred at 0 °C for 30 min, then warmed to room temperature, and stirred for further 24 h. After this time, the layers were separated and the organic phase was washed with a saturated solution of NaHCO₃ (2 × 10 mL), dried with anhydrous Na₂SO₄, and concentrated under vacuum to give a residue from which compound **29** was purified via flash column chromatography on silica gel using a 1:1 mixture of petroleum ether and EtOAc as an eluent.

White solid (160 mg, 50% yield). ¹H NMR (200 MHz, DMSO-*d*₆): δ (ppm) 7.52–7.25 (m, 10H), 4.60 (dd, *J* = 11.2, 3.6 Hz, 1H), 3.98–3.88 (m, 1H), 3.37–3.22 (m, 2H), 3.10–3.02 (m, 2H), 1.27–1.18 (m, 1H); MS (ESI): *m/z* calcd for C₁₉H₁₈N₃O₂ [M + H]⁺, 320.37; found, 320.40.

Benzylamine or 4-fluorobenzylamine (3 mmol) was added to a stirring solution of **29** (1 mmol) in DMSO (3 mL) in the presence of a catalytic amount of *p*-toluenesulfonic acid. After 18 h of stirring at 60 °C, the reaction solution was diluted with water (10 mL) and extracted with EtOAc (3 × 15 mL). The organic layers were dried over Na₂SO₄ and concentrated *in vacuo* after which crude products were purified by flash column chromatography on silica gel using a 4:1 mixture of CH₂Cl₂ and MeOH.

Method B for the Synthesis of Guanidine Derivatives 15 and 16.

Compounds **15** and **16** were alternatively synthesized according to a manual solid-phase synthesis approach described previously.¹⁸ Briefly, compounds **31a** or **31b** (0.62 mmol) was added to a suspension of 2-(4-bromomethyl-phenoxy)ethyl polystyrene HL resin (substitution: 1.23 mmol/g, 0.62 mmol) in a 2:1 mixture of CH₂Cl₂/DMF (3 mL). The mixture was heated at 50 °C until starting material consumption was observed (4 h). After that, each of the two differently functionalized resins was filtered, washed with DMF (2 × 5 mL) and CH₂Cl₂ (2 × 5 mL), and dried. Subsequently, the respective functionalized resin (0.62 mmol) was suspended in CH₃CN (2 mL) before adding compound **28** (1.55 mmol) and HgCl₂ (0.93 mmol). After heating at 90 °C for 24 h, a simple filtration was performed and the filtrates were purified by flash column chromatography on silica gel using a 4:1 mixture of CH₂Cl₂ and MeOH.

***N*-Benzyl-3-oxo-1,1-diphenyltetrahydro-3H-oxazolo[3,4-*a*]pyrazine-7(1H)-carboximidamide (15).** White solid (method A: 56 mg, 21% yield; method B: 103 mg, 39% yield); mp 68–69 °C; ¹H NMR (400 MHz, DMSO-*d*₆): δ (ppm) 8.38 (m, 1H), 7.90 (s, 2H), 7.61–7.54 (m, 2H), 7.46–7.25 (m, 14H), 4.77 (dd, *J* = 11.3, 3.5 Hz, 1H), 4.43 (d, *J* = 5.7 Hz, 2H), 3.78–3.58 (m, 2H), 3.23–3.17 (m, 1H), 3.08–3.03 (m, 1H), 2.64–2.57 (m, 1H). ¹³C NMR (DMSO-*d*₆): δ 156.79, 155.36, 142.90, 138.39, 137.37, 129.02, 128.56, 128.00, 127.57, 126.10, 85.18, 59.76, 49.02, 45.63, 45.56, 41.20. MS (ESI): *m/z* calcd for C₂₆H₂₇N₄O₂ [M + H]⁺, 427.53; found, 427.44. T_R = 17.68.

***N*-(4-Fluorobenzyl)-3-oxo-1,1-diphenyltetrahydro-1H-oxazolo[3,4-*a*]pyrazine-7(3H)-carboximidamide (16).** White solid (method A: 28 mg, 10% yield; method B: 85 mg, 31% yield); mp 82–85 °C; ¹H NMR (400 MHz, DMSO-*d*₆): δ (ppm) 8.43 (br s, 1H), 7.95 (s, 2H), 7.60 (d, *J* = 7.4 Hz, 2H), 7.52–7.30 (m, 9H), 7.29–7.09 (m, 3H), 4.84–4.74 (m, 1H), 4.42 (d, *J* = 5.5 Hz, 2H), 3.85–3.53 (m, 3H), 3.23–3.12 (m, 1H), 2.71–2.57 (m, 1H). ¹³C NMR (DMSO-*d*₆): δ 162.69, 156.14, 154.85, 142.41, 137.86, 133.08, 129.26, 129.18, 128.48, 128.03, 125.54, 115.24, 84.65, 59.26, 54.27, 48.49, 45.03, 44.37, 40.66. MS (ESI): *m/z* calcd for C₂₆H₂₆FN₄O₂ [M + H]⁺, 445.52; found, 445.39. T_R = 18.09.

General Procedure for the Synthesis of 35a–e. Enantiomerically pure monosubstituted piperazines **35a–e** were prepared starting from commercial chiral amino-esters following previously reported procedures, and the analytical data for intermediates **33–35a–e** are in agreement with data from the literature.^{19,50} A solution of di-*tert*-butyl dicarbonate (1.1 mmol) in anhydrous THF was added at 0 °C to a solution of compounds **35a–e** (1 mmol) in dry THF (10 mL). The reaction mixture was warmed at room temperature and further

stirred for 1 h. The solvent was removed in vacuo, and the residue was dissolved in CH_2Cl_2 (15 mL) and washed with water (3×10 mL) and brine (1×10 mL). The organic phase was dried over anhydrous Na_2SO_4 and concentrated to dryness. Flash column chromatography on silica gel using a 0.5:9.5 mixture of EtOAc/Pet as the eluent provided the desired compounds with good yields.

(S)-tert-Butyl 4-Benzyl-2-methylpiperazine-1-carboxylate (36a). Colorless oil (192 mg, 66% yield). ^1H NMR (200 MHz, CDCl_3 -d): δ (ppm) 7.41–7.20 (m, 5H), 4.28–4.10 (m, 1H), 3.89–3.73 (m, 1H), 3.63–3.33 (m, 2H), 3.23–3.00 (m, 1H), 2.87–2.67 (m, 1H), 2.67–2.50 (m, 1H), 2.23–1.90 (m, 2H), 1.45 (s, 9H), 1.24 (d, $J = 6.6$ Hz, 3H). MS (ESI): m/z calcd for $\text{C}_{17}\text{H}_{27}\text{N}_2\text{O}_2$ [$\text{M} + \text{H}$] $^+$, 291.42; found, 291.04.

(S)-tert-Butyl 4-Benzyl-2-isopropylpiperazine-1-carboxylate (36b). Colorless oil (223 mg, 70% yield). ^1H NMR (200 MHz, $\text{DMSO}-d_6$): δ (ppm) 7.37–7.17 (m, 5H), 3.88–3.73 (m, 1H), 3.60–3.43 (m, 2H), 3.28 (s, 1H), 3.00–2.70 (m, 3H), 2.40–2.20 (m, 1H), 2.00–1.77 (m, 2H), 1.37 (s, 9H), 0.77–0.70 (m, 6H). MS (ESI): m/z calcd for $\text{C}_{19}\text{H}_{31}\text{N}_2\text{O}_2$ [$\text{M} + \text{H}$] $^+$, 319.47; found, 319.46.

(S)-tert-Butyl 4-Benzyl-2-isobutylpiperazine-1-carboxylate (36c). Colorless oil (239 mg, 72% yield). ^1H NMR (200 MHz, $\text{DMSO}-d_6$): δ (ppm) 7.39–7.17 (m, 5H), 4.00 (br s, 1H), 3.83–3.70 (m, 1H), 3.60–3.47 (m, 1H), 3.31 (s, 1H), 3.03–2.85 (m, 1H), 2.80–2.70 (m, 1H), 2.60–2.50 (m, 1H), 2.00–1.82 (m, 2H), 1.60–1.47 (m, 2H), 1.38 (s, 9H), 1.30–1.20 (m, 1H), 0.88–0.80 (m, 6H). MS (ESI): m/z calcd for $\text{C}_{20}\text{H}_{33}\text{N}_2\text{O}_2$ [$\text{M} + \text{H}$] $^+$, 333.50; found, 333.07.

(S)-tert-Butyl 2,4-Dibenzylpiperazine-1-carboxylate (36d). Colorless oil (136 mg, 37% yield). ^1H NMR (200 MHz, $\text{DMSO}-d_6$): δ (ppm) 7.42–7.22 (m, 5H), 7.22–7.10 (m, 3H), 7.03–6.95 (m, 2H), 4.13–4.00 (m, 1H), 3.87–3.72 (m, 1H), 3.63–3.52 (m, 1H), 3.27–3.16 (m, 1H), 3.00–2.73 (m, 4H), 2.60 (m, 1H), 2.10–1.83 (m, 2H), 1.26 (s, 9H). MS (ESI): m/z calcd for $\text{C}_{23}\text{H}_{31}\text{N}_2\text{O}_2$: [$\text{M} + \text{H}$] $^+$, 367.51; found, 367.02.

(S)-tert-Butyl 4-Benzyl-2-phenylpiperazine-1-carboxylate (36e). Colorless oil (229 mg, 65% yield). ^1H NMR (200 MHz, $\text{DMSO}-d_6$): δ (ppm) 7.34–7.18 (m, 10 H), 5.17–5.06 (m, 1H), 3.90–3.73 (m, 1H), 3.60–3.44 (m, 2H), 3.30–3.20 (m, 1H), 3.00–2.83 (m, 1H), 2.83–2.70 (m, 1H), 2.37–2.25 (m, 1H), 2.13–1.93 (m, 1H), 1.39 (s, 9H). MS (ESI): m/z calcd for $\text{C}_{22}\text{H}_{29}\text{N}_2\text{O}_2$ [$\text{M} + \text{H}$] $^+$, 353.49; found, 353.45.

General Procedure for the Synthesis of 37a–e. TMEDA (2.7 mmol) was added under an argon atmosphere at room temperature to a stirring solution of 36a–e (1 mmol) in freshly distilled THF (5 mL). After cooling at -78 °C, *sec*-BuLi (2.7 mmol) was added, and the reaction solution was allowed to reach -30 °C over 2 h. A solution of benzophenone (2 mmol) in THF (5 mL) was added, and the reaction mixture was left stirring at -30 °C for 30 min, then slowly warmed to room temperature, and stirred for 18 h. The reaction was quenched with a saturated solution of NH_4Cl (15 mL), and the solvents were concentrated under vacuum to half volume giving a residue, which was extracted with EtOAc (3×15 mL). The organic layers were combined, dried over Na_2SO_4 , and the solvent was removed under vacuum. The resulting crude product was purified by flash column chromatography on silica gel using a 1:9 mixture of EtOAc/Pet as the eluent.

(5S,8aR)-7-Benzyl-5-methyl-1,1-diphenylhexahydro-3H-oxazolo[3,4-a]pyrazin-3-one (37a). Yellow oil (100 mg, 25% yield). ^1H NMR (200 MHz, CDCl_3): δ (ppm) 7.56–7.44 (m, 2H), 7.44–7.20 (m, 13H), 4.70 (d, $J = 9.1$ Hz, 1H), 4.15–4.01 (m, 1H), 3.60–3.45 (m, 1H), 3.33–3.22 (m, 1H), 2.63–2.47 (m, 2H), 2.11–1.97 (m, 1H), 1.62–1.50 (m, 2H), 1.39–1.29 (m, 2H). MS (ESI): m/z calcd for $\text{C}_{26}\text{H}_{27}\text{N}_2\text{O}_2$ [$\text{M} + \text{H}$] $^+$, 399.51; found, 399.44.

(5S,8aR)-7-Benzyl-5-isopropyl-1,1-diphenylhexahydro-3H-oxazolo[3,4-a]pyrazin-3-one (37b). Colorless oil (77 mg, 18% yield). ^1H NMR (200 MHz, CDCl_3): δ (ppm) 7.70–7.60 (m, 2H), 7.60–7.14 (m, 13H), 4.73–4.40 (m, 1H), 3.70–3.03 (m, 3H), 2.91–2.70 (m, 1H), 2.61–2.47 (m, 1H), 2.34–2.18 (m, 1H), 1.94–1.91 (m, 1H), 1.27–1.22 (m, 1H), 0.79 (s, 3H), 0.78 (s, 3H). MS (ESI): m/z calcd for $\text{C}_{28}\text{H}_{31}\text{N}_2\text{O}_2$ [$\text{M} + \text{H}$] $^+$, 427.57; found, 427.48.

(5S,8aR)-7-Benzyl-5-isobutyl-1,1-diphenylhexahydro-3H-oxazolo[3,4-a]pyrazin-3-one (37c). Yellow oil (79 mg, 18% yield). ^1H NMR (200 MHz, CDCl_3): δ (ppm) 7.57–7.47 (m, 2H), 7.43–7.29 (m, 13H), 4.76–4.64 (m, 1H), 4.06–3.86 (m, 1H), 3.56–3.47 (m, 1H), 3.27–3.16 (m, 1H), 2.69–2.25 (m, 2H), 2.11–1.98 (m, 1H), 1.65–1.63 (m, 2H), 1.03–0.89 (m, 2H), 0.86 (dd, $J = 6.5, 3.7$ Hz, 6H). MS (ESI): m/z calcd for $\text{C}_{29}\text{H}_{33}\text{N}_2\text{O}_2$ [$\text{M} + \text{H}$] $^+$, 441.60; found, 441.46.

(5S,8aR)-5,7-Dibenzyl-1,1-diphenylhexahydro-3H-oxazolo[3,4-a]pyrazin-3-one (37d). Yellow oil (247 mg, 52% yield). ^1H NMR (200 MHz, CDCl_3): δ (ppm) 7.46–7.44 (m, 2H), 7.39–7.27 (m, 13H), 7.15–7.08 (m, 3H), 7.01–6.94 (m, 2H), 4.77 (dd, $J = 11.1, 3.3$ Hz, 1H), 4.19–4.07 (m, 1H), 3.54 (d, $J = 12.9$ Hz, 1H), 3.23 (d, $J = 12.9$ Hz, 1H), 3.12–2.98 (m, 2H), 2.63 (d, $J = 11.5$ Hz, 2H), 1.95 (dd, $J = 11.7, 3.9$ Hz, 1H), 1.73–1.60 (m, 1H). MS (ESI): m/z calcd for $\text{C}_{32}\text{H}_{31}\text{N}_2\text{O}_2$ [$\text{M} + \text{H}$] $^+$, 475.61; found, 475.35.

(5S,8aR)-7-Benzyl-1,1,5-triphenylhexahydro-3H-oxazolo[3,4-a]pyrazin-3-one (37e). $\text{C}_{31}\text{H}_{28}\text{N}_2\text{O}_2$ (88 mg, 19% yield); ^1H NMR (400 MHz, CDCl_3): δ (ppm) 7.61–7.58 (m, 2H), 7.37–7.28 (m, 6H), 7.24–6.88 (m, 11H), 3.84–3.75 (m, 1H), 3.55–3.38 (m, 2H), 3.32–3.29 (m, 2H), 2.96–2.80 (m, 1H), 2.64–2.47 (m, 1H), 2.35–2.20 (m, 1H), 1.36–1.22 (m, 1H). MS (ESI): m/z calcd for $\text{C}_{31}\text{H}_{29}\text{N}_2\text{O}_2$ [$\text{M} + \text{H}$] $^+$, 461.59; found, 461.49.

General Procedure for the Synthesis of 38a–e. 9-Fluorenylmethoxycarbonyl chloride (FmocCl, 1.1 mmol) was added to a solution of 37a–e (1 mmol) in CH_3CN (5 mL). The reaction solution was heated at 90 °C for 5 h and then stirred at room temperature for 18 h. The solvent was evaporated giving a residue that was dissolved in EtOAc (15 mL), and the resulting organic phase was washed with water (3×10 mL), dried over anhydrous Na_2SO_4 , and concentrated to dryness. All crude residues were finally purified via flash column chromatography on silica gel using a 1:4 mixture of EtOAc/Pet as the eluent.

(9H-Fluoren-9-yl)methyl (5S,8aR)-5-Methyl-3-oxo-1,1-diphenyltetrahydro-3H-oxazolo[3,4-a]pyrazine-7(1H)-carboxylate (38a). White solid (440 mg, 83% yield); ^1H NMR (400 MHz, DMSO): δ (ppm) 7.97–7.84 (m, 3H), 7.47–7.22 (m, 13H), 7.06–6.93 (m, 2H), 5.02–4.91 (m, 1H), 4.51–4.33 (m, 2H), 4.33–4.21 (m, 1H), 4.13–4.05 (m, 1H), 3.11–3.00 (m, 1H), 3.00–2.87 (m, 1H), 2.87–2.75 (m, 1H), 2.33–2.11 (m, 1H), 0.87–0.79 (d, $J = 7.2$ Hz, 3H); ^{13}C NMR (400 MHz, DMSO): δ 154.61, 144.05, 141.94, 140.67, 137.74, 128.64, 128.46, 127.86, 127.60, 127.54, 127.07, 127.00, 125.43, 124.95, 120.02, 84.15, 64.96, 55.01, 47.27, 46.36, 45.96, 45.02, 24.02. MS (ESI): m/z calcd for $\text{C}_{34}\text{H}_{31}\text{N}_2\text{O}_4$ [$\text{M} + \text{H}$] $^+$, 531.63; found, 531.52.

(9H-Fluoren-9-yl)methyl (5S,8aR)-5-Isopropyl-3-oxo-1,1-diphenyltetrahydro-3H-oxazolo[3,4-a]pyrazine-7(1H)-carboxylate (38b). White solid (318 mg, 57% yield); ^1H NMR (400 MHz, CDCl_3): δ (ppm): 7.87–7.73 (m, 2H), 7.64–7.16 (m, 14H), 7.07–6.96 (m, 2H), 5.29–5.20 (dd, 1H), 4.56–4.40 (m, 1H), 4.24–4.11 (m, 2H), 3.40–3.16 (m, 1H), 2.80–2.64 (m, 1H), 2.26–2.01 (m, 1H), 1.81–1.56 (m, 2H), 1.16–1.04 (m, 1H), 0.94 (d, $J = 6.4$ Hz, 3H), 0.62 (d, $J = 6.8$ Hz, 3H); ^{13}C NMR (400 MHz, CDCl_3): δ 155.96, 144.29, 143.23, 142.11, 141.41, 138.79, 138.02, 128.61, 127.96, 127.85, 127.18, 125.64, 125.34, 124.56, 120.00, 119.63, 84.87, 64.89, 57.60, 56.77, 48.27, 46.09, 43.89, 25.64, 19.98, 19.47. MS (ESI): m/z calcd for $\text{C}_{36}\text{H}_{35}\text{N}_2\text{O}_4$ [$\text{M} + \text{H}$] $^+$, 559.69; found, 559.57.

(9H-Fluoren-9-yl)methyl (5S,8aR)-5-Isobutyl-3-oxo-1,1-diphenyltetrahydro-3H-oxazolo[3,4-a]pyrazine-7(1H)-carboxylate (38c). White solid (309 mg, 54% yield). ^1H NMR (400 MHz, CDCl_3): δ (ppm): 7.78–7.75 (m, 2H), 7.64–7.16 (m, 14H), 7.07–6.96 (m, 2H), 5.29–5.20 (m, 1H), 4.56–4.40 (m, 1H), 4.24–4.11 (m, 2H), 3.40–3.16 (m, 1H), 2.80–2.64 (m, 1H), 2.26–2.01 (m, 1H), 1.81–1.56 (m, 2H), 1.40–1.23 (m, 2H), 1.16–1.04 (m, 1H), 0.98–0.91 (d, $J = 6.4$ Hz, 3H), 0.67–0.60 (d, $J = 6.8$ Hz, 3H). MS (ESI): m/z calcd for $\text{C}_{37}\text{H}_{37}\text{N}_2\text{O}_4$ [$\text{M} + \text{H}$] $^+$, 573.71; found, 573.73.

(9H-Fluoren-9-yl)methyl (5S,8aR)-5-Benzyl-3-oxo-1,1-diphenyltetrahydro-3H-oxazolo[3,4-a]pyrazine-7(1H)-carboxylate (38d). White solid (376 mg, 62% yield). ^1H NMR (400 MHz, CDCl_3): δ (ppm) 7.84–7.71 (m, 2H), 7.71–7.01 (m, 21H), 5.22–5.11 (m, 1H),

4.63–4.47 (m, 2H), 4.26–4.15 (m, 1H), 4.13–3.89 (m, 2H), 3.42–3.31 (m, 1H), 2.89–2.82 (m, 1H), 2.82–2.61 (m, 1H), 2.61–2.44 (m, 1H), 2.27–2.00 (m, 1H). MS (ESI): m/z calcd for $C_{40}H_{35}N_2O_4$ $[M + H]^+$, 607.73; found, 607.49.

(9*H*-Fluoren-9-yl)methyl (5*S*,8*aR*)-3-Oxo-1,1,5-triphenyltetrahydro-3*H*-oxazolo[3,4-*a*]pyrazine-7(1*H*)-carboxylate (**38e**). White solid (350 mg, 59% yield); 1H NMR (400 MHz, $CDCl_3$): δ (ppm) 7.95–6.88 (m, 23H), 5.10–4.98 (m, 1H), 4.68–4.52 (m, 1H), 4.40–4.30 (m, 1H), 4.30–4.18 (m, 1H), 4.18–4.09 (m, 1H), 3.83–3.78 (m, 1H), 3.78–3.67 (m, 1H), 2.93–2.73 (m, 2H). MS (ESI): m/z calcd for $C_{39}H_{33}N_2O_4$ $[M + H]^+$, 593.70; found, 593.50.

General Procedure for the Synthesis of Final Compounds 17–21. 4-Fluorobenzyl isocyanate (2 mmol) and DBU (1.2 mmol) were sequentially added at room temperature to a stirring solution of **38a–e** (1 mmol) in anhydrous THF (5 mL). The reaction solution was stirred for 2 h and then it was quenched with a saturated solution of NH_4Cl (10 mL). The mixture was concentrated under vacuum to half volume and the aqueous phase was extracted with EtOAc (3 \times 15 mL). The organic layers were combined, dried over Na_2SO_4 , and concentrated in vacuum. The desired products were purified by preparative RP-HPLC.

(5*S*,8*aR*)-*N*-(4-Fluorobenzyl)-5-methyl-3-oxo-1,1-diphenyltetrahydro-1*H*-oxazolo[3,4-*a*]pyrazine-7(3*H*)-carboxamide (**17**). White solid (225 mg, 49% yield); mp 153–156 $^{\circ}C$; 1H NMR (400 MHz, DMSO- d_6): δ (ppm) 7.57–7.55 (m, 2H), 7.44–7.25 (m, 11H), 7.14–7.09 (m, 2H), 4.70 (dd, $J = 11.3, 3.8$ Hz, 1H), 4.28–4.14 (m, 2H), 3.98–3.84 (m, 2H), 3.79 (d, $J = 13.7$ Hz, 1H), 2.87 (dd, $J = 13.7, 3.9$ Hz, 1H), 2.15–2.01 (m, 1H), 1.15 (d, $J = 6.9$ Hz, 3H). ^{13}C NMR (DMSO- d_6): δ 162.12, 157.39, 154.69, 142.36, 138.46, 136.92, 128.83, 128.75, 128.55, 128.40, 128.24, 127.84, 125.61, 125.35, 114.83, 114.62, 84.82, 55.76, 46.83, 46.11, 45.45, 42.80, 15.33. MS (ESI): m/z calcd for $C_{26}H_{27}FN_3O_3$ $[M + H]^+$, 460.53; found, 460.49. $T_R = 23.10$. $[\alpha]_D^{22} = +1059.13$ (c 0.023).

(5*S*,8*aR*)-*N*-(4-Fluorobenzyl)-5-isopropyl-3-oxo-1,1-diphenyltetrahydro-1*H*-oxazolo[3,4-*a*]pyrazine-7(3*H*)-carboxamide (**18**). White solid (229 mg, 47% yield); mp 186–187 $^{\circ}C$; 1H NMR (400 MHz, DMSO- d_6): δ (ppm) 7.65 (d, $J = 7.5$ Hz, 2H); 7.43–7.38 (m, 6H); 7.35–7.28 (m, 2H); 7.28–7.20 (m, 3H); 7.13–7.08 (m, 2H); 4.67 (dd, $J = 11.2, 3.9$ Hz, 1H); 4.19 (dd, $J = 15.1, 5.4$ Hz, 2H); 4.01 (d, $J = 14.2$ Hz, 1H); 3.71 (dd, $J = 12.8, 3.6$ Hz, 1H); 3.26 (dd, $J = 12.3, 3.8$ Hz, 1H); 2.88 (dd, $J = 13.8, 3.9$ Hz, 1H); 2.36–2.21 (m, 1H); 1.93–1.76 (m, 1H); 0.92 (d, $J = 6.6$ Hz, 3H); 0.60 (d, $J = 6.6$ Hz, 3H). ^{13}C NMR (DMSO- d_6): δ 162.11, 159.71, 157.18, 155.27, 142.90, 138.34, 136.94, 128.82, 128.75, 128.50, 128.43, 128.15, 127.79, 125.25, 125.17, 114.80, 114.59, 84.77, 57.01, 56.58, 45.15, 43.05, 42.82, 26.10, 19.47, 18.98. MS (ESI): m/z calcd for $C_{29}H_{31}FN_3O_3$ $[M + H]^+$, 488.58; found, 488.54. $T_R = 26.07$. $[\alpha]_D^{22} = +1058.5$ (c 0.012).

(5*S*,8*aR*)-*N*-(4-Fluorobenzyl)-5-isobutyl-3-oxo-1,1-diphenyltetrahydro-1*H*-oxazolo[3,4-*a*]pyrazine-7(3*H*)-carboxamide (**19**). White solid (100 mg, 20% yield); mp 216–219 $^{\circ}C$; 1H NMR (400 MHz, DMSO- d_6): δ (ppm) 7.61–7.55 (m, 2H), 7.42–7.07 (m, 13H), 4.69 (dd, $J = 11.1, 3.6$ Hz, 1H), 4.29–4.13 (m, 3H), 3.85–3.75 (m, 2H), 2.91 (dd, $J = 13.6, 3.9$ Hz, 1H), 2.17 (m, 1H), 1.63–1.52 (m, 1H), 1.40–1.23 (m, 2H), 0.80 (d, $J = 6.4$ Hz, 3H), 0.76 (d, $J = 6.8$ Hz, 3H). ^{13}C NMR (DMSO- d_6): δ 162.12, 157.29, 155.77, 155.01, 142.58, 138.36, 136.94, 128.96, 128.85, 128.78, 128.44, 128.19, 127.79, 125.42, 125.28, 115.13, 114.96, 114.75, 114.57, 84.79, 55.89, 48.69, 45.99, 45.16, 42.75, 37.37, 24.13, 22.64, 21.65. MS (ESI): m/z calcd for $C_{30}H_{33}FN_3O_3$ $[M + H]^+$, 502.61; found, 502.40. $T_R = 26.28$. $[\alpha]_D^{22} = +794.29$ (c 0.022).

(5*S*,8*aR*)-*N*-(4-Fluorobenzyl)-5-benzyl-3-oxo-1,1-diphenyltetrahydro-1*H*-oxazolo[3,4-*a*]pyrazine-7(3*H*)-carboxamide (**20**). White solid (134 mg, 25% yield); mp 95–98 $^{\circ}C$; 1H NMR (400 MHz, DMSO- d_6): δ (ppm) 7.51–7.48 (m, 2H); 7.43–7.25 (m, 11H); 7.16–7.04 (m, 7H); 4.87 (dd, $J = 11.2, 3.7$ Hz, 1H); 4.29–4.18 (m, 2H); 4.03–3.99 (m, 1H); 3.94–3.88 (m, 1H); 3.82 (dd, $J = 13.1, 3.2$ Hz, 1H); 2.99–2.79 (m, 3H); 2.26–2.14 (m, 1H). ^{13}C NMR (DMSO- d_6): δ 162.12, 159.73, 157.43, 154.95, 142.44, 138.22, 137.71, 136.86, 128.96, 128.85, 128.37, 128.29, 128.05, 127.93,

127.79, 126.05, 125.57, 125.33, 114.82, 114.61, 84.76, 56.42, 52.19, 45.66, 45.35, 42.87, 34.85. MS (ESI): m/z calcd for $C_{33}H_{31}FN_3O_3$ $[M + H]^+$, 536.63; found, 536.38. $T_R = 26.10$. $[\alpha]_D^{23} = +539.8$ (c 0.024).

(5*S*,8*aR*)-*N*-(4-Fluorobenzyl)-3-oxo-1,1,5-triphenyltetrahydro-1*H*-oxazolo[3,4-*a*]pyrazine-7(3*H*)-carboxamide (**21**). White solid (83 mg, 16% yield); mp 105–107 $^{\circ}C$; 1H NMR (400 MHz, DMSO- d_6): δ (ppm) 7.63 (d, $J = 7.9$ Hz, 2H); 7.50 (t, $J = 7.7$ Hz, 2H); 7.39 (t, $J = 7.1$ Hz, 1H); 7.24 (t, $J = 6.9$ Hz, 2H); 7.15–6.99 (m, 11H); 6.97–6.88 (m, 2H); 5.03 (d, $J = 13.9$ Hz, 1H); 4.17–4.06 (m, 2H); 3.75–3.62 (m, 2H); 2.85–2.80 (m, 1H), 2.71–2.55 (m, 2H). ^{13}C NMR (DMSO- d_6): δ 162.04, 159.64, 155.95, 139.25, 138.42, 136.73, 134.11, 128.60, 128.01, 127.42, 125.92, 125.61, 114.69, 114.47, 87.97, 71.18, 47.37, 42.64, 42.11. MS (ESI): m/z calcd for $C_{32}H_{29}FN_3O_3$ $[M + H]^+$, 522.60; found, 522.46. $T_R = 26.72$. $[\alpha]_D^{23} = +8.8$ (c 0.025).

Pharmacology. Calcium Mobilization Assay. HEK293_{mNPSR} cells were generated as previously described³ and maintained in DMEM supplemented with 10% fetal bovine serum, 2 mM L-glutamine, and hygromycin B (100 mg/L) and cultured at 37 $^{\circ}C$ in 5% CO_2 humidified air. HEK293_{mNPSR} cells were seeded at a density of 50,000 cells/well into poly-D-lysine coated 96-well black, clear-bottom plates. The following day, the cells were incubated with medium supplemented with 2.5 mM probenecid, 3 μ M of the calcium sensitive fluorescent dye Fluo-4 AM, and 0.01% pluronic acid, for 30 min at 37 $^{\circ}C$. After that time, the loading solution was aspirated and 100 μ L/well of assay buffer (Hanks' balanced salt solution; HBSS) supplemented with 20 mM 4-(2-hydroxyethyl)-1-piperazineethanesulfonic acid (HEPES), 2.5 mM probenecid, and 500 μ M Brilliant Black (Sigma-Aldrich) was added. Concentrated solution (1 mM) of NPS was made in bidistilled water and kept at -20 $^{\circ}C$. Concentrated solutions (10 mM) of NPSR antagonists were made in DMSO and kept at -20 $^{\circ}C$. Serial dilutions were carried out in HBSS/HEPES (20 mM) buffer (containing 0.02% bovine serum albumin fraction V). After placing both plates (cell culture and master plate) into the fluorometric imaging plate reader FlexStation II (Molecular Devices, Sunnyvale, CA), fluorescence changes were measured. On-line additions were carried out in a volume of 50 μ L/well. To facilitate drug diffusion into the wells in antagonist type experiments, the present studies were performed at 37 $^{\circ}C$, and three cycles of mixing (25 μ L from each well moved up and down 3 times) were performed immediately after antagonist injection to the wells. Inhibition response curves were determined against the stimulatory effect of 10 nM NPS. Additionally, the concentration–response curve to NPS has been tested in the absence and in the presence of 100 nM of **1**, compound **16**, and compound **21** (Figure 3). NPSR antagonists were injected into the wells 24 min before adding NPS.

Mouse Locomotor Activity Test. All animal care and experimental procedures conformed with the European Communities Council Directives (2010/63/EU) and national regulations (D.L. 26/2014). Studies involving animals are reported in accordance with the ARRIVE guidelines.⁵¹ This study was approved by the Italian Ministry of Health (authorization number 120/2014-PR). The experiments were performed with CD-1 mice (2–4 month old, from the Laboratory for Preclinical Research (LARP) of the University of Ferrara, Italy). Mice were housed under standard conditions (22 $^{\circ}C$, 55% humidity, 12 h light/dark cycle, light on at 7:00 am), with free access to food and water. Appropriate environmental enrichment was present in each cage. Mice were killed with CO_2 overdose. Each animal was used only once. Experiments were performed during the light cycle (between 09.00 and 13.00) according to Guerrini et al. (2009).⁴² For *in vivo* studies, **1**, **16**, and **21** were solubilized in water containing 1% DMSO and 10% Cremophor EL (Sigma-Aldrich). NPS was solubilized in saline solution. Vehicle, **1**, **16**, and **21** were injected by the ip route 30 min before saline or NPS injection. NPS or saline were given by the i.c.v. route 15 min before the beginning of the test and the locomotor activity was recorded for 30 min. The i.c.v. injections (2 μ L/mouse) were given under light (just enough to produce loss of the righting reflex) isoflurane anesthesia into the left ventricle according to the procedure described by Laursen and Belknap (1986)⁵² and routinely adopted in our laboratory. For these

experiments, the ANY-maze video tracking system was used (Ugo Basile, application version 4.52c Beta). Mice were positioned in a square plastic cage (40 × 40 cm), one mouse per cage. Four mice were monitored in parallel. Mouse horizontal activity was monitored by a camera while vertical activity was measured by an infrared beam array. The parameters measured were cumulative distance traveled (total distance in m that the animal traveled during the test), immobility time (the animal is considered immobile when 90% of it remains in the same place for a minimum of 2.5 s), and the number of rearings (the number of beam breaks due to the vertical movements; this input is triggered only when the beam is interrupted for at least 200 ms). Previous studies performed under the present experimental conditions demonstrated that NPS stimulated locomotor activity in a dose-dependent way;⁴² from these studies, the dose of 0.1 nmol was selected as the lower dose inducing statistically significant effects.

Data Analysis and Terminology. Data are expressed as means ± standard error of the mean (SEM) of *n* experiments. Nonlinear regression analysis using GraphPad Prism software (v.4.0) allowed logistic iterative fitting of the resultant responses and the calculation of agonist potencies and maximal effects. Agonist potency was expressed as pEC₅₀, which is the negative logarithm to base 10 of the agonist molar concentration that produces 50% of the maximal possible effect of that agonist. In inhibition response experiments (i.e., increasing concentrations of antagonist vs a fixed concentration of agonist), the antagonist potency was expressed as pK_B, derived from the following equation

$$K_B = IC_{50} / (2 + ([A] / EC_{50})^{1/n} - 1)$$

where IC₅₀ is the concentration of antagonist that produces 50% inhibition of the agonist response, [A] is the concentration of agonist, EC₅₀ is the concentration of agonist producing a 50% maximal response, and *n* is the Hill coefficient of the concentration–response curve to the agonist. When the concentration–response curve to NPS has been tested in the absence and in the presence of antagonists, the antagonist potency was expressed as pA₂, derived from the following equation

$$pA_2 = -\log[(CR - 1) / [A]]$$

where CR means the ratio between agonist potency in the presence and absence of antagonist and [A] the molar concentration of the antagonist.

In vivo data are expressed as mean ± SEM of *n* animals. Data were analyzed using two-way ANOVA, followed by Bonferroni's post-hoc test. Differences were considered statistically significant when *p* < 0.05.

Molecular Modeling. hNPSR Model Construction. The query sequence of the hNPSR in its I107 variant (Q6W5P4, FASTA format) was downloaded from the Universal Protein Resource.⁵³ BLAST (Basic Local Alignment Search Tool) was used to search the homologous sequences to be used as template structures. The sequences of templates were obtained from the Uniprot web server. The human C5a anaphylatoxin chemotactic receptor 1 (P21730, PDB 6C1R),⁵⁴ the human κ opioid receptor (P41145, PDB 4DJH),³³ the human M2 muscarinic receptor (P08172, PDB 5ZKC),⁵⁵ the human neuropeptide Y Y1 Receptor (Q15761, PDB 5ZBH),²⁹ the human orexin-1 receptor (O43613, PDB 6TOD),⁵⁶ and the human type-2 angiotensin receptor (P50052, PDB 4ZUD)³⁸ were chosen as the templates. The sequence identity and coverage between hNPSR and the six templates are reported in Table S1 along with the phylogenetic tree (Figure S3) and pairwise sequence alignments (Figures S4–S9). The choice of templates was dictated by the resolution and sufficient similarity sequence coverage with the target. The alignments reported in Figures S4–S9 were used to build six hNPSR models using the Prime module within Schrödinger (Prime; Schrödinger, LLC, version 2020-1). The X-ray structures of the templates were obtained from the Protein Data Bank. Homology built models were obtained using the knowledge-based method. Validation of the model was carried by generating the Ramachandran plots for each model. This analysis

allowed supporting the viability of the constructed models that all had >90% of the residues in the allowed regions of the plot.

Docking Calculations. Docking calculations were attained employing the Glide tool implemented in Maestro 12.4.⁵⁷ The 3D structures of 1, 3–5, 7, 10, 12, and 14–21 were generated with the Maestro fragment Build tool and then energetically minimized with Macro-model.⁵⁸ The 6 models were all prepared through the Protein Preparation Wizard of the Maestro 12.4 graphical user interface, which assigns bond orders, adds hydrogen atoms, and generates appropriate protonation states.

The docking grid box was centered on the residues lining the putative binding orthosteric binding, with a grid box dimension equal to 31 Å × 31 Å × 31 Å. Finally, docking runs were carried out using the standard precision method. Pictures were rendered employing UCSF Chimera software.⁵⁹

MD Simulation System Setup. The complexes obtained from docking experiments of 1, 16, and 21 in both BM1 and BM2 employing the hNPSR model built using the human neuropeptide Y Y1 receptor (hNPY1R, PDB code 5ZBH) structure as a template were used to build an MD simulation system. The complex was embedded in a membrane of phosphatidylcholine lipids⁶⁰ using Maestro's system builder and was located in the membrane using the default parameters. Next, the system was solvated in an orthorhombic water box with a buffer distance of 10 Å.⁶¹ The system was neutralized with 9 Cl[−] ions for the complexes with 1 and 21 while 10 Cl[−] ions were included in the 16/hNPSR complexes. The salt concentration was set to 0.15 M NaCl. The OPLS3 force field was used for the constructed receptor/ligand/membrane system.⁶²

MD Simulation Protocols. The Desmond module within the Schrödinger suite was used for MD simulations.^{63–65} First, the system was relaxed using the following relaxation protocol for membrane proteins:

1. minimization with restraints on all solute-heavy atoms;
2. unrestrained minimization;
3. Brownian Dynamics in NVT ensemble (constant number of particles, constant volume, constant temperature of 300 K) using small timesteps and restraints on solute heavy atoms (50 kcal/mol) at 10 K for 50 ps;
4. NPT ensemble simulation (constant number of particles, constant pressure of 1 bar, and constant temperature of 100 K) Gaussian barrier potential on water molecules, membrane restrained in *z*, protein restrained (20 kcal/mol) for 20 ps;
5. NPγT ensemble simulation (constant number of particles, constant pressure of 1 bar, constant temperature of 100 K, and lateral surface tension of membranes) Gaussian Barrier potential on water molecules, membrane restrained in *z*, protein restrained (10 kcal/mol) for 100 ps;
6. NPγT ensemble simulation with increasing temperature from 100 to 300 K, Gaussian Barrier potential on water molecules, and gradual release of restraints for 150 ps.
7. NVT production run (constant number of particles, constant volume, and constant temperature of 300 K) without any restraint for 100 ps.

After the relaxation, 100 ns production runs were conducted under the NPγT ensemble for each of the six systems using the default protocol. In detail, the temperature was controlled using the Nosé–Hoover thermostat^{66,67} with a coupling constant of 1.0 ps. The pressure was controlled using the Martyna–Tuckerman–Klein barostat^{68,69} with a coupling constant of 2.0 ps. The cutoff distance for short-range nonbonded interactions was 9 Å, and the long-range van der Waals interactions were based on a uniform density approximation. To minimize the computation time, nonbonded forces were calculated using an r-RESPA integrator⁷⁰ where the short-range forces were updated every two steps and the long-range forces were updated every six steps. The trajectories were saved at 100.0 ps. The Desmond SID tool was used to analyze the receptor–ligand interactions during the MD trajectory. Particular attention was given to ligand–residue interactions and ligand RMSF.

■ ASSOCIATED CONTENT

Supporting Information

The Supporting Information is available free of charge at <https://pubs.acs.org/doi/10.1021/acs.jmedchem.0c02223>.

¹H NMR and NOE NMR analyses of compound **17**; sequence identity and coverage between the hNPSR and selected hGPCRs; phylogenetic tree of the hNPSR and the six selected template structures; pairwise sequence alignments of the hNPSR and the six selected template structures; ligand-root-mean-square fluctuation of compounds **1**, **16**, and **21**; and ligand–NPSR interactions for compounds **1**, **16**, and **21** (PDF)

Molecular formula strings (CSV)

3D coordinates of the energy-minimized docked pose of **1** in the constructed model of NPSR during MD simulation in BM1 (PDB)

3D coordinates of the energy-minimized docked pose of **1** in the constructed model of NPSR during MD simulation in BM2 (PDB)

3D coordinates of the energy-minimized docked pose of **16** in the constructed model of NPSR during MD simulation in BM1 (PDB)

3D coordinates of the energy-minimized docked pose of **16** in the constructed model of NPSR during MD simulation in BM2 (PDB)

3D coordinates of the energy-minimized docked pose of **21** in the constructed model of NPSR during MD simulation in BM1 (PDB)

3D coordinates of the energy-minimized docked pose of **21** in the constructed model of NPSR during MD simulation in BM2 (PDB)

■ AUTHOR INFORMATION

Corresponding Authors

Sandro Cosconati – “DiSTABiF”, Università della Campania “Luigi Vanvitelli”, 81100 Caserta, Italy; orcid.org/0000-0002-8900-0968; Email: sandro.cosconati@unicampania.it

Salvatore Pacifico – Department of Chemical, Pharmaceutical and Agricultural Sciences, University of Ferrara, 44121 Ferrara, Italy; orcid.org/0000-0002-3377-5107; Email: salvatore.pacifico@unife.it

Authors

Valentina Albanese – Department of Chemical, Pharmaceutical and Agricultural Sciences, University of Ferrara, 44121 Ferrara, Italy

Chiara Ruzza – Department of Neuroscience and Rehabilitation, Section of Pharmacology, University of Ferrara, 44121 Ferrara, Italy; LTTA Laboratory for Advanced Therapies, Technopole of Ferrara, 44121 Ferrara, Italy

Erika Marzola – Department of Chemical, Pharmaceutical and Agricultural Sciences, University of Ferrara, 44121 Ferrara, Italy

Tatiana Bernardi – Department of Chemical, Pharmaceutical and Agricultural Sciences, University of Ferrara, 44121 Ferrara, Italy

Martina Fabbri – Department of Chemical, Pharmaceutical and Agricultural Sciences, University of Ferrara, 44121 Ferrara, Italy

Anna Fantinati – Department of Chemical, Pharmaceutical and Agricultural Sciences, University of Ferrara, 44121 Ferrara, Italy

Claudio Trapella – Department of Chemical, Pharmaceutical and Agricultural Sciences, University of Ferrara, 44121 Ferrara, Italy; LTTA Laboratory for Advanced Therapies, Technopole of Ferrara, 44121 Ferrara, Italy

Rainer K. Reinscheid – Institute of Pharmacology and Toxicology, Jena University Hospital, Friedrich Schiller University, 07747 Jena, Germany; Institute of Physiology I, University Hospital Münster, University of Münster, 48149 Münster, Germany

Federica Ferrari – Department of Neuroscience and Rehabilitation, Section of Pharmacology, University of Ferrara, 44121 Ferrara, Italy

Chiara Sturaro – Department of Neuroscience and Rehabilitation, Section of Pharmacology, University of Ferrara, 44121 Ferrara, Italy

Girolamo Calò – Department of Pharmaceutical and Pharmacological Sciences, University of Padova, 35131 Padova, Italy

Giorgio Amendola – “DiSTABiF”, Università della Campania “Luigi Vanvitelli”, 81100 Caserta, Italy; orcid.org/0000-0003-4271-5031

Remo Guerrini – Department of Chemical, Pharmaceutical and Agricultural Sciences, University of Ferrara, 44121 Ferrara, Italy; LTTA Laboratory for Advanced Therapies, Technopole of Ferrara, 44121 Ferrara, Italy

Delia Preti – Department of Chemical, Pharmaceutical and Agricultural Sciences, University of Ferrara, 44121 Ferrara, Italy; orcid.org/0000-0002-1075-3781

Complete contact information is available at: <https://pubs.acs.org/doi/10.1021/acs.jmedchem.0c02223>

Author Contributions

^VV.A and C.R. contributed equally to the work. All authors have given approval to the final version of the manuscript.

Notes

The authors declare no competing financial interest.

■ ACKNOWLEDGMENTS

D.P., C.R., G.C., and R.G. were supported by the FAR (Fondo di Ateneo per la Ricerca Scientifica) grants from the University of Ferrara; C.R. was supported by a FIR (Fondo per l’Incentivazione alla Ricerca) grant from the University of Ferrara. For the determination of optical rotations, the authors thank Dr. Julie Oble, Sorbonne Université, Faculté des Sciences et Ingénierie, Campus Pierre et Marie Curie, Institut Parisien de Chimie Moléculaire.

■ ABBREVIATIONS

BLAST, Basic Local Alignment Search Tool; BM, binding mode; Boc₂O, di-*tert*-butyl dicarbonate; CL_{95%}, 95% confidence limit; CCR9, CC chemokine receptor type 9; CXCR4, chemokine receptor type 4; DMEM, Dulbecco’s modified Eagle’s medium; ECL, extracellular loop; EtOAc, ethyl acetate; FmocCl, Fmoc chloride; HBSS, Hanks’ balanced salt solution; HEPES, 4-(2-hydroxyethyl)-1-piperazineethanesulfonic acid; hNPY1R, human neuropeptide Y Y1 receptor; NPS, neuropeptide S; NPSR, neuropeptide S receptor; NTSR1, neurotensin receptor 1; OX1R, orexin receptor type 1; PAR1, protease-activated receptor 1; PEt, petroleum ether; *p*-TsOH,

p-toluenesulfonic acid; RMSF, root-mean-square fluctuation; *sec*-BuLi, *sec*-butyllithium; SEM, standard error of the mean; TM, transmembrane

REFERENCES

- (1) Syuji, S.; Yasushi, S.; Nobuyuki, M.; Koji, Y. cDNA and protein sequence of a novel human and animal G protein-coupled receptors and their uses in drug screening, diagnosis, and therapeutics. WO2002031145A1, April 18, 2002.
- (2) Xu, Y.-L.; Reinscheid, R. K.; Huitron-Resendiz, S.; Clark, S. D.; Wang, Z.; Lin, S. H.; Brucher, F. A.; Zeng, J.; Ly, N. K.; Henriksen, S. J.; de Lecea, L.; Civelli, O. Neuropeptide S: a neuropeptide promoting arousal and anxiolytic-like effects. *Neuron* **2004**, *43*, 487–497.
- (3) Reinscheid, R. K.; Xu, Y.-L.; Okamura, N.; Zeng, J.; Chung, S.; Pai, R.; Wang, Z.; Civelli, O. Pharmacological characterization of human and murine neuropeptide S receptor variants. *J. Pharmacol. Exp. Ther.* **2005**, *315*, 1338–1345.
- (4) Xu, Y.-L.; Gall, C. M.; Jackson, V. R.; Civelli, O.; Reinscheid, R. K. Distribution of neuropeptide S receptor mRNA and neurochemical characteristics of neuropeptide S-expressing neurons in the rat brain. *J. Comp. Neurol.* **2007**, *500*, 84–102.
- (5) Clark, S. D.; Duangdao, D. M.; Schulz, S.; Zhang, L.; Liu, X.; Xu, Y.-L.; Reinscheid, R. K. Anatomical characterization of the neuropeptide S system in the mouse brain by in situ hybridization and immunohistochemistry. *J. Comp. Neurol.* **2011**, *519*, 1867–1893.
- (6) Guerrini, R.; Salvadori, S.; Rizzi, A.; Regoli, D.; Calo', G. Neurobiology, pharmacology, and medicinal chemistry of neuropeptide S and its receptor. *Med. Res. Rev.* **2010**, *30*, 751–777.
- (7) Ruzza, C.; Calò, G.; Di Maro, S.; Pacifico, S.; Trapella, C.; Salvadori, S.; Preti, D.; Guerrini, R. Neuropeptide S receptor ligands: a patent review (2005-2016). *Expert Opin. Ther. Pat.* **2017**, *27*, 347–362.
- (8) Blough, B.; Namjoshi, O. Small molecule neuropeptide S and melanocortin 4 receptor ligands as potential treatments for substance use disorders. *Handb. Exp. Pharmacol.* **2020**, *258*, 61–87.
- (9) Kohji, F.; Yutaka, N.; Tarui, N.; Masaaki, M.; Hirokazu, M.; Osamu, K.; Hiroshi, B. Bicyclic piperazine compound and use thereof. WO2005021555A1, March 10, 2005.
- (10) Okamura, N.; Habay, S. A.; Zeng, J.; Chamberlin, A. R.; Reinscheid, R. K. Synthesis and pharmacological in vitro and in vivo profile of 3-oxo-1,1-diphenyl-tetrahydro-oxazolo[3,4-*a*]pyrazine-7-carboxylic acid 4-fluoro-benzylamide (SHA 68), a selective antagonist of the neuropeptide S receptor. *J. Pharmacol. Exp. Ther.* **2008**, *325*, 893–901.
- (11) Ruzza, C.; Rizzi, A.; Trapella, C.; Pela', M.; Camarda, V.; Ruggieri, V.; Filafferro, M.; Cifani, C.; Reinscheid, R. K.; Vitale, G.; Ciccocioppo, R.; Salvadori, S.; Guerrini, R.; Calo', G. Further studies on the pharmacological profile of the neuropeptide S receptor antagonist SHA 68. *Peptides* **2010**, *31*, 915–925.
- (12) Li, M. S.; Peng, Y. L.; Jiang, J. H.; Xue, H. X.; Wang, P.; Zhang, P. J.; Han, R. W.; Chang, M.; Wang, R. Neuropeptide S increases locomotion activity through corticotropin-releasing factor receptor 1 in substantia nigra of mice. *Peptides* **2015**, *71*, 196–201.
- (13) Han, R.-W.; Zhang, R.-S.; Xu, H.-J.; Chang, M.; Peng, Y.-L.; Wang, R. Neuropeptide S enhances memory and mitigates memory impairment induced by MK801, scopolamine or A β 1-42 in mice novel object and object location recognition tasks. *Neuropharmacology* **2013**, *70*, 261–267.
- (14) Ruzza, C.; Asth, L.; Guerrini, R.; Trapella, C.; Gavioli, E. C. Neuropeptide S reduces mouse aggressiveness in the resident/intruder test through selective activation of the neuropeptide S receptor. *Neuropharmacology* **2015**, *97*, 1–6.
- (15) Okamura, N.; Garau, C.; Duangdao, D. M.; Clark, S. D.; Jüngling, K.; Pape, H.-C.; Reinscheid, R. K. Neuropeptide S enhances memory during the consolidation phase and interacts with noradrenergic systems in the brain. *Neuropsychopharmacology* **2011**, *36*, 744–752.
- (16) Hassler, C.; Zhang, Y.; Gilmour, B.; Graf, T.; Fennell, T.; Snyder, R.; Deschamps, J. R.; Reinscheid, R. K.; Garau, C.; Runyon, S. P. Identification of neuropeptide S antagonists: structure-activity relationship studies, X-ray crystallography, and in vivo evaluation. *ACS Chem. Neurosci.* **2014**, *5*, 731–744.
- (17) Schmoutz, C. D.; Zhang, Y.; Runyon, S. P.; Goeders, N. E. Antagonism of the neuropeptide S receptor with RTI-118 decreases cocaine self-administration and cocaine-seeking behavior in rats. *Pharmacol. Biochem. Behav.* **2012**, *103*, 332–337.
- (18) Wang, Y.; Sauer, D. R.; Djuric, S. W. A facile and practical one-pot 'catch and release' synthesis of substituted guanidines. *Tetrahedron Lett.* **2009**, *50*, 5145–5148.
- (19) Maity, P.; König, B. Synthesis and structure of 1,4-dipiperazino benzenes: Chiral terphenyl-type peptide helix mimetics. *Org. Lett.* **2008**, *10*, 1473–1476.
- (20) Liu, B.; Xu, G. Y.; Yang, C. H.; Wu, X. H.; Xie, Y. Y. A novel and facile method to synthesize (R)- and (S)-2-methylpiperazine. *Synth. Commun.* **2004**, *34*, 4111–4118.
- (21) Reginato, G.; Di Credico, B.; Andreotti, D.; Mingardi, A.; Paio, A.; Donati, D. A new versatile and diastereoselective synthesis of polysubstituted 2-oxopiperazines from naturally occurring amino acids. *Tetrahedron: Asymmetry* **2007**, *18*, 2680–2688.
- (22) Trapella, C.; Pela, M.; Del Zoppo, L.; Calo, G.; Camarda, V.; Ruzza, C.; Cavazzini, A.; Costa, V.; Bertolasi, V.; Reinscheid, R. K.; Salvadori, S.; Guerrini, R. Synthesis and separation of the enantiomers of the neuropeptide S receptor antagonist (9R/S)-3-oxo-1,1-diphenyl-tetrahydro-oxazolo[3,4-*a*]pyrazine-7-carboxylic acid 4-fluoro-benzylamide (SHA 68). *J. Med. Chem.* **2011**, *54*, 2738–2744.
- (23) Zhang, Y.; Gilmour, B. P.; Navarro, H. A.; Runyon, S. P. Identifying structural features on 1,1-diphenyl-hexahydro-oxazolo[3,4-*a*]pyrazin-3-ones critical for Neuropeptide S antagonist activity. *Bioorg. Med. Chem. Lett.* **2008**, *18*, 4064–4067.
- (24) Yang, Y.; Xu, Z.; Zhang, Z.; Yang, Z.; Liu, Y.; Wang, J.; Cai, T.; Li, S.; Chen, K.; Shi, J.; Zhu, W. Like-charge guanidinium pairing between ligand and receptor: an unusual interaction for drug discovery and design? *J. Phys. Chem. B* **2015**, *119*, 11988–11997.
- (25) Saczewski, F.; Balewski, L. Biological activities of guanidine compounds. *Expert Opin. Ther. Pat.* **2009**, *19*, 1417–1448.
- (26) Saczewski, F.; Balewski, L. Biological activities of guanidine compounds, 2008-2012 update. *Expert Opin. Ther. Pat.* **2013**, *23*, 965–995.
- (27) Dal Ben, D.; Antonini, I.; Buccioni, M.; Lambertucci, C.; Marucci, G.; Vittori, S.; Volpini, R.; Cristalli, G. Molecular modeling studies on the human neuropeptide S receptor and its antagonists. *ChemMedChem* **2010**, *5*, 371–383.
- (28) Okada, T.; Fujiyoshi, Y.; Silow, M.; Navarro, J.; Landau, E. M.; Shichida, Y. Functional role of internal water molecules in rhodopsin revealed by X-ray crystallography. *Proc. Natl. Acad. Sci. U.S.A.* **2002**, *99*, 5982–5987.
- (29) Yang, Z.; Han, S.; Keller, M.; Kaiser, A.; Bender, B. J.; Bosse, M.; Burkert, K.; Kögler, L. M.; Wifling, D.; Bernhardt, G.; Plank, N.; Littmann, T.; Schmidt, P.; Yi, C.; Li, B.; Ye, S.; Zhang, R.; Xu, B.; Larhammar, D.; Stevens, R. C.; Huster, D.; Meiler, J.; Zhao, Q.; Beck-Sickingler, A. G.; Buschauer, A.; Wu, B. Structural basis of ligand binding modes at the neuropeptide Y Y1 receptor. *Nature* **2018**, *556*, 520–524.
- (30) Yin, J.; Babaoglu, K.; Brautigam, C. A.; Clark, L.; Shao, Z.; Scheuermann, T. H.; Harrell, C. M.; Gotter, A. L.; Roecker, A. J.; Winrow, C. J.; Renger, J. J.; Coleman, P. J.; Rosenbaum, D. M. Structure and ligand-binding mechanism of the human OX1 and OX2 orexin receptors. *Nat. Struct. Mol. Biol.* **2016**, *23*, 293–299.
- (31) Wu, B.; Chien, E. Y. T.; Mol, C. D.; Fenalti, G.; Liu, W.; Katritch, V.; Abagyan, R.; Brooun, A.; Wells, P.; Bi, F. C.; Hamel, D. J.; Kuhn, P.; Handel, T. M.; Cherezov, V.; Stevens, R. C. Structures of the CXCR4 chemokine GPCR with small-molecule and cyclic peptide antagonists. *Science* **2010**, *330*, 1066–1071.
- (32) Fenalti, G.; Giguere, P. M.; Katritch, V.; Huang, X.-P.; Thompson, A. A.; Cherezov, V.; Roth, B. L.; Stevens, R. C. Molecular

control of delta-opioid receptor signalling. *Nature* **2014**, *506*, 191–196.

(33) Wu, H.; Wacker, D.; Mileni, M.; Katritch, V.; Han, G. W.; Vardy, E.; Liu, W.; Thompson, A. A.; Huang, X.-P.; Carroll, F. I.; Mascarella, S. W.; Westkaemper, R. B.; Mosier, P. D.; Roth, B. L.; Cherezov, V.; Stevens, R. C. Structure of the human kappa-opioid receptor in complex with JD1c. *Nature* **2012**, *485*, 327–332.

(34) Zhang, C.; Srinivasan, Y.; Arlow, D. H.; Fung, J. J.; Palmer, D.; Zheng, Y.; Green, H. F.; Pandey, A.; Dror, R. O.; Shaw, D. E.; Weis, W. I.; Coughlin, S. R.; Kobilka, B. K. High-resolution crystal structure of human protease-activated receptor 1. *Nature* **2012**, *492*, 387–392.

(35) White, J. F.; Noinaj, N.; Shibata, Y.; Love, J.; Kloss, B.; Xu, F.; Gvozdenovic-Jeremic, J.; Shah, P.; Shiloach, J.; Tate, C. G.; Grisshammer, R. Structure of the agonist-bound neurotensin receptor. *Nature* **2012**, *490*, 508–513.

(36) Shihoya, W.; Nishizawa, T.; Yamashita, K.; Inoue, A.; Hirata, K.; Kadji, F. M. N.; Okuta, A.; Tani, K.; Aoki, J.; Fujiyoshi, Y.; Doi, T.; Nureki, O. X-ray structures of endothelin ETB receptor bound to clinical antagonist bosentan and its analog. *Nat. Struct. Mol. Biol.* **2017**, *24*, 758–764.

(37) Zhang, H.; Unal, H.; Gati, C.; Han, G. W.; Liu, W.; Zatselin, N. A.; James, D.; Wang, D.; Nelson, G.; Weierstall, U.; Sawaya, M. R.; Xu, Q.; Messerschmidt, M.; Williams, G. J.; Boutet, S.; Yefanov, O. M.; White, T. A.; Wang, C.; Ishchenko, A.; Tirupula, K. C.; Desnoyer, R.; Coe, J.; Conrad, C. E.; Fromme, P.; Stevens, R. C.; Katritch, V.; Karnik, S. S.; Cherezov, V. Structure of the angiotensin receptor revealed by serial femtosecond crystallography. *Cell* **2015**, *161*, 833–844.

(38) Zhang, H.; Unal, H.; Desnoyer, R.; Han, G. W.; Patel, N.; Katritch, V.; Karnik, S. S.; Cherezov, V.; Stevens, R. C. Structural basis for ligand recognition and functional selectivity at angiotensin receptor. *J. Biol. Chem.* **2015**, *290*, 29127–29139.

(39) Phillips, J. C.; Braun, R.; Wang, W.; Gumbart, J.; Tajkhorshid, E.; Villa, E.; Chipot, C.; Skeel, R. D.; Kalé, L.; Schulten, K. Scalable molecular dynamics with NAMD. *J. Comput. Chem.* **2005**, *26*, 1781–1802.

(40) Camarda, V.; Ruzza, C.; Rizzi, A.; Trapella, C.; Guerrini, R.; Reinscheid, R. K.; Calo, G. In vitro and in vivo pharmacological characterization of the novel neuropeptide S receptor ligands QA1 and P11. *Peptides* **2013**, *48*, 27–35.

(41) Ruzza, C.; Rizzi, A.; Camarda, V.; Pulga, A.; Marzola, G.; Filafiero, M.; Novi, C.; Ruggieri, V.; Marzola, E.; Vitale, G.; Salvadori, S.; Guerrini, R.; Calo', G. [³H]-Bu-D-Gly⁵]NPS, a pure and potent antagonist of the neuropeptide S receptor: in vitro and in vivo studies. *Peptides* **2012**, *34*, 404–411.

(42) Guerrini, R.; Camarda, V.; Trapella, C.; Calò, G.; Rizzi, A.; Ruzza, C.; Fiorini, S.; Marzola, E.; Reinscheid, R. K.; Regoli, D.; Salvadori, S. Synthesis and biological activity of human neuropeptide S analogues modified in position 5: identification of potent and pure neuropeptide S receptor antagonists. *J. Med. Chem.* **2009**, *52*, 524–529.

(43) Ruzza, C.; Pulga, A.; Rizzi, A.; Marzola, G.; Guerrini, R.; Calo', G. Behavioural phenotypic characterization of CD-1 mice lacking the neuropeptide S receptor. *Neuropharmacology* **2012**, *62*, 1999–2009.

(44) Duangdao, D. M.; Clark, S. D.; Okamura, N.; Reinscheid, R. K. Behavioral phenotyping of neuropeptide S receptor knockout mice. *Behav. Brain Res.* **2009**, *205*, 1–9.

(45) Zhu, H.; Mingler, M. K.; McBride, M. L.; Murphy, A. J.; Valenzuela, D. M.; Yancopoulos, G. D.; Williams, M. T.; Vorhees, C. V.; Rothenberg, M. E. Abnormal response to stress and impaired NPS-induced hyperlocomotion, anxiolytic effect and corticosterone increase in mice lacking NPSR1. *Psychoneuroendocrinology* **2010**, *35*, 1119–1132.

(46) Cannella, N.; Economidou, D.; Kallupi, M.; Stopponi, S.; Heilig, M.; Massi, M.; Ciccocioppo, R. Persistent increase of alcohol-seeking evoked by neuropeptide S: an effect mediated by the hypothalamic hypocretin system. *Neuropsychopharmacology* **2009**, *34*, 2125–2134.

(47) Kallupi, M.; Cannella, N.; Economidou, D.; Ubaldi, M.; Ruggeri, B.; Weiss, F.; Massi, M.; Marugan, J.; Heilig, M.; Bonnavion, P.; de Lecea, L.; Ciccocioppo, R. Neuropeptide S facilitates cue-induced relapse to cocaine seeking through activation of the hypothalamic hypocretin system. *Proc. Natl. Acad. Sci. U.S.A.* **2010**, *107*, 19567–19572.

(48) Paneda, C.; Huitron-Resendiz, S.; Frago, L. M.; Chowen, J. A.; Picetti, R.; Lecea, L. d.; Roberts, A. J. Neuropeptide S reinstates cocaine-seeking behavior and increases locomotor activity through corticotropin-releasing factor receptor 1 in mice. *J. Neurosci.* **2009**, *29*, 4155–4161.

(49) Waring, M. J. Lipophilicity in drug discovery. *Expet Opin. Drug Discov.* **2010**, *5*, 235–248.

(50) Jida, M.; Ballet, S. An efficient one-pot synthesis of chiral N-protected 3-substituted (diketo)piperazines via Ugi-4CR/de-Boc/cyclization Process. *ChemistrySelect* **2018**, *3*, 1027–1031.

(51) Kilkenny, C.; Browne, W.; Cuthill, I. C.; Emerson, M.; Altman, D. G.; Group, N. C. R. R. G. W. Animal research: reporting in vivo experiments: the ARRIVE guidelines. *Br. J. Pharmacol.* **2010**, *160*, 1577–1579.

(52) Laursen, S. E.; Belknap, J. K. Intracerebroventricular injections in mice. Some methodological refinements. *J. Pharmacol. Methods* **1986**, *16*, 355–357.

(53) The Universal Protein Resource (UniProt) databases. <https://www.uniprot.org/> (accessed Sept 15, 2020).

(54) Liu, H.; Kim, H. R.; Deepak, R. N. V. K.; Wang, L.; Chung, K. Y.; Fan, H.; Wei, Z.; Zhang, C. Orthosteric and allosteric action of the C5a receptor antagonists. *Nat. Struct. Mol. Biol.* **2018**, *25*, 472–481.

(55) Suno, R.; Lee, S.; Maeda, S.; Yasuda, S.; Yamashita, K.; Hirata, K.; Horita, S.; Tawaramoto, M. S.; Tsujimoto, H.; Murata, T.; Kinoshita, M.; Yamamoto, M.; Kobilka, B. K.; Vaidehi, N.; Iwata, S.; Kobayashi, T. Structural insights into the subtype-selective antagonist binding to the M2 muscarinic receptor. *Nat. Chem. Biol.* **2018**, *14*, 1150–1158.

(56) Rappas, M.; Ali, A. A. E.; Bennett, K. A.; Brown, J. D.; Bucknell, S. J.; Congreve, M.; Cooke, R. M.; Cseke, G.; de Graaf, C.; Doré, A. S.; Errey, J. C.; Jazayeri, A.; Marshall, F. H.; Mason, J. S.; Mould, R.; Patel, J. C.; Tehan, B. G.; Weir, M.; Christopher, J. A. Comparison of Orexin 1 and Orexin 2 ligand binding modes using X-ray crystallography and computational analysis. *J. Med. Chem.* **2020**, *63*, 1528–1543.

(57) *Schrödinger Release 2020-1: Maestro*; Schrödinger, LLC: New York, NY, 2020.

(58) *Schrödinger Release 2020-1: MacroModel*; Schrödinger, LLC: New York, NY, 2020.

(59) Pettersen, E. F.; Goddard, T. D.; Huang, C. C.; Couch, G. S.; Greenblatt, D. M.; Meng, E. C.; Ferrin, T. E. UCSF Chimera—a visualization system for exploratory research and analysis. *J. Comput. Chem.* **2004**, *25*, 1605–1612.

(60) Lyman, E.; Higgs, C.; Kim, B.; Lupyan, D.; Shelley, J. C.; Farid, R.; Voth, G. A. A role for a specific cholesterol interaction in stabilizing the Apo configuration of the human A_{2A} adenosine receptor. *Structure* **2009**, *17*, 1660–1668.

(61) Mark, P.; Nilsson, L. Structure and dynamics of the TIP3P, SPC, and SPC/E water models at 298 K. *J. Phys. Chem. A* **2001**, *105*, 9954–9960.

(62) Harder, E.; Damm, W.; Maple, J.; Wu, C.; Reboul, M.; Xiang, J. Y.; Wang, L.; Lupyan, D.; Dahlgren, M. K.; Knight, J. L.; Kaus, J. W.; Cerutti, D. S.; Krilov, G.; Jorgensen, W. L.; Abel, R.; Friesner, R. A. OPLS3: A force field providing broad coverage of drug-like small molecules and proteins. *J. Chem. Theory Comput.* **2016**, *12*, 281–296.

(63) Bowers, K. J. C.; Xu, H.; Dror, R. O.; Eastwood, M. P.; Gregersen, B. A.; Klepeis, J. L.; Kolossvary, I.; Moraes, M. A.; Sacerdoti, F. D.; Salmon, J. K.; Shan, Y.; Shaw, D. E. Scalable algorithms for molecular dynamics simulations on commodity clusters. *Proceedings of the ACM/IEEE Conference on Supercomputing (SC06)*, Tampa, Florida, November 11–17, 2006.

(64) *Schrödinger Release 2020-1: Desmond Molecular Dynamics System*; D. E. Shaw Research: New York, NY, 2020.

(65) *Maestro-Desmond Interoperability Tools*; Schrödinger: New York, NY, 2020.

(66) Nosé, S. A molecular-dynamics method for simulations in the canonical ensemble. *Mol. Phys.* **1984**, *52*, 255–268.

(67) Hoover, W. G. Canonical dynamics: equilibrium phase-space distributions. *Phys. Rev. A: At, Mol, Opt. Phys.* **1985**, *31*, 1695–1697.

(68) Martyna, G. J.; Tobias, D. J.; Klein, M. L. Constant-pressure molecular-dynamics algorithms. *J. Chem. Phys.* **1994**, *101*, 4177–4189.

(69) Martyna, G. J.; Tuckerman, M. E.; Tobias, D. J.; Klein, M. L. Explicit reversible integrators for extended systems dynamics. *Mol. Phys.* **1996**, *87*, 1117–1157.

(70) Tuckerman, M.; Berne, B. J.; Martyna, G. J. Reversible multiple time scale molecular dynamics. *J. Chem. Phys.* **1992**, *97*, 1990–2001.

Novel Mixed NOP/Opioid Receptor Peptide Agonists

Salvatore Pacifico, Valentina Albanese, Davide Illuminati, Erika Marzola, Martina Fabbri, Federica Ferrari, Victor A.D. Holanda, Chiara Sturaro, Davide Malfacini, Chiara Ruzza,* Claudio Trapella, Delia Preti,* Ettore Lo Cascio, Alessandro Arcovito, Stefano Della Longa,* Martina Marangoni, Davide Fattori, Romina Nassini, Girolamo Calò, and Remo Guerrini



Cite This: *J. Med. Chem.* 2021, 64, 6656–6669



Read Online

ACCESS |



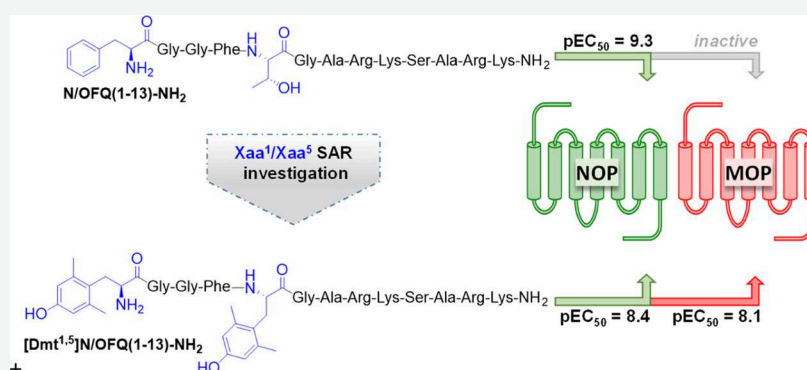
Metrics & More



Article Recommendations



Supporting Information



ABSTRACT: The nociceptin/orphanin FQ (N/OFQ)/N/OFQ receptor (NOP) system controls different biological functions including pain and cough reflex. Mixed NOP/opioid receptor agonists elicit similar effects to strong opioids but with reduced side effects. In this work, 31 peptides with the general sequence [Tyr/Dmt¹,Xaa⁵]N/OFQ(1-13)-NH₂ were synthesized and pharmacologically characterized for their action at human recombinant NOP/opioid receptors. The best results in terms of NOP versus mu opioid receptor potency were obtained by substituting both Tyr¹ and Thr⁵ at the N-terminal portion of N/OFQ(1-13)-NH₂ with the noncanonical amino acid Dmt. [Dmt^{1,5}]N/OFQ(1-13)-NH₂ has been identified as the most potent dual NOP/mu receptor peptide agonist so far described. Experimental data have been complemented by *in silico* studies to shed light on the molecular mechanisms by which the peptide binds the active form of the mu receptor. Finally, the compound exerted antitussive effects in an *in vivo* model of cough.

INTRODUCTION

Nociceptin/orphanin FQ (N/OFQ; FGGFTGARKSAR-KLANQ) is the endogenous ligand of the N/OFQ peptide receptor.^{1,2} N/OFQ and the NOP receptor display high structural homology with peptides and receptors of the opioid family but distinct pharmacology.³ The N/OFQ-NOP receptor system controls several biological functions at both central and peripheral levels including pain transmission, mood and anxiety, food intake, learning and memory, locomotion, cough and micturition reflexes, cardiovascular homeostasis, intestinal motility, and immune responses.⁴

The effects of N/OFQ and selective NOP agonists in analgesimetric assays are complex depending on the dose, administration route, type of pain, and animal species.^{5,6} On the contrary, strong and consistent experimental evidence suggests that the simultaneous activation of NOP and opioid receptors elicits synergistic analgesic effects.^{6,7} On these bases, mixed NOP/opioid receptor agonists (cebranopadol,^{8,9} AT-121,¹⁰ BU10038,¹¹ and BPR1M97¹²) have been developed and investigated for their antinociceptive properties. It was

consistently demonstrated that these drugs elicit similar analgesic effects to strong opioids but with substantially reduced side effects including respiratory depression, tolerance, and abuse liability (see the recent review by Kiguchi *et al.*¹³).

Other ligands targeting multiple opioid receptors have been studied.¹⁴ For example, dual-acting mu agonist/delta antagonist peptidomimetics demonstrated to produce antinociception *in vivo* with reduced tolerance liability compared with morphine.^{15,16} Moreover, mixed kappa agonist/mu partial agonist ligands have been investigated as potential treatment agents for cocaine and other psychostimulant abuses.¹⁷ Finally, mixed kappa agonist/delta antagonist ligands have been developed as

Received: November 27, 2020

Published: May 17, 2021



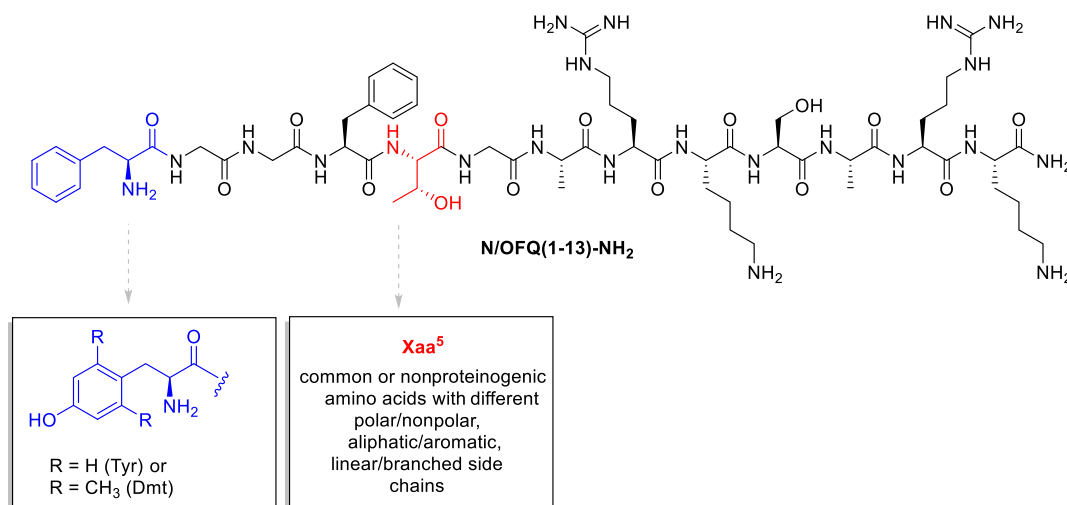


Figure 1. SAR investigation leading to a series of [Tyr/Dmt¹,Xaa⁵]N/OFQ(1-13)-NH₂ peptide derivatives as possible mixed NOP/opioid receptor ligands.

Table 1. Effects of Standard Agonists and a First Series of [Tyr¹,Xaa⁵]N/OFQ(1-13)-NH₂ Derivatives at NOP and mu Opioid Receptors in Calcium Mobilization Studies

		NOP		mu		NOP/mu
		pEC ₅₀ (CL _{95%})	E _{max} ± S.E.M.	pEC ₅₀ (CL _{95%})	E _{max} ± S.E.M.	CR
1	N/OFQ(1-13)NH ₂	9.29 (9.12–9.46)	368 ± 11	inactive		<0.001
2	dermorphin	inactive		7.71 (7.35–8.07)	380 ± 15	>50
3	[Tyr ¹]N/OFQ(1-13)-NH ₂	9.23 (9.07–9.39)	380 ± 11	crc incomplete; 10 μM: 197 ± 69		0.001
4	[Tyr ¹ ,Asn ⁵]N/OFQ(1-13)-NH ₂	8.70 (8.26–9.11)	327 ± 15	crc incomplete; 10 μM: 209 ± 29		0.002
5	[Tyr ¹ ,Val ⁵]N/OFQ(1-13)-NH ₂	8.70 (8.53–8.87)	334 ± 19	crc incomplete; 10 μM: 254 ± 19		0.002
6	[Tyr ¹ ,Lys(Ac ⁵)]N/OFQ(1-13)-NH ₂	8.55 (7.88–9.22)	370 ± 16	crc incomplete; 10 μM: 161 ± 31		0.003
7	[Tyr ¹ ,Abu ⁵]N/OFQ(1-13)-NH ₂	8.15 (7.61–8.69)	366 ± 20	crc incomplete; 10 μM: 213 ± 37		0.007
8	[Tyr ¹ ,Lys ⁵]N/OFQ(1-13)-NH ₂	7.26 (6.74–7.78)	366 ± 6	crc incomplete; 10 μM: 113 ± 35		0.05
9	[Tyr ¹ ,Dap ⁵]N/OFQ(1-13)-NH ₂	7.20 (6.95–7.45)	367 ± 9	crc incomplete; 10 μM: 144 ± 44		0.06
10	[Tyr ¹ ,Dab ⁵]N/OFQ(1-13)-NH ₂	6.43 (6.28–6.58)	340 ± 22	crc incomplete; 10 μM: 41 ± 4		0.37
11	[Tyr ¹ ,Leu ⁵]N/OFQ(1-13)-NH ₂	8.03 (7.46–8.60)	339 ± 24	6.08 (5.95–6.21)	339 ± 25	0.01
12	[Tyr ¹ ,Nle ⁵]N/OFQ(1-13)-NH ₂	8.77 (8.45–9.09)	375 ± 9	6.74 (6.15–7.33)	323 ± 4	0.01
13	[Tyr ¹ ,Nva ⁵]N/OFQ(1-13)-NH ₂	8.43 (7.55–9.31)	358 ± 14	6.25 (5.59–6.91)	313 ± 19	0.007
14	[Tyr ^{1,5}]N/OFQ(1-13)-NH ₂	7.07 (6.68–7.46)	332 ± 19	6.76 (6.34–7.18)	357 ± 21	0.49

tools for the characterization of delta and kappa-opioid receptor phenotypes.¹⁸

With the aim of generating a peptide acting as a nonselective NOP/opioid agonist, we investigated different approaches. On one hand, the peptide [Dmt¹]N/OFQ(1-13)-NH₂ has been identified as a nonselective agonist for NOP and opioid receptors¹⁹ and its tetrabranch derivative, generated using the peptide welding technology (PWT),²⁰ was demonstrated to produce a robust analgesic effect after spinal administration in nonhuman primates. However, this action was sensitive to NOP but not opioid receptor antagonists.²¹ On the other hand, N/OFQ and dermorphin-related peptides were linked together to generate the hetero-tetrabranch derivative H-PWT1-N/OFQ-[Dmt¹]dermorphin²² or the dimeric compound DeNo.²³ Despite its promising *in vitro* pharmacological profile as a mixed NOP/opioid agonist, DeNo was not effective as a spinal analgesic.²³ In the present study, we further investigate the possibility of generating a mixed NOP/opioid agonist based on the following evidence: (i) mixed NOP/kappa ligands can be obtained combining the C-terminal sequence of N/OFQ with the N-terminal of dynorphin A, where amino acids in positions 5 and 6 were particularly important for receptor selectivity;²⁴ (ii)

Thr⁵ in N/OFQ(1-13)-NH₂ can be replaced with several different residues without loss of peptide efficacy and potency at the NOP receptor;²⁵ (iii) the substitution of Phe¹ in N/OFQ with Tyr²⁶ and particularly with Dmt^{19,27,28} increases affinity/potency at classical opioid receptors. Thus, in the present study, 31 peptide derivatives with the general sequence [Tyr/Dmt¹,Xaa⁵]N/OFQ(1-13)-NH₂ were generated and tested for their action at NOP and opioid receptors (Figure 1).

Experimental data have been complemented by an *in silico* study of the binding of [Dmt^{1,5}]N/OFQ(1-9)-NH₂ to the mu receptor. This non-natural peptide has been compared with the agonist peptide DAMGO ([D-Ala², N-MePhe⁴, Gly-ol]-enkephalin) and the N-terminal fragment of N/OFQ (N/OFQ(1-9)-NH₂). The starting point of the computational study was the structure of the activated mu receptor in complex with the agonist peptide DAMGO that has been previously reported by X-ray diffraction and cryo-electron microscopy.^{29,30} The last structure of the complex DAMGO-mu receptor was used as a model, allowing the setup of the two unknown complexes with the selected peptides by molecular docking. Specifically, docking of a flexible ligand to multiple receptor conformations as already applied to the study of NOP agonists and antagonists^{31,32} was

Table 2. Effects of Standard Agonists and [Tyr¹,Xaa⁵]N/OFQ(1-13)-NH₂ Derivatives with Different Aromatic Residues as Xaa⁵ at NOP and mu Opioid Receptors in Calcium Mobilization Studies

		NOP		mu		NOP/mu
		pEC ₅₀ (CL _{95%})	E _{max} ± S.E.M.	pEC ₅₀ (CL _{95%})	E _{max} ± S.E.M.	CR
1	N/OFQ(1-13)-NH ₂	9.40 (9.19–9.61)	288 ± 15	inactive		<0.001
2	dermorphin	inactive		7.83 (7.56–8.11)	306 ± 23	>50
3	[Tyr ¹]N/OFQ(1-13)-NH ₂	9.13 (8.83–9.43)	266 ± 14	crc incomplete; 10 μM: 217 ± 29		0.001
15	[Tyr ¹ ,Phe ⁵]N/OFQ(1-13)-NH ₂	7.72 (7.56–7.87)	242 ± 11	6.41 (5.85–6.97)	315 ± 32	0.05
16	[Tyr ¹ ,His ⁵]N/OFQ(1-13)-NH ₂	7.39 (7.16–7.62)	249 ± 23	crc incomplete; 10 μM: 230 ± 37		0.05
17	[Tyr ¹ ,Trp ⁵]N/OFQ(1-13)-NH ₂	7.27 (7.19–7.35)	288 ± 28	crc incomplete; 10 μM: 193 ± 31		0.07
18	[Tyr ¹ ,hPhe ⁵]N/OFQ(1-13)-NH ₂	8.70 (8.24–9.16)	301 ± 26	crc incomplete; 10 μM: 228 ± 29		0.003
19	[Tyr ¹ ,Phg ⁵]N/OFQ(1-13)-NH ₂	7.57 (7.12–8.02)	293 ± 31	6.81 (6.33–7.29)	287 ± 48	0.17
20	[Tyr ¹ ,p(OCH ₃)Phe ⁵]N/OFQ(1-13)-NH ₂	7.88 (7.81–7.95)	246 ± 18	crc incomplete; 10 μM: 221 ± 49		0.02
21	[Tyr ¹ ,(pF)Phe ⁵]N/OFQ(1-13)-NH ₂	7.31 (6.81–7.81)	311 ± 22	crc incomplete; 10 μM: 256 ± 55		0.06
22	[Tyr ¹ ,(pNO ₂)Phe ⁵]N/OFQ(1-13)-NH ₂	7.31 (6.90–7.72)	305 ± 22	crc incomplete; 10 μM: 192 ± 64		0.06
23	[Tyr ¹ ,Dip ⁵]N/OFQ(1-13)-NH ₂	6.61 (6.13–7.09)	240 ± 26	6.78 (6.28–7.27)	331 ± 32	1.48
24	[Tyr ¹ ,Bip ⁵]N/OFQ(1-13)-NH ₂	6.93 (6.63–7.22)	272 ± 29	crc incomplete; 10 μM: 151 ± 66		0.15
25	[Tyr ¹ ,1NaI ⁵]N/OFQ(1-13)-NH ₂	7.17 (6.82–7.52)	245 ± 16	6.08 (5.67–6.49)	319 ± 31	0.08
26	[Tyr ¹ ,2NaI ⁵]N/OFQ(1-13)-NH ₂	6.82 (6.60–7.04)	266 ± 15	crc incomplete; 10 μM: 244 ± 10		0.19
27	[Tyr ¹ ,(pNH ₂)Phe ⁵]N/OFQ(1-13)-NH ₂	7.52 (7.11–7.93)	274 ± 15	6.43 (5.80–7.05)	329 ± 37	0.08
28	[Tyr ¹ ,Dmt ⁵]N/OFQ(1-13)-NH ₂	7.75 (7.22–8.27)	251 ± 22	6.71 (6.36–7.07)	301 ± 35	0.09

Table 3. Effects of Standard Agonists and [Dmt¹,Xaa⁵]N/OFQ(1-13)-NH₂ Derivatives at NOP and mu Opioid Receptors in Calcium Mobilization Studies

		NOP		mu		NOP/mu
		pEC ₅₀ (CL _{95%})	E _{max} ± S.E.M.	pEC ₅₀ (CL _{95%})	E _{max} ± S.E.M.	CR
1	N/OFQ(1-13)-NH ₂	9.59 (9.30–9.88)	289 ± 34	inactive		<0.001
2	dermorphin	inactive		8.15 (7.97–8.33)	359 ± 18	>100
3	[Tyr ¹]N/OFQ(1-13)-NH ₂	9.15 (8.48–9.82)	236 ± 13	5.80 (5.22–6.38)	251 ± 34	<0.001
29	[Dmt ¹]N/OFQ(1-13)-NH ₂	8.57 (8.26–8.87)	294 ± 22	7.37 (7.12–7.51)	311 ± 20	0.06
30	[Dmt ¹ ,Tyr ⁵]N/OFQ(1-13)-NH ₂	6.91 (6.81–7.01)	304 ± 21	7.81 (7.47–8.15)	410 ± 25	7.94
31	[Dmt ¹ ,Phe ⁵]N/OFQ(1-13)-NH ₂	7.25 (6.69–7.81)	277 ± 28	8.19 (7.71–8.66)	335 ± 22	8.71
32	[Dmt ¹ ,Phg ⁵]N/OFQ(1-13)-NH ₂	6.95 (6.78–7.12)	282 ± 12	8.54 (8.13–8.96)	339 ± 28	39
33	[Dmt ¹ ,1NaI ⁵]N/OFQ(1-13)-NH ₂	7.22 (6.91–7.54)	286 ± 19	7.80 (7.51–8.09)	349 ± 20	3.80
34	[Dmt ¹ ,(pNH ₂)Phe ⁵]N/OFQ(1-13)-NH ₂	7.58 (7.37–7.79)	258 ± 20	7.82 (7.35–8.29)	358 ± 15	1.73
35	[Dmt ^{1,5}]N/OFQ(1-13)-NH ₂	8.39 (8.05–8.72)	270 ± 25	8.08 (7.74–8.42)	354 ± 16	0.49

Table 4. Effects of Standard Agonists and [Dmt^{1,5}]N/OFQ(1-13)-NH₂ at NOP and mu Opioid Receptors in DMR Studies

		NOP		mu		mu/NOP
		pEC ₅₀ (CL _{95%})	E _{max} ± S.E.M.	pEC ₅₀ (CL _{95%})	E _{max} ± S.E.M.	CR
36	N/OFQ	9.37 (8.96–9.79)	209 ± 14	inactive		<0.001
2	dermorphin	inactive		8.92 (8.74–9.10)	151 ± 16	>500
35	[Dmt ^{1,5}]N/OFQ(1-13)-NH ₂	7.71 (6.65–8.76)	223 ± 11	8.64 (8.28–9.01)	202 ± 20	8.51

carried out to provide the best binding pose of the two peptides [Dmt^{1,5}]N/OFQ(1-9)-NH₂ and N/OFQ(1-9)-NH₂. This docking procedure was further challenged by long-lasting molecular dynamics (MD) simulations and compared with an MD simulation of the DAMGO-mu receptor-G_i protein complex to identify the key interactions necessary for a successful nonselective NOP/opioid agonist. Finally, considering that NOP receptor agonists have demonstrated antitussive effects *in vivo*^{33–37} and that opioids are effective drugs currently in use to treat cough,³⁸ the most potent mixed NOP/opioid agonist has been evaluated *in vivo* for its antitussive effects in guinea pigs.

RESULTS

Chemistry. The peptide derivatives reported in Tables 1–4 were prepared through automated Fmoc/*t*Bu-based solid-phase

peptide synthesis (SPPS) on a Rink amide MBHA resin. Commercially available protected amino acids were employed as synthetic precursors of the target peptides except for Fmoc-2',6'-dimethyl-tyrosine (Fmoc-Dmt-OH) that was instead synthesized in analogy to an approach previously published by Wang *et al.*³⁹ (Scheme S1 of the Supporting Information). Specifically, H-Tyr-OH was first esterified to H-Tyr-OMe under standard conditions, and then, the phenolic hydroxyl was protected with a *tert*-butyldimethylsilyl ether moiety before the following coupling with picolinic acid. The latter function worked as a directing group for the subsequent Pd(OAc)₂-catalyzed C–H alkylation with CH₃I and K₂CO₃ allowing the simultaneous and regioselective introduction of two methyl groups at the ortho-positions of the aromatic ring. Then, full deprotection under strongly acidic conditions, followed by treatment with Fmoc-Cl, led to the desired 2',6'-dimethyl

tyrosine scaffold (detailed procedures and analytical characterizations of Fmoc-Dmt-OH and its precursors have been reported in the Supporting Information). The structures of other nonproteinogenic amino acids employed in this work have been depicted in Table S1.

In Vitro Structure–Activity Relationship. N/OFQ(1-13)-NH₂ stimulated calcium mobilization with high potency and maximal effects in cells coexpressing NOP receptors and chimeric G proteins, while being inactive in cells expressing the mu opioid receptor. On the contrary, dermorphin stimulated calcium mobilization with high potency and maximal effects in mu expressing cells, while it was inactive in NOP cells (Table 1). The substitution of Phe¹ with Tyr as in [Tyr¹]N/OFQ(1-13)-NH₂ did not affect NOP potency while promoting a minor increase in mu potency. Thr⁵ in [Tyr¹]N/OFQ(1-13)-NH₂ was replaced with a series of both proteinogenic and non-proteinogenic amino acids with different polar/nonpolar, aliphatic/aromatic, linear/branched side chains with the aim to explore the effect of several structural parameters on the biological activity. The substitution of Thr⁵ with Asn, Val, Lys(Ac) caused a slight (<10-fold) reduction in NOP potency and no modification of mu potency. The same substitution with Abu, Lys, Dap, and Dab induced a larger loss (>10-fold) of NOP potency. The introduction in position 5 of Leu, Nle, and Nva promoted a moderate decrease in NOP potency associated with a significant increase in mu potency. A similar increase in mu potency was achieved with [Tyr^{1,5}]N/OFQ(1-13)-NH₂, which however displayed a larger decrease in NOP potency; thus, the NOP/mu concentration ratio for this peptide was near 1 (Table 1). None of the amino acid substitutions evaluated in Table 1 modified ligand efficacy at both NOP and mu receptors. Based on these results, aromatic residues were selected for further modifications of position 5 of [Tyr¹]N/OFQ(1-13)-NH₂.

As shown in Table 2, 14 compounds with an aromatic residue substituting Thr⁵ in [Tyr¹]N/OFQ(1-13)-NH₂ were assayed in NOP and mu receptor expressing cells. The different amino acids did not modify ligand efficacy but produced different effects on NOP and mu potency. In particular, the NOP potency of these derivatives was in the range of 8.70–6.61, while the mu potency of these compounds was <6 with the exceptions of peptides substituted with Phe, Phg, 1Nal, (pNH₂)Phe, and Dmt (range 6.08–6.81). Then, for further investigation, we selected those sequences showing pEC₅₀ values >7 for the NOP receptor and >6 for the mu receptor associated with an NOP/mu concentration ratio >0.05. These criteria were matched by [Tyr¹]N/OFQ(1-13)-NH₂ derivatives substituted in position 5 with Tyr, Phe, Phg, 1Nal, (pNH₂)Phe, and Dmt.

The third series of peptides was generated by substituting Tyr¹ with Dmt that is known to increase opioid receptor potency.⁴⁰ In fact, as shown in Table 3, [Dmt¹]N/OFQ(1-13)-NH₂ displayed a moderate (10-fold) decrease in NOP potency compared to [Tyr¹]N/OFQ(1-13)-NH₂ associated to a more pronounced increase (approx. 40-fold) in mu potency. The substitution of Thr⁵ of [Dmt¹]N/OFQ(1-13)-NH₂ with the above-mentioned amino acids generated results similar to those obtained with [Tyr¹]N/OFQ(1-13)-NH₂, that is, a slight to moderate decrease in NOP potency associated to a large increase in mu potency. The most exciting result has been obtained with [Dmt^{1,5}]N/OFQ(1-13)-NH₂ that displayed similar and high potency at both NOP and mu receptors.

[Dmt^{1,5}]N/OFQ(1-13)-NH₂ was further evaluated in dynamic mass redistribution (DMR) experiments performed on CHO cells expressing the human NOP and mu receptors. As

summarized in Table 4, N/OFQ elicited a concentration-dependent positive DMR signal in cells expressing the NOP receptor being inactive in mu expressing cells. Opposite results were obtained with dermorphin that behaves as a mu-selective agonist. [Dmt^{1,5}]N/OFQ(1-13)-NH₂ elicited a robust DMR response in both cell lines with similar maximal effects to standard agonists. [Dmt^{1,5}]N/OFQ(1-13)-NH₂ displayed nanomolar potency at both NOP and the mu receptor with a mu/NOP potency ratio of 8.51 (Table 4).

Finally, the agonist properties of [Dmt^{1,5}]N/OFQ(1-13)-NH₂ were evaluated at delta and kappa opioid receptors in calcium mobilization experiments. As shown in Figure 2,

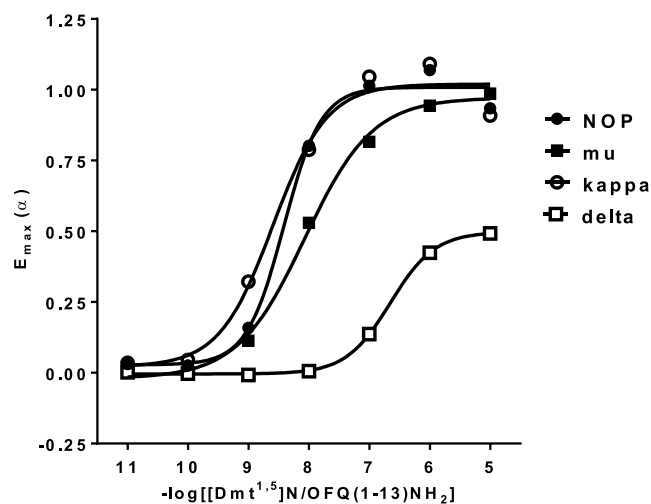


Figure 2. Effects of [Dmt^{1,5}]N/OFQ(1-13)-NH₂ at NOP and classical opioid receptors in calcium mobilization studies.

[Dmt^{1,5}]N/OFQ(1-13)-NH₂ displayed low potency and efficacy at the delta receptor. On the contrary, the peptide showed at the kappa opioid receptor high potency (pEC₅₀ = 8.49) similar to that displayed at NOP (pEC₅₀ = 8.39) and mu (pEC₅₀ = 8.08) receptors. Thus, [Dmt^{1,5}]N/OFQ(1-13)-NH₂ should be classified as a mixed NOP/mu/kappa full agonist.

Molecular Dynamics. As explained in the Experimental Section, MD simulations have been performed setting up nine-residue long peptides (i.e., [Phe/Dmt¹,Thr/Dmt⁵]N/OFQ(1-9)-NH₂) due to the fact that longer peptides lack reliable starting conformations by molecular docking. Moreover, in the following, we will focus on the first five residues of the peptides, those entering the mu opioid receptor orthosteric site, as residues 6–9 represent the more flexible part of the peptides along the MD simulation. The results obtained for [Dmt^{1,5}]N/OFQ(1-9)-NH₂ were compared with those obtained by similar simulations performed on the mu agonist peptide DAMGO and also on N/OFQ(1-9)-NH₂ as a sort of negative control since this peptide lacks mu receptor affinity.²⁶

In Figure 3A, the 3D conformation obtained after docking and MD for [Dmt^{1,5}]N/OFQ(1-9)-NH₂ (colored purple) is superimposed to the known one reported for DAMGO (colored yellow, PDB code 6DDF).³⁰ Subsequent panels (Figure 3B–E) show the main interactions relating to each of the three aromatic residues, that is, Dmt¹, Phe⁴, and Dmt⁵. Furthermore, a general comparison between the results of MD simulations performed on DAMGO (blue), [Dmt^{1,5}]N/OFQ(1-9)-NH₂ (green), and N/OFQ(1-9)-NH₂ (red) is shown in Figure 4. In this figure, patterns of the main receptor-peptide interactions provided are

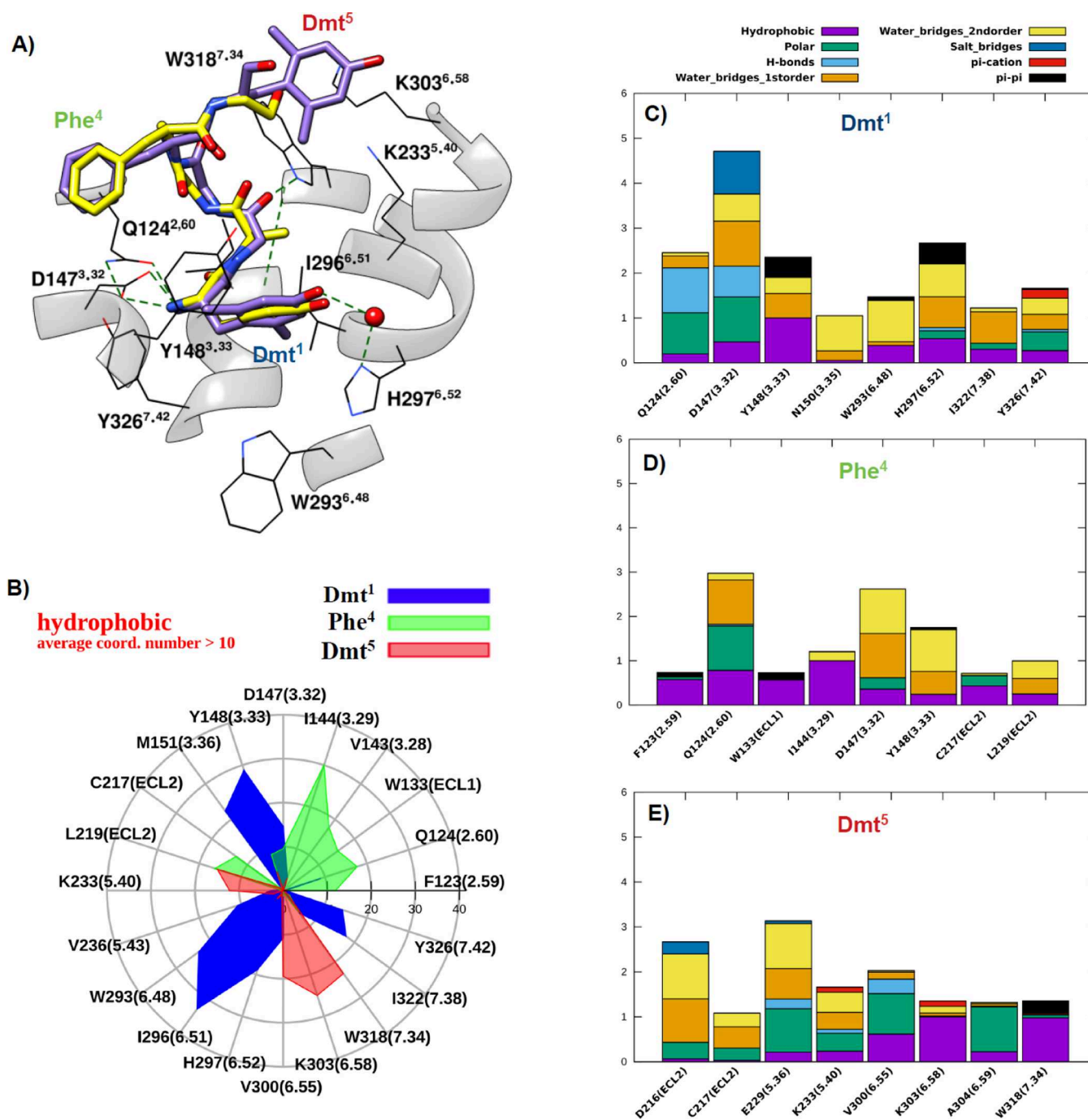
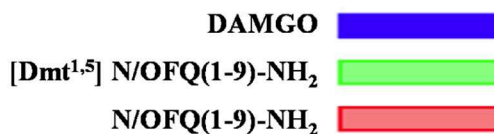
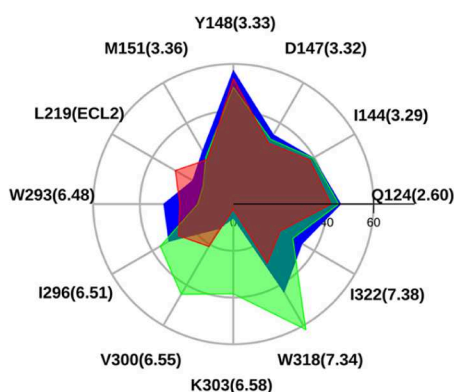


Figure 3. (A) Orthosteric site of [Dmt^{1,5}]N/OFQ(1-9)-NH₂ (colored purple) in the active mu receptor, according to “*in silico*” docking and MD (starting receptor structure from PDB code 6DDF). Only the first five residues are shown. The reported DAMGO conformation (the same PDB code) is superimposed (yellow). (B) Hydrophobic contacts between Dmt¹, Phe⁴, and Dmt⁵ with their neighboring residues. (C–E) Interaction histograms of residues Dmt¹, Phe⁴, and Dmt⁵, respectively, including hydrophobic, polar, H-bonds, water bridges of first and second order, salt bridges, and π -cation and π - π stacking as derived from long-lasting MD.

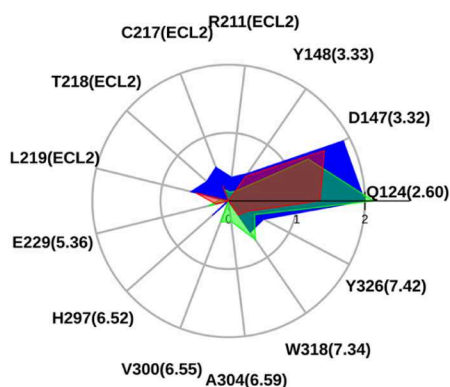
displayed and superimposed, that is, hydrophobic and polar average number of contacts (Figure 4A,B), percentage of formation of hydrogen bonds, and average “strength” of π - π stacking and π -cation interaction (Figure 4C–E, respectively). Accordingly, the representative conformation of [Dmt^{1,5}]N/OFQ(1-9)-NH₂ in the orthosteric site largely overlaps with that of DAMGO (Figure 3A). The N-terminus of Dmt¹ forms salt bridge/hydrogen bond contacts with D¹⁴⁷ (a residue conserved all along the opioid family) similar to both DAMGO and the morphinan agonist BU72 (PDB code 5C1M).²⁹ MD

simulations show that this important interaction is strongly stabilized by the presence of another conserved residue, Q¹²⁴ (TM2), whose nitrogen and oxygen side-chain atoms reinforce the hydrogen bond network by contacts with both the carboxyl oxygen of D¹⁴⁷ and the N-terminus of Dmt¹. Moreover, water bridges fill the small remaining volume between the D¹⁴⁷ and Q¹²⁴ side chains and the backbone donor/acceptors of Dmt¹, Gly³, and Gly², with the latter being in direct H-bond with W³¹⁸ of TM7.

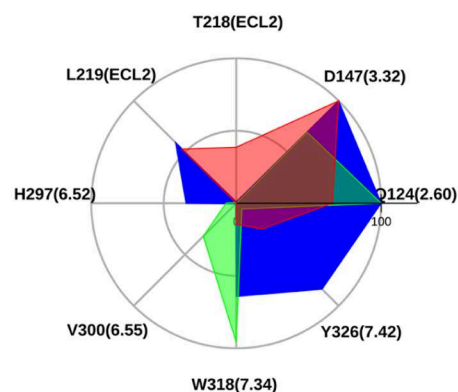
A) **hydrophobic**
average coord. number > 25



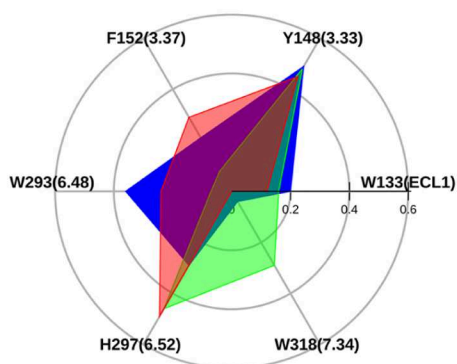
B) **polar**
average coord. number > 0.3



C) **H-bonds**
percentage > 25%



D) **pi-pi stacking**
strength > 0.2



E) **pi-cation**
strength > 0.05

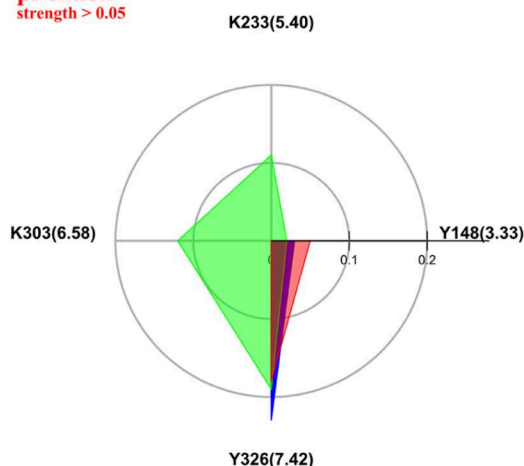


Figure 4. Maps of hydrophobic (A), polar (B), H-bond (C), π - π stacking (D), and π -cation (E) interactions between the mu receptor and the studied ligands along MD trajectories. Only residues 1–5 are considered for [Dmt^{1,5}]N/OFQ(1-9)-NH₂ and N/OFQ(1-9)-NH₂.

Dmt¹ is also in direct hydrophobic contact with TM6 residues (W²⁹³, H²⁹⁷, and especially I²⁹⁶, Figure 3B,C). Along the MD trajectories, its aromatic head moves alternating first- and second-order water bridges with H²⁹⁷ of TM6 (Figure 3C). Partial π - π stacking between the Dmt¹ and H297 rings is also observed during the simulations. Hydrophobic, π -stacking, and water bridge contacts between Dmt¹ and Y¹⁴⁸ (TM3), H²⁹⁷ and W²⁹³ (TM6) frequently occur (Figure 3C). The latter residue, in

the so-called receptor polar cavity, is thought to be very important for the activation mechanism in many class A GPCRs, and these interactions, although not fully stable, could contribute to stabilize the receptor active state.

The formation of alternating second-order water bridges (along 78% of the trajectory) shows that the N-terminus of Dmt¹, together with D¹⁴⁷, is also in contact with N¹⁵⁰ (Figure 3C), an important conserved residue that in the reported high-

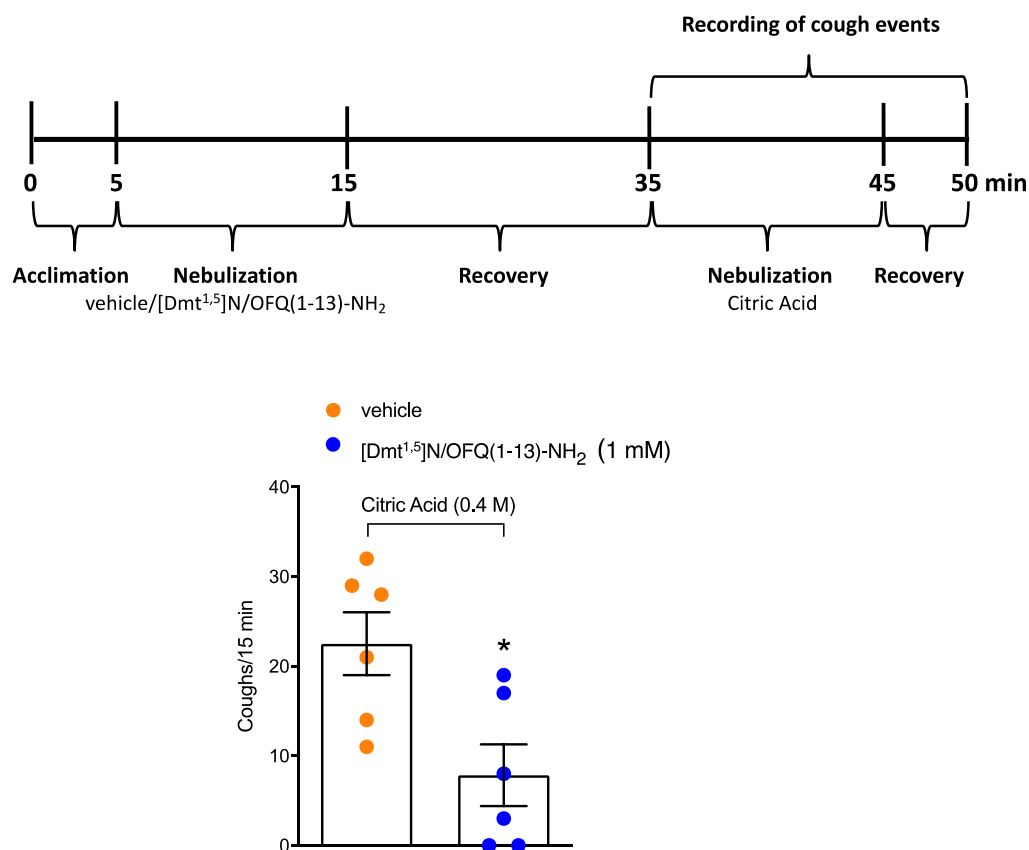


Figure 5. Effect of [Dmt^{1.5}]N/OFQ(1-13)-NH₂ on citric acid-induced cough in conscious guinea pigs. Schematic representation of the experimental procedure for the cough measurement in conscious guinea pigs and pooled data of cough number after [Dmt^{1.5}]N/OFQ(1-13)-NH₂ (1 mM) or vehicle (0.9% NaCl) nebulization, 30 min before the nebulization of the tussive agent, citric acid (0.4 M). Values are the mean \pm SEM of the numbers of coughs/15 min, with data points overlaid ($n = 6$ guinea pigs for each condition). * $p < 0.05$ vs vehicle, Student's t -test.

resolution structure of the inactive delta receptor⁴¹ is shown to connect the orthosteric site to the sodium pocket in the central part of the receptor.

While Dmt¹ interacts with both TM3 (more than 40 contacts with residues Y¹⁴⁸ and M¹⁵¹) and TM6 (about 80 contacts with residues W²⁹³, I²⁹⁶, and H²⁹⁷), Phe⁴ is immersed in the same hydrophobic pocket as the phenyl group of DAMGO between TM2 (residues F¹²³ and Q¹²⁴) and TM3 (residues V¹⁴³ and I¹⁴⁴) (Figure 3B,D), still participating with its amidic nitrogen and water bridges to the main hydrogen bond network linking the peptide to D¹⁴⁷ and Q¹²⁴ (Figure 3D).

The Dmt⁵ peptide residue mainly interacts with residues not conserved within the opiate family, that is, E²²⁹ and K²³³ of TM5, V³⁰⁰, and K³⁰³ of TM6, and W³¹⁸ of TM7. Movements of this ring allow an alternation of nonpolar interactions with the aliphatic chains of K³⁰³ (TM6) and K²³³ (TM5) (Figure 3B) and of possible π -cation interactions with the positively charged amine of both the same K residues (Figure 3E). Similarly, the amidic oxygens of Gly³, Dmt⁵, and Gly⁶ alternate in H-bond or water bridge contacts with R²¹¹ (ECL2) and E²²⁹ (TM5) on two opposite sides of the receptor.

Details on the MD simulations of DAMGO and [Dmt^{1.5}]N/OFQ(1-9)-NH₂ in complex with the mu receptor are given in Figures S1 and S2, reporting the root-mean-square deviation (RMSD) analyses and clustering outcomes for each of the investigated peptides. Moreover, the RMSD analysis (Figure S3) and the representative conformation of residues 1–5 of N/OFQ(1-9)-NH₂ (purple) are shown, compared to DAMGO (yellow). MD shows that the interactions of N/OFQ(1-9)-NH₂

with TM6 are strongly diminished; in addition to the absence of polar contacts and the water density between residues 1–5 of the peptide and TM6, there are only about 20 nonpolar contacts (between Phe¹ and W²⁹³ and between Phe¹ and F²³⁶), while both polar and nonpolar interactions with TM3 increase.

In Figure 4, the maps of hydrophobic, polar, hydrogen bond, π - π stacking, and π -cation interactions for the peptides under study are superimposed for an overall immediate comparison. The hydrophobic and polar interaction maps are widely superimposable on all peptides (Figure 4A,B), attesting the similarity of their conformation inside the orthosteric site, with an increase of nonpolar contacts between [Dmt^{1.5}]N/OFQ(1-9)-NH₂ and TM6 (I²⁹⁶, V³⁰⁰, and K³⁰³) essentially due to the aromatic ring of Dmt⁵. The N-terminus of all three peptides forms hydrogen bonds with D¹⁴⁷ and Q¹²⁴ (Figure 4C). More interestingly, according to our simulation, the H-bond contact reported in the crystal structure between the amidic oxygen of Gly³ of DAMGO and the indole nitrogen of W³¹⁸ is not fully stable; in the same time, the phenolic head of Tyr¹ tends to extend toward the so-called “polar cavity” between Y³²⁶ and W²⁹³ in the intracellular side (Figure S1C), with the possibility to form π -stacking with W²⁹³ (Figure 4D) and a H-bond besides a π -cation contact between its N-terminus and the phenol group of Y³²⁶. On the other hand, the H-bond between Gly² of [Dmt^{1.5}]N/OFQ(1-9)-NH₂ and W³¹⁸ remains quite stable, as reinforced by partial π -stacking between W³¹⁸ and Dmt⁵ (Figures 3E and 4D), while the Dmt¹ phenolic head, sterically hindered by the two methyl groups, does not extend toward the polar cavity. Concerning N/OFQ(1-9)-NH₂, Phe¹ has

negligible hydrogen and water bond contacts with the inner side of the receptor, and the contacts between Phe⁴, Thr⁵ of the peptide and T²¹⁸, L²¹⁹ of extracellular loop 2 (ECL2) are stronger (Figure 4C). The N-terminus of the three peptides can form π -cation interactions with the aromatic ring of Y³²⁶, while as mentioned above, π -cation contributions due to interactions of K²³³ and K³⁰³ are exclusive of [Dmt^{1,5}]N/OFQ(1-9)-NH₂ (Figure 4E).

In Vivo Experiments: [Dmt^{1,5}]N/OFQ(1-13)-NH₂ Effect on Citric Acid-Induced Cough in the Conscious Guinea Pig. To test the antitussive effect of [Dmt^{1,5}]N/OFQ(1-13)-NH₂, we used a model of cough induced by citric acid in guinea pigs. Data showed that the coadministration of [Dmt^{1,5}]N/OFQ(1-13)-NH₂ with citric acid did not affect the tussive response (coughs/15 min: vehicle = 17.83 ± 3.95 vs [Dmt^{1,5}]N/OFQ(1-13)-NH₂ 17.67 ± 1.73). However, the nebulization with [Dmt^{1,5}]N/OFQ(1-13)-NH₂ before (30 min) the challenge with the tussive agent significantly reduced the cough number induced by citric acid (Figure 5).

DISCUSSION

This structure activity investigation was aimed at the identification of novel peptides acting as mixed NOP/mu receptor agonists. To this aim, we substituted Phe¹ of N/OFQ(1-13)-NH₂ with amino acids containing a phenol moiety and Thr⁵ with several proteinogenic and nonproteinogenic residues. Novel peptides were investigated in calcium mobilization experiments performed in cells expressing the human recombinant receptors and chimeric G proteins. The structure activity investigation led to the identification of the potent mixed agonist [Dmt^{1,5}]N/OFQ(1-13)-NH₂ whose NOP and mu agonist properties were confirmed in DMR studies. Moreover, [Dmt^{1,5}]N/OFQ(1-13)-NH₂ was also able to potently stimulate kappa but not delta opioid receptors. The capability of this peptide to bind the mu receptor has been also investigated in MD studies that suggested a similar active conformation for [Dmt^{1,5}]N/OFQ(1-13)-NH₂ and DAMGO and crucial interactions with D¹⁴⁷ and H²⁹⁷. Moreover, the binding of [Dmt^{1,5}]N/OFQ(1-13)-NH₂ is reinforced by additional polar interactions of Dmt⁵ with K²²³ and K³⁰³. Finally, [Dmt^{1,5}]N/OFQ(1-13)-NH₂ elicited a robust antitussive action *in vivo* in a model of cough induced by nebulization of citric acid in conscious guinea pigs.

Previous studies demonstrated that the substitution of Phe¹ in N/OFQ with Tyr reduces NOP selectivity over opioid receptors^{26,42} and that Thr⁵ of N/OFQ(1-13)-NH₂ can be substituted with different amino acids with no changes in peptide efficacy and relatively little modifications of potency.²⁵ Thus, we selected a series of amino acids to substitute Thr⁵ in [Tyr¹]N/OFQ(1-13)-NH₂ in order to increase the mu receptor activity of the peptide derivatives. The results obtained with [Tyr¹]N/OFQ(1-13)-NH₂ derivatives were similar to those previously obtained with N/OFQ(1-13)-NH₂ derivatives in terms of NOP receptor activity. As far as the mu receptor is concerned, an increase in potency has been obtained with Leu, Nle, Nva, and Tyr. These results are not unexpected since Leu in position 5 is found in naturally occurring opioid ligands (Leu-enkephalin and dynorphin) and Nle (and possibly Nva) may mimic methionine, which is also present in position 5 of other endogenous opioid peptides (Met-enkephalin, beta-endorphin). In addition, the same can be said for Tyr⁵, which is found in amphibian opioid peptides such as the mu-selective agonist dermorphin. Moreover, previous studies demonstrated that

position 5 of enkephalin can be replaced with aromatic residues⁴³ or non-natural aliphatic residues⁴⁴ with no major changes of bioactivity. Interestingly, [Tyr^{1,5}]N/OFQ(1-13)-NH₂ displayed very similar potency at NOP and the mu opioid receptor; thus, with the aim to identify potent mixed NOP/mu agonists, further studies were performed substituting position 5 with aromatic amino acids.

Despite the investigation of 14 chemically different aromatic residues, no clear structure activity information was obtained. In fact, with the exception of hPhe⁵, little changes in NOP potency were measured and the same can be said for mu receptor activity. Thus, for further studies, we selected compounds matching the following criteria: pEC₅₀ > 7 for the NOP receptor and >6 for the mu receptor, with NOP/mu ratio > 0.05. This let us to select Tyr, Phe, Phg, 1Nal, (pNH₂)Phe, and Dmt to be substituted in position 5 of [Dmt¹]N/OFQ(1-13)-NH₂.

The opioid receptor binding enhancing properties of Dmt in position 1^{19, 27, 28} were confirmed by the present results. In fact, compared to [Tyr¹]N/OFQ(1-13)-NH₂, [Dmt¹]N/OFQ(1-13)-NH₂ displayed approximately 3-fold reduced potency at NOP associated with almost 100-fold increased potency at the mu receptor. The same pattern of effects, that is, no change or modest reduction of NOP potency associated with a large increase in mu potency was obtained with [Dmt¹]N/OFQ(1-13)-NH₂ derivatives substituted in position 5 with Tyr, Phe, Phg, 1Nal, and (pNH₂)Phe. [Dmt^{1,5}]N/OFQ(1-13)-NH₂ is however the exception to this rule; in fact, this peptide displayed, compared to [Tyr¹,Dmt⁵]N/OFQ(1-13)-NH₂, increased potency at both NOP and mu receptors. This led to an NOP/mu ratio of potency of [Dmt^{1,5}]N/OFQ(1-13)-NH₂ near 1. Interestingly, a very similar NOP/mu ratio was displayed by [Tyr^{1,5}]N/OFQ(1-13)-NH₂, which was however approximately 30-fold less potent at both receptors.

The calcium mobilization assay used in the present study has been previously set up^{45,46} in our laboratories and then validated by investigating a large number of NOP and opioid receptor ligands.^{19,23,47} However, this assay is based on the aberrant signaling generated by the expression of chimeric G proteins; therefore, we reassessed the pharmacological effects of [Dmt^{1,5}]N/OFQ(1-13)-NH₂ with the DMR assay. This test measures the physiological G_i-dependent signaling of NOP and opioid receptors as demonstrated by its sensitivity to pertussis toxin treatment.^{48,49} DMR studies confirmed the mixed mu/NOP full agonist properties of [Dmt^{1,5}]N/OFQ(1-13)-NH₂.

Finally, the effects of [Dmt^{1,5}]N/OFQ(1-13)-NH₂ at kappa and delta opioid receptors were investigated. At delta receptors, [Dmt^{1,5}]N/OFQ(1-13)-NH₂ displayed low potency and efficacy, while it behaved as a potent full agonist at the kappa receptor. Of note, the kappa potency of [Dmt^{1,5}]N/OFQ(1-13)-NH₂ was similar to that shown at NOP and mu receptors. These results were not unexpected. In fact, binding experiments performed in guinea-pig brain membranes demonstrated the following rank order of affinity for [Tyr¹]N/OFQ(1-13)-NH₂: NOP > mu = kappa > delta.²⁶ Moreover, similar results have been previously obtained in functional studies performed with human recombinant receptors with [Dmt¹]N/OFQ(1-13)-NH₂ that displayed the following rank order of potency: NOP = mu > kappa > delta.¹⁹ Collectively, these findings indicate that modifications of position 1 of N/OFQ such as Tyr and Dmt are sufficient for increasing mu and kappa but not delta receptor binding. Most probably, this is due to the fact that the C-terminal portion of N/OFQ is enriched in positively charged

residues that may favor mu and kappa interactions but are detrimental for delta receptor binding.⁵⁰

To get insights into the mechanisms by which [Dmt^{1,5}]N/OFQ(1-13)-NH₂ binds the mu receptor, MD studies were performed using the recently solved DAMGO-mu receptor-G_i complex.³⁰ The results obtained with [Dmt^{1,5}]N/OFQ(1-9)-NH₂ were compared with those of DAMGO and N/OFQ(1-9)-NH₂ used as the positive and negative control, respectively. These studies show that beyond the pivotal and expected interaction between the [Dmt^{1,5}]N/OFQ(1-9)-NH₂ N-terminus and D¹⁴⁷, the phenol oxygen of Dmt¹ can make first- or second-order water bridges with H²⁹⁷ (Gln in NOP) of TM6 of the mu receptor. This is in good agreement with the observation of a water bridge between the agonist BU72 and H²⁹⁷ in the active mu receptor and other small molecules or peptide mimetic agonists of kappa and delta receptors³⁰ and can account for the reduction of NOP selectivity and the increase of mu potency as simply induced by the presence of the phenol groups of Tyr¹ or Dmt¹ in N/OFQ instead of the phenyl group of Phe¹. Partial π - π stacking between Dmt¹ (or Tyr¹) and H297 could further contribute to peptide stabilization in the orthosteric site, thus enhancing these effects. Analogous contacts have been reported for cocrystallized mu⁵¹ and delta⁵² but not NOP⁵³ antagonists. Importantly, Phe¹ of the N/OFQ sequence cannot form water bridges with H²⁹⁷, and this is most probably the reason for the lack of mu affinity of the peptide.

Interestingly, as stated above, Dmt⁵ mainly interacts with residues that differ within the opiate family, that is, E²²⁹ (G in NOP, D in kappa and delta) and K²³³ (A in NOP) of TMS, V³⁰⁰ (I in kappa), and K³⁰³ (W, E, and Q in delta, kappa, and NOP receptor, respectively) of TM6, and W³¹⁸ (L in NOP) of TM7. While the carbonyl oxygen of Dmt⁵ is in water bridge contact with E²²⁹, its aromatic bulky head is stacked between the aliphatic chains of K³⁰³ and K²³³, making possible π -cation interactions with the positively charged amine of both lysines (Figure 3B,E). In the reported crystal structure of mu-DAMGO³⁰ (PDB code 6DDF), the K³⁰³ positive charge is found at a 3.3 Å distance of the carbonyl oxygen of N(Me)-Phe of DAMGO, compatible with a weak H-bond, whereas K²³³ does not appear to contribute to the stabilization of the mu active state induced by both DAMGO and BU72,²⁹ the K²³³ amine group is found covalently linked to the antagonist β -funaltrexamine in the crystal structure of the inactive mu receptor.⁵¹ As K³⁰³ and K²³³ are present in the mu but not the NOP receptor, the above-mentioned interactions between Dmt⁵ and the two lysine residues could contribute to explain the mu-selective increase of affinity of [Dmt^{1,5}]N/OFQ(1-13)-NH₂ compared to [Dmt¹]N/OFQ(1-13)-NH₂, thus making [Dmt^{1,5}]N/OFQ(1-13)-NH₂ a mixed mu/NOP agonist. Last, as observed along the MD runs, the indole nitrogen of W³¹⁸ in TM7 does not interact with N/OFQ but can form H-bond contact with Gly² of [Dmt^{1,5}]N/OFQ(1-9)-NH₂ as well as with DAMGO (49 and 63% of the trajectory, respectively). Thus, beyond differences in steric hindrance of Tyr¹ and Dmt¹ that may generically contribute to a larger hydrophobic core for the last one, the entity of the interaction between W³¹⁸ and Gly² could also contribute to explain the enhanced potency of [Dmt^{1,5}] N/OFQ(1-13)-NH₂. Data obtained from this molecular modeling investigation are in agreement with those reported by recent studies performed on a series of cyclic opioid peptides.⁵⁴

The role of the N/OFQ-NOP receptor system has been widely reported in several biological functions at the central and peripheral levels, including the cough reflex.⁴ Previous studies

showed that NOP receptor agonists given centrally or peripherally suppress capsaicin and acid inhalation-induced cough in guinea pigs.^{33–37} Moreover, opioid drugs are widely used as antitussive agents,³⁸ and inhalation of encephalin was shown to be effective in reducing cough reflex *in vivo*.⁵⁵ The novel mixed NOP/opioid agonist [Dmt^{1,5}]N/OFQ(1-13)-NH₂ showed an inhibitory activity against citric acid-induced cough in guinea pigs, thus demonstrating the *in vivo* activity of the compound. However, further studies are needed to investigate the receptor mechanism involved in the antitussive action of the molecule.

CONCLUSIONS

In this study, starting from the NOP-selective sequence of N/OFQ(1-13)-NH₂, we developed a structure activity investigation focused on positions 1 and 5. Regarding position 1, a phenol moiety is required to increase mu receptor binding, and regarding position 5, aromatic residues generated the best results in terms of similar potency at NOP and mu receptors. This study led to the identification of [Dmt^{1,5}]N/OFQ(1-13)-NH₂ as the most potent mixed peptide agonist for NOP and mu receptors so far described in the literature. MD studies shed light on the molecular mechanisms adopted by this peptide to bind the active form of the mu receptor: some features of the mode of binding of [Dmt^{1,5}]N/OFQ(1-9)-NH₂ are superimposable to those of DAMGO, that is, the ionic bond with D¹⁴⁷ of TM3 and the H-bond network with H²⁹⁷ of TM6, while others are peculiar of [Dmt^{1,5}]N/OFQ(1-9)-NH₂, that is, polar interactions of Dmt⁵ with K²²³ and K³⁰³ of TMS and TM6, respectively.

[Dmt^{1,5}]N/OFQ(1-13)-NH₂ is a novel mixed agonist for NOP and mu receptors that exerted antitussive effects in an *in vivo* model of cough. The compound will be evaluated in future studies for its antinociceptive properties. In fact, mixed NOP/mu agonists of both peptide and nonpeptide structures have been consistently demonstrated in preclinical studies to promote antinociceptive effects similar to those of morphine being however better tolerated particularly in terms of respiratory depression, tolerance, and abuse liability.¹³ Importantly, phase II and III clinical studies performed with the mixed NOP/mu agonist cebranopadol have confirmed this favorable profile in pain patients.^{9,56} Nowadays, the availability of safer analgesic drugs is particularly needed for facing the opioid epidemic that leads to a progressive increase of fatal overdoses over the past 2 decades.⁵⁷

EXPERIMENTAL SECTION

Chemistry. Materials and Methods. All solvents and reagents were purchased from Sigma-Aldrich and Fisher Scientific. Enantiopure Fmoc-protected amino acids and the resins for SPPS were purchased from AAPPTEC. Peptides were synthesized using a standard Fmoc/*t*-butyl strategy⁵⁸ with a Syro XP multiple peptide synthesizer (MultiSynTech GmbH, Witten Germany) on a Rink amide MBHA resin (4-(2',4'-dimethoxyphenyl-Fmoc-aminomethyl)-phenoxyacetamido-norleucyl-MBHA resin; loading 0.55 mmol/g). Fmoc-amino acids were used with a 4-fold excess on a 0.11 mM scale of the resin and coupled to the growing peptide chain using *N,N'*-diisopropylcarbodiimide and 1-hydroxybenzotriazole (DIC/HOBt, 4-fold excess) for 1 h at room temperature. Each Fmoc removal step was performed using 40% piperidine in *N,N*-dimethylformamide, and all the subsequent couplings were repeated until the desired peptide-bound resin was completed. The cleavage cocktail to obtain the peptides from the resin consisted of 95% trifluoroacetic acid, 2.5% water, and 2.5% triethylsilane, and cleavages were conducted for 3 h at room temperature. After filtration of the resin, diethyl ether was added to

the filtrate to promote precipitation of the peptide products that were finally isolated by centrifugation. Reverse-phase purification of crude peptides was carried out on a Waters Prep 600 high-performance liquid chromatography (HPLC) system with a Jupiter column C18 (250 × 30 mm, 300 Å, 15 μm spherical particle size) using a gradient, programmed time by time, of acetonitrile/water [with 0.1% trifluoroacetic acid (TFA)] at a flow rate of 20 mL/min. Nonpeptide derivatives were purified through flash column chromatography using a Biotage System Isolera One. Analytical HPLC was performed with a Beckman 116 liquid chromatograph furnished with a UV detector. The purity of peptides in Table 1 was assessed with a Symmetry C18 column (4.6 × 75 mm, 3.5 μm particle size, SYSTEM GOLD) at a flow rate of 0.5 mL/min using a linear gradient from 100% of A (water + 0.1% TFA) to 100% of B (acetonitrile + 0.1% TFA) over a period of 25 min. The purity of peptides in Tables 2 and 3 was assessed with an Agilent Zorbax C18 column (4.6 × 150 mm, 3.5 μm particle size, KARAT32) at a flow rate of 0.7 mL/min using a linear gradient from 100% of A (water + 0.1% TFA) to 100% of B (acetonitrile + 0.1% TFA) over a period of 25 min. All final compounds were monitored at 220 nm showing ≥95% purity, and their molecular weights were confirmed using an ESI Micromass ZQ, Waters (HPLC chromatograms and ESI mass spectra of the final peptide derivatives have been reported in the Supporting Information). ¹H and ¹³C NMR spectra were recorded for nonpeptide derivatives on a Varian 400 MHz instrument, and all experiments were performed in deuterated DMSO using its residual shifts as reference (s: singlet, d: doublet, dd: double doublet, t: triplet, m: multiplet).

In Vitro Pharmacological Studies. Drugs and Reagents. [D-Pen²,D-Pen⁵]enkephalin (DPDPE) and naltrexone were purchased from Tocris Bioscience (Bristol, UK). Concentrated solutions (1 mM) were made in bidistilled water and kept at −20 °C until use. The medium and reagents for cell culture were from Euroclone (Milan, Italy). Fluo-4 AM and pluronic acid were from Invitrogen/Thermo-Fisher Scientific (Waltham, USA). *N*-(2-Hydroxyethyl)piperazine-*N'*-ethanesulfonic acid (HEPES), probenecid, brilliant black, and bovine serum albumin (BSA) fraction V were from Sigma-Aldrich (St. Louis, USA).

Calcium Mobilization Assay. CHO cells stably coexpressing the human NOP or kappa or the mu receptor and the C-terminally modified G_{αq15} and CHO cells coexpressing the delta receptor and the G_{αqG66D15} protein were generated and cultured as described previously.^{45,46} Cells were maintained in Dulbecco's modified Eagle's medium/nutrient mixture F-12 (DEMEM/F-12) supplemented with 10% FBS, 100 U/mL penicillin and 100 μg/mL streptomycin, 100 μg/mL hygromycin B, and 200 μg/mL G418 and cultured at 37 °C in 5% CO₂ humidified air. Cells were seeded at a density of 50,000 cells/well into 96-well black, clear-bottom plates. The following day, the cells were incubated with Hanks' balanced salt solution (HBSS) supplemented with 2.5 mM probenecid, 3 μM of the calcium-sensitive fluorescent dye Fluo-4 AM, and 0.01% pluronic acid for 30 min at 37 °C. After that time, the loading solution was aspirated and 100 μL/well of HBSS supplemented with 20 mM HEPES, 2.5 mM probenecid, and 500 μM brilliant black was added. Serial dilutions were carried out in HBSS/HEPES (20 mM) buffer (containing 0.02% BSA fraction V). After placing both plates (cell culture and master plate) into the fluorometric imaging plate reader FlexStation II (Molecular Devices, Sunnyvale, CA), fluorescence changes were measured. On-line additions were carried out in a volume of 50 μL/well. To facilitate drug diffusion into the wells, the present studies were performed at 37 °C. Maximum change in fluorescence, expressed as percent over the baseline fluorescence, was used to determine agonist response.

DMR Assay. CHO cells stably expressing the human NOP and mu receptors were kindly provided by D.G. Lambert (University of Leicester, UK). Cells were cultured in DMEM/F-12 medium supplemented with 10% FBS, 100 U/mL penicillin, 100 μg/mL streptomycin, and 2 mmol/L L-glutamine. The medium was supplemented with 400 μg/mL G418 to maintain expression. Cells were cultured at 37 °C in 5% CO₂ humidified air. For DMR measurements, the label-free EnSight Multimode Plate Reader (Perkin Elmer, MA, US) was used. Cells were seeded 15,000 cells/well in a volume of 30 μL onto fibronectin-coated 384-well DMR microplates

and cultured for 20 h to obtain confluent monolayers. Cells were starved in the assay buffer (HBSS with 20 mM HEPES, 0.01% BSA fraction V) for 90 min before the test. Serial dilutions were made in the assay buffer. After reading the baseline, compounds were added in a volume of 10 μL; then, DMR changes were recorded for 60 min. Responses were described as picometer (pm) shifts over time (sec) following subtraction of values from vehicle-treated wells. Maximum picometer (pm) modification (peak) was used to generate concentration response curves. All the experiments were carried out at 37 °C.

Data Analysis and Terminology. The pharmacological terminology adopted in this paper is consistent with IUPHAR recommendations.³⁹ All data are expressed as the mean ± standard error of the mean (SEM) of at least three experiments performed in duplicate. For potency values, 95% confidence limits (CL_{95%}) were indicated. Agonist potencies are given as pEC₅₀, that is, the negative logarithm to base 10 of the molar concentration of an agonist that produces 50% of the maximal effect of that agonist. Concentration-response curves to agonists were fitted to the classical four-parameter logistic nonlinear regression model:

$$\text{Effect} = \text{Baseline} + (E_{\text{max}} - \text{Baseline}) / (1 + 10^{(\text{LogEC}_{50} - \text{Log}[\text{compound}]) \times \text{Hillslope}})$$

Curve fitting was performed using PRISM 6.0 (GraphPad Software Inc., San Diego).

Molecular Dynamics. The setup of an *in silico* model of the non-natural peptides [Dmt^{1,5}]N/OFQ(1-9)-NH₂ and N/OFQ(1-9)-NH₂ in complex with the human mu receptor has been described in the Supporting Information. Classical MD simulations of these two receptor-peptide complexes were performed and compared with an MD simulation of the experimental system DAMGO-mu receptor-G_i protein complex as derived by the PDB file 6DDF.³⁰ The GROMACS 2018.3 package⁶⁰ was used under the AMBER parm99sb force field⁶¹ at the full atomistic level using a TIP3P water solvent and an explicit pre-equilibrated phospholipid bilayer of 128 POPC (1-palmitoyl-2-oleoyl-*sn*-glycero-3-phosphocholine) molecules obtained by the Prof. Tieleman website (<http://moose.bio.ucalgary.ca>). All the MD sessions were performed in a water-membrane system prepared as previously described.^{31,32} The receptor-peptide-membrane systems were solvated in a triclinic water box (having basis vector lengths of 7, 7.4, and 9.3 nm) under periodic boundary conditions for a total number of about 45,000 atoms (6400 solvent molecules). The total charge of the system was neutralized by randomly substituting water molecules with Na⁺ ions and Cl⁻ ions to obtain neutrality with a 0.15M salt concentration. Following a steepest descent minimization algorithm, the system was equilibrated under canonical ensemble (NVT) conditions for 300 ps using a V-rescale, modified Berendsen thermostat with position restraints for both the receptor-peptide complex and the lipids and thereafter in a isothermal-isobaric ensemble (NPT) for 500 ps, applying position restraints to the heavy atoms of the protein-peptide complex, and using a Nose-Hoover thermostat and a Parrinello-Rahman barostat at 1 atm with a relaxation time of 2.0 ps. The MD simulation of the mu receptor-DAMGO-G_i protein was carried out on the whole ternary complex without positional restraints. On the other hand, in order to reduce the computational time, in the two mu receptor-peptide complexes, the G_i protein was not included in the system, but all residues within 5 Å of the G_i protein interface were restrained to the initial structure of the activated receptor using 5.0 kcal mol⁻¹ Å⁻² harmonic restraints applied to non-hydrogen atoms. Using such restraints ensures that the receptor maintains an active conformation throughout the simulation. MD runs were performed under NPT conditions at 300 K with a T-coupling constant of 1 ps. van der Waals interactions were modeled using a 6–12 Lennard-Jones potential with a 1.2 nm cutoff. Long-range electrostatic interactions were calculated, with a cutoff for the real space term of 1.2 nm. All covalent bonds were constrained using the LINCS algorithm. The time step employed was 2 fs, and the coordinates were saved every 5 ps for analysis.

The MD analysis of the DAMGO-mu receptor-G_i protein complex (Figure S1) shows an overall stability of the starting configuration (corresponding to the crystal structure) with some motion of the phenolic head toward the intracellular side of the receptor, still conserving the water bridge contact with H²⁹⁷. A non-negligible rearrangement is observed (Figures S2 and S3) along the MD sessions,

starting from the docked conformations of [Dmt^{1,5}]N/OFQ(1-9)-NH₂ and N/OFQ(1-9)-NH₂, probably due to the limitations of the docking procedures applied to molecules with a large number of torsions, and confirms the importance of performing long-lasting MD sessions. Analysis of MD trajectories was performed using state-of-the-art computational tools, as described in the [Supporting Information](#).

Artwork. 3D images of peptide-receptor structures were obtained by the Chimera software.⁶²

In Vivo Pharmacological Studies. Animals. Guinea pigs (Dunkin Hartley, male, 400–450 g, Charles River, Milan, Italy) were used. The group size of $n = 6$ animals was determined by sample size estimation using G*Power (v3.1)⁶³ to detect the size effect in a post-hoc test with type 1 and 2 error rates of 5 and 20%, respectively. Allocation concealment to the vehicle(s) or treatment group was performed using a randomization procedure (<http://www.randomizer.org/>). The assessors were blinded to the identity (allocation to the treatment group) of the animals. Guinea pigs were housed in a temperature- and humidity-controlled vivarium (12 h dark/light cycle, free access to food and water) for at least 1 week before the start of the experiments. Cough experiments were done in a quiet, temperature-controlled (20–22 °C) room between 9 am and 5 pm and were performed by an operator blinded to the treatment. All experiments were carried out according to the European Union (EU) guidelines for animal care procedures and the Italian legislation (DLgs 26/2014) application of the EU Directive 2010/63/EU. All animal studies were approved by the Animal Ethics Committee of the University of Florence and the Italian Ministry of Health (permit #450/2019-PR) and followed the animal research reporting *in vivo* experiment (ARRIVE) guidelines.

Measurement of Cough in Conscious Guinea Pigs. Cough experiments were performed using a whole-body plethysmography system (Buxco, Wilmington, NC, USA, upgraded version 2018).⁶⁴ The apparatus consists of four plethysmographs (four transparent Perspex chambers) ventilated with a constant airflow and each provided by a nebulizing head (Aerogen) and adjustable bias flow rates for acclimation and nebulization. The particle size presents an aerodynamic mass median diameter of 6 μm, and the output of the nebulizing heads can be set in the range between 0 and 0.4 mL per minute. The number of elicited coughs was automatically counted using the instrument. The nebulization rate used in the following experiments was 0.15 mL/min, and the air flows were 1750 mL/min during the acclimation phase and 800 mL/min during nebulization. These rates were previously found in our lab to elicit a significant number of cough events in the citric acid-induced cough model.

On the day of experiments, guinea pigs were individually placed into the chambers and let to acclimate for 10 min. To test the antitussive effect of [Dmt^{1,5}]N/OFQ(1-13)-NH₂, two different protocols were used. Protocol 1: after acclimation, a mixture of [Dmt^{1,5}]N/OFQ(1-13)-NH₂ (1 mM) or its vehicle (0.9% NaCl) and the tussive agent, citric acid (0.4 M), was nebulized for 10 min. During the 10 min of nebulization and for 5 min immediately post challenge (recovery period), the number of elicited coughs was automatically recorded using the BUXCO system. Protocol 2: after acclimation, [Dmt^{1,5}]N/OFQ(1-13)-NH₂ (1 mM) or its vehicle (0.9% NaCl) was nebulized for 10 min. After 20 min of recovery, the tussive agent, citric acid (0.4 M), was delivered by aerosol via a nebulizer for 10 min. During the 10 min of the citric acid challenge and 5 min immediately post challenge (recovery period), the number of elicited coughs was automatically recorded using the BUXCO system.

For the *in vivo* experiment, the statistical significance of differences between groups was assessed using Student's *t*-test.

■ ASSOCIATED CONTENT

SI Supporting Information

The Supporting Information is available free of charge at <https://pubs.acs.org/doi/10.1021/acs.jmedchem.0c02062>.

Synthesis of Fmoc-2',6'-dimethyltyrosine; synthetic procedures for the preparation of Fmoc-2',6'-dimethyltyrosine; structures of nonproteinogenic amino acids;

HPLC chromatograms and ESI mass spectra of the final peptide derivatives; model setup of non-natural peptides for MD; model setup of the mu receptor; model setup of the peptide-mu receptor complexes; and analysis of MD trajectories (PDF)

Molecular formula strings (CSV)

Model coordinates: representative structure of the [Dmt^{1,5}]N/OFQ(1-9)-NH₂-mu receptor complex (PDB)

Model coordinates: representative structure of the N/OFQ(1-9)NH₂-mu receptor complex (PDB)

■ AUTHOR INFORMATION

Corresponding Authors

Chiara Ruzza – Department of Neuroscience and Rehabilitation, Section of Pharmacology, University of Ferrara, Ferrara 44121, Italy; Technopole of Ferrara, LTTA Laboratory for Advanced Therapies, Ferrara 44121, Italy; Phone: +39-0532-455220; Email: chiara.ruzza@unife.it

Delia Preti – Department of Chemical, Pharmaceutical and Agricultural Sciences, University of Ferrara, Ferrara 44121, Italy; orcid.org/0000-0002-1075-3781; Phone: +39-0532-455501; Email: delia.preti@unife.it

Stefano Della Longa – Department of Life, Health and Environmental Sciences, University of L'Aquila, L'Aquila 67100, Italy; orcid.org/0000-0002-8157-9530; Phone: +39-0862-433568; Email: stefano.dellalonga@univaq.it

Authors

Salvatore Pacifico – Department of Chemical, Pharmaceutical and Agricultural Sciences, University of Ferrara, Ferrara 44121, Italy; orcid.org/0000-0002-3377-5107

Valentina Albanese – Department of Chemical, Pharmaceutical and Agricultural Sciences, University of Ferrara, Ferrara 44121, Italy

Davide Illuminati – Department of Chemical, Pharmaceutical and Agricultural Sciences, University of Ferrara, Ferrara 44121, Italy

Erika Marzola – Department of Chemical, Pharmaceutical and Agricultural Sciences, University of Ferrara, Ferrara 44121, Italy

Martina Fabbri – Department of Chemical, Pharmaceutical and Agricultural Sciences, University of Ferrara, Ferrara 44121, Italy

Federica Ferrari – Department of Neuroscience and Rehabilitation, Section of Pharmacology, University of Ferrara, Ferrara 44121, Italy

Victor A.D. Holanda – Department of Neuroscience and Rehabilitation, Section of Pharmacology, University of Ferrara, Ferrara 44121, Italy

Chiara Sturaro – Department of Neuroscience and Rehabilitation, Section of Pharmacology, University of Ferrara, Ferrara 44121, Italy

Davide Malfacini – Department of Pharmaceutical and Pharmacological Sciences, University of Padova, Padova 35131, Italy

Claudio Trapella – Department of Chemical, Pharmaceutical and Agricultural Sciences, University of Ferrara, Ferrara 44121, Italy; Technopole of Ferrara, LTTA Laboratory for Advanced Therapies, Ferrara 44121, Italy

Ettore Lo Cascio – Dipartimento di Scienze Biotechologiche di Base, Cliniche Intensivologiche e Perioperatorie, Università Cattolica del Sacro Cuore, Roma 00168, Italy

Alessandro Arcovito – Dipartimento di Scienze Biotechologiche di Base, Cliniche Intensivologiche e Perioperatorie, Università Cattolica del Sacro Cuore, Roma 00168, Italy; Fondazione Policlinico Universitario A. Gemelli IRCCS, Roma 00168, Italy

Martina Marangoni – Department of Health Sciences, Section of Clinical Pharmacology and Oncology, University of Florence, Florence 50139, Italy

Davide Fattori – Department of Health Sciences, Section of Clinical Pharmacology and Oncology, University of Florence, Florence 50139, Italy

Romina Nassini – Department of Health Sciences, Section of Clinical Pharmacology and Oncology, University of Florence, Florence 50139, Italy

Girolamo Calò – Department of Pharmaceutical and Pharmacological Sciences, University of Padova, Padova 35131, Italy

Remo Guerrini – Department of Chemical, Pharmaceutical and Agricultural Sciences, University of Ferrara, Ferrara 44121, Italy; Technopole of Ferrara, LTTA Laboratory for Advanced Therapies, Ferrara 44121, Italy

Complete contact information is available at:

<https://pubs.acs.org/10.1021/acs.jmedchem.0c02062>

Notes

The authors declare the following competing financial interest(s): S.P., V.A., D.I., C.T., E.M., C.R., D.P., G.C., and R.G. are inventors of the patent application (10202000025972) focused on NOP/mu mixed agonists. G.C. and R.G. are founders of the University of Ferrara spin off company UFPeptides s.r.l., the assignee of such patent application. C.R. is CEO of UFPeptides s.r.l.

ACKNOWLEDGMENTS

FAR (Fondo di Ateneo per la Ricerca Scientifica) grants from the University of Ferrara support D.P., C.R., G.C., and R.G. C.R. is supported by an FIR (Fondo per l'Incentivazione alla Ricerca) grant from the University of Ferrara. S.P., F.F., D.P., G.C., and R.G. are supported by the grant PRIN 2015 (Prot. 2015WX8YSB_002) from the Italian Ministry of Research and Education.

ABBREVIATIONS

CHO cells, chinese hamster ovary cells; CL_{95%}, 95% confidence limits; CR, concentration ratio; crc, concentration–response curve; DAMGO, [D-Ala², N-MePhe⁴, Gly-ol]-enkephalin; DIC, N,N'-diisopropylcarbodiimide; DIPEA, N,N'-diisopropylethylamine; DMEM/F-12, Dulbecco's modified Eagle's medium/nutrient mixture F-12; DMR, dynamic mass redistribution; DPDPE, [D-Pen², D-Pen⁵]enkephalin; EtOAc, ethyl acetate; FBS, fetal bovine serum; FmocCl, Fmoc chloride; HATU, hexafluorophosphate azabenzotriazole tetramethyl uronium; HBSS, Hanks' balanced salt solution; LINCS, LINear Constraint Solver; MBHA resin, 4-methylbenzhydrylamine resin; N/OFQ, nociceptin/orphanin FQ; NPT, isothermal–isobaric ensemble; NVT, canonical ensemble conditions; PWT, peptide welding technology; SEM, standard error of the mean; SPPS, solid-phase peptide synthesis

REFERENCES

- (1) Meunier, J.-C.; Mollereau, C.; Toll, L.; Suaudeau, C.; Moisand, C.; Alvinerie, P.; Butour, J. L.; Guillemot, J. C.; Ferrara, P.; Monsarrat, B.; Mazarguil, H.; Vassart, G.; Parmentier, M.; Costentin, J. Isolation and structure of the endogenous agonist of opioid receptor-like ORL1 receptor. *Nature* **1995**, *377*, 532–535.
- (2) Reinscheid, R. K.; Nothacker, H. P.; Bourson, A.; Ardati, A.; Henningsen, R. A.; Bunzow, J. R.; Grandy, D. K.; Langen, H.; Monsma, F. J., Jr.; Civelli, O. Orphanin FQ: a neuropeptide that activates an opioidlike G protein-coupled receptor. *Science* **1995**, *270*, 792–794.
- (3) Toll, L.; Bruchas, M. R.; Calò, G.; Cox, B. M.; Zaveri, N. T. Nociceptin/Orphanin FQ receptor structure, signaling, ligands, functions, and interactions with opioid systems. *Pharmacol. Rev.* **2016**, *68*, 419–457.
- (4) Lambert, D. G. The nociceptin/orphanin FQ receptor: a target with broad therapeutic potential. *Nat. Rev. Drug Discovery* **2008**, *7*, 694–710.
- (5) Schröder, W.; Lambert, D. G.; Ko, M. C.; Koch, T. Functional plasticity of the N/OFQ-NOP receptor system determines analgesic properties of NOP receptor agonists. *Br. J. Pharmacol.* **2014**, *171*, 3777–3800.
- (6) Toll, L.; Ozawa, A.; Cippitelli, A. NOP-related mechanisms in pain and analgesia. *Handb. Exp. Pharmacol.* **2019**, *254*, 165–186.
- (7) Kiguchi, N.; Ko, M. C. Effects of NOP-related ligands in nonhuman primates. *Handb. Exp. Pharmacol.* **2019**, *254*, 323–343.
- (8) Linz, K.; Christoph, T.; Tzschenke, T. M.; Koch, T.; Schiene, K.; Gautrois, M.; Schröder, W.; Kögel, B. Y.; Beier, H.; Englberger, W.; Schunk, S.; De Vry, J.; Jahnel, U.; Frosch, S. Cebranopadol: a novel potent analgesic nociceptin/orphanin FQ peptide and opioid receptor agonist. *J. Pharmacol. Exp. Ther.* **2014**, *349*, 535–548.
- (9) Calò, G.; Lambert, D. G. Nociceptin/orphanin FQ receptor ligands and translational challenges: focus on cebranopadol as an innovative analgesic. *Br. J. Anaesth.* **2018**, *121*, 1105–1114.
- (10) Ding, H.; Kiguchi, N.; Yasuda, D.; Daga, P. R.; Polgar, W. E.; Lu, J. J.; Czoty, P. W.; Kishioka, S.; Zaveri, N. T.; Ko, M.-C. A bifunctional nociceptin and mu opioid receptor agonist is analgesic without opioid side effects in nonhuman primates. *Sci. Transl. Med.* **2018**, *10*, No. eaar3483.
- (11) Kiguchi, N.; Ding, H.; Cami-Kobeci, G.; Sukhtankar, D. D.; Czoty, P. W.; DeLoid, H. B.; Hsu, F.-C.; Toll, L.; Husbands, S. M.; Ko, M.-C. BU10038 as a safe opioid analgesic with fewer side-effects after systemic and intrathecal administration in primates. *Br. J. Anaesth.* **2019**, *122*, e146–e156.
- (12) Chao, P. K.; Chang, H. F.; Chang, W. T.; Yeh, T. K.; Ou, L. C.; Chuang, J. Y.; Tsu-An Hsu, J.; Tao, P. L.; Loh, H. H.; Shih, C.; Ueng, S. H.; Yeh, S. H. BPR1M97, a dual mu opioid receptor/nociceptin-orphanin FQ peptide receptor agonist, produces potent antinociceptive effects with safer properties than morphine. *Neuropharmacology* **2020**, *166*, 107678.
- (13) Kiguchi, N.; Ding, H.; Ko, M.-C. Therapeutic potentials of NOP and MOP receptor coactivation for the treatment of pain and opioid abuse. *J. Neurosci. Res.* **2020**, DOI: 10.1002/jnr.24624.
- (14) Azzam, A. A. H.; McDonald, J.; Lambert, D. G. Hot topics in opioid pharmacology: mixed and biased opioids. *Br. J. Anaesth.* **2019**, *122*, e136–e145.
- (15) Anand, J. P.; Kochan, K. E.; Nastase, A. F.; Montgomery, D.; Griggs, N. W.; Traynor, J. R.; Mosberg, H. I.; Jutkiewicz, E. M. In vivo effects of μ -opioid receptor agonist/ δ -opioid receptor antagonist peptidomimetics following acute and repeated administration. *Br. J. Pharmacol.* **2018**, *175*, 2013–2027.
- (16) Aceto, M. D.; Harris, L. S.; Negus, S. S.; Banks, M. L.; Hughes, L. D.; Akgun, E.; Portoghese, P. S. MDAN-21: a bivalent opioid ligand containing mu-agonist and delta-antagonist pharmacophores and its effects in rhesus monkeys. *Int. J. Med. Chem.* **2012**, *2012*, 327257.
- (17) Greedy, B. M.; Bradbury, F.; Thomas, M. P.; Grivas, K.; Cami-Kobeci, G.; Archambeau, A.; Bosse, K.; Clark, M. J.; Aceto, M.; Lewis, J. W.; Traynor, J. R.; Husbands, S. M. Orvinols with mixed kappa/mu opioid receptor agonist activity. *J. Med. Chem.* **2013**, *56*, 3207–3216.

- (18) Daniels, D. J.; Kulkarni, A.; Xie, Z.; Bhushan, R. G.; Portoghesi, P. S. A bivalent ligand (KDAN-18) containing δ -antagonist and κ -agonist pharmacophores bridges $\delta 2$ and $\kappa 1$ opioid receptor phenotypes†. *J. Med. Chem.* **2005**, *48*, 1713–1716.
- (19) Molinari, S.; Camarda, V.; Rizzi, A.; Marzola, G.; Salvadori, S.; Marzola, E.; Molinari, P.; McDonald, J.; Ko, M.; Lambert, D.; Calò, G.; Guerrini, R. [Dmt¹]N/OFQ(1-13)-NH₂: a potent nociceptin/orphanin FQ and opioid receptor universal agonist. *Br. J. Pharmacol.* **2013**, *168*, 151–162.
- (20) Guerrini, R.; Marzola, E.; Trapella, C.; Pelà, M.; Molinari, S.; Cerlesi, M. C.; Malfacini, D.; Rizzi, A.; Salvadori, S.; Calò, G. A novel and facile synthesis of tetra branched derivatives of nociceptin/orphanin FQ. *Bioorg. Med. Chem.* **2014**, *22*, 3703–3712.
- (21) Cerlesi, M. C.; Ding, H.; Bird, M. F.; Kiguchi, N.; Ferrari, F.; Malfacini, D.; Rizzi, A.; Ruzza, C.; Lambert, D. G.; Ko, M. C.; Calò, G.; Guerrini, R. Pharmacological studies on the NOP and opioid receptor agonist PWT2-[Dmt¹]N/OFQ(1-13). *Eur. J. Pharmacol.* **2017**, *794*, 115–126.
- (22) Pacifico, S.; Albanese, V.; Illuminati, D.; Fantinati, A.; Marzola, E.; Ferrari, F.; Neto, J. A.; Sturaro, C.; Ruzza, C.; Calò, G.; Preti, D.; Guerrini, R. Tetrabrached hetero-conjugated peptides as bifunctional agonists of the NOP and mu opioid receptors. *Bioconjugate Chem.* **2019**, *30*, 2444–2451.
- (23) Bird, M. F.; Cerlesi, M. C.; Brown, M.; Malfacini, D.; Vezzi, V.; Molinari, P.; Micheli, L.; Mannelli, L. D. C.; Ghelardini, C.; Guerrini, R.; Calò, G.; Lambert, D. G. Characterisation of the novel mixed μ -NOP peptide ligand dermorphin-N/OFQ (DeNo). *PLoS One* **2016**, *11*, No. e0156897.
- (24) Lapalu, S.; Moisan, C.; Mazarguil, H.; Cambois, G.; Mollereau, C.; Meunier, J.-C. Comparison of the structure-activity relationships of nociceptin and dynorphin A using chimeric peptides. *FEBS Lett.* **1997**, *417*, 333–336.
- (25) Guerrini, R.; Marzola, E.; Trapella, C.; Pacifico, S.; Cerlesi, M. C.; Malfacini, D.; Ferrari, F.; Bird, M. F.; Lambert, D. G.; Salvadori, S.; Calò, G. Structure activity studies of nociceptin/orphanin FQ(1-13)-NH₂ derivatives modified in position 5. *Bioorg. Med. Chem.* **2015**, *23*, 1515–1520.
- (26) Varani, K.; Rizzi, A.; Calò, G.; Bigoni, R.; Toth, G.; Guerrini, R.; Gessi, S.; Salvadori, S.; Borea, P. A.; Regoli, D. Pharmacology of [Tyr¹]nociceptin analogs: receptor binding and bioassay studies. *Naunyn-Schmiedeberg's Arch. Pharmacol.* **1999**, *360*, 270–277.
- (27) Yamamoto, T.; Nair, P.; Largent-Milnes, T. M.; Jacobsen, N. E.; Davis, P.; Ma, S.-W.; Yamamura, H. I.; Vanderah, T. W.; Porreca, F.; Lai, J.; Hruby, V. J. Discovery of a potent and efficacious peptide derivative for δ/μ opioid agonist/Neurokinin 1 antagonist activity with a 2',6'-dimethyl-l-tyrosine: In vitro, In vivo, and NMR-Based Structural Studies. *J. Med. Chem.* **2011**, *54*, 2029–2038.
- (28) Giri, A. K.; Apostol, C. R.; Wang, Y.; Forte, B. L.; Largent-Milnes, T. M.; Davis, P.; Rankin, D.; Molnar, G.; Olson, K. M.; Porreca, F.; Vanderah, T. W.; Hruby, V. J. Discovery of novel multifunctional ligands with μ/δ opioid agonist/Neurokinin-1 (NK1) antagonist activities for the treatment of pain. *J. Med. Chem.* **2015**, *58*, 8573–8583.
- (29) Huang, W.; Manglik, A.; Venkatakrishnan, A. J.; Laeremans, T.; Feinberg, E. N.; Sanborn, A. L.; Kato, H. E.; Livingston, K. E.; Thorsen, T. S.; Kling, R. C.; Granier, S.; Gmeiner, P.; Husbands, S. M.; Traynor, J. R.; Weis, W. I.; Steyaert, J.; Dror, R. O.; Kobilka, B. K. Structural insights into μ -opioid receptor activation. *Nature* **2015**, *524*, 315–321.
- (30) Koehl, A.; Hu, H.; Maeda, S.; Zhang, Y.; Qu, Q.; Paggi, J. M.; Latorraca, N. R.; Hilger, D.; Dawson, R.; Matile, H.; Schertler, G. F. X.; Granier, S.; Weis, W. I.; Dror, R. O.; Manglik, A.; Skiniotis, G.; Kobilka, B. K. Structure of the μ -opioid receptor-Gi protein complex. *Nature* **2018**, *558*, 547–552.
- (31) Della Longa, S.; Arcovito, A. "In silico" study of the binding of two novel antagonists to the nociceptin receptor. *J. Comput.-Aided Mol. Des.* **2018**, *32*, 385–400.
- (32) Della Longa, S.; Arcovito, A. Microswitches for the activation of the nociceptin receptor induced by cebranopadol: hints from microsecond molecular dynamics. *J. Chem. Inf. Model.* **2019**, *59*, 818–831.
- (33) McLeod, R. L.; Bolser, D. C.; Jia, Y.; Parra, L. E.; Mutter, J. C.; Wang, X.; Tulshian, D. B.; Egan, R. W.; Hey, J. A. Antitussive effect of nociceptin/orphanin FQ in experimental cough models. *Pulm. Pharmacol. Ther.* **2002**, *15*, 213–216.
- (34) McLeod, R. L.; Jia, Y.; Fernandez, X.; Parra, L. E.; Wang, X.; Tulshian, D. B.; Kiselgof, E. J.; Tan, Z.; Fawzi, A. B.; Smith-Torhan, A.; Zhang, H.; Hey, J. A. Antitussive profile of the NOP agonist Ro-64-6198 in the guinea pig. *Pharmacology* **2004**, *71*, 143–149.
- (35) McLeod, R. L.; Tulshian, D. B.; Ho, G. D.; Fernandez, X.; Bolser, D. C.; Parra, L. E.; Zimmer, J. C.; Erickson, C. H.; Fawzi, A. B.; Jayappa, H.; Lehr, C.; Erskine, J.; Smith-Torhan, A.; Zhang, H.; Hey, J. A. Effect of a novel NOP receptor agonist (SCH 225288) on guinea pig irritant-evoked, feline mechanically induced and canine infectious tracheo-bronchitis cough. *Pharmacology* **2009**, *84*, 153–161.
- (36) McLeod, R. L.; Parra, L. E.; Mutter, J. C.; Erickson, C. H.; Carey, G. J.; Tulshian, D. B.; Fawzi, A. B.; Smith-Torhan, A.; Egan, R. W.; Cuss, F. M.; Hey, J. A. Nociceptin inhibits cough in the guinea-pig by activation of ORL1 receptors. *Br. J. Pharmacol.* **2001**, *132*, 1175–1178.
- (37) Lee, M.-G.; Udem, B. J.; Brown, C.; Carr, M. J. Effect of nociceptin in acid-evoked cough and airway sensory nerve activation in guinea pigs. *Am. J. Respir. Crit. Care Med.* **2006**, *173*, 271–275.
- (38) Gibson, P. G.; Ryan, N. M. Cough pharmacotherapy: current and future status. *Expert Opin. Pharmacother.* **2011**, *12*, 1745–1755.
- (39) Wang, X.; Niu, S.; Xu, L.; Zhang, C.; Meng, L.; Zhang, X.; Ma, D. Pd-catalyzed dimethylation of tyrosine-derived picolinamide for synthesis of (S)-N-Boc-2,6-dimethyltyrosine and its analogues. *Org. Lett.* **2017**, *19*, 246–249.
- (40) Bryant, S. D.; Jinsmaa, Y.; Salvadori, S.; Okada, Y.; Lazarus, L. H. Dmt and opioid peptides: a potent alliance. *Biopolymers* **2003**, *71*, 86–102.
- (41) Fenalti, G.; Giguere, P. M.; Katritch, V.; Huang, X.-P.; Thompson, A. A.; Cherezov, V.; Roth, B. L.; Stevens, R. C. Molecular control of δ -opioid receptor signalling. *Nature* **2014**, *506*, 191–196.
- (42) Shimohigashi, Y.; Hatano, R.; Fujita, T.; Nakashima, R.; Nose, T.; Sujaku, T.; Saigo, A.; Shinjo, K.; Nagahisa, A. Sensitivity of opioid receptor-like receptor ORL1 for chemical modification on nociceptin, a naturally occurring nociceptive peptide. *J. Biol. Chem.* **1996**, *271*, 23642–23645.
- (43) Morley, J. S. Structure-activity relationships of enkephalin-like peptides. *Annu. Rev. Pharmacol. Toxicol.* **1980**, *20*, 81–110.
- (44) Ndong, D. B.; Blais, V.; Holleran, B. J.; Proteau-Gagne, A.; Cantin-Savoie, I.; Robert, W.; Nadon, J. F.; Beauchemin, S.; Leduc, R.; Pineyro, G.; Guerin, B.; Gendron, L.; Dory, Y. L. Exploration of the fifth position of leu-enkephalin and its role in binding and activating delta (DOP) and mu (MOP) opioid receptors. *Pept. Sci.* **2019**, *111*, No. e24070.
- (45) Camarda, V.; Calò, G. Chimeric G proteins in fluorimetric calcium assays: experience with opioid receptors. *Methods Mol. Biol.* **2013**, *937*, 293–306.
- (46) Camarda, V.; Fischetti, C.; Anzellotti, N.; Molinari, P.; Ambrosio, C.; Kostenis, E.; Regoli, D.; Trapella, C.; Guerrini, R.; Severo, S.; Calò, G. Pharmacological profile of NOP receptors coupled with calcium signaling via the chimeric protein Gαq5. *Naunyn-Schmiedeberg's Arch. Pharmacol.* **2009**, *379*, 599–607.
- (47) Rizzi, A.; Cerlesi, M. C.; Ruzza, C.; Malfacini, D.; Ferrari, F.; Bianco, S.; Costa, T.; Guerrini, R.; Trapella, C.; Calò, G. Pharmacological characterization of cebranopadol a novel analgesic acting as mixed nociceptin/orphanin FQ and opioid receptor agonist. *Pharmacol. Res. Perspect.* **2016**, *4*, No. e00247.
- (48) Codd, E. E.; Mabus, J. R.; Murray, B. S.; Zhang, S. P.; Flores, C. M. Dynamic mass redistribution as a means to measure and differentiate signaling via opioid and cannabinoid receptors. *Assay Drug Dev. Technol.* **2011**, *9*, 362–372.
- (49) Malfacini, D.; Simon, K.; Trapella, C.; Guerrini, R.; Zaveri, N. T.; Kostenis, E.; Calò, G. NOP receptor pharmacological profile - A dynamic mass redistribution study. *PLoS One* **2018**, *13*, No. e0203021.
- (50) Schwyzer, R. Molecular mechanism of opioid receptor selection. *Biochemistry* **1986**, *25*, 6335–6342.

(51) Manglik, A.; Kruse, A. C.; Kobilka, T. S.; Thian, F. S.; Mathiesen, J. M.; Sunahara, R. K.; Pardo, L.; Weis, W. I.; Kobilka, B. K.; Granier, S. Crystal structure of the μ -opioid receptor bound to a morphinan antagonist. *Nature* **2012**, *485*, 321–326.

(52) Granier, S.; Manglik, A.; Kruse, A. C.; Kobilka, T. S.; Thian, F. S.; Weis, W. I.; Kobilka, B. K. Structure of the δ -opioid receptor bound to naltrindole. *Nature* **2012**, *485*, 400–404.

(53) Thompson, A. A.; Liu, W.; Chun, E.; Katritch, V.; Wu, H.; Vardy, E.; Huang, X.-P.; Trapella, C.; Guerrini, R.; Calò, G.; Roth, B. L.; Cherezov, V.; Stevens, R. C. Structure of the nociceptin/orphanin FQ receptor in complex with a peptide mimetic. *Nature* **2012**, *485*, 395–399.

(54) Stefanucci, A.; Dimmito, M. P.; Macedonio, G.; Ciarlo, L.; Pieretti, S.; Novellino, E.; Lei, W.; Barlow, D.; Houseknecht, K. L.; Streicher, J. M.; Mollica, A. Potent, efficacious, and stable cyclic opioid peptides with long lasting antinociceptive effect after peripheral administration. *J. Med. Chem.* **2020**, *63*, 2673–2687.

(55) Adcock, J. J. Peripheral opioid receptors and the cough reflex. *Respir. Med.* **1991**, *85*, 43–46.

(56) Tzschentke, T. M.; Linz, K.; Koch, T.; Christoph, T. Cebranopadol: A novel first-in-class potent analgesic acting via NOP and opioid receptors. *Handb. Exp. Pharmacol.* **2019**, *254*, 367–398.

(57) Volkow, N. D.; Blanco, C. The changing opioid crisis: development, challenges and opportunities. *Mol. Psychiatry* **2021**, *26*, 218–233.

(58) Benoiton, N. L. *Chemistry of Peptide Synthesis*; Taylor & Francis: London, 2006; pp 125–155.

(59) Neubig, R. R.; Spedding, M.; Kenakin, T.; Christopoulos, A. International union of pharmacology committee on receptor nomenclature and drug classification. XXXVIII. Update on terms and symbols in quantitative pharmacology. *Pharmacol. Rev.* **2003**, *55*, 597–606.

(60) Abraham, M. J.; Murtola, T.; Schulz, R.; Páll, S.; Smith, J. C.; Hess, B.; Lindahl, E. GROMACS: High performance molecular simulations through multi-level parallelism from laptops to super-computers. *SoftwareX* **2015**, *1–2*, 19–25.

(61) Hornak, V.; Abel, R.; Okur, A.; Strockbine, B.; Roitberg, A.; Simmerling, C. Comparison of multiple Amber force fields and development of improved protein backbone parameters. *Proteins* **2006**, *65*, 712–725.

(62) Pettersen, E. F.; Goddard, T. D.; Huang, C. C.; Couch, G. S.; Greenblatt, D. M.; Meng, E. C.; Ferrin, T. E. UCSF Chimera? A visualization system for exploratory research and analysis. *J. Comput. Chem.* **2004**, *25*, 1605–1612.

(63) Faul, F.; Erdfelder, E.; Lang, A.-G.; Buchner, A. G*Power 3: a flexible statistical power analysis program for the social, behavioral, and biomedical sciences. *Behav. Res. Methods* **2007**, *39*, 175–191.

(64) Belvisi, M. G.; Patel, H. J.; Freund-Michel, V.; Hele, D. J.; Crispino, N.; Birrell, M. A. Inhibitory activity of the novel CB2 receptor agonist, GW833972A, on guinea-pig and human sensory nerve function in the airways. *Br. J. Pharmacol.* **2008**, *155*, 547–557.



Article

Synthesis and NLRP3-Inflammasome Inhibitory Activity of the Naturally Occurring Velutone F and of Its Non-Natural Regioisomeric Chalconoids

Tiziano De Ventura ^{1,†}, Mariasole Perrone ^{2,3,†}, Sonia Missiroli ^{2,3}, Paolo Pinton ^{2,3,4}, Paolo Marchetti ¹, Giovanni Strazzabosco ¹, Giulia Turrin ¹, Davide Illuminati ¹, Virginia Cristofori ¹, Anna Fantinati ⁵, Martina Fabbri ¹, Carlotta Giorgi ^{2,3,*}, Claudio Trapella ^{1,3,*} and Vinicio Zanirato ¹

¹ Department of Chemistry, Pharmaceutical and Agricultural Sciences, University of Ferrara, Via Luigi Borsari 46, 44121 Ferrara, Italy

² Department of Medical Sciences, Section of Experimental Medicine, University of Ferrara, Via Fossato di Mortara, 64/b, 44121 Ferrara, Italy

³ Laboratory for Technologies of Advanced Therapies (LTTA), Via Fossato di Mortara, 70, 44121 Ferrara, Italy

⁴ Maria Cecilia Hospital, GVM Care & Research, 48033 Cotignola, Italy

⁵ Department of Environmental and Prevention Sciences, University of Ferrara, Via Fossato di Mortara 17, 44121 Ferrara, Italy

* Correspondence: carlotta.giorgi@unife.it (C.G.); trap@unife.it (C.T.);
Tel.: +39-0532-455802 (C.G.); +39-0532-455924 (C.T.)

† These authors contributed equally to this work.



Citation: De Ventura, T.; Perrone, M.; Missiroli, S.; Pinton, P.; Marchetti, P.; Strazzabosco, G.; Turrin, G.; Illuminati, D.; Cristofori, V.; Fantinati, A.; et al. Synthesis and NLRP3-Inflammasome Inhibitory Activity of the Naturally Occurring Velutone F and of Its Non-Natural Regioisomeric Chalconoids. *Int. J. Mol. Sci.* **2022**, *23*, 8957. <https://doi.org/10.3390/ijms23168957>

Academic Editor: Atsushi Matsuzawa

Received: 13 July 2022

Accepted: 9 August 2022

Published: 11 August 2022

Publisher's Note: MDPI stays neutral with regard to jurisdictional claims in published maps and institutional affiliations.



Copyright: © 2022 by the authors. Licensee MDPI, Basel, Switzerland. This article is an open access article distributed under the terms and conditions of the Creative Commons Attribution (CC BY) license (<https://creativecommons.org/licenses/by/4.0/>).

Abstract: Plant-derived remedies rich in chalcone-based compounds have been known for centuries in the treatment of specific diseases, and nowadays, the fascinating chalcone framework is considered a useful and, above all, abundant natural chemotype. Velutone F, a new chalconoid from *Milletia velutina*, exhibits a potent effect as an NLRP3-inflammasome inhibitor; the search for new natural/non-natural lead compounds as NLRP3 inhibitors is a current topical subject in medicinal chemistry. The details of our work toward the synthesis of velutone F and the unknown non-natural regioisomers are herein reported. We used different synthetic strategies both for the construction of the distinctive benzofuran nucleus (**BF**) and for the key phenylpropenone system (**PhP**). Importantly, we have disclosed a facile entry to the velutone F via synthetic routes that can also be useful for preparing non-natural analogs, a prerequisite for extensive SAR studies on the new flavonoid class of NLRP3-inhibitors.

Keywords: flavonoid; chalcone-based compounds; NLRP3-inflammasome inhibitors

1. Introduction

Chalcone-based compounds can act as photoinitiators of polymerization under visible light with an excellent profile for (i) free radical polymerization, (ii) cationic polymerization, (iii) synthesis of interpenetrating polymer networks (IPNs), and (iv) thiol-ene reactions [1]. Additionally, fluorescent chalcone derivatives have been used for the development of a mouse embryonic stem cell probe [2]. On the other hand, in-depth pharmacological studies concluded that natural extracts containing chalcone-based compounds exhibit an impressive array of biological activities, including anti-inflammatory/anticancer effects [3–5]. Actually, chalcones may inhibit specific enzymes such as different kinases [6–8], the aldose reductase [9,10], cyclooxygenases [11,12], and inducible nitric oxide synthase [13,14]. Moreover, it has been shown that both synthetic and natural chalconoids play a healthy role in several diseases by inhibiting the NLRP3-inflammasome formation [15–19]. The NLRP3 inflammasome is a large protein complex controlling the production of caspase-1 and ultimately of pro-inflammatory cytokines (IL-1 and IL-18). In this context, it was reported that velutone F (**1**) (Figure 1), a retrochalcone [20–22] recently identified in the ethanolic extract of the

leguminous plant *Millettia velutina* [23,24], inhibits the formation of the NLRP3 active complex. Among the eight new flavonoids identified in the lipophilic crude residue derived from 10 kg of dry vine stems of *Millettia velutina*, compound **1** exhibited the most potent inhibitory effect against nigericin-induced IL-1 release in THP-1 cells. Velutone F, featuring the 1-phenyl-2-propen-1-one moiety (PhP) and a substituted benzofuran core (BF), can be classified as a hybrid chalcone. The development of hybrid molecules incorporating different pharmacophores, each with its own molecular target, is an important area of research in medicinal chemistry [25]. Actually, both natural and synthetic benzofuran-derived compounds have potential therapeutic interests ranging from antibacterial, antifungal, anti-inflammatory, analgesic, antidepressant, anticonvulsant, anticancer, anti-HIV, antidiabetic, antituberculosis, and antioxidant [26–29].

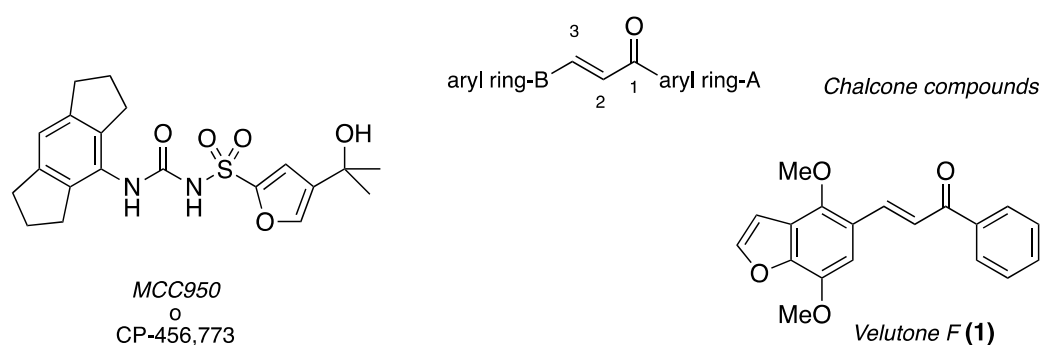


Figure 1. Natural and non-natural inhibitors of the NLRP3 inflammasome activation.

We are currently involved in a multidisciplinary study aimed at identifying new anti-inflammatory/anticancer compounds that mimic the MCC950 molecular structure (Figure 1). It has been demonstrated that the diarylsulfonylurea MCC950 powerfully inhibits the NLRP3 activation selectively [30,31]. In detail, MCC950 would seem to reversibly bind the NLRP3 multi-protein complex making it unable to generate the active complex, namely the NLRP3-inflammasome [32,33]. Because of the profoundly different chemical structures of the synthetic MCC950 compared to the one of velutone F (**1**), it is reasonable to assume that they can block the activation of the NLRP3-inflammasome by interfering with different bio-chemical targets. We were intrigued by the possibility of disposing of multi-milligrams amount of the natural substance **1** for the purpose of undertaking pharmacological investigations and mostly to shed some light on the mechanism by which compound **1** inhibits the nigericin-induced IL-1 release. Actually, when we started the search, the chemical identity of **1** was ascertained by spectroscopic means exclusively, primarily 2D NMR [23]. However, very recently [24], the same research teams got proof of the chalconoid structure of compound **1** by its semi-synthesis from Khellin.

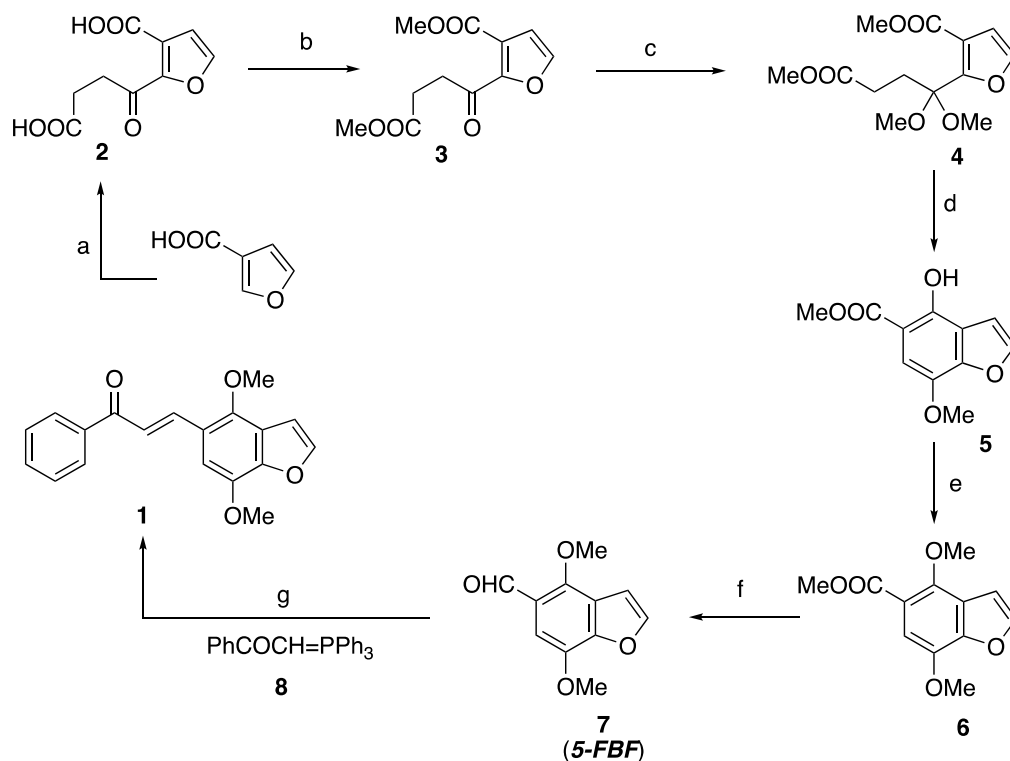
The reasons mentioned above prompted us to design/develop synthetic routes for preparing both the natural substance originally extracted from the tropical plant *Millettia velutina* and analogs to be studied by the biologist team as promising anti-inflammatory agents.

2. Results and Discussion

A host of synthetic strategies has been developed to create the trans-carbon-carbon double bond of the 1,3-diaryl-2-propen-1-one moiety featuring chalcone compounds, including Claisen-Schmidt's condensations, Wittig, and Julia-Kocienski olefinations. Instead, palladium-catalyzed reactions, namely Heck, Sonogashira, and Suzuki-Miyaura cross couplings, have been used to establish the 1,3-diaryl-enone framework through A-ring/C-1 and/or C1/C2 bond formation [34].

Initially, we planned a synthetic strategy to compound **1** based on the introduction of the required alkene by Wittig olefination of 5-formyl-4,7-dimethoxy benzofuran **7** (5-FBF) with the 1-phenyl-2-(triphenylphosphoranylidene)ethanone counterpart **8** [35]. To this end we elaborated two synthetic approaches for the preparation of the key intermediate

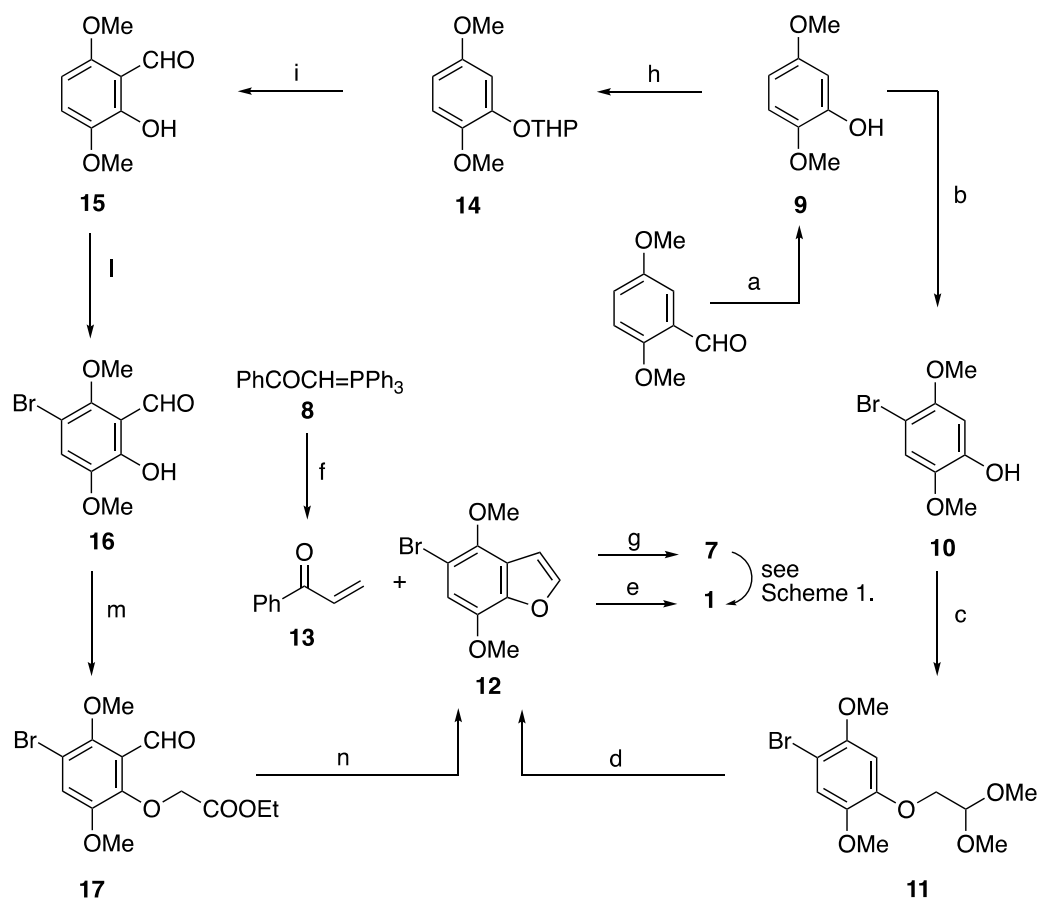
5-FBF differing in the way the benzofuran core (**BF**) could be formed via annellation of the carbocyclic ring system onto a preformed furan, synthetic pathway A (Scheme 1), or alternatively, by creating the furan ring by intramolecular cyclization on a preexistent carbocyclic, synthetic pathway B (Scheme 2).



Scheme 1. Synthetic pathway A for target compound **1**. Reagents and conditions: (a) i: LDA, THF, $-78\text{ }^{\circ}\text{C}$, succinic anhydride; ii: dil.HCl; 35%; (b) MeOH, H_2SO_4 , 90%; (c) $\text{HC}(\text{OMe})_3$, p-TsOH, MeOH reflux, 36 h, 90%; (d) i: t-BuOK, THF, $-78\text{ }^{\circ}\text{C}$; ii: dil.HCl, 62%; (e) MeI, Cs_2CO_3 , DMF, rt, 16 h, 96%; (f) i: LiAlH_4 , Et_2O , 12 h; ii: PCC, CH_2Cl_2 , rt, 1.5 h, 60% two steps; (g) MeCN, MW, $135\text{ }^{\circ}\text{C}$, 1.5 h, 70%.

2.1. Synthetic Pathway A for Target Compound 1

The first route starts by treating the 3-furoic acid with excess LDA to produce the corresponding C-2 lithiated carboxylate lithium salt, which, by reacting with succinic anhydride, gave the dicarboxylic acid **2**. The desired acyl derivative **3** could be isolated in a modest yield after esterification of **2** [36,37]. The subsequent carbonyl group protection as dimethyl ketal **4** opened the way to the creation of the annellated six-membered carbocyclic ring. Thus, the Dieckmann cyclization, performed with potassium tert-butoxide at $-78\text{ }^{\circ}\text{C}$, occurred with simultaneous elimination of MeOH from the dimethyl ketal group yielding the aromatic derivative **5**, which was taken to the benzofuran derivative **6** by etherification. Subsequently, the methoxycarbonyl group was converted to the required formyl group by a two-step process entailing reduction with LiAlH_4 and oxidation of the resulting primary alcohol with pyridinium chlorochromate (PCC). The resulting **5-FBF** was eventually reacted with the stabilized phosphorous ylide **8**, in turn, prepared according to the literature [35]. The Wittig olefination under microwave irradiation provided velutone F (**1**) in 70% yield after chromatographic purification. As expected, NMR spectroscopic data for the synthesized velutone F were superimposable to the ones originally reported for the retrochalcone isolated from *Millettia velutina*.



Scheme 2. Synthetic pathway B for target compound 1. Reagents and conditions: (a) i: H_2O_2 , *t*-BuOH, cat. SeO_2 , rt, 12 h; ii: MeOH, K_2CO_3 , 90% two steps; (b) NBS, MeCN, 0 °C, 30 min, 97%; (c) $\text{BrCH}_2\text{CH}(\text{OMe})_2$, KOH, DMA, 140 °C, 1.5 h, 83%; (d) PPA, PhCl, reflux, 30 min, 50%; (e) $\text{Pd}(\text{OAc})_2$, Tri(*o*-tolyl)phosphine, DIPEA:DMF (1:1), 32%; (f) CH_2Cl_2 -formalin, reflux, 12 h, 80%; (g) i: BuLi, THF, −78 °C; ii: DMF, 50%; (h) DHP, PPTS, CH_2Cl_2 , rt, 12 h, 91%; (i) i: BuLi, Et_2O , 0 °C, 2 h; ii: DMF, −78 to rt, 2 h; iii: HCl 6M, 80% overall; (l) Br_2 -AcOH, AcONa, rt, 30 min, 80%; (m) $\text{BrCH}_2\text{COOEt}$, DMF, Cs_2CO_3 , rt, 1 h, 85%; (n) i: LiOH, THF- H_2O , rt, 12 h; ii: AcONa, Ac_2O , 130 °C, 2 h; iii: EtOH, 60 °C, 2 h, 57%.

2.2. Synthetic Pathway B for Target Compound 1

The starting move of the alternative synthetic approach to 7 entailing the creation of the furan ring by intramolecular cyclization of the bromobenzene derivative 11 (Scheme 2) was the Dakin-like oxidation of the cheap 2,5-dimethoxybenzaldehyde by using the H_2O_2 /cat. SeO_2 system in *tert*-BuOH [38]. Methanolysis of the resulting arylformate promptly furnished the 2,5-dimethoxyphenol 9, which underwent regioselective bromination with NBS affording 10. The exclusive C-4 bromination accounted for the marked para orienting effect of the phenolic hydroxyl group [39].

At this stage, with the aim of creating the annellated 2,3-unsubstituted furan ring, we needed to introduce an O-tethered functionalized two carbon fragment. Thus, compound 10 was easily converted to the aryl ether 11 by treatment with bromoacetaldehyde dimethyl acetal and KOH in dimethylacetamide (DMA) [40]. The anticipated intramolecular electrophilic aromatic substitution was carried out with polyphosphoric acid (PPA), providing the benzofuran derivative 12 in a 50% yield. Transformation of the 5-bromo benzofuran derivative 12 into 5-formyl-4,7-dimethoxy benzofuran 7 (5-FBF) was achieved through halogen-metal exchange with BuLi followed by reaction with DMF [41].

In order to make the critical furan ring annellation step more efficient, we turned our attention to a recently reported protocol for the synthesis of 6-hydroxybenzofuran based

on an unusual cycloaddition-cycloreversion sequence [42]. To this end, we prepared the penta-substituted benzene derivative **16** starting from the tri-substituted phenol derivative **9** (Scheme 2), exploiting the well-known ability of the OTHP as an ortho-directing group for the metalation [43]. Accordingly, compound **9** was promptly transformed into the corresponding tetrahydropyranyl ether **14** that was at first ortho-lithiated by treatment with BuLi and later reacted with DMF to give the tetra-substituted phenyl derivative **15**. The subsequent bromination para to the phenol group [44] afforded the desired penta-substituted benzene **16**, to which the O-ethoxycarbonylmethylene fragment was easily inserted by standard etherification reaction. In previous saponification, compound **17** was treated with the Ac₂O-AcONa system with heating to give the required 5-bromo benzofuran derivative **12** in an appreciable 57% yield. The mechanism proposed for the interesting cyclization reaction entails dehydration of the carboxyl group to give an unstable ketene intermediate that is trapped intramolecularly by the formyl group. The thermal [2 + 2] heterocycloaddition reaction is followed by a cycloreversion with the expulsion of CO₂ and production of the 2,3-unsubstituted benzofuran derivative **12** [42].

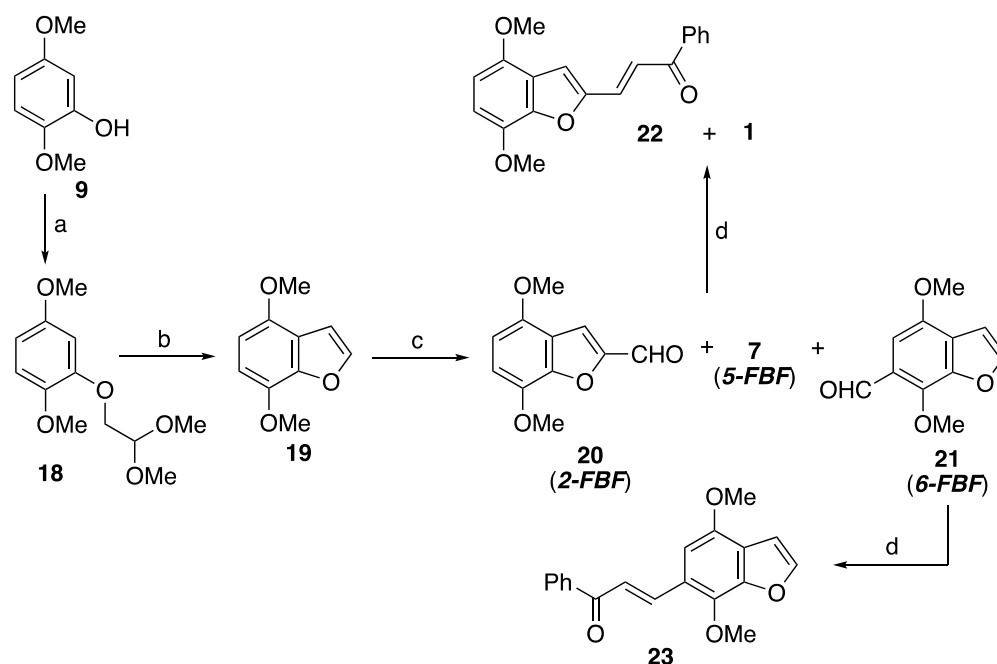
Having the suitably derivatized aryl ring-B moiety in hand, we conceived preparing compound **1** by exploiting the Mizoroki-Heck cross-coupling reaction between **12** and 1-phenyl-2-propen-1-one **13**. The latter reagent was, in turn, easily prepared by reacting phosphorous ylide **8** and formaldehyde according to a known Wittig protocol [45] (Scheme 2). Disappointingly, the Pd(0)-catalyzed reaction provided the retrochalcone **1** with a modest 32% yield [46].

2.3. Synthetic Pathways Providing the Non-Natural Regioisomers of Velutone F

With the aim of learning about stereo-electronic properties of the hybrid benzofuran-retrochalcone scaffold, we decided to prepare the non-natural compounds **22**, **23**, and **28** featuring the PhP moiety attached, respectively, at C-2, C-6, and C-3 of the 4,7-dimethoxy benzofuran core (BF). The non-natural regioisomers of velutone F are previously unknown compounds.

2.3.1. Synthetic Pathways to the Isomers 22 and 23

The direct formylation of electron-rich arenes can be conveniently accomplished via the Vilsmeier-Haack (V-H) reaction. Indeed, the benzo[b]furan nucleus is reported to yield the 2-formyl derivative by reaction with the V-H electrophilic species [47]. We anticipated that the regioselectivity of the V-H reaction could change if electron-donating groups were present on the phenyl ring of the benzo-fused system. In line with our hypothesis, we decided exploring the behavior of 4,7-dimethoxy benzo[b]furan **19** under V-H reaction conditions (Scheme 3). We planned to build the substituted benzo[b]furan **19** from **9** by creating the annellated 2,3-unsubstituted furan ring according to our previously sound synthetic pathway B for target compound **1** (Scheme 2). Thus, once etherified the phenolic group of **9** with the functionalized two carbon fragment, the resulting compound **18** was cyclized to **19** under the action of PPA (Sn-β zeolite also showed to efficiently promote this transformation [48]). As expected, we found the subsequent electrophilic aromatic substitution reaction was poorly regioselective: all but one of the regioisomeric formyl benzofuran derivatives **2-FBF**, **5-FBF**, and **6-FBF** were formed. In detail, chromatographic purification of the residue from the V-H reaction led us to isolate compounds **20** (**2-FBF**) together with **7** (**5-FBF**) in 37% yield (¹H NMR and HPLC analysis showed the isomers were in a 3.5:6.5 ratio), and compound **21** (**6-FBF**) in 30% yield. At this stage, we submitted the separated fractions to the Wittig olefination with the stabilized phosphorous ylide **8**. We obtained chalcone **23** from **6-FBF**, while in the same manner, the inseparable mixture of **2-FBF** and **5-FBF** furnished chalcones **22** and **1**, which, gratifyingly, could be easily separated by column chromatography.



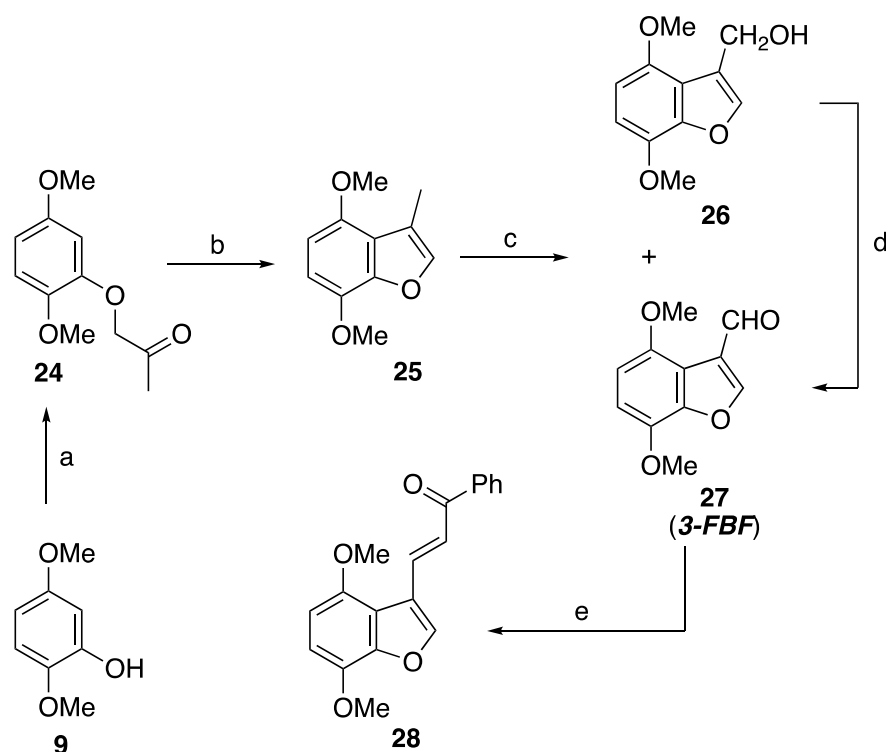
Scheme 3. Synthetic pathways to regioisomers **22** and **23**. Reagents and conditions: (a) KOH, DMAC, BrCH₂CH(OMe)₂, 140 °C, 2 h, 70%; (b) Sn-β zeolite, PhCl, 105 °C, 5 h, 62%; (c) POCl₃, DMF, 80 °C, 12 h, (**20**, 24%), (**7**, 13%), (**21**, 30%); (d) **8**, toluene, reflux, 12 h 50%.

2.3.2. Synthetic Pathway to the Isomer **28**

We envisaged setting up the **PhP** moiety of **28** by reaction of 3-formyl benzofuran derivative **27** (**3-FBF**) with the ylide **8** according to the previously tested protocol entailing a classical Wittig olefination. About **3-FBF** preparation, we selected compound **25** as the direct precursor having in mind a controlled oxidation of its C-3 methyl substituent in order to derive the pivotal electrophilic functional group [49,50] (Scheme 4). Thus, we devised preparing compound **25** in two steps from phenol **9**, namely: etherification with bromoacetone followed by acid-promoted cyclization of the resulting aryloxy acetone derivative **24**. The planned SeO₂-oxidation of the C-3 methyl residue of compound **25** furnished a 1:1 mixture of the primary alcohol **26** and the aldehyde **27**, which were separable by chromatography. However, we found it very easy to carry out the oxidation of **26** to **3-FBF** by using the Corey–Suggs reagent (PCC). Eventually, the microwave-promoted Wittig reaction between the aryl aldehyde **27** (**3-FBF**) and the phosphorous ylide **8** provided the aimed chalconoid **28** in good yield.

2.3.3. Inhibition of IL-1β Release In Vitro and In Vivo

Among the inflammasomes, NLRP3 is the most studied and characterized due to its implication in the pathogenesis of different human diseases [51]. The activation of NLRP3 inflammasomes consists of caspase-1 activation, which in turn induces secretion of the inflammatory cytokine IL-1β. Hence, IL-1β release is the most used read-out for NLRP3 inflammasome activation. In this study, IL-1β release was determined by ELISA assay to assess the inhibitory effects of synthesized compounds on NLRP3 inflammasome activation both in mouse bone marrow-derived macrophages (BMDMs) and in human PMA-differentiated lipopolysaccharide (LPS)-primed THP-1 macrophages (Figure 2). Velutone F (**1**) and the non-natural compounds **22**, **23**, and **28** demonstrated a high inhibitory capacity on the release of IL-1β.



Scheme 4. Synthetic pathway to regioisomer 28. Reagents and conditions: (a) $\text{BrCH}_2\text{COCH}_3$, Cs_2CO_3 , DMF, rt, 12 h, 63%; (b) PPA, PhCl, 110°C , 20 min, 50%; (c) SeO_2 , dioxane, 75°C , 96 h, 80%; (d) PCC, CH_2Cl_2 , rt, 12 h, 95%; (e) 8, MeCN, MW, 135°C , 2 h, 65%.

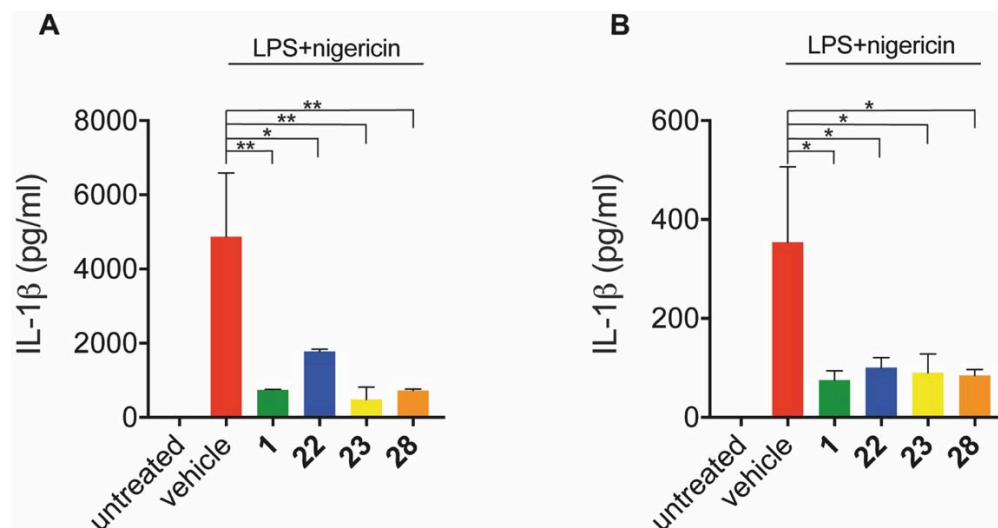


Figure 2. In vitro inhibition of IL-1 β release. (A) BMDMs were stimulated with LPS ($1\ \mu\text{g}/\text{mL}$) for 2 h, then treated with compounds for 30 min, and then activated with nigericin ($10\ \mu\text{M}$) for 1 h. (B) LPS-primed PMA-differentiated THP-1 cells were stimulated with LPS ($1\ \mu\text{g}/\text{mL}$) for 3 h, then treated with compounds for 30 min, and then activated with nigericin ($10\ \mu\text{M}$) for 1 h. Cell supernatants were analyzed with ELISA test for the evaluation of IL-1 β release ($n = 3$, mean \pm SEM). Statistics differences were analyzed using one-way ANOVA: ** $p < 0.01$, * $p < 0.05$.

To confirm the anti-inflammatory activity of these compounds in vivo, we used an LPS-induced inflammation treatment. Mice were intraperitoneally (IP) pre-injected with velutone F (1) and the non-natural isomers 22, 23, and 28 or vehicle at $25\ \text{mg}/\text{kg}$ and then were IP injected with LPS ($1\ \text{mg}/\text{kg}$). After 4 h, plasma and peritoneal exudate were collected from mice and analyzed for evaluation of IL-1 β release. The mice that received

pre-treatment with our compounds displayed a dramatic reduction in IL-1 production both in peritoneal exudate and blood samples (Figure 3).

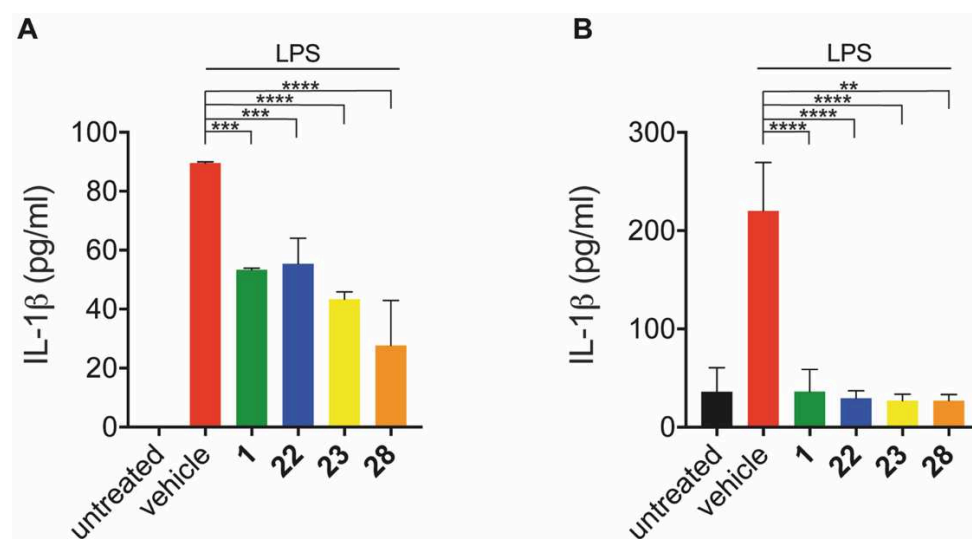


Figure 3. In vivo inhibition of IL-1 β release. (A) Exudate and (B) plasma levels of IL-1 β from C57BL/6 mice pretreated with compounds or vehicle control as determined by ELISA 4 h after intraperitoneally IP LPS (1 mg/kg) injection, n = 6/group. Data are shown as mean \pm SEM. Statistical differences were analyzed using one-way ANOVA: **** $p < 0.0001$, *** $p < 0.001$, ** $p < 0.01$.

Taken together, these results revealed that synthesized velutone F (1), as well as its regioisomers 22, 23, and 28, exerted a strong inhibition on the NLRP3 inflammasome activation both in vitro and in vivo.

3. Materials and Methods

3.1. Chemistry: Materials and General

All reagents and solvents that were commercially purchased were directly used without prior treatment. Reaction temperatures were recorded using a regular thermometer without correction. Melting points were determined on the Reichert Termovar apparatus and are uncorrected. Reactions were monitored by analytical thin-layer chromatography (TLC) on silica gel F254 glass plates (Merck, Darmstadt, Germany) and visualized under UV light 254 nm and KMnO_4 . Mobile phases abbreviations: A = Ethyl acetate, P = petroleum ether, DCM = dichloromethane. ^1H NMR spectra were recorded with a Mercury Place Varian 400 MHz NMR spectrometer (Varian Palo Alto, CA, USA) at room temperature. Chemical shifts (in ppm) were recorded as parts per million (ppm) downfield to tetramethylsilane (TMS). The following abbreviations are used for a multiplicity of NMR signals: s, singlet; d, doublet; t, triplet; q, quartet; m, multiplet; dd, double doublet; dt, double triplet; ddd, doublet of doublet of doublets; dtd, doublet of triplet of doublets. MS was carried out using electrospray ionization (ESI MICROMASS ZQ 2000, Waters, Milford, MA, USA). HRMS was acquired by CIGS University of Modena e Reggio Emilia (Modena, Italy) using a Q-Exactive Hybrid Quadrupole Orbitrap (Thermo Scientific, Waltham, MA, USA). IR spectra were taken on a Perkin-Elmer FT-IR spectrum 100 spectrometer (Foster City, CA, USA). Analytical HPLC was performed with Beckman System Gold 168 (Milan, Italy) using a C18 100 A Phenomenex Kinetex (150 \times 4.6 mm) and UV-DAD detection. [A]: 0.1% TFA in water and [B]: 0.1% TFA in acetonitrile was used as a binary mobile phase at a flow rate of 0.7 mL/min. Gradient: from 0% to 100% [B] in 25 min. Microwave reactions were performed in a Biotage Initiator Plus reactor (Biotage, Sweden) using 2–5 mL glass vials with a rubber cap. For all experimental spectra see Supplementary Materials.

3.1.1. Methyl 3-(4-Methoxy-4-oxobutanoyl)furan-2-carboxylate (3)

A solution of 3-Furoic acid (1 g, 8.92 mmol, 1 equiv.) in anhydrous THF (6 mL) was added dropwise, under argon atmosphere, to a cooled ($-78\text{ }^{\circ}\text{C}$) solution of LDA, which was previously prepared from *n*-BuLi (12.5 mL, 1.6 M in hexane, 19.96 mmol, 2.2 equiv.) and *i*-Pr₂NH (2.9 mL, 19.96 mmol, 2.2 equiv.) in THF (25 mL). The reaction mixture was stirred at $-78\text{ }^{\circ}\text{C}$ for 2 h, then a solution of succinic anhydride (1 g, 9.99 mmol, 1.1 equiv.) in anhydrous THF (8 mL) was added to the reaction flask. The cooling bath was removed, and aqueous 2 M HCl (30 mL) was added at room temperature. The mixture was extracted with chloroform, the organic phase was dried over Na₂SO₄, and solvent was evaporated. The solid residue was dissolved in MeOH (50 mL), cooled at $0\text{ }^{\circ}\text{C}$, and H₂SO₄ (0.45 mL, 95%) was added dropwise. The mixture was stirred at room temperature for 24 h, then a saturated NaHCO₃ solution was added, and the mixture was extracted with AcOEt. The organic phase, dried over Na₂SO₄, was evaporated under reduced pressure to give a crude that was purified by silica gel column chromatography with A/P 1:9, *v/v* as a solvent system. Title compound (3) was isolated as a colorless oil. Yield 32% over two steps. ¹H NMR (400 MHz, Chloroform-*d*) δ 7.51 (d, *J* = 1.7 Hz, 1H), 6.81 (d, *J* = 1.7 Hz, 1H), 3.89 (s, 3H), 3.68 (s, 3H), 3.31 (t, *J* = 6.7 Hz, 2H), 2.73 (t, *J* = 6.6 Hz, 2H). ¹³C NMR (101 MHz, Chloroform-*d*) δ 187.72, 172.96, 162.89, 150.83, 144.36, 122.29, 113.62, 52.46, 51.83, 34.92, 27.47 [36,37].

3.1.2. Methyl 3-(1,1,4-Trimethoxy-4-oxobutyl)furan-2-carboxylate (4)

A solution of compound 3 (0.9 gr, 3.75 mmol, 1 equiv.), HC(OMe)₃ (2.1 mL, 19.48 mmol, 5.2 equiv.), and *p*-TsOH (0.05 gr) in MeOH (8 mL) was refluxed for 48 h. The reaction mixture was cooled to room temperature, pyridine (0.18 mL) was added, and the solvent evaporated. The residue was purified by silica gel column chromatography with A/P 1:4, *v/v* as a solvent system. Title compound 4 was obtained as a transparent oil. Yield 90%. ¹H NMR (400 MHz, Chloroform-*d*) δ 7.36 (d, *J* = 1.7 Hz, 1H), 6.66 (d, *J* = 1.7 Hz, 1H), 3.81 (s, 3H), 3.58 (s, 3H), 3.20 (s, 6H), 2.47 (t, *J* = 6.7 Hz, 2H), 2.16 (t, *J* = 6.6 Hz, 2H). ¹³C NMR (101 MHz, Chloroform-*d*) δ 173.51, 163.81, 154.87, 141.84, 117.12, 112.38, 111.59, 101.72, 52.18, 51.97, 49.51, 30.35, 28.92 [36,37].

3.1.3. Methyl 4-Hydroxy-7-methoxybenzofuran-5-carboxylate (5)

tert-BuOK (0.61 g, 5.45 mmol, 2.2 equiv.) was poured into anhydrous THF (65 mL) under an argon atmosphere, and the suspension was cooled to $-78\text{ }^{\circ}\text{C}$. A solution of compound 4 (0.71 g, 2.48 mmol, 1 equiv.) in anhydrous THF (2 mL) was added dropwise, and the mixture turned orange. After 1.5 h of stirring at $-78\text{ }^{\circ}\text{C}$, anhydrous HCl (4 M in 1,4-dioxane) was added. The resulting transparent yellow reaction mixture was allowed to room temperature and stirred for 1 h. The precipitate was filtered through a Gooch filter, and the solvent was evaporated under reduced pressure. Chromatographic purification of the residue with A/P 1:9 *v/v* as the eluent phase provided title compound 5 as a white solid. Melting point: 125–127 $^{\circ}\text{C}$. Yield 62%. ¹H NMR (400 MHz, Chloroform-*d*) δ 11.14 (s, 1H), 7.60 (dd, *J* = 2.1 Hz, 1H), 7.17 (s, 1H), 6.98 (d, *J* = 2.1 Hz, 1H), 3.97 (d, *J* = 1.6 Hz, 6H). ¹³C NMR (101 MHz, Chloroform-*d*) δ 171.09, 152.43, 149.52, 144.76, 139.19, 118.90, 105.66, 105.38, 105.02, 56.51, 52.29 [36,37].

3.1.4. Methyl 4,7-Dimethoxybenzofuran-5-carboxylate (6)

A mixture of compound 5 (0.21 g, 0.95 mmol, 1 equiv.), Cs₂CO₃ (1.55 g, 5.75 mmol, 5 equiv.), and CH₃I (0.29 mL, 4.75 mmol, 5 equiv.) in anhydrous DMF (6 mL) was stirred at room temperature for 16 h under an argon atmosphere. After complete conversion of starting material (checked by TLC A/P 1:9), the reaction was partitioned between HCl 2 M and AcOEt; the organic phase was washed with HCl 2 M ($\times 2$) and brine, dried over Na₂SO₄, and the solvent was evaporated to dryness. Purification of the crude by column chromatography with A/P 1:4 as the eluent phase afforded title compound 6 as a colorless oil. Yield 96%. ¹H NMR (300 MHz, Chloroform-*d*) δ 7.63–7.61 (m, 1H), 7.26 (s, 1H), 6.95–6.94

(m, 1H), 4.00 (d, $J = 0.8$ Hz, 6H), 3.94 (d, $J = 0.8$ Hz, 3H). ^{13}C NMR (75 MHz, Chloroform-*d*) δ 167.04, 149.35, 148.04, 145.57, 141.84, 123.31, 117.58, 108.69, 105.80, 62.46, 56.77, 52.52.

3.1.5. 4,7-Dimethoxybenzofuran-5-carbaldehyde (7)

A solution of compound **6** (0.2 g, 0.84 mmol, 1 equiv.) in dry Et_2O (4 mL) was added dropwise to a stirred to a cooled (0°C) suspension of LiAlH_4 (0.08 g, 2.1 mmol, 2.5 equiv.) in anhydrous Et_2O (5 mL) under argon atmosphere. The reaction mixture was stirred at room temperature overnight, then it was cooled to 0°C , and aqueous NaOH solution (5 mL, 2 M) was added. After 30 min, the mixture was filtered on a celite pad, and the phases were separated. The aqueous phase was extracted with Et_2O . The combined organics were dried over Na_2SO_4 , and the solvent was evaporated to give (4,7-dimethoxybenzofuran-5-yl)methanol as a white crystalline solid, which was used in the next oxidative step without further purification.

A solution of the primary alcohol (0.14 g, 1.29 mmol, 1 equiv.) in anhydrous DCM (5 mL) was added to a suspension of PCC (0.42 g, 1.93 mmol, 1.5 equiv.) in DCM (5 mL). The dark brown reaction mixture was magnetically stirred at room temperature for 1.5 h then Et_2O was added. The supernatant was decanted from the black insoluble residue, which was further washed with Et_2O ($\times 3$). The combined organic phases were filtered through a pad of silica, and the solvent was evaporated. Purification of the crude by column chromatography with A/P 1:4 *v/v* as a solvent system furnished title compound **7** as a white crystalline solid. Melting point: $142\text{--}145^\circ\text{C}$. Yield 50%. ^1H NMR (400 MHz, Chloroform-*d*) δ 10.46 (s, 1H), 7.67 (dd, $J = 2.3, 0.4$ Hz, 1H), 7.25 (s, 1H), 7.02 (d, $J = 2.3$ Hz, 1H), 4.15 (s, 3H), 4.00 (s, 3H). ^{13}C NMR (101 MHz, Chloroform-*d*) δ 189.09, 149.92, 145.30, 142.04, 122.24, 120.30, 105.88, 103.45, 61.74, 56.29.

3.1.6. 2,5-Dimethoxyphenol (9)

H_2O_2 (2.4 mL, 30% *w/w*, 78.21 mmol, 5.4 equiv.) was added dropwise to a magnetically stirred mixture of 2,5-dimethoxybenzaldehyde (2.42 g, 14.56 mmol, 1 equiv.), SeO_2 (0.038 g, 0.342 mmol, 0.023 equiv.) in *tert*-BuOH (6 mL). The reaction mixture was stirred overnight at room temperature then Et_2O (20 mL) was added. The resulting mixture was washed with brine ($\times 3$), the organic phase was dried over Na_2SO_4 , and the solvent was evaporated to dryness. The residue was dissolved in MeOH (10 mL), and a solution of K_2CO_3 (2 g) in H_2O (10 mL) was added to the solution. After 1 h, HCl 6M was added to reach pH 1, and the reaction mixture was extracted with DMC (20 mL $\times 3$). The combined organic phases were dried over anhydrous Na_2SO_4 , and the solvent was evaporated to dryness. Purification was carried out by silica gel column chromatography with A/P 1.5:8.5 *v/v* to obtain compound **9** as a transparent oil. Yield 90%. ^1H NMR (400 MHz, Chloroform-*d*) δ 6.77 (d, $J = 8.8$ Hz, 1H), 6.56 (d, $J = 2.9$ Hz, 1H), 6.38 (dd, $J = 8.8, 2.9$ Hz, 1H), 5.66 (s, 1H), 3.84 (s, 3H), 3.75 (s, 3H). ^{13}C NMR (101 MHz, Chloroform-*d*) δ 154.56, 146.44, 140.96, 111.45, 104.23, 101.73, 56.58, 55.66 [38].

3.1.7. 4-Bromo-2,5-dimethoxyphenol (10)

NBS (1.16 g, 6.55 mmol, 1 equiv.) was added to a cooled (0°C) solution of **9** (1.0 g, 6.55 mmol, 1 equiv.) in acetonitrile (130 mL). Stirring at 0°C was continued for 30 min. Then, $\text{Na}_2\text{S}_2\text{O}_3$ saturated solution was added, and the mixture was extracted with AcOEt ($\times 3$). The combined organic phases were washed with brine, dried over Na_2SO_4 , and the solvent was evaporated. Purification of the residue by column chromatography by eluting with A/P 1:4 *v/v* gave **10** as a transparent oil. Yield 97%. ^1H NMR (400 MHz, Chloroform-*d*) δ 7.02 (s, 1H), 6.61 (s, 1H), 5.65 (s, 1H), 3.83 (s, 3H), 3.81 (s, 3H). ^{13}C NMR (101 MHz, Chloroform-*d*) δ 150.66, 145.71, 140.94, 115.77, 100.51, 99.81, 56.77, 56.74.

3.1.8. 1-Bromo-4-(2,2-dimethoxyethoxy)-2,5-dimethoxybenzene (11)

$\text{BrCH}_2\text{CH}(\text{OMe})_2$ (1.0 mL, 8.82 mmol, 1.5 equiv.) was added dropwise to a stirred solution of **10** (1.37 g, 5.88 mmol, 1 equiv.) and KOH (0.66 g, 11.756 mmol, 2 equiv.) in

DMAC (12 mL). The reaction mixture was stirred at 140 °C for 1.5 h and then cooled to room temperature. H₂O (20 mL) was added, and the resulting mixture was extracted with Et₂O (40 mL × 3). The combined organic phases were washed with aqueous NaOH (30 mL, 5%) and H₂O (30 mL), dried over Na₂SO₄, and the solvent was evaporated to dryness. Purification of the residue by column chromatography with A/P 1:4 *v/v* as the eluent furnished **11** as a white crystalline solid. Melting point: 57–60 °C. Yield 83%. ¹H NMR (400 MHz, Chloroform-*d*) δ 7.05 (s, 1H), 6.63 (s, 1H), 4.72 (t, *J* = 5.2 Hz, 1H), 4.04 (d, *J* = 5.2 Hz, 0H), 3.83 (s, 3H), 3.80 (s, 3H), 3.46 (s, 6H). ¹³C NMR (101 MHz, Chloroform-*d*) δ 150.30, 148.22, 144.66, 117.47, 102.52, 102.07, 69.94, 57.10, 56.87, 54.51.

3.1.9. 5-Bromo-4,7-dimethoxybenzofuran (**12**) by Cyclization of (**11**)

A solution of compound **11** (0.37 g, 1.55 mmol, 1 equiv.) in chlorobenzene (3 mL) was added dropwise to a heated (120 °C) mixture of polyphosphoric acid (0.5 g) in chlorobenzene (15 mL). After 30 min, the reaction mixture was cooled to room temperature, diluted with Et₂O, and washed with H₂O. The removal of volatiles under reduced pressure gave a residue that was purified by column chromatography with A/P 0.5:9.5 *v/v*. Compound **12** was isolated as a white crystalline solid. Melting point: 63–65 °C. Yield 50%. ¹H NMR (400 MHz, Chloroform-*d*) δ 7.59 (dd, *J* = 2.2, 0.5 Hz, 1H), 6.92 (s, 1H), 6.87 (dd, *J* = 2.1, 0.4 Hz, 1H), 3.97 (d, *J* = 1.7 Hz, 6H). ¹³C NMR (101 MHz, Chloroform-*d*) δ 145.11, 144.54, 143.95, 142.09, 122.44, 110.55, 107.66, 104.60, 61.06, 56.57.

3.1.10. 4,7-Dimethoxybenzofuran-5-carbaldehyde (**7**) via Halogen-Metal Exchange

n-BuLi (1.32 mL, 1.6 M in hexane, 2.1 equiv.) was added to a cooled (−78 °C) solution of compound **12** (0.26 g, 1.0 mmol, 1.0 equiv) in dry THF (5 mL) under argon atmosphere. The reaction mixture was stirred at −78 °C for 20 min. Then, DMF (0.25 mL, 3.25 equiv.) was added, and the cooling bath was removed. After 12 h, AcOEt (10 mL) was added, and the reaction was quenched with NH₄Cl saturated aqueous solution. The organic layer was separated, washed with brine, dried over Na₂SO₄, and the solvent was evaporated to dryness. Chromatographic purification of the residue with A/P 1:4 *v/v* afforded the aldehyde **7** as a white crystalline solid. Melting point: 142–145 °C. Yield 50%. ¹H NMR (400 MHz, Chloroform-*d*) δ 10.46 (s, 1H), 7.67 (dd, *J* = 2.3, 0.4 Hz, 1H), 7.25 (s, 1H), 7.02 (d, *J* = 2.3 Hz, 1H), 4.15 (s, 3H), 4.00 (s, 3H). ¹³C NMR (101 MHz, Chloroform-*d*) δ 189.09, 149.92, 145.30, 142.04, 122.24, 120.30, 105.88, 103.45, 61.74, 56.29.

3.1.11. 1-Phenylprop-2-en-1-one (**13**)

Formalin (0.8 mL, 37%, 10 mmol, 5 equiv.) was added to a solution of the ylide **8** (0.76 g, 2 mmol, 1 equiv.) in DCM (8 mL), and the mixture was heated at reflux overnight. After washing with brine, the organic phase was dried over anhydrous Na₂SO₄ and evaporated to dryness. Purification of the residue by column chromatography with A/P 1:4 *v/v* as the eluent phase furnished compound **13** as a clear oil. Yield 80%. ¹H NMR (400 MHz, Chloroform-*d*) δ 7.97–7.93 (m, 2H), 7.58–7.55 (m, 1H), 7.51–7.45 (m, 2H), 7.16 (ddd, *J* = 17.2, 10.6, 0.6 Hz, 1H), 6.44 (dd, *J* = 17.2, 1.7 Hz, 1H), 5.95–5.91 (m, 1H). ¹³C NMR (101 MHz, Chloroform-*d*) δ 191.14, 137.35, 133.06, 132.47, 130.26, 129.00, 128.77, 128.70, 128.07 [45].

3.1.12. 2-(2,5-Dimethoxyphenoxy) tetrahydro-2H-pyran (**14**)

DHP (4.16 mL, 46 mmol, 10 equiv.) was added to a solution of compound **9** (0.71 g, 4.6 mmol, 1 equiv.) and PPTS (0.115 g, 0.46 mmol, 0.1 equiv.) in DCM (10 mL). The reaction mixture was stirred at room temperature overnight, then it was diluted with DCM and washed with NaOH solution and brine. The organic phase was dried over Na₂SO₄ and evaporated. Purification was performed by column chromatography using A/P 1:9 *v/v* as the eluent phase. Compound **14** was isolated as a clear oil. Yield 91%. ¹H NMR (400 MHz, DMSO-*d*₆) δ 6.89 (d, *J* = 8.8 Hz, 1H), 6.68 (d, *J* = 2.9 Hz, 1H), 6.50 (dd, *J* = 8.9, 2.9 Hz, 1H), 5.39 (t, *J* = 3.3 Hz, 1H), 3.82 (ddd, *J* = 11.1, 8.9, 3.8 Hz, 1H), 3.71 (s, 3H), 3.67 (s, 3H), 3.53 (dtd, *J* = 11.5, 4.3, 1.2 Hz, 1H), 1.94–1.38 (m, 7H) [44].

3.1.13. 2-Hydroxy-3,6-dimethoxybenzaldehyde (**15**)

n-BuLi (4 mL, 1.6 M in hexane, 6.37 mmol, 1.1 equiv.) was added dropwise to a cooled (0 °C) solution of compound **14** (1.38 g, 5.79 mmol, 1 equiv.) in anhydrous Et₂O (60 mL) under argon atmosphere. The reaction mixture turned purple, then yellow, and stirring was continued at room temperature for 2 h. The reaction flask was cooled to −78 °C, and anhydrous DMF (1.78 mL, 23.16 mmol, 4 equiv.) was added. The reaction mixture was stirred at room temperature for 2 h, quenched with HCl (5 mL, 6 N), and stirred at room temperature for 1 h. The aqueous phase was extracted with AcOEt (×3), the combined organics were dried over Na₂SO₄, and the solvent was evaporated. Purification of the residue was performed by column chromatography with A/P 1:4 *v/v* as the eluent phase. Compound **15** was isolated as bright yellow solid. Melting point: 67–69 °C. Yield 80%. ¹H NMR (400 MHz, Chloroform-*d*) δ 12.17 (s, 1H), 10.31 (s, 1H), 7.02 (d, *J* = 8.9 Hz, 1H), 6.27 (d, *J* = 8.9 Hz, 1H), 3.84 (d, *J* = 0.8 Hz, 6H). ¹³C NMR (101 MHz, Chloroform-*d*) δ 194.91, 155.87, 153.58, 142.08, 120.27, 111.09, 99.36, 56.90, 55.78 [44].

3.1.14. 3-Bromo-6-hydroxy-2,5-dimethoxybenzaldehyde (**16**)

AcONa (0.091 gr, 1.1 mmol, 1.1 equiv.) and then Br₂ (0.056 mL, 1.1 mmol, 1.1 equiv.) was added to a cooled (0 °C) solution of compound **15** (0.182 g, 1 mmol, 1 eq) in acetic acid (3 mL). The reaction mixture was stirred at room temperature for 30 min. Then, H₂O (10 mL) was added, and the mixture was extracted with DCM (10 mL × 3). The combined organic phases were washed with H₂O (10 mL), dried over Na₂SO₄, and evaporated. Purification of the residue by column chromatography with A/P 1:4 *v/v* as the eluent phase furnished compound **16** as a light-yellow solid. Melting point: 92–95 °C. Yield 80%. ¹H NMR (400 MHz, Chloroform-*d*) δ 11.89 (s, 1H), 10.21 (s, 1H), 7.19 (s, 1H), 3.92 (s, 3H), 3.87 (s, 3H). ¹³C NMR (101 MHz, Chloroform-*d*) δ 194.91, 152.63, 152.47, 145.51, 122.50, 115.15, 104.06, 63.41, 56.67 [44].

3.1.15. Ethyl 2-(4-bromo-2-formyl-3,6-dimethoxyphenoxy)acetate (**17**)

Cs₂CO₃ (0.36 g, 1.1 mmol, 1.1 equiv.) and BrCH₂COOEt (0.12 mL, 1.1 mmol, 1.1 equiv.) were added to a solution of compound **16** (0.261 g, 1 mmol, 1 equiv.) in DMF (5 mL). The reaction mixture was stirred at room temperature for 1 h. H₂O (10 mL) was added, and the mixture was extracted with AcOEt (20 mL × 3). The combined organic phases were washed with H₂O (20 mL), dried over Na₂SO₄, and the solvent was evaporated. Compound **17** was isolated as a white grainy solid after trituration with petroleum ether. Melting point: 85–86 °C. Yield 85%. ¹H NMR (400 MHz, Chloroform-*d*) δ 10.49 (s, 1H), 7.27 (s, 1H), 4.76 (s, 2H), 4.23 (q, *J* = 7.1 Hz, 2H), 3.85 (d, *J* = 2.1 Hz, 6H), 1.28 (t, *J* = 7.1 Hz, 3H). ¹³C NMR (101 MHz, Chloroform-*d*) δ 189.32, 168.96, 150.74, 148.89, 148.75, 121.27, 112.82, 69.75, 62.64, 61.36, 56.66, 14.24.

3.1.16. 5-Bromo-4,7-dimethoxybenzofuran (**12**) via Cyclization of (**17**)

LiOH·H₂O (0.032 g, 0.78 mmol, 3 equiv.) was added to a magnetically stirred solution of compound **17** (0.09 g, 0.26 mmol, 1 equiv.) in a 3:1 THF/H₂O (4 mL) mixture. After stirring at room temperature overnight, the reaction mixture was acidified with 1 M HCl and extracted with AcOEt (10 mL × 3). The combined organics were washed with brine, dried over anhydrous Na₂SO₄, and evaporated to dryness. The white solid residue was dissolved in Ac₂O (3 mL), AcONa (0.085 g, 1.035 mmol, 1.5 equiv.) was added, and the mixture was heated at 130 °C for 2 h. Successively, the temperature was lowered to 60 °C, and EtOH (3 mL) was added dropwise to consume acetic anhydride. The stirring was continued at 60 °C for 2 h. then, the reaction mixture was cooled to room temperature. H₂O (3 mL) was added, and the mixture was extracted with AcOEt (10 mL). The organic phase was washed with NaOH (5 mL 2 N) and with H₂O (5 mL), dried over Na₂SO₄, and evaporated. Chromatographic purification of the residue with A/P 0.5:9.5 provided compound **12** as a white crystalline solid. Melting point: 63–65 °C. Yield 57%. ¹H NMR (400 MHz, Chloroform-*d*) δ 7.59 (dd, *J* = 2.2, 0.5 Hz, 1H), 6.92 (s, 1H), 6.87 (dd, *J* = 2.1, 0.4 Hz,

1H), 3.97 (d, $J = 1.7$ Hz, 6H). ^{13}C NMR (101 MHz, Chloroform-*d*) δ 145.11, 144.54, 143.95, 142.09, 122.44, 110.55, 107.66, 104.60, 61.06, 56.57.

3.1.17. Synthesis of (1) from (12) via Mizoroki-Heck

A reaction flask containing DMF (1 mL) and DIPEA (1 mL) was charged with phenylpropenone **13** (0.165 g, 1.25 mmol, 1.25 equiv.), aryl bromide **12** (0.257 g, 1 mmol, 1 equiv.), $\text{P}(\text{o-tol})_3$ (0.121 g, 0.4 mmol), and $\text{Pd}(\text{OAc})_2$ (0.011 g, 0.05 mmol, 0.05 equiv.). The reaction mixture was stirred under an argon atmosphere at 110 °C for 5 h. Then, AcOEt (10 mL) and H_2O (10 mL) were added to the residue after solvent evaporation. The insoluble solid was filtered on celite, and the organic phase was washed with brine and dried over Na_2SO_4 . The solvent was evaporated, and Chromatographic purification of the residue with A/P 1:4 *v/v* provided compound **1** [10] as a yellow crystalline solid. Melting point: 98–103 °C. Yield 32%. ^1H NMR (400 MHz, Chloroform-*d*) δ 8.22 (d, $J = 15.8$ Hz, 1H), 8.05–8.01 (m, 2H), 7.62 (d, $J = 2.2$ Hz, 1H), 7.59–7.48 (m, 4H), 7.05 (s, 1H), 6.95 (dd, $J = 2.2, 0.6$ Hz, 1H), 4.05 (s, 3H), 4.04 (s, 3H). ^{13}C NMR (101 MHz, Chloroform-*d*) δ 191.00, 148.07, 144.97, 141.96, 140.32, 138.60, 132.53, 128.54, 128.50, 121.68, 121.47, 120.74, 105.34, 104.97, 61.51, 56.50. HPLC r.t. = 23,233 min. ESI = 309,2086 $[\text{M} + \text{H}]^+$. HRMS *m/z*: $[\text{M} + \text{H}]^+$ calc for $\text{C}_{19}\text{H}_{16}\text{O}_4$ 309.11214, found 309.1121; $[\text{M} + \text{Na}]^+$ calc 331.09408 found 331.0937. I.R. (neat) $\text{cm}^{-1} = 3126, 1654, 1598, 1586, 1572, 1480, 1440, 1354, 1287, 1231, 1202, 1185, 1159, 1072, 1013, 995, 935, 875, 853, 771, 738, 718, 704, 685, 662.$

3.1.18. Synthesis of (1) from (7) via Wittig

A microwave vial was charged with aldehyde **7** (0.065 g, 0.3 mmol, 1 equiv.), ylide **8** (0.125 g, 0.33 mmol, 1.1 equiv.), and acetonitrile (3 mL); microwave was set at 135 °C for 1.5 h. The solvent was evaporated and the residue chromatographed by eluting with A/P 1:4 *v/v*. Yield 70%.

3.1.19. (E)-3-(4,7-Dimethoxybenzofuran-2-yl)-1-phenylprop-2-en-1-one (22)

A microwave vial was charged with aldehyde (**20**, in mixture ratio 65:35 with **7**) (0.08 g, 0.38 mmol, 1 equiv.), ylide **8** (0.144 g, 0.38 mmol, 1 equiv.), and acetonitrile (3 mL); microwave was set at 135 °C for 1.5 h. The solvent was evaporated and the residue chromatographed by eluting with A/P 1:4 *v/v*. Yield 70%. Melting Point: 155–160 °C. ^1H NMR (400 MHz, Chloroform-*d*) δ 8.12–8.06 (m, 2H), 7.71 (d, $J = 4.9$ Hz, 2H), 7.59 (ddt, $J = 8.3, 6.6, 1.4$ Hz, 1H), 7.55–7.47 (m, 2H), 7.13 (s, 1H), 6.80 (d, $J = 8.6$ Hz, 1H), 6.54 (d, $J = 8.6$ Hz, 1H), 4.01 (s, 3H), 3.91 (s, 3H). ^{13}C NMR (101 MHz, Chloroform-*d*) δ 189.04, 151.81, 147.38, 145.17, 139.38, 137.41, 132.41, 130.13, 128.09, 128.05, 121.06, 120.40, 110.05, 108.56, 102.49, 56.09, 55.25. HPLC r.t. = 22,617 min. ESI = 3,092,086 $[\text{M} + 1]$. HRMS *m/z*: $[\text{M} + \text{H}]^+$ calc for $\text{C}_{19}\text{H}_{16}\text{O}_4$ 309.11214, found 309.1122; $[\text{M} + \text{Na}]^+$ calc 331.09408 found 331.094.

3.1.20. Synthesis of (22 and 1) from (20 and 7) via Wittig by Convectonal Heating

A round bottom flask vial was charged with aldehydes (**20**, in mixture ratio 65:35 with **7**) (0.08 g, 0.38 mmol, 1 equiv.), ylide **8** (0.144 g, 0.38 mmol, 1 equiv.), and toluene (3 mL); the mixture was refluxed overnight. After complete conversion of the starting material, the solvent was evaporated and the residue chromatographed by eluting with A/P 1:4 *v/v*. Yield 70%.

3.1.21. (E)-3-(4,7-Dimethoxybenzofuran-6-yl)-1-phenylprop-2-en-1-one (23)

A microwave vial was charged with aldehyde **21** (0.08 mg, 0.38 mmol, 1 equiv.), ylide **8** (144 mg, 0.38 mmol, 1 equiv.), and acetonitrile (3 mL); the microwave was set at 135 °C for 1.5 h. The solvent was evaporated and the residue chromatographed by eluting with A/P 1:4 *v/v*. Yield 70%. Melting Point 138–141 °C ^1H NMR (400 MHz, Chloroform-*d*) δ 8.23 (d, $J = 15.9$ Hz, 1H), 8.05–8.02 (m, 2H), 7.62 (d, $J = 2.1$ Hz, 1H), 7.61–7.49 (m, 4H), 6.89 (d, $J = 2.1$ Hz, 1H), 6.87 (s, 1H), 4.17 (s, 3H), 3.97 (s, 3H). ^{13}C NMR (101 MHz, Chloroform-*d*) δ 191.16, 148.59, 147.46, 145.45, 140.43, 138.72, 132.61, 128.64, 128.61, 122.92, 122.26, 122.11,

105.07, 101.56, 61.41, 55.92. HPLC r.t. = 24,183 min. ESI = 3,092,086 [M + 1]. HRMS m/z : [M + H]⁺ calc for C₁₉H₁₆O₄ 309.11214, found 309.1121; [M + Na]⁺ calc 331.09408 found 331.0937.

3.1.22. 2-(Dimethoxymethoxy)-1,4-dimethoxybenzene (18)

Bromoacetaldehyde dimethyl acetale (1.14 mL, 9.73 mmol, 1.5 equiv.) was added dropwise to a solution of **9** (1 g, 6.49 mmol, 1 equiv.), KOH (727 mg, 13 mmol, 2 equiv.) in DMAC (13 mL) at room temperature. The mixture was heated at 140 °C and stirred for 2 h until the starting material was no longer detected by TLC (A/P 1:4). It was allowed to cool down to room temperature and quenched with H₂O (20 mL). The crude was extracted with Et₂O (40 mL × 3), and combined organic phases were washed with an aqueous solution of 5% NaOH (30 mL) and H₂O (30 mL). After drying over anhydrous Na₂SO₄, the ether extraction phase was evaporated in vacuo. The residue was purified by silica gel column chromatography (elution system A/P 1:4 *v/v*) to obtain **18** as a white crystalline solid. Yield 70%. ¹H NMR (400 MHz, Chloroform-*d*) δ 6.80 (d, *J* = 8.8 Hz, 1H), 6.56 (d, *J* = 2.9 Hz, 1H), 6.44 (dd, *J* = 8.8, 2.8 Hz, 1H), 4.77 (t, *J* = 5.2 Hz, 1H), 4.03 (d, *J* = 5.2 Hz, 2H), 3.78 (d, *J* = 21.9 Hz, 6H), 3.46 (s, 6H). ¹³C NMR (101 MHz, Chloroform-*d*) δ 154.26, 149.08, 144.18, 113.21, 104.69, 102.73, 102.37, 69.16, 56.84, 55.73, 54.35.

3.1.23. 4,7-Dimethoxybenzofuran (19)

Compound **18** (1 g, 4.12 mmol, 1 equiv.) and Sn-β zeolite (4.12 g) (kindly prepared by the analytical chemistry division of the University of Ferrara, Prof. Pasti Luisa) were poured in chlorobenzene (42 mL). The heterogeneous mixture was stirred at 105 °C. After 5 h, it was allowed to cool down to room temperature, filtered through a Gooch filter, and evaporated under reduced pressure. The residue was purified by silica gel column chromatography (elution system A/P 1:9 *v/v*) to obtain a white crystalline solid. Yield 62%. ¹H NMR (400 MHz, Chloroform-*d*) δ 7.56 (d, *J* = 2.1 Hz, 1H), 6.86 (d, *J* = 2.1 Hz, 1H), 6.70 (d, *J* = 8.5 Hz, 1H), 6.54 (d, *J* = 8.5 Hz, 1H), 3.97 (s, 3H), 3.90 (s, 3H). ¹³C NMR (101 MHz, Chloroform-*d*) δ 147.60, 143.90, 140.38, 119.45, 106.43, 104.43, 102.72, 56.53, 55.80.

3.1.24. 1-(2,5-Dimethoxyphenoxy)propan-2-one (24)

Compound **9** (560 mg, 4.21 mmol, 1 equiv.) was dissolved in DMF (0.2 M), then Cs₂CO₃ (1.5 g, 4.631 mmol, 1.1 equiv.) and bromoacetone (0.63 gr, 4.63 mmol, 1.1 equiv.) were added. The mixture was stirred overnight at room temperature and quenched with brine and H₂O. The mixture was extracted with AcOEt, dried over Na₂SO₄, and the solvent was evaporated. The residue was purified by silica gel column chromatography (elution system A/P 1:4 *v/v*) to obtain **24** as a yellowish oil. Yield 63%. ¹H NMR (400 MHz, Chloroform-*d*) δ 6.83 (d, *J* = 8.8 Hz, 1H), 6.47 (dd, *J* = 8.8, 2.8 Hz, 1H), 6.39 (d, *J* = 2.8 Hz, 1H), 4.57 (s, 2H), 3.84 (s, 3H), 3.74 (s, 3H), 2.28 (s, 3H). ¹³C NMR (101 MHz, Chloroform-*d*) δ 206.07, 154.22, 148.22, 144.00, 113.22, 105.29, 102.74, 74.46, 56.73, 55.77, 26.56.

3.1.25. 4,7-Dimethoxy-3-methylbenzofuran (25)

A mixture of polyphosphoric acid (0.52 g) in chlorobenzene (15 mL) was heated at 120 °C, and a solution of **24** (370 mg, 1.55 mmol, 1 equiv.) in chlorobenzene (3 mL) was added. The mixture turned black, and after 20 min, it was allowed to cool at room temperature. The chlorobenzene phase was decanted, and the residue was rinsed three times with 20 mL of Et₂O. The ether was evaporated, and cyclized product **25** was purified on silica gel column chromatography by eluting with A/P 0.2:9.8, *v/v*, to obtain a yellowish solid. Yield 50%. ¹H NMR (400 MHz, Chloroform-*d*) δ 7.28 (d, *J* = 1.4 Hz, 1H), 6.66 (d, *J* = 8.5 Hz, 1H), 6.49 (d, *J* = 8.5 Hz, 1H), 3.95 (s, 3H), 3.86 (s, 3H), 2.35 (d, *J* = 1.3 Hz, 3H). ¹³C NMR (101 MHz, Chloroform-*d*) δ 149.34, 145.93, 140.50, 140.36, 120.11, 116.40, 106.33, 102.40, 56.58, 55.80, 29.78.

3.1.26. (4,7-Dimethoxybenzofuran-3-yl)methanol (**26**), 4,7-Dimethoxybenzofuran-3-carbaldehyde (**27**)

Compound **25** (109 mg, 0.57 mmol, 1 equiv.) and SeO₂ (125 mg, 1.134 mmol, 2 equiv.) in 1,4-dioxane were stirred at 75 °C for 96 h. The cooled mixture was filtered through Gooch, and the solvent evaporated under reduced pressure. Chromatographic purification of the residue using A/P 3:7 v/v as the eluent phase provided title compounds **26** and **27** in 1:1 ratio as brown and red solid, respectively. Yield 80%. ¹H NMR (400 MHz, Chloroform-*d*) δ 7.47 (d, *J* = 1.0 Hz, 1H), 6.71 (d, *J* = 8.6 Hz, 1H), 6.56 (d, *J* = 8.6 Hz, 1H), 4.73 (d, *J* = 0.9 Hz, 2H), 3.95 (s, 3H), 3.94 (s, 3H), 2.85 (s, 1H). ¹³C NMR (101 MHz, Chloroform-*d*) δ 147.06, 146.03, 140.71, 140.55, 120.85, 118.54, 106.82, 102.70, 56.55, 55.94.

3.1.27. 4,7-Dimethoxybenzofuran-3-carbaldehyde (**27**)

A solution of **26** (50 mg, 0.24 mmol, 1 equiv.) in anhydrous DCM (5 mL) was added to a suspension of PCC (129 mg, 0.6 mmol, 2.5 equiv.) in anhydrous DCM (5 mL). The red mixture turned dark brown and was stirred at room temperature overnight. The insoluble cake was rinsed three times with anhydrous Et₂O. The ether portions were combined, filtered through a pad of Florisil, and evaporated. Compound **27** was afforded by chromatographic purification using A/P 3:7 v/v as the eluent phase. Yield 95%. ¹H NMR (400 MHz, Chloroform-*d*) δ 10.41–10.41 (m, 1H), 8.21–8.18 (m, 1H), 6.77 (d, *J* = 8.6 Hz, 1H), 6.65 (d, *J* = 8.6 Hz, 1H), 3.96 (s, 3H), 3.92 (s, 3H). ¹³C NMR (101 MHz, Chloroform-*d*) δ 187.31, 148.52, 148.25, 145.99, 140.31, 123.46, 107.68, 104.36, 56.57, 55.82.

3.1.28. (E)-3-(4,7-Dimethoxybenzofuran-3-yl)-1-phenylprop-2-en-1-one (**28**)

A microwave vial was charged with aldehyde **27** (65 mg, 0.3 mmol, 1 equiv.), ylide **8** (125 mg, 0.33 mmol, 1.1 equiv.), and acetonitrile (3 mL); the microwave was set at 135 °C for 2 h. The solvent was evaporated, and the residue was purified on silica gel chromatography eluting with A/P 1:4 v/v to obtain the desired product **28** as a yellow-ocher solid. Yield 65%. ¹H NMR (400 MHz, Chloroform-*d*) δ 8.08–8.02 (m, 3H), 7.97–7.84 (m, 2H), 7.61–7.48 (m, 3H), 6.78 (d, *J* = 8.6 Hz, 1H), 6.65 (d, *J* = 8.7 Hz, 1H), 3.98 (s, 3H), 3.96 (s, 3H). ¹³C NMR (101 MHz, Chloroform-*d*) δ 190.58, 148.41, 146.56, 145.78, 140.38, 138.38, 134.75, 132.62, 128.56, 128.46, 124.00, 119.85, 116.75, 107.53, 104.04, 56.56, 55.96. HPLC r.t. = 23.017 min. ESI = 3,092,086 [M + 1]. HRMS *m/z*: [M + H]⁺ calc for C₁₉H₁₆O₄ 309.11214, found 309.1121; [M + Na]⁺ calc 331.09408 found 331.0937.

3.1.29. Cell Cultures and Stimulation

Bone marrow-derived macrophages (BMDMs) were isolated from C57BL/6 mice as described [52] and differentiated for 7 days in Iscove's Modified Dulbecco's Medium supplemented with 15% fetal bovine serum (FBS, Gibco), 1% penicillin/streptomycin (P/S) and 10 ng/mL M-CSF. THP-1 cells were grown in RPMI medium supplemented with 10% FBS, 100 U/mL penicillin, and 100 mg/mL streptomycin. THP-1 cells were stimulated by 100 ng/mL PMA overnight to differentiate into macrophages. All cells were grown in a 5% CO₂ incubator at 37 °C. BMDMs were seeded at 5 × 10⁵ in 24 well plates. After 12 h, the medium was removed, and cells were treated with LPS from *Escherichia coli* 055:B5 (1 µg/mL) in fresh Iscove's Modified Dulbecco's Medium for 2 h. After that, the medium was removed and replaced with a serum-free medium containing DMSO or compounds (10 µM) for 30 min. Cells were then stimulated with Nigericin (10 µM) for 1 h. Human THP-1 cells were seeded at 3 × 10⁵ cells per well in 24 well plates. The following day, the overnight medium was replaced, and cells were stimulated with LPS (1 µg/mL) for 3 h. The medium was removed and replaced with a serum-free medium containing DMSO or compounds (10 µM) for 30 min. Cells were then stimulated with Nigericin (10 µM) for 1 h.

3.1.30. In Vivo LPS Challenge

C57BL/6 mice were IP injected with compounds (25 mg/kg) or vehicle control (DMSO) 30 min before IP injection of LPS 1 mg/kg (4 h) and then were euthanized, and blood and

peritoneal exudate were isolated. Mouse plasma was collected after blood centrifugation ($1000 \times g$, 15 min at 4 °C). ELISA for IL-1 β was performed according to the manufacturer's instructions (R&D Systems).

3.1.31. ELISA

Supernatants from BMDMs and THP-1 cell culture were assayed for mouse or human IL-1 β , respectively, by ELISA according to the manufacturer's instructions (R&D Systems).

4. Conclusions

We succeeded in synthesizing the bioactive compound velutone F (**1**), the chalconoid contained in *Millettia velutina* stem, together with other 21 flavonoids. Our chemical total synthesis of velutone F is advantageous compare to the recently reported [24] seven steps semi-synthesis requiring the naturally occurring furanochromone derivative Khellin as the costly starting material (25 G > 800 USD). We could develop synthetic routes A and B; the first one establishes the benzofuran nucleus by creating the annellated carbocyclic ring onto a furan ring, while the second one proceeds exactly the other way. Instead, the Wittig olefination and the Heck coupling reaction are the featuring steps allowing for the assemblage of the 1,3-diaryl enone scaffold. Both the multi-step synthetic routes A and B establish the enone moiety at position C-5 of the 4,7-dimethoxybenzofuran thus, slightly modified synthetic approaches were designed in order to achieve the non-natural chalconoids **22**, **23**, and **28**, which formally are the C-2, C-3, and C-6 regioisomers of velutone F (**1**). The anti-inflammatory effects of the newly synthesized compounds are also reported.

Supplementary Materials: The following supporting information can be downloaded at: <https://www.mdpi.com/article/10.3390/ijms23168957/s1>.

Author Contributions: Conceptualization, C.T., V.Z. and C.G.; methodology, T.D.V., M.P. and S.M.; validation, P.P., C.G. and V.Z.; synthesis of chalconoids, T.D.V., D.I., P.M., G.T., V.C., G.S. and M.F.; writing—original draft preparation, V.Z., A.F., C.T., S.M. and C.G.; writing—review and editing, A.F., C.T. and T.D.V.; supervision, P.P., C.G. and C.T.; funding acquisition, C.T., P.P. and C.G. All authors have read and agreed to the published version of the manuscript.

Funding: The authors are greatly thankful to the University of Ferrara for the support. The Signal Transduction Laboratory is supported by the Italian Association for Cancer Research (IG-23670 to P.P., IG-19803 to C.G.), A-ROSE, Progetti di Rilevante Interesse Nazionale (PRIN2017E5L5P3 to P.P. and PRIN20177E9EPY to C.G.), the Italian Ministry of Health (GR-2019-12369646 to S.M.), the European Research Council (853057-InflaPML to C.G.) and local funds from the University of Ferrara to C.G., P.P., V.Z. and C.T. M.P. is supported by AIRC research fellowship (ID: 26665). P.P. is grateful to C. Degli Scrovegni for her continuous support.

Institutional Review Board Statement: Procedures involving animals and their care were in conformity with institutional guidelines, and Animal Ethics Committee approved all experimental protocols (Authorization N° 481/2017-PR and CBCC2.N.BH4 approved by Italian Ministry of Health).

Acknowledgments: The authors thank Giorgia Macedonio for NMR analysis and Erika Marzola for HPLC analysis.

Conflicts of Interest: The authors declare no conflict of interest.

References

1. Tehfe, M.-A.; Dumur, F.; Xiao, P.; Delgove, M.; Graff, B.; Fouassier, J.-P.; Gignes, D.; Lalevée, J. Chalcone Derivatives as Highly Versatile Photoinitiators for Radical, Cationic, Thiol-ene and IPN Polymerization Reactions Upon Visible Lights. *Polym. Chem.* **2014**, *5*, 382–390. [[CrossRef](#)]
2. Lee, S.-C.; Kang, N.-Y.; Park, S.-J.; Yun, S.-W.; Chandran, Y.; Chang, Y.-T. Development of a fluorescent chalcone library and its application in the discovery of a mouse embryonic stem cell probe. *Chem. Commun.* **2012**, *48*, 6681–6683. [[CrossRef](#)]
3. Nowakowska, Z. A review of anti-infective and anti-inflammatory chalcones. *Eur. J. Med. Chem.* **2007**, *42*, 125–137. [[CrossRef](#)] [[PubMed](#)]

4. Zhou, B.; Xing, C. Diverse Molecular Targets for Chalcones with Varied Bioactivities. *Med. Chem.* **2015**, *5*, 388–404. [[CrossRef](#)] [[PubMed](#)]
5. Zhuang, C.; Zhang, W.; Sheng, C.; Zhang, W.; Xing, C.; Miao, Z. Chalcone: A Privileged Structure in Medicinal Chemistry. *Chem. Rev.* **2017**, *117*, 7762–7810. [[CrossRef](#)]
6. Funakoshi-Tago, M.; Tanabe, S.; Tago, K.; Itoh, H.; Mashino, T.; Sonoda, Y.; Kasahara, T. Licochalcone A Potently Inhibits Tumor Necrosis Factor α -Induced Nuclear Factor- κ B Activation through the Direct Inhibition of I κ B Kinase Complex Activation. *Mol. Pharmacol.* **2009**, *76*, 745–753. [[CrossRef](#)]
7. Pandey, M.K.; Sandur, S.K.; Sung, B.; Sethi, G.; Kunnumakkara, A.B.; Aggarwal, B.B. Butein, a Tetrahydrochalcone, Inhibits Nuclear Factor (NF)- κ B and NF- κ B-regulated Gene Expression through Direct Inhibition of I κ B α Kinase β on Cysteine 179 Residue. *J. Biol. Chem.* **2007**, *282*, 17340–17350. [[CrossRef](#)]
8. Wang, J.P.; Tsao, L.T.; Raung, S.L.; Lin, C.N. Investigation of the inhibitory effect of broussouchalcone A on respiratory burst in neutrophils. *Eur. J. Pharmacol.* **1997**, *320*, 201–208. [[CrossRef](#)]
9. Maccari, R.; Ottana, R. Targeting Aldose Reductase for the Treatment of Diabetes Complications and Inflammatory Diseases: New Insights and Future Directions. *J. Med. Chem.* **2015**, *58*, 2047–2067. [[CrossRef](#)]
10. Aida, K.; Tawata, M.; Shindo, H.; Onaya, T.; Sasaki, H.; Yamaguchi, T.; Chin, M.; Mitsuhashi, H. Isoliquiritigenin: A New Aldose Reductase Inhibitor from Glycyrrhizae Radix. *Planta Med.* **1990**, *56*, 254–258. [[CrossRef](#)]
11. Song, N.R.; Kim, J.E.; Park, J.S.; Kim, J.R.; Kang, H.; Lee, E.; Kang, Y.G.; Son, J.E.; Seo, S.G.; Heo, Y.S.; et al. Licochalcone A, a Polyphenol Present in Licorice, Suppresses UV-Induced COX-2 Expression by Targeting PI3K, MEK1, and B-Raf. *Int. J. Mol. Sci.* **2015**, *16*, 4453–4470. [[CrossRef](#)] [[PubMed](#)]
12. Nyandoro, S.S.; Nkunya, M.H.H.; Josepha, C.C.; Odalo, J.O.; Sattler, I. New Glucopyranosylglyceryl-N-Octenyl Adipate and Bioactivity of Retro and Condensed Chalcones from *Toussaintia orientalis*. *Tanz. J. Sci.* **2012**, *38*, 108–126, eISSN: 2507–7961. Print ISSN 0856-1761.
13. Lee, M.H.; Kim, J.Y.; Ryu, J.-H. Prenylflavones from *Psoralea corylifolia* Inhibit Nitric Oxide Synthase Expression through the Inhibition of I- κ B- α Degradation in Activated Microglial Cells. *Biol. Pharm. Bull.* **2005**, *28*, 2253–2257. [[CrossRef](#)]
14. Daikonya, A.; Katsuki, S.; Kitanaka, S. Antiallergic Agents from Natural Sources 9. Inhibition of Nitric Oxide Production by Novel Chalcone Derivatives from *Mallotus philippinensis* (Euphorbiaceae). *Chem. Pharm. Bull.* **2004**, *52*, 1326–1329. [[CrossRef](#)]
15. Chen, H.; Chen, X.; Sun, P.; Wu, D.; Yue, H.; Pan, J.; Li, X.; Zhang, C.; Wu, X.; Hua, L.; et al. Discovery of dronedarone and its analogues as NLRP3 inflammasome inhibitors with potent anti-inflammation activity. *Bioorg. Med. Chem. Lett.* **2021**, *46*, 128160. [[CrossRef](#)]
16. Zhang, C.; Yue, H.; Sun, P.; Hua, L.; Liang, S.; Ou, Y.; Wu, D.; Wu, X.; Chen, H.; Hao, Y.; et al. Discovery of chalcone analogues as novel NLRP3 inflammasome inhibitors with potent anti-inflammation activities. *Eur. J. Med. Chem.* **2021**, *219*, 113417. [[CrossRef](#)] [[PubMed](#)]
17. Choi, H.R.; Lim, H.; Lee, J.H.; Park, H.; Kim, H.P. Interruption of *Helicobacter pylori*-Induced NLRP3 Inflammasome Activation by Chalcone Derivatives. *Biomol. Ther.* **2021**, *29*, 410–418. [[CrossRef](#)]
18. Swanson, K.V.; Deng, M.; Ting, J.P.Y. The NLRP3 inflammasome: Molecular activation and regulation to therapeutics. *Nat. Rev. Immunol.* **2019**, *19*, 477–489. [[CrossRef](#)] [[PubMed](#)]
19. Wang, Z.; Xu, G.; Gao, Y.; Zhan, X.; Qin, N.; Fu, S.; Li, R.; Niu, M.; Wang, J.; Liu, Y.; et al. Cardamonin from a medicinal herb protects against LPS-induced septic shock by suppressing NLRP3 inflammasome. *Acta Pharm. Sin. B* **2019**, *9*, 734–744. [[CrossRef](#)]
20. Aybe, S.I.; Furuya, T. Studies on Plant Tissue Cultures. Part 36. Biosynthesis of a Retrochalcone, Echinatin, and Other Flavonoids in the Cultured Cells of *Glycyrrhiza echinata*. A New Route to a Chalcone with Transposed A- and B-Rings. *J. Chem. Soc. Perkin Trans.* **1982**, *1*, 2725–2734. [[CrossRef](#)]
21. Aybe, S.I.; Furuya, T. Biosynthesis of a Retrochalcone, Echinatin: A Feeding Study with Advanced Precursors. *Tetrahedron Lett.* **1981**, *22*, 2097–2098. [[CrossRef](#)]
22. Ayabe, S.I.; Yoshikawa, T.; Kobayashi, M.; Furuya, T. Biosynthesis of a Retrochalcone, Echinatin: Involvement of O-Methyl Transferase to Licodione. *Phytochemistry* **1980**, *19*, 2331–2336. [[CrossRef](#)]
23. Ma, X.; Zhao, M.; Tang, M.-H.; Xue, L.-L.; Zhang, R.-J.; Liu, L.; Ni, H.-F.; Cai, X.-Y.; Kuang, S.; Hong, F.; et al. Flavonoids with Inhibitory Effects on NLRP3 Inflammasome Activation from *Millettia velutina*. *J. Nat. Prod.* **2020**, *83*, 2950–2959. [[CrossRef](#)] [[PubMed](#)]
24. Zhang, R.; Hong, F.; Zhao, M.; Cai, X.; Jiang, X.; Ye, N.; Su, K.; Li, N.; Tang, M.; Ma, X.; et al. New Highly Potent NLRP3 Inhibitors: Furanochalcone Velutone F Analogues. *ACS Med. Chem. Lett.* **2022**, *13*, 560–569. [[CrossRef](#)]
25. Mishra, S.; Singh, P. Hybrid molecules: The privileged scaffolds for various pharmaceuticals. *Eur. J. Med. Chem.* **2016**, *124*, 500–536. [[CrossRef](#)]
26. Miao, Y.H.; Hu, Y.H.; Yang, J.; Liu, T.; Sun, J.; Wang, X.J. Natural source, bioactivity and synthesis of benzofuran derivatives. *RSC Adv.* **2019**, *9*, 27510–27540. [[CrossRef](#)]
27. Chand, K.; Hiremathad, A.; Singh, M.; Santos, M.A.; Keri, R.S. A review on antioxidant potential of bioactive heterocycle benzofuran: Natural and synthetic derivatives. *Pharm. Rep.* **2017**, *69*, 281–295. [[CrossRef](#)]
28. Radadiya, A.; Shah, A. Bioactive benzofuran derivatives: An insight on lead developments, radioligands and advances of the last decade. *Eur. J. Med. Chem.* **2015**, *97*, 356–376. [[CrossRef](#)]
29. Khanam, H. Bioactive Benzofuran derivatives: A review. *Eur. J. Med. Chem.* **2015**, *97*, 483–504. [[CrossRef](#)]

30. Schwaid, A.G.; Spencer, K.B. Strategies for Targeting the NLRP3 Inflammasome in the Clinical and Preclinical Space. *J. Med. Chem.* **2021**, *64*, 101–122. [[CrossRef](#)]
31. Zhang, X.; Xu, A.; Lv, J.; Zhang, Q.; Ran, Y.; Wei, C.; Wu, J. Development of small molecule inhibitors targeting NLRP3 inflammasome pathway for inflammatory diseases. *Eur. J. Med. Chem.* **2020**, *185*, 1118222. [[CrossRef](#)]
32. Coll, R.C.; Hill, J.R.; Day, C.J.; Zamoshnikova, A.; Boucher, D.; Massey, N.L.; Chitty, J.L.; Fraser, J.A.; Jennings, M.P.; Robertson, A.A.; et al. MCC950 directly targets the NLRP3 ATP-hydrolysis motif for inflammasome inhibition. *Nat. Chem. Biol.* **2019**, *15*, 556–559. [[CrossRef](#)]
33. Tapia-Abellán, A.; Angosto-Bazarra, D.; Martínez-Banaolocha, H.; de Torre-Minguela, C.; Cerón-Carrasco, J.P.; Pérez-Sánchez, H.; Arostegui, J.I.; Pelegrin, P. MCC950 closes the active conformation of NLRP3 to an inactive state. *Nat. Chem. Biol.* **2019**, *15*, 560–564. [[CrossRef](#)]
34. Goyal, K.; Kaur, R.; Goyal, A.; Awasthi, R. Chalcones: A review on synthesis and pharmacological activities. *J. Appl. Pharm. Sci.* **2021**, *11* (Suppl. S1), 1–14. [[CrossRef](#)]
35. Chen, Z.; Hu, F.; Huang, S.; Zhao, Z.; Mao, H.; Qin, W. Organocatalytic Enantioselective Selenosulfonylation of a C–C Double Bond to Form Two Stereogenic Centers in an Aqueous Medium. *J. Org. Chem.* **2019**, *84*, 8100–8111. [[CrossRef](#)]
36. Gammill, R.B. Synthetic Routes to Benzofurans and Benzothiophenes and Intermediates Therefor. U.S. Patent 4,609,739, 2 September 1986.
37. Gammill, R.B. Preparing 4,7-Dialkoxybenzofurans, and Intermediates Used Therein. European Patent 95,835, 7 December 1983.
38. Guzman, J.A.; Mendoza, V.; Garcia, E.; Garibay, C.F.; Olivares, L.Z.; Maldonado, L.A. Baeyer-Villiger Oxidation of β -Aryl Substituted Unsaturated Carbonyl Compounds with Hydrogen Peroxide and Catalytic Selenium Dioxide. *Synth. Commun.* **1995**, *25*, 2121–2133. [[CrossRef](#)]
39. Pang, Y.; An, B.; Lou, L.; Zhang, J.; Yan, J.; Huang, L.; Li, X.; Yin, S. Design, Synthesis, and Biological Evaluation of Novel Selenium-Containing Isocombretastatins and Phenstatins as Antitumor Agents. *J. Med. Chem.* **2017**, *60*, 7300–7314. [[CrossRef](#)]
40. Ma, W.; Huang, J.; Huang, X.; Meng, S.; Yang, Z.; Li, C.; Wang, Y.; Qi, T.; Li, B. Direct construction of 2,3-unsubstituted benzofurans and benzothiophenes via a metal-free catalyzed intramolecular Friedel-Crafts reaction. *Org. Chem. Front.* **2019**, *6*, 493–497. [[CrossRef](#)]
41. Liu, H.; Ge, L.; Wang, D.; Chen, N.; Feng, C. Photoredox-Coupled F-Nucleophilic Addition: Allylation of *gem*-Difluoroalkenes. *Angew. Chem. Int. Ed.* **2019**, *58*, 3918–3922. [[CrossRef](#)]
42. Song, S.-Y.; Lu, H.-L.; Wang, G.-F.; Yang, Y.-Q.; Huang, Y.-S. An improved and scale-up synthesis of 6-hydroxybenzofuran. *Res. Chem. Intermed.* **2016**, *42*, 4433–4442. [[CrossRef](#)]
43. Bunce, R.A.; Moore, J.D. Tetrahydropyranloxy-Directed *ortho* Lithiation of Aromatic Systems. Synthesis of *o*-Hydroxycinnamate Esters from Phenols. *Org. Prep. Proc. Int.* **1997**, *29*, 293–299. [[CrossRef](#)]
44. Wriede, U.; Fernandez, M.; West, K.F.; Harcour, D.; Moore, H.W. Synthesis of Halodimethoxy-1,2-benzoquinones. *J. Org. Chem.* **1987**, *52*, 4485–4489. [[CrossRef](#)]
45. Ma, T.; Fu, X.; Kee, C.W.; Zong, L.; Pan, Y.; Huang, K.-W.; Tan, C.-H. Pentanidium-Catalyzed Enantioselective Phase-Transfer Conjugate Addition Reactions. *J. Am. Chem. Soc.* **2011**, *133*, 2828–2831. [[CrossRef](#)]
46. Mikami, S.; Kitamura, S.; Negoro, N.; Sasaki, S.; Suzuki, M.; Tsujihata, Y.; Miyazaki, T.; Ito, R.; Suzuki, N.; Miyazaki, J.; et al. Discovery of Phenylpropanoic Acid Derivatives Containing Polar Functionalities as Potent and Orally Bioavailable G Protein-Coupled Receptor 40 Agonists for the Treatment of Type 2 Diabetes. *J. Med. Chem.* **2012**, *55*, 3756–3776. [[CrossRef](#)]
47. Sayson, L.V.; Custodio, R.J.P.; Ortiz, D.M.; Lee, H.J.; Kim, M.; Jeong, Y.; Lee, Y.S.; Kim, H.J.; Cheong, J.H. The potential rewarding and reinforcing effects of the substituted benzofurans 2-EAPB and 5-EAPB in rodents. *Eur. J. Pharmacol.* **2020**, *885*, 173527. [[CrossRef](#)]
48. Sun, N.; Huang, P.; Wang, Y.; Mo, W.; Hu, B.; Shen, Z.; Hu, X. Zeolite-catalyzed synthesis of 2,3-unsubstituted benzo[b]furans via the intramolecular cyclization of 2-aryloxyacetaldehyde acetals. *Tetrahedron* **2015**, *71*, 4835–4841. [[CrossRef](#)]
49. Zaidlewicz, M.; Chechlowska, A.; Prewysz-Kwinto, A. Enantioselective Synthesis of 2- and 3-benzofuryl β -amino alcohols. *Heterocycles* **2001**, *55*, 569–577. [[CrossRef](#)]
50. Ando, K.; Kawamura, Y.; Akai, Y.; Kunitomo, J.I.; Yokomizo, T.; Yamashita, M.; Ohta, S.; Ohishi, T.; Ohishi, Y. Preparation of 2-, 3-, 4- and 7-(2-alkylcarbamoyl-1-alkylvinyl)benzo[b]furans and their BLT1 and/or BLT2 inhibitory activities. *Org. Biomol. Chem.* **2008**, *6*, 296–307. [[CrossRef](#)]
51. Missiroli, S.; Perrone, M.; Boncompagni, C.; Borghi, C.; Campagnaro, A.; Marchetti, F.; Anania, G.; Greco, P.; Fiorica, F.; Pinton, P.; et al. Targeting the NLRP3 inflammasome as a new therapeutic option for overcoming cancer. *Cancers* **2021**, *13*, 2297. [[CrossRef](#)]
52. Ying, W.; Cheruku, P.S.; Bazer, F.W.; Safe, S.H.; Zhou, B. Investigation of macrophage polarization using bone marrow derived macrophages. *J. Vis. Exp.* **2013**, *76*, 50323. [[CrossRef](#)]